

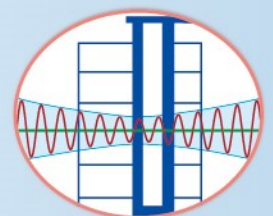
2020

NCREE Research

Programs and Accomplishments



National Center for Research on Earthquake Engineering
National Applied Research Laboratories



Contents

- 1 **Dominated Waves of Vertical Ground Motion in Taiwan**
Shu-Hsien Chao, Che-Min Lin, Chun-Hsiang Kuo, and Jyun-Yan Huang
- 5 **The Time-dependent Seismic Microzonation Map of Near Fault Area in Taiwan**
Yu-Wen Chang, Chih-Wei Chang, Hsun-Jen Liu and Wen-Yu Chien
- 9 **Source Radiation Pattern Database Calculated from 1-D Velocity Structure in Taiwan**
Jyun-Yan Huang, Che-Min Lin and Shu-Hsien Chao
- 12 **Established Vs30 Grid Data for Taiwan Area By Weighted Kriging**
Chia Li Chen, Chun Hsiang Kuo and Xue Min Lu
- 16 **Stiffness Configuration of Strongbacks to Reduce Inter-story Drift Concentraion**
Jui-Liang Lin, Meng-Kwee Kek, and Keh-Chyuan Tsai
- 20 **Nonlinear Dynamic Analysis Research Based on TEASPA Fiber Section Model**
Yeong-Kae Yeh and Te-Kuang Chow
- 24 **Pushover Analysis of the E-defense 10-Story RC Building Test by TEASPA 4.0**
Yu-Chih Lai, Tsung-Chih Chiou, Lap-Loi Chung, Ming-Chieh Chuang, Juin-Fu Chai, Shyh-Jiann Hwang, Jae-Do Kang, and Koichi Kajiwara
- 28 **Study on Seismic Retrofitting of Structures using High-Strength Fiber Resin Mortar**
Fu-Pei Hsiao, Chia-Yi Ho, Pu-Wen Weng, Chia-Chen Lin, and Chih-Ming Kuo
- 32 **Reduced Scale Shaking Table Test and Numerical Study on a Simply Supported Bridge Crossing Fault**
Hsiao-Hui Hung, Yuan-Shuo Tseng, and Chang-Wei Huang

- 36 **Development of Advanced Bridge Information System's High-Performance Web Server**
Kuang-Wu Chou and Chia-Chuan Hsu
- 40 **Development of Advanced Bridge Information System: Database Design**
Chia-Chuan Hsu and Kuang-Wu Chou
- 43 **Study on Smart Nanofluid Viscous Damper (II)**
Fang-Yao Yeh, Chung-Han Yu, Shen-Kai Peng and Kuo-Chun Chang
- 47 **Displacement-Dependent Tuned Mass Damper Feasibility Study**
Bo-Han Lee, Chun-Chung Chen, Sheng-Yuan Shiao, Chi-Rung Jiang and Fang-Yao Yeh
- 51 **Experimental Study on the Evaluation Method for Bridge Structures by Using Load Tests**
Chun-Chung Chen, Chi-Rung Jiang, Sheng-Yuan Siao, and Bo-Han Lee
- 55 **Application And Design of Automatic Water Supplement for Bridge Fiber Optic Settlement Sensor**
Zheng-Kuan Lee
- 59 **Study on Lightweight Truss-type Composite Temporary Bridge for Disaster Relief**
Fang-Yao Yeh, Bo-Han Lee, Kuo-Chun Chang, Sheng-Yuan Shiao, Chi-Lon Jang and Chun-Lung Chen
- 63 **A Study of Rotational Loads on the Supporting Structure of an Onshore Wind Turbine by Time-Frequency Analysis**
Kung-Chun Lu, Wei-Chen Tseng, Yu-Shu Kuo, Peng Heng-Chu, and Yi-Cheng Chen
- 67 **Experimental study of Suspended Fire Sprinkler Systems**
Wei-Chung Chen, Chen-Pei Hsu, George C. Yao, Juin-Fu Chai, Fan-Ru Lin, Wei-Hung Hsu, and Bai-Yi Huang

- 71 **Effects of Non-linear behavior of Building Structure on Critical Equipment**
Min-Chi Ko, Fan-Ru Lin, Bai-Yi Huang, Wei-Chung Chen, Juin-Fu Chai, and George C. Yao
- 75 **Modification of Sloped Rolling-type Isolation Bearing with Stepwise Variable Designs**
Chung-Han Yu, Shiang-Jung Wang, Wang-Chuen Lin, and Cho-Yen Yang
- 79 **Preliminary Design Procedure for Structural Retrofitting with an Isolation System including a Friction Pendulum Bearing**
Cho-Yen Yang, Peng-Yu Lin, Lap-Loi Chung, Wang-Chuen Lin, Chung-Han Yu, and Shiang-Jung Wang
- 83 **Seismic Performance Evaluation of Existing High-Rise Steel Structures**
Sheng-Jhih Jhuang, Ker-Chung Lin, Kai-Ning Chi, Sish-Siou Gao, and Yung-Chih Wang
- 87 **Experimental Study on Buckling-Restrained Brace Stability**
An-Chin Wu and Keh-Chyuan Tsai
- 91 **Seismic Performance of Steel Panel Dampers**
An-Chin Wu, Ming-Chieh Chuang, and Keh-Chyuan Tsai
- 95 **Influence of steel Grade on Development Length in Tension for High-Strength Reinforced Concrete**
Ker-Chun Lin , Yuan-Yan Lin , Kai-Ning Chi , Sheng-Jhih Jhuang, and Yung-Chih Wang
- 99 **Performance Evaluation of an Entropy-based Structural Health Monitoring by Utilizing Composite Cross-sample Entropy**
Tzu-Kang Lin, Yi-Hsiu Chien and Pei-Yang Lin
- 103 **Post-earthquake Building Safety Assessment Using Crowdsourcing-based Interstory Drifts Measurement**
Ting Y. Hsu, Cheng Y. Liu , Yo M. Hsieh , and Chi T. Weng, Pei Y. Lin

- 107 **Modal Property Extraction Based on Frequency-Domain Stochastic Subspace Identification Using Out-of-Plane Video Motion**
Chia-Ming Chang, Jau-Yu Chou, and Meng-Huang Gu
- 111 **Machine-Learning Based Optimal Active Seismic Control for Earthquake-Excited Building Structures**
Pei-Ching Chen and Kai-Yi Chien
- 115 **Sensor Fusion for Trajectory Reconstruction from Inertial Measurement Unit to Estimate Structural Residual Displacements**
Yi-Jie Chuang, Shieh-Kung Huang, and Chia-Ming Chang
- 118 **Analysis on Experimental Database of the Deformation Capacity of Reinforced Concrete Rectangular Column Members**
Kai-Ning Chi, Ker-Chun Lin, Sheng-Jhih Jhuang and Jun-Wei Wu
- 122 **Centrifuge Modeling of the Dynamic Behavior of Low-rise Buildings on Sandy Ground with Different Water Table Depths**
Hu-Lin Mao, Chih-Chieh Lu, and Kuan-Yu Chen
- 126 **The Soil Liquefaction Potential Map of Taipei Basin Based on a Refined Borehole Database**
Chih-Chieh Lu, Yuan-Chang Deng, and Jin-Hung Hwang
- 130 **Research of the Seismogenic and Velocity Structures in Kaohsiung and Pingtung Areas**
Yu-Chih Huang, Yi-Zen Chang, Strong Wen, Che-Min Lin, Hung-Hao Hsieh, and Chih-Wei Chang
- 134 **Statistical Analysis of Radon Time Series Data from San-Jie Monitoring Station in Northern Taiwan**
Vivek Walia, Arvind Kumar, Shih-Jung Lin and Hsiao-Fen Lee

- 138 **Draft Revision of Guidelines for Seismic Installation of Suspended Ceiling Systems**
Wei-Chung Chen, Juin-Fu Chai, Fan-Ru Lin, George C. Yao, Bai-Yi Huang, and Wei-Hung Hsu
- 142 **Effects of Near-Fault Ground Motions on Seismic Isolated buildings and Corresponding Design Strategies**
Wang-Chuen Lin , Jenn-Shin Hwang , Cho-Yen Yang , Chung-Han Yu and Shiang-Jung Wang
- 146 **Shaking Table Test of Unidirectional Shear Box**
Hsuan-Chih Yang, Kuan-Yu Chen, Wei-Kuang Chang, Shang-Yi Hsu, and Che-Yu Chang
- 150 **Database of Near-Fault Highway Bridge Damage in Recent Taiwan Earthquakes and Preliminary Fragility Investigation**
Gee-Yu Liu, Pao-Ching Chou, and Lee-Hui Huang
- 154 **The Development of the 5D Smart City Platform**
Ren-Zuo Wang and Chih-Shian Chen
- 158 **Preliminary Study on Acceleration Control of Seismic Simulators using Deep Learning**
Po-Hui Hsieh, Pei-Ching Chen and Chuin-Shan Chen
- 161 **Benchmark of GPGPU for Artificial Intelligence**
Wei-Tze Chang
- 165 **Nonlinear Response History Analyses of NCREE Research Building Extension**
Ming-Chieh Chuang, Keh-Chyuan Tsai, Guan-Hong Lin, and Jui-Liang Lin
- 169 **A Case Study of Rescue Route Planning**
Yang-Tao Yang, Chi-Hao Lin, Zheng-Xuan Li, Ya-Chu Tsao, and I-Tien Lo
- 172 **The Post-earthquake Crowdedness of a First-aid Hospital by Non-urgent Patients**
You-Xuan Lin and Chi-Hao Lin

- 176 **Site-Effect Model for Wide-area Seismic Damage Assessment**
Chin-Hsun Yeh, Lee-Hui Huang and Yin-Nan Huang
- 180 **Assessment of Redundancy Factors for the Seismic Design for Building Structures**
Yuan-Tao Weng, Lap-Loi Chung, Eliot Chen, Li-Tzung Huang, Xi-Qing Guo, and Tsung-Jen Teng
- 184 **Influence of Prestressing on the Fundamental Frequency of Uncracked Concrete Beams**
Marco Bonopera
- 188 **Bridge Displacement Monitoring using a Fiber Bragg Grating–Differential Settlement Measurement Sensor System**
Marco Bonopera and Zheng-Kuan Lee
- 192 **Mapping a 3D Geometric Model of the Décollement in the Western Foothills of Central Taiwan**
Chiu-Ping Fan, Kuan-Yu Chen, Yu-Wen Chang, Chih-Wei Chang, and Hsun-Jen Liu
- 196 **Taiwan Seismic Microzonation Map of the Design Basis Earthquake: Construction of A Geometric Model of the Chukou and Lunghou Faults**
Kuanyu Chen, Chiuping Fan, Yuwen Chang, Chihwei Chang, and Hsunjen Liu
- 200 **Discussion on the seismic and geochemical monitoring data of Tatun Volcano Group in 2020**
Ya-chuan Lai, Hsiao-fen Lee, Min-Hung Shih, Li-Chin Chang, Chin-hsing Liu and Chia-Jui Teng, and Teng-Yang Shao
- 204 **Taiwan Recorded Ground-Motion Database for Structural Response-History Analysis**
Hsun-Jen Liu, Wen-Yu Jean, and Yu-Wen Chang
- 208 **Evaluation of DIP with CLSM Backfill under Truck Loading for the Water Pipeline System**
Hsuan-Chih Yang, Che-Yu Chang, Gee-Yu Liu, and Pao-Ching Chou

Dominant Waves in Vertical Ground Motion in Taiwan

Shu-Hsien Chao¹, Che-Min Lin², Chun-Hsiang Kuo³, Jyun-Yan Huang⁴

趙書賢¹ 林哲民² 郭俊翔³ 黃雋彥⁴

Abstract

This study aims to compile information about the arrival times of P-waves and S-waves, peak occurrence times of ground motion, and structural responses for the ground motion records observed in Taiwan. From these, we evaluate the percentages of the vertical peak ground motions and structural vertical peak responses that occur in P-wave and S-wave windows. We observe that most vertical ground motions and structural vertical peak responses occur in S-wave windows, especially the vertical peak responses of long-period structures. Given the nonlinear hysteretic behavior of soil under large shear strain induced by S-waves, this observation provides a physical basis for the observed nonlinear site effect of vertical ground motion in Taiwan.

Keywords: vertical ground motion, nonlinear site effect, P-wave and S-wave arrival times.

Introduction

Vertical ground motion significantly affects the seismic behavior of structures such as isolated buildings and bridges, pipes, and equipment. Several studies have focused on the evaluation of vertical ground-motion characteristics and developed vertical ground-motion prediction equations (GMPE). Five research teams that worked in the Enhancement of Next Generation Attenuation Relationships for Western US (NGA-West2) project held by the Pacific Earthquake Engineering Research (PEER) Center have proposed five horizontal GMPEs and four vertical GMPEs (Bozorgnia and Campbell, 2016; Gülerce *et al.*, 2017; Stewart *et al.*, 2016; PEER, 2014). Unlike these proposed horizontal GMPEs, the vertical GMPEs derived from the observation and regression analysis of the vertical ground-motion records either do not consider or consider an insignificant nonlinear site effect term. This could be attributed to that the vertical ground motion in NGA-West2 database is dominated by the pressure wave (P-wave), implying that the observed peak ground motion and peak structural response occur in the P-wave window before the arrival of the shear wave (S-wave). In general, the behavior of the soil layer under constrained pressure strain is almost linear with no hysteresis. As a result, the nonlinear site effect will not be observed in vertical

ground motion.

Chao *et al.* (2019, 2020) proposed horizontal and vertical GMPEs that are applicable for crustal and subduction earthquakes in Taiwan; we call these the NCREE19 horizontal and vertical GMPEs in this study. In contrast to the observations from the four vertical GMPEs in the NGA-West 2 project, Chao *et al.* proposed that the nonlinear site effect can be observed from the vertical ground motion in Taiwan, with its level similar to that of the nonlinear site effect observed from the horizontal ground motion. The nonlinear site effects of horizontal and vertical components are highly correlated. This means that we can observe the nonlinear site effect in the horizontal component as well as the vertical component of the same ground motion record. Hence, the observations from the NCREE19 vertical GMPE and the four vertical GMPEs in the NGA-West 2 project are not consistent. It is necessary to evaluate the possible cause of nonlinear site effects observed in vertical ground motion in Taiwan because the vertical ground motion in Taiwan may be dominated by the S-wave, implying that the observed peak ground motion and structural response occur in the S-wave window after the arrival of the S-wave. Moreover, the behavior of the soil layer under shear strain is nonlinear with a significant hysteresis. Under this premise, the nonlinear site effect can also be observed in the

¹ Associate Research Fellow, National Center for Research on Earthquake Engineering

² Research Fellow, National Center for Research on Earthquake Engineering

³ Assistant Professor, National Central University

⁴ Assistant Research Fellow, National Center for Research on Earthquake Engineering

vertical component of ground motion in Taiwan.

In this study, we aim to compile information about the arrival times of P-waves and S-waves, peak occurrence times of ground motion, and structural responses for the ground motion records observed in Taiwan, and we evaluate the percentages of the vertical peak ground motions and structural vertical peak responses that occur in P-wave and S-wave windows. We observe that most vertical peak ground motions and structural vertical peak responses occur in S-wave windows, especially those of long-period structures. Given the nonlinear hysteretic behavior of soil under large shear strain, likely induced by S-waves, this observation provides a physical basis for the observed nonlinear site effect of vertical ground motion in Taiwan from the NCREE19 vertical GMPE.

Definition of Dominating Waves

Seismic waves can be classified as either body waves, which travel inside the earth, or surface waves, which travel along the surface of the earth. Body waves include primary or pressure waves (P-waves) and shear waves (S-waves). The velocity of P-waves is higher than that of S-waves. As a result, the S-wave arrives at a target site later than the P-wave. In general, the amplitude of horizontal ground motion induced by the S-wave is higher than that of vertical ground motion. By contrast, the amplitude of vertical ground motion induced by the P-wave is generally higher than that of horizontal ground motion, but their difference is not significant. In this study, we will denote the ground motion record as P-dominated when the peak occurs in the P-wave window before the arrival of the S-wave and as S-dominated when the peak occurs in the S-wave window after the arrival of the S-wave. It should be noted that the peak of S-dominated records may be induced by not only S-waves but also surface waves.

Nonlinear Site Amplification

The levels of site amplification for soil sites will decrease for large input ground motions. This phenomenon is due to the hysteresis of the soil layer under large shear strain induced by the S-wave with large input ground motion. Generally, because the horizontal ground motion is S-dominated, the nonlinear site amplification has been observed in several horizontal ground motion datasets and has been considered in several published horizontal GMPEs.

From the analysis of the NCREE19 horizontal GMPE, the nonlinear site amplification of the horizontal component can also be observed from the ground motion records in Taiwan. Figure 1(a) shows the site amplification of horizontal peak ground acceleration (PGA) with respect to (w.r.t.) the

reference site condition of $V_s = 760$ m/s versus the PGA predicted by the NCREE19 horizontal GMPE for the reference site condition by using ground motion records with V_{s30} from 120 m/s to 200 m/s. This plot clearly shows the nonlinear site amplification for the horizontal PGA.

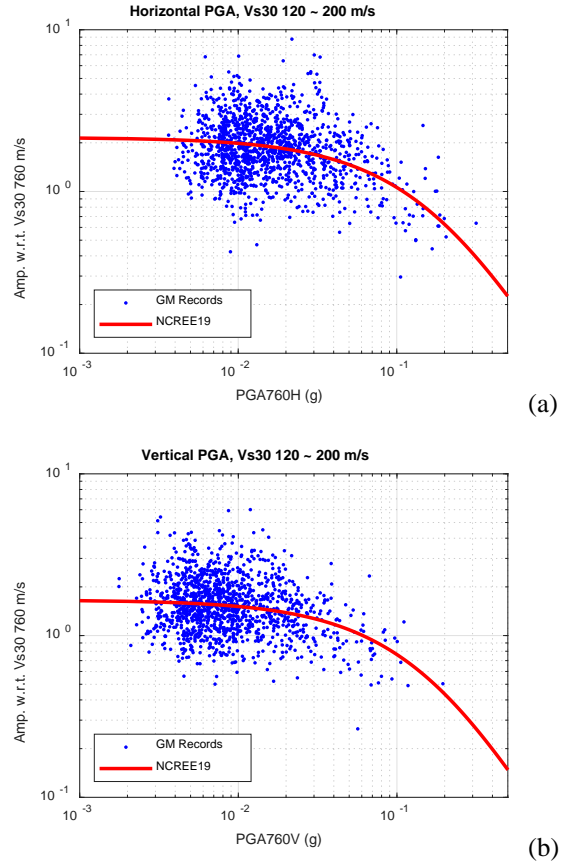


Fig. 1. Site amplification w.r.t. the reference site condition of $V_s = 760$ m/s versus predicted PGA by the NCREE19 GMPE for the reference site condition using ground motion records with V_{s30} from 120 m/s to 200 m/s. (a) Horizontal PGA and (b) vertical PGA.

In addition to the NCREE19 horizontal GMPE, the NCREE vertical GMPE, which is applicable for crustal and subduction earthquakes in Taiwan, has also been developed in parallel by using the same ground motion records and the functional form. Figure 1(b) shows the site amplification of the vertical PGA w.r.t. the reference site condition versus the PGA predicted by the NCREE19 vertical GMPE for the reference site condition by using ground motion records with V_{s30} from 120 m/s to 200 m/s. Nonlinear site amplification can be clearly observed for the vertical PGA. The level of nonlinear site amplification of the vertical component is similar to that of the horizontal component. This is not consistent with some published vertical GMPEs that indicate non-significant nonlinear site amplification of vertical ground motion, which could be attributed to that the vertical ground motion in the used database is mostly P-dominated, and the

soil layer behavior under pressure strain to be linear with no hysteresis.

Arrival Times of P-Waves and S-Waves

The observation of nonlinear site amplification in the NCREE19 vertical GMPE can be attributed to the possibility that the vertical ground motion in Taiwan is S-dominated, meaning that the observed peak ground motion and peak structural responses occur in the S-wave window after the arrival of the S-wave. The behavior of the soil layer under shear strain is nonlinear with a significant hysteresis. Given this, the nonlinear site effect can also be observed in vertical ground motion in Taiwan.

Based on this assumption, we try to compile the arrival time information of ground motion records in Taiwan. A total of 37,888 ground motion records from both crustal and subduction earthquakes observed in Taiwan with available arrival times of P-waves and S-waves are manually selected. The magnitude versus distance plot for these ground motion records is shown in Figure 2.

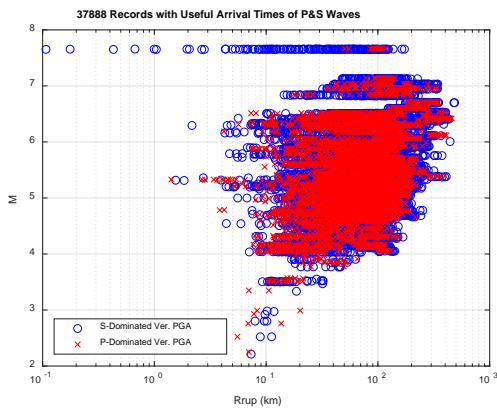


Fig. 2. Magnitude versus distance plot for the ground motion records with available arrival times of P-waves and S-waves from manual selection.

The occurrence times of the peak ground motion and structural peak response can be also evaluated from the time histories of the ground motion records and dynamic analysis of a single-degree-of-freedom system. First, we calculate the vector sum of two horizontal components present in one ground motion record; then, we determine the occurrence time of the peak in the vector sum of two horizontal components as the occurrence time of peak horizontal ground motion or horizontal structural response.

Based on the arrival time information and the occurrence times of the peak ground motions and structural peak responses, we can identify each ground motion record as P-dominated or S-dominated for each ground motion intensity measurement. For example, if a ground motion record had a vertical PGA that

occurred after the arrival of the S-wave, then it is identified as a record with S-dominated vertical PGA. In contrast, if the vertical PGA occurred before the arrival of the S-wave, then it is identified as a record with P-dominated vertical PGA.

Figure 3 shows the three-axis acceleration time histories of two ground motion records observed during the March 31, 2002, earthquake in Taiwan from the TUC024 station, which is a record with an S-dominated vertical PGA, and from the TAP017 station, which is a record with a P-dominated vertical PGA. Note that one record can be identified as both a P-dominated vertical PGA and an S-dominated horizontal PGA. For example, both records in Figure 3 are identified as S-dominated horizontal PGA records as well.

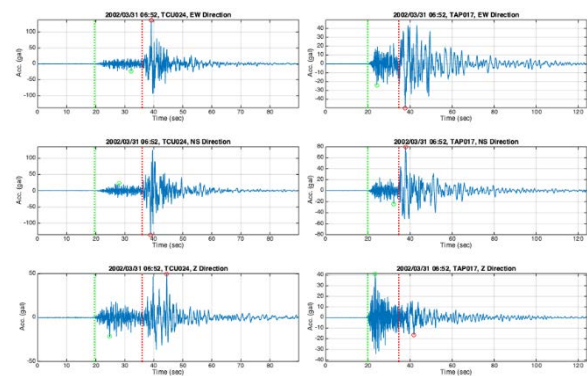


Fig. 3. Three-axis acceleration time histories of two ground motion records observed in the 03/31/2002 earthquake in Taiwan from the TUC024 (S-dominated vertical PGA) and the TAP017 (P-dominated vertical PGA) stations. The green and red lines indicate the arrival times of P-waves and S-waves, respectively.

Percentages of P-Dominated and S-Dominated Records

As described above, the percentage of P-dominated and S-dominated records will be related to the used ground motion intensity measurements. For vertical PGA as an example, a total of 27,830 S-dominated vertical PGA records and 10,058 P-dominated vertical PGA records exist. Most ground motion records with vertical PGA observed in Taiwan are S-dominated, accounting for a percentage of approximately 73%. This result is consistent with the assumption made previously that most of the vertical ground motion in Taiwan is dominated by S-waves.

The blue and red markers shown in Figure 2 represent the S-dominated and P-dominated vertical PGA records, respectively. The vertical PGA of ground motion records observed in the Mw 7.6 Chi-Chi earthquake from the stations within a 40 km distance are all S-dominated. This may be because the

Chi-Chi earthquake was caused by the activity of a reverse fault with a large magnitude. For other earthquakes with small to middle magnitudes, some records with a P-dominated vertical PGA can be observed in a near-source region. The mechanism for the occurrence of a P-dominated vertical PGA is still not clear based on current collected data and observation.

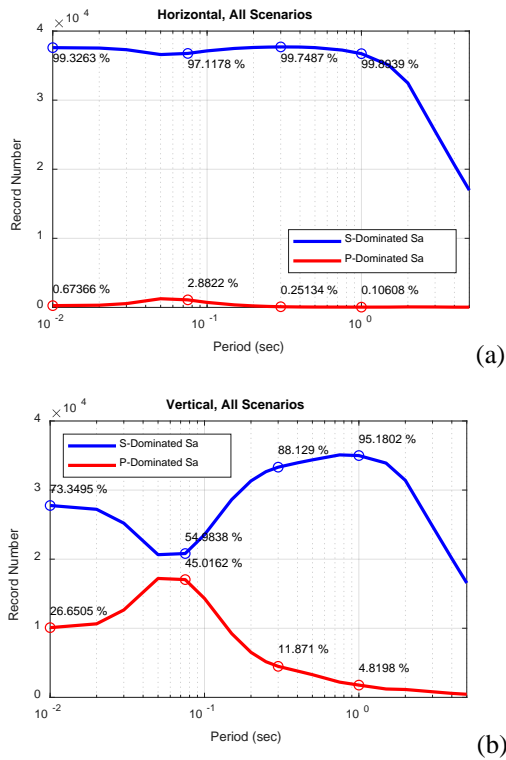


Fig. 4. Record numbers and percentages of S- and P-dominated records for (a) horizontal SA and (b) vertical SA.

In addition to PGA, we also evaluate the occurrence time of spectral acceleration (SA), which is the peak structural acceleration response. If a ground motion record has the vertical SA occurring after the arrival of the S-wave, then it is identified as a record with S-dominated vertical SA. In contrast, if the vertical SA occurred before the arrival of the S-wave, then it is identified as a record with P-dominated vertical SA. All the ground motion records used in this study are high-pass filtered for baseline correction. We only consider the ground motion records with 1.25 times the cut-off frequency of the high-pass filter, which is lower than the structural frequency of SA, to evaluate the occurrence time of SA in this study. For a lower structural frequency or a longer structural period SA, the number of ground motion used records will be fewer.

Figures 4(a) and (b) show the record numbers and percentages of S-dominated and P-dominated records with horizontal and vertical SA, respectively. Almost all horizontal SA is dominated by S-waves. The percentage of S-dominated vertical SA records

depends on the structural period. However, the percentage of S-dominated records is higher than 50% for all structural periods of vertical SA. The percentage of P-dominated records is the highest for a structural period of 0.075 s; it is higher for shorter periods and lower for longer structural periods. This may be due to the frequency content of P-waves being higher than that of S-waves.

Conclusions

In this study, we compiled information about the arrival times of P-waves and S-waves, peak occurrence times of ground motion, and structural responses for ground motion records observed in Taiwan. Based on this information, we evaluated the percentages of the vertical peak ground motions and structural vertical peak responses that occurred in P-wave and S-wave windows. We found that the vertical PGA and SA of ground motion records in Taiwan are significantly dominated by S-waves. It provides a physical basis for the analysis of the nonlinear site effect of vertical ground motion in Taiwan from the NCREE19 vertical GMPE.

References

- Bozorgnia, Y., Campbell, K.W. (2016). Vertical Ground Motion Model for PGA, PGV, and Linear Response Spectra Using the NGA-West2 Database. *Earthquake Spectra*; 32(2):979-1004.
- Chao, S.H., Chiou, B., Hsu, C.C., and Lin, P.S. (2019). Development of horizontal and vertical ground motion model for crustal earthquakes and subduction earthquakes in Taiwan, NCREE (National Center for Research on Earthquake Engineering) Report, No. NCREE-19-003.
- Chao S-H, Chiou B, Hsu C-C, Lin P-S. (2020) A horizontal ground-motion model for crustal and subduction earthquakes in Taiwan. *Earthquake Spectra*; 36(2):463-506.
- Gülerce, Z., Kamaı, R., Abrahamson, N.A., Silva, W.J. (2017). Ground Motion Prediction Equations for the Vertical Ground Motion Component Based on the NGA-W2 Database. *Earthquake Spectra*; 33(2):499-528.
- Pacific Earthquake Engineering Research (PEER) Center (2013). NGA-West2 Ground Motion Prediction Equations for Vertical Ground Motions. PEER Report No. 2013/24.
- Stewart, J.P., Boore, D.M., Seyhan, E., Atkinson, G.M. (2016). NGA-West2 Equations for Predicting Vertical-Component PGA, PGV, and 5%-Damped PSA from Shallow Crustal Earthquakes. *Earthquake Spectra*; 32(2):1005-1031.

The Time-dependent Seismic Microzonation Map of Near Fault Area in Taiwan

Yu-Wen Chang¹, Chih-Wei Chang², Hsun-Jen Liu³ and Wen-Yu Chien⁴

張毓文¹、張志偉²、劉勛仁³、簡文郁⁴

Abstract

Time-dependent probability model are considered because studies of paleoseismic records on well-studied faults in Taiwan have found them to be technically defensible characterizations of the timing of earthquakes. If the behavior of earthquake recurrence is credible evidence of recurrence behavior, then a time-dependent recurrence model for describing the probability of earthquake occurrence must be part of the uncertainty in the hazard assessment. A relative hazard factor that is used to consider the time-dependent hazard estimation is the Equivalent Poisson Ratio (EPR). It is expressed as an effective Conditional Probability ratio of the time-dependent to the time-independent hazard estimate. That is, a seismic hazard ground motion map relative the particular periods near the faults can be estimated in the principles of probabilistic seismic hazard analysis (PSHA). The conditional probability in the next subsequent time windows (T_p) corresponds to a renewal model with the coefficient of variation of the recurrence interval. The time-dependent seismic microzonation map of near for the 25 major faults area in Taiwan is developed in this study.

Keywords: Probabilistic Seismic Hazard Analysis, Time-dependent, Equivalent Poisson Ratio

Introduction

According to the principles of probabilistic seismic hazard analysis (PSHA), Probabilistic seismic hazard analysis (PSHA) requires technically accurate models of fault behavior. The model most commonly used in the PSHA for earthquake occurrence, the Poisson process, assumes that earthquakes occur randomly in time when viewed over a long interval; This method assumes memory lessness in which time, size and location of preceding events are independent.

In reality, there is increasing evidence showing that the behavior of earthquake occurrence, which is related to individual fault sources, follows an inherent time model. During repeated rupture episodes on an individual fault (or fault system), some characteristics remain approximately constant over a long timescale. This means that characterization of recurrent ruptures of an earthquake does not match the assumption used

in the Poisson process. It is important to properly consider the variability in recurrence rates caused by multiple-segment ruptures that change from event to event due to fault interactions.

The frequency of large earthquake occurrence forms the basis for seismic hazard assessments, and the concept of stress-driven earthquake renewal has inspired time-dependent earthquake probability calculations. The U.S. Geological Survey's Working Group on California Earthquake Probabilities (WGCEP, 2003) considered time-dependent hazard analysis in a study of the San Francisco Bay region using the probability models for the major Bay Area faults. In this study, the group performed time-dependent probability calculations for the next 30 years using historic earthquake data from the segmentation of active faults.

The concept of time-dependent earthquake occurrence in PSHA applies to fault-specific seismic

¹ Associate Researcher, National Center for Research on Earthquake Engineering

² Assistant Technologist, National Center for Research on Earthquake Engineering, Taipei, Taiwan

³ Assistant Researcher, National Center for Research on Earthquake Engineering

⁴ Research Fellow, National Center for Research on Earthquake Engineering

sources. Given the prominence of the Poisson model for earthquake occurrence in PSHA, most computer codes for hazard estimation have, until recently, assumed the Poisson model. The recognition that earthquake occurrence may be time-dependent has created interest in establishing methods to use current PSHA calculations even to model time-dependent sources in hazard codes. The equivalent Poisson's ratio (EPR) estimates are the relative adjustments to time-independent rupture rates that are necessary to produce the equivalent time-dependent rupture rate. The EPR formulation can be applied in hazard codes as a constant multiplier for time-independent hazards. Unknown parameters that affect the hazard estimate, such as earthquake recurrence interval and the coefficient of variation (CV) for recurrence are included as geologically bounded ranges.

The Fault Model

An active fault is defined as one that has moved repeatedly in recent geological time and has the potential to cause earthquakes in the future. The Taiwan Central Geological Survey (CGS) has had a project for active fault research since 1997. Until 2010, thirty-three active fault locations in Taiwan were published by CGS (<https://www.moeacgs.gov.tw/>). The study congregates relevant seismic, geological, and geophysical data of the faults to develop the database for the CGS version. On the other hand, thirty-eight on-land active seismogenic structures were identified by Shyu et al. (2016). The model combined information from pre-existing databases and a digitized three-dimensional seismogenic structure map for Taiwan. The fault parameters in both the databases include fault geometry, slip rate, the time of the most recent earthquake, etc. Specifically, some active faults consisting of the same geometry characteristic are combined in both the models.

In this study, the parameters relating to the geometry and activity of the twenty-five on-land active faults in Taiwan have been summarized using the CGS and Shyu et al. (2016) studies. Although time-independent earthquake occurrence behavior characterization requires only an assessment of the mean recurrence interval (T_r) for a given magnitude, this study considers the elapsed time since the previous earthquake (T_e) in a time-dependent probability model for these major faults. Time-dependence can be incorporated into PSHA using alternative models to account for the active fault rupture cyclic characteristics from the present time up to a particular lifetime. The conditional probability in the next subsequent time windows (T_p) corresponds to a renewal model with a coefficient of variation for the recurrence interval.

Conditional Probability in T_p years

Let $f(\xi)$ denote a probability density function of the recurrence interval for the fault rupture that causes an earthquake. If the elapsed time of a time-dependent active fault is given as T_e , the hazard analysis involves an estimation of the occurrence probability of the fault during the subsequent T_p -year. For most structures, the earthquake design is estimated on the basis of the structural lifetime. In this case, T_p is set as the structural lifetime, and the seismic hazard due to the active fault can be estimated using engineering reliability theory. Given a condition that the fault has survived during $[0, T_e]$, the probability of causing a fault rupture during $[T_e, T_e+T_p]$ is called the posterior failure probability (or recurrence probability):

$$P_{cod} = Q_c(T_e + T_p | T_e) = \frac{Q_c[T_e + T_p, T_e]}{Q_c[T_e]} = \frac{\int_{T_e}^{T_e+T_p} f(\xi) \cdot d\xi}{\int_{T_e}^{\infty} f(\xi) \cdot d\xi} \quad (1)$$

The probability $Q_c(T_e+T_p|T_e)$ represents the conditional probability (P_{cod}) in the subsequent time period. Fig. 1 shows the comparison of five probability models used to estimate the conditional probabilities of an earthquake during the subsequent 50-year period ($T_p = 50$ years) using Eq.(1). All models have a mean recurrence interval of 100 years and a CV of 0.5. The conditional probability of the renewal model is consistent with the Poisson model when CV is large.

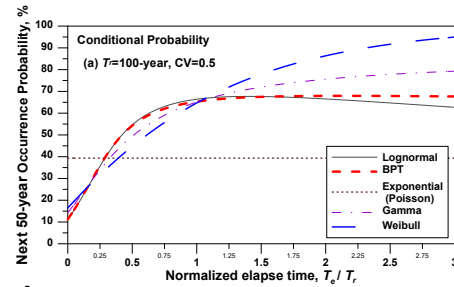


Fig. 1 Comparison of the five probability models used to estimate the conditional probability for earthquake occurrence during the next 50-year period ($T_p = 50$). All models have a mean recurrence interval of 100 years and $CV = 0.5$.

Sensitivity Analysis with Respect to CV of the Renewal Model

Most faults do not have sufficient fault-crossing trenching to constrain the history of past events. A time-dependent model properly considers the variability in recurrence rates caused ruptures in multiple segments that may change from event to event due to fault interactions. The occurrence probability sensitivity analysis for CV indicates that the occurrence probability depends on the different CV values used in the renewal model. The width parameter of the time-dependent probability density function (PDF) governs the regularity of earthquake occurrence on the fault.

As with the recurrence interval, a best possible estimation is unavailable. However, an informed range can be adopted from the following references:

- In Taiwan, a high confidence, $CV = 0.35$, was estimated from the high-quality paleoseismic data of the Chelungpu Fault, which is a reverse fault.
- A range was observed at high-quality paleoseismic sites on strike-slip faults in California in the Western United States. The range expresses the greatest confidence for CV values between 0.5 and 0.8 and a low confidence for $CV < 0.5$, which represents a more random recurrence (Pacific Gas & Electric (PG&E), 2015).
- WGCEP (1995) assumed renewal processes with a larger CV of 0.5 ± 0.2 for the most active fault segments in the San Francisco Bay area.

For the above studies, a conservative CV of 0.5 is an reasonable value for a fault that has limited information on the active behavior. Similarly, a CV value of 0.7–0.8 is acceptable for a fault for which only the location information is known. The locations and geometries of most faults in Taiwan can be identified on the basis of geological evidence, but there is a lack of information relating to the activity, such as the recurrence interval and the last event. Consequently, a wider range of CV values (between 0.5 and 0.8) is considered to cover the realistic possibilities.

Fig. 2 shows the conditional probability ratios (CPRs) for the Brownian Passage Time (BPT) distribution and values of CV ranging from 0.3 to 0.8; for the probability estimation plot, we assumed that the recurrence interval T_r was 100 years and the subsequent T_p was 50 years. In fact, the ratios between the conditional probability of the time-dependent and exponential models, which correspond to a constant recurrence interval, decrease with increasing CV. As anticipated by the hazard function, the initial CP ratio is almost zero immediately after an earthquake; it then increases with the increasing CV over the elapsed time.

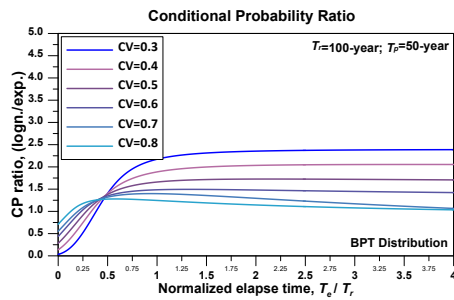


Fig. 2 Comparison of the CPR using BPT distributions with CV ranging from 0.3 to 0.8 to estimate the occurrence of earthquakes in the subsequent 50 years (T_p).

Equivalent Poisson Ratio

Since the Poisson model is used in baseline hazard calculations, the time dependence of the subsequent T_p years is implemented using a factor that can be applied to the earthquake rate (relative to the slip rate) that increases (or, in principle, could lower) the hazard. This factor is called the equivalent Poisson's ratio (EPR). This concept was proposed by the Senior Seismic Hazard Analysis Committee (SSHAC) project, which involved the seismic hazard analysis for the Diablo Canyon Power Plant (DCPP) in the US (PG&E, 2015).

Substituting the T_p -year conditional probability (P_{cod}) for the Poisson probability per year into the Poisson process, an effective Poisson rate (λ_{eff} , WGCEP, 2003) can be solved as follows:

$$\lambda_{eff} = -\ln(1 - P_{cond}) / T_p \quad (2)$$

EPR estimates are the relative adjustments to time-independent rupture rates (λ_{pois}) necessary to produce the equivalent time-dependent rupture rate, which is described by:

$$EPR = \frac{\lambda_{eff}}{\lambda_{pois}} \quad (3)$$

For including the possibility of the occurrence probability model, the EPR is the multiple of the slip rate for a fault in the hazard calculation.

Based on the recurrence interval and CV values of each fault, the EPR distributions for each fault can be calculated. In the analysis, the CV=0.5 and 0.7 have used to consider the variability of the recurrence interval. For the earthquake behavior, the weight use 0.8 for time-dependent model and 0.2 for the time-independent model.

In addition, both of the time-independent and time-dependent models for describing the fault activity behavior will be included in hazard calculation.

The Near Fault Seismic Hazard Map Considering the Time-Dependent Model

Based on the PSHA procedure and the parameters of the faults, the next 50-year seismic hazard map of peak ground acceleration (PGA) of the 25 major faults considering the time-independent model and time-dependent model can be estimated including the 10% and 2% probabilities of exceedances in 50 years as shown in Fig. 3. In the hazard calculation, the seismic source only considers the 26 major faults, and Taiwan ground motion prediction equations (GMPEs) (NCREE&TPC, 2019) are adopted to evaluate the seismic-hazard assessment in terms of strong ground

motion (assume equal weighting in hazard calculation). The average shear-wave velocity in the top 30 m, V_{S30} , is assumed to be 360 m/sec in order to focus on the near-fault effect in the PSHA. This study neglects the site effect. The study sites are located on the hanging-wall and footwall in around the fault; the distance of site to fault is 5km and 10km, respectively.

From the next 50-year seismic hazard map, it indicates that the high conditional probability of the faults leads to the greater ground motion in the particular site. Oppositely, when the seismic moment of the fault is announced in the near future, the requirement for ground motion level at the sites will be smaller during the structure lifetime.

Conclusion

Considering the uncertainty of the fault recurrence interval, the slip rate is one of the parameters used to estimate the range of the uncertainty. Given the prominence of the Poisson model of earthquake occurrence in the PSHA, EPR estimates are the relative adjustments to time-independent rupture rates necessary to produce the equivalent time-dependent rupture rate. The EPR method provides a framework within which to estimate relative time dependence on faults that lack sufficient data for a direct estimate.

Therefore, the next 50-year seismic hazard map of the PGA near the 25 major faults considering the time-dependent model can be estimated, including the 10% and 2% probabilities of exceedances in 50 years. The map shows that the seismic requirement for the hanging-wall is almost double than the footwall due to the hanging-wall effect. It is more important to develop the GMPE model that includes the hanging-wall effect because of Taiwan's geologic environment.

References

Matthews, M. V., W. L. Ellsworth, and P. A. Reasenberg (2002). A Brownian model for recurrent earthquakes, *Bull. Seismol. Soc. Am.* 92.

Pacific Gas and Electric Company (PG&E) (2015). Seismic Source Characterization for the Diablo Canyon Power Plant, San Luis Obispo County, California, Report on the results of a SSHAC level 3 study Rev. A. Available online at <http://www.pge.com/dcpp-1tsp>.

Shyu, J. B. H., Y. R. Chuang, Y. L. Chen, Y. R. Lee, and C. T. Cheng (2016). A new on-land seismogenic structure source database from the Taiwan Earthquake Model (TEM) project for seismic hazard analysis of Taiwan, *Terr. Atmos. Ocean. Sci.* 27(3), 311-323, doi:10.3319/TAO.2015.11.27.02(TEM).

Working Group on California Earthquake Probabilities (WGCEP) (1995). Seismic hazards in Southern California: probable earthquake, 1994 to 2024, *Bull. Seismol. Soc. Am.* 85, 379-439.

Working Group on California Earthquake Probabilities (WGCEP) (2003). Earthquake Probabilities in the San Francisco Bay Region: 2002-2031. U.S. Geological Survey, Open-File Report 03-214, 234 pp.

Taiwan Power Company and National Center for Research on Earthquake Engineering (2019). "Reevaluation of Probabilistic Seismic Hazard of Nuclear Facilities in Taiwan Using SSHAC Level 3 Methodology – Ground Motion Characterization Technical Report," Draft Version, Project No.: 027040000101.

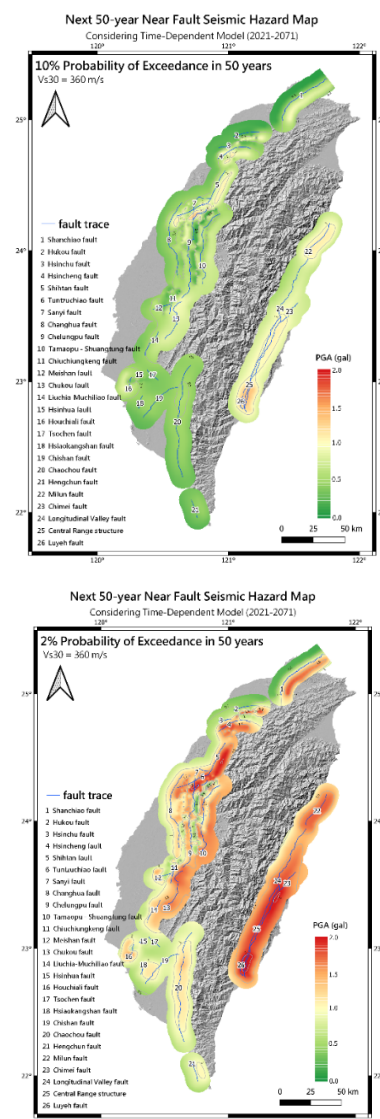


Fig.3 The next 50-year seismic hazard map of peak ground acceleration (PGA) (10% and 2% probability of exceedance in 50 years) of the 26 major faults considering the time-dependent model

Source Radiation Pattern Database Calculated from the 1-D Seismic Velocity Structure in Taiwan

Jyun-Yan Huang¹, Che-Min Lin² and Shu-Hsien Chao³

黃雋彥¹、林哲民²、趙書賢³

Abstract

The National Center for Research on Earthquake Engineering hosted the Senior Seismic Hazard Analysis Committee Level III project in Taiwan (NCREE, 2018) and rearranged the ground motion database and flat-file in the ground motion characteristics (GMC) team. The flat-file was built in an attempt to develop spectral acceleration based ground motion models (GMM) for application to seismic hazard evaluation. However, some complex effects or indices were not considered or calculated in the database and still require careful consideration. These include the Fourier amplitude spectrum, and hanging wall, directivity, seismic duration, and radiation pattern effects. In this study, to update the ground motion database in Taiwan, the necessary information from the GMC flat-file is gathered to upgrade systematically the applicability of the database. The theoretical source radiation pattern is calculated from the pseudo-bending ray-tracing method in a three-dimensional grid and the one-dimensional velocity structure for each record in the Taiwanese database. Specifically, takeoff angles and S wave radiation coefficients were added to the database for each record for future applications in GMM in Taiwan.

Keywords: Radiation pattern, ground motion database, Taiwan

Introduction

Ground motion prediction for high probability faults is an important issue and traditionally the ground motion prediction equation (GMPE) has been widely used for this purpose in many regions. Various researchers have given significant effort to increase the accuracy of the GMPE prediction and reduce its uncertainty using supplementary geophysical considerations. However, the aleatory uncertainty is still significant in worldwide ground motion models owing to a lack of sufficient observational records to describe certain phenomena such as hanging walls, directivity, seismic duration, and radiation patterns. Near source and large earthquake records are deficient due to limited operating periods of the strong motion stations. Therefore, accurate consideration of most of the abovementioned effects remains challenging in worldwide GMPEs. The present study attempts to address these considerations, with a focus on source radiation pattern calculations. The seismic source radiation pattern can be computed from several geometrical relations using a combination of fault plane strike, dip, rake, takeoff angle, and source-station related angles (Aki and Richards, 1980, 2002). Takemura et al. (2016) verified the velocity records of

thirteen events in the Japan Hi-net network and indicated a possible frequency dependence for the S wave radiation pattern between long and short periods, with periodic trends being established for frequencies of 0.5-1.0 Hz from amplitude fluctuations. Kotha et al. (2019) demonstrated periodic trends over a short distance for strike slip events from a larger dataset in which the trend fitted a normalized residual of Japanese database well. In Taiwan, the ground motion characteristics (GMC) team in the Senior Seismic Hazard Analysis Committee (SSHAC) project developed a strong motion database from a Taiwan strong motion instrumentation program (TSMIP) with a recording period from the 1990s to 2016. This included 44600 records gathered for the entire Taiwanese region (NCREE, 2018) and several next generation GMPEs were generated (Chao et al., 2020; Phung et al., 2020a, 2020b). Fig. 1 shows the magnitude-distance relationship (M-R) for the current GMC database for a Mw magnitude range of 2.2-7.6 and rupture distance Rrup from < 100 m to > 500 km. The results provide an opportunity to supplement extra indices based on the current database to further upgrade its applicability for more precise GMPEs in the future.

¹ Assistant Research Fellow, National Center for Research on Earthquake Engineering

² Research Fellow, National Center for Research on Earthquake Engineering

³ Associate Research Fellow, National Center for Research on Earthquake Engineering

Theoretical Shear Wave Radiation Patterns

Aki and Richards (1980, 2002) indicated that amplitudes of strong motion would behave spatially with a petal shape (Fig. 2) related to fault strike direction, as can be readily observed for a pure strike slip fault. Given that the observations of the present study are mainly on the surface, there is a need to further consider geographical curvature to capture the four-lobed shape in 3D. Using the relevant angles, including fault strike ϕ_s , fault dip δ , fault rake λ , takeoff angle i_ξ from the source and source-receiver azimuth ϕ (Fig. 3), the shear wave radiation pattern can be obtained from

$$\begin{aligned} \mathcal{F}^{SV} &= \left[(\boldsymbol{\gamma} \cdot \boldsymbol{\nu})(\hat{\mathbf{u}} \cdot \hat{\mathbf{p}}) + (\boldsymbol{\gamma} \cdot \hat{\mathbf{u}})(\boldsymbol{\nu} \cdot \hat{\mathbf{p}}) \right] / \hat{u} \\ &= \sin \lambda \cos 2\delta \cos 2i_\xi \sin(\phi - \phi_s) - \cos \lambda \cos \delta \cos 2i_\xi \cos(\phi - \phi_s) \\ &\quad + \frac{1}{2} \cos \lambda \sin \delta \sin 2i_\xi \sin 2(\phi - \phi_s) \\ &\quad - \frac{1}{2} \sin \lambda \sin 2\delta \sin 2i_\xi (1 + \sin^2(\phi - \phi_s)), \\ \mathcal{F}^{SH} &= \left[(\boldsymbol{\gamma} \cdot \boldsymbol{\nu})(\hat{\mathbf{u}} \cdot \hat{\boldsymbol{\phi}}) + (\boldsymbol{\gamma} \cdot \hat{\mathbf{u}})(\boldsymbol{\nu} \cdot \hat{\boldsymbol{\phi}}) \right] / \hat{u} \\ &= \cos \lambda \cos \delta \cos i_\xi \sin(\phi - \phi_s) + \cos \lambda \sin \delta \sin i_\xi \cos 2(\phi - \phi_s) \\ &\quad + \sin \lambda \cos 2\delta \cos i_\xi \cos(\phi - \phi_s) \\ &\quad - \frac{1}{2} \sin \lambda \sin 2\delta \sin i_\xi \sin 2(\phi - \phi_s). \end{aligned}$$

where F^{SV} is the radiation coefficient of the SV wave and F^{SH} is that for the SH wave. The shear wave radiation pattern F_s can then be given by

$$F_s = \sqrt{(F^{SV})^2 + (F^{SH})^2}, \quad (3)$$

and it is associated with the far field displacement. Therefore, in order to calculate the takeoff angle i_ξ , a pseudo-bending ray-tracing technique (Um and Thurber, 1987; Koketsu and Sekine, 1998) was applied to a 3D grid and 1D velocity structure to generate F_s for entire records in the database. The 1D velocity structure was obtained from Taiwan's Central Weather Bureau (Table 1, Chen and Shin, 1998).

Table 1. 1D shear wave velocity model used in the pseudo-bending ray tracing technique applied in this study (Chen and Shin, 1998)

thick	depth	Vp	dVp	Vs	dVs
		(km/sec)	(km/sec)	(km/sec)	(km/sec)
2	0 - 2	3.48	-0.013	1.96	-0.017
2	2 - 4	4.48	-0.013	2.62	0.006
5	4 - 9	5.25	0.020	3.03	0.014
4	9 - 13	5.83	0.014	3.35	0.003
4	13 - 17	6.21	0.003	3.61	0.000
8	17 - 25	6.41	0.004	3.71	0.001
5	25 - 30	6.83	0.012	3.95	0.007
5	30 - 35	7.29	0.007	4.21	-0.008
15	35 - 50	7.77	0.015	4.49	-0.008
20	50 - 70	8.05	0.001	4.68	0.000
20	70 - 90	8.16	0.000	4.72	0.002
20	90 - 110	8.34	0.002	4.79	-0.007
30	110 - 140	8.35	0.020	4.80	0.004
30	140 - 170	8.20	-0.013	4.74	-0.009
30	170 - 200	8.40	-0.003	4.86	-0.001
40	200 - 240	8.51	0.003	4.92	0.008
half space	240 -	8.70	0.000	5.49	0.000

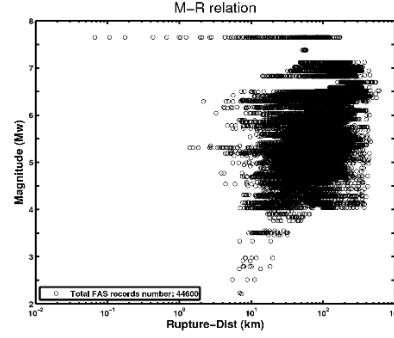


Fig. 1 M-R relationship for the GMC database from the NCREE (2018)

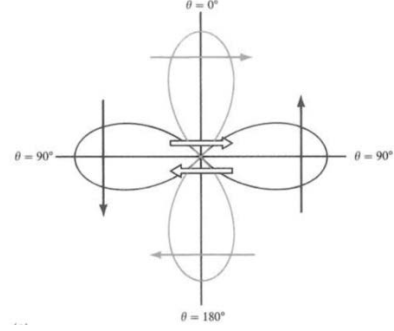


Fig. 2. Theoretical S wave radiation pattern of the transverse component of displacement due to a double couple mechanism (Aki and Richards, 2002)

The takeoff angle was identified while the first arrival ray path was traced and the shear wave radiation pattern coefficient was calculated from these parameters.

Results and Conclusions

Fig. 4 shows samples of the first arrival ray path and the corresponding shear wave radiation pattern coefficient. The theoretical S wave radiation pattern has an amplified range of seismic energy from 0 to 1 in the source effect, suggesting the generation of high or low energy regions from a double-coupled fault rupture in different locations relative to a fault. While the radiation pattern was a 3D pattern in the underground structure, strong motions were mostly observable at the surface; this means that the radiation pattern could not always show obvious four-lobbed features from various stations if the fault dip was not perpendicular to the surface (Figs 4(a), (d)). Therefore, in this study, a radiation pattern coefficient of total record numbers of 24416, 2811, 3974, and 10665 was respectively used for shallow crustal, deep crustal, subduction interface, and subduction intra-slab events.

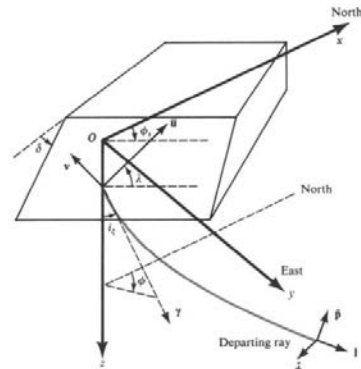


Fig. 3. Definition of the Cartesian coordinates (x, y, z) used to obtain the explicit dependence of P, SV, and SH radiation patterns (Aki and Richards, 2002)

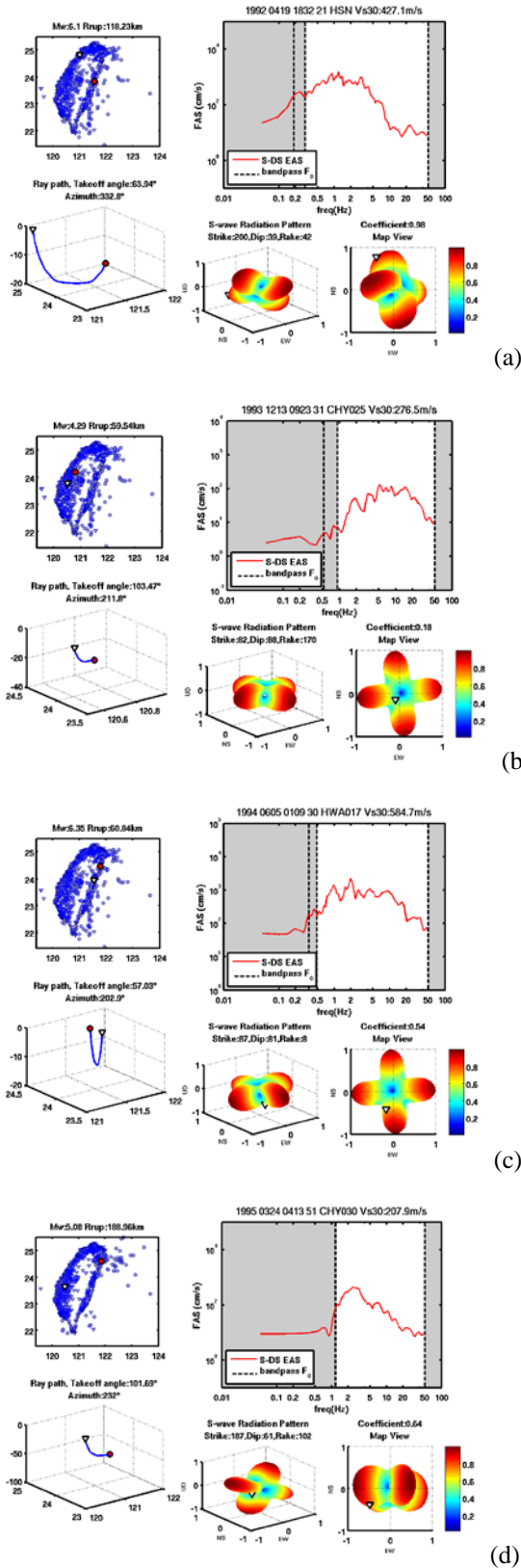


Fig. 4. Examples of the calculated ray path and radiation pattern of selected station-source pairs for (a) a 1992 Mw 6.1 earthquake, (b) a 1993 Mw 4.3 earthquake, (c) a 1994 Mw 6.3 earthquake, and (d) a 1995 Mw 5.1 earthquake. White triangles are the recording strong motion stations, the red circles are the seismic sources, blue triangles denote the locations of entire stations, the blue curves are the first arrival ray path, and the colored petals show the main S wave radiation pattern in 3D at two different viewing angles

References

- Aki, K. and Richards, P. G. (1980). “Quantitative seismology. University Science Books, Freeman, San Francisco.
- Aki, K. and Richards, P. G. (2002). “Quantitative seismology- second edition”, University science books, Mill Valley, California.
- Chao, S. H., Chiou, B., Hsu, C. C. and Lin, P. S. (2020). “A horizontal ground motion model for crustal and subduction earthquakes in Taiwan”, *Earthq. Spectra* 36, (2), 463–506.
- Chen, Y.L. and Shin, T. C. (1998), “Study on the earthquake location of 3-d velocity structure in the taiwan area”, *Meteorological Bulletin* 42(2), 135-169. (in Chinese with English abstract)^{[1][SEP]}
- Koketsu, K. and Sekine, S. (1998), “Pseudo-bending method for three-dimensional seismic ray tracing in a spherical earth with discontinuities”, *Geophys. J. Int.* 132, 339-346.
- Kotha, S. R., Cotton, F. and Bindi, D. (2019), “Empirical models of shear-wave radiation pattern derived from large datasets of ground-shaking observations”, *Scientific reports* 9, 981.
- National Center for Research on Earthquake Engineering (NCREE), (2018). Web page for reevaluation of probabilistic seismic hazard of nuclear facilities in Taiwan using SSHAC level 3 methodology project, available at <http://sshac.ncree.org.tw>.
- Phung, B. V., Loh, C. H., Chao, S. H. and Abrahamson, N. A. (2020a) “Ground motion prediction equation for Taiwan subduction zone earthquakes”, *Earthq. Spectra* 36(3), 1331-1358.
- Phung, B. V., Loh, C. H., Chao, S. H., Chiou, B. and Huang, B. S. (2020), “Ground motion prediction equation for crustal earthquakes in Taiwan”, *Earthq. Spectra* 36(4), 2129-2164
- Takemura, S., Kobayashi, M. and Yoshimoto K. (2016), “Prediction of maximum P- and S-wave amplitude distributions incorporating frequency- and distance-dependent characteristics of the observed apparent radiation patterns”, *Earth, Planets and Space* 68, 166.
- Um, J. and Thurber, C. (1987), “A fast algorithm for two-point seismic ray tracing”, *Bull. Seism. Soc. Am.* 77(3), 972-986.

Established Vs30 Grids Data for Taiwan Areas by Weighted Kriging

Chia Li Chen¹, Chun Hsiang Kuo^{2,3} and Xue Min Lu¹

Abstract

Although the Taiwan strong motion instrumentation program (TSMIP) has compiled many reliable site-effect parameters in the Engineering Geological Database for TSMIP (EGDT), the drilling survey stations are not uniformly distributed. Since resolution is not high enough to represent characteristics of local areas, this study attempted to establish Vs30 grid data for the Taiwan area using weighted kriging. Weighted kriging considers not only distance factors, but also confidence of different Vs30 methods. It can control grid values to yield higher confidence values. In this study case, we chose data points where distance was less than 6 kilometers for interpolation purposes. We also evaluated interpolation results five times using the cross validation method. First, we randomly removed 5% of samples from each Vs30 method by program code, then re-interpolated the data. Finally, we analyzed errors between sampled and interpolated results. Our statistical analysis showed high reliability in plain areas and large errors in mountainous areas or areas with rapidly altered terrain. Obtaining more Vs30 data in mountainous areas in the future will allow further control points to improve reliability and accuracy for ground motion predictions and disaster applications.

Keywords: Kriging, Vs30

Introduction

Taiwan is located at a complex convergent plate boundary with a high level of seismicity. Uplift, weathering, erosion, and other geological processes have generated many broad and deep alluvial basins. Soft alluvium amplifies the seismic waves giving strong ground motion. The seismic site effect of a soft site may lead to an earthquake disaster. To accurately estimate earthquake response, many earthquake engineering studies and hazard analyses have considered ground motion parameters, in which Vs30 is an important site effect parameter.

Since 2000, the National Center for Research on Earthquake Engineering (NCREE) and the Central Weather Bureau (CWB) have collaborated to execute the Taiwan strong motion instrumentation program (TSMIP) and upload drilling data onto the Engineering Geological Database for TSMIP (EGDT). The average distance between drilling survey stations is 5 kilometers (Wang and Kuo, 2006; Lin et al., 2017), but the velocity result only includes effects of site characteristics below the station. Therefore, it is not possible to clearly determine site characteristics of

local areas. Despite some authors using other methods to estimate Vs30 values (Liu et al., 2015; Lin et al., 2018), their estimated Vs30 values are from a single station, making it difficult to immediately apply these data to seismic hazard analyses.

We chose geostatistical methods to attempt to establish reliable grid values by using available Vs30 data. Second order stationarity and intrinsic hypotheses are basic theories of geostatistical methods, in which expectations and variances of regionalized variables only relate to distance. The various available Vs30 methods have intrinsic uncertainties, so we quantified a data weight for each method. We then modified the kriging method to consider distance parameters and data weights for each method. We expected to obtain results that closely approximated real situations and that can be immediately applied.

To confirm the modified kriging method, we compared our output to the output obtained using a different interpolation method. The results show that both methods returned similar distributions. Selecting an appropriate theoretical semi-variogram model is subjective. Therefore, we used cross validation, which

¹ Research Assistant, National Center for Research on Earthquake Engineering

² Research Fellow, National Center for Research on Earthquake Engineering

³ Assistant Professor, National Central University

requires removing part of the sample data and re-interpolating the modified database. Finally, we analyzed the error between estimated values and sample values.

Description of Vs30 Database

The EGDT provides different Vs30 values from different methods, including drilling and other estimates (Kwok et al., 2018; Lin et al., 2018). Our data count was approximately 800. The TSMIP drilling survey stations were located in metropolitan and high seismic hazard potential areas, with the terrain typically forming plains or basins. However, there is a paucity of Vs30 data in mountainous areas. This study used (1) a Vs30 estimation for the central mountain area of Taiwan (C17) and (2) a Vs30 estimation base for topographic slopes (AW09) to solve the lack of data in the mountainous areas. We also added (3) a Vs30 base for the micro tremor method (MHVSR) to our Vs30 database to increase the number of data points located in the plains (Figure 1)

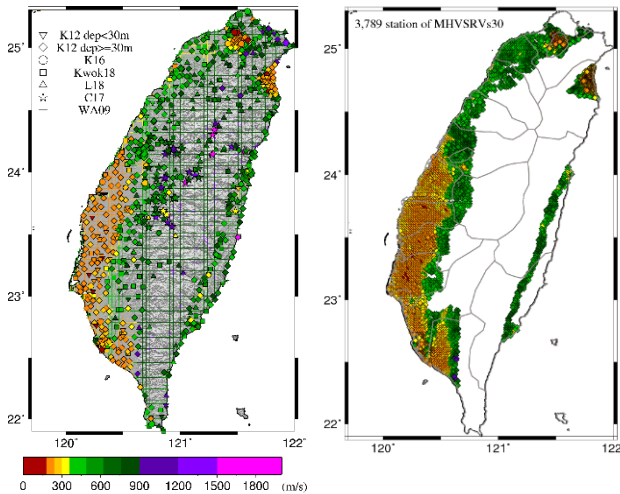


Figure 1. Vs30 database for this study. The left panel shows the distribution of EGDT and AW09 data. The right panel shows velocity survey locations by micro tremor

Weighted Kriging

Geostatistical methods estimate entire area distributions using a small sample. Ordinary kriging is a common class of geostatistical method applied to a wide variety of problems, including hydrological regimes and weather patterns. The most important technological aspect of kriging is the semi-variogram. The theoretical semi-variogram model is a function related to distance. Initially, we calculated the experimental semi-variogram model assuming a reasonable distance interval when selecting a suitable theoretical semi-variogram model. We selected a type of theoretical semi-variogram model and adjusted its

parameters to fit the experimental semi-variogram model.

We selected Vs30 values with a distance less than 6 kilometers between point locations and the grid center and substituted distance into a experimental semi-variogram model to calculate variability. This allowed us to obtain the distance weight for each point via an inverse matrix to estimate Vs30 values for the grid. The standard kriging method only considers distance, but the Vs30 data used here included observations made using different methods which have different uncertainties. Therefore, this study used the error results of Kuo et al. (2017) and Ancheta et al. (2013), modified by the weighting function of Seyhan et al. (2014), to calculate data weights for each method (Table 1).

Table 1. Vs30 data weight for each method. MA = micro tremor array. μ is median. σ is standard deviation.

Method	μ	σ	Weight
drilling	0.02	0.06	15.81
MA	-0.03	0.15	6.54
Kwok18	-0.02	0.3	3.33
L18	-0.13	0.31	2.97
C17	-0.1	0.16	5.37
WA09	0.01	0.36	2.78
MHVSRV	-0.06	0.2	4.79

Preliminary Analytical Results

This study develop the program to implement the weight kriging method by ourselves, so first important thing is ensure the correctness and similarity. Figure 2 and figure 3 show our result is similar to another result from GMT interpolate command. In order to quantify the difference between the theoretical semi-variogram models, we statistically analyzed the common statistics variable with the error between estimation and sample, it include error mean and standard deviation. Our Vs30 database is not sensitive for theoretical semi-variogram models. We try to interpolate by different theoretical semi-variogram model, but it was unavailable to reduce the maximum error value. The reason why it can't reduce the maximum error value was that we selected the data point less than 6 kilometer but their Vs30 value still rapid changes. The grid size too large will lead to smooth the estimation and unable to response real situation. We think our database is enough, especially on the plain. So we adapt to 500 meter \times 500 meter for each grid and the result show it is indeed reduce the error effectively.

We used cross validation repeat 5 times in order to evaluate our interpolate result. Its process is remove part of sample from database and interpolate again by other data. We random took out 5% data point of each kind of Vs30 method. Finally, we calculate the error between new interpolate result and plot the error distribution of sample at figure 4 and figure 5. The sample be take out on plain have not a significant effect on the interpolate result. That mean the count of Vs30 points is enough, like Kaohsiung, Yunlin, Chiayi and Tainan. A few sample located on Taichung basin, Taipei basin, Longitudinal Valley and foothills region have significant effect because the sample located on the rapid terrain changes or difference geology.

We cross-validated our results and calculated means and standard deviations for the error values. The error analysis showed that results based on C17 method have a maximum error value of 831 m/s (Figure 6). The samples were CH-13 (Wu-ling), CH-17 (Qin-ai), and EH-13 (Swallow Grotto). The drilling report showed the rock types were slate, quartzite, and marble, and their Vs30 estimations were larger than 1000 m/s. The velocities for mountainous areas showed a wide range of values, with scattered data points. Although we added method AW09 to mitigate the lack of data points in mountainous areas, the maximum Vs30 value for AW09 was 900 m/s. Therefore, removing samples located in these areas resulted in a significant effect on the interpolation. Figures 4 and 5 show that maximum error values larger than ± 200 m/s are often located in mountainous area. The mean square standard error (MSSE) result also showed that the C17 and L18 methods still yield significant error values at figure 7.

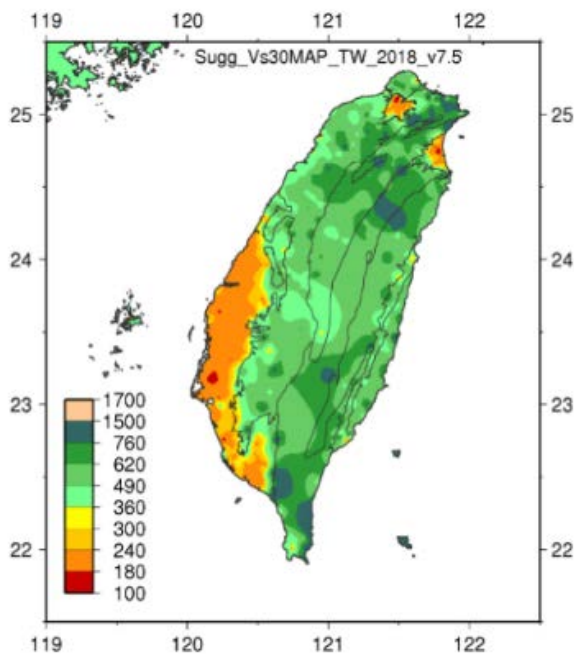


Figure 2. EGDT image of the study site

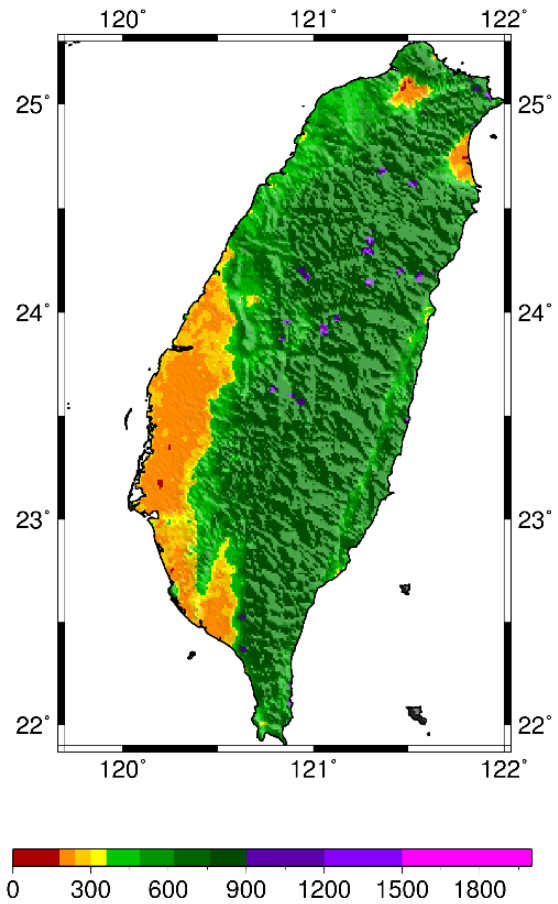


Figure 3. The kriging result from this study.

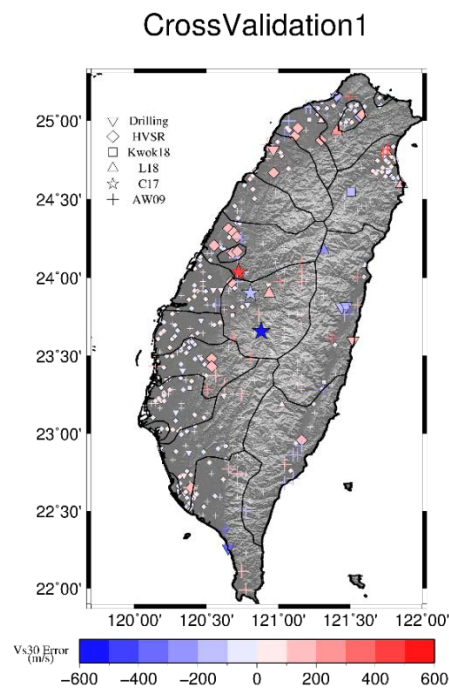


Figure 4. The error distribution of the sample based on cross validation. This figure refers to Case 1

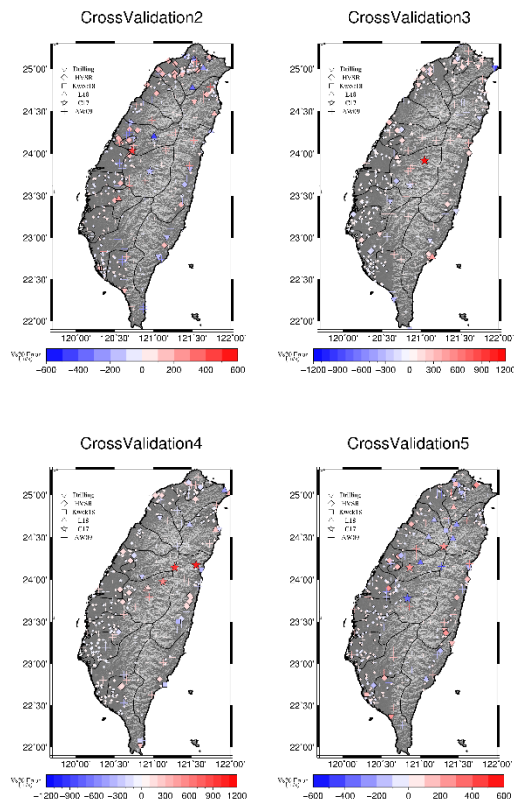


Figure 5. The error distribution of the sample based on cross validation. This figure refers to Cases 2–5

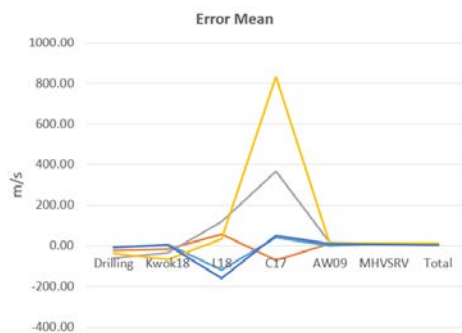


Figure 6. Mean error value based on cross validation. Each color represents a different case. C17 and L18 show a larger error value

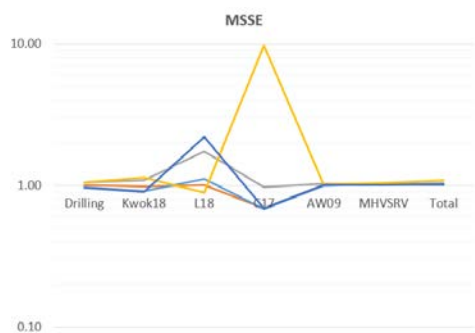


Figure 7. Mean Square Standard Error value base on cross validation. Each color represents different case. C17 and L18 still have a larger error value.

Conclusion

We test model and result show our database can obtain 500 meter \times 500 meter Vs30 grid result. The cross validation sample located on metropolitan are stable. We also control the estimation by data weight for others located on the value rapid changes area. On mountain area we only have AW09 data. There are 14 station for C17 that Vs30 value between 900 m/s and 1941 m/s. If we can obtain more Vs30 data on mountain area in the future, we will consider to add them to our database to improve the confidence.

Reference

- Allen, T. I., & Wald, D. J. (2009). On the use of high-resolution topographic data as a proxy for seismic site conditions (VS 30). *Bulletin of the Seismological Society of America*, 99(2A), 935-943.
- Ancheta, T. D., Darragh, R. B., Stewart, J. P., Seyhan, E., Silva, W. J., Chiou, B. S.-J., Wooddell, K. E., Graves, R. W., Kottke, A. R., Boore, D. M., Kishida, T., and Donahue, J. L., 2013. PEER NGA-West2 Database, PEER Report No. 2013/03, Pacific Earthquake Engineering Research Center, University of California, Berkeley, CA, 134 pp.
- Kwok, O. L. A., J. P. Stewart, D. Y. Kwak, and P. L. Sun (2018). Taiwan-Specific Model for V S30 Prediction Considering Between-Proxy Correlation. *Earthquake Spectra*
- Liu, K. S., & Tsai, Y. B. (2015). A Refined Vs30 Map for Taiwan Based on Ground Motion Attenuation Relationships. *Terrestrial, Atmospheric & Oceanic Sciences*, 26(6).
- Seyhan, E., and Stewart, J. P., 2014. Semi-empirical nonlinear site amplification from NGA-West2 data and simulations, *Earthquake Spectra* 30, 1241–1256.
- Thompson, E. M., & Wald, D. J. (2012, September). Developing VS30 site-condition maps by combining observations with geologic and topographic constraints. In *The 15th World Conference on Earthquake Engineering: September (pp. 24-28)*.
- 林哲民、郭俊翔、黃雋彥、謝宏灝、思敬章、溫國樑，「臺灣 TSMIP 強震站之淺層剪力波速度構造研究」，NCREE-18-019，2018，141 頁。
- 陳家立、郭俊翔、陳棋炫、林燕初、謝宏灝（2017），「估算台灣中部山區淺部地層之速度構造」，中華民國地球物理學會與中華民國地質學會 106 年會暨學術研討會，S4-P-185，台南，台灣。
- 陳俊德、郭俊翔、林哲民、黃雋彥、溫國樑(2020)，「使用為地動方法估算全臺淺部剪力波速剖面」，中華民國第 15 屆結構工程暨第 5 屆地震工程研討會，台南，台灣，9 月 2 日至 4 日。
- 郭俊翔、林哲民、章順強、溫國樑、謝宏灝（2017）。臺灣強震測站場址資料庫，國家地震工程研究中心，NCREE-17-004，共 80 頁。

Stiffness Configuration of Strongbacks for Reducing Inter-story Drift Concentration

Jui-Liang Lin¹ Meng-Kwee Kek² and Keh-Chyuan Tsai³

林瑞良¹、郭銘桂²、蔡克銓³

Abstract

This paper examines the stiffness configuration of strongbacks to effectively mitigate inter-story drift concentration in buildings. We first develop a simplified numerical model for simulating buildings with strongbacks. This model is capable of reflecting the various deformation types of the strongbacks and original buildings, where the story stiffness and story mass distribution types are not limited. We used this model to conduct a parametric analysis of the ratio of the strongback stiffness to that of the original buildings with different heights and deformation types. Buildings with uniform story mass and story stiffness distributions over building height were considered in the parametric analysis, rather than other specific distributions. One nine-story steel moment-resisting frame building was investigated to verify the effectiveness of the proposed strongback stiffness configuration.

Keywords: seismic design, strongback, inter-story drift, generalized building model

Introduction

Excessive inter-story drift concentrated on one or few stories risks the premature failure of buildings, such as by an overall building collapse or “pancake” crush of a few stories. Such building damage usually results in major casualties during seismic events. Therefore, many researchers have proposed innovative designs to unify and optimize the inter-story drift distribution over the building height (Al-Ansari and Senouci, 2011; Lin et al., 2019). On the other hand, using strongbacks, which act like relatively stiff spines that constrain the deformation of original buildings (Fig. 1a), has been proven as an effective alternative to reduce inter-story drift concentration (Qu et al., 2014; Simpson and Mahin, 2018).

It is understood that moment-resisting frames tend to have a pure shear deformation type (Fig. 1b). In contrast, buildings with walls, braces, or cores tend to have a pure flexural deformation type (Fig. 1c). In addition, higher mode effects on inter-story drift distribution increase as building height increases. The present study aims to look at the effect of strongback stiffness configuration on mitigating inter-story drift

concentration in buildings with various deformation types and numbers of stories. Although Fig. 1a conceptually depicts the strongback as a rigid pole alongside the original building, a real strongback with limited stiffness also undergoes deformation. Therefore, the deformation type of the strongback itself is also a key factor considered in this study.

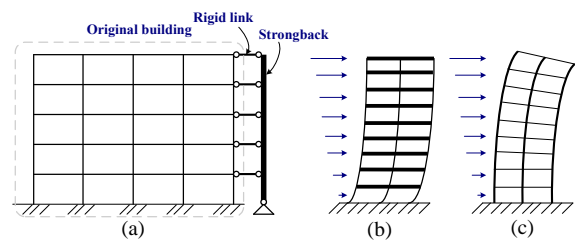


Fig. 1. Depictions of (a) a building with a strongback, and the deformations of (b) a shear-type building and (c) a flexural-type building.

Simplified Numerical Model

The generalized building model (GBM), a simplified numerical model modified from the cantilever beam model (Miranda and Taghavi, 2005),

¹ Research Fellow, National Center for Research on Earthquake Engineering

² Graduate Student, Department of Civil Engineering, National Taiwan University

³ Professor, Department of Civil Engineering, National Taiwan University

is capable of simulating buildings with any deformation type (Lin et al., 2019). In addition to an arbitrary number of stories, the GBM (Fig. 2) uniquely simulates buildings with an arbitrary story mass and stiffness distribution over the building height, unlike the cantilever beam model. The present study further extends the GBM to simulate buildings with strongbacks (Fig. 1a). This extended GBM, designated as GBMSB herein, is introduced as follows.

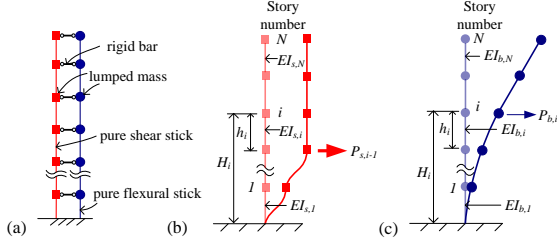


Fig. 2. (a) The GBM and (b) the pure shear stick and (c) pure flexural stick deform under lateral loads $P_{s,i-1}$ and $P_{b,i}$, respectively.

The GBMSB consists of two parts: one is the GBM representing the original building and the other representing the strongback, which are modeled as a shear stick rigidly connected to a flexural stick. The two parts are combined together through rigid links (Fig. 3a). Compared with the GBM's two sticks with lumped masses and fixed bases, the two sticks of the strongback model are pinned to the ground and have zero mass (Fig. 3a). Therefore, the mass matrix of the GBMSB is the same as the GBM's mass matrix, which is a diagonal matrix straightforwardly secured from the original building. The pure shear stick of the strongback has the following lateral stiffness matrix:

$$\mathbf{K}_s^{SB} = k_{s,1}^{SB} \mathbf{E}_s^{SB} \quad (1)$$

where $k_{s,1}^{SB} = EI_{s,1}^{SB}/h_1^3$ and $EI_{s,1}^{SB}$ is the flexural rigidity of the pure shear stick's lowest segment (Fig. 3b). In addition, the matrix \mathbf{E}_s^{SB} (Eq. 1) is a matrix with non-zero elements on its diagonal band. Moreover, κ_r^{SB} , $r = 1$ to N , is the ratio of the r -th segment's lateral stiffness to that of the lowest segment, obtained while treating the base of the pure shear stick as a fixed end. Because the bottom of the pure shear stick of the strongback is a hinge, the second term of the bottom-right corner element is $\kappa_1^{SB}/4$, rather than κ_1^{SB} . The pure flexural stick of the strongback has the following lateral stiffness matrix:

$$\mathbf{K}_b^{SB} = (\mathbf{F}_b^{SB})^{-1} \quad (2)$$

where \mathbf{F}_b^{SB} is the pure flexural stick's $N \times N$ flexibility matrix. \mathbf{F}_b^{SB} is obtained by applying the unit-load method to the stand-alone pure flexural stick with an added rotational spring at its bottom. The purpose of adding a rotational spring is to

make the stand-alone pure flexural stick stable so that the unit-load method is applicable to the stick. The rotational stiffness of the added rotational spring is expressed as $k_\theta = \mu EI_{b,1}^{SB}/h_1$, where μ is a scalar, and $EI_{b,1}^{SB}$ is the flexural rigidity of the pure flexural stick's lowest segment (Fig. 3b). The desired boundary condition, a hinge at the bottom of the pure flexural stick, is achieved by approximating μ as zero. Therefore, the i -th row and j -th column element of \mathbf{F}_b^{SB} , denoted as f_{ij}^{SB} , is

$$f_{ij}^{SB} = \frac{e_{ij}^{SB}}{k_{b,1}^{SB}} \quad (3)$$

where $k_{b,1}^{SB} = EI_{b,1}^{SB}/h_1^3$ and e_{ij}^{SB} (Eq. 3) is

$$e_{ij}^{SB} = \begin{cases} \begin{matrix} \bar{H}_{N+1-j}^1 \bar{H}_{N+1-i}^1 \\ \mu \\ \bar{H}_{N+1-j}^r \bar{H}_{N+1-i}^r (\bar{H}_r^r - \bar{H}_{r-1}^r) \\ - \frac{(\bar{H}_{N+1-j}^r + \bar{H}_{N+1-i}^r)}{2} [(\bar{H}_r^r)^2 - (\bar{H}_{r-1}^r)^2] \\ + \frac{1}{3} [(\bar{H}_r^r)^3 - (\bar{H}_{r-1}^r)^3] \end{matrix} & i \geq j \\ e_{ji}^{SB}, & i < j \end{cases} \quad (4)$$

In Eq. 4, $\bar{H}_s^r = H_s/h_r$, where h_r is the r -th story's height, and H_s is the height from the ground to the s -th story (Fig. 3b). The strongback's pure flexural stick thus has the following lateral stiffness matrix:

$$\mathbf{K}_b^{SB} = k_{b,1}^{SB} \mathbf{E}_b^{SB} \quad (5)$$

where \mathbf{E}_b^{SB} is the inverse of the matrix composed of the element e_{ij}^{SB} for i and $j = 1$ to N , with the scalar μ set equal to zero. Therefore, the lateral stiffness matrix of the strongback, denoted as \mathbf{K}_{SB} , is the sum of the stiffness matrices of its two sticks:

$$\mathbf{K}_{SB} = \mathbf{K}_s^{SB} + \mathbf{K}_b^{SB} = k_{SB} [\alpha_{SB} \mathbf{E}_s^{SB} + (1 - \alpha_{SB}) \mathbf{E}_b^{SB}] \quad (6)$$

where

$$k_{SB} = k_{s,1}^{SB} + k_{b,1}^{SB} = \frac{E(I_{s,1}^{SB} + I_{b,1}^{SB})}{h_1^3} = \frac{EI_{SB}}{h_1^3}$$

$$\alpha_{SB} = \frac{k_{s,1}^{SB}}{k_{s,1}^{SB} + k_{b,1}^{SB}} \quad (7)$$

Eq. 7 indicates that α_{SB} ranges from zero to one. The strongback has a pure flexural deformation type ($\mathbf{K}_{SB} = k_{b,1}^{SB} \mathbf{E}_b^{SB}$) while $\alpha_{SB} = 0$ (i.e., $k_{s,1}^{SB} = 0$). The strongback has a pure shear deformation type ($\mathbf{K}_{SB} = k_{s,1}^{SB} \mathbf{E}_s^{SB}$) while $\alpha_{SB} = 1$ (i.e., $k_{b,1}^{SB} = 0$). Finally, the lateral stiffness matrix of the GBMSB, denoted \mathbf{K}_{GBMSB} , is the sum of the stiffness

matrices of the GBM (\mathbf{K}_{GBM}) and the strongback (\mathbf{K}_{SB}):

$$\begin{aligned} \mathbf{K}_{GBMSB} &= \mathbf{K}_{GBM} + \mathbf{K}_{SB} \\ &= k \left\{ \left[\alpha \mathbf{E}_s + (1-\alpha) \mathbf{E}_b \right] + \beta \left[\alpha_{SB} \mathbf{E}_s^{SB} + (1-\alpha_{SB}) \mathbf{E}_b^{SB} \right] \right\} \end{aligned} \quad (8)$$

where $\beta = k_{SB}/k$. The definitions of all the parameters related to the GBM (\mathbf{K}_{GBM} , \mathbf{E}_s , \mathbf{E}_b , α , and k) are similar to their strongback counterparts (\mathbf{K}_{SB} , \mathbf{E}_s^{SB} , \mathbf{E}_b^{SB} , α_{SB} , and k_{SB}) and are reported previously (Lin et al., 2019).

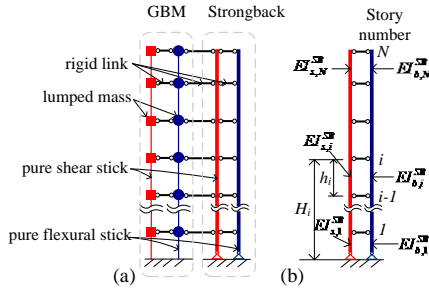


Fig. 3. The models of (a) the GBMSB and (b) the strongback.

Strongback Stiffness Configuration

The stiffness ratio of the strongback to the original building is considered in this study. It is natural that the effectiveness of a strongback becomes more substantial when its stiffness increases. Nevertheless, due to the limits imposed by engineering cost, the practical stiffness of a strongback should be reasonable. Figures 4a and 4b show the vertical distributions of the peak inter-story drift ratio, denoted IDR_{peak} , for 20-story GBMSBs with $\beta = 1$ and 5, respectively. Comparing the first plot ($\alpha = 0$) with the last plot ($\alpha = 1$) of Fig. 4 shows that adding a strongback is more effective in mitigating the inter-story drift concentration in pure-flexural buildings compared with pure-shear buildings. In addition, comparing Fig. 4a with Fig. 4b indicates that the effectiveness of strongbacks increases when the value of β increases from one to five. Figure 4 also shows that when α_{SB} increases from 0 to 1, the distributions of the IDR_{peak} gradually approach vertical straight lines, in addition to an overall decrease in IDR_{peak} . That is to say, shear-type strongbacks (i.e., with greater α_{SB} values) are more effective than flexural-type strongbacks (i.e., with smaller α_{SB} values).

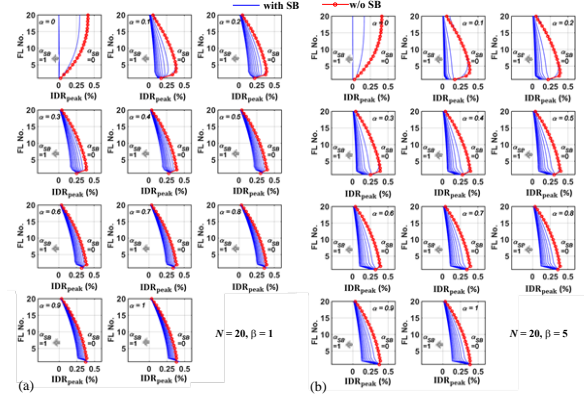


Fig. 4. IDR_{peak} distributions for 20-story GBMSBs: (a) $\beta = 1$ and (b) $\beta = 5$.

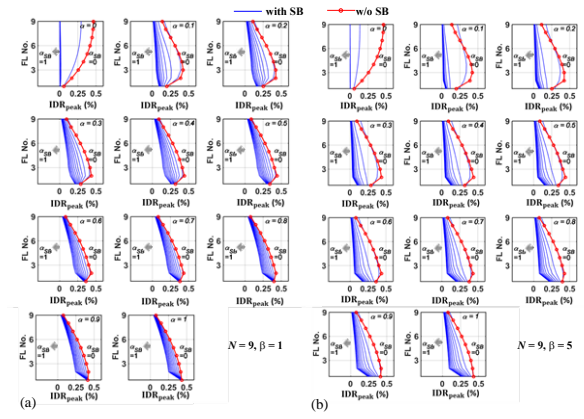


Fig. 5. IDR_{peak} distributions for nine-story GBMSBs: (a) $\beta = 1$ and (b) $\beta = 5$.

Figures 5a and 5b show the vertical distributions of the peak inter-story drift ratio for nine-story GBMSBs with $\beta = 1$ and 5, respectively. Comparing the curve of Fig. 5a with its counterpart shown in Fig. 4a as $\alpha = \alpha_{SB} = \beta = 1$ shows that the curve of the nine-story GBMSB is straighter than the twenty-story GBMSB. The effect of the strongback on reducing the inter-story drift concentration therefore decreases when the building height increases.

Numerical Verification

The example nine-story steel building is the SAC research project prototype for buildings in Los Angeles (FEMA-355, 2000). This building, designated SAC9 in this study, is a typical office building with perimeter moment frames located on stiff soil. Figures 6a and 6b show the typical floor plan and elevation. Each story mass is concentrated at the geometric center of the floor plan. All the floor slabs are assumed to be rigid diaphragms. A set of 20 ground motion records with a 475-year return period is applied in the building's z-direction. The ground motion records, denoted as la1-la20, were those that the SAC research project exerted on the prototype buildings of

Los Angeles. Figure 6c shows the 5% damped pseudo-acceleration response spectra of la1–la20.

Figures 7a and 7b show the IDR distributions over the heights of SAC9 and SAC9-SB, respectively, subjected to la1–la10. Each line in each plot of Fig. 7 depicts the IDR distribution at the point in time that a certain story reaches its minimum or maximum IDR. Therefore, the maximum number of blue and red lines in each plot is equal to nine when the minimum or maximum IDRs of the nine stories occur at completely different points in time. Figure 6 clearly shows that using the strongback makes it so that more stories of SAC9 simultaneously reach their minimum or maximum IDR. The IDR distributions of SAC9-SB subjected to la1–la10 are also much more uniform than those of SAC9. Accordingly, the proposed strongback stiffness configuration is effective in mitigating inter-story drift concentration for SAC9.

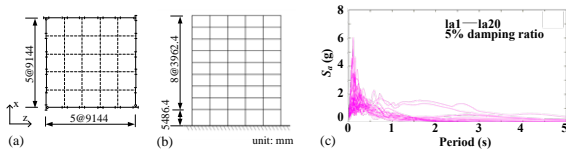


Fig. 6. (a) Floor plan and (b) elevation of SAC9, and (c) pseudo-acceleration response spectra of la1–la20.

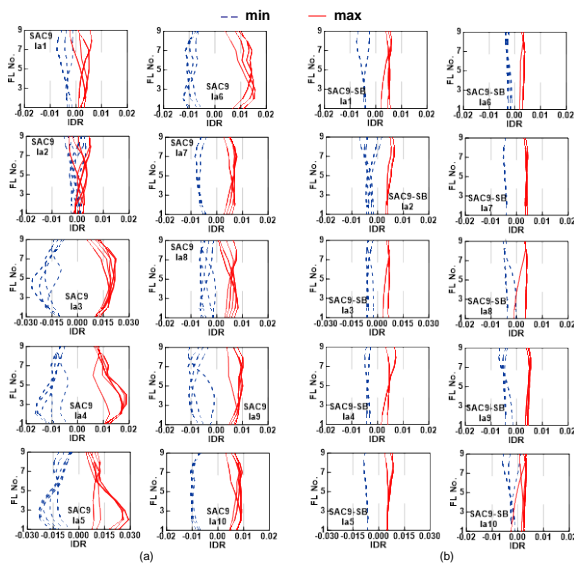


Fig. 7. IDR distributions over the building heights of (a) SAC9 and (b) SAC9-SB subjected to la1–la10.

Conclusions

The proposed GBMSB considers not only varied story masses and story stiffnesses, but also the various building and strongback deformation types. We conducted a comprehensive parametric study of the stiffness configuration of strongbacks for mitigating inter-story drift concentration in buildings using the GBMSB. The results indicate that using strongbacks to mitigate inter-story drift concentration is more

effective in low- or mid-rise buildings compared to high-rise buildings. In addition, adding strongbacks to mitigate inter-story drift concentration is more effective for buildings with a flexural deformation type. In contrast, strongbacks with shear deformation types outperform those with flexural deformation types. The numerical verification results from a nine-story steel moment-resisting frame building consistently confirm the effectiveness of the proposed strongback stiffness configuration.

References

- Al-Ansari, M. and Senouci, A. (2011), “Drift optimization of high-rise buildings in earthquake zones”, *The Structural Design of Tall and Special Buildings*, 20, 208–222.
- FEMA-355C. (2000), “State of the art report on systems performance of steel moment frames subject to earthquake ground shaking”, prepared by the SAC Joint Venture for the Federal Emergency Management Agency.
- Lin, J. L., Dai, J. Y. and Tsai, K. C. (2019), “Optimization approach to uniformly distributed peak inter-story drifts along building heights”, *Journal of Structural Engineering*, ASCE, 145(5), 04019032.
- Miranda, E., and Taghavi, S. (2005), “Approximate floor acceleration demands in multistory buildings I: formulation”, *Journal of Structural Engineering*, ASCE, 131(2), 203–211.
- Qu, B., Sanchez-Zamora, F. and Pollino, M. (2014), “Mitigation of inter-story drift concentration in multi-story steel concentrically braced frames through implementation of rocking cores”, *Engineering Structures*, 70, 208–217.
- Simpson, B. G., and Mahin, S. A. (2018), “Experimental and Numerical Investigation of Strongback Braced Frame System to Mitigate Weak Story Behavior”, *Journal of Structural Engineering*, 144 (2), 04017211.

Nonlinear Dynamic Analysis Research Based on TEASPA Fiber Section Model

Yeong-Kae Yeh¹ and Te-Kuang Chow²

葉勇凱¹、周德光²

Abstract

Using PERFORM-3D software, Replace nonlinear hinge with fiber section to explore and simulate the backbone curve of TEASPA's RC component. It also associated with the function of mutual control of axial force and bending moment and free setting of hysteresis loop rules. At the same time, the analysis results of the fiber section model and the nonlinear hinge model are compared with the three-story and seven-story structures of the South Laboratory of the NCREC. The analysis results show that the nonlinear dynamic analysis of the overall structure based on the fiber section model is efficient and feasible. It is compared that the experimental values, nonlinear hinges and fiber section models with each other. The results explain that fiber section model can reflect the axial force and bending moment of PM interaction. The convergence of the descending for fiber section model is better than the nonlinear hinge model. It can be use in nonlinear dynamic analysis. It means that the fiber section can make up for the shortcomings of PM non-linear hinges in ETABS that cannot freely set hysteresis behavior. Based on the fiber section model obtained by TEASPA method, the analysis results of the three-story and seven-story structures show that there is a certain degree of accuracy with the experimental values.

Keywords: detailed seismic evaluation, fiber section model, nonlinear hinge model, TEASPA

Introduction

At present, the detailed evaluation method of TEASPA earthquake resistance commonly used by engineers in our country [1,2], adopts TEASPA's non-linear model of concrete structure, and uses non-linear lateral push analysis to obtain the capacity curve of the building structure, that is, to establish the structural base shear force and the roof displacement relationship curve, and then based on the performance requirements of the building, set the performance target point on the capacity curve, and then use the Capacity Spectrum Method [3] to find the performance target earthquake with the roof displacement response of the performance target point. The performance target design earthquake is presented in terms of the seismic response spectrum and the maximum surface acceleration during the earthquake. If the performance target earthquake is greater than the 475 design earthquake, it means that the building has sufficient earthquake resistance; otherwise, the

building needs to strengthen its earthquake resistance. TEASPA2.0[4] uses M3 non-linear hinge. After TEASPA3.1 version [5], it switched to PM non-linear hinge with mutual axial force and bending moment, which also lifted the limit on the number of floors and obtained certification from the Construction and Construction Administration. For the seismic evaluation of mid-to-high-rise buildings, nonlinear static lateral thrust analysis is still used in China. However, the higher the floor, the higher the error of the analysis. It is necessary to check the seismic performance of the building with nonlinear dynamic analysis; however, General software packages cannot freely set the hysteresis energy dissipation mode of PM nonlinear hinges. Therefore, this study explores replacing nonlinear hinges with fiber sections and simulating the spine curve of TEASPA's RC members, which has mutual axial force and bending moments. And freely set the function of hysteresis energy dissipation mode.

¹ Research Fellow, National Center for Research on Earthquake Engineering, ykyeh@ncrec.narl.org.tw

² Assistant Technician, National Center for Research on Earthquake Engineering, tkchow@ncrec.narl.org.tw

The fiber section model was established for the three-story and seven-story frame specimens of the southern laboratory of the National Earthquake Center [6], based on the single-column lateral thrust analysis as a benchmark, so that the frame model can establish its fiber based on the single-column lateral thrust analysis. The cross-section model adopts the TEASPA seismic evaluation program developed by the National Earthquake Center. The resulting fiber cross-section model can fully conform to the TEASPA's nonlinear model. The three-story and seven-story structures of the fiber section model are used to perform nonlinear dynamic analysis to obtain the overall structural response. The results are compared with experimental values, nonlinear hinges, and fiber section models, based on the fiber section obtained by TEASPA. For the model, the analysis results of the three-story and seven-story structures show a certain degree of accuracy with the experimental values. This paper adopts the recommendations of the second edition of the National Earthquake Center Technical Manual [4] to set the bending moment nonlinear hinge of the member, and perform the nonlinear dynamic analysis with the package software PERFORM-3D [7].

Fiber Section Introduction

The fiber element model, also known as the section discrete element, is the most detailed analysis model in the nonlinear analysis of reinforced concrete frame structures and is close to the actual structural force performance. It has a wide range of applications; its principle is to divide the component into several sections longitudinally. The deformation of a certain section in the middle of each section represents the deformation of the section. The section is divided into several concrete fibers and reinforcing steel fibers. The force state of the fiber element is only one-dimensional. Strain, through the integration of each sub-block or layer along the section to obtain the generalized stiffness relationship between the internal force of the section and the corresponding deformation, and then obtain the stiffness matrix of the component element.

PERFORM-3D provides a beam-column fiber section model [7]. For the beam fiber section model, only the fiber division in one direction of the section is considered. Therefore, only one-way compression and bending interaction (PM) can be considered, section torsion, Shear force and out-of-plane bending are assumed to be elastic and are dedicated to simulating the unidirectional nonlinear bending of the beam section; as for the column fiber section model, the fiber division in two directions can be considered, so the bidirectional compression and bending interaction can be considered (PMM), the same cross-section torsion and shear are assumed to be elastic, which is mainly used for double-bending simulation of column cross-section.

In PERFORM-3D, the beam-column element is composed of a Frame Member Compound Component, and a frame composite component can be composed of multiple basic components (such as nonlinear hinges, elastic sections, node rigid domains, strength sections, etc.) ; If the fiber section model is used, the fiber section can be assembled into the frame composite component. For beam-column members, under the action of earthquakes, nonlinear deformations are mainly concentrated at both ends. Therefore, in addition to the rigid areas of the beam-column joints at both ends, they can be assembled in the form of "fiber section + elastic section + fiber section". , Where the fiber section is used to simulate the non-linear behavior that may occur at the end of the component.

Single Column Test

The NCREC produced two reinforced concrete three-dimensional structure specimens with non-ductile reinforcement for three-story and seven-story buildings. The first floor is high, the first and second floors have only columns without any walls, and the floors above the third floor. Reinforced concrete walls are installed on the two outer sides of the short direction to highlight the characteristics of the weak ground floor, and to explore the seismic performance of typical composite mid-to-high-rise buildings in Taiwan under the action of near-fault earthquakes. Before conducting three-story and seven-story shaking table experiments, one should understand the mechanical properties of structural members. Therefore, two-pillar member specimens are made with the same cross-sectional dimensions and steel bar configuration, using the multi-axial test of the National Seismological Center Taipei Laboratory The test system (MATS) performs repeated load tests [6]. Among them, the two-pillar component specimens are single-column specimens A-pillar (30×30 cm) and B-pillar (30×75 cm). The following is a single-pillar specimen nonlinear hinge model and fiber Cross-sectional model comparison. The comparison between the lateral capacity curve of the fiber section model of A-pillar and the hysteresis loop of the single-column test is shown in Figure 1, and the comparison of the lateral capacity curve of the fiber section model of the B-pillar and the hysteresis loop of the single-column test is shown in Fig. 2. It can be found The fiber model is quite close to the test value no matter in the capacity curve or the hysteresis loop.

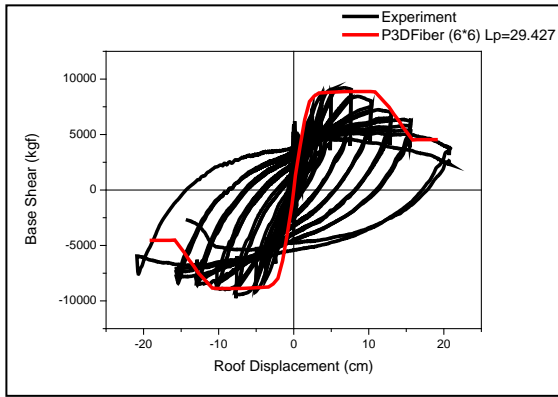


Fig. 1 Comparison of A-Column Capacity Curve of Single-Column Specimen with Test Value Hysteresis Circle Drawing

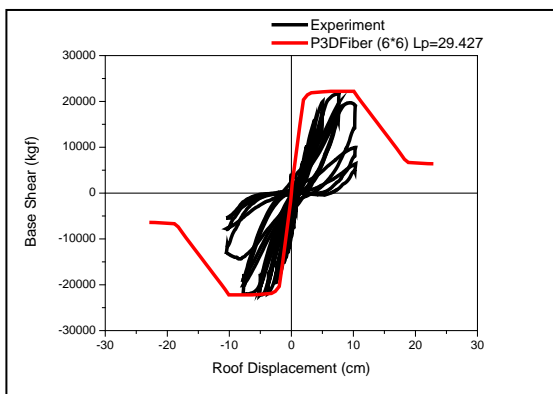


Fig. 2 Comparison of B-Column Capacity Curve of Single-Column Specimen with Test Value Hysteresis

Three-Story Structure Test

The NCREC produced a three-story non-ductile reinforced concrete three-dimensional structure specimen [4]. The first floor is high, the first and second floors have only columns without any walls, and the third floor is in the short direction. Reinforced concrete walls are set on the outside to highlight the characteristics of the weak ground floor, and to explore the seismic performance of typical high-rise buildings in Taiwan under the action of near-fault earthquakes. The southern laboratory of the National Earthquake Center officially conducted public seismic tests on the three-story test specimen [6]. There are four groups, in order, the 0728 TCU052_350gal near-field earthquake and 0728 CHY047_420gal far-field earthquake on July 28, 2006, and the Republic of China. For 0809 TCU052_800gal and 0809 TCU052_1000gal on August 9, 106, the PGA value after the earthquake record name is the target setting value, and the actual shaking table output is slightly different; set the seismic chronological analysis sequence of the frame specimen, except for the three-story frame specimen. In addition to its own weight, the earthquake duration analysis is performed first with 0809TCU052_800gal and its 1000gal, and then the post-earthquake test body is used as the prototype test body, and then four sets of seismic tests

are officially carried out continuously [11]. For the nonlinear hinge model and fiber section model of the three-story structure specimen, follow the input seismic sequence described in the previous section, and use PERFPRM-3D to perform the non-linear hinge model and fiber section model of the three-story structure. Linear dynamic analysis, comparison of the roof displacement duration records of the analysis values of the two models, the small earthquake TCU052_350gal and the large earthquake TCU052_1000gal are shown in Figure 3 and Figure 4.

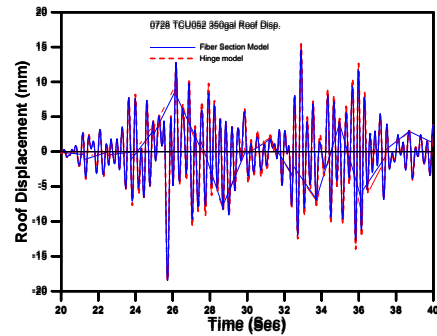


Fig. 3 TCU052_350gal roof displacement comparison

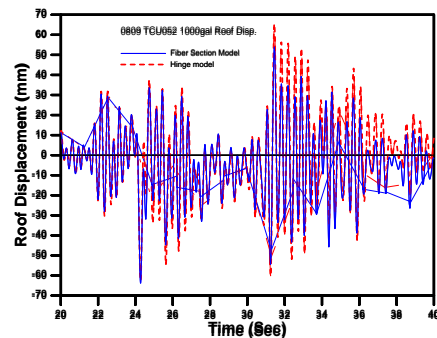


Fig. 4 TCU052_1000gal roof displacement comparison

Seven-Story Structure Test

The NCREC assembled the seven-story structure test body and carried out follow-up related tests. Refer to the blind test analysis test [12] of the reinforced concrete three-dimensional frame specimen of the seven-story building with non-ductile reinforcement. The earthquake duration and maximum surface acceleration PGA [12] of the CHY015 and CHY063 stations set by the test are used. Set the sequence of earthquake duration analysis as follows: In addition to its own weight, the sequence of earthquake duration input is CHY015_70%, CHY063_50%, CHY063_100%, CHY063_150%, and CHY063_200%; the earthquake duration event name CHY015 is a remote earthquake, and CHY063 is Near-field earthquake. PERFPRM-3D is used to perform nonlinear dynamic analysis on the nonlinear hinge model and fiber section model of the seven-story structure. The roof displacement histories of the analysis values of the two models are compared, and the small earthquake CHY015_70% and the large earthquake CHY063_200 are selected. % Is shown in Figure 5 and Figure 6.

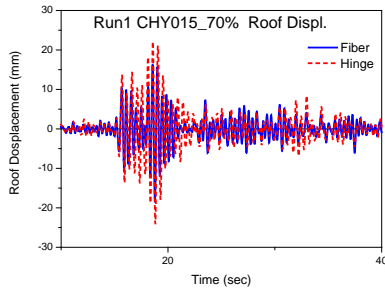


Fig. 5 CHY015_70% Roof displacement comparison

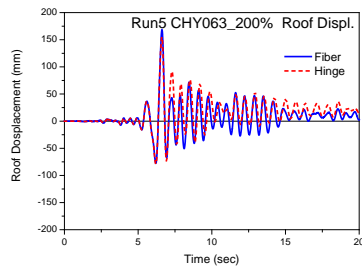


Fig. 6 CHY015_200% Roof displacement comparison

Conclusions

In this paper, based on the lateral push analysis of the fiber section model of A and B double curvature columns and the TEASPA bending moment nonlinear hinge model, the material parameters of the fiber section model are adjusted so that the capacity curves of the two are consistent, and then used as A The fiber cross-section model of the B-pillar and the three-story building and the seven-story building structure are respectively used for nonlinear dynamic analysis based on the selected far-field and near-field seismic records, and the acceleration, displacement, and floor center of each floor are analyzed. The interlayer displacement angle is compared with the experimental values of the nonlinear hinge and fiber section model to discuss the rationality and accuracy of the compared fiber section model. The comprehensive analysis results can get the following conclusions:

1. The fiber cross-section model ratio of the single-column specimen is quite close to the test data whether it is the spine curve or the hysteresis loop.
2. The analysis results of the non-linear hinge model and the fiber section model of the three-story and seven-story structures are quite close in the medium and small earthquakes. When a large near-field earthquake is applied, the analysis results begin to have obvious differences. The analysis results of the hinge model and the fiber section model are still close to the test.

3. The bending moment strength of the fiber section and the PM nonlinear hinge can change in response to the change of the axial pressure, while the nonlinear hinge cannot be changed. The fiber section model can accurately simulate the PM nonlinear hinge, and the dynamic hysteresis of structural elements can be set freely The behavior, and indeed reflects the changes in the axial force of the components in the earthquake duration, can be used in the seismic evaluation program for weak ground-floor buildings and mid-to-high-rise buildings.

References

1. Seismic Evaluation of Reinforced Concrete Structure with Pushover Analysis , NCREE-09-015 , Taipei , 2009 .
2. Technology Handbook for Seismic Evaluation and Retrofit of School Buildings Third Edition , NCREE-13-023 , Taipei , 2013 .
3. Applied Technology Council (ATC), ATC-40 Seismic Evaluation and Retrofit of Concrete Buildings, prepared by the Applied Technology Council, Redwood City, Calif., 1996.
4. Technology Handbook for Seismic Evaluation and Retrofit of School Buildings Second Edition , NCREE-09-023 , Taipei , , 2009 .
5. Taiwan Earthquake Assessment for Structures by Pushover Analysis (TEASPA V3.1) , NCREE-18-015 , Taipei , 2018 .
6. Shaking TbleTests, Instrumental Technology, Structural Identification and Npnonlinear Dyanmic Analysis of a 3-story RC Frame Specimen , NCREE-19-004 , Taipei , 2019 .
7. CSI, PERFORM-3D: Nonlinear Analysis and Performance Assessment for 3DStructures, Version 4, Computers and Structures, Inc., Berkeley, California, 2006.
8. Technology Handbook for Seismic Evaluation and Retrofit of School Buildings , NCREE-08-023 , Taipei , 2008 .
9. Laura N Lowes., and Carson Baker, Recommendations for Modeling the Nonlinear Response of Slender Reinforced Concrete Walls Using PERFORM-3D, SEAOC 2016 .
10. Priestley, M.J.N., Seible, F. and Calvi, M., Seismic Design and Retrofit of Bridges, Wiley & Sons, New York, 1996.
11. Nonlinear Dynamic Analysis Research Based on TEASPA Fiber Section Model , NCREE-20-012 , Taipei , 2020 .
12. Blind Analysis Contest on a 7-story Reinforced Concrete Building under Near-fault Earthquakes 2018~2019, Taiwan Tainan <https://www.ncree.org/conference/index.aspx?n=C20180501A0>

Pushover Analysis of a 10-Story RC Building on E-defense by TEASPA 4.0

Yu-Chih Lai¹, Tsung-Chih Chiou², Lap-Loi Chung³, Ming-Chieh Chuang⁴
Juin-Fu Chai⁵, Shyh-Jiann Hwang⁶, Jae-Do Kang⁷, and Koichi Kajiwara⁸

賴昱志¹、邱聰智²、鍾立來³、莊明介⁴、柴駿甫⁵、黃世建⁶、姜在道⁷、梶原浩一⁸

Abstract

TEASPA (Taiwan Earthquake Assessment for Structures by Pushover Analysis) is a seismic performance evaluation method proposed by the National Center for Research on Earthquake Engineering (NCREE) for analyzing existing buildings. TEASPA 4.0 adopts P-M hinges for simulation of the nonlinear behavior of columns. The P-M hinges of columns are suitable for the seismic simulation of mid- and high-rise buildings. Shaking-table tests are conducted on a 10-story full-scale RC building frame on the E-Defense in Japan. The tested building is designed in accordance with the provisions of a new building design code in Japan. In this study, we conduct pushover analysis on the tested building by using the nonlinear hinge properties using TEASPA and ASCE 41-13. We compare the simulation and test results. The analysis results show that the TEASPA method can effectively simulate a specimen, yielding conservative results that agree well with the test results. Consequently, the TEASPA method can be applied to predict the seismic performance of newly designed buildings.

Keywords: TEASPA, detailed evaluation, P-M hinge, full-scale shaking-table test.

Introduction

TEASPA (Taiwan Earthquake Assessment for Structures by Pushover Analysis) is a method proposed by the National Center for Research on Earthquake Engineering (NCREE) for evaluating the seismic performance of existing RC buildings in Taiwan. After the 1999 Chi-Chi earthquake in Taiwan, many old buildings were severely damaged. To upgrade the seismic capacity of old school buildings in Taiwan, the NCREE conducted numerous studies and experiments and proposed a detailed evaluation method (version 1) for old school buildings in 2008. NCREE, was used to conduct *in situ* experiments of

real school buildings from 2005 to 2007 to confirm that the method is conservative for old school buildings. TEASPA V4.0, proposed in 2020, improves the simulation accuracy for members, functions, and retrofit methods and also imports a web-system for online user service.

TEASPA was originally developed for existing buildings in Taiwan. However, owing to the law in Taiwan, new buildings may also need to be subjected to detailed evaluation in the future. In this study, we conducted pushover analysis using TEASPA 4.0 for a 10-story full-scale RC building frame by performing a shaking-table test on E-Defense in 2015. Here, we

¹ Assistant Technologist, National Center for Research on Earthquake Engineering

² Associate Researcher, National Center for Research on Earthquake Engineering and Jointly Appointed Associate Professor, Department of Civil and Construction Engineering, National Taiwan University of Science and Technology

³ Deputy Director General, National Center for Research on Earthquake Engineering and Professor, Department of Civil Engineering, National Taiwan University and Jointly Appointed Professor, National Cheng Kung University

⁴ Associate Researcher, National Center for Research on Earthquake Engineering

⁵ Deputy Director General, National Center for Research on Earthquake Engineering and Jointly Appointed Professor, National Taiwan University of Science and Technology

⁶ Director General, National Center for Research on Earthquake Engineering and Distinguished Professor, Department of Civil Engineering, National Taiwan University

⁷ Visiting Researcher, Earthquake Disaster Mitigation Research Division, National Research Institute for Earth Science and Disaster Resilience, Miki, Japan

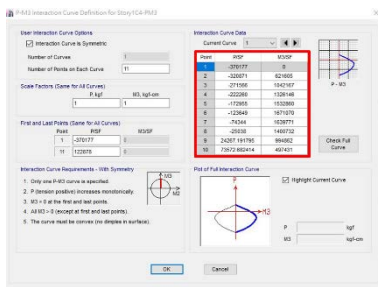
⁸ Director General, Earthquake Disaster Mitigation Research Division, National Research Institute for Earth Science and Disaster Resilience, Miki, Japan

compare the simulation results not only with the experiment results but also with the results of the method suggested by ASCE in order to discuss whether TEASPA can be used for newly constructed buildings.

Introduction of TEASPA 4.0

There are many new functions, methods, and services proposed in TEASPA 4.0, and in this section, we will introduce the simulation method for members and the pushover analysis method that will be used on a specimen. Readers can find more details in the handbook of TEASPA 4.0.

To use the method for mid-to-high-rise buildings, from V3.1 onward, NCREC has cooperated with Sinotech to develop P-M hinges of columns. In addition, the Construction and Planning Agency of Ministry of Interior, CPAMI, confirmed that the method is no longer limited to six-floor buildings but can be used for mid-to-high-rise buildings. Same as V3.1, V4.0 also considers various axial forces acting on columns. To consider the effect of axial forces and moments, V4.0 uses P-M hinges to simulate the behavior of columns (Fig. 1). To obtain the hinge properties of beam members in TEASPA 4.0, the suggestion of ASCE is followed.



(a) P-M curve of a column



(b) Hinge properties of each point on the P-M curve

Fig. 1. Details of P-M hinges in the analysis software.

V4.0 uses the fiber section method to evaluate the nominal flexural strength of members. The “modified Kent and Park model” is used to simulate the behavior of concrete with the assumption that the steel bar is

perfectly elastic. To obtain the rigidity coefficient after cracking of members, the V4.0 handbook revised the method of analyzing members. To determine the elastic rigidity coefficient of columns, V4.0 refers to the suggestion of ASCE, considering the working force of the column. To determine the elastic rigidity coefficient of beam members, V4.0 also refers to the suggestion of ASCE.

To obtain the scale of the lateral force during pushover, V4.0 follows the suggestion of ATC-40, using:

$$V_i = V \left[w_i \phi_i / \sum_j w_j \phi_j \right], \quad (1)$$

where w_i is the weight of the i th floor and ϕ_i are the components of the control mode of the i th floor.

Introduction to the 10-Story RC Building Model

The National Research Institute for Earth Science and Disaster Resilience, NIED, conducted an experiment for a 10-story RC building that was designed in accordance with the RC code in Japan in 2015. The specimen configurations are shown in Fig. 2. The details of the sections are shown in Figs. 3 and 4. The material properties of the concrete and rebar for the analysis model are shown as Tables 1 and 2. The weight of the specimen is shown in Fig. 5.

Table 1. Specifications of the concrete of each floor (kgf/cm^2).

FLOOR	f'_c	FLOOR	f'_c
2FL	700.31	7FL	492.86
3FL	733.95	8FL	499.49
4FL	587.16	9FL	529.05
5FL	490.32	10FL	447.50
6FL	463.81	RFL	417.94

Table 2. Yielding strength of rebar (kgf/cm^2).

REBAR	f_y	REBAR	f_y
D10	3876.00	D19	3969.00
D13	3680.00	D22	3954.00
D16	3007.00	S10	9493.00

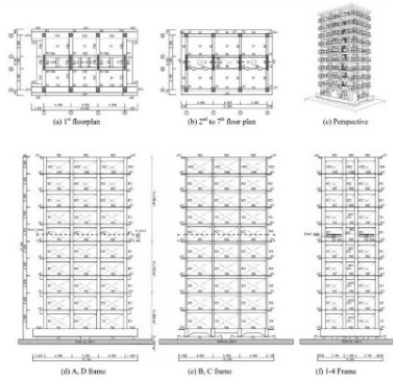


Fig. 2. Plan and elevations of the specimen.

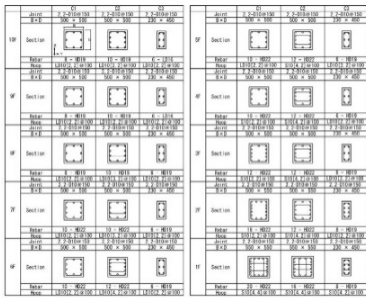


Fig. 3. Column section details.



Fig. 4. Beam section details.

	D.L. [kN]	L.L. [kN]	Sum. [kN]
R	725	0	725
10	740	57	1,522
9	694	28	2,244
8	716	28	2,988
7	949	28	3,965
6	618	188	4,771
5	780	28	5,579
4	798	28	6,405
3	817	28	7,250
2	889	57	8,196
1	1,830	29	10,055

Fig. 5. Weights of the floors of the specimen.

First, to observe the behavior of the structure, the response of the base slip was obtained experimentally. Next, a procedure was performed to make the base into a fixed base and NIED tested the response of the specimen. The test case is shown in Fig. 6. In this study, we first discuss the frame direction of specimen, using pushover analysis to compare with the fixed-base case with a 100% magnification. The pushover analysis was conducted using the auxiliary program

ETABS2016, and the derived 3D model is shown in Fig. 7.

No.	Test case	Input wave	Magnification
1	Base slip	JMA-Kobe	10%
2			25%
3			50%
4			100%
5	Fixed base	JMA-Kobe	10%
6			25%
7			50%
8			100%
9			60%

Fig. 6. Test case and input wave.

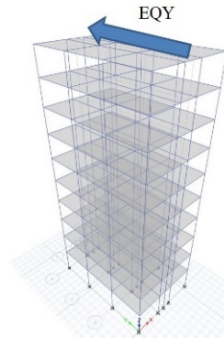


Fig. 7. 3D Model in the auxiliary program.

Analysis Results

By using the auxiliary program and TEASPA 4.0, we can conduct a pushover analysis of the specimen. To discuss the feasibility of applying TEASPA 4.0 to new buildings, we first study the frame direction of the specimen. After establishing the structure model and assigning necessary settings, we can assign nonlinear hinges from the web service. In this study, we also conducted nonlinear pushover analysis using the ASCE method for comparison with TEASPA 4.0.

The result of the pushover analysis with TEASPA 4.0 is shown in Fig. 7. The beam members in 5FL have flexural damage. The maximum base shear is 309.24 tf, and the relative displacement in the roof is 39.70 cm. The failure mode obtained with TEASPA is similar to the test result (Fig. 8). The maximum base shear obtained by the TEASPA method is 75.19% of the test result, whereas that obtained by ASCE is 67.18%. The maximum story drift by both the TEASPA and test results is at 5FL, while that by ASCE occurs at 4FL. The maximum story drift with the TEASPA method is 86.35% of the test result. The results for the relation between base shear and roof displacement and the maximum story drift are shown in Figs. 9 and 10. The figures indicate that all these parameters in the case of the TEASPA method are relatively more accurate.

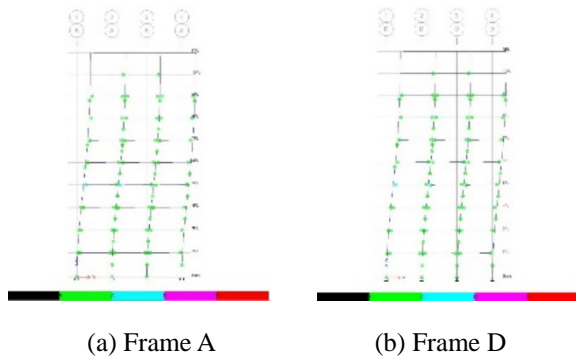


Fig. 7. Last step of the pushover analysis (TEASPA 4.0).

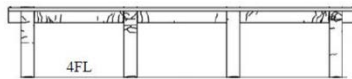


Fig. 8. Damage of specimen frame A (50% fixed base).

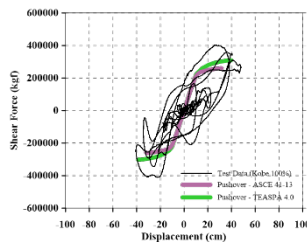


Fig. 9. Comparison of the TEASPA 4.0 and ASCE results with the test results in terms of the relationship between base shear and roof displacement.

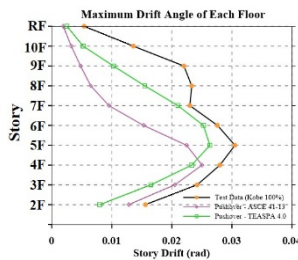


Fig. 10. Comparison of the TEASPA 4.0 and ASCE results with the test results in terms of the maximum story drift.

Conclusions

In this study, both the TEASPA method and ASCE were used on the frame direction of the test specimen. The results showed that the TEASPA method proposed by NCREE accurately simulates strength, damage mode, and drift tendency in comparison to the test results. The study also confirmed that TEASPA 4.0 yielded a good simulation for performing pushover analysis of newly constructed buildings. Thus, this method can be effectively applied for seismic performance prediction of new buildings

in the future.

References

- Tsung-Chih Chiou, Lap-Loi Chung, Yaw-Shen Tu, Yu-Chih Lai, Chien-Chuang Tseng, Pu-Wen Weng, Ming-Chieh Chuang, Yeong-Kae Yeh, Chi-Hang Li, Min-Lang Lin, Jia-Xian Wang, Wen-Cheng Shen, Fu-Pei Hsiao, Qiang Xue, and Shyh-Jiann Hwang, "Technical Handbook for Taiwan Earthquake Assessment and Strengthening of Structures by Pushover Analysis (TEASPA V4.0)," NCREE, Taiwan, Taipei, Report NO. NCREE-20-005.
- ASCE/SEI 41-13, "Seismic Evaluation and Retrofit of Existing Buildings (41-13)," American Society of Civil Engineers (ASCE), Reston, VA, 2014, 518 pp.
- Scott, B. D., Park, R., and Priestley, M. J. N., "Stress-Strain Behavior of Concrete Confined by Overlapping Hoops at Low and High Strain Rates," ACI Journal, Proceedings, V. 79, No. 1, 1982, pp. 13-27.
- ATC-40, Seismic evaluation and retrofit of concrete buildings. Report No. SSC 96-01, Applied Technology Council, 1996.
- K. Kajiwara, Y. Tosauchi, E. Sato, K. Fukuyama, T. Inoue, H. Shiohara, T. Kabeyasawa, T. Nagae, H. Fukuyama, T. Kabeyasawa and T. Mukai, (2017). "2015 Three-dimensional Shaking Table Test of a 10-story Reinforced Concrete Building on the E-Defense Part 1: Overview and Specimen Design of the Base Slip and Base Fixed Tests", Proceedings of the 16th WCEE, Santiago, Chile, Paper N° 4012.
- E. Sato, Y. Tosauchi, K. Fukuyama, T. Inoue, K. Kajiwara, H. Shiohara, T. Kabeyasawa, T. Nagae, H. Fukuyama, T. Kabeyasawa and T. Mukai, (2017). "2015 Three-dimensional Shaking Table Test of a 10-story Reinforced Concrete Building on the E-Defense Part 2: Specimen Fabrication and Construction, Test Procedure, and Instrumentation Program" Proceedings of the 16th WCEE, Santiago, Chile, Paper N° 4007.
- Y. Tosauchi, E. Sato, K. Fukuyama, T. Inoue, K. Kajiwara, H. Shiohara, T. Kabeyasawa, T. Nagae, H. Fukuyama, T. Kabeyasawa and T. Mukai, (2017). "2015 Three-dimensional Shaking Table Test of a 10-story Reinforced Concrete Building on the E-Defense Part 3: Base Slip and Base Fixed Test Results," Proceedings of the 16th WCEE, Santiago, Chile, Paper N° 4016.
- K. Kajiwara, Y. Tosauchi, E. Sato, K. Fukuyama, T. Inoue, H. Shiohara, T. Kabeyasawa, T. Nagae, H. Fukuyama, T. Kabeyasawa and T. Mukai, (2017). "3-direction shaking table test of 10 story RC frame (2015) at E-defense : Outline of the test, part 1," Proceedings of the 16th WCEE, Santiago, Chile, Paper N° 4012.
- NIED, (2015). "自体研究 現行耐震設計基準に基づく 10 層 RC 造骨組の崩壊メカニズムと普及型高耐震技術に関する実験実験計画書", reference provided by NIED.
- NIED, Test details of "2015 Three-dimensional Shaking Table Test of a 10-story Reinforced Concrete Building on the E-Defense," reference provided by NIED.

Study on Seismic Retrofitting of Structures using High-Strength Fiber Resin Mortar

Fu-Pei Hsiao¹, Chia-Yi Ho², Pu-Wen Weng³, Chia-Chen Lin⁴
and Chih-Ming Kuo²

蕭輔沛¹、何家儀²、翁樸文³、林佳蓁⁴、郭至明²

Abstract

Traditional seismic retrofitting methods often affect the regular operation of buildings and require considerable time during the retrofit process. Thus, it is challenging to carry out retrofitting work in private houses. This research aims to develop new seismic retrofitting methods for existing reinforced concrete structures using high-strength fiber resin mortar. This approach can effectively improve the performance of seismic retrofitting methods, and its expected strength can be achieved within two weeks. It has a minimal impact during installation and therefore does not affect the existing functions of the building. It is particularly applicable to hospitals, commercial buildings, and private residences. In this study, different kinds of seismic retrofitting methods were tested at the National Center for Research on Earthquake Engineering laboratory. The experimental specimens were tested using horizontal cyclic loading to compare the seismic behavior of the different seismic retrofitting methods. The study uses popular seismic assessment methods for each test and compares them with our experimental results.

Keywords: Seismic retrofitting of structures; steel-brace frames; RC shear walls; stub columns

Introduction

In this study, three retrofitting methods are studied and tested: steel frame diagonal bracing retrofitting, shear wall retrofitting, and steel panel damper retrofitting. Drawing on the results of previous studies, a design test was carried out when high-strength fiber resin mortar was incorporated in the beam-column joint area of the external frame. The joint area did not suffer damage during the test. We observed that the high-strength fiber resin mortar has good stress behavior, and the strength of the external frame can be fully utilized. This research recommends that high-strength fiber resin mortar be applied to the general retrofitting method, with the aim of reducing the damage caused by shear zones and the interface connection transfer zones and of effectively improving the earthquake resistance of buildings.

Specimen Design

This study investigates three kinds of seismic retrofitting methods using six test bodies: an existing basic structural specimen (BS), two steel frame diagonal bracing retrofitting specimens (FS1 and FS2), two reinforced concrete (RC) shear wall retrofitting specimens (SS1 and SS2), and a steel panel damper retrofitting specimen (SPD). The existing basic structural specimen (BS) is designed to simulate the first-floor structure of a mid-to-high-rise building in Taiwan. Due to the limitations of the test platform, the six test bodies were designed at half the real scale.

The base structural specimen is a portal structure. The length of the test body is 4000 mm, the height is 2000 mm, and the span is 2900 mm, as shown in Fig. 1. The side column has a cross-sectional length of 300 mm, a width of 300 mm, and a clear height of 1400 mm. The retrofitting design is configured with No. 5 steel bars, and the stirrup is

¹ Research fellow, National Center for Research on Earthquake Engineering

² Graduate student, National Taipei University of Technology

³ Research assistant, National Center for Research on Earthquake Engineering

⁴ Project assistant, National Center for Research on Earthquake Engineering

configured with No. 3 steel bars with a spacing of 100 mm. The length of the upper and lower beams is 4000 mm, their cross-sectional width is 600 mm, and their depth is 300 mm. In the steel design, the main retrofitting structure is configured with No. 6 steel bars, and the stirrup is configured with No. 3 steel bars with a spacing of 100 mm. The design compressive strength of the concrete in side columns and the upper and lower beams is 210 kgf/cm².

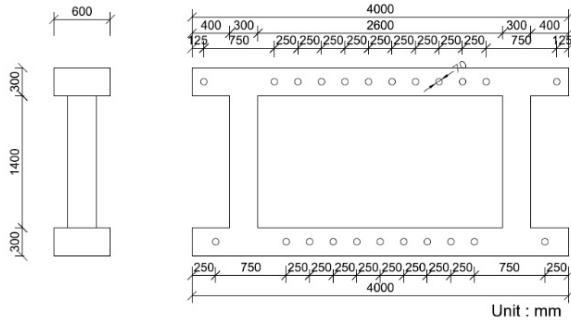


Fig. 1. Schematic diagram showing the dimensions of the basic specimen

Experimental Methods and Test Setup

The six test bodies were tested at the National Center for Research on Earthquake Engineering (NCREE) Tainan Laboratory using the Bi-Axial Testing System (BATS) shown in Fig. 2. The vertical part of the BATS includes six dynamic actuators and one static actuator at the bottom of the platform to provide vertical force and displacement; a total of four static actuators in the lateral part allow the system to be fine-tuned in this direction. The long direction is operated on by four dynamic actuators and can meet the demand of large static displacement.

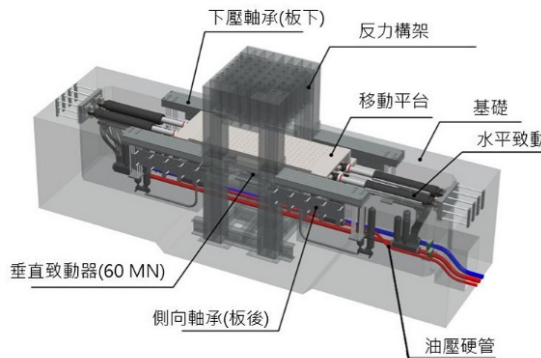


Fig. 2. Bi-Axial Testing System (BATS)

The test specimen is fixed by two sets of clamping beams. The clamping beams were fixed to the test specimen before the test, and the lower clamping beam was preloaded. The test specimen and the clamping beams were then lifted together into the BATS. In the process of assembling the test body and applying the preloading-force, it is important to avoid damage to the test body, which may cause unexpected failure and affect the test results.

Test Results

The behavior of the basic frame specimen and the five reinforced frame specimens in response to repeated load tests is discussed individually below. For each interlayer displacement angle, the lateral force is the total load applied to the moving platform by the horizontal actuator. The positive (+) symbol indicates that the test body is moving in the positive direction, while the negative (-) symbol indicates that the body is moving in the negative direction. For each interlayer displacement angle, the maximum value of the first loop is considered to be the maximum lateral force of the interlayer displacement angle.

1. Basic structural specimen (BS)

The test results, in the form of a hysteresis loop and envelope, for the base structural specimen (BS) are shown in Fig. 3. When the drift ratio is 1.5% in the first loop, both the positive and negative directions reach the maximum bearing capacity, 406 kN and -428 kN, respectively. From then until the drift ratio reaches 3.0%, the strength of the specimen is only 241 kN, which is 56% of the maximum load capacity.

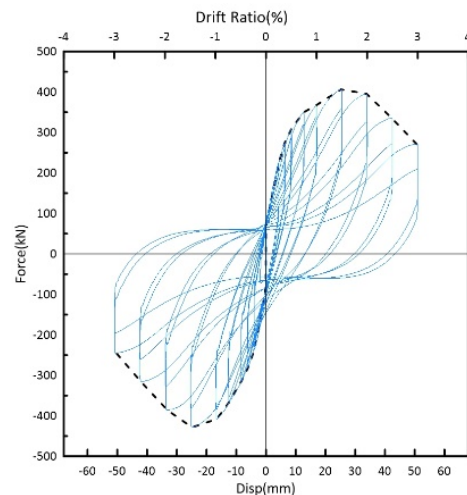


Fig. 3. Hysteresis loop and envelope for specimen BS

2. Steel frame inclined support specimen (FS1)

Results for steel frame inclined support retrofitting specimen FS1 are shown in Fig. 4. When the drift ratio = 1% in the first loop, both the positive and negative directions reach maximum load capacity, 1488 kN and -1285 kN, respectively. At this time, the reinforcing joint corner mortar spalled off and slipped with the foundation specimen, making it impossible to improve the strength. Thus, the diagonal bracing reinforcing member on the steel frame did not achieve the expected strength. When the drift ratio = 3.0%, the strength of the specimen is only 460 kN, which is 30% of the maximum load capacity, and the protective layer of the boundary column peeled off.

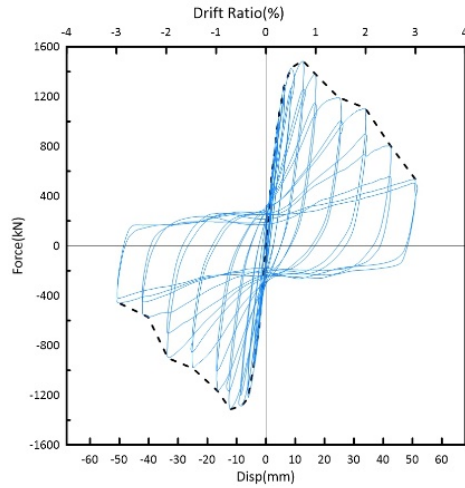


Fig. 4. Hysteresis loop and envelope of FS1

3. Steel frame inclined support specimen (FS2)

The behavior of the second steel frame inclined support retrofitting specimen (FS2) is shown in Fig. 5. When the drift ratio = 0.75%, the steel frame diagonal brace buckled during the second loop. The strength of the specimen decreases slightly, until the drift ratio = 1 %; then, the steel frame diagonal brace exerts its yield strength to make the specimen strength rise. When the drift ratio = 1.5% in the first loop, the positive and negative directions reach maximum load capacities of 1915 kN and -1733 kN, respectively. When the drift ratio = 5.0%, the strength of the specimen is only 910 kN, which is 50% of the maximum load capacity. The boundary columns and both sides of the steel frame diagonal braces separated from the retrofitting joint mortar.

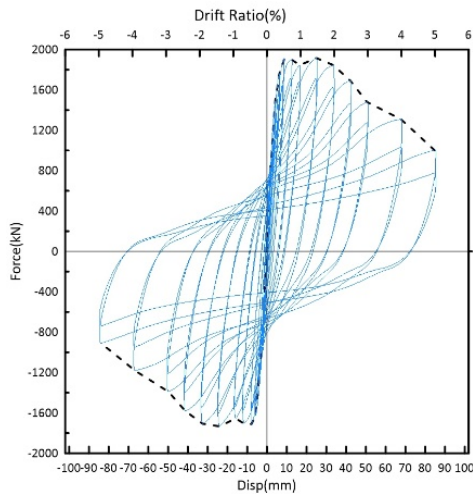


Fig. 5. Hysteresis loop and envelope for FS2

4. Open RC shear wall retrofitting specimen (SS1)

The results for the open RC shear wall retrofitting specimen SS1 are shown in Fig. 6. When the drift ratio = 1%, the maximum load capacities in the positive and negative directions for the first loop are 1561.49 kN and -1393.52 kN, respectively. In the second positive loop, the strength of the

specimen drops dramatically. At a drift ratio of 1.5%, the strength of the test body is only 622 kN, which is 40% of the maximum load capacity. The boundary columns were damaged by deflection shear, and a large amount of block mortar spalled on both sides of the openings, therefore exposing the wall retrofitting.

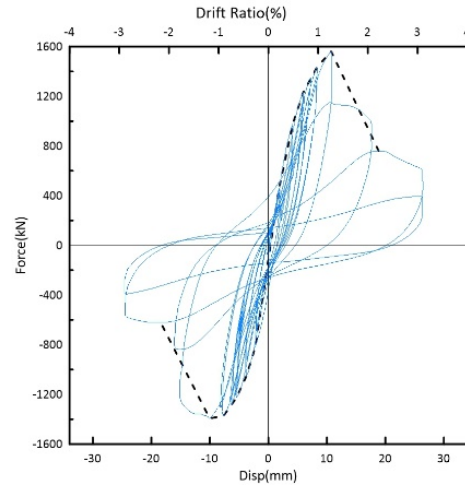


Fig. 6. Hysteresis loop and envelope for SS1

5. Inclined reinforced shear wall retrofitting specimen (SS2)

The behavior of the second inclined reinforced shear wall retrofitting specimen (SS2) is shown in Fig. 7. When the drift ratio = 1%, the maximum load capacities in the positive and negative directions in the first loop are 2807.83 kN and -2723.97 kN, respectively. In the second positive loop, the strength of the specimen drops dramatically. When the drift ratio = 2.5%, the strength of the specimen is only 164 kN in the positive direction of the first loop, which is 6% of the maximum bearing capacity. A large amount of block mortar peeled off the specimen used for the shear wall retrofitting, and the wall retrofitting became exposed and bent. The boundary column was damaged by flexural shear, and the main retrofitting and stirrups were seriously deformed.

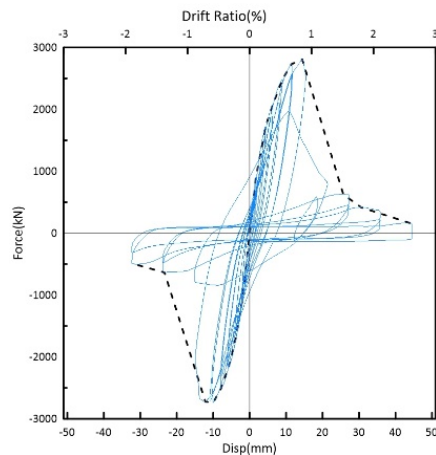


Fig. 7. Hysteresis loop and envelope for SS2

6. Steel panel damper specimen (SPD)

The steel panel damper specimen (SPD) results are shown in Fig. 7. When the drift ratio = 1.5%, the maximum load capacities in the positive and negative directions for the first loop are 665.16 kN and -660.31 kN, respectively. At this time, the mortar spalled at the corner of the reinforced joint and slipped with the foundation specimen. Thus, the strength could not be improved, and the expected strength was not achieved. When the drift ratio = 3.0%, the strength of the test body was only 466 kN, which is 70% of the maximum load capacity, and the protective layer of the boundary column spalled off. At the end of the test, we observed that unexpected horizontal cracks had appeared in the upper beam part of the test body of the foundation structure. We conclude that the reason for this may be that the concentrated stresses generated by the reinforcing members caused the test body to be damaged.

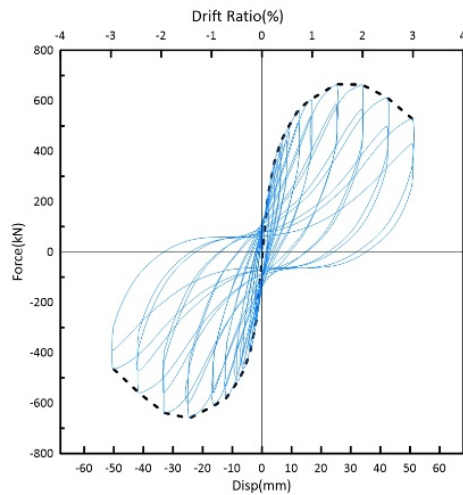


Fig. 8. Hysteresis loop and envelope for SPD

Conclusions

This research uses high-strength fiber resin mortar for seismic structural retrofitting. Test results on six model specimens showed that this mortar is effective in transmitting force, whether as a joint design or as a substitute for general concrete, and improves the shear strength of the specimens. We make the following conclusions:

1. Specially adapted steel frames with diagonal bracing and joint parts that use high-strength fiber resin mortar in their design provide good interface shear strength and reduce the logistical and time difficulties associated with retrofitting. Reinforcing steel frames with diagonal bracing members can be made in a factory. If there are challenges to construction, they can be filled with high-strength fiber resin mortar. Compared with on-site welding, retrofitting using this process potentially provides closer fits to existing structures.

2. In the second steel frame diagonal bracing specimen (FS2), high-strength fiber resin mortar was used as the filling material for the retrofitting joint. Without the use of

confining stirrups, the retrofitted member still provided sufficient strength. There was no slippage at the interfaces, which reduces construction challenges.

3. The high-strength fiber resin mortar can reach its expected compressive strength in 14 days. Applying it to the retrofitting method can shorten the installation period and reduce the impact on normal operation of existing buildings. This approach is suitable for commercial buildings and hospitals that require retrofitting.

References

- Yu-Lung Chu. (2014). Study on Existing Reinforced Concrete Structures Retrofitting by Steel-braced Frame with Direct Connection. Degree Thesis of the Institute of Civil and Disaster Prevention Engineering, National Taipei University of Technology.
- Wei-Li Yen .(2018). Research on Seismic Retrofitting for Existing Buildings with Exterior Reinforced Concrete Frames. Degree Thesis of the Institute of Civil and Disaster Prevention Engineering, National Taipei University of Technology.
- ZI-En Gu. (2019). A study on the improvement of retrofit method using RC shear wall and its damage detection. Degree Thesis of the Institute of Civil and Disaster Prevention Engineering, National Taipei University of Technology.
- Qiao-Han Jian. (2015). Study of Steel Frame Bracing System with Indirect Connection on Seismic Retrofitting of RC Frame. Department of Civil Engineering National Taiwan University.
- Chinese Society of Structure Engineering. (2005). Steel Structure Design Handbook (Limit States Design). Scientific & Amp Technical Publishing Co., Ltd.
- Hilti Taiwan Company Ltd. (2018). Anchor Fastening technical manual.
- Chung-Hsiang Hsu, Chao-Hsien Li, Pu-Yuan Chin, Keh-Chyuan Tsai. (2017). Seismic Design , Tests and Analysis of Steel Panel Dampers for Steel Moment Frames , Structural Engineering, Vol. 32, No. 2.
- Keh-Chyuan Tsai, An-Chien Wu, Pao-Chun Lin, Chih-Yu Wei, Ming-Chieh Chuang. (2012). Study on the welded end-slot buckling restrained brace and delamination materials. Structural Engineering Vol.27, No. 3.
- Construction and Planning Agency, Ministry of the Interior. (2011). Seismic Design Specifications and Commentary of Buildings.
- Construction and Planning Agency, Ministry of the Interior. (2011). Design Specifications for Concrete Structures.

Reduced scale shaking table test and numerical study on a simply supported bridge crossing fault

Hsiao-Hui Hung¹ Yuan-Shuo Tseng² and Chang-Wei Huang³

洪曉慧¹、曾院碩²、黃仲偉³

Abstract

In order to understand the response of a simply supported bridge under the action of a cross-fault earthquake, this study investigated a set of 1:81 scale two-span simply supported bridge experimental models. Through small-scale shaking table experiments, we were able to compare the displacement and acceleration responses of such bridges during near-fault and cross-fault earthquakes. In addition, this study established a numerical model for comparison with the experimental results and calculated the corresponding internal force in the bridge column. The experiment used two small shaking tables to simulate near-fault and cross-fault effects using synchronous and non-synchronous inputs. The variables considered included the effect of the seismic stoppers and the direction of fault movement. Nonlinear dynamic time history analysis for displacement-input earthquake forces was conducted using SAP 2000N software. The experimental and simulation results show that the cross-fault effect was mainly reflected in the displacement of the structure. If the displacement is restricted, the internal force of the bridge pier is increased significantly. On the other hand, the dynamic acceleration of the bridge deck is mainly caused by the dynamic effect of near-fault acceleration. The research results also show that if the experiment uses a single shaking table to simulate the cross-fault effect, the calculation of the relative displacements of the bridge is not significantly different from the simulation using double shaking tables; however, the acceleration responses and the internal forces of the bridge pier may be incorrectly estimated.

Keywords: cross-fault bridges, scaled shaking table test, seismic block, near-fault earthquake.

Introduction and scope of the research

Taiwan is located at the junction of the Eurasian Plate and the Philippine Sea Plate, where active faults are densely distributed. According to the latest report published by the Central Geological Survey in Taiwan (MOEA 2012), there are 33 active faults and four suspected faults in Taiwan. Therefore, it is difficult for existing bridges and newly designed bridges to completely avoid crossing faults. In addition to being threatened by the enhanced ground motions and long-period velocity pulses from near-fault earthquakes, cross-fault bridges must also withstand the large demand for displacement caused by the permanent differential displacement of the fault. For instance, the 921 Chi-Chi earthquake that occurred in central Taiwan in 1999 (Chang 1999), the two earthquakes that occurred in Turkey (Ulusay et al. 2002) in the

same year, and the Kumamoto earthquake in Japan in 2016 (JBA 2016) all caused serious problems in many bridges that crossed faults, including adverse effects on adjacent traffic arteries. However, the domestic code for the seismic design of bridges currently only considers the effect of near-fault earthquakes, but not the effect of cross-fault earthquake. The code recommends that bridge construction should avoid cross faults, and that the code is not applicable to the design of bridges that cross active faults. Because Taiwan is intensively faulted, it is often necessary to address unexpected cross-fault threats. Therefore, it is necessary to conduct an in-depth study on the impact of cross-fault effects on bridges.

There are many existing bridges in Taiwan that are simply supported. During the 921 Chi-Chi earthquake, many simply supported bridges collapsed

¹ Research Fellow, National Center for Research on Earthquake Engineering

² Graduate Student, Department of Civil Engineering, Chung Yuan Christian University

³ Professor, Department of Civil Engineering, Chung Yuan Christian University

or were severely damaged because they crossed faults. To address this problem, this study investigates simply supported bridges by performing experimental tests on scaled-down bridge models. Two shaking tables and synchronous and non-synchronous inputs were used to simulate the effects of near-faults and cross-faults. The experimental results are compared with results of numerical finite element numerical modelling to further investigate the internal forces acting in such bridges. Finally, results of the two-table tests are compared with tests using a single shaking table, in order to evaluate the accuracy of the latter experiments.

Experimental setup and procedures

In this experiment, a two-span simply supported beam bridge was designed and established on two small scale shake tables. The earthquake simulations were applied synchronously and asynchronously to represent a bridge subjected to near-fault and cross-fault earthquakes, respectively. In the case of an asynchronized input (cross-fault earthquakes), the experiment was divided into relative and absolute dislocation to compare the differences in the response of the bridge across the fault under two different forms of seismic excitation. The reason for doing this was to understand the error in the bridge responses during experiments with only one shaking table for cross-fault experiments (in anticipation of future large-scale experiments).

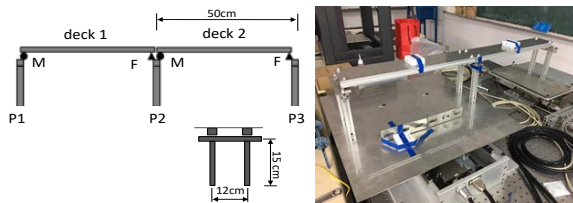


Fig. 1. Experimental model

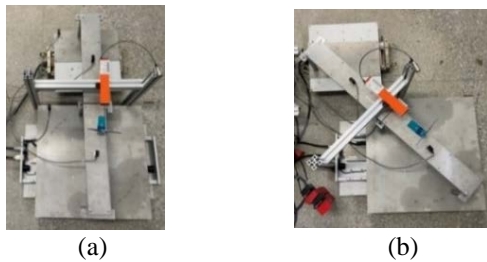


Fig. 2. Experimental setup (a) 90 degree fault line; (b) 45 degree fault line

Because of the weight-bearing limit of the small shaking tables adopted in current study, we used a small-scaled bridge model for the double shaking table test. A two-span simply supported beam bridge with a span of 40.5 m and a column height of 12.15 m was used as the prototype model and this was reduced at a scale of 1:81. The scaled-down model is shown in Fig. 1. The superstructure consisted of two side-by-side main beams with a single-span length of 50 cm. The

substructure was a double-column frame pier with a column height of 15 cm and a column spacing of 12 cm. The bridge support configuration is M-FM-F, where M is a two-way sliding support and F is a hinge support. Because it is not easy to use reinforced concrete to build a 1:81 scale bridge specimen, we selected an aluminum extrusion as the main structure of the bridge body for this experiment. The bridge columns, cap beams, and main girders were all made of aluminum extrusion of the same cross-section. The extrusion model used in this study was made from an A6N01S-T5 aluminum alloy and had a cross-sectional area of 160 mm², a tensile strength of 25 kgf/mm², and a yield strength of 21 kgf/mm². The bridge deck was erected using an iron plate.

In this test, welded round-iron rods were used to simulate the support at both ends of the main beam. The rods at the hinge support end were also spot welded to the top surface of the cap beam of the substructure to limit the displacement of the support in the driving and transverse directions. On the roller support end, the rods were directly placed on the top plate of the cap beam of the substructure, allowing the support to slide freely in the longitudinal and transverse directions. In addition, in order to explore the impact of seismic stoppers, we conducted experiments with seismic stoppers in the transverse direction. The stoppers were simulated with nuts, and the distance between the vibration stoppers and the main beam was 3 mm. There were no seismic stoppers in the longitudinal direction, but the support length in the driving direction was set to 12 mm by installing a white iron plate on the cap beam.

The experiment considered two different horizontal fault angles, 90 degrees and 45 degrees. As shown in Fig. 2(a), in the case of the 90-degree fault, the bridge was erected on two parallel shaking tables, and the direction of the bridge and the fault line were perpendicular. As shown in Fig. 2(b), the case in which the fault angle was 45 degrees investigates performance when the angle between the bridge driving direction and the fault line is 45 degrees.

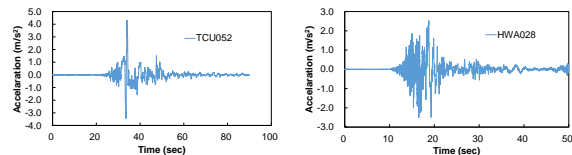


Fig. 3. Acceleration time histories for station TCU052 and HWA028

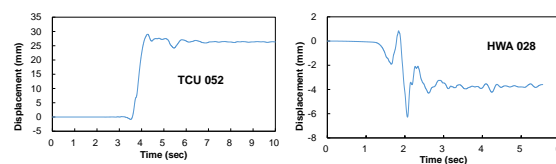


Fig. 4. Input displacement time histories

In order to explore the cross-fault effect on simply supported bridges, the experiment incorporated two sets of earthquake motions with obvious permanent displacements. One was collected during the 1999 Chi-Chi earthquake at seismic station TCU052, and the other was collected during the 2018 Hualien earthquake at station HWA028. Fig. 3 shows the original acceleration motions of these records. For the shaking table test with displacement control, the acceleration time history must be integrated twice to obtain the displacement time history. In addition, because this experiment was a scaled-down test, the input time history for the experiment was also scaled down according to scaling rule. The maximum displacement of TCU052 after scaling was nearly 9 cm, which surpassed the vibration table displacement protection mechanism. Thus, the scaling displacement time history was further reduced to one-third. The input displacement time history used for this study is shown in Fig. 4. The maximum displacements at TCU052 and HWA028 were approximately 30 mm and 6 mm, respectively.

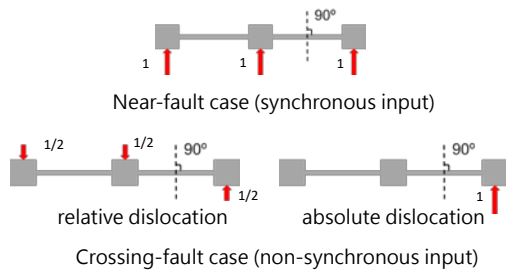


Fig. 5. Schematic diagram of displacement input

In this study, two small shaking tables were adopted to simulate near-fault and cross-fault effects with synchronous and non-synchronous input. The experiment on the two tables was carried out using the displacement input method. Because the shaking tables could only vibrate horizontally in one direction, we restricted the input to the displacement time histories in one direction during the experiment, i.e., along the assumed direction of the fault line. As shown in Fig. 5, the near-fault case was tested with two shaking tables that simultaneously applied the displacement time history given in Fig. 4 in the same direction. Under these conditions, the relative displacement between the columns of the two-span bridge approached zero. The case of a cross-fault was tested using two methods. In the first, referred to as relative dislocation, the two shaking tables simultaneously reversed input at 0.5 times the displacement time history, so that the relative displacement of the two shaking tables was the same as the input displacement time history given in Fig. 4. In the other method, referred to as absolute dislocation, the input of one shaking table was the same as the input displacement given in Fig. 4, while the other shaking table remained stationary. Thus, the relative displacements between the two shaking tables were

also the same as the displacement time history shown in Fig. 4. The test can represent the case with only one shaking table because only one shaking table was applied earthquake motions. We used these two different cross-fault simulation methods because not every experiment can be tested with double shaking tables, especially large shaking tables.

Experimental results

The two sets of scaled earthquake ground motions used in this study, TCU052 and HWA028, represent two cases in which different levels of fault dislocation displacement were experienced. In addition, we compared the influence of different variables, including two cross-fault angles (90 degrees and 45 degrees), the presence or absence of seismic stoppers, and near-fault or cross-fault effects (measured using relative dislocation and absolute dislocation). Therefore, a total of 24 tests were conducted. Figs. 6 and 7 compare the maximum responses during the tests. The comparison items include the transverse sliding displacement of the movable support on the bridge column P2, the longitudinal displacement of Deck 2, and the acceleration of both decks (Deck 1 and Deck 2) in the transverse direction. Figs. 6 and 7 respectively compare the displacement and acceleration responses. For the sliding displacement of the movable support in the transverse direction, the results of the cross-fault cases were notably larger than those of the non-cross-fault (near-fault) cases. However, if there is a seismic stopper, the displacement is limited to the gap distance between the stopper and the main girder, (approximately 3mm). Figs. 6 and 7 do not show the results of TCU052 for a fault angle of 45 degrees. The reason for this is that the displacement for TCU052 was large. When the fault angle was 45 degrees, the relative displacement of the bridge piers P2 and P3 in the longitudinal direction also increased. Therefore, the sliding displacement of the movable support of Deck 2 was greater than the support length of the pier P2 during excitation, which caused the bridge deck to unseat. The case of the unseated bridge is not included in the figures, so the test results corresponding to the 45-degree fault angle for TCU 052 are missing. For HWA028, the input displacements were less than those for TCU052, and the longitudinal displacements caused by the tests were not greater than the support length, so the bridge deck did not become unseated. In addition, it can be observed from Fig. 6 that the displacement responses obtained from the cross-fault tests with relative and absolute dislocation were not significantly different. This indicates that the simulation of the cross-fault condition with a single shaking table is reliable for the displacement responses.

In terms of the transverse acceleration measured at Deck 2 (as shown in Fig. 7(a)), the experimental results show that the responses for a bridge under a

near-fault earthquake is larger than that for a bridge subjected to cross-fault excitation with relative dislocation input in the absence of a seismic stopper. The large deck acceleration possibly reflects the input displacement time history for this cross-fault case, which was half the original; thus, its dynamic acceleration is also halved. For the same reason, the acceleration of Deck 2 across a fault with absolute dislocation, in which the input displacement has not been halved, is approximately equal to the acceleration of the near-fault case. This result not only confirms that the two cross-fault test methods generate different acceleration values, but also confirms that the main influence of the cross-fault effect on the bridge is displacement, while its impact on acceleration is relatively small. Regarding the acceleration of Deck 1 (as shown in Fig. 7(b)), the absolute dislocation test requires that pier P3 has a displacement input, piers P1 and P2 are static, and the supporting conditions of the beams of Deck 2 on P2 are two-way sliding; thus, the acceleration of Deck 1 is less than that of Deck 2.

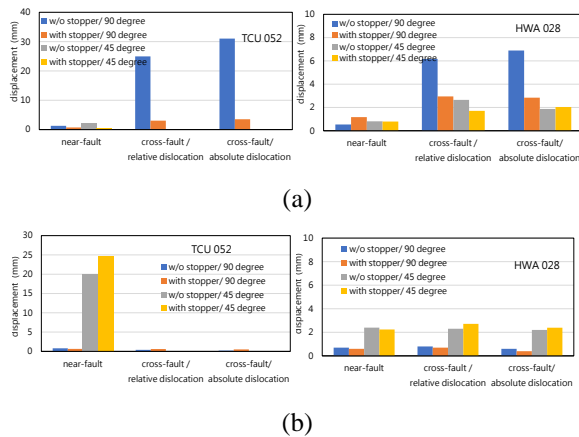


Fig. 6. Influence of seismic stoppers and fault angle on the displacement responses: (a) transverse sliding displacements of the movable support at P2; (b) longitudinal displacements for Deck 2

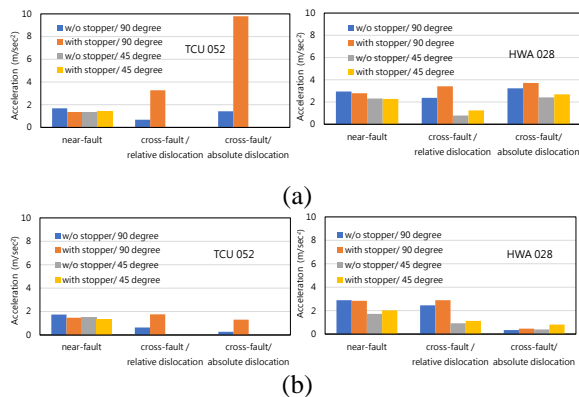


Fig. 7. Influence of seismic stopper and fault angle on acceleration response for different earthquakes: (a) acceleration at Deck 2; (b) acceleration at Deck 1

Since the scaled-down bridge specimen used in the experiment is constructed of aluminum extrusion,

the amount of deformation was small during the experiments, and it was difficult to measure its internal force through strain measurements. Therefore, this study also established a scaled bridge numerical model using the commercial finite element software SAP 2000N and conducted a dynamic time history analysis. Through this analysis, the displacement and internal force response of the bridge can be obtained at the same time. Compared with the experimental results, the displacement response was not significantly different, and the reliability of the analysis results can be verified. The analytical results also show that the internal force of the bridge column is related to the displacement input method and whether it hits the seismic stoppers. It can be found that although the stopper restricts the transverse displacement of the girders and prevents the bridge from unseating, it also causes the internal force of the column to increase, thereby increasing the probability of the bridge column damages. In addition, compared with near-fault cases, bridge with cross-fault cases will bear larger torque at columns. Due to space limitations, the comparison charts for the analysis result mentioned above are omitted in this article.

Conclusions

This study investigates the near-fault and cross-fault effect on the responses of simply supported bridges through experimental and numerical approaches. According to the experimental results and numerical simulations, several key parameters that affect the responses are identified and discussed. The results also show that for an experiment that uses a single shaking table to simulate the cross-fault effect on multiple-span simply supported bridges, the calculations of the relative displacement of the bridge show that the result is not significantly different from the experimental result for the dual shaking table. However, this approach may not properly estimate the acceleration response in the bridge deck and the internal force of the bridge pier according to the numerical simulations.

References

- Central Geological Survey, MOEA, 2012, <http://fault.moeacgs.gov.tw/MgFault/>
- Chang K. C., 1999, 921 Chi-Chi Earthquake Reconnaissance Report - Bridge Investigation, NCREE-99-055. (in Chinese)
- Ulusay, R., Aydan, O., Hamada, M., 2002, The behaviour of structures built on active fault zones: Examples from the recent earthquakes of Turkey, Structural Engineering & Earthquake Engineering, JSCE, 19 (2), 149-167.
- Japan Bridge Association (JBA), 2016, Bridge Damage Investigation Report for Kumamoto Earthquake. (in Japanese)

Development of Advanced Bridge Information System's High-Performance Web Server

Kuang-Wu Chou¹ and Chia-Chuan Hsu²

周光武¹、許家銓²

Abstract

This study was to develop an efficient bridge information system that could afford time-consuming computations or simulations on the web. The web server of the system was created by using two C++ libraries coming from the famous Boost: Beast and Asio. The server also implemented the HTTPS (Hyper Text Transfer Protocol Secure) protocol, providing secure communication between the server and users. Besides, the web server offered a Web API (Application Programming Interface) to enable the SPA (Single Page Application) design of the bridge information system. Preliminary tests were carried out to ensure that Beast and Asio sufficed to create a secure Web API and the web server was able to timely respond to user requests for bridge information.

Keywords: C++, Boost, Asio, Beast, networking programming, Web API, HTTP, HTTPS

Introduction

This study was to create an efficient bridge information system that could afford time-consuming computations or simulations on the web. Though aiming to run time-consuming simulations, this system was supposed to be responsive, able to quickly respond to user requests. That is, if this system were a desktop application, at least two threads would be required to concurrently run a simulation and the user interface, respectively. The thread running the interface would check anytime the progress of the simulation and immediately report that progress to the user before the simulation ends. Meanwhile, the other thread keeps running the simulation without interruption until the simulation ends. The performance of this simulation thread, in fact, determines how much time the desktop application will take. In this study, the bridge information system will behave as the desktop application. This system is designed as a web application that can serve users through browsers without the issue of which operating system to run and without the need to install this system. In addition, this system was created as a single-page application (SPA) to offer users efficient, responsive interfaces. In our SPA approach, the back-end development of the system was separated from the system's front-end development. The system's back

end is web servers, implemented as web APIs (Application Programming Interface) to offer data manipulations requested by the front end of the system. The front end shows in browsers the results of those data manipulations. The front end was implemented by using Angular, a Javascript framework supplying the system's SPA user interface.

Because the back-end web servers are supposed to perform time-consuming simulations efficiently, these servers should be implemented by calling the frameworks or libraries that not only offer high-performance services of Hyper Text Transfer Protocol (HTTP) but also can efficiently work with the code carrying out simulations. While the C++ programming language is used to program the simulation code, there are several back-end frameworks or libraries from which we can choose. But they are supposed to be implemented by the same programming language C++, in order to be easily integrated with the simulation code.

Web Server Development Method

Boost.Beast was used to prototype the web servers of the bridge information system. *Beast* is a C++ header-only library, which provides low-level types and algorithms for developers to implement

¹ Associate Researcher, National Center for Research on Earthquake Engineering

² Assistant Researcher, National Center for Research on Earthquake Engineering

protocols of networking, WebSocket, and HTTP. This library may be used to create either clients or servers running these protocols. *Beast*'s support for HTTP, in particular, can facilitate the creation of web servers.

Beast is used because of being based on a famous network programming library: *Boost.Asio*. As a cross-platform C++ library, *Asio* supports low-level networking programming and modern C++ programming language features.

Asio implements two protocols of the transport layer of the internet protocol suite: Transmission Control Protocol (TCP) and User Datagram Protocol (UDP). Fig. 1 shows that the two protocols support all the upper protocols belonging to the application layer of the DARPA (Defense Advanced Research Projects Agency) model. One of those application-layer protocols is HTTP. *Beast* implements the standard HTTP/1.

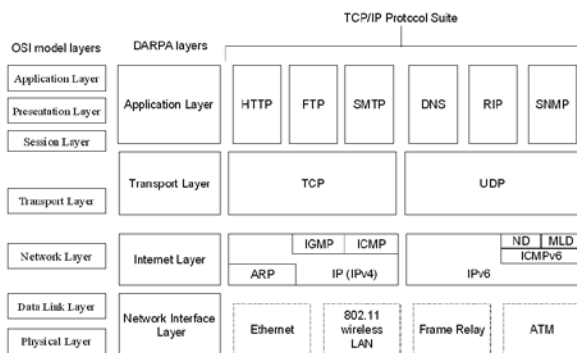


Fig. 1. The architecture of the TCP/IP protocol suite (Microsoft 2007)

More importantly, *Asio* implements the protocol of Transport Layer Security (TLS), which provides secure communication between applications. Fig. 2 shows that TLS runs on TCP in the transport layer and works inside the application layer (TLS comprises the alert protocol, the change cipher spec protocol, the handshake protocol, and the record layer protocol). The HTTP protocol cooperating with TLS is called the HTTPS (Hyper Text Transfer Protocol Secure), which web servers assuring secure communications are required to implement. While *Asio* plays the role of TLS and is responsible for majority of secure communications initiated by *Beast*, it could benefit the long-term development of web servers to familiarize the low-level *Asio*. In fact, the sample codes of *Asio* show that one can use *Asio* alone to create a web server, without using *Beast*. Therefore, as one policy of this study, *Beast* is replaceable.

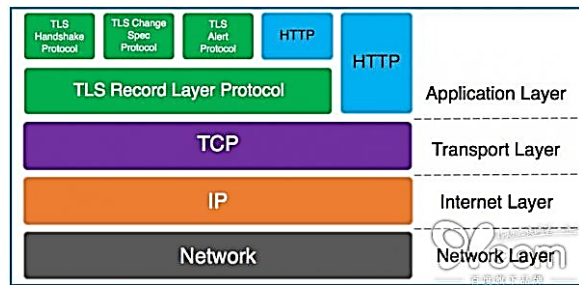


Fig. 2. The relationship between TLS, HTTP, and TCP (Ithead01.com 2018)

In addition to HTTP/1, there are two newer protocol standards supporting more efficient communication mechanisms. Currently as a standard draft, faster than HTTP/2, HTTP/3 is supposed to be the successor of HTTP/2. Since *Beast* supports only HTTP/1 that might satisfy the current requirements of this study, we would need to implement the two newer standards ourselves by writing codes using *Asio* or parts of *Beast*. Fortunately, the C++ library `libnghttp2_asio`, developed by Tatsuhiro Tsujikawa (2016), uses *Asio* to implement HTTP/2, proving that *Asio* is still able to afford the requirements of HTTP/2. On the other hand, there seems no C++ library to implement HTTP/3 so far. This is an important issue that we should think about how to resolve.

Preliminary Test of The Boost.Beast Web Server

This preliminary test is to know whether *Beast* is sufficient to implement a Web API offering information of bridges. To perform this test, this study created a web server by using the *Beast* library and connected this server with a database that offers the basic information of the bridges in Taiwan. The bridge information database is maintained by a *PostgreSQL* relational database management system (RDBMS). The web server offered a Web API that the front-end programs can call to show or modify bridge data according to the user's request.

In the test, two functions of the Web API were carried out, supposed to output data in the JSON (Javascript Object Notation) format in browsers. One function was to list the names and identifiers of all bridges in the city specified; the other function, the basic information of the bridge specified with its identifier.

As required to securely communicate with users, the web server implemented the HTTPS protocol. Because the HTTPS server used a self-signed certificate not signed by any certificate authority (CA), users would see a warning in their browser before actually accessing this server, as shown in Fig. 3. They may choose to click either the *advanced* button to access this server or the *back-to-safety* button to back

to the former page. Once the *advanced* button being clicked, another prompt would be shown in the browser, expressing that the self-signed certificate was not trusted by the operating system, yet giving a hyper link to let users proceed to access this server, as shown in Fig. 4. After clicking such a link, users could see the JSON data that this server responded to browsers, as shown in Fig. 5 and 6.

Fig. 5 shows the result of querying the bridges in Taichung City (台中市) by inputting into the browser the URL (Uniform Resource Locator): <https://61.56.6.172/Bridges?city=台中市>. This URL called one of the two Web API functions in the test, the function listing in the browser the name and identifier (id) of the bridges in Taichung City. In the listed output, the bridge with the name 保安橋 and the id 7219 was chosen for the browser to further show the bridge's basic information (See Fig. 6). The URL template to call the other aforementioned function showing a bridge's basic information is <https://61.56.6.172/Bridge/id>. In Fig. 6, the id of this template was substituted by 7219 to create a URL to show the basic information of the bridge 保安橋.

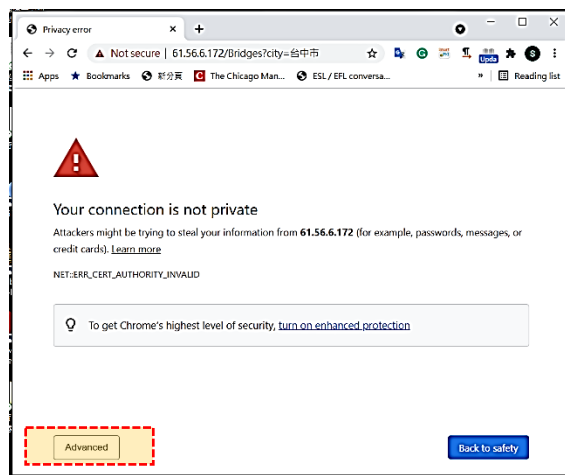


Fig. 3. A warning message shown in a browser that tried to access a Web API function of the Beast web server through the url, <https://61.56.6.172/Bridges?city=台中市>

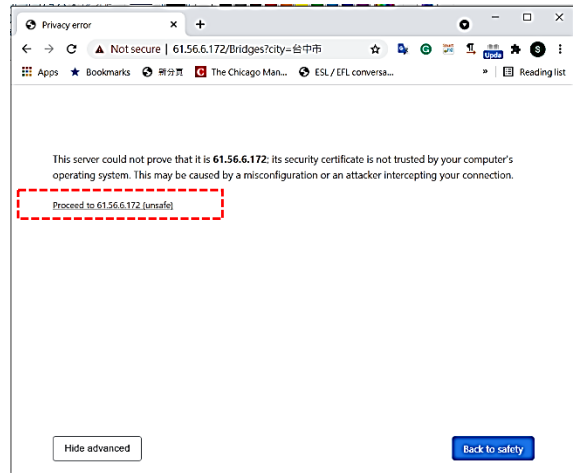
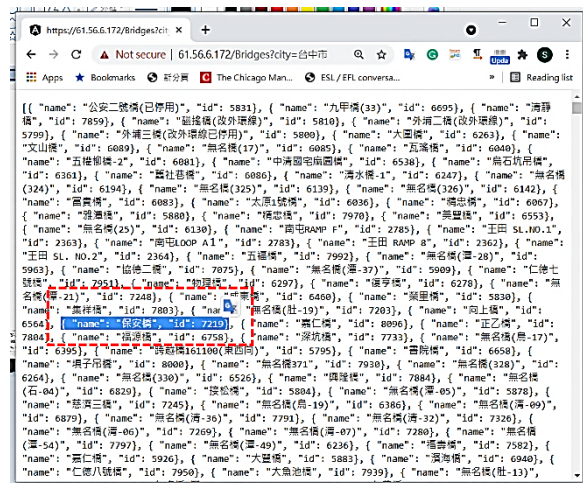


Fig. 4. The prompt providing a hyper link to proceed to access a Web API function of the Beast web server through the url, <https://61.56.6.172/Bridges?city=台中市>



Conclusions

This study created a web server by using the C++ open source *Boost.Beast*. This server was directly executed by the Ubuntu operating system of a computer, without depending on any existing web server like Apache or Nginx. This server was able to efficiently respond to requests of querying bridge-information database, quickly deliver the query results to browsers.

The C++ web server created in this study will work with C++ simulation codes to examine if this server could allow multiple users to perform their simulations and show non-blocking I/O (Input/Output). In addition, to examine the performance of the proposed web server development, we will construct web servers by using another famous open source, *Node.js*, comparing its performance with that of the proposed method. Meanwhile, *Node.js* will also work with the same C++ simulation codes as the proposed server development is supposed to call. In fact, *Node.js* is another technology we aim at in order to create efficient web servers because it not only can reduce our development time but also can timely support the newest standard of the HTTP protocol. These *Node.js* servers will be used to deliver Web applications that perform computations taking less time.

References

- Boost Software License (2021). Boost C++ Library [Programming libraries]. Available from <https://boost.org>.
- Canonical Ltd (2021). Ubuntu [Operating system]. Available from <https://ubuntu.com>.
- Google LLC (2021). Angular [Web programming framework]. Available from <https://angular.io>.
- Itread01.com (2018). "Explain the difference and the relationship between HTTPS, TLS, SSL, and HTTP". Available from <https://www.itread01.com/content/1544660134.html> (In Chinese).
- Microsoft (2007). "Chapter 2 – Architectural Overview of the TCP/IP Protocol Suite". Available from <https://technet.microsoft.com/en-us/library/bb726993.aspx>.
- NGINX, Inc. (2021). Nginx [Web server software]. Available from <https://nginx.org>
- OpenJS Foundation (2021). Node.js [Web programming framework]. Available from <https://nodejs.org>.
- Tatsuhiko Tsujikawa (2016). "libnghttp2_asio: High level HTTP/2 C++ library". Available from https://nghttp2.org/documentation/libnghttp2_asio.html

The Apache Software Foundation (2021). The Apache HTTP Server Project [Web server software]. Available from <https://httpd.apache.org>.

The PostgreSQL Global Development Group (2021). PostgreSQL [Database management system]. Available from <https://postgresql.org>.

Developing an Advanced Bridge Information Management Application: Database Design

Chia-Chuan Hsu¹ and Kuang-Wu Chou²

許家銓¹、周光武²

Abstract

The development of computers in the last few decades has made the concept of using storage media (e.g., disks, hard drives, and CDs) to store data possible. These storage media were widely used in the mid-1960s. This study investigates ways to design a database that could support development of an advanced bridge management information system. The investigation focuses on relational databases and relational database management systems.

Keywords: Database, DBMS, Database Design

Introduction

There are more than 20,000 bridges in Taiwan, which are managed by different agencies. The data from these bridges are crucial for the development of a bridge information system. The designed database should support the system, which will be in the form of web applications. The system can not only help manage bridge information, but can also perform simulations through the Internet. This means that the application server may use databases to access bridge model data and store simulation results through the webserver. The purposes of developing a bridge information system include updating and breaking through existing bridge management system mechanisms and combining information technology to make bridge management more effective.

Many applications and systems use relational databases to store data. The biggest feature of these databases is the linking of different tables through key-value (primary/foreign key) and the association of complete data. Relational databases usually adopt database normalization and the entity-relationship (ER) model (Chen, 1976) to carry out the database design. After formalizing the database design or ER model, a schema of the relational database can be designed, which includes the name of the table, the name of each field in the table, the data type, the data restriction conditions, and the association between the data tables. Structured query language (SQL) is used to retrieve and display the data that meet the query conditions in the application or website.

Database management system

Nowadays, a database usually refers to a database management system (DBMS), which is software that can capture and analyze data. Codd (1970) described a concept for storing and working with large databases, which was the introduction of the relational database management system (RDBMS).

Fig. 1 shows that each piece of data is a record in a table, and different tables are assembled to become a relational database.

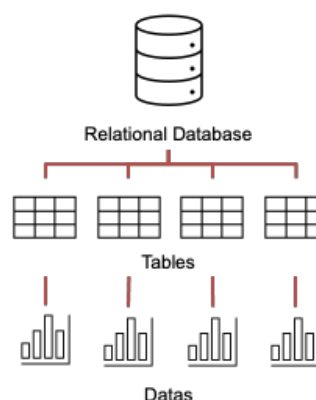


Fig. 1. Data are stored in one or more tables

For example, the database of a shopping website might include a sellers table, a users table, and a products table (Fig. 2).

¹ Assistant Researcher, National Center for Research on Earthquake Engineering

² Associate Researcher, National Center for Research on Earthquake Engineering

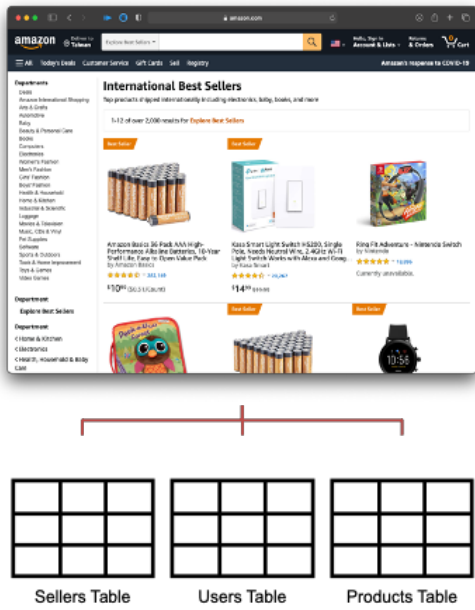


Fig. 2. Tables of a shopping website

Relational databases are the most popular database type of the past few decades, and are still used by most developers because of their ease of use and stability. According to DB-Engines in April 2021, relational databases accounted for seven of the top ten databases (Fig. 3).

Rank			DBMS	Database Model
Apr 2021	Mar 2021	Apr 2020		
1.	1.	1.	Oracle	Relational, Multi-model
2.	2.	2.	MySQL	Relational, Multi-model
3.	3.	3.	Microsoft SQL Server	Relational, Multi-model
4.	4.	4.	PostgreSQL	Relational, Multi-model
5.	5.	5.	MongoDB	Document, Multi-model
6.	6.	6.	IBM Db2	Relational, Multi-model
7.	7.	8.	Redis	Key-value, Multi-model
8.	8.	7.	Elasticsearch	Search engine, Multi-model
9.	9.	9.	SQLite	Relational
10.	10.	10.	Microsoft Access	Relational

Fig. 3. DB-Engines April 2021 rankings

Relational databases are generally used to store structured data, and most of the data are clearly related. As an example, a course arrangement could be divided into three categories: classrooms, classes, and students. A direct relationship needs to be established between them. In a relational database, these three types of data will be stored in three tables (Fig. 4).

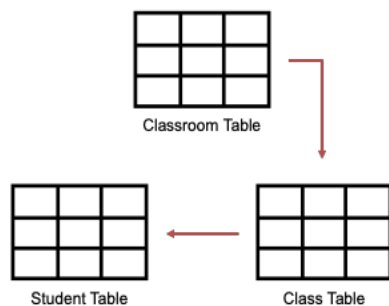


Fig. 4. Relationships between the tables

Relational databases can be operated in SQL, which has helped them become the most popular

DBMS. SQL is a programming language specially used to manage and query relational databases. The general structure of a relational database is shown in Fig. 5. Users can create, read, update, and delete data (CRUD) in a relational database through SQL. Furthermore, SQL can also create and modify database models.

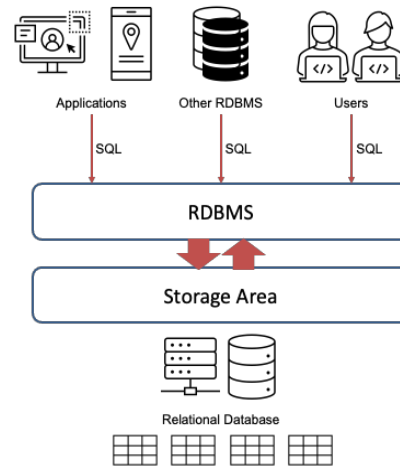


Fig. 5. The general structure of a relational database

Database design

Database design is the process of creating a detailed data model during the software or application development process. Mostly, database design involves the logical design of basic data structures used to keep and store data. Database design can also refer to a collection of base relationships (e.g., relationships between data tables) and a collection of derived relationships in a relational database.

The process of designing a database generally consists of many tasks, including determining which data should be persistently stored in the database and determining a collection of relationships between different data elements. A flowchart of the database design process is represented in Fig. 6 (Nian, 2017).

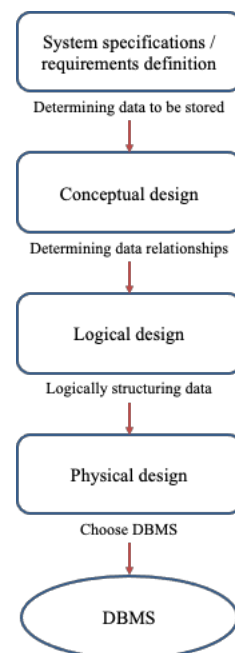


Fig. 6. The database design process

As shown in Fig. 6, there are four stages in the design process:

1. Defining system specifications/requirements

It is necessary to collect data and understand the operation situation. Data are usually collected through scientific methods, which include extract, transform, and load (ETL), data cleansing, and data mining. This stage also includes determining the design requirements.

2. Conceptual design

The main task at this stage is to analyze and classify the collected data through classification analysis, clustering analysis, regression analysis, time series analysis, associative analysis, and sequential pattern analysis to design a database model that can fit end-user needs.

3. Logical design

The concept at this design stage is to convert the ER model into actual data tables and conform to the data table normalization to ensure the integrity of the data.

4. Physical design

This stage involves selecting the DBMS (e.g., MySQL, MS Access, or PostgreSQL) and creating the designed tables.

Database Creation

Fig. 7 shows the created bridge database of the developing system. The database includes management data, geometric data, geographic data, and structural data.

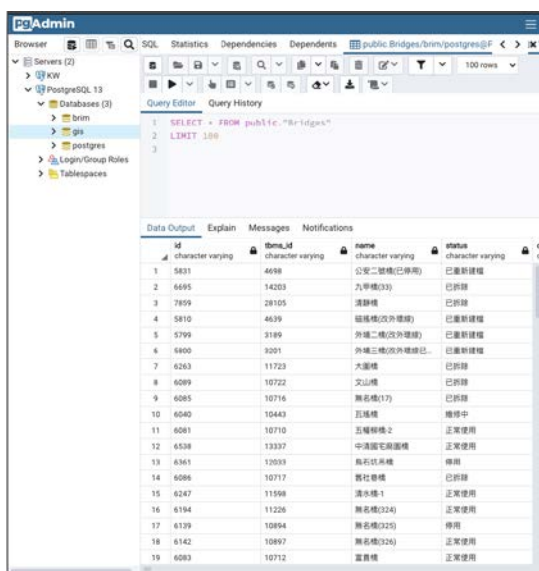


Fig. 7. Bridge database of the developing system

The collected bridge data are imported and preliminary collections are illustrated in Fig. 7. The distribution of the bridges is shown in Fig. 8.

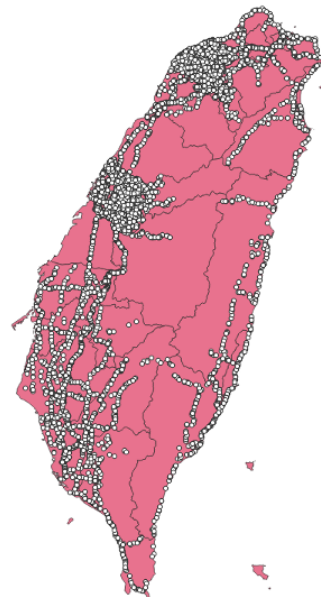


Fig. 8. Distribution of the created bridge database

Conclusion

A relational database is introduced in this study, the primary purpose of which is to describe the design procedure. A convoluted or poor database design can cause many problems, including inability to match demands, low performance, and poor scalability. Based on the design process, a preliminary bridge database was created, and this could support the development of an advanced bridge management information system.

References

Peter P. Chen (1976), “The Entity-Relationship Model - Toward a Unified View of Data”. *ACM Transactions on Database Systems (TODS)*, 1 (1), 9-36.

Edgar F. Codd (1970), “A Relational Model of Data for Large Shared Data Banks”, *Communications of the ACM*, 13 (6), 377–387.

ALPHA Camp (2020). What is SQL / NoSQL? Understanding of database management system DBMS. Available from <https://tw.alphacamp.co/blog/sql-nosql-database-dbms-introduction> (in Chinese)

DB-Engine (2021), DB-Engines Ranking. Available from <https://db-engines.com/en/ranking>

Tian-Shou Nian (2017), Introduction to database system (including logic design). Available from http://www.tsnien.idv.tw/DataBase_WebBook/Database.htm (in Chinese)

Smart Nanofluid Viscous Dampers (II)

Fang-Yao Yeh¹, Chung-Han Yu², Shen-Kai Peng³ and Kuo-Chun Chang⁴

葉芳耀¹、游忠翰²、彭聖凱³、張國鎮⁴

Abstract

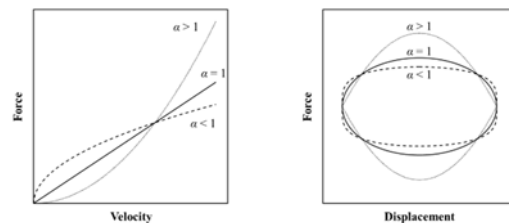
Nanofluid dampers feature a force–velocity curve described by a dual nonlinear exponent, in which an exponent with $\alpha > 1$ describes the low-velocity range while $\alpha < 1$ describes the working-velocity range, typical of deformations induced by earthquake excitations. This property can be used in bridge systems to significantly decrease the inner pressure of dampers and the wear on oil seals, which increases the durability of the dampers. This study attempts to use the shear thickening and thinning characteristics of a nanofluid and a damper with a simple solid piston head. This study aims to show that the performance of the damper can be adjusted by changing the formula and concentration of the nanofluid to achieve dual-nonlinear-exponent force–velocity mechanical properties in the damper. The results of this study indicate that (1) the initial viscosity of the nanofluid is greater than that of the corresponding pure polypropylene glycol (PPG) fluid; (2) the initial viscosity is proportional to the PPG polymer chain length and fluid concentration; (3) the shear thickening, cluster effect, and maximum viscosity are all proportional to fluid concentration; (4) as the temperature increases, the viscosity corresponding to shear strain rate decreases, although the shear strain rate corresponding to relatively low and high viscosities increases with temperature; and (5) the area enclosed by the hysteresis loop for the nanofluid damper is proportional to frequency and maximum velocity. Finally, after temperature correction, the force curve and regression equation of the nanofluid damper show the mechanical characteristics associated with a dual nonlinear exponent.

Keywords: nanomaterial, rheology, nanofluid rheological property test, damper performance test.

Introduction

In recent years, extensive applied research on fluid viscous dampers has been conducted. In the field of structural engineering, fluid viscous dampers can be used to reduce the responses of buildings and bridges to earthquakes, and they can also improve buildings with insufficient earthquake resistance. When the damper moves, a velocity-dependent damping force is generated by the pressure difference generated by the fluid when the piston head moves relative to the sides. The relationship between the output force of the damper and the velocity of the piston head can be written as $F_D = CV^\alpha$, where F_D is the damping force, C is the damping coefficient, V is the damper velocity, and α is its exponent. A damper with $\alpha = 1$ is called a linear fluid viscous damper,

whereas a damper with $\alpha \neq 1$ is called a nonlinear fluid viscous damper, as shown in Fig. 1.



(a) Force–velocity relationship (b) Hysteresis loop
Fig. 1. Comparison between viscous dampers with different α values.

Viscous dampers with an exponent of less than 1 are popular because of the characteristics of their damping force, which can quickly reach the force demand at low velocities but does not increase rapidly at high velocities, as shown by the red dashed line in

¹ Division Director, Bridge Engineering Division, National Center for Research on Earthquake Engineering

² Assistant Researcher, Structural Monitoring and Control Division, National Center for Research on Earthquake Engineering

³ Ph. D. Candidates, Department of Civil Engineering, National Taiwan University

⁴ Professor, Department of Civil Engineering, National Taiwan University

Fig. 2. In recent years, however, engineers have discovered that the large damping force generated at low velocities limits other structural control functions, such as seismic isolation. In addition, the characteristics of an idealized nanofluid damper are represented by the solid blue line in Fig. 2, which comprises two continuous exponential curves. This feature enables the nanofluid damper to generate low damping force at low velocities but to sharply increase the force over a specific velocity range, so that it performs like a normal viscous damper in the working-velocity range.

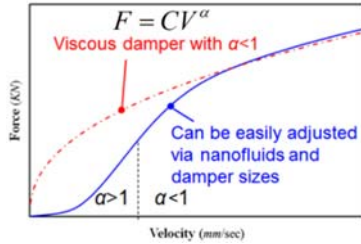


Fig. 2. Comparison between idealized nanofluid damper (blue line) and conventional damper (red line).

The present research team has confirmed the output behavior of nanofluid dampers in previous studies [1]. This study aims to use the shear thickening and thinning characteristics of a nanofluid and a damper with a simple solid piston head to achieve a damper with mechanical properties described by a dual nonlinear exponent. This was attempted by changing the formula and concentration of the nanofluid.

Nanofluid rheology test

A rheological test was conducted in order to understand the influence of various parameters on the nanofluid's properties. The parameters that were varied were the type of silica nanoparticle (R812, R972, and R974), the molecular weight of the polypropylene glycol (PPG) solution (PPG400, PPG1000, PPG2000, PPG3000, and PPG4000), and the weight concentration (4%, 6%, 8%, 10%, 12%, and 14%).

Preparation of the nanofluid

The process of preparing the nanofluid was kept constant, to ensure that the quality of the nanofluid was consistent. The mixing steps were as follows (Fig. 3). (1) First, place the container of PPG under the mixer, turn on the mixer, and ensure that the carrier fluid rotates continuously at a low speed. (2) Second, gradually add the silica nanoparticles to the container, and continue rotating the fluid at a low speed to gradually stir the nanoparticles into the liquid. (3) Third, when there are no more silica nanoparticles suspended on the surface of the fluid, increase the stirring speed slightly to accelerate the dispersion of the nanoparticles. (4) Finally, when the fluid became

transparent and there are no more white agglomerated nanoparticles in suspension, switch the mixer to high-speed stirring mode and continue stirring the fluid for at least ten minutes to ensure that the silica nanoparticles have been uniformly dispersed throughout the solution.



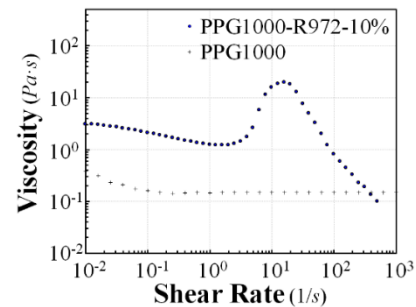
Fig. 3. BLDCM BLG-3D digital blender and process of producing nanofluid.

Test results

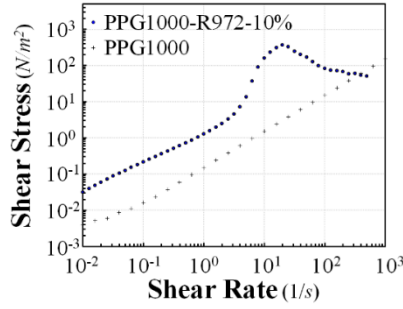
The rheological test in this study was carried out at the Institute of Polymer Research, National Taiwan University. The instrument used was an AR2000ex rheometer. Constant temperature and steady-state rheological tests were carried out on each of the nanofluids, and the range of controlled shear strain rates was $0.01\text{--}1000\text{ S}^{-1}$. This range was divided into fifty parts at equal logarithmic intervals, so each shear strain rate measuring point was separated by $10^{0.1}\text{ S}^{-1}$. During the constant temperature tests, the temperature was set to $25\text{ }^{\circ}\text{C}$.

This study also conducted temperature tests on the nanofluids. The rheometer's liquid tray was used for temperature control and a series of constant-temperature tests were conducted for temperatures from $5\text{ }^{\circ}\text{C}$ to $50\text{ }^{\circ}\text{C}$ in increments of $5\text{ }^{\circ}\text{C}$. Of the large number of types and quantities of nanofluid tested, the PPG1000-R972-10% nanofluid was selected as the standard.

Figure 4 shows a comparison of the viscosity curve for the standard nanofluid with pure PPG (of the same molecular weight as was used in the nanofluid) obtained in the rheology test. The experimental results show that: (1) the initial viscosity of the nanofluid was greater than that of the pure PPG fluid; (2) the initial viscosity was proportional to the PPG polymer chain length and fluid concentration; (3) and the shear thickening, cluster effect, and maximum viscosity were all proportional to the fluid concentration.



(a) Viscosity curve



(b) Flow curve

Fig. 4. Rheological properties of sample PPG1000-R972-10%.

The results of the temperature test are shown in Fig. 5. The viscosity curve shifts to the lower right as the temperature rises. Therefore, as the temperature increased, the viscosity corresponding to each shear strain rate decreased, but the shear strain rate corresponding to the relatively low and to the highest viscosities increased with temperature. This indicates that the viscosity of the nanofluid as a whole decreased when the temperature was relatively high. It can be inferred that the increase in the output force of the nanofluid damper will slow down as the temperature increases.

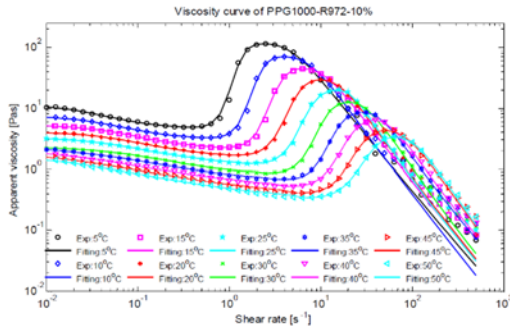


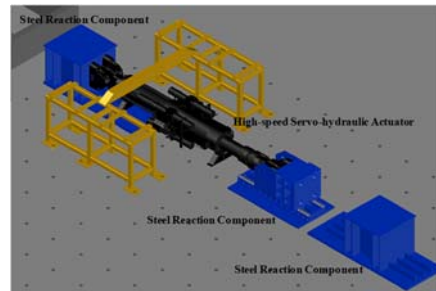
Fig. 5. Influence of temperature on nanofluid PPG1000-R972-10%.

Performance test of nanofluid dampers

Test plan

The dampers were subjected to performance tests by the Energy Dissipation Device Test System at the National Center for Research on Earthquake Engineering (NCREE) in Taiwan (Fig. 6). The tests to which the dampers were subjected were designed according to a technical report published by NCREE [2] and the earthquake-resistance design codes of various countries [3–7]. Performance tests of nanofluid dampers can take one of two forms – temperature tests and frequency tests – and displacement control is used in both types of test. Before the temperature test, the specimen was placed in a constant-temperature chamber and isolated for more than twelve hours to ensure that it was completely stable at a constant temperature. For each

set of experiments, the specimen was subjected to six complete sinewaves with a frequency of 0.5 Hz and an amplitude of 30 mm. The temperature tests were conducted after the specimen had been removed from the constant temperature chamber, and the test temperatures ranged from 10.0 °C to 48.7 °C. In the frequency tests, the specimen was subjected to triangle waves and sinewaves, corresponding to the extremely low-velocity range and the medium-velocity range, respectively. The constant-velocity characteristic of the triangle wave test can cause the damper to produce a stable output at a low velocity. The triangle-wave tests were performed at velocities of less than 10 mm/s, while the sinewave tests were performed at velocities of greater than 15 mm/s. Each test was run for six cycles.



(a) Test system for the energy dissipation device



(b) Test setup for the nanofluid damper specimen

Fig. 6. High-performance damper test system and setup.

Test results

The results of the triangle-wave and sinewave tests of the specimen are shown in Figs 7 and 8, respectively. From the test results, it can be seen that the area enclosed by the hysteresis loop was proportional to the test frequency and maximum velocity. In addition, from the sinewave test results, it can be seen that the hysteresis loop for the low-frequency test was approximately elliptical, indicating that the behavior of the damper was identical or similar to that of a linear fluid viscous damper. In contrast, the hysteresis loop for the high-frequency test was close to rectangular, and thus the damper's behavior was similar to that of a nonlinear fluid viscous damper. The output curves after temperature correction are plotted in Fig. 9. Regression of the experimental results produces the following output force equation for the test specimen:

$$F_D = 1.85V_D^{1.3} \quad \text{for } V_D \leq 3.48 \text{ mm/sec}$$

$$F_D = 4.37V_D^{0.61} \quad \text{for } V_D > 3.48 \text{ mm/sec}.$$

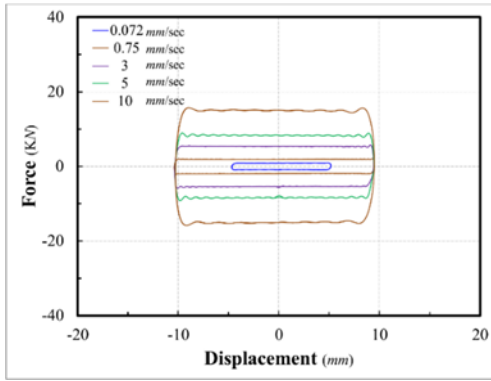


Fig. 7. Hysteresis loops from the triangular-wave tests of the nanofluid damper PPG1000-R972-10%.

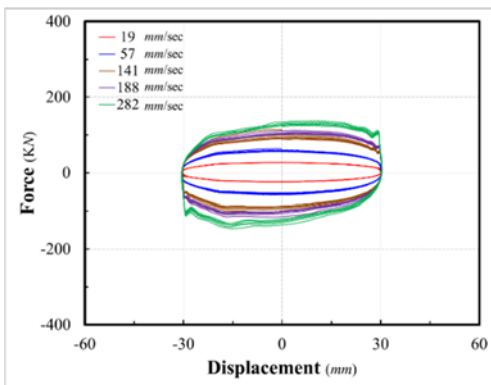
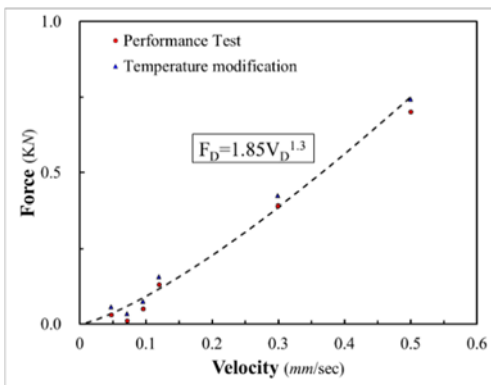
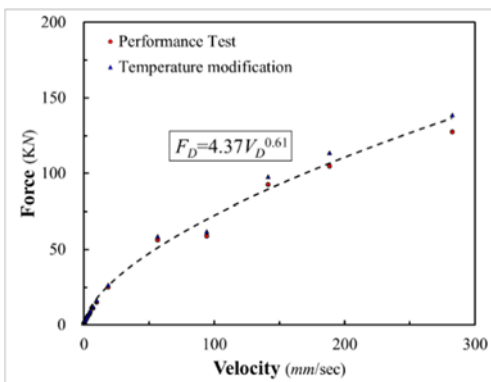


Fig. 8. Hysteresis loops from the sine-wave tests on the nanofluid damper PPG1000-R972-10%.



(a) Low-velocity range



(b) Working-velocity range

Fig. 9. Force curves for the nanofluid damper PPG3000-R972-10%.

Conclusions

The results of this study showed that (1) the initial viscosity of the nanofluid is greater than that of the corresponding pure PPG fluid; (2) the initial viscosity is proportional to the PPG polymer chain length and fluid concentration; (3) the shear thickening, cluster effect, and maximum viscosity are all proportional to the fluid concentration; (4) the viscosity corresponding to shear strain rate decreases with increasing temperature, although the shear strain rate corresponding to relatively low and high viscosities increases with increasing temperature; and (5) the area of the hysteresis loop for the nanofluid damper is proportional to frequency and maximum velocity. Finally, after temperature correction, the force curve and regression equation for the nanofluid damper exhibit the mechanical characteristics associated with a dual nonlinear exponent.

References

1. Yeh, F. Y., Chang, K. C., Chen, T. W., Yu, C. H. "The dynamic performance of a shear thickening fluid viscous damper." *Journal of the Chinese Institute of Engineers* 37.8 (2014): 983-994.
2. National Center for Research on Earthquake Engineering, "Study on test requirements for seismic isolators and velocity-dependent dampers," NCREE-2014-016, December, 2014. (In Chinese)
3. Construction and Planning Agency, Ministry of the Interior, "Seismic Design Specifications and Commentary of Buildings," January, 2011. (In Chinese)
4. American Society of Civil Engineers (ASCE), "Minimum design loads for buildings and other structures," ASCE/SEI 7-10, ASCE, Reston, VA, 2010.
5. AASHTO, "LRFD Bridge Construction Specifications," American Association of State Highway and Transportation Officials, Washington, DC, 2010.
6. "EN 15129:2009 - Anti-seismic devices," European Committee for Standardization (CEN), November, 2009.
7. "A Test Plan for the Characterization and Qualification of Highway Bridge Seismic Isolator and Damping Devices," Energy Technology Engineering Center Highway Innovative Technology Evaluation Center California Department of Transportation, 1995.

Displacement-Dependent Tuned Mass Damper Feasibility Study

Bo-Han Lee¹, Chun-Chung Chen², Sheng-Yuan Shiao³, Chi-Rung Jiang³ and Fang-Yao Yeh⁴

李柏翰¹、陳俊仲²、蕭勝元³、江奇融³、葉芳耀⁴

Abstract

Tuned mass dampers (TMD) are used to reduce the vibrations of high-rise buildings due to wind disturbance. Specifically, the displacement-dependent tuned mass damper (DTMD) is an effective energy absorber that is connected to a primary structure to reduce the vibration response of the structure under harmonic and external force disturbances. Its natural frequency is adjusted to be close to the fundamental vibration frequency of the primary structure, which leads to an antiphase resonance that dissipates the external force-induced disturbance energy. Several studies have proposed different objective optimization design functions and researchers have developed active and semi-active TMD systems to significantly improve control efficiency. In this study, a reasonable mass and objective function were considered using a simplified degree-of-freedom structural model (DTMD and primary structure) to derive an optimized design method and evaluate the feasibility of structural reinforcement through numerical analysis of the TMP and shaking table tests. The fundamental retrofit design used in this study can facilitate the development of specialized DTMDs that can be applied in practical engineering contexts.

Keywords: Tuned mass damper, seismic performance, shaking table test

Introduction

In recent years, many studies have focused on structural components or materials, particularly low floors that undergo long-term aging and deterioration, which affect structural safety. Designing reinforcements to improve earthquake resistance is a common countermeasure for this problem. The earthquake resistance of a degraded structure can be enhanced by improving its strength, increasing the damping ratio, and extending the primary vibration period.

In the past, many studies have applied a tuned mass damper (TMD) concept in the seismic design of civil structures. The primary structural system is first subjected to harmonic excitation of fixed acceleration and displacement amplitude without damping. The theoretical formulae of the optimal TMD damping ratio and the primary structure's frequency ratio under the minimum steady-state response is then derived [1]. Warburton derived an optimal TMD design formula for the damping of a single degree of freedom (SDOF)

system in a primary structural system subjected to external harmonic and random white noise excitation. Structural systems also experience damping effects, and the influence of structural damping needs to be considered for optimal TMD design. Therefore, Warburton used the value method to investigate the behavior of a primary structural system with damping, optimized the TMD design parameters, and created a chart for practical design reference.

Tsai and Lin used curve-fitting to confirm the optimized TMD design parameter formula [2]. Villaverde and Toshihiko et al. proposed another optimal damping ratio design formula and conducted a series of numerical simulations to verify its applicability. However, this formula is not applicable when the tuning mass is greater than the primary structure mass. Moreover, the results obtained using the optimized damping ratio formula do not correspond to the damping ratios of the first two modes of vibration [3]. Matta discussed the effectiveness of a TMD with regard to the base excitation input pulse. Nagarajaiah and Varadarajan considered the benefits of TMD frequency variation

¹ Assistant Researcher, National Center for Research on Earthquake Engineering

² Associate Researcher, National Center for Research on Earthquake Engineering

³ Associate Technologist, National Center for Research on Earthquake Engineering

⁴ Division Director and Research Fellow, National Center for Research on Earthquake Engineering

for a structure affected by wind. Soong et al. also optimized TMD parameters for structures with a SDOF and with multiple degrees of freedom.

The effect of the inherent damping of the primary structure on the TMD optimization parameters has also been discussed [4]. Narasimhan and Chey conducted a series of investigations on the optimization design parameters of semi-active TMD controls. Several scholars in China have also discussed TMD optimization parameters [5]. Lin et al. proposed a necessary condition for determining the optimal parameters of a TMD when there is a minimum phase difference between the TMD and the primary structure [6]. Lin et al. proposed that a multiple TMD (MTMD) design can both effectively obviate the necessity for a high tuning mass ratio and control the multi-modal response of the primary structure. An MTMD design effectively reduces the off-frequency effect of the traditional TMD on the damping of the primary structure [7].

Sadek et al. used the state space method to derive theoretical formulae for optimal TMD frequency and damping ratios under the following condition: for the main structure containing the TMD, the first two modes have the most extensive and almost equal damping ratios. Numerical analysis proved that an increase in mass ratio results in a smaller design frequency ratio and a larger design damping ratio. The objective function of TMD design is thus to optimize these dynamic characteristics [8]. Generally, when designing TMD parameters, if the primary structural system is subjected to harmonic excitations, the formula or regression chart obtained in the linear elastic phase is still applicable. TMD system designs based on the harmonization of external excitations can reduce the response of the primary structure.

In Rana and Soong's research, an SDOF structure was equipped with a TMD designed with parameters based on a formula derived from the harmonic excitations. Time history analysis results from earthquake excitations suggested that the TMD reduced the seismic effect. After the primary structural system began yielding, the natural frequency of the TMD decreased with a reduction in stiffness. Consequently, the effectiveness of the TMD system decreased due to detuning effects. Lukkunaprasit and Wanitkorkul installed a TMD on a five-story structure and a significant reduction in structural response and hysteresis energy was observed under seismic excitations. Pinkaew et al. simulated a 20-story structure equivalent to an SDOF system. The frame that was equipped with a TMD experienced less structural damage after yielding during seismic excitations than the frame without a TMD. Abé proposed the concept of a bilinear hysteresis TMD system. Under the assumption that the relationship between the force and displacement of the primary structural system is elastoplastic, the frequency of the

TMD system was found to be consistent with that of the primary structure after yielding; this enables the TMD system to continue to act as a shock absorber.

Moon et al. proposed a method for designing a friction damping system comprised of a braced frame and friction dampers to retrofit existing old low- to mid-rise reinforced concrete buildings governed primarily by the first mode. The collapse intensity of the retrofitted structure was better than that of the original structure. Kaneko proposed a practical method for evaluating the vibration control performance of TMDs mounted on building rooftops without using time history analysis. Performance curve diagrams were plotted depicting the response reduction factor of the building and the amplification factor of the TMD in terms of the mass ratio and the damping factor. Designing TMD parameters based on this diagram has been reported to be useful in engineering applications [38]. In the formulated design procedure, the TMD mass required is determined based on the idea that the damping factor loss is equal to the additional damping factor introduced by a TMD [9].

This study explores the application of a displacement-dependent TMD (DTMD) to enhance structural seismic performance. To evaluate the feasibility of such an enhancement, shaking table tests were conducted to compare the responses of a two-story bare frame with and without a DTMD. The duration of the test earthquakes was decided by considering different peak ground acceleration (PGA) and seismic characteristics.

Displacement-dependent Tuned Mass Damper

The equations of motion that govern the response of a structure when it is subjected to ground excitation can be expressed as follows:

$$\mathbf{M}\ddot{\mathbf{u}}(t) + \mathbf{C}\dot{\mathbf{u}}(t) + \mathbf{K}\mathbf{u}(t) = -\mathbf{M}\mathbf{r}\ddot{\mathbf{u}}_g(t) \quad (1)$$

where \mathbf{M} , \mathbf{C} , and \mathbf{K} are the mass, damping, and stiffness matrices of the structure, respectively; $\ddot{\mathbf{u}}(t)$, $\dot{\mathbf{u}}(t)$, and $\mathbf{u}(t)$ are the acceleration, velocity, and displacement vectors of the structure relative to the ground, respectively; \mathbf{r} is the influence coefficient vector, which represents the displacement vector; and $\ddot{\mathbf{u}}_g(t)$ is the acceleration of the input ground motion.

As illustrated in Fig. 1, the DTMD consists of a mass m_t , which slides relative to the primary structure and is attached to it through a spring with stiffness k_t and a friction support with coefficient c_t . The parameters of the DTMD are its tuning, mass, and damping ratios. The tuning ratio f depends on the balance of the fundamental frequency of the DTMD ω_t with that of the primary structure ω_p . Thus, the

dynamic characteristics of the linear system are as follows:

$$\omega_t = \sqrt{\frac{k_t}{m_t}} \quad (2)$$

$$\zeta_t = \frac{c_t}{2m_t\omega_t} \quad (3)$$

$$\omega_p = \sqrt{\frac{k_p}{m_p}} \quad (4)$$

where ω_t and ζ_t are the apparent circular frequency and damping ratio of the DTMD, respectively, and the corresponding circular frequency ω_p is defined by assuming an effective mass of m_p and an elastic stiffness of k_p for a controlled building.

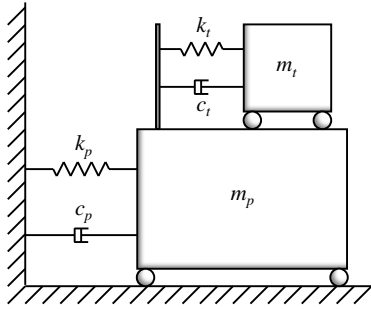


Fig. 1. Tuned mass damper mounted on primary structure

Seismic Excitations

We considered the influence of input excitations with different characteristics on the DTMD. The experiment involved near-fault, far-fault, and long-term ground motions, including earthquake excitations measured at stations TCU047 and TCU068 for the 1999 Chi-Chi earthquake in Taiwan, at station I-ELC270 for the 1940 Northridge Earthquake in California (El Centro), at station KJM000 for the 1995 Hanshin Earthquake in Japan (Kobe), and at station MYG013 for the 2011 Tohoku Earthquake in Japan (THU). Researchers often use the uniform frequency connotations of the far-fault El Centro earthquake and near-fault Kobe earthquake with the velocity pulse period. The two different station records of the Chi-Chi earthquake include TCU047, a far-fault earthquake, and TCU068, a near-fault earthquake with a high peak ground velocity (PGV) and an extensive velocity pulse. The maximum PGV at TCU068 reached 383 cm/s, surpassing the previous highest PGV value measured during the 1994 Northridge earthquake. The 2011 Tohoku earthquake off the Pacific coast was Japan's first recorded earthquake with a moment magnitude scale of more than 9.0 and a long-term duration of more than 2 min.

The acceleration histories for the excitations of the five earthquakes were determined and the normalized displacement and acceleration response

spectra are depicted in Fig. 2.

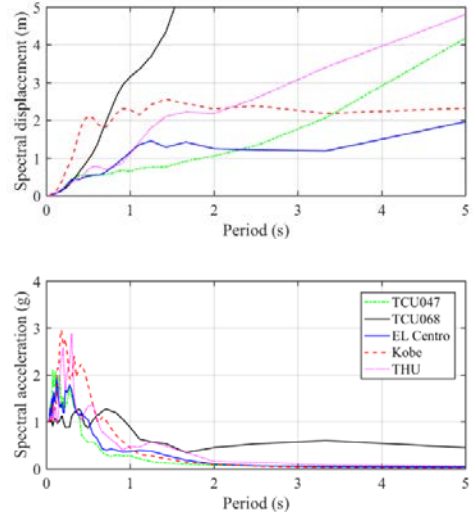


Fig. 2. 5% damped acceleration and displacement response spectra of time-scaled ground motions with PGA of 1 g

Comparing Seismic Responses of a Structure With and Without a Displacement-Dependent Tuned Mass Damper

For an intuitive and comprehensive comparison, the maximum acceleration ratio (AR_{max}) and the minimum acceleration ratio (AR_{min}) from the second floor (2F) of the bare structure and the structure with the DTMD under the five seismic excitations were calculated using Eqs. (5) and (6), respectively, and the values are depicted in Fig. 3. The abscissae in the figure indicate the different PGA ratios for the seismic excitation inputs. If the ordinate value is greater than 100%, the 2F response is amplified.

$$AR_{max} = MAXAcc_{DTMD,i} / MAXAcc_{Bare,i} \quad (5)$$

$$AR_{min} = MINAcc_{DTMD,i} / MINAcc_{Bare,i} \quad (6)$$

where the subscript i indicates the maximum X-directional acceleration responses at the i^{th} floor of the specimens.

On average, the 2F acceleration response of the structure with the DTMD under the El Centro, Kobe, and THU seismic excitations was reduced by approximately 7%, with different excitation magnification ratios from the test results. The interaction between the DTMD and the structure and the out-of-phase motion of the larger PGA reduces the structural response under earthquake excitations. This verifies that the DTMD effectively reduces vibration under the TCU047, TCU068, and THU earthquake excitations.

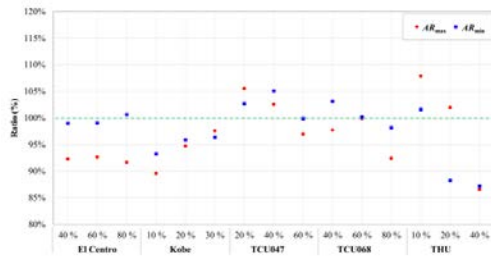


Fig. 3. AR_{\max} and AR_{\min} for the bare structure and the structure with the DTMD

For an intuitive and comprehensive comparison, the maximum relative displacement (RD_{\max}) and minimum relative displacement (RD_{\min}) of the structure with the DTMD with respect to the bare specimen at 2F under the five seismic excitations were calculated using Eqs. (7) and (8), respectively, and the values are depicted in Fig. 4. The structure with the DTMD remained stable throughout the shaking table tests with no generated torsion or rotation. The design of the proposed mechanism using a DTMD can thus enhance structural seismic performance.

$$RD_{\max} = \text{MAX}(Disp_{DTMD,i} - Disp_{Bare,i}) \quad (7)$$

$$RD_{\min} = \text{MIN}(Disp_{DTMD,i} - Disp_{Bare,i}) \quad (8)$$

where the subscript i indicates the maximum X-directional displacement responses at the i^{th} floor of the test specimens.

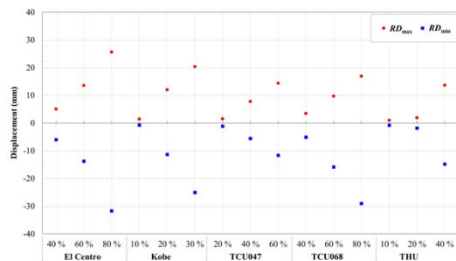


Fig. 4. RD_{\max} and RD_{\min} for the bare structure and the structure with the DTMD

Conclusions

In this study, we considered different PGAs and seismic excitations for a scaled two-story test specimen to verify the reduction in structural responses achieved using a DTMD. In previous studies, TMDs have been used to design wind-resistant high-rise buildings. In this study, we investigated the proposed use of DTMDs in improving the seismic performance of old and low-rise buildings with insufficient seismic resistance. This method provides a buffer for older and low-rise buildings that have not yet undergone urban renewal, ensuring their safety during strong earthquakes. Based on the experimental

success of the DTMD, they seem to be a feasible option for structural vibration reduction.

In summary, using a DTMD, which produces an antiphase resonance to dissipate external force-induced disturbance energy, enhances structural seismic performance. Results indicate that the test specimen equipped with a DTMD did not exhibit a significantly reduced inter-story drift ratio, but the observed acceleration response reduction could be beyond 10% with a properly designed DTMD mechanism and parameters. Using compression springs to provide stiffness and friction supports to improve energy dissipation is possible. The modularly designed mass, compression springs, and friction supports together could thus form a viable mechanism for enhancing structural seismic performance.

References

- [1] Den Hartog JP. Mechanical vibrations. 4th ed. New York: McGraw-Hill; 1956.
- [2] Tsai HC, Lin GC. Optimum tuned-mass dampers for minimizing steady-state response of support-excited and damped systems. Earthq Eng Struct Dyn 1993;22(11):957-73.
- [3] Asami T, Wakasono T, Kameoka K, Hasegawa M, Sekiguchi H. Optimum design of dynamic absorbers for a system subjected to random excitation. JSME Int J III-Vib C 1991;34(2):218-26. <https://doi.org/10.1299/jsmec.1988.34.218>.
- [4] Hadi MNS, Arfiadi Y. Optimum design of absorber for MDOF structures. J Struct Eng 1998;124(11):1272-80.
- [5] Narasimhan S, Nagarajaiah S. A STFT semi-active controller for base isolated buildings with variable stiffness isolation systems. Eng Struct 2005;27(4):514-23.
- [6] Lin PY, Chung LL, Loh CH. Semiactive control of building structures with semiactive tuned mass damper. Comput-Aided Civ Inf 2005;20(1):35-51.
- [7] Lin CC, Hu CM, Wang JF, Hu RY. Vibration control effectiveness of passive tuned mass dampers. J Chin Inst Eng 1994;17(3):367-76.
- [8] Sadek F, Mohraz B, Taylor AW, Chung RM. A method of estimating the parameters of tuned mass dampers for seismic applications. Earthq Eng Struct Dyn 1997;26(6):617-35.
- [9] Kaneko K. Optimal design method of tuned mass damper effective in reducing overall bending vibration in steel buildings with inter story dampers. J Struct Constr Eng Trans AIJ 2017;82(737):1003-12.

Experimental Study on the Evaluation Method for Bridge Structures Using Load Tests

Chun-Chung Chen¹, Chi-Rung Jiang², Sheng-Yuan Siao³, Bo-Han Lee⁴

陳俊仲¹、江奇融²、蕭勝元³、李柏翰⁴

Abstract

For old bridges or those with unique structural systems, the field load test can effectively and accurately assess and verify bridge structure safety. This study presents an experimental study of the evaluation methods for bridges using loading tests. A series of flatcar loading tests are conducted to evaluate the structural safety of bridges. Improving bridge evaluation technologies can effectively assist bridge authorities in implementing bridge maintenance and management operations, as well as extend the service life of bridges to perform service functions. With increasing use of artificial intelligence analysis and the demand for practical applications, transforming a large amount of bridge inspection and monitoring data into useable information that assists in evaluation processes is needed. Therefore, this study applied data science methods to analyze experimental data. Intelligent data promotes effective decision-making for bridge disaster prevention, as well as management and maintenance actions to maintain safety during the bridge life cycle, improve bridge disaster prevention technology, and implement business applications.

Keywords: bridge, structural evaluation, load test

Introduction

The bridge vehicle load test is a direct method to evaluate and verify actual structural bearing capacity of field bridges. Generally, there are static and dynamic load tests. The static load test evaluates stress behavior and structural characteristics of the bridge structure to verify its safety and bridge structure design theory and calculation method, the results of which are used for evaluating similar structural bridges. During design and construction, the dynamic load test can determine the dynamic characteristics of a bridge structure, such as natural vibration frequency, vibration state, or damping characteristics. Further, it can elucidate the dynamic impact effect of the bridge under heavy vehicle weight. The vehicle load test must use a loading vehicle with a known weight as the test load. Therefore, it has to record the actual vehicle load before the vehicle enters the bridge deck for the test and moves slowly to its predetermined position according to the experimental procedure.

The static vehicle load test primarily measures

the relative vertical deflection at each measurement point on the bridge deck or the change in bridge profile under experimental loading. Moreover, the test data should also include inclination or displacement of the related static parameters of the bridge structure. Since the load-bearing capacity and deformation behavior of the system are related to the time characteristics of the loaded weight, the loading program must be carefully selected to understand the load-bearing capacity and deformation behavior of the structure. There must be a sufficient interval between each loading case. Obtaining the essential dynamic characteristics of the bridge requires measuring the vibration acceleration at different bridge positions, including the fundamental vibration frequency, representative vibration state, or damping. The dynamic vehicle load test should use installed vibration signal measuring instruments and equipment on the bridge to record the vibration signal during the dynamic vehicle load driving.

While the load test is a useful method to assess bridge structure safety, further methods are needed to effectively quantify and evaluate structural safety. This

¹ Associate Researcher, National Center for Research on Earthquake Engineering

² Associate Technologist, National Center for Research on Earthquake Engineering

³ Associate Technologist, National Center for Research on Earthquake Engineering

⁴ Assistant Researcher, National Center for Research on Earthquake Engineering

study explores assessing bridge structure safety using an experimental load test platform. A series of load test cases with scaled bridge specimens are considered that apply controllable static and dynamic loads in the laboratory and measure the response of the bridge specimen.

Application of Data Science Methods

In recent years, artificial intelligence and big data analysis has received increasing attention from many research fields and has gradually developed practical application requirements. Data science is a multidisciplinary field of applied technology, including statistical scientific methods and data analysis and processing. This study applies monitoring and inspection data processing to the bridge load test data using lifecycle-based bridge management and maintenance concepts.

Flatcar load tests were performed. The known load-bearing load was used as the input value to measure output responses of the bridge specimen structure. The data science analysis method was applied to a series of experimental data. A series of experimental, data science models can be used for long-term monitoring data references. Figure 1 shows the application of scientific data analysis methods to select parameter categories. Data processing tools can be divided into three categories: structural analysis, data regression, and structural status classification. The input parameters of structural analysis include structural system characteristics, geometric dimensions, material parameters, and boundary support conditions. The corresponding output continuity long-term monitoring data covers field and laboratory test data. Traditional analytical methods can then build a structural analysis model for verification that can appropriately evaluate structural response.

Regression analysis is a common data processing method when collecting long-term monitoring data and is suitable for exploring long-term trends to determine relative management and maintenance outputs. Field bridge monitoring items typically include physical quantities such as temperature, strain, displacement, inclination, and velocity or acceleration, which feed directly into the structural safety assessment method. Using the structural state classification method, structural safety classification of the structural assessment results relies on a large amount of measurement or monitoring data. In addition to the structural safety level, the classified output can also be used to estimate the limit state of the structure, predict possible disaster modes in advance, and prepare for disasters when they occur.

Analysis		Regression		Classification
Structural Parameters (Identifiable)	Data Sources (Measures)	Features (Input)	Responses (Output)	Results (Trends or Predictions)
Structural Systems	Field Monitoring (Bridges)	Temperature	Deflection	Safety Levels (Notice Value, Warning Value, Action Value)
			Displacement	
			Inclination	Limit States (Failure Modes)
Geometry Dimensions	Field Monitoring (Transmission Tower)	Temperature	Acceleration	Maintenance Strategies (Inspection Frequencies, Methods, Budget)
		Wind	Strain	
		Earthquake		
Material Properties	Field Experiments (Loading Tests)	Vehicle Load	Deflection	Disaster Response (Emergency Action)
		Vehicle Position	Strain	
Boundary Conditions	Lab. Experiments	Vehicle Velocity	Acceleration	

Fig. 1. Selected parameters for the data science analysis method in this study.

Laboratory Experiments of Loading Tests

The planned analysis process and study details are shown in Figure 2. Using the field bridge long-term monitoring system and the load test of the experimental specimen returns a considerable amount of measurement data. This study verified the scientific analysis measurements with data. On-site monitoring data mainly uses the environmental temperature change as an input parameter and matches the vehicle load test results. The laboratory load test can accurately show applied load values and loading position and conditions and measure the precise response of the structural specimen. In addition to the traditional finite element analysis method using the structural model for analytical solutions, load tests can also be analyzed using the structural influence line theory to obtain the analytical solution for the corresponding load condition.

The structural analysis model and test measurement data can be compared. Data science methods can perform regression calculations and classification analyses. Sorting and screening data is required to formulate applicable analyses for monitoring and measurement data, as well as define representative measurement parameters corresponding to safety, after which a quantitative index process that assesses bridge safety and disaster prevention can be developed.

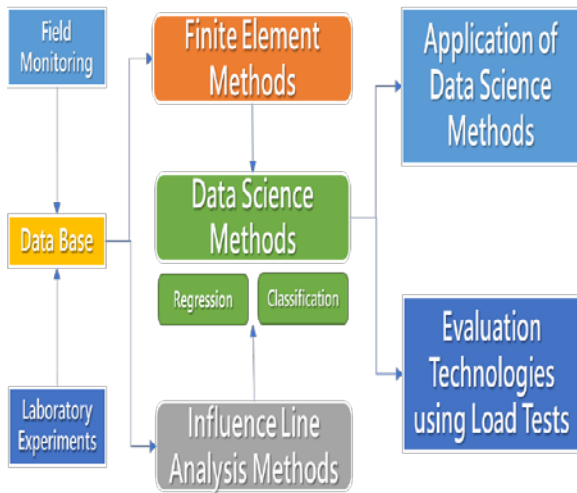


Fig. 2. Research analysis process and the studied content.

This study designed a set of research and development platforms for load test technology. The hardware components of the platform include test landslide lanes for loaded flatcars and bridge specimens, as shown in Figure 3. The test platform can perform both static and dynamic load tests. The static load test is equipped with various flatcar loads at different locations on the bridge specimen that provide static data measurements. In the dynamic load test, a pulley system is installed above the landslide section. The pulley system and the counterweight device behind the ramp section connect a flatcar with a given load to a steel cable. The steel cable lifts the flatcar to a specific elevation and fixes the flatcar temporarily in position.

Furthermore, a decoupling release allows the test flatcar to detach from the steel cable during the test. The flatcar will freely slide down by gravity and enter the test section lane of the bridge specimen. As gravitational potential energy may be converted to other forms of energy, such as kinetic energy, the free sliding entry speed of the flatcar at a specific height can be calculated. The bridge specimen in this study was a single-span simply supported steel bridge with a span of 3 m, a bridge deck width of 1 m, and two-way lanes. The structural system includes three steel girders (section H150 × 45 × 2.3) and a steel bridge deck (thickness of 5 mm). Figure 4 shows the configuration of the load test measuring instrument.

The measuring instruments include optical fiber and electronic strain gauges installed on the steel member to measure the strain response of the girders under load application. Furthermore, an optical displacement measuring instrument is used to record the output response of the dynamic relative displacement of the bridge specimen as flatcars travel through the test section. Furthermore, because of the possible vibration problems caused by vehicles

passing over the bridge, this test technology research platform aims to combine developmental requirements of structural vibration reduction technology in the future, such as coordinated mass dampers mounted on the bridge specimen, using vibration reduction experiments.



Fig. 3. Load test landslide lane and test bridge specimen.

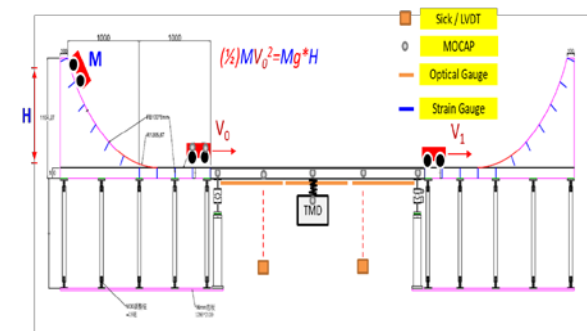


Fig. 4. Load test measurement instrument configuration.

This study used commercial structural analysis software MIDAS Civil to build the bridge specimen's structural analysis model shown in Figure 5. The main components of the analysis model include three girders and the bridge deck. The measurement data of the test load applied during the test can provide feedback to the analysis model and the simulation can further evaluate the ultimate state and the related dynamic characteristics of the bridge specimen. Finally, the input and output parameters of the measurement records must be defined.

This study applied a data science method to analyze experimental data. Therefore, test loading cases must be planned more systematically. The dynamic load test involves releasing the elevation from the landslide, calculating and setting the average speed of the test vehicle on the bridge deck, and measuring the displacement and stress of the main girder and deck plate of the test bridge, as well as any structural vibration signals.

The maximum displacement or strain data can be obtained via a series of flatcar load tests and the test load and average speed of the corresponding flatcar are used as key input analysis parameters. In this study, the data science method explores possible correlations and establishes a data science analytical model. The established model can evaluate the safety level or state of the bridge structure. Figure 6 shows the test measurement input and output parameter table.

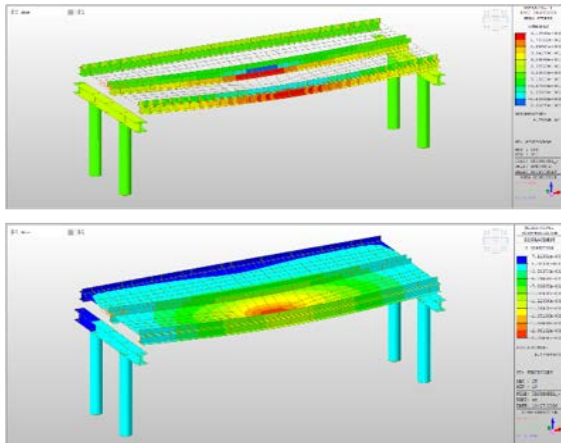


Fig. 5. Structural analysis model of the bridge specimen.

Figure 7 shows the preliminary static load tests used in this study. The maximum vertical load of each flatcar with eight layers of mass pieces is 125 kg in total weight. There are four sets of flatcar that can be used with different masses so that various vertical loads can be applied according to test configurations for different flatcar positions. For the dynamic load test, each flatcar is equipped with a sliding rail support frame and low-friction bearings so that the moving flatcar can travel smoothly on the deck lane without deviating while simultaneously ensuring that the flatcar can easily pass over the entire bridge. The steel plate elevation of the expansion joint between the landslide section and the bridge deck must be smooth.

Time / Items	Ramp Load Testing Bridge (Measurement / Input)					Target (Response)		
	Loading (Li)	Velocity (Vi)	Deflection (Di)	Stress (Si)	Acceleration (Ai)	Max Deflection (Dmax)	Loading (Li)	
Record ₁	L ₁	V ₁	D ₁	S ₁	A ₁	Dmax	L ₁	
Record ₂	L ₂	V ₂	D ₂	S ₂	A ₂		L ₂	
...
Record _n	L _n	V _n	D _n	S _n	A _n		L _n	
Weightings	Try to find the "key feature" / Representative sensors or locations					Safety / Warning / Action		

Fig. 6. Test measurement record input and output parameters.



Fig. 7. The static load test configuration with flatcars.

Conclusions

This study proposed an innovative experimental platform for evaluating bridge structures using load tests. A series of flatcar load tests was conducted and data science methods were applied to the test data for assessing bridge structure safety. The feasibility of the dynamic load test was presented in the laboratory. Finally, the study aimed to collect large amounts of data using experiments or field projects to select and discuss the applicability of the data science models.

For old bridges or bridges with unique structural systems, the field load test is a practical method to assess structural safety in detail. With the increasing trend in the use of artificial intelligence analysis, a large amount of data from field monitoring, inspection, or experiments can be obtained and transformed for use in evaluation via scientific data analysis methods. We are now moving toward intelligent decision-making in bridge disaster prevention and management, ensuring bridge service safety during the bridge lifecycle, achieving complete lifecycle management and maintenance, improving bridge disaster prevention technology, and implementing business applications.

Application And Design of Automatic Water Supplement for Bridge Fiber Optic Settlement Sensor

Zheng-Kuan Lee¹

李政寬

Abstract

This paper is about the design and application of optical fiber differential settlement measurement (DSM) sensors for bridges. In particular, an automatic water supplement tank is introduced to reduce the maintenance work required. By using the law of connected vessels, the buoyancy principle, the two-force member equilibrium condition, and the photo elasticity of fiber Bragg grating (FBG), the DSM sensor is easily manufactured and sensitive to level changes. Besides describing the design principles, this study also illustrates the application of the DSM sensors on underpass bridges. From the field case, the proposed DSM sensors are demonstrated to be stable and precise for monitoring the behavior of multiple-span underpass bridges. Sharing the field experience of the optical fiber DSM sensor is the aim of this study.

Keywords: bridge safety monitoring, settlement sensor, FBG, sensor maintenance

Introduction

Bridges are large-scale linear structures used to extend traffic routes (e.g., roads and railways), cross natural barriers (e.g., rivers, straits, and canyons), or cross artificial barriers (e.g., highways and railway lines). Bridges connect urban and rural areas, as well as transport water and energy, making them indispensable structures in modern civilization [1].

Bridges are profoundly affected by the environment and external forces of nature including earthquakes, typhoons, and floods, as well as by the aging of materials, such as in the case of bridge deformation due to the creep and shrinkage of concrete [2]. Regular manual level surveys for bridge elevation are therefore important during bridge inspections.

Because of the growth of cities, the increasing number of bridges demands more inspection efforts. Adapting technologies from other domains of knowledge for bridge level surveys to save human resources and enhance efficiency has been a continuing concern for bridge managers and engineers. With the advent of the Internet of Things (IOT), automatic bridge safety monitoring technologies are expected to expand.

This study designed and produced a fiber Bragg grating (FBG)-based differential settlement sensor (DSM), which was applied to in situ monitoring of bridges for elevation changes. Based on the results of its application, the proposed DSM sensor can be used as an instrument for the automatic leveling of bridge elevation.

Brief Review on the Development of Laser, Optical Fiber, and Fiber Bragg Grating

The invention of lasers and optical fibers in the mid-20th century has substantially improved quality of life and facilitated convenient worldwide communication, an influence that was difficult to imagine at the time they were invented. Key events in optical communication history are as follows: (1) Albert Einstein first predicted the possibility of stimulated emission in his 1917 paper [3]; (2) light-transmitting optical fibers were invented in the 1930s, though they could only be used as art lighting and endoscopes; (3) in 1960, Maiman produced a laser by stimulating a ruby with high-intensity light, thereby providing the first necessary conditions for light to transmit information; (4) in 1966, Kao and Hockham discovered that rapid loss of light was mainly due to impurities within optical fibers, and determined that increasing the purity of glass enabled the transmission distance of optical signals to exceed 100 km; (5) in

¹ Associated Research Fellow, National Center for Research on Earthquake Engineering

1970, a low-loss optical fiber was mass-produced by Corning Inc.; (6) in 1977, the world's first optical fiber communication system was developed for commercial use in Chicago in the United States; (7) in 1978, Hill and colleagues discovered the photosensitivity of an erbium-doped optical fiber and used an argon-ion laser to induce chemical changes in photosensitive optical fibers [4]; (8) in 1989, Meltz and colleagues employed high-energy ultraviolet lasers by using the transverse holographic method to change the molecular structure of a photosensitive optical fiber, turning it into an optical filter [5]; and (9) in 1993, Hill and colleagues developed the phase-mask method to produce FBG, thereby enabling the technology to mature [6]. Today, FBGs are mass-produced and commercialized, allowing for them to be purchased and applied in various fields.

Introduction to Fiber Bragg Grating

This study only describes an application of FBG; a more detailed explanation can be found elsewhere [7]. Fig. 1 shows its optical and mechanical behavior: the changes in the wavelengths of reflected light depend on the changes in strain and temperature.

If both ends of one FBG are clamped using a heat-shrink tube as in Fig. 2, through which the force medium is introduced, the local organization forms sensing elements.

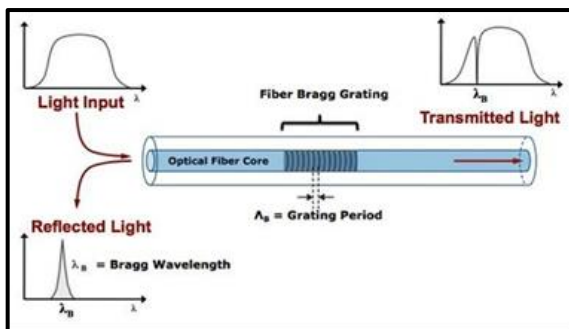


Fig. 1. Structure and spectral response of FBG

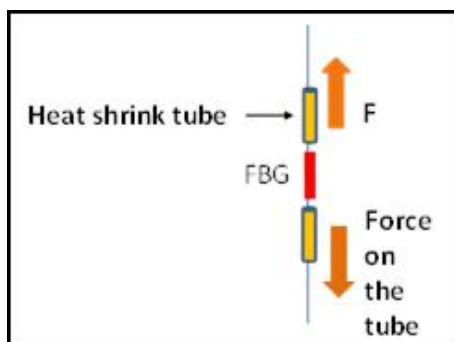


Fig. 2. Heat-shrink tubes placed on both ends of the FBG act as the application medium for external force F.

Fiber Bragg Grating-based Differential Settlement Sensor

Fig. 3 shows the structure of a set of FBG-based differential settlement sensors, which contain two water-filled containers connected by a communicating tube. The upper and lower ends of the FBG were clamped by two heat-shrink tubes, with one end fixed at the top of the container and the other end fixed with the cylinder buoy to withstand part of the cylinder weight [8]. The elevations of the two sensors in Fig. 3 may change into those depicted in Fig. 4. From wavelength signals, the elevation difference between Fig. 3 and Fig. 4 can be calculated.

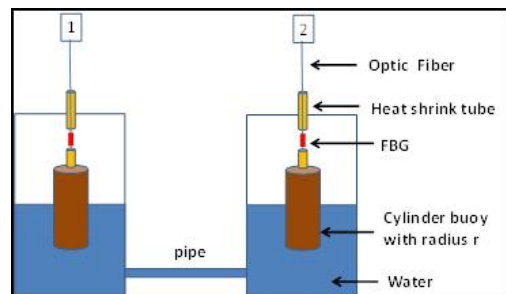


Fig. 3. FBG-based differential settlement sensors

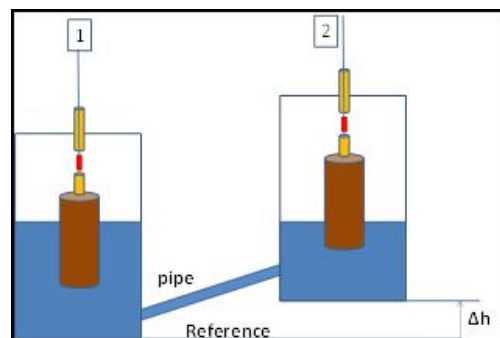


Fig. 4. Sensor elevation change

Bridge Monitoring Project

Fig. 5 shows three DSM sensors that were deployed within each box girder and connected by pipes to observe the midpoint deflection as well as the elevation difference at both ends of the girder. In addition, optical fiber thermometers were placed on the roof plate and base plate inside some girders of a continuous 14-span underpass bridge in Tainan City, Taiwan. [9]

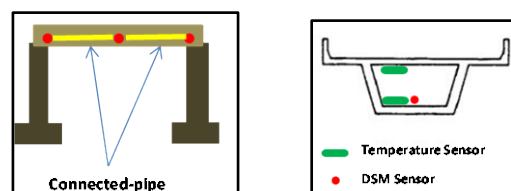


Fig. 5. Three DSM sensors deployed at each span; optical fiber thermometers in some girders

Fig. 6 shows approximately 24 hours of monitoring data from Span 1, with the abscissa and ordinate representing time (min) and length (cm), respectively. The blue line shows the deflection variations at the midpoints in Span 1, while the red line indicates the elevation changes at both ends of the girder. Fig. 7 presents the temperature ($^{\circ}\text{C}$) data collected by the optical fiber thermometer in the box girder. The blue line and the red line show the temperature variation on the roof plate and the base plate inside the girder, respectively. The deflection of the girder is obviously affected by temperature with a time-delay effect.

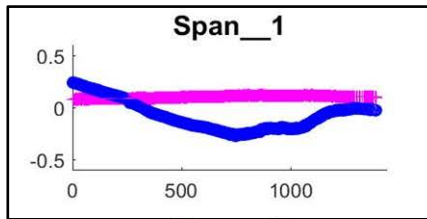


Fig. 6. Observation from 19:00 on June 10, 2018 to 18:30 on June 11, 2018. The blue line represents changes at the midpoint girder deflection and the red line represents the elevation changes at both ends of the girder. Abscissa and ordinate represent minutes and centimeters, respectively.

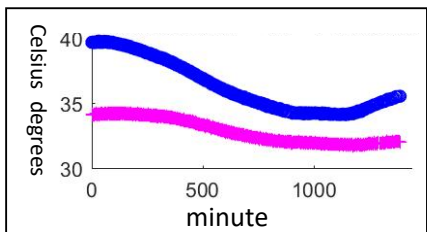


Fig. 7. Temperature observations from the box girder. The blue line and the red line indicate the temperature changes of the roof plate and the base plate, respectively.

Discussion of Bridge Structure Based on Monitoring Data

Monitoring was conducted for more than one year with a sampling rate 0.5 Hz. Fig. 8 graphs the maximum deflections (absolute value) by month and by span. The maximum deflections took place at the abutment spans (Span 1 and Span 14) and at those spans on both sides of the expansion joint between Span 7 and Span 8. Fig. 8 shows that the bridge deflection was stable with a fixed “W” pattern. Fig. 9 graphs the maximum elevation difference between two ends of each girder by month and by span, revealing that all spans were stable within a range from 0.03 to 0.37 cm.

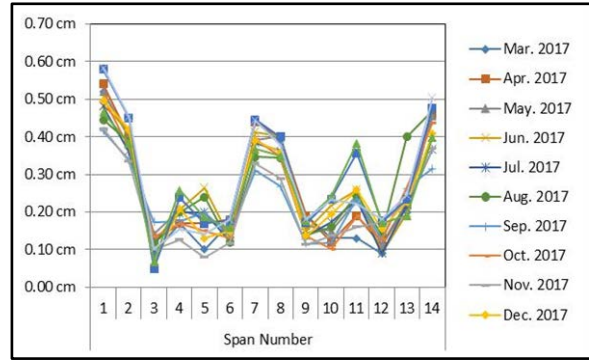


Fig. 8. Maximum girder deflection (absolute value) by month and by span.

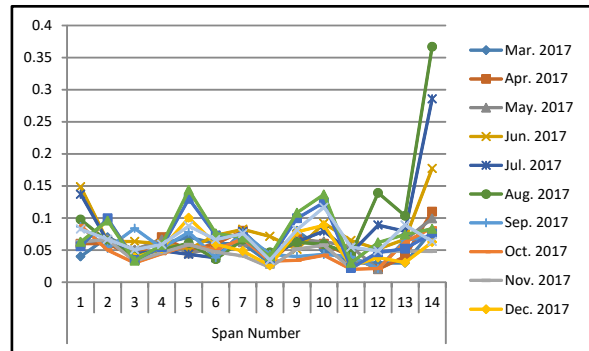


Fig. 9. Maximum elevation difference (absolute value) between two ends of each girder by month and by span.

Discussion of the Sensor Maintenance

Water in the sensors can vaporize at any time. On average, maintenance work is required every three months to refill the sensors. It is tedious and laborious work inside the girder. The water vaporizing problem should be further considered in the future.



Fig. 9. Refilling the sensors

Automatic Water Supplement Design for Fiber Optic Settlement Sensor

To reduce the frequency of the maintenance work, a water supplement tank using the siphon principle was designed and is shown in Fig. 10.

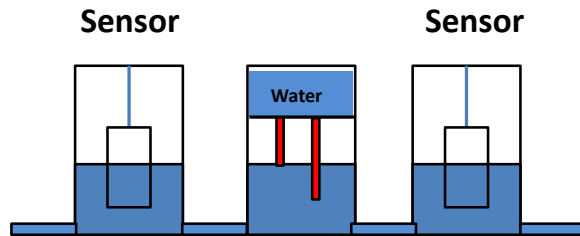


Fig. 10. A water supplement tank linked with sensors

There are two tubes in the water supplement tank. The shorter tube controls the level of the connected sensors, while the longer one delivers water from the upper level to the lower level. In this way, the frequency of the maintenance work could be reduced. In another bridge monitoring case, the upper water tank was 30 cm in height and lowered approximately 1 cm per month to maintain the water level of the connected sensors.

Conclusions

1. This study briefly introduces the historical development of lasers, optical fibers, and FBG. It is recognized that science together with material-science facilitates the progress of engineering technologies.
2. This paper proposes a simple design for DSM sensor integrated with the law of connected vessels, the buoyancy principle, the two-force member equilibrium condition, and the photo elasticity of FBG.
3. A 14-span underpass bridge was monitored with the DSM sensors. This proved that the sensors are sufficiently sensitive and reliable to clarify some subtle bridge structural behaviors.
4. From the field case in this study, optical fiber and FBG sensors demonstrate great advantages, especially for long and multiple-span bridges.
5. A water supplement tank using the siphon principle was introduced to reduce the frequency of maintenance work. From field cases; the mechanism was proven to work.

Reference

- [1] "Bridge," Wikipedia, Retrieved July 18, 2018 from <https://en.wikipedia.org/wiki/Bridge>
- [2] "Koror–Babeldaob Bridge," Wikipedia, Retrieved July 18, 2018 from https://en.wikipedia.org/wiki/Koror%E2%80%93Babeldaob_Bridge
- [3] "Einstein Predicts Stimulated Emission," APS NEWS, American Physical Society, Retrieved July 18, 2018 from <https://www.aps.org/publications/apsnews/200508/history.cfm>
- [4] K. O. Hill, Y. Fujii, D. C. Johnson, and B. S. Kawasaki, "Photosensitivity in optical fiber waveguides: application to reflection fiber fabrication," *Appl. Phys. Lett.* 32 (10): 647, 1978.
- [5] G. Meltz, W. W. Morey, W. H. Glenn, "Formation of Bragg gratings in optical fibers by a transverse holographic method," *Opt. Lett.* 14, 823-825, 1989.
- [6] K. O. Hill, B. Malo, F. Bilodeau, D. C. Johnson, and J. Albert, "Bragg gratings fabricated in monomode photosensitive optical fiber by UV exposure through a phase mask" *Appl. Phys. Lett.* 62, 1035, 1993.
- [7] "Fiber Bragg grating," Wikipedia, Retrieved July 18, 2018 from https://en.wikipedia.org/wiki/Fiber_Bragg_grating
- [8] Z.K. Lee, "Bridge safety monitoring integrated system with full optical fiber and the method for sensing thereof," U.S. Patent No. 9183739, November 10, 2015.
- [9] B. S. Huang, C. H. Chiang, Y. H. Chen, "Restoration of Lateral Deviation in Bridge No. 24 at Provincial Highway 86 after the 2016 Southern Taiwan Earthquake," *Journal of the Chinese Institute of Civil & Hydraulic Engineering*, Vol. 44, No. 3, pp.20–26, June 2017.

Study on Lightweight Truss-type Composite Temporary Bridges for Disaster Relief

Fang-Yao Yeh¹, Bo-Han Lee², Kuo-Chun Chang³, Sheng-Yuan Shiao⁴,
Chi-Lon Jang⁴ and Chun-Lung Chen⁵

葉芳耀¹、李柏翰²、張國鎮³、蕭勝元⁴、江奇融⁴、陳君隆⁵

Abstract

Typhoons and earthquakes, which occur frequently in Taiwan, often lead to the washout or collapse of river bridges, subsequently causing traffic interruptions. When a bridge structure loses workability, constructing a temporary rescue bridge is effective for disaster relief. In this study, a truss-type composite temporary rescue bridge is proposed to improve the stiffness of longer span (50 m) bridges. A 50-m span asymmetric self-anchored truss-type cable-stayed bridge is designed and experimentally validated. The rapid assembly technology proposed for construction is validated via simulations. It is found that the assembly process improved worker safety during bridge construction and shortened the assembly duration. Two construction processes, namely the cantilever erection method and the incremental launching method, are compared to improve worker safety. The results of this study indicate that (1) the truss-type segmental composite bridge can improve the stiffness of a 50-m span temporary rescue bridge, thus meeting the required deflection-to-span ratio, (2) rapid assembly technology for bridge construction significantly improved worker safety and shortened assembly time of the temporary rescue bridge, (3) the incremental launching method had greater operational efficiency than the cantilever erection method, (4) the incremental launching method can avoid bridge construction over rivers, thus providing better worker safety, and (5) considering construction safety, the maximum allowable wind speed for construction should be set to maintain worker safety.

Keywords: temporary rescue bridge, truss type structure, safety of workers, rapid assembly

Introduction

Typhoons and earthquakes, which occur frequently in Taiwan, often lead to the washout or collapse of river bridges, thereby causing traffic interruptions. When a bridge structure loses its workability, constructing a temporary rescue bridge is an effective disaster relief option. Yeh *et al.* applied glass fiber-reinforced plastic (GFRP) material to a segmental temporary rescue bridge design, making it lightweight and reusable [1]. The live load capacity of the GFRP bridge was 5 tons and the span length was 20 m. However, when considering the working environment, the span length may be too short and assembly of this bridge may be difficult due to unsuitable weather for construction and difficulties in

ensuring safety of on-site construction workers.

To address these problems, a truss-type segmental structure is used here to improve the stiffness of a longer span (50 m) bridge and the process of constructing the GFRP temporary rescue bridge is analyzed. The assembly process is critical, as it significantly affects construction progress and worker safety during bridge construction. Two different processes, namely the cantilever erection method and incremental launching method, are compared in terms of worker safety.

Design and experiment of a composite temporary bridge

¹ Division Director, Bridge Engineering Division, National Center for Research on Earthquake Engineering

² Assistant Researcher, Bridge Engineering Division, National Center for Research on Earthquake Engineering

³ Professor, Department of Civil Engineering, National Taiwan University

⁴ Associate Technologist, Bridge Engineering Division, National Center for Research on Earthquake Engineering

⁵ Assistant Technologist, Bridge Engineering Division, National Center for Research on Earthquake Engineering

Design of a truss-type composite bridge

For the design, a case of communities isolated by Typhoon Morakot in 2009 was considered. A river bridge with a 50 m span length was washed away by the floods, interrupting traffic to and from surrounding areas. A temporary rescue bridge was required within eight hours to ensure small trucks weighing 3.5 tons could access and transport relief materials into the isolated area.

A temporary rescue bridge system using a self-balancing approach with a cantilever erection method and incremental launching method is herein developed and an asymmetric self-anchored truss-type segmental composite cable-stayed bridge is proposed. Truss-type GFRP segmental bridge systems were studied to assess the structural requirements necessary to meet the following design requirements recommended by USDA: 50-m span, 3-m width, 5-ton live load capability, and a deflection-to-span ratio of $L/400$ [2]. Fig. 1(a) shows the deformed shape and finite element method (FEM) model of the asymmetric self-anchored truss-type segmental composite cable-stayed bridge. The main girders of the bridge system with truss-type structural segments were composed of 203 mm \times 60 mm \times 9.5 mm C-shaped and 101 mm \times 101 mm \times 6 mm box-shaped GFRP composite members. The GFRP had a Young's modulus of 20.03 GPa, a density of 1.72 g/cm³, and an allowable stress of 207 MPa. Fig. 1(b) shows the deflections under various loading positions. The maximum displacement was 10.67 cm, which meets the design requirements for a deflection-to-span ratio of $L/400$.

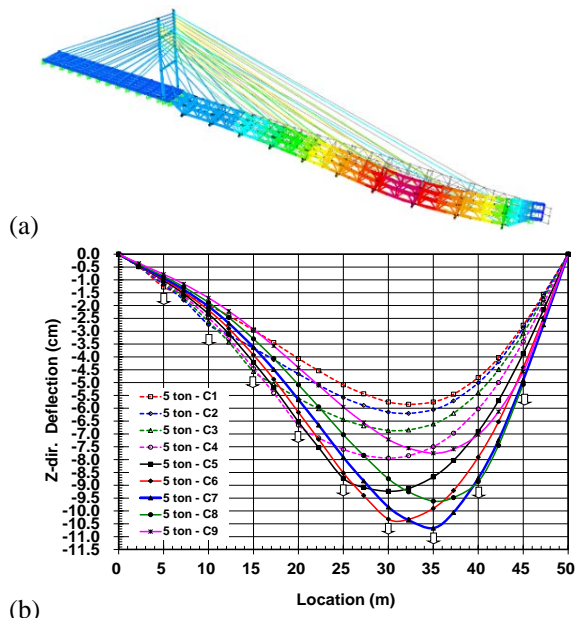


Fig. 1. Design results for a 50-m span temporary rescue bridge: (a) the deformed shape and (b) deflections (for various loading positions).

Experiment for a truss-type composite segment

The typical experimental setup for a flexural test is shown in Fig. 2. The test program included a flexural test to measure the deflection and stiffness of the truss-type composite segment to calibrate the FEM model.

The specimen was tested using flexural loadings applied at the mid-span of the specimen. The tests were performed by controlling the load with a design target loading of 50 kN. Comparisons of laboratory measurements and analytical results obtained using the FEM model are presented in Fig. 3, showing the deflection of the G2 girder at an applied load of $P = 20\text{--}50$ kN at the mid-span. The solid and dashed lines denote the analytical results and experimental measurements, respectively. As shown in these figures, the FEM model can predict the GFRP bridge deflection with satisfactory accuracy. Therefore, the FEM model was validated by comparing the analytical and experimental results.



Fig. 2. Experimental setup for the flexural test with the applied loading at the mid-span of the specimen.

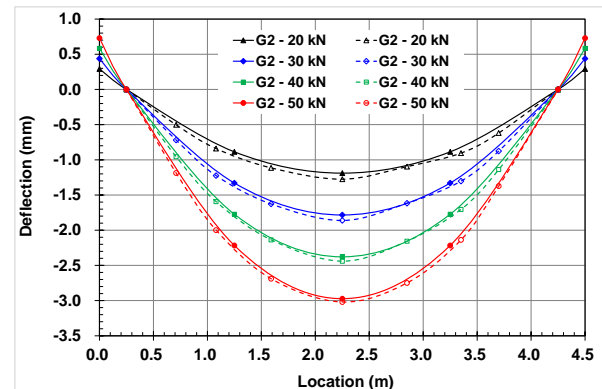


Fig. 3. Comparison of results for the deflection of the specimen at an applied load of $P = 20\text{--}50$ kN.

Fig. 4 shows the strain measurement positions at the top of the upper chord, bottom of the upper chord, vertical strut, diagonal brace, top of the lower chord, and bottom of the lower chord. Fig. 5 shows that the maximum longitudinal strains were 3.23×10^{-4} , which occurred in the main girder G2, on the bottom of the upper chord. Nevertheless, the minimum longitudinal strains were -3.51×10^{-4} , which occurred in the main girder G2 on the top of the upper chord.

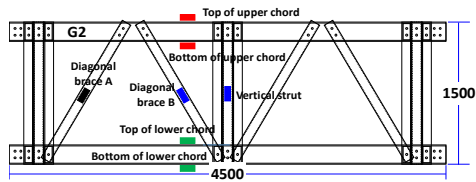


Fig. 4. Location of strain gauges for main girder G2 of the specimen.

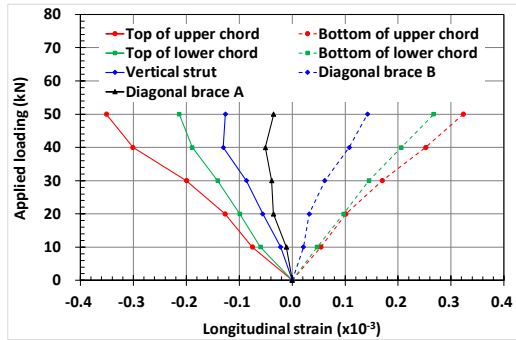


Fig. 5. Test results for the longitudinal strains of main girder G2 at the applied load of $P = 0\text{--}50$ kN.

Rapid assembly technology for construction

Design of truss-type segment joints

Considering the force transmission and ease of assembly, the pin connection is the key component of the joint design. Fig. 6 shows the design results for the segmented male joint, the female joint, and the combined joint. This joint only transmits axial and shear forces.

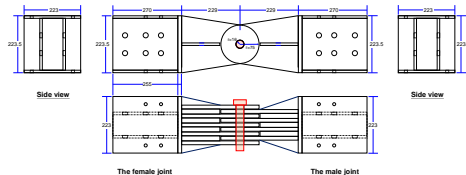


Fig. 6. Design drawing of the truss-type segment joints.

Development of rapid assembly technology

The joint between the segments of the cantilever erection method is guided by the central joint of the upper chord, after which the bottom chord joint can be assembled in a rotating manner. In the proposed construction method (Fig. 7), the section can be hoisted by a miniature crawler crane. The upper chord joint section is first combined with a bolt, after which the section is assembled in a rotating manner.

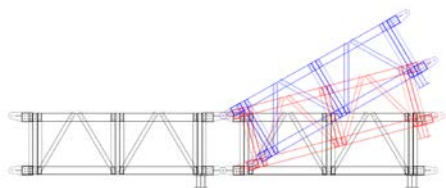


Fig. 7. Segment joint assembly by the rotation method.

Construction operational efficiency and safety analysis

Description of efficiency analysis

The operational efficiency analysis for the task of disaster relief using temporary rescue bridges compares operational efficiency indicators from the cantilever erection (Fig. 8) and incremental launching (Fig. 9) methods. The efficiency indicators include (1) worker safety, (2) construction time, (3) equipment and labor required for construction, and (4) counterweight demand.

Worker safety is the first indicator under consideration. For the cantilever erection method, a mini-crawler crane is used instead of workers for the river-crossing process, thus improving worker safety. For the incremental launching method, the assembly is performed on the riverbank, after which the bridge is pushed forward to the isolated end to avoid construction over the river, which ensures worker safety.

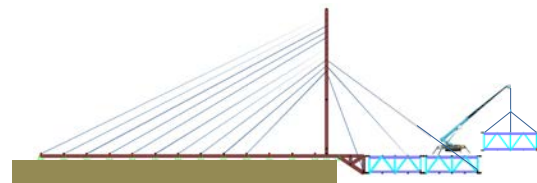


Fig. 8. Cantilever erection method for rescue bridges.

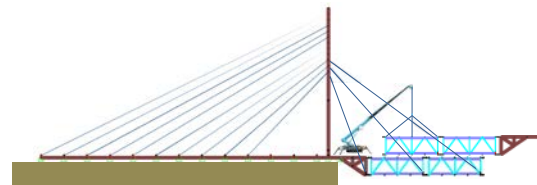


Fig. 9. Incremental launching method for rescue bridges.

Construction time analysis

The construction time analysis for a 50-m span temporary rescue bridge compared the total construction time taken by the original construction method without autonomous assembly technology, using the cantilever erection method with autonomous assembly technology, and using the incremental launching method.

Fig. 10 shows the construction time results for the three different construction processes for a 50-m span temporary rescue bridge. The gray line represents the original construction method, whose total construction time was approximately 540 minutes. This does not meet the requirement of being within eight hours. The red line represents the cantilever erection method. Owing to the autonomous assembly technology, the total construction time was shortened to 430 minutes, thus meeting the < 8 -hr requirement. The blue line

represents the incremental launching method. As the construction process over the river was avoided, the total construction time was drastically shortened to 370 minutes, thus meeting < 8-hr requirement.

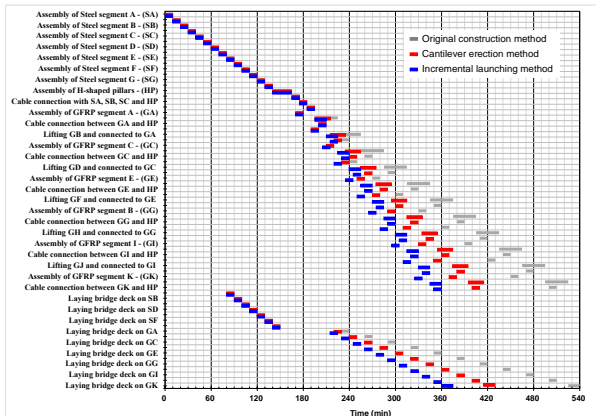


Fig. 10. Results of the construction time analysis of the three construction processes for a 50-m span temporary rescue bridge.

Demand for additional counterweight

The truss-type composite temporary rescue bridge was constructed using a self-balancing approach with either the cantilever erection method or incremental launching method. Before completion of the composite bridge, additional counterweight is needed for balancing the weight of the mini-crawler crane and the self-weight of composite segments during construction.

Fig. 11 shows the results for additional counterweight demand of both construction processes for a 50-m span temporary rescue bridge. The red line represents the cantilever erection method, where the required additional counterweight was 1.8–25.8 tons during the river-crossing process. The blue line represents the incremental launching method, where the required additional counterweight was 3.8–8.9 tons during the river-crossing process.

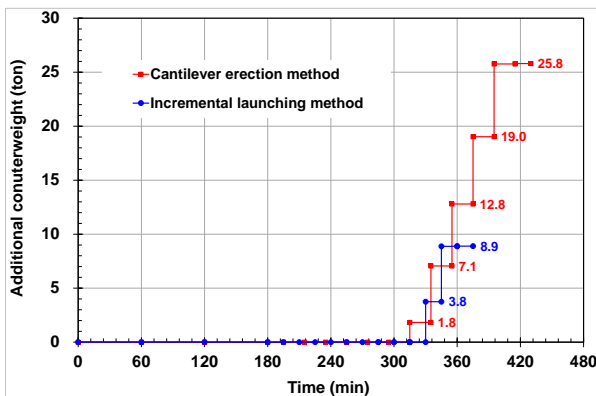


Fig. 11. Results of additional counterweight demand for the two construction processes for a 50-m span temporary rescue bridge.

Analysis of wind effects during construction

During the erection of the temporary bridge for disaster relief, lateral wind was the most important factor affecting construction safety. Wind force calculations were performed according to current highway bridge design specifications. Fig. 12 shows the lateral displacement of the front end of the bridge under different wind speeds at a length of 42.5 m (before bridge completion) for a 50-m span truss composite disaster relief bridge. As the skew angle of the wind increased, the maximum lateral displacement decreased accordingly. Nevertheless, as the wind speed increased, the maximum lateral displacement rapidly increased.

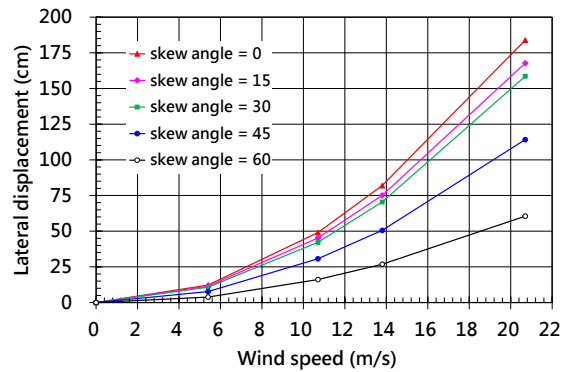


Fig. 12. Lateral displacements under different wind speeds for a 50-m span temporary rescue bridge.

Conclusions

This study showed that (1) a truss-type segmental composite bridge can improve stiffness of a 50-m span rescue bridge to meet the required deflection-to-span ratio, (2) autonomous assembly technology for bridge construction can contribute significantly to improving worker safety and shortening assembly time of rescue bridges, (3) the incremental launching method has greater operational efficiency than the cantilever erection method, (4) the incremental launching method can avoid construction over the river, thus ensuring better worker safety, and (5) considering construction safety, the maximum allowable wind speed for construction should be set to maintain worker safety.

References

1. Yeh, F.Y., K.C. Chang, Y.C. Sung, H.H. Hung and C.C. Chou, A novel composite bridge for emergency disaster relief: Concept and verification, *Composite Structures*, 2015, 127 (Supplement C): p. 199-210.
2. USDA Forest Service, A guide to fiber-reinforced polymer trail bridges, 2nd edition, United States Department of Agriculture, 2011.

A Study of Rotational Loads on the Supporting Structure of an Onshore Wind Turbine by Time-Frequency Analysis

Kung-Chun Lu¹, Wei-Chen Tseng², Yu-Shu Kuo³, Peng Heng-Chu⁴, Yi-Cheng Chen⁵

盧恭君¹ 曾韋禎² 郭玉樹³ 彭珩筑⁴ 陳一成⁵

Abstract

Structural health monitoring (SHM) is of primary importance in wind turbine monitoring systems because the integral functionality of the turbine relies heavily on the robustness of the supporting structure. Traditional frequency domain tools limit the precise interpretation of the in situ vibration signals of an onshore wind turbine. In this study, we employ time-frequency analysis to identify the structural as well as mechanical dynamic characteristics of an onshore wind turbine (Zephyros Z72, 1.5 MW), based on the vibration signals of the supporting structure under parked (idling) and operational conditions. The dynamic signatures of the structure could be estimated from the vibration signals by system identification tools. However, several non-structurally dynamic patterns unexpectedly appeared in the time-frequency representation while analyzing the vibration signals by short-time Fourier transform (STFT). We thus employed STFT in combination with the concepts of mechanical vibration and rotor dynamics to resolve these implicit clues into explicit illustrations of probable events that occurred in the machinery, such as the run-up of the rotor, blade shadowing effects, and the subsequent beating phenomena over its supporting structure.

Keywords: TFA, SHM, Wind turbine, wireless sensing

Introduction

A variety of loads may act on onshore wind turbines. These include self-weight, accidental impacts, inertia forces induced by seismic events, wind blows, aerodynamic turbulence, and rotational loads due to the eccentricity of the rotor-nacelle-assembly (RNA).

Except for self-weight, these loads are intrinsically non-stationary. From a practical viewpoint, a greater understanding of the nature of external loads translates into greater potential robustness of the whole structural design and higher effectivity of a structural health monitoring (SHM) system. We therefore use time-frequency analysis as the primary approach to analyze the vibration signals measured from the supporting structure of an onshore wind turbine.

Time-frequency analysis (TFA) combines the analysis of both time and frequency domains. Due to the emergent properties of the approach, it is more effective at describing the complexity of non-stationary processes than either of these on their own. It well approximates the overall interactions between external loads and the complete turbine in a space of three parameters—time, frequency, and magnitude of

the corresponding energy. In other words, the detailed time-frequency representation (TFR) can provide a comprehensive image of how the structural system responds to external loads in combination. We here focus only on the rotational loading pattern components.

In this study, the onshore wind turbine is conceptually modeled as the combination of two distinct parts. Its operating RNA is treated as a forcing source to excite the supporting structure, which behaves like a sink. We then investigate how the vibration signals physically link to the rotating imbalance during operations.

The framework of this study is as follows. Section 2 gives a brief introduction to time-frequency analysis, particularly to short-time Fourier transform. In section 3, we provide details about the in situ experiments. In section 4, we attempt to relate the results from TFA to the RNA-induced events that probably occurred in the supporting structure. The parked state is first examined to find the fundamental frequency of the wind turbine. Then, in the operational scenario, the tower's responses to the corresponding excitations from RNA are shown by comparing TFRs of the vibration signals of different sensors. Section 5 offers conclusions and discusses future research

directions.

In Situ Experiment

With the increasing demands leveled on wind power, the effective management of wind turbines in service is crucial to ensure uninterrupted energy supply from wind. An integral SHM system for offshore wind turbine was proposed by Rolfes et al. [4], who also introduce the concept of safety monitoring for support structures of wind turbines.

For our experiment, we used an on-shore wind turbine of model Zephyros Z72, 1.5 MW, with a 65 m tower and a pile foundation. The profile and specification of the Z72 turbine are given in Figure 1. In the following, we provide some further details about the wireless sensing system, sensor instrumentation, measurements, and the time signal setup.



Rated shaft power	1670 kW	Temperature rise class	F
Rated electrical power	1562 kW	Insulation class	F (H)
Rated air gap torque	262 kNm	Standards	IEC 614
Rated voltage	3000 V	Protection by enclosure	IP54
Rated current	327 A	Cooling type	IC40
Power factor	0.92	Rotor inertia	35000 kgm ²
Frequency	2-9.25 Hz (rated)	Total weight	47200 kg
Rotational speed	9-18.5 rpm (rated)	Stator weight	23600 kg
Pole number	40	Rotor weight	12500 kg
Pole angle	33.5 deg.	Bearing support cone	2000 kg
Torque harmonics	100% fundamental (162 kNm)	Bearing weight	4000 kg
	< 1% 6 th harmonic (55.5 Hz)	PT 100 motor	6
	< 1% 12 th harmonic (111 Hz)	PT 100 generator air	2
	< 1% 24 th harmonic (222 Hz)	PT 100 bearing	2
Short circuit current	549 A (sustained)	Airgap distance sensors	4
Ambient temperature	40 °C	Bearing measuring unit	1
Radial pull	98 kN/mm between stator and rotor disc in eccentricity	Maximum magnetic pulling force of ring pole	

Figure 1. Z72 wind turbine profile (1.5 MW/65 m height)

A wireless sensing system (NTU-WSU), developed by NCRE and NTU, and a high sensitivity velocity meter (VSE-15D1) designed by Tokyo Sokushim Co. Ltd., were adopted as the structural monitoring system of wind turbine to address the issues of sensor wiring and layout in the support structure.



Figure 2. Wireless sensing system (NTU-WSU)

As shown in Figure 3, each measurement location was installed with a velocity meter unit consisting of three uniaxial velocity meters (VSE-15D1). To identify the modal parameters and investigate the tower motion and the interactions between soil and the foundation, eight measurement locations were instrumented to record the responses of the whole structure.

Along the tower, the sensors were instrumented on four different levels. U12 and U14 were on the

ground; U11 and U10 were instrumented at levels D1 (elevation 15 m) and D2 (elevation 40 m). At the top of the tower (elevation 60 m), four sensors were installed at equal intervals around the circumference. Figure 2 shows the server and one sensor installed on the supporting structure.

The records of each sensor were labeled systematically based on four spots (A, B, C, D; Figure 3). Therefore, the codes of all records from U3, U10, U11, and U14 begin with the letter ‘‘C’’; those from U9 and U12 begin with the letter A, and so on.

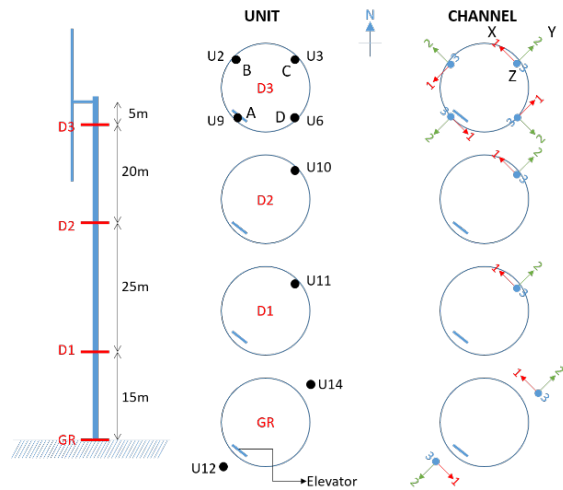


Figure 3. Instrumentation on Z72

The entire wireless sensing system is coordinated with a laptop as the server. The server provides the functions of data storage, signal analysis, and sensor management. The system must ensure that the sensitivities of all sensors are calibrated; to perform this calibration, all sensors were co-located and recorded in the same time segment and the sensitivities were evaluated through the comparison of the signals of different sensors. Figure 2 shows the server and the wireless sensing system prior to the calibration.

Duplicated measuring is essential to ensure a robust estimate of the vibrations of the structure. The measurement list is shown in Table 1 and includes both parked and operating conditions. Under the parked condition, Z72 is subjected only to ambient excitations. Under the operational condition, the responses of the wind turbine are subject to a great number of other disturbances, such as vibrations from the power generator, aerodynamics, and interactions between the foundation and the soil. Responses under the operating condition thus contain a great amount of information that could be used to analyze many interactions between the foundation and other forcing effects. To gather sufficient data for analysis, four tests were carried out for each instrumentation case, each recording one minute of response histories at a 200 Hz sampling rate.

Table 1. Measurements on Z72

NO	Status	Time
1	Parked	2014_09_25_12_44
2	Parked	2014_09_25_12_50
3	Parked	2014_09_25_12_53
4	Parked	2014_09_25_12_57
5	Parked	2014_09_25_13_01
6	Parked	2014_09_25_13_05
7	Parked	2014_09_25_13_08
8	Parked	2014_09_25_13_12
9	Parked	2014_09_25_13_17
10	Parked	2014_09_25_13_23
12	Parked	2014_09_25_13_27
13	Operation	2014_09_25_13_40
14	Operation	2014_09_25_13_45
15	Operation	2014_09_25_13_50
16	Operation	2014_09_25_13_54



Figure 4. Server (laptop) of NTU-WSU



Figure 5. Sensor at D2 level (40 m height)

Of the 16 records, record 1 (parked) was selected as representative of parked states, and record 13 (run-up/transient stage) was selected for the purpose of transient analysis. Record 15 (steady operation) was chosen for the steady operational state. The respective corresponding signals in the time domain are shown in Figures 6, 7, and 8.

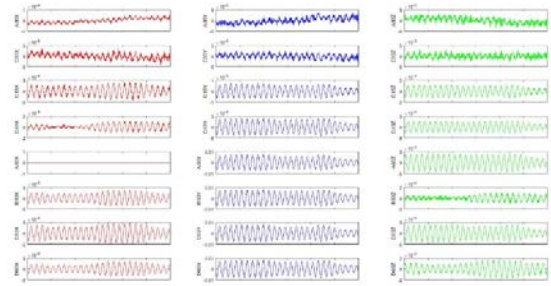


Figure 6. Signals of record 1 (parked/A60X sensor went down)

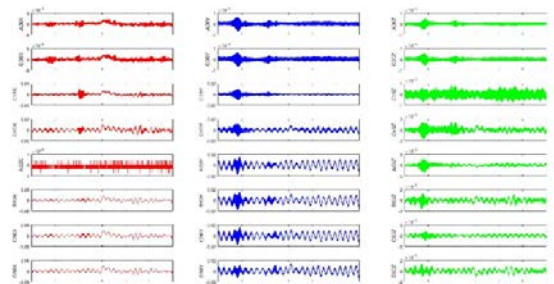


Figure 7. Signals of record 13 (transient operation/A60X sensor went down)

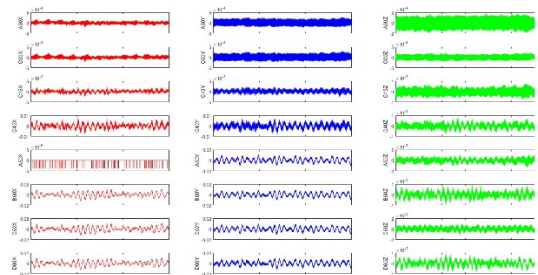


Figure 8. Signals of record 15 (stable operation/A60X sensor went down)

Interpretations of TFR

As a basic parameter of a wind turbine, the first natural frequency of Z72 (0.4395 Hz) was first identified. The data of A60Y and C60X in record 1 were used for this purpose. Figure 10 demonstrates the consistency between fast Fourier transform (FFT) and TFA; the latter is considered a generalization of the former. The peaks of the curves of the FFT (upper half) correspond to the red stripe of the TFR (lower half), and both of them indicate 0.4395 Hz. As the duration of the measurement (1 minute) is not long enough, the closing modes of Z72 were not observed.

Record 13, as a transient part in the operational state, was selected for observing the rotor run-up, as shown in Figure 10 (measurement on the ground) and Figure 11 (measurement at the top of the tower). Both curves in the lower panels have a flattened sigmoidal form that corresponds to rotor acceleration during the

run-up stage. Some peaks observed in both TFR graphs suggest momentary pulses.

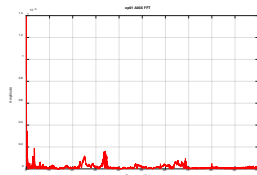


Figure 10 C00X FFT & TFR (Record 13)

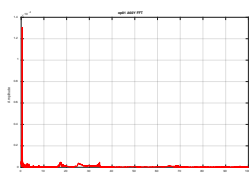


Figure 11 A60Y TFR (Record 13)

Conclusions and further research

In this study, a Z72 wind turbine was modeled as the combination of a forcing component (RNA; power generating device) and a supporting structure (tower). The TFA of the measured data of structural vibrations provided a more precise interpretation of the dynamic events (rotational load patterns in this case) occurring in the onshore wind turbine. Rotor run-up, the blade shadowing effect, tower beating, and orientation of RNA were clearly observed in TFR. Whether the design criterion of the “soft-stiff” resonance-avoidance principle is met can be confirmed through the transformation of the blade shadowing effect by either TFA or FFT during the stable operation state. Continued periodic wave impacts on the supporting structure may lead to material fatigue in the tower in the long term. These identified dynamic loads during normal operations may be incorporated into the design of sub-structures, and hopefully result in a co-design work of the whole wind turbine system.

Acknowledgements

The authors acknowledge funding from NEP-II (MOST 107-3113-E-006-011: the decision-making database and display platform for the design of offshore wind turbine underwater).

References

1. Timothy D. Dorney. Time frequency analysis. Rice University, 1999.
2. Maria Sandsten. Time-frequency analysis of non-stationary processes: an introduction, Centre for Mathematical Science, Lund University, 2013.
3. F. Hlawatsch, G.F. Boudreaux-Bartels. Linear and quadratic time-frequency signal representation. IEEE Signal Processing Magazine. April, 1992.

4. R Rolfes, S Zerbst, G Haake, J Reetz, J P Lynch. Integral SHM-system for offshore wind turbines using smart wireless sensors. Proceedings of the 6th International Workshop on Structural Health Monitoring, Stanford, CA, September 11-13, 2007.
5. Wenping Cao, Ying Xie, Zheng Tan. Wind turbine generator technologies. InTech. Nov. 21, 2012.
6. K.C. Lu, H.C. Peng, Y.S. Kuo. Structural health monitoring of the support structure of wind turbine using wireless sensing system. 7th European Workshop on Structural Health Monitoring, 2014.
7. B. Petersen, M. Pollack, B. Connell. Evaluate the effects of turbine period of vibration requirements on structural design parameters. Applied Physical Sciences. Sep. 1, 2010.
8. Daniel A. Russel. Superposition of waves. <http://www.acs.psu.edu/drussell/Demos/superposition/superposition.html>. Jan., 27, 2014.

Experimental Study of Suspended Fire Sprinkler Systems

Wei-Chung Chen¹, Chen-Pei Hsu², George C. Yao³, Juin-Fu Chai¹, Fan-Ru Lin¹,

Wei-Hung Hsu¹, and Bai-Yi Huang¹

陳威中¹、許宸珮²、姚昭智³、柴駿甫¹、林凡茹¹、徐瑋鴻¹、黃百誼¹

Abstract

A suspended fire sprinkler system is a key nonstructural component in buildings and its damage during earthquakes can have major impacts on both fire safety and building functionality. This is especially critical in buildings of significant importance, such as hospitals, where immediate post-earthquake functionality is paramount. However, observations of past earthquakes have highlighted that even minor damage to fire sprinkler systems can result in building impairment, primarily due to flooding caused by piping leakage.

To better understand the dynamic behavior of suspended fire sprinkler systems, this study analyzes a series of full-scale shaking-table tests conducted at the National Center for Research on Earthquake Engineering (NCREE) Tainan Laboratory. It attempts to identify the seismic performance of fire sprinkler systems in accordance with the conventional construction method followed in Taiwan and with seismic restraints required by NFPA 13. A conceptual computational model is developed based on tests conducted on components such as the hangers, angles, and rigid bracings installed in fire sprinkler systems. In comparison with the shaking-table test results, this model provides relatively accurate time-history analysis and helps simulate the dynamic response of different conditions of fire sprinkler systems.

Keywords: suspended fire sprinkler systems, shaking table tests, nonstructural components, computational model.

Introduction

Seismic events dating back to the 1999 Chi-Chi earthquake have caused damage to suspended fire-sprinkler systems (Fig. 1(a)), as documented in several post-earthquake studies. The reported damage primarily consists of joint failure (Fig. 1(b)) or fractured piping, hanger pull-out (Fig. 1(c)), and ceiling panel-sprinkler head interaction, leading to torn ceiling panels or broken sprinkler heads (Fig. 1(d)). This damage not only is a critical threat to fire safety but also leads to a substantial reduction in functionality of buildings and other facilities. From a fire-safety perspective, a failure in the level of fire protection is a serious concern. Fortunately, to date, such a failure has not occurred frequently and not resulted in fires causing large property loss. Historically, the primary impact of fire-sprinkler system failure during earthquakes is piping leakage that ensues when system components are damaged and

water is subsequently released into the buildings.



Fig. 1. Failure patterns of fire sprinkler systems.

Several studies with respect to the strength capacity of the components of fire-sprinkler systems have been conducted over the past few years in Taiwan. However, it is still difficult to verify if the seismic

¹ National Center for Research on Earthquake Engineering

² Graduate Student, National Cheng Kung University

³ Distinguished Professor, National Cheng Kung University

second configurations, respectively. For the unbraced system, the maximum relative displacement of 309 mm occurred at the branch line in the X direction and that of 137 mm was observed at the 4-inch-diameter main run in the Y direction. In contrast, the maximum relative displacement observed in the braced system was less than 5 mm in both horizontal directions.

In addition, the seismic measures as per NFPA13 substantially increased the fundamental frequencies of the braced system in the horizontal directions, which adequately prevented resonance effects between the fire sprinkler systems and the building structure. The original fundamental frequencies of the unbraced system in the X and Y directions were approximately 2 Hz. In contrast, the fundamental frequencies of the braced system in the horizontal directions increased to 20 Hz.

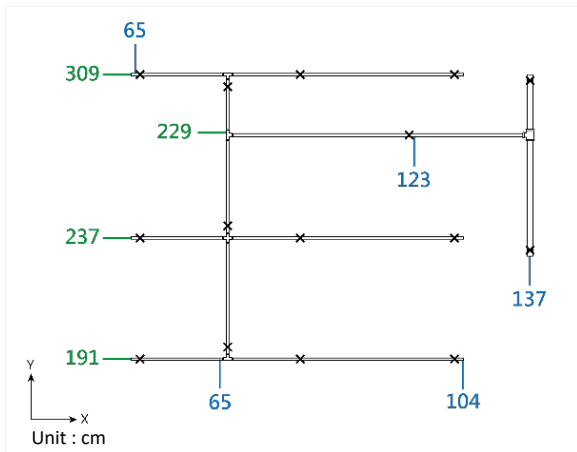


Fig. 8. Maximum response of the unbraced system.

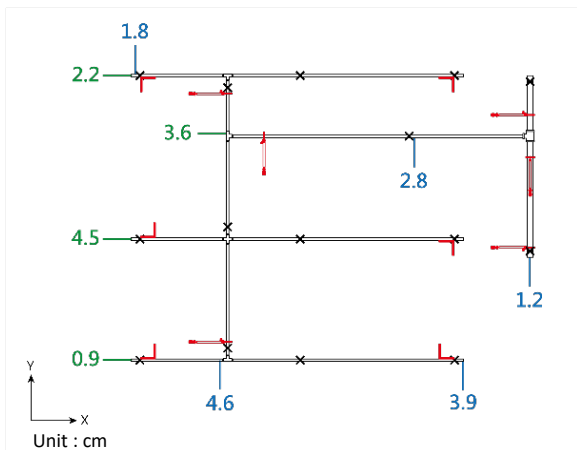


Fig. 9. Maximum response of the braced system.

Numerical Results

Cyclic-loading tests of the hangers, angles, and rigid bracings (Fig. 10) were performed in this study to investigate their mechanical behavior. Based on the hysteretic load–displacement responses recorded from

the tests, computational models of each component were developed and calibrated by subjecting the component to cyclic loading (Fig. 11).

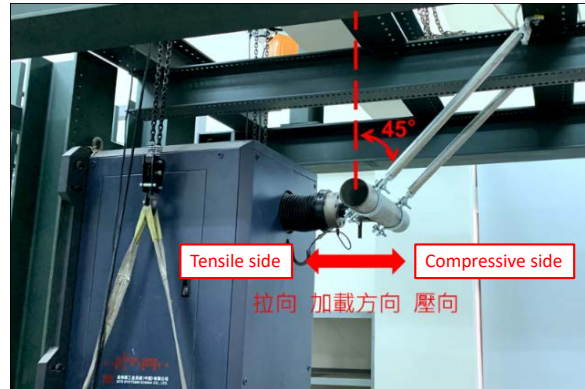


Fig. 10. Cyclic-loading test of the rigid bracing.

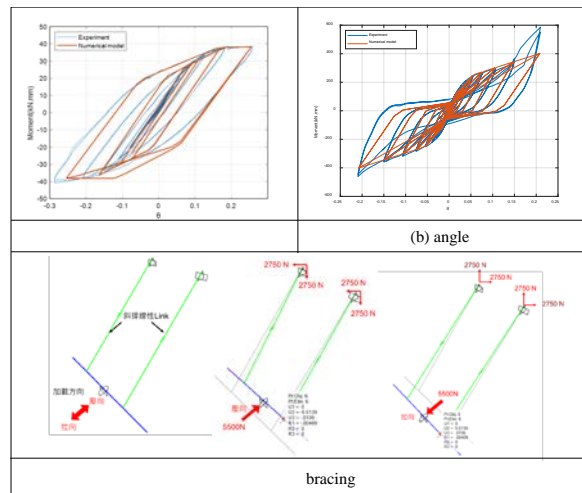


Fig. 11. Computational models of the components.

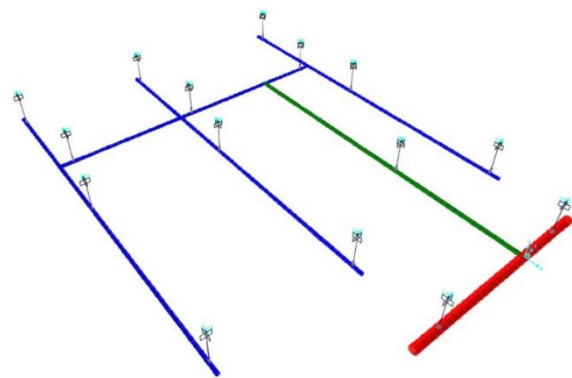


Fig. 12. Computational model of the unbraced system.

The structural analysis software SAP2000 was used to generate a computational model. Figure 12 illustrates the computational model of the unbraced system. All of the setting information, including the material property, frame section property, and

boundary conditions, followed the same specifications as for the test specimen. The fundamental frequencies of this model in the X and Y directions were 1.9 and 2.1 Hz, respectively; thus, the accuracy of the computational model in comparison with the test results was verified.

Figs. 13 and 14 show the relative displacement responses generated by the model in the horizontal directions. In comparison with the test records, the proposed computational model provides a reliable simulation of the unbraced fire sprinkler system.

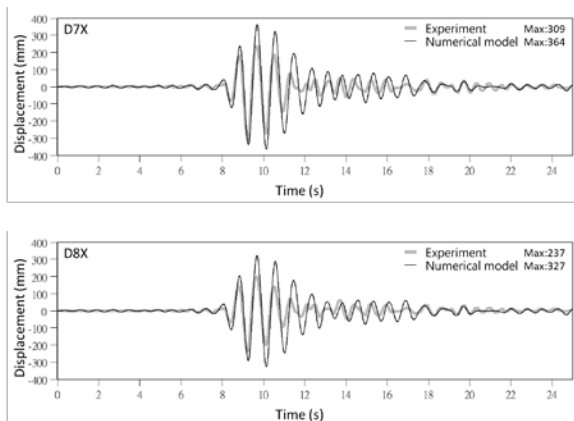


Fig. 13. Time-history response in the X direction.

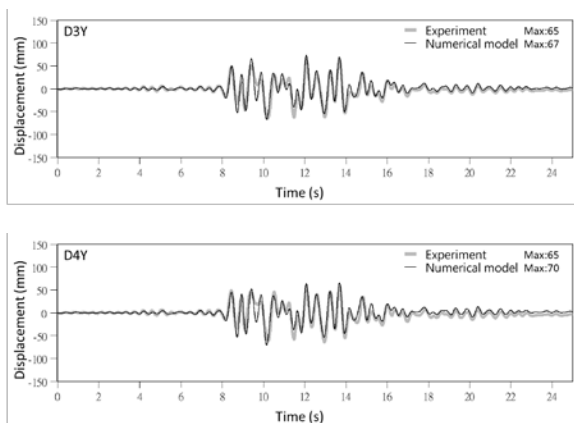


Fig. 13. Time-history response in the Y direction.

Conclusions

Past earthquake observations have conclusively highlighted that damage to suspended fire-sprinkler systems can lead to interruptions to post-earthquake operations of critical facilities. However, the current standards in Taiwan provide only limited guidance for the seismic design. In this study, to determine the seismic performance of fire-sprinkler systems, a series of full-scale shaking table tests was conducted. The test results showed that seismic restraints, including the angles and the rigid bracings, required by NFPA 13 effectively helped reduce the dynamic responses of the suspended fire-sprinkler systems.

A computational model of the unbraced fire-sprinkler system was developed and provided a time-history analysis with reliable accuracy. However, it should be noted that a computational model of the braced system was not explicitly addressed in this paper. Further study is required to develop computational models of both unbraced and braced systems under various conditions during earthquakes.

References

- Huang JJ (2003). “A Study on Earthquake Performance of Fire Sprinkler Systems” Master Thesis, National Cheng Kung University, Tainan, Taiwan.
- Huang JG (2013). “A Study on Seismic Behavior of Joints of Fire Protection Sprinkler Piping Systems in Hospital” Master Thesis, National Taiwan University, Taipei, Taiwan.
- Chung MF (2013). “A Study on Seismic Behavior Fire Protection Sprinkler Piping System” Master Thesis, National Taipei University of Technology, Taipei, Taiwan.
- Lin FR (2017). “Seismic Evaluation Methods for Fire Protection Sprinkler Piping Systems in Buildings” Doctoral Dissertation, National Taiwan University, Taipei, Taiwan.
- Huang CL (2018). “A Study on Seismic Retrofit of Suspension Piping Systems in Buildings: A Case Study of Fire Protection Sprinkler Piping System” Master Thesis, National Cheng Kung University, Tainan, Taiwan.
- Hsu CP (2020). “A Research on Suspension Fire Sprinkler Piping System Simulation” Master Thesis, National Cheng Kung University, Tainan, Taiwan.
- National Fire Protection Association. (2010) “Standard for the Installation of Sprinkler” *NFPA 13*, USA.

Effects of the Non-linear Behavior of Building Structures on Critical Equipment

Min-Chi Ko¹, Fan-Ru Lin², Bai-Yi Huang³, Wei-Chung Chen³, Juin-Fu Chai⁴

George C. Yao⁴

柯敏琪¹ 林凡茹² 黃百誼³ 陳威中³ 柴駿甫⁴ 姚昭智⁴

Abstract

According to the building performance-based design framework in FEMA P58, there are three seismic performance levels for building structures: repairable, not collapsed but irreparable, and collapsed. Only when the building structure is classified as repairable would the repaired time, costs, and functionality of non-structural components in the building be considered in the building performance. On the other hand, the response of the structure of the building under different earthquake intensities represents the seismic demand of non-structural components. In order to decrease the uncertainty of the performance evaluation for nonstructural components, this study adopted a stick model for a mid-rise building structure to discuss the structural response according to nonlinear and linear analyses. The simulation parameters for the numerical model are discussed to determine better seismic demands for nonstructural components to aid in future building performance designs.

Keywords: performance-based seismic design, nonlinear analysis, numerical analysis

Introduction

The performance design of buildings has been carried out for thousands of cases using FEMA P58. One integer from 1 to 100 is chosen at random to determine the probability of irreparable damage or collapse. If the integer is in the designated range corresponding to irreparable damage or a collapsed state, the building structure is considered irreparable or collapsed. Therefore, under high-intensity earthquakes, the building is occasionally recognized as being repairable and not collapsed; therefore, related non-structural components and equipment should be assessed for damage. However, linear analysis for building structures under large ground motion may not be suitable for determining actual nonlinear dynamic behavior. Meanwhile, different types of strong motions may affect the uncertainty and may be representative of the seismic demands of non-structural components.

In order to investigate the influence of the results of the numerical analysis for the building structure on the building performance-based design in FEMA P58, a stick model was established to simplify time-

consuming numerical analyses that usually involve a detailed finite element model (Su, 2018). Seismic responses under different seismic input intensities such as the floor response spectrum and the drift ratio were obtained from linear and nonlinear numerical analyses. These findings are discussed to investigate the influences of ground motion parameters on the seismic demands of nonstructural components. Proper far-field and near-fault ground motions were chosen from the PEER database.

Numerical Model and Input Motions

In this study, an existing stick model was established using an actual fourteen-story 69.6-m tall steel structure. The stick model was composed of kinematic link elements and lumped mass joints. The bi-axial linear stiffness of the link elements for each floor was analyzed according to the pushover analysis of a full-scale 3D numerical model with real material characteristics. The total mass at each floor was lumped at the joints of the stick model to reduce analysis time. This model was also confirmed using modal and time history simulations. Fig. 1 and Table 1 depict the process of establishing the model and the

1 Ph. D Student, National Cheng Kung University

2 Associate Researcher, National Center for Research on Earthquake Engineering

3 Assistant Researcher, National Center for Research on Earthquake Engineering

4 Deputy Director General, National Center for Research on Earthquake Engineering

modal analysis results.

Referring to FEMA P-695, the far-field (FQ) and near-fault (NQ) ground motions (Table 2) were chosen from the PEER NGA Database. According to the Taiwan Seismic Design Building Code (TBC), the maximum design spectral acceleration S_{DS} is 1.136 g, the maximum considered acceleration S_{MS} is 1.32 g, and the medium design acceleration $1/4S_{DS}$ is 0.284 g. The peak ground accelerations of biaxial horizontal time history were scaled to the three different intensities. On the other hand, FQ Duzce and NQ Duzce time histories were adopted to establish two groups of artificial motions that are compatible with the building-code response spectrum (BRS). Table 2 lists the input motions for the numerical analysis of the stick model. Taking the Duzce earthquake event as an example, Fig. 2 shows the scaled records and artificial motions in one horizontal direction at the maximum considered earthquake level. Fig. 3 depicts the corresponding acceleration response spectrum of the input motion at the maximum considered earthquake level.

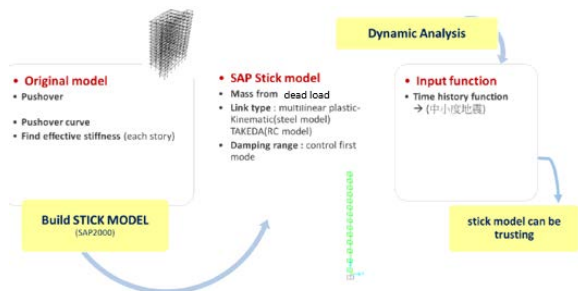


Fig. 1. Process for establishing the model.

Table 1. Modal analysis results.

	X dir. (U2)	Y dir. (U3)
1 st mode	2.11	1.88
2 nd mode	0.78	0.75
Modal participating mass ratios	1 st -80% 2 nd -11%	1 st -74% 2 nd -13%

Table 2. Far-field and near-fault input motions.

FQ	FQ Duzce (BRS)
	FQ Duzce
	FQ Capitola
	FQ 0304CHY004
	FQ 0921CHY039
NQ	NQ Duzce
	NQ 0921TCU065
	NQ Duzce (BRS)

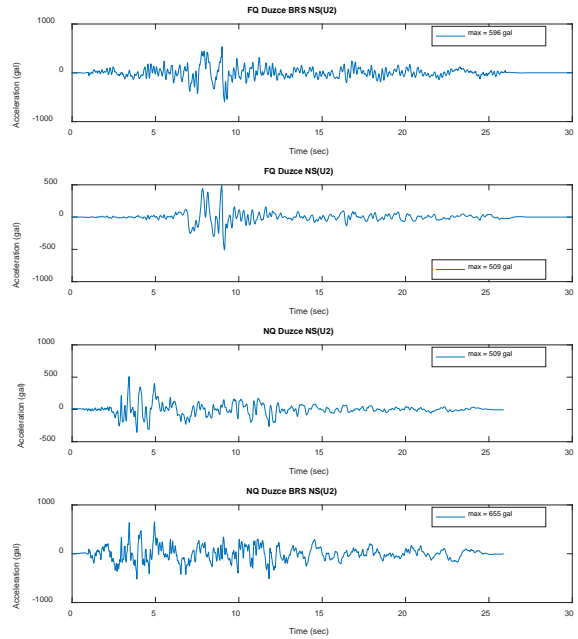


Fig. 2. Input motions at the maximum considered earthquake level for the Duzce event.

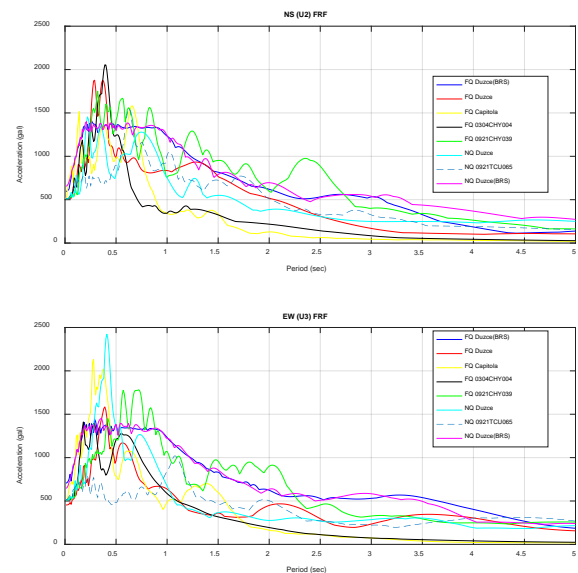


Fig. 3. Maximum considered earthquake response spectrum.

Numerical Analysis Results

In this study, the linear and nonlinear analyses were executed at the medium, design, and maximum earthquake levels. As the representative nonstructural seismic demands, the floor response spectrum and story drift ratio were adopted to investigate the influence of the numerical analysis for the building on the nonstructural analysis. Referring to ASCE 7-16 and TBC, the designated acceptable criteria for the drift ratio at three seismic intensity levels were adopted to judge the seismic performance of the building structure for each numerical analysis (Table 3). Fig. 4 to Fig. 6 show the response spectrum, drift ratio, and shear force for each floor according to the

biaxial numerical analysis.

Table 3. Acceptable criteria for the drift ratio.

Drift ratio	Corresponding seismic intensity
<0.5%	medium earthquake
<1%	design based earthquake (DBE)
1%~2%	maximum considered earthquake (MCE)

1. Drift Ratio: According to the results shown in Fig. 5, the response of the stick model exceeds the yielding strength in each time history analysis. Most drift ratios for the floors were in the range of 1% to 2%. This result meets the expected building performance since this building is designed according to the current TBC standard, which requires that buildings resist collapse at the MCE level. Only the drift ratio under the motions of FQ Duzce (BRS) and FQ 0921CHY039 were over 2%, corresponding to buildings that could enter the collapse stage. Overall, eight floors and three floors exceeded a drift ratio of 2% in the linear and nonlinear analyses, respectively.

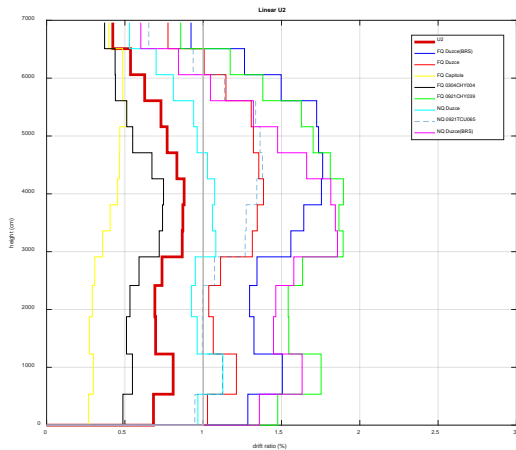


Fig. 4. Drift ratio at the MCE level.

2. Floor Response Spectrum: Similar to the DBE analysis results, Fig. 4 shows the roof floor (RF) response spectrum, (i.e., the frequency contents of time history have a significant influence on the floor response spectrum). It can be seen that the nonlinear analysis results are smaller than the linear analysis results, which may be caused by decreasing frequency or hysteric behavior during the plastic stage. These phenomena are further discussed in the free vibration analysis section.
3. Free Vibration Analysis: In the nonlinear MCE time history numerical analysis, the analysis shows that the performance of the building was better than obtained from the linear analysis. On

the other hand, it can be seen that the nonlinear floor spectral accelerations were calculated to be much smaller than in the linear analysis. In order to determine the major cause of the differences between the linear and nonlinear analyses, the free vibration behavior was observed after strong motion inputs to exclude the effects of excitation. The duration of the data acquisition was increased by increasing the steps of the output duration in the numerical model for the FQ Duzce (BRS) and NQ Duzce (BRS) analysis. Free vibrations were observed between 25 s and 60 s in the numerical analysis (Fig. 7 and Fig. 8). According to the acceleration of the free vibration response in the RF, the natural frequency can be analyzed by a fast Fourier transform. As shown in Fig. 9 and Fig. 10, the natural frequency was 0.5 Hz in the horizontal direction and approximately equal to the first mode, which had a period of 2.1 s (Table 1).

As shown in Fig. 11 and Fig. 12, the path of the RF hysteresis loops indicates that the slopes are similar in the positive loading and reverse unloading directions in both the linear and nonlinear analyses. Due to the behavioral characteristics of the kinematic links, when the link motion is in the plastic stage, the initial stiffness in the elastic stage would be adopted during the unloading path. The animation of the path of the free vibration hysteresis loop between 25 and 60 s shows that the internal force and deformation were in the elastic stage. The decreased stiffness in the plastic stage only occurred during the loading states. This explains why the maximum floor spectral accelerations were approximately at the same frequency in the linear and nonlinear analyses.

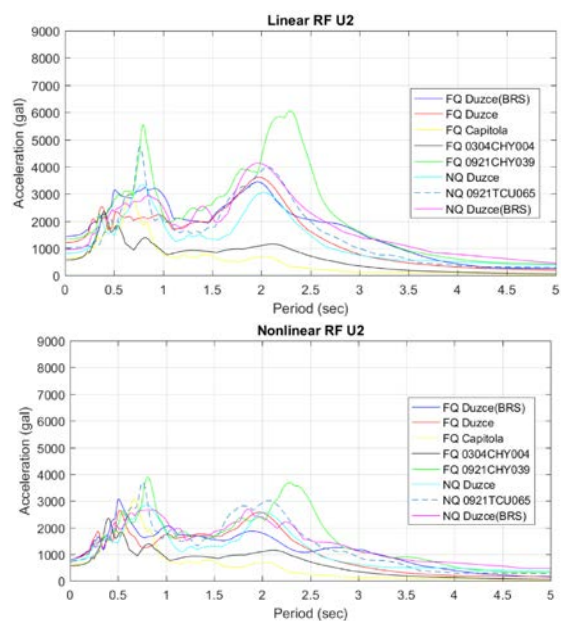


Fig. 5. Floor response spectrum of the roof floor at the MCE level.

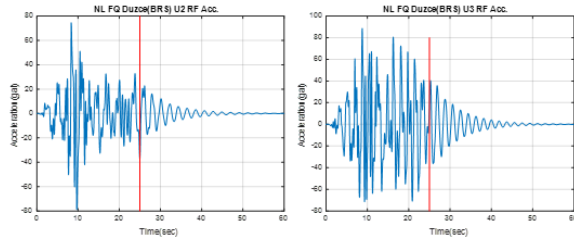


Fig. 6. FQ Duzce (BRS) RF acceleration response.

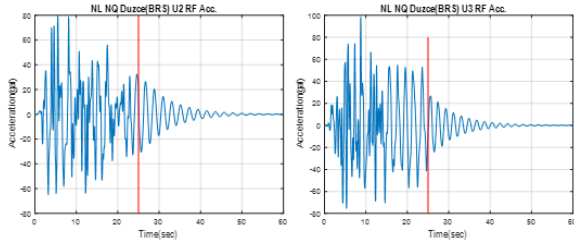


Fig. 7. NQ Duzce (BRS) RF acceleration response.

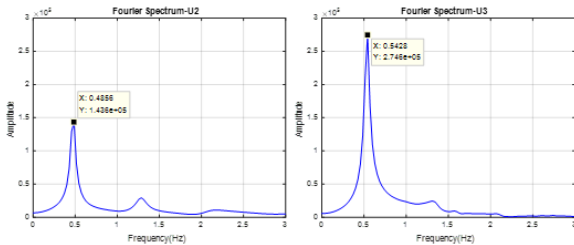


Fig. 8. Transfer function of free vibration in the FQ Duzce (BRS) analysis.

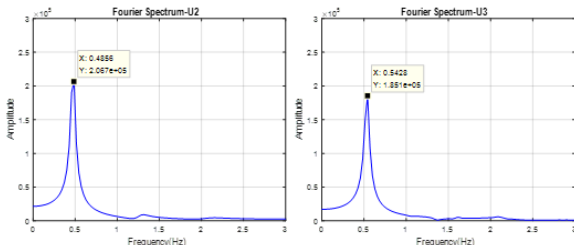


Fig. 9. Transfer function of free vibration in the NQ Duzce (BRS) analysis at the MCE level.

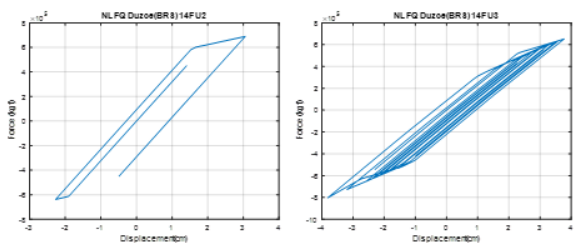


Fig. 10. Hysteresis loop of the fourteenth floor in the FQ Duzce (BRS) analysis at the MCE level.

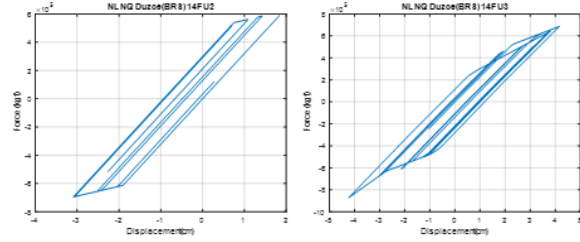


Fig. 11. Hysteresis loop of the fourteenth floor in the NQ Duzce (BRS) analysis at the MCE level.

Conclusion

In order to increase to confidence in seismic demand analyses (floor response spectrum and drift ratio) and the performance assessment for nonstructural components, this study aimed to investigate the linear and nonlinear time history analyses for building structures under different excitation conditions. The simulation parameters of the numerical model were discussed to evaluate properly the seismic demands of nonstructural components to improve future building performance designs.

References

- Applied Technology Council. Seismic Performance Assessment of Buildings. FEMA P-58, 2012, Federal Emergency Management Agency, USA.
- Pacific Earthquake Engineering Research Center, PEER NGA Database. PEER, 2006a. University of California, Berkeley, California, Available at <http://peer.berkeley.edu/nga/>.
- Quantification of Building Seismic Performance Factors. FEMA P-695, 2009, Federal Emergency Management Agency, USA.
- Seismic Design Specifications and Commentary of Buildings. 2011, Construction and Planning Agency Ministry of the Interior, Taiwan,
- Lin, F.R. (2017). Seismic Evaluation Methods for Fire Protection Sprinkler Piping Systems in Buildings, National Taiwan University, Taiwan, Taipei.
- Su, Y.H. (2018). A Research on Analysis of Seismic Demands for Non-Structural Components of System in Mid-to-High-Rise Buildings, National Taipei University of Technology, Taiwan, Taipei.
- Tseng, S.C. (2020). A Study on Seismic Behavior of Fire Protection Sprinkler Piping Systems in Hospital, National Cheng Kung University, Taiwan, Tainan.

Modification of a Sloped Rolling-type Isolation Bearing with Stepwise Variable Designs

Chung-Han Yu¹, Shiang-Jung Wang², Wang-Chuen Lin³, Cho-Yen Yang³

游忠翰¹、汪向榮²、林旺春³、楊卓諺³

Abstract

In this study, we numerically investigated the horizontal displacement control performance of sloped rolling-type seismic isolators with the same horizontal control performance by passively varying parameters in a stepwise pattern, and keeping others variables constant. The first design incorporated stepwise increased sloping angles and a stepwise decreased damping force with increasing horizontal isolation displacement. The second design used the opposite philosophy, in which the stepwise sloping angles were decreased and the stepwise damping force was increased with increasing horizontal isolation displacement. A series of numerical results show that for sloped rolling-type seismic isolators designed with a constant sloping angle and damping force, larger damping forces (smaller sloping angles) generally correspond to a smaller horizontal maximum and a larger residual displacement response. In summary, to ensure acceptable displacement control performances without sacrificing acceleration control performance under diverse seismic demands, we compared designs with constant parameters. Adopting the second design appears to be a better choice.

Keywords: sloped rolling-type seismic isolator, sloping angle, damping force, isolation displacement, residual displacement,

Introduction

Sloped rolling-type seismic isolators (Fig. 1) feature a constant horizontal acceleration control (or a zero post-elastic stiffness) performance and an inherent gravity-based self-centering capability. Although their in-plane seismic isolation performance has already been numerically and experimentally demonstrated in many previous works, their sloping angle and damping force have usually been designed as constant, which may prevent passive control performances at different stages (or displacement levels). This kind of demand is particularly important and necessary for some specific industries, such as high-tech factories, if different seismic performances or protective objectives are required for different levels of external disturbance. Previous numerical and statistical studies by Wang et al. have shown that for systems that do not maintain the same horizontal acceleration control performance, larger designed sloping angles and damping forces in particular generally correspond to a smaller horizontal isolation

displacement. However, when the roller is in motion on a sloped surface, an increase in sloping angles and damping force will lead to a larger horizontal acceleration transmitted to the protected object above the isolator. Therefore, although increasing the sloping angles and damping force can effectively mitigate horizontal isolation displacement, this will reduce the horizontal acceleration control performance. Moreover, an increase in damping force to suppress horizontal isolation displacement under major earthquakes may cause sloped rolling-type seismic isolators to have unacceptable self-centering performances during major earthquakes and even during other frequent or minor earthquakes

In this study, to maintain the unique features of sloped rolling-type seismic isolators, (i.e., the constant horizontal acceleration performance), we implemented passively stepwise variable sloping angles and damping force in the mechanism designs. By conducting a numerical study using a large number of ground motions with different seismic

¹ Assistant Researcher, National Center for Research on Earthquake Engineering

² Associate Professor, National Taiwan University of Science and Technology

³ Associate Researcher, National Center for Research on Earthquake Engineering

characteristics, we compare and discuss the horizontal displacement control performances of two different design philosophies. This is the main purpose of this study, namely to numerically compare the seismic responses of sloped rolling-type seismic isolators designed with stepwise variable and constant parameters under a constant horizontal acceleration control performance, rather than to seek their optimum design parameters.

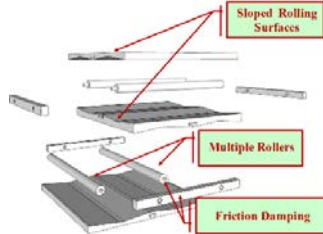


Fig. 1 Sloped rolling-type isolation bearing

Design concept

Based on the simplified model shown in Fig. 2(a), in which a roller is in motion between a sloped surface and a flat surface the simplified and linearized equation of motion for the horizontal dynamic behavior of sloped rolling-type seismic isolators can be obtained from Eq. (1), and its hysteretic behavior, without considering the effect of \ddot{z}_g , is shown in Fig. 2(b).

$$\ddot{x} + \ddot{x}_g = \frac{-(g + \ddot{z}_g)\theta}{2} \text{sgn}(x) - \frac{F_D}{(M + m_1)} \text{sgn}(\dot{x}) \quad (1a)$$

where $\ddot{x}(x)$ is the horizontal acceleration (displacement) response of the protected object and the bearing plate above the roller relative to the fixed base; \ddot{x}_g and \ddot{z}_g are the horizontal and vertical acceleration excitations, respectively; θ is the sloping angle of the V-shaped surface; F_D is the horizontal friction damping force; M , m_1 , and m_2 are the seismic reactive masses of the protected object, superior bearing plate, and roller, respectively; and r is the cross-sectional radius of the roller.

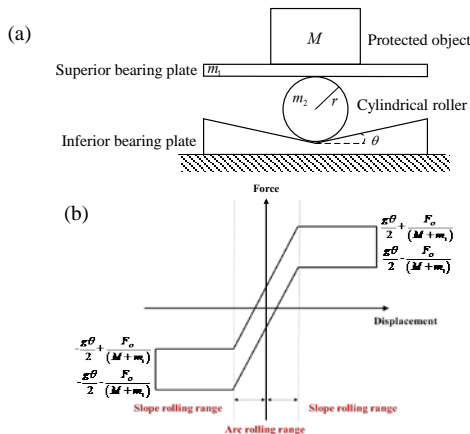


Fig. 2 A simple model that considers a roller in motion between sloped and flat surfaces

In this study, to maintain their unique feature, two patterns were designed and examined numerically. For the first design pattern, denoted as Design I, the sloping angle of the V-shaped surface in contact with the roller increased stepwise while the damping force decreased stepwise as the horizontal isolation displacement increased. The multi-linear elastic behavior that accounted for the two sloping angles increased in a stepwise fashion as the horizontal isolation displacement (or slope rolling ranges) and two transition ranges (or arc rolling ranges) increased. This is illustrated in Fig. 3(a). The hysteretic behavior corresponding to the plots in Fig. 3(a) considers two damping forces that decreased stepwise with increasing horizontal isolation displacement. There is one intermediate transition range (i.e., the second transition range), as illustrated in Fig. 3(b). A greater damping force design corresponded to greater horizontal hysteretic loop areas in the second and fourth quadrants, as indicated by the dashed and gray lines shown in Figs. 3(b)-(c).

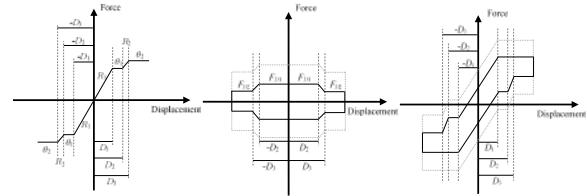


Fig. 3 Illustrations of the displacement-force relationship in Design I

For the second design pattern, denoted as Design II, the sloping angle of the V-shaped surface in contact with the roller decreased stepwise while the damping force increased stepwise as the horizontal isolation displacement increased. In contrast with Fig. 3(a), the multi-linear elastic behavior for the two sloping angles decreased stepwise with increasing horizontal isolation displacement; the two transition ranges are illustrated in Fig. 4(a). In contrast with Fig. 3(b), the hysteretic behavior of the two damping forces increased stepwise with increasing horizontal isolation displacement; one intermediate transition range (i.e., the second transition range) is illustrated in Fig. 4(b). Designs with greater damping forces correspond to greater horizontal hysteretic loop areas in the second and fourth quadrants, as indicated by the dashed and gray lines shown in Figs. 4(b)-(c).

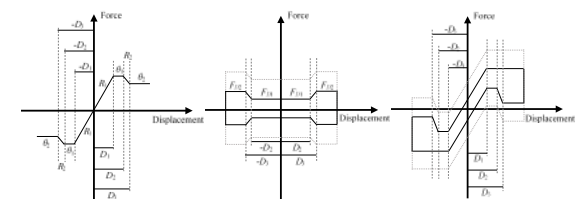


Fig. 4 Illustrations of the displacement-force relationship in Design II

Numerical analysis and discussions

For the numerical models and analyses we assumed that the object to be protected above the isolators has a seismic reactive mass of 1000 kg. For simplicity, the external disturbance and dynamic responses in only one horizontal principal direction are considered.

Four Design I models, denoted by VSD-36A, VSD-48A, VSD-36B, and VSD-48B, were designed with the same first slope rolling range, 10 mm. Model VSD-36A had a smaller sloping angle but a larger damping force in both the first and second slope rolling ranges (i.e., $\theta_1 = 3$ degrees, $\theta_2 = 6$ degrees, $F_{D1} = 550$ N, and $F_{D2} = 300$ N) than model VSD-48A (with, $\theta_1 = 4$ degrees, $\theta_2 = 8$ degrees, $F_{D1} = 460$ N, and $F_{D2} = 120$ N). The design parameters of VSD-36B and VSD-48B are identical to those of VSD-36A and VSD-48A, respectively, except for their first slope rolling range, which was 20 mm. Following this notation, four similar Design II models were generated and are denoted as VSD-63A, VSD-84A, VSD-63B, and VSD-84B.

In addition to these eight models (which have stepwise variable sloping angles and damping force), another four counterpart models were designed with constant sloping angles and damping force. These models are denoted as CSD-3, CSD-4, CSD-6, and CSD-8. For an objective comparison (i.e., to maintain the same maximum horizontal acceleration that is transmitted to the protected object), the constant values of sloping angles and damping force (θ , F_D) were applied to the four counterpart models in sequence. The angle and force values were equal to 3 degrees and 550 N for CSD-3, 4 degrees and 460 N for CSD-4, 6 degrees and 300 N for CSD-6, and 8 degrees and 120 N for CSD-8.

The ground motion records contain 2,553 sets of local ground motions, with peak ground accelerations varying from 0.082 g to 1.260 g and peak ground velocities varying from 0.006 m/s to 2.800 m/s. We incorporated these records as horizontal acceleration inputs. The data were collected by the Taiwan Strong Motion Instrument Program from July 29th, 1992 to December 31st, 2006. Eighteen of these records are classified as pulse-like near-fault ground motions (Shahi and Baker 2014), and the remaining are classified as far-field ground motions.

The maximum and residual horizontal displacements for models CSD-3, CSD-6, VSD-36A, VSD-36B, VSD-63A, and VSD-63B, after being subjected to ground motions are shown in Fig. 5. The corresponding results for models CSD-4, CSD-8, VSD-48A, VSD-48B, VSD-84A, and VSD-84B are shown in Fig. 6. Figure 5 presents the amounts of ground motion by which the displacement control performance of models VSD-36A, VSD-36B, VSD-

63A, and VSD-63B are better than those of CSD-3 and CSD-6, respectively. The average responses for CSD-3 and CSD-6 are also presented. Similarly, the values shown in Fig. 6 are for models VSD-48A, VSD-48B, VSD-84A, and VSD-84B relative to models CSD-4 and CSD-8, respectively.

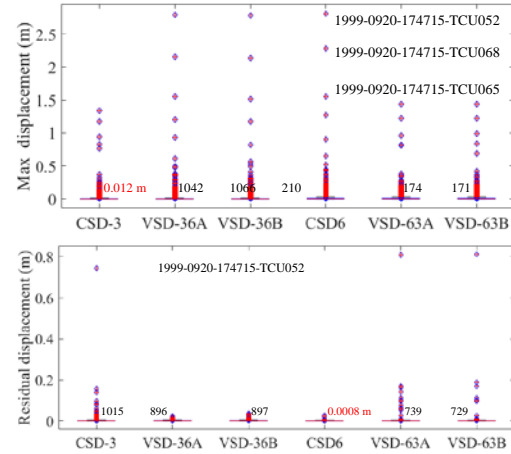


Fig. 5 Numerical analysis results for Design I experiments. Top, maximum displacement responses, and bottom, residual displacement responses

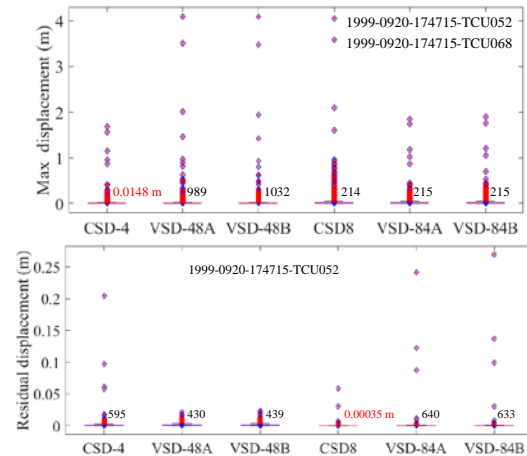


Fig. 6 Numerical analysis results of Design II experiments. Top, maximum displacement responses, and bottom, residual displacement responses

We reiterate that the objective of this study was to numerically compare the merits and limitations of Design I and Design II models, rather than to design a sloped rolling-type seismic isolator for ground motion that minimizes the horizontal isolation displacement..

When subjected to ground motions, CSD-3 and CSD-4 obviously have better performances in suppressing horizontal maximum displacement responses according to the average values and distributions, as shown in Figs. 5(a) and 6(a). This may be because of their larger damping force designs during the entire motion compared with the other models. Models CSD-6 and CSD-8 have worse performances because of their smaller damping force designs. In other words, for the same horizontal

acceleration control performance, adopting a design with a smaller sloping angle (or larger damping force) is more effective for suppressing horizontal isolation displacement compared with designs that adopt a larger sloping angle (or smaller damping force). For the same reasons, the opposite tendency is observed for the re-centering performance, as shown in Figs. 5(b) and 6(b).

As shown in Fig. 5(a) (and correspondingly in Fig. 6(a)), the Design I models VSD-36A and VSD-36B (VSD-48A and VSD-48B in Fig. 6(a)), are comparable with CSD-3 (and CSD-4) in their suppression of horizontal maximum displacement responses when under a smaller horizontal isolation displacement demand. However, Design II models VSD-63A and VSD-63B in Fig. 5(a) (and, correspondingly, models VSD-84A and VSD-84B in Fig. 6(b)) do the opposite when under a larger horizontal isolation displacement demand, as indicated by green squares. This may be because the first and second sloping ranges include larger damping force designs (as large as those for CSD-3 or CSD-4). Adopting a combination of sloping angles of 3 and 6 degrees was better for the suppression of the horizontal isolation displacement than adopting a combination of sloping angles of 4 and 8 degrees. Since most ground motions are classified as far-field ground motions, which usually do not cause an excessive horizontal isolation displacement demand for the design of seismic isolation, it is not surprising that Design I models outperformed Design II models when subjected to increased ground motions. As shown in Figs. 5(b) and 6(b), on average, (i.e., if extremes are precluded), there are no significant discrepancies for the re-centering performances of the different models. In terms of distribution, the residual displacement responses of the Design I models may not be as scattered as those of the Design II models. Adopting a combination of sloping angles of 4 degrees and 8 degrees to reduce residual displacement results in a better performance than adopting a combination of slope angles of 3 and 6 degrees.

Conclusions

On the premise of maintaining the same horizontal acceleration control performance, sloped rolling-type seismic isolators designed with a constant sloping angle and damping force may be unable to control their horizontal maximum and residual displacement responses simultaneously. More precisely, the increase in damping force or decrease in sloping angle will lead to a decrease in horizontal isolation displacement. However, this will also cause an increase in residual displacement. In conventional approaches, the acceleration control performance is usually sacrificed in order to achieve acceptable displacement control performance under diverse seismic demands. Therefore, in this study, we propose to implement the ideas of stepwise variable sloping

angles and damping force in sloped rolling-type seismic isolators. By subjecting the isolators to a large number of ground motions and further classifying ground motions as far-field and pulse-like near-fault motions, we could statistically compare and discuss the horizontal displacement control performances of the isolators in terms of maximum and residual displacement responses. Our aim is to consider the diverse ground motions; and the models designed in this study were created to obtain wide-ranging seismic responses for the models, rather than to passively minimize their seismic responses or to propose their optimum design approaches.

To implement acceptable displacement control performance without sacrificing acceleration control performance under diverse seismic demands, we compared two variable model designs with constant parameters. We concluded that a design in which the sloping angle of the V-shaped surface in contact with the roller decreases in a stepwise fashion while the damping force increases stepwise would be a better choice.

The current conclusions were based on the numerical results of limited combinations of design parameters and only one acceleration performance objective. For more conclusive results, combinations of design parameters and more acceleration performance objectives should be studied in a numerical or experimental approach in the future.

References

- Wang, S.J., Sung, Y.L. and Hong, J.X. (2020), "Sloped rolling-type bearings designed with linearly variable damping force", *Earthquakes and Structures*, 19(2), 129-144.
- Wang, S.J., Hwang, J.S., Chang, K.C., Shiao, C.Y., Lin, W.C., Tsai, M.S., Hong, J.X. and Yang, Y.H. (2014), "Sloped multi-roller isolation devices for seismic protection of equipment and facilities", *Earthquake Engineering and Structural Dynamics*, 43(10), 1443-1461.
- Wang, S.J., Yu, C.H., Lin, W.C., Hwang, J.S. and Chang, K.C. (2017), "A generalized analytical model for sloped rolling-type seismic isolators", *Engineering Structures*, 138, 434-446.
- Wang, S.J., Yu, C.H., Cho, C.Y. and Hwang, J.S. (2019), "Effects of design and seismic parameters on horizontal displacement responses of sloped rolling-type seismic isolators", *Structural Control and Health Monitoring*, 26(5).

Preliminary Design Procedure for Structural Retrofitting with an Isolation System including a Friction Pendulum Bearing

Cho-Yen Yang¹, Peng-Yu Lin², Lap-Loi Chung³, Wang-Chuen Lin¹,
Chung-Han Yu⁴, and Shiang-Jung Wang⁵

楊卓諺¹、林芃妤²、鍾立來³、林旺春³、游忠翰⁴、汪向榮⁵

Abstract

Many existing structures in Taiwan were built according to an outdated Design Code of Buildings, and some of these buildings, especially historical ones, did not even include consideration of seismic forces in their design. Such buildings are dangerous according to evaluations for seismic capacity using current design codes. Therefore, it is important that evaluations include a check on their seismic capacity, and if it is insufficient, retrofitting is necessary to increase seismic capacity and to meet the seismic demand. Conventional retrofitting such as reinforced concrete jacketing and use of shear walls and wing walls are possible solutions. However, these conventional retrofit methods may change the appearance of structures, which is not desirable for historical buildings. Seismic isolation is an alternative way to retrofit historical buildings by reducing the seismic demand. In this paper, a preliminary design procedure for structural retrofitting with an isolation system using a friction pendulum is introduced. The design procedure is demonstrated with a two-story reinforced concrete benchmark structure as the retrofit target.

Keywords: seismic isolation, retrofit, seismic evaluation, friction pendulum bearing, seismic design

Introduction

When a structure is confirmed to have insufficient seismic capacity by seismic evaluation, a structural retrofit must be installed. Conventionally, several methods of structural retrofitting have been used to increase the seismic capacity of structures, including use of reinforced concrete (RC) jackets, steel jackets, shear walls, and flange walls. A different approach to address the problem is to reduce seismic demand by introducing an isolation system. Using structural isolation, the seismic force is transmitted to the superstructure by the isolation system. For historical buildings that must be retrofitted, the appearance of the building can thus be preserved. In this article, we consider an isolation system with a friction pendulum bearing, and we establish the preliminary design procedure. The design procedure is demonstrated using an example structure as a target for

retrofitting.

Retrofit design procedure

The first step in the procedure, before implementation of structural retrofits with isolation, is to confirm the seismic capacity of a structure using a seismic evaluation. Based on structural information such as member size, arrangement of the reinforcement, properties of the material, and site location, the pushover analysis can be conducted to obtain the capacity curve of the structure (the relationship between base shear (V_{bs}) and roof displacement (Δ_{RF})). The superstructure is usually considered to be elastic under seismic excitations if it is equipped with an isolation system. Thus, the performance point of the base shear, which is equal to $0.8V_{max}$, is determined. Second, due to the isolation system, the demand for the seismic design force can

¹ Associate Researcher, National Center for Research on Earthquake Engineering

² Postgraduate Student, National Taiwan University

³ Professor, National Taiwan University

⁴ Assistant Researcher, National Center for Research on Earthquake Engineering

⁵ Associate Professor, National Taiwan University of Science and Technology

be decreased to $S_a^{(R)}W$ by the effective period of isolation T_e , where W is the weight of the isolated structure and $S_a^{(R)}$ is the spectral acceleration. To ensure that the isolation system is effective, the demand of base shear $S_a^{(R)}W$ must be smaller than the capacity V_{bs} ; thus:

$$S_a^{(R)}W = \frac{S_{D1}}{B_1 T_e} W \leq V_{bs} \Rightarrow T_e B_1 \geq \frac{S_{D1} W}{V_{bs}} \quad (1)$$

Thirdly, the isolation period must be long enough for the isolation system to perform effectively. However, it cannot be too long because the displacement would then be too large. Therefore, a medium to long isolation period should be used:

$$2 \leq T_e \leq 5 \text{ s} \quad (2)$$

Fourthly, if the effective damping ratio ζ is less than 2%, then the one-second modification factor of the seismic force due to damping, B_1 , will be 0.8, and if ζ is greater than 50%, B_1 will be 1.75:

$$0.80 \leq B_1 \leq 1.75 \quad (3)$$

Fifthly, because the isolated structure has a medium-to-long period, the spectral acceleration $S_a^{(R)}$ will be $S_{D1}/B_1 T_e$. The displacement $D = S_a^{(R)} g T_e^2 / 4\pi$ should be less than the allowable displacement of the isolation system, D_a

$$S_a^{(R)} g T_e^2 / 4\pi^2 \leq D_a \Rightarrow \frac{B_1}{T_e} \geq \frac{S_{D1} g}{4\pi^2 D_a} \quad (4)$$

where g is the acceleration due to gravity.

Using Eqs. (1) to (4), the available design range for B_1 and T_e can be obtained. Then, according to the Seismic Design Code of Buildings (2011), the available ranges for B_1 and T_e can be converted into the ranges for ζ and T_e . Finally, at a specific displacement D , the effective stiffness K_e and effective period T_e can be determined using the radius of curvature R and the coefficient of friction μ for the friction pendulum bearing.

$$K_e = \frac{W}{R} \left(1 + \frac{\mu R}{D} \right) \quad (5a)$$

$$T_e = 2\pi \sqrt{\frac{W}{K_e g}} = 2\pi \sqrt{\frac{R}{g} \sqrt{\frac{1}{1 + \frac{\mu R}{D}}}} \quad (5b)$$

The effective damping ratio ζ can be calculated using the energy dissipation of friction W_D and the strain energy W_S ; thus,

$$W_D = 4\mu D \quad (6a)$$

$$W_S = \frac{1}{2} K_e D^2 \quad (6b)$$

$$\zeta = \frac{W_D}{4\pi W_S} = \frac{2\mu}{\pi \left(\frac{D}{R} + \mu \right)} \quad (6c)$$

By solving Eqs. (5b) and (6c), the displacement D is determined to be $S_{D1} g T_e / 4\pi^2 B_1$, and R and μ can be

expressed using the following equations:

$$R = \frac{T_e^2 g}{2\pi^2 (2 - \pi\zeta)} \quad (7a)$$

$$\mu = \frac{2\pi^3 \zeta D}{T_e^2 g} \quad (7b)$$

The available ranges for T_e and ζ can be converted into the available ranges of R and μ using Eqs. (7a) and (7b). Therefore, engineers can easily design the two parameters for the friction pendulum bearing.

Example Structure

The example structure is a conventional moment-resisting RC frame (Chung 2018). The plan dimension is 5 m by 8 m with respect to the x- and y-directions, with the x-axis representing the main direction during pushover analysis. The structure had two stories, each of which was 3.6 m high. The example structure is situated in Ruisui Township, Hualien County, and the site is classified as a soft site (type III). The distance to the nearest fault is greater than 12 km. According to the site conditions and the Seismic Design Code of Buildings (2011), the design spectral acceleration for the short-period structure S_{DS} is 0.8, and spectral acceleration for the one-second-period structure S_{D1} is 0.675. In this structure, the thickness of the slab is 15 cm, the beam is 24 cm wide and 60 cm deep, and the column is 50 cm wide (x direction) and 30 cm deep (y direction). The reinforcements of the beam and column are shown in Fig. 4. The compression strength of the concrete is 190 kgf/cm² and the yielding strength of the steel is 3200 kgf/cm². The size of the plan and section can be used to determine the total volume of the structure and thus its weight. In accordance with the Application of Concrete Engineering Design Specifications, we also considered the weights of the mortar, paving, ceiling, and wires. The total weight, W is 75.63 tf. The example structure is an emergency shelter, so we incorporated an importance factor $I = 1.5$ in compliance with the Seismic Design Code of Buildings (2011). Using the Manual for Seismic Assessment and Retrofit of School Buildings (v3) (2013), the pushover curve of the structure was obtained by pushover analysis with ETABS software. The result is shown in Fig. 5. If a structure is slightly damaged during the design basis earthquake, the base shear will develop to 80% of its maximum value. Therefore, the base shear of the performance point is $V_{bs} = 0.8V_{max} = 21.88$ tf and the corresponding roof displacement Δ_{RF} is 4.44 cm.

According to the Manual for Seismic Assessment and Retrofit of School Buildings (v3) (2013), the pushover curve (capacity curve) can be converted into a capacity spectrum (a plot of S_a versus S_d) as shown in Fig. 6, which indicates that, at the performance point,

the spectrum acceleration S_a is 0.3132 g and its corresponding spectrum displacement S_d is 3.682 cm. Using these values for S_a and S_d , the performance peak ground acceleration A_P is calculated to be 0.1564 g, and the design peak ground acceleration A_T is $0.4S_{DS}$, or 0.32 g; therefore, the capacity to demand ratio is given by $R_{CD}=A_P/A_T=0.4887<1$. Since R_{CD} is less than 1, the structure needs to be retrofitted. At the performance point, T_{eq} is 0.688 s and the equivalent damping ratio ζ_{eq} is 0.0876. From Eq. (1), $S_a^{(R)}W$ is smaller than V_{bs} , so Eq. (1) can be used to determine $T_e B_1 \geq S_{D1} W / V_{bs} = 0.675(75.63) / 21.88 = 2.331$. The effective vibration period for the isolated structure is $2 \leq T_e \leq 5$ s (from Eq. (2)), and the one-second modification factor of the seismic force due to damping is $0.80 \leq B_1 \leq 1.75$ (from Eq. (3)). The allowable displacement D_a is assigned to be 50 cm, so $B_1 / T_e \geq 0.675(981) / 4\pi^2(50) = 0.3355$ can be obtained from Eq. (4). The design solutions, including values for the isolation period T_e and one-second modification factor of seismic force due to damping B_1 (Fig. 7), are constrained by these four inequalities Table 1 shows the relationship between B_1 and the damping ratio ζ . In addition to this, the available range of B_1 and T_e can be used to find the available range of T_e and ζ (Fig. 8). According to Eqs. (7a) and (7b), the available ranges of T_e and ζ can be used to determine the available ranges of the radius of curvature R and coefficient of friction, μ (Fig. 9). We selected values within the acceptable ranges, namely $R=4$ m and $\mu=0.04$, and after iteration using the procedure of equivalent lateral force, we determined the following parameters: design displacement $D=38.6 < D_a=50$ cm, the isolation period $T_e=3.37$ s, the damping ratio $\zeta=0.1866$, and $B_1=1.466$. We also found the demand for base shear to be $S_{D1} W / B_1 T_e = 0.675(75.63) / 1.466(3.37) = 10.33$ tf, a value smaller than the capacity $V_{bs}=21.88$ tf. We therefore achieved our goal of seismic retrofitting the structure to within the specifications.

Table 1. One-second damping modification factor from Seismic Design Code of Buildings (2011)

damping ratio ζ (%)	B_1
<2	0.80
5	1.00
10	1.25
20	1.50
30	1.63
40	1.70
>50	1.75

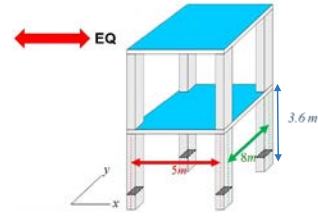


Fig. 1. 3D schematic diagram of the example structure

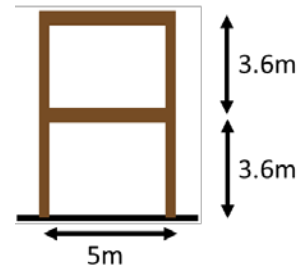


Fig. 2. Elevation view of example structure in the x direction (earthquake direction)

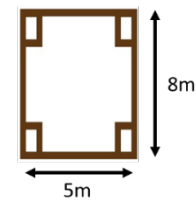


Fig. 3. Plan view of the example structure

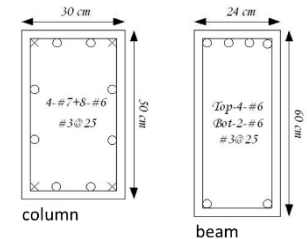


Fig. 4. Beam, column section, and their respective reinforcements

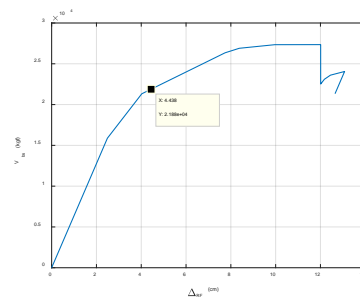


Fig. 5. Pushover curve (capacity curve) of the example structure and the performance point

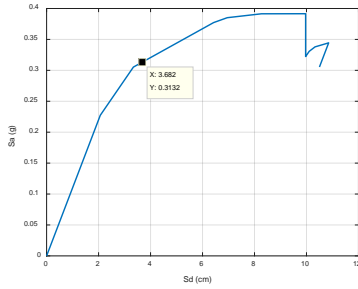


Fig. 6. Capacity spectrum and the performance point

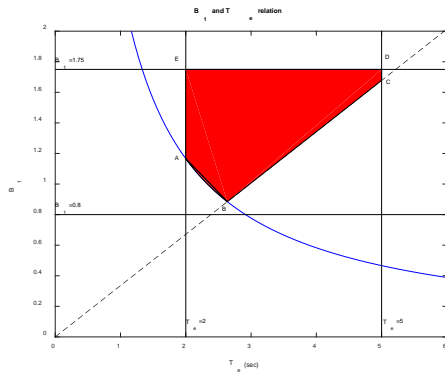


Fig. 7. Available range for isolation period T_e and one-second modification factor for the seismic force due to damping B_1 (red area)

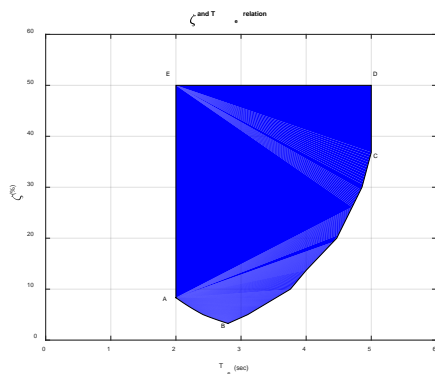


Fig. 8. Available range for T_e and ζ (blue area)

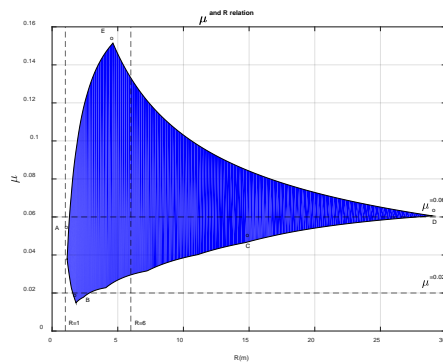


Fig. 9. Available range for radius of curvature R and coefficient of friction μ (blue area)

Conclusions

In the practical applications, engineers can refer to this study if an existing structure needs to be retrofitted with an isolation system with a friction pendulum bearing. This article presents a design procedure for installing an isolation system and demonstrates its application with an example structure using detailed structural information. First, the capacity-to-demand ratio R_{CD} of a structure must be evaluated; if it is less than 1, the structure needs retrofitting. Second, the design range of B_1 and T_e can be obtained using four conditions: $R_{CD} > 1$, the range of the effective period T_e , the range of B_1 , and $D \leq D_a$. Then, linear interpolation is used to find ζ corresponding to B_1 , resulting in the design range of ζ and T_e . This range can be used to find suppliers that provide friction pendulum systems and to determine the design parameters R and μ of the system. Finally, the displacement D can be calculated and used to check whether R_{CD} is greater than 1 after implementing the isolation system. If it is, the demand of the structure is decreased successfully, and the goal of seismic retrofitting is achieved.

References

- Chinese Institute of Civil and Hydraulic Engineering (2011), "Application of concrete engineering design specifications (civil engineering 404-100) (Volume II)", *Taiwan, Technology book*.
- Chung, L. L., Chen, C. H., Yang, Y. S. and Lai, Y. C. (2018), "Structure Seismic Assessment: Real Earthquakes as Demand", *Engineers Times (submitting)*.
- Ministry of Interior (2011), "Seismic Design Code of Buildings", from <https://goo.gl/h7dU6V>.
- National Center for Research on Earthquake Engineering (2013), "Manual for seismic assessment and retrofit of school buildings (v3)", NCREE-2013-023, from <https://goo.gl/RwuGrP>.

Ugkuo le'Rgt hqt o cpeg'Gxcnwc vkqp'qhi'Gz kumpi '' J li j /Tkg'UygnUvt wewwt gu'

Sheng-Jhih Jhuang¹ Ker-Chung Lin² Kai-Ning Chi³ Sish-Siou Gao⁴
and Yung-Chih Wang⁵

莊勝智¹、林克強²、紀凱甯³、高墀修⁴、王勇智⁵

Cduwt cev'

Steel structures in Taiwan have been developed for nearly 40 years. Due to specification revisions and building material strength and joint performance attenuation by earthquakes, there are doubts about whether existing steel structures have adequate seismic performance. The main objective of this study is to establish a seismic performance evaluation procedure and retrofit method for high-rise steel structures to understand the characteristics of high-rise building responses and common retrofit methods. We considered a 15-floor (15F) steel building model designed according to past specifications, which needs to be retrofitted. We adopted the Taiwan and United States standards for the seismic performance evaluation process to establish a recommended methodology and evaluate design using this case study. The results of this study show that inelastic pushover responses may be similar to dynamic analysis responses due to the absence of higher mode effects on the interstory drift of the 15F steel structure. If there are obvious higher mode effects in steel structures with a greater number of floors, dynamic time-history analysis should be carried out. In addition, the 15F building retrofitted with buckling restrained braces has acceptable displacement control efficiency. We recommend performing inelastic time-history analysis and reviewing the retrofit method. Each building retrofit is case-specific, and the building requirements as well as the advantages and disadvantages of each retrofit strategy must be understood before effectively carrying out the retrofit design.

Mg{y qtf u steel structure, seismic performance evaluation, retrofit, dynamic time-history analysis

30Hqtgy qtf

During the 921 Chi-Chi earthquake in 1999, a large number of casualties and considerable economic losses occurred due to the destruction and collapse of building structures. Therefore, when the Seismic Design Specifications and Commentary of Buildings (Construction and Planning Agency, 2005) were revised, the required seismic force demand for building structures was increased. Based on these current specifications, many existing buildings may not be able to meet the seismic force requirements. For existing building structures to meet these requirements and to theoretically verify safety requirements according to past earthquake activity, updated specifications, and analytical technology advancements, the structures need to be re-evaluated for earthquake resistance.

In response to the seismic issues and considering

economic factors, domestic specifications allow existing structures to be evaluated using inelastic analysis methods instead of traditional elastic analysis. The inelastic performance of existing structures is thus used to test their seismic resilience. This can greatly reduce the cost of retrofitting and meet economic value expectations for existing buildings. In addition, for high-rise buildings, the higher mode effects become more significant as the number of floors increases. Inelastic pushover analysis methods therefore may not be able to adequately test the high mode amplification effect behavior of high-rise buildings. An inelastic dynamic time-history method should be used instead to analyze these structures and to control the unfavorable high mode behavior.

40Ugkuo le'r gt hqt o cpeg'gxcnwc vkqp'et kgt kc
40'Ugkuo le'gxcnwc vkqp'itcuk'

¹ Research Assistant Fellow, National Center for Research on Earthquake Engineering

² Research Fellow, National Center for Research on Earthquake Engineering

³ Research Assistant Fellow, National Center for Research on Earthquake Engineering

⁴ Master, Department of Civil Engineering, National Central University

⁵ Professor, Department of Civil Engineering, National Central University

The seismic performance evaluation in this study is based on the provisions in Chapter 8 of the Seismic Design Specifications and Commentary for Buildings (Construction and Planning Agency, 2005) regarding seismic performance evaluation and seismic retrofitting of existing buildings. According to the commentary of section 8.2:

The seismic performance of existing buildings that are expected to be used for more than 50 years should reach the ground acceleration for a site return period of 475 years.

The seismic performance evaluation and seismic retrofitting of the existing buildings in this study are thus based on a designed earthquake level with a return period of 475 years (a 2% exceedance probability during a 50-year useful life). We used this evaluation criterion as the basis for our retrofit design.

40'Ugko le'gxcnecvqpp'cpcrf ulu'b gvj qf u'

The seismic performance evaluation of existing buildings used in this study separately considers three performance targets: strength, displacement ductility, and story drift. These three performance targets are obtained by elastic static analysis, inelastic static analysis, and inelastic dynamic time-history analysis. This study will use these three analytical methods to confirm the existing seismic performance of the building.

2.2.1 Elastic static analysis

Elastic static analysis results should meet the strength performance target. Based on the strength design of new buildings of the building seismic design specification, the demand of earthquake force are the largest of minimum design level total transverse force, design earthquake force to avoid collapse of maximum consideration earthquake, and design earthquake force to avoid yield of moderate and small earthquake. And analyze it by elastic static analysis method. The structural members could not yield under the specified design load combination.

2.2.2 Inelastic static analysis

The results from inelastic static analysis should meet the displacement ductility target. A structural model of the building is established, inelastic static analysis is performed, and the pushover capacity curve between the top floor displacement and the base shear force is obtained. This is achieved using the seismic demand response spectrum (designed earthquake spectrum with a return period of 475 years and maximum considered earthquake spectrum with a return period of 2500 years) of the building performance target while considering the equivalent damping ratio of the structural system. In accordance with the capacity spectrum method in ATC 40 (Applied Technology Council, 1996), the building pushover capacity curve and the earthquake demand response spectrum curve (i.e., the relationship between

acceleration and period) are then converted into acceleration-displacement response spectra (ADRS). The ADRS describe the spectral acceleration and spectral displacement coordinates, and the intersection of the two lines, when plotted in the same graph, yields the performance point of the structure. The pushover capacity curve of the structure can be simplified into a bilinear capacity curve by selecting an equivalent theoretical yield point to facilitate the determination of the elastic displacement Δ_y and the plastic displacement Δ_p as shown in Figure 1. Table 1, read in conjunction with Figure 1, summarizes recommended building performance targets used to judge whether the building meets seismic performance targets.

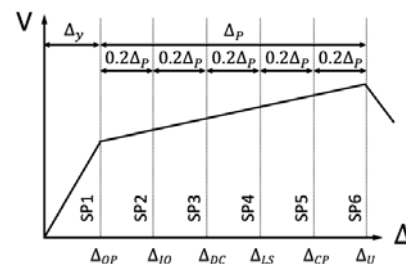


Figure 1 Displacement ductility targets (Architecture and Building Research Institute, 2005)

Table 1 Seismic performance targets (Architecture and Building Research Institute, '2005)

Seismic Performance Objective	Earthquake Return Period (years)		
	Importance of Architecture		
	I & II (I=1.5)	III (I=1.25)	IV (I=1.0)
Operational (OP)	75	50	30
Immediate Occupancy (IO)	475	-	-
Damage Control (DC)	2500	475	-
Life Safety (LS)	-	2500	475
Collapse Prevention (CP)	-	-	2500

2.2.3 Inelastic dynamic time-history analysis

The main purpose of inelastic dynamic time-history analysis is to (1) verify that the overall structure meets the interstory displacement target specified by the design, and (2) confirm that the deformation requirements of each member meet the deformation capacity used in the analysis. This method is based on a 3D structural analysis model, where actual earthquake acceleration records or artificial acceleration records are selected for inelastic dynamic analysis. According to ASCE 7-16 (the American Society of Civil Engineers, 2016), at least eleven earthquake acceleration records must be used for inelastic dynamic time-history analysis. Care should be taken to make the earthquake acceleration history consistent with the site ground motion characteristics or the design acceleration response spectrum. This can be achieved by taking earthquake acceleration history records from the site or a nearby station and making

adjustments using scaling and matching methods. For the seismic design of buildings, it is generally believed that relevant research is well advanced in the United States (e.g., the Uniform Building Code, the International Building Code, ASCE 7, and ASCE 41). However, there have been considerable changes in the provisions on the adjustment of earthquake acceleration history in past editions of these specifications. Ways to adjust the scaling and matching methods have not yet converged.

50Ecug'twfw {

The case analysis is for an existing steel structure building with 15 floors (15F). The height of the first floor is 5.1 m, the height of each floor above the first floor is 3.4 m, and the total height of the building is 52.7 m. The building is assumed to be an office block. The building belongs to the third building type according to the classification based on the importance of the structure (type III, $I=1.25$, Table 1), and the site is in Taipei's Second District. The plane of this building is shown in Figure 2, and the base shear force of the building is given in Table 2.

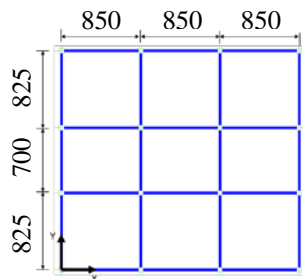


Figure 2 Model plane

Table 2 Base shear coefficient of 15F building (X direction)"

	1983 & 1994 Specification	2011 Specification
Weight	6840	
Period	2.05	
Maximum stress ratio	0.646	1.073
Base shear coefficient	0.072	0.133

50'Ugko le'tgt hqt o cpeg'gxcncvkap'dghqtg'tgt qhkv'

1. Strength target

First, the earthquake force in the current specification (Construction and Planning Agency, 2011) is calculated, and elastic pushover analysis is performed. The allowable interstory drift of each floor is shown in Table 3. This value exceeded 0.005 for many floors, which means that some members have yielded and the building does not meet the requirement for member strength.

2. Displacement ductility target

The ductility target is judged using inelastic pushover analysis. The results are shown in Figure 3.

The design response spectrum is reduced by considering the extra hysteresis damping produced by the plastic hinge. The performance point is the intersection of the response spectrum and the performance curve. According to the suggestions made by the Architectural and Building Research Institute of the Ministry of Interior (Architectural and Building Research Institute, 2005), the performance target adopts damage control. The quantification standard is $\Delta_y + 0.4\Delta_p$. The performance point is lower than the standard, indicating that the ductility target meets the recommended provisions.

3. Story drift target

The interstory displacement target is judged using inelastic dynamic time-history analysis. The scaling method was adopted to adjust the earthquake history. The results of the inelastic dynamic analysis are shown in Figure 4. The interstory drift of some floors exceeded the 0.015 requirement.

From the analysis results of the aforementioned three targets, the failure to meet the three seismic performance targets indicates that the building needs to be retrofitted to improve its seismic performance.

Table 3 Interstory drift of 15F building before retrofit

U _q t {	F t h/z	F t h/z	U _q t {	F t h/z	F t h/z
37H	0.0024	0.0024	9H	0.0053	0.0053
36H	0.0031	0.0031	8H	0.0053	0.0053
35H	0.0038	0.0038	7H	0.0054	0.0054
34H	0.0044	0.0044	6H	0.0054	0.0054
33H	0.0049	0.0049	5H	0.0052	0.0052
32H	0.0053	0.0053	4H	0.0049	0.0048
:H	0.0054	0.0053	3H	0.0031	0.0031
:H	0.0054	0.0053			

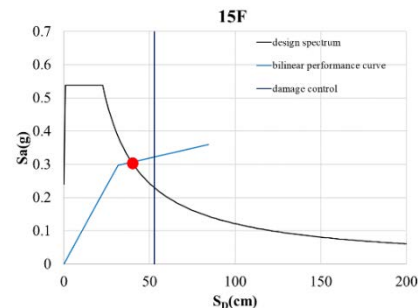


Figure 3 Pushover analysis results of 15F steel building

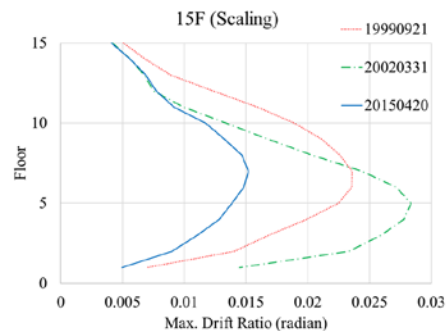


Figure 4 Dynamic analysis results of 15F steel building (X direction)

50'Ugko le'fgt hqt o cpeg'gxcnvcvkqp'c'ngt't'gvt qhls'

The aforementioned 15F steel structure was retrofitted using buckling restrained braces (BRBs). The axial force and the quantity of braces are shown in Table 4.

1. Strength target

Because of retrofitting with BRBs, the structural stiffness of the overall building and the earthquake force increase. This works together with the force transmission mechanism of BRBs to transfer the maximum stress ratio after retrofitting to the columns of the first and second floors. The maximum stress ratio of the columns reaches 0.93 but does not exceed 1.0, which meets the strength target.

2. Displacement ductility target

The results of the inelastic pushover analysis after BRB retrofitting are shown in Figure 5. In terms of ductility, the structure meets the requirements of the increase in earthquake force. Comparing the results in Figures 3 and 5, it is clear that the earthquake force and the structural stiffness increase.

Table 4 Axial force and quantity of BRBs

Uqt{	F gułi p CzlcilHqteg *qp+	S wcpvls{	Uqt{	F gułi p CzlcilHqteg *qp+	S wcpvls{
37H	0	0	9H	220	4
36H	0	0	8H	260	4
35H	0	0	7H	260	4
34H	180	4	6H	260	4
33H	180	4	5H	300	4
32H	180	4	4H	300	4
;H	220	4	3H	320	4
:H	220	4			

3 Story drift target

Figure 6 shows the inelastic dynamic analysis results of the retrofitted 15F steel structure. The interstory drift was reduced and all drifts satisfy the provision that they do not exceed 0.015.

The seismic performance of the retrofitted steel structure is in line with the provisions. Using BRBs is an effective way to control interstory drift, but it is also necessary to pay attention to the increase in earthquake force caused by the increase in building stiffness.

Eqpemvkqp'c'pf 'Uwi i guvkpu'

Comparing the past earthquake force specifications in Taiwan (Ministry of the Interior, 1982; 1994) and the current specifications (Construction and Planning Agency, 2011) with current US specifications (ASCE 7, 2016) for the same period (approximately 1.8 s) and the same site (Taipei Second District) reveals that the current earthquake force provision in Taiwan is nearly twice as large as it was in the past, while the earthquake force specified in the US is similar to the past specification in Taiwan. If the current specification is taken as the performance target, existing buildings need to be retrofitted, especially

when a larger stress ratio was used in the original building design.

In the analyses, it is necessary to select earthquake histories that are close to the design response spectrum before adjustment. It is not recommended that the two horizontal component earthquake histories are used as two separate earthquake records; it is far preferable if the two horizontal time-history analyses are performed at the same time.

The results of the seismic evaluation in this study indicate that before retrofitting, the existing 15F steel structure buildings cannot meet the strength, displacement ductility, and displacement targets at the same time under the designed earthquake with a return period of 475 years. After the retrofit is configured using BRBs, the structure can meet the required targets.

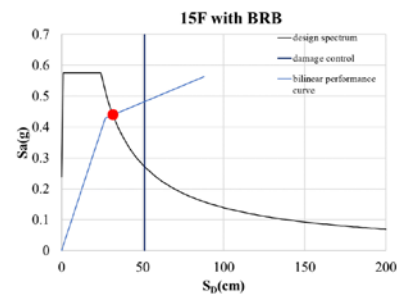


Figure 5 Pushover analysis results of 15F steel building after configuring BRB retrofit

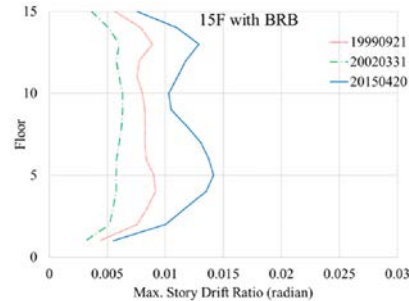


Table 6 Dynamic analysis results of 15F steel building after configuring BRB retrofit (X direction)

T'ghgt gpegu'

ATC40(1996), "Seismic Evaluation and Retrofit of concrete buildings", Applied Technology Council, Redwood City, California.

ASCE7(2016), "Minimum Design Loads for Buildings and Other Structures", American Society of Civil Engineers, New York, Manual of Practice.

Ministry of the Interior(1982,1994), "Building Technical Regulations" .

Construction and Planning Agency, Ministry of the Interior(2005), "Seismic Design Specifications and Commentary of Buildings" .

Construction and Planning Agency, Ministry of the Interior(2011), "Seismic Design Specifications and Commentary of Buildings" .

Architecture and Building Research Institute, Ministry of the Interior(2005), "Research on Seismic Design Specifications of Buildings" .

Experimental Study on Buckling-Restrained Brace Stability

An-Chien Wu¹, Keh-Chyuan Tsai²

吳安傑¹、蔡克銓²

Abstract

Experimental results indicate that global stability of buckling-restrained braces (BRBs) and gusset connections is critical to the seismic performance of buckling-restrained braced frames (BRBFs). This study presents experimental results testing a simplified analytical method that has been developed to incorporate the concept of a notional load and the flexural effects of the restrainer in assessing the global stability of a welded-end BRB and its connection. Cyclic loading tests on four full-scale BRBs with varying steel casing sizes and gusset connection stiffnesses were performed with various initial imperfections and out-of-plane (OOP) drifts to demonstrate the effectiveness of the proposed method. Test results confirm that the effects of the initial imperfection, OOP drift, and gusset edge stiffener on the BRB buckling strength can be satisfactorily predicted. It is concluded that the global stability is vulnerable to the OOP drift and adequately stiffening the gusset is recommended in BRB applications.

Keywords: buckling-restrained brace, global stability, flexural restrainer, notional load

Introduction

Buckling-restrained braces (BRBs) are designed as seismic dampers to yield both in tension and compression through gusset plates as the interface between the structural frame and the damper. However, out-of-plane (OOP) buckling of the BRB gussets has been reported and investigated in a series of buckling-restrained braced frame (BRBF) tests [Tsai and Hsiao 2008, Chou and Liu 2012, Mahrenholtz et al. 2015, Wu et al. 2017]. Recently, Takeuchi et al. [2014] proposed a set of equations for evaluating BRB global stability considering the restrainer moment transfer capacity, gusset rotational stiffness, initial imperfection, and OOP drift. It was validated through cyclic loading tests on both diagonal and chevron configured BRB-and-gusset sub-assemblages. Nevertheless, the collapse mechanisms illustrated in Takeuchi's models involve an un-deformed restrainer, which is somewhat inconsistent with the buckling mode observed in a recent frame test [Wu et al. 2017]. As a result, Tsai et al. [2018] and Chen et al. [2019] proposed an evaluation procedure

extended from Takeuchi's approach but by incorporating consideration of the flexural restrainer and gusset rotations to describe the observed buckling mechanism. This refined model requires finite element model analyses to determine the rotational stiffness and strength of the gussets, as well as additional moment demands induced by the initial imperfection and OOP drift. Zaboli et al. [2018] adopted the notional load yield line method to propose a simplified stability design procedure for both concentrically braced frames and BRBFs. Again, this method was also based on the collapse mechanisms of Takeuchi's models, which neglects the buckling mode with a flexural deformed restrainer.

This study is an experimental follow-up on a proposed analytical model that draws on the key advantages of the above-mentioned methods and incorporates welded-end BRB's OOP stability assessment by considering the notional load yield line method and restrainer flexibility. In order to verify the effectiveness of the proposed model, experimental results of four full-scale BRB specimens are investigated in

¹ Associate Researcher, National Center for Research on Earthquake Engineering, acwu@ncree.narl.org.tw.

² Professor, Department of Civil Engineering, National Taiwan University, kctasi@ntu.edu.tw.

this study. It is confirmed that the proposed method is able to predict satisfactorily the overall buckling strengths of the specimens.

Table 1. Design dimensions of specimens.

Specimen	t_c (mm)	B_c (mm)	R_f (mm)	t_r (mm)	L_{BRB} (mm)	t_g (mm)
G18			216			18
G16	16	103	216	7	5760	16
G18LC			267			18
G16ES			216			16

Specimen Profiles

Four specimens of G18, G16, G18LC, and G16ES were designed to represent a typical BRBF

with a 6000-mm bay width and a 4000-mm story height. The detailed dimensions are illustrated in Fig. 1 and given in Table 1. The specimens are denoted such that the first three alphanumeric letters indicate the gusset thickness. "LC" denotes a larger restrainer, while "ES" denotes the gusset edge stiffeners. The cores of the specimens were fabricated using CNS SN490B steel with a nominal yield capacity of 988 kN, while the steel casings were made from CNS STK490 steel. In order to understand the flexural effects of the restrainers, two sizes of restrainers were considered, both filled with high-strength mortar. Specimens G16ES and 2G16ES were fabricated with a 10-mm thick stiffener along the long side of the gusset free edges to investigate the effects of a stiffened gusset.

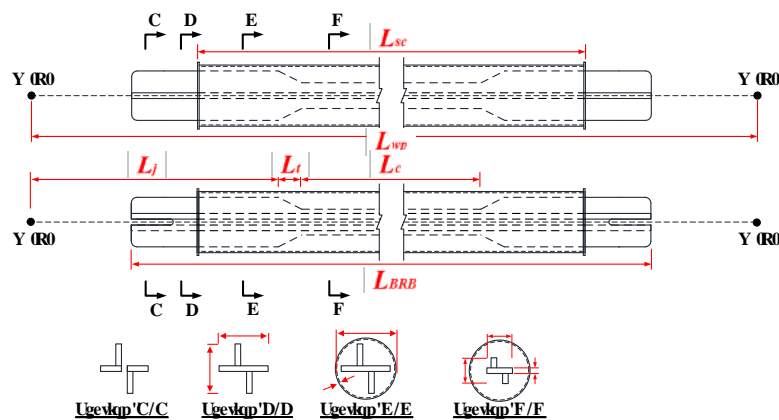


Fig 1. Profiles of the specimens.

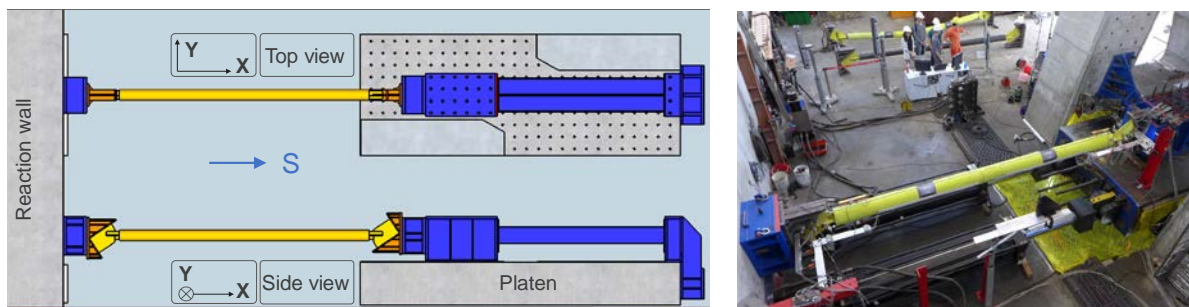


Fig 2. Test setup.

The experiment was conducted using the Multi-Axial Testing System (MATS) at the National Center for Research on Earthquake Engineering (NCEE) in Taiwan. As shown in Fig. 2, the experimental layout was set up to have the positive X-direction toward the south (the platen side) and the positive Y-direction toward the east. This coordinate system was applied for both the loading protocol and the instrumentation. Two displacement transducers were mounted at each brace end to measure axial deformation. An array of uniaxial strain gauges was attached to the elastic portion between the restrainer and the gusset to recover the axial forces. The specimens were tested by applying

cyclically increasing displacements. The loading protocol shown in Fig. 3 consisted of two parts as the standard and the extended cyclic loading tests. The standard loading cycles followed the specifications of AISC 314-16 [2016] for BRBs, where the first two cycles considered the yield displacement of the test specimen. Then, the loading proceeded with an increasing inter-story drift ratio (IDR) ranging from 1% to 4% for two cycles at each level. In order to trigger the instability of the specimens, two additional cycles with 5% IDR were adopted following the last 4% IDR cycle if necessary. If the specimen underwent these loading cycles without failure, constant loadings with a

constant displacement of 3% IDR were repeated until specimen failure.

V_{gu}T_{gum}'

As shown in Fig. 4 [Ou et al. 2020], specimen G18LC exhibited stable hysteresis behavior throughout the prescribed loading cycles without any observable instability or damage. Its core fatigue fractured at the 16th cycle in the subsequent fatigue loadings. The total cumulative plastic deformation (CPD) exceeded 674 before the end of the test. During the test, the developed maximum compressive strength of 2178kN was recorded. Specimens G18, G16, and G16ES buckled, with plastic hinges forming at the gussets, and significant flexural deformation developed along their

restrainers. Specimen G18 buckled at the first cycle of 5% IDR loading and the axial strength dropped drastically after reaching 2118 kN. Specimen G16 buckled during the first 3% IDR loading cycle with a buckling strength of 1721 kN and a CPD of approximately 80.

Table 2. Test results.

Specimen	IDR	OOP	a_0 (mm)	δ_0 (mm)	P_{exp} (kN)
G18	5.0%	-	7.6	7.3	2118
G16	3.0%	-	9.0	57.4	1721
G18LC	5.0%	-	16.3	72.7	2178*
G16ES (I)	5.0%	-	21.0	0.3	2126*
G16ES (II)	5.0%	1.4%	-	57.1	1942

*Peak compressive strength of stable specimens measured during the loading cycle.

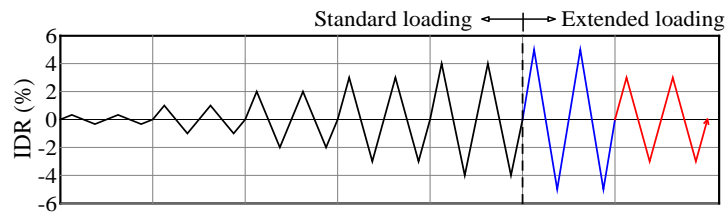


Fig 3. Loading protocol.

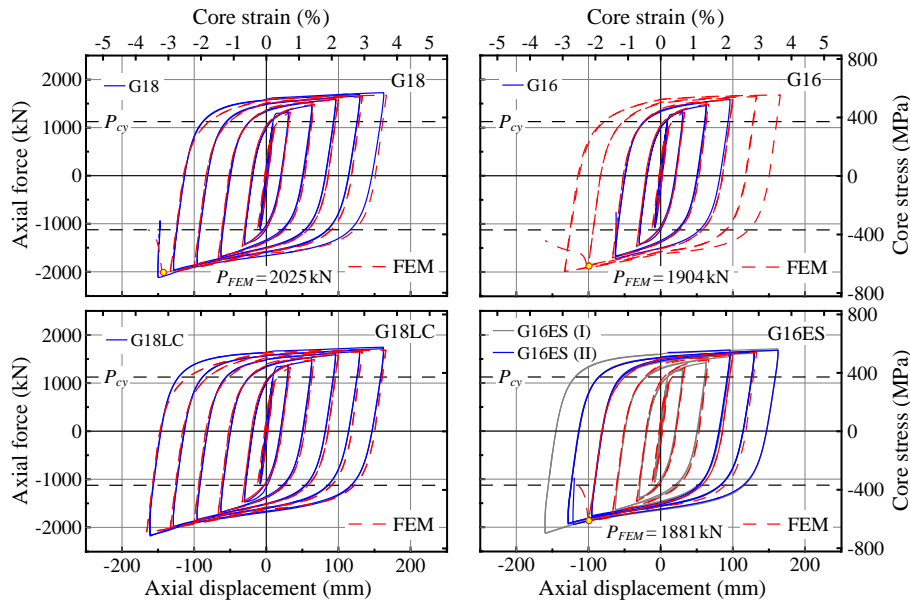
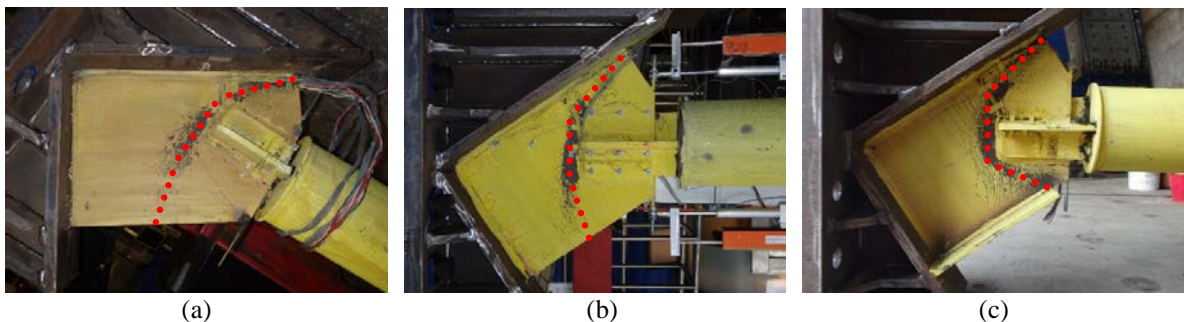


Fig 4. Experimental responses of specimens.



(a)

(b)

(c)

Fig 5. Folding lines at the gussets of specimens (a) G18, (b) G16, and (c) G16ES.

It should be noted that non-negligible imperfections (a_0) at the restrainer mid-span and OOP end drifts (δ_0) of the specimens were measured at the initial states, which were attributed to the fabrication error and experimental misalignment as tabulated in Table 2. Considering the unintentional OOP end drift measured from the above-mentioned tests, specimen G16ES was carefully calibrated without any initial drift. This specimen showed stable performance throughout the standard cycle and additional 5% IDR loading cycles without any damage. Thus, it was further subjected to an OOP IDR of approximately 1.4% and loaded from the 3% IDR cycle to investigate the effects of end drift on the overall stability. Eventually, G16ES buckled at the first 5% IDR loading cycle with a buckling strength of 1942 kN and a CPD of 491. The experimental responses with no end drift and with end drift are designated as “G16ES (I)” and “G16ES (II)”, respectively. Figure 5 shows the folding line that developed on the gussets of the buckled specimens. The overlapping portion between the gusset and the BRB joint segment formed a rigid zone, which pushed the folding line inward to the gussets, causing a curved folding line. The distance between the end of the BRB member and the folding line is approximately twice the gusset thickness. Substantially, the yield line pattern on the regular gusset (Figs. 5a and 5b) runs from the corner of the gusset to the underside of the brace end and back to the middle of the other gusset edge. For the stiffened gusset shown in Fig. 5c, the yield line spreads from the corner of the gusset to the underside of the brace end and back to the tip of the stiffened gusset edge. In addition, from the axial force versus deformation relationships in Fig. 4, it can be seen that the axial stiffness rose slightly during compression in the 4% IDR cycles, and even increased further during the 5% IDR cycle. This phenomenon should be caused by the effects of severe high-mode buckling developing along the core.

Conclusions

An OOP stability assessment procedure for welded-end BRBs considering the notional load yield line method and restrainer flexibility has been proposed [Ou et al. 2020]. Test results presented in this study indicate that the effects of initial imperfections, OOP drift, and gusset edge stiffeners on the BRB global stability could be reasonably captured by the model in terms of buckling strength predictions. It is noted that adequately stiffening the gusset is recommended in the application of BRBs.

References

Tsai KC, Hsiao PC, 2008. Pseudo-dynamic test of a full-scale CFT/BRB frame-Part II: Seismic

performance of buckling-restrained braces and connections. *Earthquake Engineering and Structural Dynamics*, 37(7), 1099-1115.

Chou CC, Liu JH, 2012. Frame and brace action forces on steel corner gusset plate connections in buckling-restrained braced frames. *Earthquake Spectra*, 28(2), 531-551.

Mahrenholtz C, Lin PC, Wu AC, Tsai KC, Hwang SJ, Lin RY, Bhayusukma MY, 2015. Retrofit of reinforced concrete frames with buckling-restrained braces. *Earthquake Engineering and Structural Dynamics*, 44(1), 59-78.

Wu AC, Tsai KC, Yang HH, Huang JL, Li CH, Wang KJ, Khoo HH, 2017. Hybrid experimental performance of a full-scale two-story buckling-restrained braced RC frame. *Earthquake Engineering and Structural Dynamics*, 46(8), 1223-1244.

Takeuchi T, Ozaki H, Matsui R, Sutcu F, 2014. Out-of-plane stability of buckling-restrained brace including moment transfer capacity. *Earthquake Engineering and Structural Dynamics*, 43(6), 851-869.

Tsai CY, Chen LW, Wu AC, Tsai KC, 2018. Seismic performance analysis of BRBs and gussets in a full-scale two-story BRB-RCF specimen. *Earthquake Engineering and Structural Dynamics*, 47(12), 2366-2389.

Chen LW, Tsai KC, Tsai CY, Wu AC, 2019. Evaluating out-of-plane stability for welded BRBs considering flexural restrainer and gusset rotations. *Journal of Constructional Steel Research*, 159, 161-175.

Zaboli B, Clifton GC, Cowie K, 2018. BRBF and CBF gusset plates: out-of-plane stability design using a simplified notional load yield line (NLYL) method. *Journal of the Structural Engineering Society of New Zealand Inc.*, 31(1), 64-76.

American Institute of Steel Construction (AISC), 2016. *Seismic Provisions for Structural Steel Buildings (AISC 341-16)*. Chicago, Illinois.

Ou IC, Chen LW, Tsai CY, Wu AC, Tsai KC, 2020. Buckling-restrained brace out-of-plane stability assessment using notional load and failure mechanism analysis with multi-case study. *Structural Engineering*, 35(1), 78-105. (In Chinese)

Ugkwo le'Rgt hqt o cpegu'qh'UvggnRcpgnF co rgt u'

An-Chien Wu¹, Ming-Chieh Chuang¹, Keh-Chyuan Tsai²

吳安傑¹、莊明介¹、蔡克銓²

Cduwcev'

A ductile Vierendeel frame can be constructed by incorporating steel panel dampers (SPDs) into a moment-resisting frame. The stiffness, strength, and ductility of the lateral force-resisting system can thereby be enhanced. The three-segment SPD proposed in this study possesses a central inelastic core (IC) and top and bottom elastic joints. This study discusses the mechanical properties, capacity design method, and buckling-delaying stiffeners of SPDs using cyclic loading tests for two specimens. Tests confirm that SPDs' cyclic force versus deformation relationships can be accurately predicted using either the Abaqus or PISA3D model analyses. The peak shear deformation of the ICs in the SPDs reached 0.11 rad. The experimental cumulative plastic deformation of the proposed SPD was 242 times its yield deformation, and was capable of sustaining the maximum considered earthquake at least eight times before failure.

Mg(y qtf u steel panel damper, capacity design, seismic design, energy dissipation

Kpvt qf wevkqp''

The stiffness and strength of a lateral force resisting system can be enhanced by incorporating steel panel dampers (SPDs) into the structural design of a building. Figure 1 schematically shows an example of a moment resisting frame that incorporates SPDs. The proposed SPDs shown here include three segments using two different steel wide-flange sections. The middle segment is defined as an

inelastic core (IC), while the top and bottom segments, which use a stronger section, are referred to as elastic joints (EJs). During severe earthquakes, the IC webs are highly likely to undergo large inelastic shear deformations, thereby dissipating seismic energy. To sustain such large deformations and delay the shear buckling of the IC web, properly detailed stiffeners must be attached to the web, flange, and the top and bottom ends of the IC.

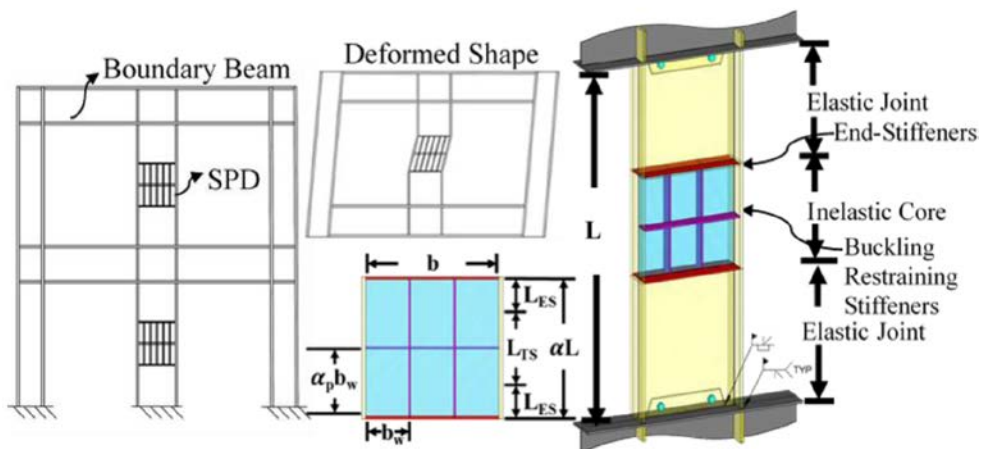


Fig 1. Schematics and stiffener locations of the SPDs in a moment-resisting frame.

¹ Associate Researcher, National Center for Research on Earthquake Engineering, acwu@ncree.narl.org.tw.

² Professor, Department of Civil Engineering, National Taiwan University, kctasi@ntu.edu.tw.

Previously, Liu et al. [2007], Otani et al. [2001], and Tanaka and Sasaki [2000] investigated the hysteretic behavior of shear panel damper components made of low-yield-stress steel and found that a well-designed shear panel damper exhibited a favorable energy dissipation capacity. Otani et al. [2001] investigated the influences of axial loads on the shear panel damper performance and found that a large axial compression force could adversely affect a damper's ability to resist buckling and dissipate energy. The effects of the stiffeners' configuration, mechanical properties, and spacing on the web buckling of the dampers were thoroughly studied by Liu et al. [2007], Otani et al. [2001],

and Koike et al. [2008]. Most of the research has focused on the details of the stiffeners and the experimental responses of an isolated short wide-flange section. Research on the design of the EJ segments, capacity design methods for the boundary beams, and the SPD-to-beam panel zones has been limited. Therefore, this study first discusses the seismic-resistance requirements of a three-segment SPD. Two full-scale SPD specimens were fabricated and tested at Taiwan's National Center for Research on Earthquake Engineering (NCEE). This study presents the experimental performance and compares the Abaqus and PISA3D numerical simulation results with the experimental responses [Hsu et al. 2017].

Table 1. Dimensions of the specimens.

Specimen	Segment	Section (mm)	Length (mm)	Stiffeners (mm)		
				Long.	Trans.	End
SPD-2L1T	Core	H 600×250×8×30	1200	12×100	25×100	12×200
	Joint	H 600×250×22×30	2×700	-	-	-
SPD-2L0T	Core	H 600×250×8×30	1200	12×100	-	12×200
	Joint	H 600×250×22×30	2×700	-	-	-



Fig 2. Dimensions and photos of the specimens.

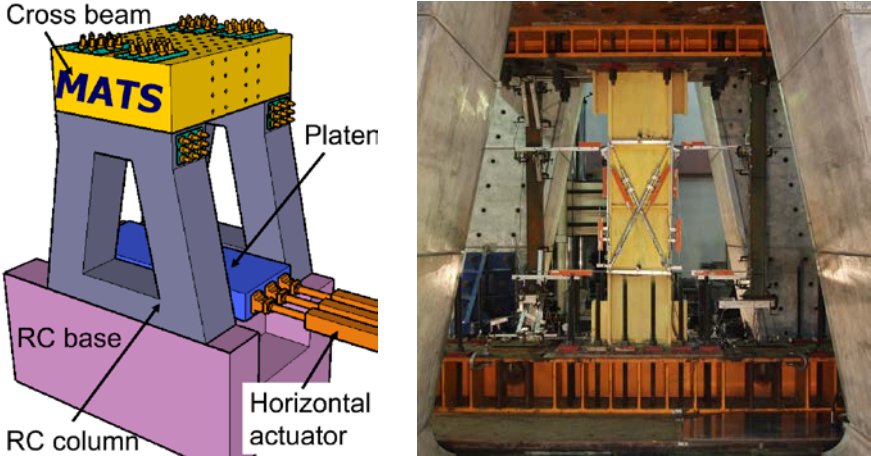


Fig 3. Experimental setup.

Vgu'Rt qi tco "

To investigate the seismic performance of the proposed SPDs, 2 full-scale SPD specimens, namely SPD-2L1T and SPD-2L0T, were fabricated and tested using the Multi-Axial Testing System (MATS) at the NCREE (Fig. 2). Table 1 and Fig. 3 provide the dimensions and photos of the specimens. The web of the IC is made of SN400B steel, while SN490B steel is adopted for the other parts. The only difference between the 2 specimens is that one side of the IC web in specimen SPD-2L1T is stiffened with one additional 100-mm by 25-mm-thick transverse or horizontal stiffener. The thickness of the end stiffeners of both specimens is 12 mm. All stiffeners were SN490B steel.

The MATS platen can move in six degrees of freedom with controlled forces or displacements using servo-hydraulic actuators acting on the platen's bottom surface and 3 side surfaces in 2

orthogonal horizontal directions. The vertical clearance between the MATS's top cross beam and platen is 5 m. During the test, no net axial loads were imposed on the SPD specimens.

In addition to the load cells in the actuators used to measure the shear and bending in the SPD specimens, a number of displacement transducers, tilt meters, and dial gauges were adopted to measure the SPD's as well as the IC's top, bottom end translation, and rotation. The loading protocol shown in Fig. 4 follows the AISC341-10 specifications [2010] for steel moment connection tests. The story height is assumed to be 3.6 m. Upon applying the platen's longitudinal translations without introducing rotations or vertical forces, the in-plane target cyclic inter-story drift ratios (IDRs) are 0.125%, 0.375%, 0.50%, 0.75%, 1.0%, 1.5%, 2%, 3%, 4%, and 5%, each determined with the required number of cycles.

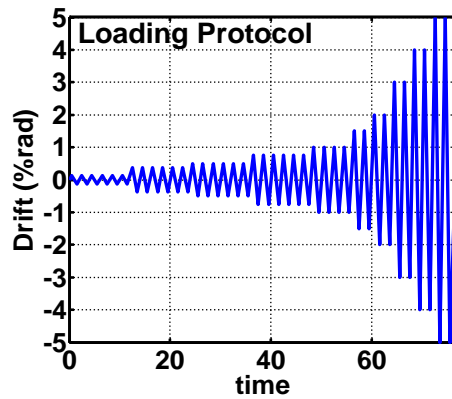


Fig 4. Loading protocol.

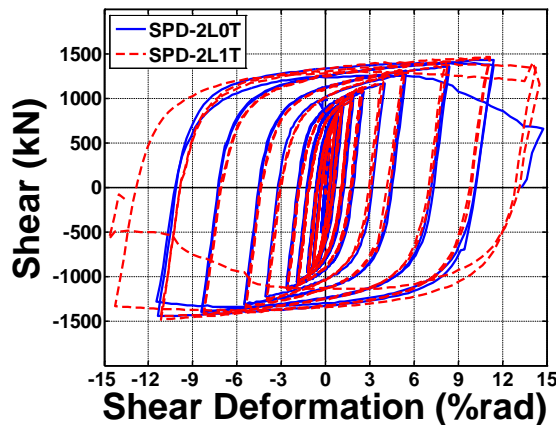


Fig 5. Experimental shear vs inelastic core rotation relationships.

Vgu'Tgummu'

Both specimens performed very well in the tests. Both sustained rather large inelastic deformations with an IDR exceeding 4% without evident strength or stiffness degradation. As shown in Fig. 5, the maximum IC shear deformations of

both SPDs exceeded 0.11 rad before failure. Test results confirmed that the design and details of the stiffeners were effective in delaying the cyclic IC web buckling. Both specimens stably dissipated a significant amount of strain energy. The shear versus shear deformation relationships of the 2 specimens were very similar, as evidenced in Fig. 5.

Nonetheless, the deformational capacity of SPD-2L1T was slightly greater than that of SPD-2L0T, suggesting that the transverse stiffener in the mid-height of the IC somewhat improved the deformational capacity of the IC. In each specimen, IC cracks were first initiated near the stiffener-to-web welds before propagating into the IC web. The EJs of the 2 specimens remained elastic throughout the tests. Test results confirmed that the details of the stiffeners and the capacity design methods for the proposed SPD are effective. The calculated cumulative plastic deformation (CPD) capacities of the 2 specimens were 249 and 242, respectively. The difference between the 2 CPDs is only 3%. These test results suggest that even without the horizontal transverse stiffener, the SPD specimen can perform satisfactorily as long as the IC web slenderness factor meets the specified requirements.

Conclusions

Tests confirmed that the peak IC shear deformations were greater than 0.11 rad. The CPD was greater than 242, indicating that the proposed SPD could sustain an maximum considered earthquake on an moment-resisting frame with SPDs at least 8 times before failure. Test results suggested that the capacity design methods and the fabrication details are sufficient to allow the proposed 3-segment SPD to achieve excellent ductility and energy dissipation capacities. Test results also confirmed that the experimental elastic stiffness can be accurately predicted using the analytical effective stiffness by considering the shear and bending deformations of all three segments of the SPD. Numerical results indicate that the experimental elastic stiffness of the SPDs can be satisfactorily predicted using the Abaqus and PISA3D model analyses, with errors of +13.8% and +1.3%, respectively. The stiffness and strength of the proposed SPD can be decoupled. It was demonstrated that both the elastic and inelastic stiffness of the proposed SPD can be significantly enhanced by reducing the IC height or increasing the EJ web thickness without altering the SPD yield strength or the boundary beam strength requirements.

References

- Liu Y, Aoki T, Takaku T, Fukumoto Y, 2007. Cyclic loading tests of shear panel damper made of low yield steel, *Journal of Structural Engineering*, 53A. (in Japanese)
- Otani M, Inai E, Matsuura T, Ito Y, 2001. Structural performance of shear panel dampers using low yield strength steel, parts 1–3. *Abstract Volume of Technical Papers of Annual Meeting, Architectural Institute of Japan*. (in Japanese)
- Tanaka K, Sasaki Y, 2000. Hysteretic performance of shear panel dampers of ultra low-yield strength steel for seismic response control of buildings. *Proceedings of 12th World Conference on Earthquake Engineering*, New Zealand.
- Koike Y, Yanaka T, Usami T, Ge HB, Oshita S, Sagou D, Uno Y, 2008. An experimental study on developing high-performance stiffened shear panel dampers. *Journal of Structural Engineering*, 54A: (in Japanese)
- Hsu CH, Li CH, Chin PY, Tsai KC, 2017. Seismic design, tests and analysis of steel panel dampers for steel moment frames. *Structural Engineering*, 32(2), 5-34.
- American Institution of Steel Construction (AISC), 2010. *Seismic Provisions for Structural Steel Buildings (341-10)*. AISC, Chicago.

Kphwpeg'qh'Uvgnl t cf g'qp'F gxgnr o gpv'Ngpi vj 'kp'Vgpukqp'' hqt 'J li j /Uvt gpi vj 'Tgkphqt egf 'Eqpet gvg''

Ker-Chun Lin¹, Yuan-Yan Lin², Kai-Ning Chi³ and Sheng-Jih Jhuang³, Yung-Chih Wang⁴

Cduwcev'

This paper reports on testing of twenty beam-end specimens (ASTM A944) for bond behaviors between deformed reinforcements and concrete. Three grades of deformed reinforcements with yield stresses of 420, 550, and 690 MPa and five types of concrete with compressive strengths of 28, 49, 70, 85, and 100 MPa were used. This study was designed to investigate the influence of steel grade on the development length in tension stipulated in the American Concrete Institute (ACI) 318-19 Code. Fifteen of the twenty specimens underwent the concrete splitting anticipated in the ACI 318 code. The results demonstrated that the modification factor for steel grade using the development length in tension specified in the ACI 318-19 Code need not be considered; the ACI 318-14 Code provides sufficiently conservative results.

Mgfy qtf u development length, steel grade modification factor, bond stress

30 Kpvt qf wevkqp

In the existing Concrete Structures Design Code in Taiwan (CPAMI 2019), the design formula and tensile development length provisions for deformed bars were drawn up primarily based on the related provisions of the ACI 318-05 Code (ACI 2005). However, these specifications were retrospective to the ACI 318-95 Code (ACI 1995), and the design formula and provisions on the development length in tension in these code versions were stipulated primarily based on the research results of Orangun et al. (1977). For these ACI 318 Code versions, the design formulas for the straight development length in tension of deformed bars are identical and are given in Eq. (1).

$$l_{d,14} = 0.9 \frac{f_y}{\lambda \sqrt{f'_c}} \frac{\Psi_t \Psi_e \Psi_s}{(c_b + K_{tr})} d_b \quad \text{for} \quad (1)$$

$$1 \leq \frac{(c_b + K_{tr})}{d_b} \leq 2.5 \quad \text{and} \quad (2)$$

K_{tr}

$$= \frac{40A_{tr}}{sn} \quad (3)$$

where f_y is the yield strength of the bar being developed, f'_c is the design compressive strength of concrete, c_b is the smaller of the distance from the bar being developed to the nearest concrete surface or half the center-to-center spacing of the bars being developed, K_{tr} is the transverse reinforcement index (for the Taiwan code, shown in Eq. (3a)) · A_{tr} is the cross-sectional area of all transverse reinforcements within spacing s , n is the number of longitudinal bars being developed, and s is the center-to-center spacing of transverse reinforcements. Ψ_t , Ψ_e , and Ψ_s are factors used to modify development length based on reinforcement location, reinforcement coating, and reinforcement size, respectively.

$K_{tr,TW}$

$$= \frac{A_{tr} f_{yt}}{10.5sn} \quad (3a)$$

Parameter f_{yt} is the yield strength of the transverse reinforcement.

¹ Research Fellow, National Center for Research on Earthquake Engineering (NCREE)

Professor, Department of Civil and Construction Engineering, National Taiwan University of Science and Technology

² Graduated student, Department of Civil and Construction Engineering, National Central University

³ Assistant Research Fellow, National Center for Research on Earthquake Engineering (NCREE)

⁴ Professor, Department of Civil Engineering, National Taiwan Central University

For the 2019 version of the ACI 318 Code (ACI 2019), the allowable strength of reinforcement was raised to 690 MPa from the 420 MPa stipulated in the 2014 version (ACI 318-14). The design formula for l_d , the straight development length in tension, from these versions were almost the same, and is designated as $l_{d,19}$ (MPa, mm) as shown in Eq. (1a), which indicates that the 2019 version includes a modification factor based on reinforcement strength grade Ψ_g .

$$l_{d,19} = 0.9 \frac{f_y}{\lambda \sqrt{f'_c}} \frac{\Psi_t \Psi_e \Psi_s \Psi_g}{(c_b + K_{tr})} d_b \quad (1a)$$

According to ACI 318-19 stipulations, Ψ_g is equal to 1.0, 1.15, or 1.3 for 420 MPa (60 ksi), 550 MPa (80 ksi), or 690 MPa (100 ksi) grade reinforcements being developed, respectively.

In this study, straight development bond behaviors under the condition of bar cutting were considered, especially the stipulations surrounding the factor of Ψ_g prescribed in the ACI 318-19 Code. The rationality of Ψ_g in Eq. (1a) was also of concern. The key purposes of this paper include proposing a rational design formula for straight development length in tension and providing a reference for revising the design code in Taiwan.

40 Gzrgtko gpcvnrtp

The bond behavior of straight development length in tension for longitudinal deformed reinforcements within flexural reinforced concrete (RC) members with transverse (confined) reinforcement was experimentally investigated in this study. The demand of development length for bar cutting at a critical section was of particular concern. The necessity of Ψ_g in Eq. (1a), which uses a value greater than 1.0 for steel yield grades higher than 420 MPa, was expected to be verified.

408'Vgu'fctco gygtu'c'pf 'tr'gelo gp'f guli p''

Twenty beam-end specimens designed on the basis of the Standard ASTM A994 were tested in this study. The dimensions of the beam-end RC specimens were identical (180, 450, and 1000 mm corresponding to their width, height, and length, respectively). Single longitudinal reinforcement was developed for each specimen. Four design parameters were considered: the design compressive strength of concrete, f'_c ; the reinforcement yield strength grade, f_y ; the splitting index, $(c_b + K_{tr})/d_b$; and the type of rib. There were five f'_c values namely 28, 49, 70, 85, and 100 MPa. Three grades of #10 (D32) reinforcements with f_y values of 420, 550, and 690 MPa were adopted as longitudinal reinforcements. For all specimens, two values of splitting index, 3.87 and 4.92, were selected. These values were determined using an identical c_b

of 90 mm and two transverse reinforcements, #4@150 mm and #4@75 mm, respectively, in which the yield strength of the transverse reinforcement was 420 MPa for all specimens. The demand development length for the specimens was calculated as $l_{d,14}$ (from Eq. (1)), according to the provisions of the ACI 318-14 Code. To prevent significant necking of the reinforcements during testing and in anticipation of the occurrence of concrete splitting, the design test (actual anchorage) lengths ($l_{d,test}$) for all specimens ranged from 0.47 to 0.78 times $l_{d,14}$. Two test lengths, 450 and 600 mm, were used for all specimens. The design parameters and results are listed in Table 1. In the table, f'_c is the compressive strength of concrete; f_y is the development length of the reinforcement being developed; d_b is the diameter of the reinforcement (D32 in this paper); R_r is the ratio of the actual rib height of the reinforcement to rib spacing based on requirements in the National Standards of the Republic of China (CNS) 560 $C_{b,s}$ or $C_{b,t}$ represent the distance from the center of the reinforcement being developed to the side or top concrete surface, respectively; S_s is the spacing of the transverse reinforcement; $(c_b + K_{tr})/d_b$ is the splitting index; $l_{d,14}$ is the straight development length in tension according to ACI 318-14 Code provisions; and $l_{d,test}$ is the actual anchorage length of the reinforcement.

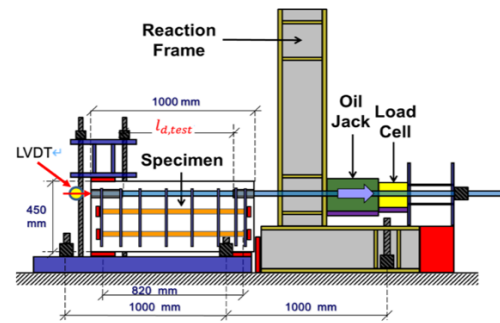


Fig. 1. Test setup

404'Vgu'tgwrr''

The test setup for this study is shown in Fig. 1. An L-shape frame was established as the reaction fixture for applying a tensile force on the reinforcement being considered in the bond specimen. As shown in Fig. 1, the test specimen was placed on the left side of the L-frame. On the right side of the frame, two oil jacks and two load cells were arranged horizontally at the same distances from the test reinforcement and were fixed in place by steel rods. On the other side of the oil jacks, a double-webbed H-shape steel as a part of the reaction system during testing. The central and two side portions of the H-shape steel had three holes for insertion of the reinforcement and two rods lining the oil jacks and load cells. A bolt was welded to the end of the test reinforcement and a nut was fastened in place to the

bolt on the right side of the H-shape steel. The oil jacks were the source of force in this test, and load cells were used to measure the strength responses of the reinforcements during testing.

50 Vgu't gwnu'cpf 'Fkewukqp

508'Utgpi vj 'cpf 'lckwtg'b qf g'

Table 2 shows the test results for the strength and failure modes of all specimens. P_{test} was the maximum tensile force tested. All ratios of P_{test} to P_y were larger than 1.0 and the maximum value was 1.49. The corresponding development length ratios of $l_{d,test}$ to $l_{d,14}$ ranged from 0.47 to 0.78 (Table 1). Comparing the strength and development length ratios, it can be concluded that the straight development length in tension according to the ACI 318-14 or ACI 318-19 Code, while excluding the Ψ_g effect (i.e., $\Psi_g = 1.0$), was quite conservative for deformed bars with R_r values no less than 0.087 under the condition of bar cutting. Four failure modes were observed: (a) concrete splitting, (b) bar fracture, (c) splice fracture, and (d) bolt fracture. All failure modes are indicated in Table 2. Fifteen specimens underwent the concrete splitting expected in the ACI 318 Codes of 1995 to 2019. Failure modes for the remaining five specimens, imply that their concrete splitting strengths were higher than their test strengths (Table 2).

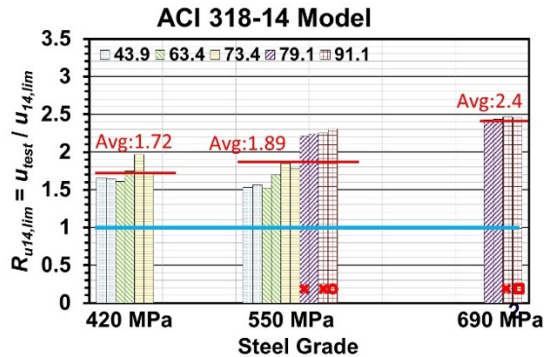


Fig. 2. Bond stress ratio for one ACI 318-14 Code model with upper limits of 70 MPa for concrete strength and 2.5 for splitting index.

504'kphwpeg'qhi'Ψ_g'

Fig. 2 shows the stress ratio $R_{u14,lim}$, plotted against steel grade. This is the ratio of the test bond stress to the theoretical bond stress based on the development length of the ACI 318-14 Code, $l_{d,14}$ (Eq. (1)), or the ACI 318-19 Code, $l_{d,19}$ (Eq. (1a)), without Ψ_g (i.e., $\Psi_g=1.0$) and with the nominal yield stress f_y . Two upper bound limits, 70 MPa for concrete strength and 2.5 for splitting index, were considered when computing the development length from the ACI 318-14 Code. Results show that the bond stress ratios for all specimens have safety factors

ranging from 1.72 to 2.4. In the same way, $R_{u19,lim}$ ratios which include the effect of Ψ_g were obtained for all specimens, and their values ranged between 1.72 and 3.17 (Lin et al. 2020). It is thus clear that for the straight development length in tension demand for deformed bars, the safety factors (ranging from 1.72 to 2.4 for the bond stress ratio using the ACI 318-14 Code) formula are sufficient for practical applications.

60 Eqpenwukqp'cpf 'Tgeqo o gpf cvkqp

Based on the above test results and discussion, one conclusion and one recommendation are offered:

1. Experimental results showed four observed failure modes, concrete splitting, bar fracture, splice fracture, and bolt fracture. The concrete splitting expected in the ACI 318 Codes of 1995 to 2019 occurred in fifteen specimens. Under design conditions where anchorage length ($l_{d,test}$) was between 0.47 and 0.78 $l_{d,14}$, the bond stress ratios ($R_{u14,lim}$) were between 1.72 and 2.4.
2. This study indicates that for the development length in tension under conditions of bar cutting, the modification factor for reinforcement strength grade (Ψ_g) specified in the ACI 318-19 Code was not necessary, and Ψ_g can be taken as 1.0. Consequently, when Eq. (1), specified in the ACI 318-14 Code, was applied for high-strength reinforcement and concrete materials, the tensile development length of $l_{d,14}$ was sufficiently conservative.

Cenpqy igf i go gpwu'

The authors would like to express appreciation to Tung Ho Steel Enterprise Corporation and Feng Hsin Steel Co. Ltd. for their donations of high-strength reinforcements. The financial support provided by the Ministry of Science and Technology of the Republic of China, Taiwan (Grant no: MOST 108-2625-M-492-006), is also sincerely acknowledged.

Tghgt gpegu'

ACI (1995, 2005, 2008, 2014, 2019), *Building Code Requirements for Structural Concrete and Commentary*, Committee 318, American Concrete Institute, Farmington Hills.

Orangun, C. O.; Jirsa, J. O.; and Breen, J. E., 1977, "A Reevaluation of Test Data on Development Length and Splices," *ACI Journal Proceedings*, V. 74, No. 3, Mar., pp. 114-122. doi: 10.14359/10993

CPAMI, 2019, *Design Code for Structural Concrete*, Construction and Planning Agency, Ministry of the Interior, Taipei, Taiwan.

Ker-Chun Lin, Yuan-Yan Lin, Kai-Ning Chi, Sheng-Jih Jhuang and Yung-Chih Wang, 2020, "Bond Performance of Concrete Splitting for High-

Table 1. Specimen design parameters

Specimens	f'_c (MPa)	f_y (MPa)	d_b (mm)	R_r	$C_{b,s}$ (mm)	$C_{b,t}$ (mm)	S_s (mm)	$\frac{(C_b + K_{tr})}{d_b}$	$l_{d,14}$ (mm)	$l_{d,test}$ (mm)	$\frac{l_{d,test}}{l_{d,14}}$
BC28Y42S15De	28	420	32	0.097	90	90	150	3.87	914	450	0.492
BC28Y55S15De	28	550	32	0.094	90	90	150	3.87	1197	600	0.501
BC28Y42S15Di	28	420	32	0.154	90	90	150	3.87	914	450	0.492
BC28Y55S15Di	28	550	32	0.133	90	90	150	3.87	1197	600	0.501
BC49Y42S15De	49	420	32	0.090	90	90	150	3.87	691	450	0.651
BC49Y55S15De	49	550	32	0.097	90	90	150	3.87	905	600	0.663
BC49Y42S15Di	49	420	32	0.145	90	90	150	3.87	691	450	0.651
BC49Y55S15Di	49	550	32	0.138	90	90	150	3.87	905	600	0.663
BC70Y42S15De	70	420	32	0.087	90	90	150	3.87	578	450	0.779
BC70Y55S15De	70	550	32	0.094	90	90	150	3.87	757	450	0.594
BC70Y42S15Di	70	420	32	0.134	90	90	150	3.87	578	450	0.779
BC70Y55S15Di	70	550	32	0.130	90	90	150	3.87	757	450	0.594
BC85Y55S75De	85	550	32	0.099	90	90	75	4.93	757	450	0.594
BC85Y69S75De	85	690	32	0.102	90	90	75	4.93	950	450	0.474
BC85Y55S75Di	85	550	32	0.121	90	90	75	4.93	757	450	0.594
BC85Y69S75De-BC	85	690	32	0.101	90	90	75	4.93	950	450	0.474
BC10Y55S75De	100	550	32	0.093	90	90	75	4.93	757	450	0.594
BC10Y69S75De	100	690	32	0.095	90	90	75	4.93	950	450	0.474
BC10Y55S75Di	100	550	32	0.136	90	90	75	4.93	757	450	0.594
BC10Y69S75De-BC	100	690	32	0.099	90	90	75	4.93	950	450	0.474

f'_c : design compressive strength of concrete f_y : nominal yield strength of developed bar
 d_b : nominal diameter of developed bar R_r : actual height-to-spacing ratio of rib
 $C_{b,s}, C_{b,t}$: distances from center of developed bar to side and top surfaces of concrete, respectively
 S_s : spacing of transverse reinforcements
 $\frac{(C_b + K_{tr})}{d_b}$: actual split index
 $l_{d,14}$: development length in tension based on ACI 318-14 Code
 $l_{d,test}$: design embedded length of reinforcement in concrete with bond

Table 2. Test results and failure modes

Specimens	f'_{ca} (MPa)	f_y (MPa)	d_b (mm)	P_y (kN)	P_{test} (kN)	$\frac{P_{test}}{P_y}$	Failure Mode
BC28Y42S15De	43.9	420	32	338	342	1.012	Concrete splitting
BC28Y55S15De	43.9	550	32	442	421	0.952	Concrete splitting
BC28Y42S15Di	43.9	420	32	338	339	1.003	Concrete splitting
BC28Y55S15Di	43.9	550	32	442	427	0.966	Concrete splitting
BC49Y42S15De	63.5	420	32	338	394	1.166	Concrete splitting
BC49Y55S15De	63.5	550	32	442	509	1.152	Concrete splitting
BC49Y42S15Di	63.5	420	32	338	427	1.263	Concrete splitting
BC49Y55S15Di	63.5	550	32	442	552	1.249	Concrete splitting
BC70Y42S15De	73.5	420	32	338	505	1.494	Concrete splitting
BC70Y55S15De	73.5	550	32	442	476	1.077	Concrete splitting
BC70Y42S15Di	73.5	420	32	338	448	1.325	Concrete splitting
BC70Y55S15Di	73.5	550	32	442	457	1.034	Concrete splitting
BC85Y55S75De	79.1	550	32	442	569	1.287	Bar fracture ❌
BC85Y69S75De	79.1	690	32	555	631	1.137	Concrete splitting
BC85Y55S75Di	79.1	550	32	442	582	1.317	Concrete splitting
BC85Y69S75De-BC	79.1	690	32	555	625	1.126	Concrete splitting
BC100Y55S75De	91.1	550	32	442	583	1.319	Bar fracture ❌
BC100Y69S75De	91.1	690	32	555	641	1.155	Bar fracture ❌
BC100Y55S75Di	91.1	550	32	442	600	1.357	Splice fracture
BC100Y69S75De-BC	91.1	690	32	555	640	1.153	Rod fracture 🟩

f'_{ca} : actual compressive strength of concrete f_y : nominal yield stress of developed bar
 P_y : nominal tensile force of developed bar P_{test} : maximum test tensile force

Performance Evaluation of an Entropy-based Structural Health Monitoring by Utilizing Composite Cross-sample Entropy

Tzu-Kang Lin¹, Yi-Hsiu Chien² and Pei-Yang Lin³

林子剛¹ 簡義修² 林沛暘³

Abstract

This study aimed to solve the issue of unstable entropy values when multiscale cross-sample entropy (MSCE) was employed to assess the damage of real structure. Therefore, composite multiscale cross-sample entropy (CMSCE) was utilized to enhance the reliability of entropy value under every scale. Additionally, the first mode of structure was extracted by using ensemble empirical mode decomposition (EEMD) to conduct entropy analysis and evaluate the performance of damage assessment. A seven-story model was created to validate the efficiency of proposed method and damage index. Subsequently, a seven-story steel benchmark experiment, including fifteen damage cases, was conducted to compare the difference between numerical and experimental model. The confusion matrix was applied to classify the results and evaluate the performance by three indexes: accuracy, precision, and recall. The result showed the feasibility of modified structural health monitoring system and demonstrated the potential on the field of long-term monitoring.

Keyword: structural health monitoring, multi-scale, composite cross-sample entropy

1. Introduction

This project uses cross-sample entropy as the main analysis method, and cross-sample entropy (Cross-SampEn) analysis is performed on the signals of the adjacent two floors, and discuss the effectiveness of empirical mode decomposition method to establish a more efficient structural health diagnosis system. According to the numerical simulation results, further experiments are designed for verification. Conducted the environmental micro-vibration test of the seven-story scale-down benchmark structure at the National Earthquake Engineering Research Center, and designed 15 uniaxial failure modes to analyze the composite multiscale cross-sample entropy (CMSCE), and then tried to quantify the graph with the damage index, eventually reach the health diagnosis of the overall structure.

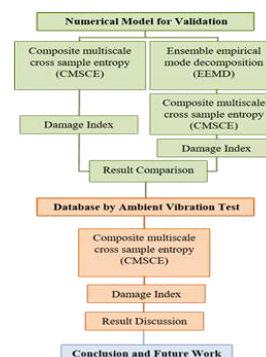


Fig. 1. Flowchart of the study

2. Methodologies

2.1 Cross-sample Entropy(Cross-SampEn)

Cross-SampEn is used to evaluate the degree of dissimilarity between two time series from the same system. The procedure of Cross-SampEn is similar to SampEn and can be summarized as follows. First, consider two individual time series $\{X_i\} = \{x_1, \dots, x_i, \dots, x_N\}$ and $\{Y_j\} = \{y_1, \dots, y_j, \dots, y_N\}$ with length N . Two signals are divided into the templates of length m : $u_m(i) = \{x_i, x_{i+1}, \dots, x_{i+m-1}\}$, $1 \leq i \leq N - m + 1$ and

¹ Professor, Department of Civil Engineering, National Yang Ming Chiao Tung University

² Master, Department of Civil Engineering, National Yang Ming Chiao Tung University

³ Research Fellow, National Center for Research on Earthquake Engineering

$v_m(j) = \{y_j, y_{j+1}, \dots, y_{j+m-1}\}, 1 \leq j \leq N-m+1$. Therefore, two template spaces, T_x and T_y , are presented as follows:

$$T_x = \begin{pmatrix} x_1 & x_2 & \cdots & x_m \\ x_2 & x_3 & \cdots & x_{m+1} \\ \vdots & \vdots & \ddots & \vdots \\ x_{N-m+1} & x_{N-m+2} & \cdots & x_N \end{pmatrix} \quad (1)$$

$$T_y = \begin{pmatrix} y_1 & y_2 & \cdots & y_m \\ y_2 & y_3 & \cdots & y_{m+1} \\ \vdots & \vdots & \ddots & \vdots \\ y_{N-m+1} & y_{N-m+2} & \cdots & y_N \end{pmatrix} \quad (2)$$

The number of similarities between $u_m(i)$ and $v_m(j)$ is defined as $n_i^m(r)$ which can be expressed as follows:

$$n_i^m(r) = \sum_{j=1}^{N-m} d[u_m(i), v_m(j)] \quad (3)$$

where $d[u_m(i), v_m(j)]$ is the maximum distance of two templates i and j . $n_i^m(r)$ can be calculated under the criterion: the maximum distance is within r which is a predetermined threshold.

$$d[u_m(i), v_m(j)] \leq r, \quad 1 \leq j \leq N-m \quad (4)$$

The similarity probability of templates is calculated by the following equations:

$$U_i^m(r)(v||u) = \frac{n_i^m(r)}{(N-m)} \quad (5)$$

Subsequently, the average probability of similarity of template m is calculated as follows:

$$U^m(r)(v||u) = \frac{1}{(N-m)} \sum_{i=1}^{N-m} U_i^m(r)(v||u) \quad (6)$$

where $U^m(r)(v||u)$ is the degree of asynchrony between the two template spaces which are segmented with length m . Next, new template spaces T_x and T_y are created with different template length $m+1$, then the procedure of calculating probability of similarity is repeated to obtain the average probability of similarity $U^{m+1}(r)(v||u)$. Cross-SampEn is defined as:

$$CS_E(m, r, N) = -\ln \left\{ \frac{U^{m+1}(r)(v||u)}{U^m(r)(v||u)} \right\} \quad (7)$$

2.2 Composite Multiscale Entropy(CMSE)

Composite multiscale entropy was proposed by Wu et al. [18] to improve the accuracy of MSE. The k th coarse-grained time series for a scale factor of τ , $y_k^{(\tau)} = \{y_{k,1}^{(\tau)}, y_{k,2}^{(\tau)} \dots y_{k,p}^{(\tau)}\}$ is defined. Therefore, each coarse-grained time series can be obtained using the following equation:

$$y_{k,j}^{(\tau)} = \frac{1}{\tau} \sum_{i=(j-1)\tau+k}^{j\tau+k-1} x_i, \quad 1 \leq j \leq N/\tau, \quad 1 \leq k \leq \tau \quad (8)$$

The algorithm of CMSE produces total τ coarse-grained time series at the scale factor τ . Subsequently, SampEn for all coarse-grained time series are calculated and CMSE value is defined as the mean value of τ SampEn values as equation below:

$$CMSE(x, \tau, m, r) = \frac{1}{\tau} \sum_{k=1}^{\tau} SampEn(y_k^{(\tau)}, m, r) \quad (9)$$

2.3 Damage index (DI)

Inspired by a series of studies in biomedical using the area of MSE curve as an index for quantifying complexity, damage index (DI) was proposed for rapidly and efficiently diagnosing the damaged floor in the structure. Signals are viewed as having more complexity when the entropy values are higher than the other signal. For a structure with F floors, the CMSCE curves under the undamaged and damaged conditions can be respectively expressed as:

$$CMSCE_{\text{undamaged}} = \left\{ \begin{matrix} H_1 \\ H_2 \\ \vdots \\ H_F \end{matrix} \right\} \quad (10)$$

$$CMSCE_{\text{damaged}} = \left\{ \begin{matrix} D_1 \\ D_2 \\ \vdots \\ D_F \end{matrix} \right\} \quad (11)$$

Hence, the general expression of Cross-SampEn on the F floor is expressed as follows:

$$\{CS_E^{DF_1}, CS_E^{DF_2}, CS_E^{DF_3}, \dots, CS_E^{DF_r}\} \quad (12)$$

The DI is evaluated by calculating the difference between the area of CMSCE curves from scale 1 to τ . The damage index of a specific floor F can be expressed as follows:

$$DI_F = \sum_{q=1}^{\tau} (CS_E^{DF_q} - CS_E^{HF_q}) \quad (13)$$

A positive DI indicates that the floor is damaged, whereas a negative DI indicates no damage occurred on the floor.

3. Numerical Simulation

3.1 Results of the original velocity response

According to the previous researches, which discussed the performance of detection accuracy under different combinations of parameters, the parameters, such as the template length m , threshold r , and signal length N , were optimized as $4, 0.08 \times$

standard deviation (SD) of the time series, and 20000 points.

The case of a single-floor damage was illustrated in Figure 2a-b. The curve of the second floor jumped to the top among all curves. Furthermore, Figure 2a showed a large gap between the second-floor curve and the remaining curves; the increase of the complexity can be clearly observed due to the loss of story stiffness. From DI results shown in Figure 2b, a positive index indicated the damage occurred on the second floor.

Figure 3 illustrated the case of damage from the fourth to the seventh floor. The curves were significantly higher than those on the undamaged case at scale 5 to 15. The peak values of the damaged curves slightly shifted from scale 3 to 6, indicating the maximum complexity showed up after the coarse-graining procedure. The DI diagram for multistory damage was shown in Figure 3b. The positive indexes on the fourth to seventh floor can be easily identified as damage, oppositely, the undamaged curves remained the almost identical complexity, resulting in small negative or approaching zero values.

In the analysis without EEMD, a high accuracy of 93.9% was obtained. A precision of 92% was obtained since two floors were misclassified as damaged. Subsequently, a recall of 85.2% showed the high percentage for detecting the actual damage.

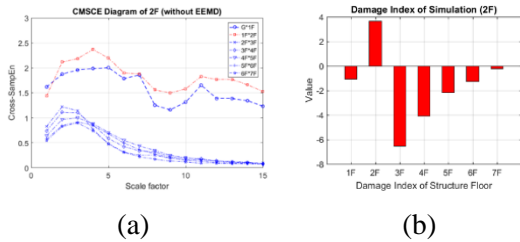


Fig. 2. (a) CMSCE diagram of damage on the second floor (2F); (b) Damage index of damage on the second floor.

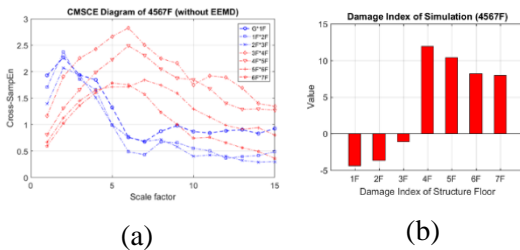


Fig. 3. (a) CMSCE diagram of damage on the second floor (4567F); (b) Damage index of damage on the fourth to the seventh floor.

3.2 Results of the extracted first mode time series (IMF4)

After EEMD procedure, the frequency analysis of each IMF had confirmed that the first mode was extracted in IMF4. Therefore, IMF4 was selected to

conduct CMSCE to evaluate the complexity between two signals. The damage assessment using IMF was examined to conclude the effectiveness of filtering the structural mode signal.

Figure 4 illustrated the CMSCE diagram for the second-floor damage. The entropy values of the second floor were gradually rise to the top at scale 10, so was the curve of the first floor. The complexity of all floors was nearly identical before the time scale 5; the curves diverged between long scales. From the result of DI, positive value on the second floor showed the damage occurred. Hence, the removal of bracings could result in the significant differences on the entropy curve.

Figure 5 illustrated the curves of the fourth to seventh floor gradually ascended and reached a plateau at the scale 10. However, the overall entropy values were almost identical. when Figure 5a was compared with the undamaged case, which revealed that the damage location was not be detected only depending on the first mode signal. The obscure change in the CMSCE diagram resulted in the failure on the DI results for diagnosing the damaged floor.

An accuracy of 77.6% was obtained in the analysis with EEMD. A precision of 66.7% was obtained, which was too conservative to precisely classify the healthy floor. A recall was only of 37% because the inconspicuous change of the complexity resulted in the mistake on detecting the damaged floors. The method without EEMD was thought as an appropriate method to validate the structural monitoring system for a scaled-down benchmark structure.

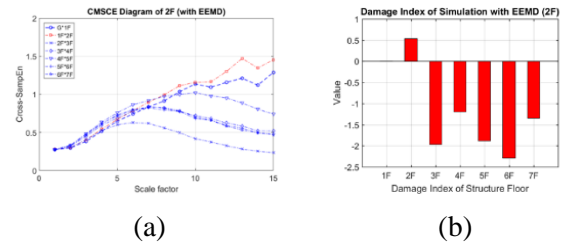


Fig. 4. (a) CMSCE diagram of damage on the second floor (2F) with EEMD; (b) Damage index of damage on the second floor with EEMD.

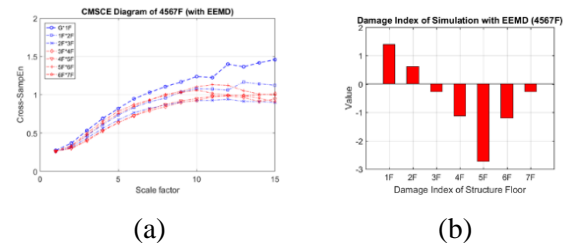


Fig. 5. (a) CMSCE diagram of damage from the fourth to the seventh floor (4567F) with EEMD; (b) Damage index of damage from the fourth to the seventh floor with EEMD.

4. Experimental Verification

In order to verify the practicality of the SHM system, an ambient vibration experiment for a scaled-down steel benchmark structure was conducted. In every damage case, the original velocity signals were analyzed to evaluate the complexity between floors. The parameters, such as the template length m , threshold r , and signal length N , were optimized as 4, $0.08 \times$ standard deviation (SD) of the time series, and 20000 points.

The CMSCE diagram for the second floor damage was illustrated in Figure 6. The rise of the second floor was evident, however the damage resulted in the rise of the first floor. Even the undefined entropies appeared from the scale 12, the DI result was not influenced because the range was decided from 1 to 10. From the DI results, the index on second floor was apparently higher than others, whereas the first and the fourth set revealed the outlier on the first floor.

The results for the damage on fourth to seventh floor was illustrated in Figure 7. A trend can be observed, which revealing the damaged curves climbed up rapidly at the scale 4. Besides the damaged curves, the curve for the first floor rose up at the scale 5 to 10, resulting in a small positive value on the DI. The DI diagram was presented in Figure 7b. Apparently, the damage on the fourth to seventh floor can be detected rapidly.

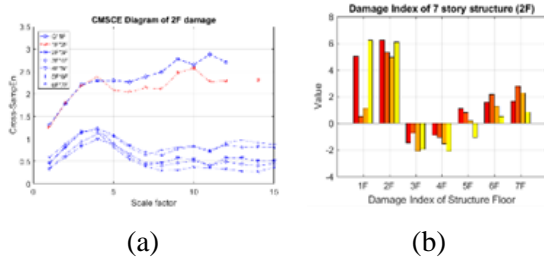


Figure 6. (a) The experimental CMSCE diagram of damage on the second floor (2F); (b) Damage index of damage on the second floor.

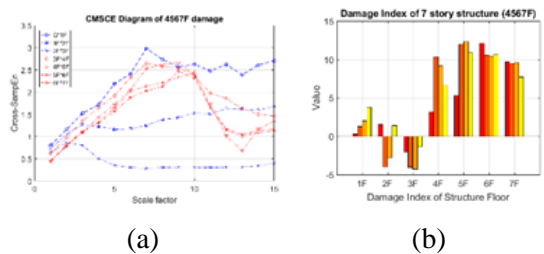


Figure 7. (a) The experimental CMSCE diagram of damage from the fourth to the seventh floor (4567F); (b) Damage index of damage from the fourth to the seventh floor..

Subsequently, the confusion matrix was utilized to evaluate the performance of the DI results. The accuracy of 78.6% was obtained. However, a

precision of 56.8% indicated the method was too conservative to classify the healthy floor. A recall of 92.6% showed that most of the floors that had been diagnosed as damaged were correctly classified as the damaged floors.

5. Conclusions

As the entropy analysis had been widely applied in the fields of biomedical, finance, and mechanical engineering, few studies utilized the entropy analysis in structural health monitoring for the entire structure. In this study, the feasibility of detecting damage location in the numerical model and the scaled-down specimen by CMSCE method was verified. In addition, the effectiveness of extracting the signals of the first mode by EEMD was examined in the numerical simulation. The experimental verification strongly indicated that the proposed entropy-based SHM system can reduce the outliers through the long-term monitoring. The reliability and viability of the proposed SHM system were examined through 15 damage cases in 5 categories representing several degrees of damage severity. The results of the numerical model without EEMD showed that 93.9% of the floors were correctly classified into the right categories, and 85.2% of the actual damaged floors can be correctly diagnosed. Moreover, the results of the scaled-down benchmark structure showed 78.6% of the floors were correctly classified into the right categories, and 92.6% of the actual damaged floors can be correctly diagnosed. The proposed entropy-based SHM system showed a great potential for the large and complex structures, even extending to the non-classical structure in the near future.

References

- T. K. Lin and A. G. Lainez, "Entropy-Based Structural Health Monitoring System for Damage Detection in Multi-Bay Three-Dimensional Structures," *Entropy*, vol. 20, p. 49, 2018.
- J. Maeck, M. M. Abdel Wahab, B. Peeters, G. De Roeck, J. De Visscher, W. P. De Wilde and J. M. Ndambi, "Damage identification in reinforced concrete structures by dynamic stiffness determination," *Engineering Structures*, vol. 22, no. 10, pp. 1339-1349, 2000.
- Z. H. Wu and N. E. Huang, "Ensemble empirical mode decomposition: a noise-assisted data analysis method," *Advances in Adaptive Data Analysis*, vol. 1, no. 1, pp. 1-41, 2009.
- M. Costa, A. L. Goldberger and C. K. Peng, "Multi-scale entropy analysis of biological signals," *Physical Review E*, vol. 71, pp. 021906-1-021906-18, 2005.

Post-earthquake Building Safety Assessment Using Crowdsourcing-based Interstory Drifts Measurement

Ting Y. Hsu^{123*}, Cheng Y. Liu^a, Yo M. Hsieh^{1b}, and Chi T. Weng^{1c} Pei Y. Lin^{3d}

許丁友^{123*} 劉政言^{1a} 謝佑明^{1b} 翁琪婷^{1c} 林沛暘^{1d}

Abstract

This study proposes to employ people's smartphones to assess a building's post-earthquake safety. The goal is to measure the maximum interstory drift ratios during earthquake excitation by using people's smartphones. Beacons inside the building are required to provide the location and relevant building information for the smartphones via Bluetooth. Wi-Fi Direct is employed between nearby smartphones to conduct peer-to-peer time synchronization and exchange the acceleration data measured. We propose an algorithm that can be used to align the orientations of nearby smartphones, and we studied the performance of the orientation alignment, interstory drift measurement, and damage level estimation numerically. The results presented in this study illustrate the potential of using people's smartphones with the proposed approach to record building motions during earthquakes and using that data to estimate a building's safety based on the interstory drift ratios measured.

Keyword: crowdsourcing, smartphones, interstory drifts, post-earthquake building safety, orientation alignment, Wi-Fi Direct.

Introduction

Among many damage parameters, the interstory drift ratio (IDR) is widely accepted as a reliable indicator for evaluating the exceedance of selected limit states and the corresponding potential for building damage. Although many studies have investigated the possibility of using a low-cost sensor network, it is still challenging to implement these networks widely because the total cost of sensors, human labor, and system maintenance is still high. If the numerous private smartphones distributed in buildings can be used to collect a building's seismic vibration response, then this could overcome the substantial challenge of deploying a costly structural health monitoring (SHM) system in buildings and provide a way to assess a building's post-earthquake safety with very low hardware and maintenance costs. However, to use private smartphones to estimate IDR, information on

the smartphones' orientation and location is required and acceleration signals from different smartphones must be synchronized. In this study, we explore the possibility of crowdsourcing using smartphones to estimate IDR and assess post-earthquake building safety. We propose an algorithm to align smartphones' orientation based on the vibration signals measured. We also propose solutions to synchronize the smartphones and identify their locations. In the next section, we explain the methodology with which smartphones are used to measure IDRs to estimate a building's safety.

Methodology

To explain the procedures involved in using smartphones to perform post-earthquake building safety assessments, a flow chart is shown in Figure 1. The first two procedures have already been developed

¹ Department of Civil and Construction Engineering, National Taiwan University of Science and Technology, Taipei 10607, Taiwan

² Taiwan Building Technology Center, National Taiwan University of Science and Technology, Taipei 10607, Taiwan

³ National Center for Research on Earthquake Engineering, Taipei 106219, Taiwan

*Corresponding author, Associate Professor, E-mail: tyhsu@ntust.edu.tw

^a Master. Student, E-mail: oulivedd@gmail.com

^b Ph.D. Associate Professor, E-mail: ymhsieh@ntust.edu.tw

^c Research Assistant, E-mail: m10305502@gapps.ntust.edu.tw

^d Researcher, E-mail: pylin@ncree.narl.org.tw

and utilized in earthquake early-warning systems (Hsu and Nieh 2020), so only a brief introduction of these two procedures is provided here. In this study, we investigated whether smartphones in a stable state could be harnessed for IDR measurement using the smartphone application developed in this study. As stated above, information on the smartphones' orientations and locations is required and the acceleration signals from different smartphones should be synchronized.

The first procedure in the overall process consists of detecting the occurrence of an earthquake event. To that end, the smartphones are triggered and de-triggered based on the short-term average/long-term average (STA/LTA) algorithm. The second procedure consists of distinguishing whether the recorded acceleration signals are due to an earthquake event.

If an event is classified as an earthquake event, then the third procedure is performed. The procedure consists of obtaining the necessary building information and the smartphones' locations, which are provided by the pre-installed Bluetooth beacons in the building. In this study, we took advantage of Bluetooth beacons to provide information about the beacons' location, structural type, number of stories, story height, and seismic design level for the smartphone application.

The fourth procedure consists of establishing a wireless connection between nearby smartphones

using Wi-Fi Direct technology. Once the wireless link is established, two smartphones can communicate with each other at typical Wi-Fi speed.

The fifth procedure consists of synchronizing the smartphones. Although each smartphone has a built-in

clock, the time on the clock may not be sufficiently accurate because of drift; the smartphone may not update its clock from Internet time servers regularly. We employed the NTP mechanism through a Wi-Fi Direct link to synchronize the time of the acceleration signals recorded.

The sixth procedure consists of performing orientation alignment of the smartphones. Following this, the damage level of the building can be estimated by directly calculating the IDR straightforwardly.

In this study, we propose the least Fourier spectrum difference (LFSD) method to address orientation alignment in the frequency domain. We assumed that the Fourier spectra of the acceleration data measured in the two horizontal components are distinct; hence, the pattern of the Fourier spectra will change as the smartphones' orientations change. When the orientations of two smartphones on two adjacent floors are identical, the difference between their Fourier spectra $\Delta U_k(\omega_j, \theta)$ in both horizontal components should be very small. The difference is defined as:

$$\begin{aligned} \Delta U_k^x(\omega_j, \theta) &= |U_{k+1}^x(\omega_j, \theta) - U_k^x(\omega_j)| \\ \Delta U_k^y(\omega_j, \theta) &= |U_{k+1}^y(\omega_j, \theta) - U_k^y(\omega_j)| \end{aligned} \quad (1)$$

in which U_{k+1}^x represents the Fourier spectrum on the $k+1^{\text{th}}$ floor in the smartphone's local x -direction and ω_j represents the j^{th} discrete frequency. The orientation of the smartphone on the $k+1^{\text{th}}$ floor, θ , is defined according to the orientation of the smartphone on the k^{th} floor. It will rotate at an interval of $\Delta\theta$ and the rotated Fourier spectra of the $k+1^{\text{th}}$ floor are calculated as:

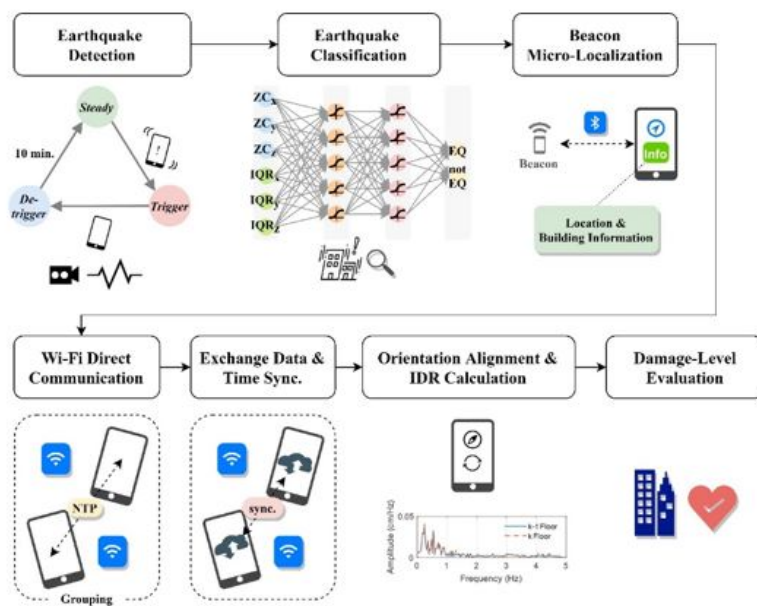


Fig. 1 The flow chart of the procedures using crowds' smartphones to perform post-earthquake building safety assessment.

$$\begin{aligned}
U_{k+1}^x(\omega_j, \theta) &= U_{k+1}^x(\omega_j) \cos \theta + U_{k+1}^y(\omega_j) \sin \theta \\
U_{k+1}^y(\omega_j, \theta) &= -U_{k+1}^x(\omega_j) \sin \theta + U_{k+1}^y(\omega_j) \cos \theta \quad (2)
\end{aligned}$$

The summation of the Fourier spectra difference $\Delta U_k(\theta)$ is calculated as:

$$\Delta U_k(\theta) = \sum_{j=1}^M (\Delta U_k^x(\omega_j, \theta) + \Delta U_k^y(\omega_j, \theta)) \quad (3)$$

in which M represents the total number of discrete frequencies considered. The orientation with the smallest value of $\Delta U_k(\theta)$ was selected as the best estimation of the orientation, denoted as θ_B . As a result, the interstory drifts in both horizontal directions between the k^{th} and $k+1^{\text{th}}$ floor were calculated using the orientation selected. The maximum value of the Euclidean norm of the interstory drifts in both horizontal directions during an earthquake excitation were calculated and used to determine the damage level of the story.

Experimental Study

A scaled, four-story steel building structure designed and constructed at the National Center for Research on Earthquake Engineering (NCREE) in Taiwan was used to experimentally test the proposed post-earthquake building safety assessment using smartphones. Each story of the building was 4.0 m wide by 2.0 m deep by 2.0 m high. The additional mass of each floor was approximately 388.1 kg/m² and the total mass of the building was 24,509 kg. Each beam and column was made of A572Gr50 steel and had H-shaped cross-sections of 125×60×6×8 mm and 150×150×7×10 mm, respectively. The column's weak axis was along the global X-direction of the building. The fundamental natural frequencies of the building were 0.77 and 0.86 Hz.

There were six stories in the steel building structure in the initial tests. However, a severe rocking interaction between the shaking table and the structure was observed, even during small excitations. To allow the structural responses to cover a larger range of IDRs and avoid the rocking interaction simultaneously, the number of stories was reduced to four, and the dimensions of the bottom of the columns on the first story were reduced to 150×50×7×10 mm. The fundamental natural frequencies were 1.17 and 1.88 Hz along the X- and Y-directions, respectively.

Five different earthquakes with scales of 10%, 20%, and 30% were used to excite the structure were used to excite the structure. However, because of safety considerations, we did not consider the 30% scale for the Kobe earthquake. The 20% Kobe earthquake already induced a large nonlinear interstory drift and the larger 30% Kobe earthquake may have caused the

structure to collapse. In total, fourteen earthquakes were excited during the shaking-table tests and their PGAs were between 28 and 199 cm/s².

Five Sharp Aquos V smartphones were mounted on each floor. The typical arrangement of the orientation of the smartphones is shown on the fourth floor. The measured accelerations from the smartphones were very close to those measured by the accelerometers. During the tests, the smartphones were connected to each other using Wi-Fi Direct. Thus, the IDRs were calculated using the smartphones on each story. Although the maximum acceleration response of lower stories was smaller, the IDR of lower stories was much larger, especially the first story.

In addition to the smartphones, three LVDTs and three accelerometers were installed on each floor of the building specimen, as shown in Figure 2. The LVDTs and accelerometers' signals were digitized at 200 Hz, while the smartphones' sampling rate was 50 Hz. Five Bluetooth low-energy beacons based on Texas Instruments CC2541 were mounted under/on the floors. The smartphones can detect the Bluetooth signals of several nearby beacons and the beacon with the largest received signal strength indicator (RSSI) was selected automatically. The selected beacon can then provide information on the story height and location.

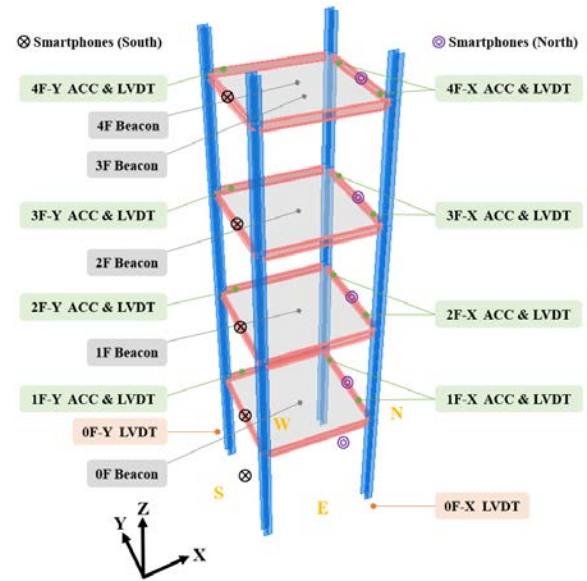


Fig. 2 The scaled, four-story steel building structure.

In this study, we studied the performance of the proposed approach in 106 cases during the earthquake excitations. Because the actual orientations of the smartphones on each floor were known, the errors in their estimated orientations, denoted as E_0 , using the proposed orientation alignment approach, *i.e.*, the LFSD method, were calculated, which indicates that more than half of the E_0 values were within $\pm 2^\circ$, and some of the outliers reached 9° and -11° . The root

mean square error (RMSE) of E_{θ} was 4.260.

The interstory drifts during the earthquakes can be calculated using the LVDTs, and the maximum drifts that the LVDTs measured were used as the reference. We then calculated the errors of the maximum IDRs, denoted as E_{IDR} , for the 106 cases during the earthquake excitations. Approximately half of them were within $\pm 0.05\%$, and some of the outliers reached approximately 0.3% and -0.2% . The RMSE of E_{IDR} was 0.091%.

With respect to the estimated damage levels of the 106 cases during the earthquake excitations, two cases in which the damage level was extensive were underestimated. It was confirmed that, even if the orientation alignment was perfect, the damage levels in these two cases—the smartphones on the north and south sides of the first story during the 20% Kobe earthquake—were still underestimated. The maximum IDR that the LVDT measured was 2.14%, while the IDRs that the smartphones measured were 1.96%, an under-estimation of approximately 0.17%. One of the reasons for these errors could be that the low-pass filter filtered out the nonlinear low-frequency drifts after double integration of the acceleration signals. Other reasons could be errors in synchronizing the time and the discrete measurement using different sampling rates between the smartphones and the LVDTs. Nevertheless, the damage level estimation's accuracy was 92.0%, which supported the feasibility of the proposed approach.

The amplitudes of earthquake excitations seem to affect the RMSEs of the estimated orientations only slightly, it seems that the RMSEs of the estimated IDR increased and the accuracy of the damage level estimation decreased as the amplitudes of the earthquake excitations increased. These results imply that some nonlinear response could occur during larger earthquake excitations, and that some of these signals could be filtered out and hence induce larger errors in IDR estimation.

In general, the errors in the smartphones' orientations were much larger than those in the numerical study (not included in this brief paper), which could be caused primarily by the extraordinarily large background excitation. As a result, the performance of interstory drift measurement and damage level estimation were affected.

Conclusions

This study proposed to use people's smartphones that are distributed in a building to estimate a building's damage level during earthquake excitation based on the estimated maximum IDRs. Originally, the information on the smartphones' orientations and

locations was not known, and the acceleration signals of different smartphones measured were not synchronized. In this study, the LFSD method was proposed to align the smartphones' orientations based on the vibration signals measured. Nearby beacons used Bluetooth to broadcast the locations and relevant building information. Wi-Fi Direct was employed to identify and connect nearby smartphones and exchange data between them; hence, the smartphones could be synchronized based on the NTP mechanism and their orientation could be aligned using the proposed LFSD method.

The necessary algorithms were embedded in the smartphone applications and the proposed approach was verified using shaking table tests of a scaled, four-story steel building. The time difference between the smartphones when they were synchronized using the NTP algorithm via Wi-Fi Direct was 0.00458 s on average, approximately one-quarter of the acceleration records' sampling interval, *i.e.*, 0.02 s. Although the error in the estimated best orientation during the experimental tests in the presence of extraordinarily large background excitation could reach 11° at maximum, the RMSE of the E_{IDR} was smaller than 0.1%. As a result, the accuracy of the damage level estimation can reach 92%. Thus, the numerical and experimental results illustrate the potential of using people's smartphones to evaluate a building's post-earthquake safety using the proposed approach. Since large earthquakes do not often occur, in order to validate the proposed approach, it may be necessary to conduct an experiment in a tall building during typhoon season in the future.

References

- Hsu, T.Y., Nieh, C.P. (2020), On-site Earthquake Early Warning Using Smartphones", *Sensors*, 20, 2928.

Modal Property Extraction Based on Frequency-Domain Stochastic Subspace Identification Using Out-of-Plane Video Motion

Chia-Ming Chang¹, Jau-Yu Chou², and Meng-Huang Gu³

張家銘¹、周肇昱²、古孟晃³

Abstract

Understanding the dynamic behavior of as-built structures is important because structural condition can often be inferred from dynamic response changes. To this end, modal properties such as natural frequencies, damping ratios, and mode shapes can be extracted from acceleration measurements. Associated installations require sensors, cabling, and data acquisition systems that can be expensive and time-consuming. Alternatively, proposed computer vision-based approaches offer non-contact measurements and substantial cost savings. However, such approaches usually only focus on the structural responses within the plane of the image. For complex structures that possess asymmetries, out-of-plane behavior is critical to understanding their dynamic responses. Determining the dynamic response of the entire structure requires multiple cameras and can be computationally demanding. In this study, imagery from a commercially available stereo camera is combined with a multi-level image pyramid approach and frequency-domain stochastic subspace identification (SSI) to extract out-of-plane modal properties. The advantages and limitations of the proposed approach are illustrated numerically for a continuous beam. Experimental validation is then performed with a three-story model building using an Intel® RealSense™ D415 depth camera. The results demonstrate that the proposed approach can give an accurate picture of the dynamic characteristics of a structure, offering the potential for effective long-term structural health monitoring.

Keywords: Structural health monitoring, image pyramid, out-of-plane motion capture, frequency-domain stochastic subspace identification

Introduction

Conventional structural health monitoring systems usually require surface-contact sensors to record structural responses. For example, accelerometers are commonly installed on columns or beams to measure dynamic responses. However, sensor deployment is often costly and labor-intensive due to the complexity and size of typical civil structures. Additionally, when testing models in the laboratory, the self-weight of installed sensors may distort the associated responses, resulting in a misrepresentation of dynamic behavior (Chen et al., 2015). Alternatively, vision-based techniques can be a good option for acquiring the vibrations of structural

components (Yoon et al., 2016).

Commercially available cameras today are capable of shooting video with both high resolution and high frame rates, which enables the extraction of precise information about a structure's dynamic response (Spencer et al., 2019). For example, Feng et al. (2015) and Ye et al. (2016) proposed a motion-tracking method employing markers whose movements were recorded with a high-speed camera. This approach allows a limited number of regions of interest to be tracked. Digital image correlation (DIC) is a popular method for measuring structural deformation at all points in a video image (i.e., full-field measurements). DIC determines structural movements by estimating blocks of pixels from a

¹ Associate Professor, National Taiwan University

² Ph.D. Candidate, National Taiwan University

³ Associate Researcher, National Center for Research on Earthquake Engineering.

speckled surface (Keating et al., 1975; Castellini et al., 2017). To date, these approaches require attaching markers to surfaces to determine dynamic responses, which could be difficult to implement on full-scale structures. Instead, Yoon et al. (2016) developed a target-free approach for vision-based structural system identification, and Xu et al. (2018) proposed a non-contact vision-based system for monitoring the multipoint displacement of a cable-stayed footbridge. Wadhwa et al. (2013) proposed a phase-based motion structural component magnification method for modal response extraction. In this method, motions in a specific frequency band can be filtered and magnified through manipulating the local phase difference of each pixel, and full-field modal responses of a structure are then extracted. Chen et al. (2015) further applied the phase-based motion magnification method to extract the modal properties of a pipe and continuous beam. Numerous video-based motion extraction algorithms have been proposed in recent years. Still, most of these algorithms only focus on responses within the image plane of the camera.

The objective of this study is to develop an out-of-plane modal property extraction method based on frequency-domain stochastic subspace identification (SSI) using stereophotogrammetry. This method first uses an image pyramid to decompose and compress each frame into spatial sub-bands. After decomposing each frame, the image intensity time history, which represents the depth information of each pixel, can be employed for system identification. In this method, frequency-domain SSI is applied. The identified mode shapes from each pyramid level can then be reconstructed using an inverse image pyramid algorithm. Next, a correction filter is developed based on the linear transformation between the input frame when the structure is still and the reconstructed image from the decomposition of that frame. Finally, the modal properties (natural frequency and mode shape) can be identified.

In this study, a numerical example using a continuous cantilever beam is developed to investigate the performance of the proposed approach. An experiment based on a three-story building structure is then conducted using an Intel® RealSense™ D415 depth camera for verification. The proposed approach was demonstrated to provide reliable identification of natural frequencies and full-field, detailed mode shapes from out-of-plane motion videos. Moreover, modal property identification can be expeditiously performed using multi-level image pyramid reconstruction.

Out-of-Plane Modal Property Extraction

Fig. 1 demonstrates the flowchart for the out-of-plane modal property extraction method. This method first utilizes the image pyramid technique to

decompose each frame into numerous levels with respect to different image resolutions. In real-world images, object information is usually contained in low-spatial frequency regions of a 2D Fourier space, while only contours and lines are preserved in high-spatial frequency regions (Dogra and Bhalla, 2014). Thus, the highest level of the pyramid (lowest resolution) is capable of identifying the modal properties of a structure. However, using only the highest level may cause errors due to the missing high-spatial frequency portions of the image, and further corrections are required for accurate mode shape determination.

After image decomposition, the intensity time histories are extracted from each pixel and exploited by the frequency-domain SSI. By repeating the identification procedure at each level of the image pyramid, mode shapes can be reconstructed at the input image resolution. In this study, using a correction filter is suggested so a reconstruction with fewer pyramid levels can be modified to the input image resolution even with slight errors. Eventually, the proposed approach is capable of identifying modal properties such as natural frequency and mode shape.

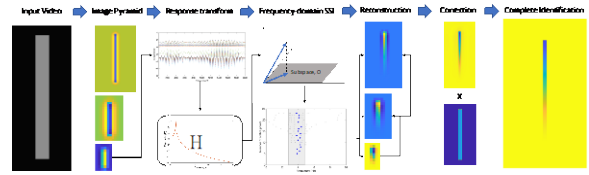


Fig. 1. Flowchart of the proposed out-of-plane identification method

The image pyramid method recursively decomposes the image into numerous spatial sub-bands using low-pass and high-pass filters. In this study, a low-pass filter H_L and high-pass filter H_H should satisfy the following criteria:

$$\begin{aligned} |H_L(\omega)|^2 + |H_H(\omega)|^2 &= 1 \\ |H_L(\omega)| &= 0 \text{ for } |\omega| > \pi/2 \end{aligned} \quad (1)$$

where the second criterion is utilized to prevent aliasing during the downsampling procedure. A single sub-band intensity, denoted \mathbf{y} , can be used to construct the following frequency-domain Hankel matrix:

$$\mathcal{H} = \begin{bmatrix} \mathbf{Y}[0] & \mathbf{Y}[1] & \dots & \mathbf{Y}[p] \\ W_p^{-1}\mathbf{Y}[0] & W_p^{-1}\mathbf{Y}[1] & \dots & W_p^{-1}\mathbf{Y}[p] \\ \vdots & \vdots & \ddots & \vdots \\ W_p^{-(N-p)}\mathbf{Y}[0] & W_p^{-(N-p)}\mathbf{Y}[1] & \dots & W_p^{-(N-p)}\mathbf{Y}[p] \end{bmatrix} \quad (2)$$

where \mathcal{H} denotes the frequency-domain Hankel matrix, \mathbf{Y} is the discrete Fourier transformation at a specific frequency point, and W_p^n is the phase shift while converting time-series response to frequency-domain, which will not affect the identification result. The modal properties can be identified by projecting

the Hankel matrix to a subspace and are determined using eigen analysis. To reconstruct the mode shapes of multiple sub-bands, a correction factor, C , is given by

$$C_{xy} = \mathbf{I}_{xy} / \mathbf{I}_{rec,xy} \quad (3)$$

where \mathbf{I}_{xy} is the input image at location (x,y) and \mathbf{I}_{rec} is the reconstructed image based on multiple levels of the image pyramid.

Results

In this study, a continuous cantilever beam was designed for numerical study. The flexural rigidity was $EI = 10^{12} \text{ N} - \text{m}^2$, the mass was $\rho A = 1000 \text{ kg/m}$, and the height was $\ell = 140 \text{ m}$. The modal damping was 0.01 for each mode. For multi-level image pyramid reconstruction, Fig. 2a represents the identified shape of the second mode using different image pyramid methods. Note that the correction factors used are based on different image pyramid techniques and were separately calculated. All methods reconstructed the image with a level 5 pyramid and utilized frequency-domain SSI. The proposed approach shows better performance compared to results using a Laplacian pyramid (Burt and Adelson, 1983) or Wavelet pyramid (Pommer and Uhl, 2003), shown in Fig. 2b.

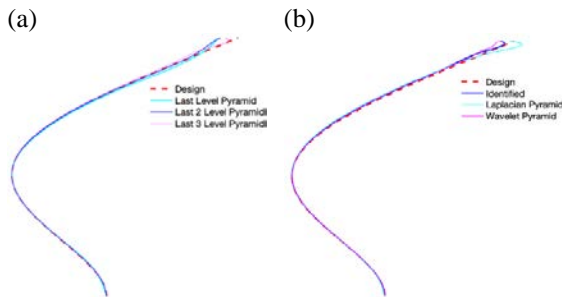


Fig. 2. Identification results for a) different levels of image pyramid reconstruction and b) different image pyramid methods

A three-story frame building was used to experimentally evaluate the proposed approach in the Smart Structures and Technology Laboratory (SSTL) at the University of Illinois at Urbana-Champaign. The out-of-plane vibrational responses were captured with the Intel® RealSense™ D415 depth camera. Fig. 3 depicts the specimen and depth image.

Fig. 4a shows the mode shapes from the reconstruction of the top two pyramid levels after correction. Because floors with mass blocks can introduce rigidity to the structure, differentiated mode shapes between the proposed method and acceleration-based results were obtained. To further verify our hypothesis, a three-story structure considering floor rigidity was simulated. Each element

consisted of 31 nodes, and the stiffness of the slabs were designed to be much higher than the columns. As shown in Fig. 4b, the mode shapes of the numerical model are similar to the ones based on the proposed approach, indicating that the proposed approach performs well at identifying continuous structural mode shapes and demonstrating how much information has been neglected while using discrete sensors for identification. However, due to the difference between the model and the structure, variations can be observed in the figure, resulting in mismatches at certain pixel points. Moreover, because the numerical model assumes that the slab is a single node, rather than a line, the effective area of mass rigidity will be different.

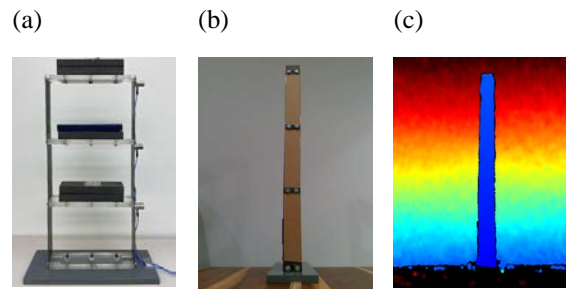


Fig. 3. a) Sensor locations, b) RGB camera, and c) disparity map in respect to depth map using RealSense Camera

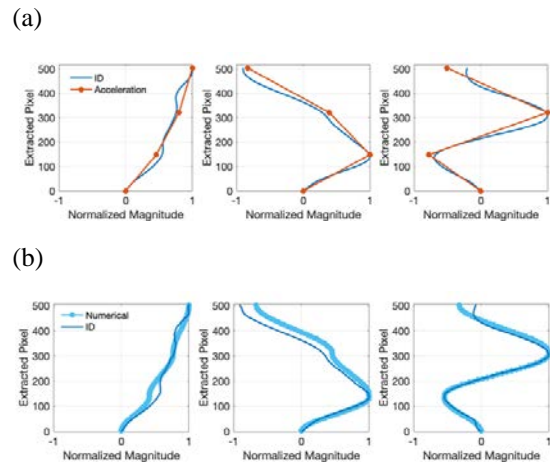


Fig. 4. a) Two-level pyramid reconstruction compared to acceleration-based results. b) Numerical model considering lateral and rotational stiffness.

Conclusions

In this study, we propose an innovative modal property extraction method for out-of-plane image motion measurements using an image pyramid and frequency-domain SSI. The out-of-plane response was captured with a dual-camera system. The depth information was then determined based on stereo vision algorithms. After recording structural motions, each frame was decomposed using an image pyramid

to filter and compress the structural response. Frequency-domain SSI was then applied to the magnitude of each effective pixel at each pyramid level, and the modal properties were extracted. Finally, to maintain the quality of the mode shapes, identifications at each pyramid level were utilized for image reconstruction.

A numerical study using a continuous beam was developed to evaluate the effectiveness of the proposed approach. With the image pyramid correction, the reconstructed mode shapes were consistent with the designed ones, indicating a high accuracy. Moreover, different types of image pyramids (Laplacian and Wavelet) were used and compared to our proposed approach. Our approach was capable of identifying mode shapes with the lowest error.

During experimental evaluation, a three-story model building was used to examine performance. The Intel® RealSense™ D415 depth camera was used to capture the depth responses of the structure. As reflected in the identification results, using two levels of the image pyramid for reconstruction would introduce errors. These errors were derived from the mass rigidity after comparing with the simulation. When more levels of the image pyramid are employed, more continuous details can be obtained. Overall, the proposed approach was able to identify near-continuous mode shapes from out-of-plane responses. A better picture of continuous out-of-plane mode shapes of structures can be derived using multi-level image pyramid reconstruction.

References

- Burt, P. and Adelson, E. (1983), "The Laplacian pyramid as a compact image code," *IEEE Transactions on Communications*, 31(4), 532-540.
- Chen, J.G., Wadhwa, N., Cha, Y.J., Durand, F., Freeman, W.T., and Buyukozturk, O. (2015), "Modal identification of simple structures with high-speed video using motion magnification," *Journal of Sound and Vibration*, 345, 58-71.
- Castellini, P., Chiariotti, P., Martarelli, M., Zappa, E., and Lavetelli, A. (2017), "Experimental modal analysis on vibration data measured by digital image correlation," *Conference Proceedings of the Society for Experimental Mechanics*.
- Dogra, A. and Bhalla, P. (2014), "Image sharpening by Gaussian and Butterworth high pass filter," *Biomedical and Pharmacology Journal*, 7(2), 707-713.
- Feng, D., Feng, M.Q., Ozer, E., and Fukuda, Y. (2015), "A vision-based sensor for noncontact structural displacement measurement," *Sensors*, 15, 16557-16575.
- Keating, M.A., Wolf, P.R., and Scarpace, F.L. (1975), "An improved method of digital image correlation," *Photogramm Engineering and Remote Sensing*, 41(8), 993-1002.
- Pommer, A. and Uhl, A. (2003), "Selective encryption of wavelet-packet encoded image data: efficiency and security," *Multimedia Systems*, 9, 279-287.
- Spencer, Jr., B.F., Hoskere, V., and Narazaki, Y. (2019), "Advances in computer vision-based civil infrastructure inspection and monitoring," *Engineering*, 5, 199-222.
- Wadhwa, N., Rubinstein, M., Durand, F., and Freeman, W. (2013), "Phase-based video motion processing," *ACM Transactions on Graphics*, 32(4).
- Xu, Y., Brownjohn, J., and Kong, D. (2018), "A non-contact vision-based system for multipoint displacement monitoring in a cable-stayed footbridge," *Structural Control and Health Monitoring*, 25, e2155.
- Yoon, H., Elanwar, H., Choi, H., Fard, G., and Spencer, Jr., B.F. (2016), "Target-free approach for vision-based structural system identification using consumer-grade cameras," *Structural Control and Health Monitoring*.
- Ye, X.W., Dong, C.Z., and Liu, T. (2016), "A review of machine vision-based structural health monitoring: methodologies and applications," *Journal of Sensors*, 2016, 7103039.

Machine-Learning Based Optimal Active Seismic Control for Earthquake-Excited Building Structures

Pei-Ching Chen¹ and Kai-Yi Chien²

陳沛清¹、簡楷益²

Abstract

In recent years, Linear-Quadratic Regulator (LQR) has been recognized as one of the most effective methods for structural vibration control which minimizes a cost function formulated by weighted states and control inputs. Optimal control requires structural states which may not be measurable in real application; therefore, state estimation is essential which inevitably takes additional computation time. However, time delay and state estimate error could affect the control performance. In this study, a multilayer perceptron (MLP) model and an autoregressive with exogenous inputs (ARX) model in machine learning are applied to learn the control force generated from an LQR with weighting matrices optimized by applying symbiotic organisms search algorithm. A shear building is adopted as a benchmark model for training and validation of the MLP and ARX models. In the numerical simulation, the dynamic analysis of the structure subjected to earthquakes is carried out with 8 sets of seismic accelerations to verify the performance of the controller. The results show that the neural network models are able to emulate the LQR control force from the acceleration response directly, reducing the necessity of a state estimator to achieve effective control performance in practice.

Keywords: machine learning; multilayer perceptron; autoregressive neural network; optimal control; active mass damper; seismic performance; shake table testing

Introduction

Structural control systems have been widely used to suppress the vibration response of structures subjected to dynamic loads (especially seismic excitations). Modern structural control systems can be divided into passive control, active control, semi-active control, and hybrid control systems according to the characteristics of control devices and approaches [1]. Among the four strategies, Active control can adapt to the structural response during dynamic loads and then take control actions on the structure. In other words, active control reduces or eliminates structural damage after strikes of earthquakes by adjusting structural response within linear behavior. For the realization of active control, two critical issues must be considered. The first issue is a structural control algorithm that is robust and clear enough to compute the control force to be imposed on the structure in real time. Another problem is the actuator controller, which can apply the required control force to the structure with acceptable real-time tracking error.

LQR is considered as one of the most effective controllers in structural active control; however, it requires structural states for feedback, which may not be measurable in practical applications. As a result, a state observer or estimator is necessary, which may increase the amount of calculation and cause a time delay in the control loop. An estimator that is not well-designed could reduce the control performance or even lead to inferior structural response. Meanwhile, control performance of LQR depends on the selection of weighting matrices in the cost function. Therefore, the objectives of this study are (1) to optimize the weighting matrices of LQR that lead to effective control performance; (2) to replace the LQR with a controller that intends to emulate the control performance of the LQR without a state estimator; and (3) to demonstrate the control performance of the LQR and the emulated ones through numerical and experimental approaches. In this study, a machine learning-based control model is proposed and trained to simulate LQR by applying a weighted matrix optimized by a novel and simple metaheuristic

¹ Associate professor, Department of Civil and Construction Engineering, National Taiwan University of Science

² Graduate student, Department of Civil and Construction Engineering, National Taiwan University of Science

algorithm called Symbiotic Organisms Search (SOS).

Modal LQR

Consider a N-degrees-of-freedom building with an active mass damper (AMD) at the top, the state-space formulation of the building in modal space can be represented as: The state-space formulation of the building in modal space can be represented as:

$$\begin{aligned} \dot{\mathbf{z}}_m(t) &= \mathbf{A}_m \mathbf{z}_m(t) + \mathbf{B}_m u(t) + \mathbf{E}_m \ddot{\mathbf{x}}_g(t) \\ \mathbf{y}_m(t) &= \mathbf{C}_m \mathbf{z}_m(t) + \mathbf{D}_m u(t) \end{aligned} \quad (1)$$

where $\dot{\mathbf{z}}_m(t) = [\mathbf{q}(t) \quad \dot{\mathbf{q}}(t)]^T$ defines the modal states. Accordingly, the system matrix \mathbf{A}_m , the control force distribution matrix \mathbf{B}_m , and the disturbance location matrix \mathbf{E}_m in modal space. On the other hand, the output $\mathbf{y}_m(t)$ is selected as the modal absolute acceleration of each mode.

As mentioned previously, LQR intends to minimize a cost function related to the states and control inputs with weighting matrices \mathbf{Q} and R determined by users. In the modal LQR design, the modal absolute acceleration is taken as the state to be regulated. Therefore, the quadratic cost function of LQR for structural control is defined as:

$$J = \int_0^{\infty} (\mathbf{y}_m^T \mathbf{Q} \mathbf{y}_m + u^T R u) dt \quad (2)$$

The dimension of the weighting matrix \mathbf{Q} depends on the number of selected modes to be controlled. The weighting R is a scalar since there is merely one control force imposed on the top of the structure. The state feedback gain matrix \mathbf{K}_m can be obtained by solving the Riccati equation:

$$\mathbf{K}_m = R^{-1} \mathbf{B}_m^T \mathbf{P} \quad (3)$$

The control force for modal LQR control becomes $u(t) = -\mathbf{K}_m \mathbf{z}_m(t)$. In order to convert the control input from the modal space to the configuration space, the gain matrix \mathbf{K}_m needs to be converted into \mathbf{K}_g through:

$$\mathbf{K}_g = \mathbf{K}_m \begin{bmatrix} \Phi^{-1} & 0 \\ 0 & \Phi^{-1} \end{bmatrix} \quad (4)$$

Corresponding to these equation and conversion, the state feedback gain matrix \mathbf{K}_g can be used to calculate the control force for the structure by $u(t) = -\mathbf{K}_g \mathbf{z}(t)$ where \mathbf{z} is the states in the configuration space which contains the displacement and velocity vectors, i.e., $\dot{\mathbf{z}}(t) = [\mathbf{x}(t) \quad \dot{\mathbf{x}}(t)]^T$.

Neural Network Models

Multilayer perceptron (MLP) is a supervised

learning algorithm that learns a function from inputs to outputs. Generally, an MLP model is composed of an input layer, an arbitrary number of hidden layers, and an output layer as depicted in Figure 1. In this study, the input of the MLP model is the structural acceleration responses at each floor with previous multiple time steps while the output is the control force of the AMD.

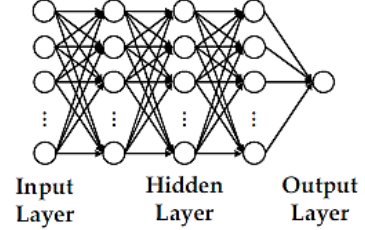


Figure 1. Illustration of a multilayer perceptron model.

An autoregressive with exogenous inputs (ARX) model, which is a recurrent dynamic neural network has been used in various applications of time-series modeling. In the ARX architecture as shown in Figure 2 In this study, the input of the ARX model is the structural acceleration responses at each floor with previous multiple time steps and the control force at the previous step. The output is the control force of the AMD at the predicting step. Since an ARX model requires output as input, it is considered as a recurrent neural network model.

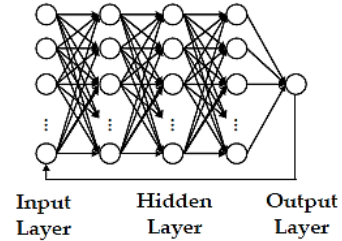


Figure 2. Illustration of an autoregressive with exogenous inputs model.

Experimental Validation

The machine learning based optimal control performance was evaluated by conducting shake table testing in the small-scale structural laboratory located in National Center for Research on Earthquake Engineering (NCREE). Figure 3 shows the experimental setup. A single-degree-of-freedom (SDOF) shear building specimen made of aluminum alloy was designed and fabricated for experimental validation. The AMD installed on the top of specimen was composed of an AC motor, a guide screw, and a mass block. Three accelerometers were installed on the bottom rigid plate connected to the shake table, the roof of specimen, and the mass block to measure the absolute acceleration. The control force of AMD was

obtained by multiplying the mass of the mass block by the absolute acceleration measured from the accelerometer. A linear-position sensor was installed between the roof and the platen of shake table to measure the relative displacement of the specimen.

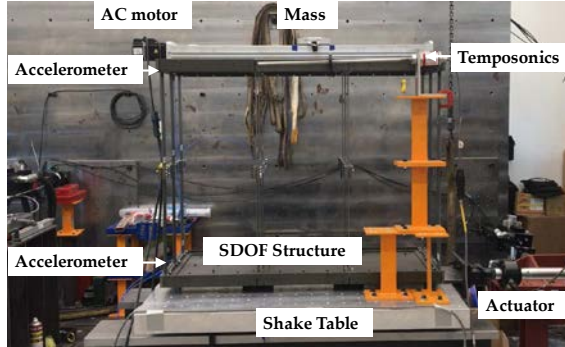


Figure 3. Experimental setup

In order to implement the controller of AMD, a Micro-Box 2000 was adopted which provided multi-function platform for rapid control prototyping applications. Three controllers were designed and implemented including the LQR-SOS, MLP-150, and ARX. The LQR-SOS required structural states for feedback control which were not measurable during the tests. As a result, a Kalman filter was essential to estimate the structural states for feedback control. In addition, the MLP and ARX took the measured acceleration as the input to calculate the control force. The hardware and software layout for the experimental validation is depicted in Figure 4.

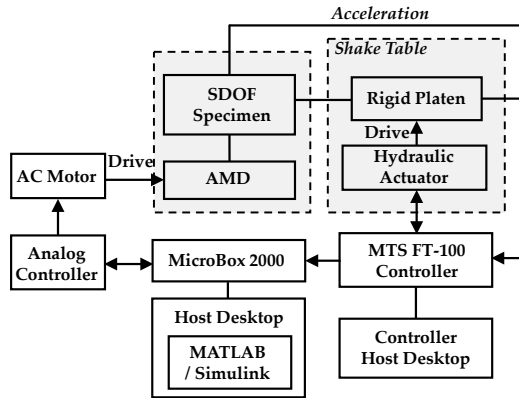


Figure 4. Hardware and software layout

Prior to LQR design for AMD, it's necessary to systematically identify a SDOF shear building specimen used as the structure to be controlled in the laboratory. The natural frequency and damping ratio of the identified model are 0.905 Hz and 0.25 %, respectively. During the optimization of weighting matrices using symbiotic organisms search, a band-limited white noise with a PGA of 0.8 m/s², a bandwidth from 0 to 15 Hz, and a duration of 140 s was used to excite the identified structural model with a time step of 0.005 sec. Accordingly, the weightings

Q and R in the cost function shown in Equation (2) were optimized and the optimal value of Q and R were 1.8357 and 100, respectively in the experimental validation. Therefore, the state feedback gain K_g was obtained as [-0.2393, 0.1329]. Afterwards, the structural model was subjected to the band-limited white noise excitation again and the control force and structural acceleration were obtained. Then, MLP with 150 steps of acceleration (MLP-150) and the ARX controllers were trained offline using these data.

In order to realize how accurately the MLP and ARX models were able to emulate the LQR, four of the performance indices used by Jansen and Dyke were adopted. The first performance index denotes the maximum normalized floor relative displacement which can be expressed as:

$$J_1 = \max_{t,i} \left(\frac{|x_i(t)|}{x^{\max}} \right) \quad (5)$$

where $x_i(t)$ is the relative displacement of the i -th floor during the excitation; and x^{\max} represents the maximum displacement of the uncontrolled shear building. The second performance index is the maximum normalized inter-story drift which can be represented as:

$$J_2 = \max_{t,i} \left(\frac{|d_i(t)/h_i|}{d_n^{\max}} \right) \quad (6)$$

where $d_i(t)$ is the inter-story drift of the i -th floor during the excitation; h_i is the story height of the i -th floor; and d_n^{\max} represents the maximum normalized inter-story drift of the uncontrolled shear building. The third performance index is the normalized peak absolute acceleration which can be expressed as:

$$J_3 = \max_{t,i} \left(\frac{|\ddot{x}_{ai}(t)|}{\ddot{x}_{ai}^{\max}} \right) \quad (7)$$

where $\ddot{x}_{ai}(t)$ is the absolute acceleration of the i -th floor during the excitation; and \ddot{x}_{ai}^{\max} is the maximum absolute acceleration of the i -th floor of the uncontrolled shear building. The last performance index considers the maximum control force normalized by the weight of the structure which is formulated as:

$$J_4 = \max_t \left(\frac{|u(t)|}{W} \right) \quad (8)$$

where $u(t)$ is the control force of AMD and W is the weight of the 10-story shear building.

Table 9 shows the experimental results of the three controllers with respect to the performance indices. Note that the specimen used in the validation was a SDOF shear building. Therefore, the

performance indices J_1 and J_2 were identical. The overall performance of the trained MLP-150 and ARX models is considered fairly well comparing with the LQR-SOS. Figures 5 and 6 illustrate the time histories of control force and structural response of the specimen, respectively when the specimen was subjected to El Centro earthquake. It can be seen from Figure 5 that in the three control situations, there is a tracking error between the desired control force and the achieved control force. However, considering the friction between the lead screw and the mass, the tracking performance is considered acceptable. In addition, the control force time histories of the three control cases are similar in both frequency and magnitude. As shown in Figure 6, a similar trend can be observed in the structural response. This shows that MLP and ARX can simulate the LQR controller quite successfully in experimental verification.

Table 1. Seismic control performance of the tests.

Controller	LQR-SOS			MLP-150			ARX		
	J_1/J_2	J_1	J_2	J_1/J_2	J_1	J_2	J_1/J_2	J_1	J_2
Earthquakes									
El Centro	0.473	0.455	0.036	0.431	0.437	0.033	0.456	0.544	0.036
Chichi	0.668	0.690	0.021	0.672	0.752	0.026	0.693	0.728	0.027
Kobe	0.447	0.438	0.056	0.519	0.567	0.042	0.525	0.515	0.036
Northridge	0.899	0.885	0.030	0.776	0.841	0.032	0.843	0.832	0.038
Parthfield	0.449	0.414	0.039	0.389	0.446	0.036	0.441	0.501	0.031
Montenegro	0.671	0.641	0.043	0.613	0.616	0.035	0.635	0.642	0.034
Meinong	0.637	0.616	0.048	0.644	0.621	0.033	0.647	0.679	0.045
Capemendocino	0.743	0.685	0.041	0.764	0.839	0.051	0.790	0.787	0.041
Average	0.623	0.603	0.039	0.601	0.640	0.036	0.629	0.653	0.036

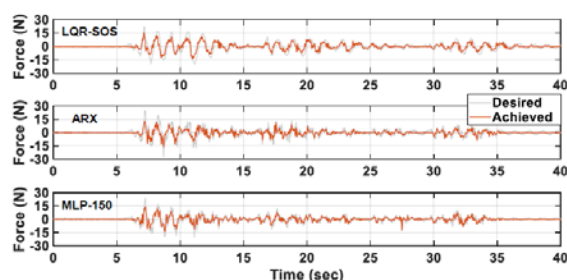


Figure 5. Time histories of the desired and achieved control force of the three controllers.

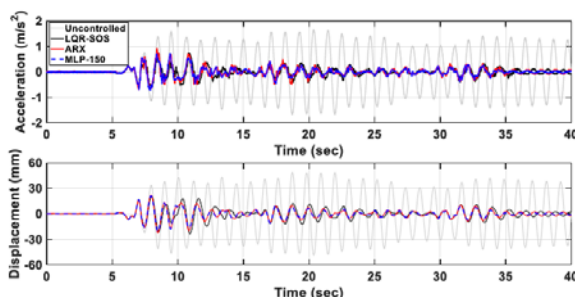


Figure 6. Time histories of the structural responses in the experimental validation.

Conclusions

Linear-quadratic regulator (LQR) has been widely applied to structural control because of minimizes a cost function formulated by weighted

states and control inputs. However LQR controller will encounter time delay caused by unobservable and additional calculation time, and the estimator is also a key factor affecting LQR. In the experimental validation, the control force time histories of the MLP and ARX models are close to that of the LQR in both frequency and magnitude. It proves that MLP and ARX can simulate the LQR controller well in practical applications. Future work will focus on the inverse training strategy to directly calculate the control force based on the relationship between the control device and the acceleration of the structure.

References

- Bani-Hani, K.; Ghaboussi, J. Nonlinear structural control using neural networks. *J. Eng. Mech.* 1998, 124, 319–327.
- Kim, J.T.; Jung, H.J.; Lee, I.W. Optimal structural control using neural networks. *J. Eng. Mech.* 2000, 126, 201–205.
- Lin, T.K.; Chang, K.C.; Chung, L.L.; Lin, Y.B. Active control with optical fiber sensors and neural networks. I: Theoretical analysis. *J. Struct. Eng.* 2006, 132, 1293–1303.
- Chen, C.J.; Yang, S.M. Application neural network controller and active mass damper in structural vibration suppression. *J. Intell. Fuzzy Syst.* 2014, 27, 2835–2845.
- Cheng, M.Y.; Prayogo, D. Symbiotic organisms search: A new metaheuristic optimization algorithm. *Comput. Struct.* 2014, 139, 98–112.
- Jansen, L.M.; Dyke, S.J. Semiactive control strategies for MR dampers: Comparative study. *J. Eng. Mech.* 2000, 126, 795–803.
- Chen, P.C.; Ting, G.C.; Li, C.H. A versatile small-scale structural laboratory for novel experimental earthquake engineering. *Earthq. Struct.* 2020, 18, 337–348.

Sensor Fusion for Trajectory Reconstruction from an Inertial Measurement Unit to Estimate Structural Residual Displacements

Yi-Jie Chuang¹, Shieh-Kung Huang², and Chia-Ming Chang³

莊奕婕¹、黃謝恭²、張家銘³

Abstract

Earthquakes can strike the ground with tremendous force. This can cause structures to undergo inelastic deformations, resulting in critical issues about their safety. Thus, residual displacement measurements are effective indicators to evaluate structural performance after earthquakes. In this study, readings from inertial measurement units (IMUs) are exploited to estimate the spatial trajectories and displacements of structures through a sensor fusion technique with the quaternion calculation. To explore the workability of the sensor fusion technique, various simplified tests are carried out. The spatial translational accelerations and angular velocities are acquired from the IMU and converted into translational and rotational displacements. These displacements are also compared with and validated by values obtained from simulation results of the IMU sensor. As found in the results, the combination of the sensor fusion method with IMUs is applicable for the displacement estimation with some constraints, and this sensor fusion method is expected to be applied to estimate the earthquake-induced displacements of structures in the future.

Keywords: trajectory reconstruction; quaternion; inertial measurement unit

Introduction

The application of inertial measurement units (IMUs) on various products has gained increasing popularity recently. Its characteristics such as small size and high precision are very useful in applications in the aerospace industry (Tiliakos 2013), the precise positioning of navigation systems (Wang 2009), the sensor orientation estimation (Teng 2009; Kim and Golnaraghit 2004; Wu *et al.* 2016; Groÿekathöfer and Yoon 2012; Smaiah *et al.* 2018; Renaudin and Combettes 2014), and the trajectory reconstruction of sensor motion (Zhang *et al.* 2018; Smaiah *et al.* 2018). In general, an IMU includes an accelerometer and a gyroscope to provide information on its acceleration and angular velocity, respectively; sometimes, a Global Positioning System (GPS) or a magnetometer is also included to fulfill the special needs.

Some applications of structural health monitoring (SHM) in civil engineering require the installation of various sensors (or monitoring devices) in different positions on the target structure to provide the full dynamic response of the structure. Moreover, it may be necessary to use additional frames to support the

devices during monitoring, which increases the cost of installing and maintaining the SHM system. The different techniques for SHM include measuring the residual displacement (or permanent displacement) of the structures after the earthquake, and installing a displacement meter and a goniometer (angle gauge) on the structure to obtain the deformation. This inevitably increases the complexity of the monitoring process. However, the advantages of IMUs, specifically the application of trajectory reconstruction, can be used to replace these sensors in the field of civil engineering. If an IMU is installed on a structure and techniques of orientation estimation and trajectory reconstruction are applied, the displacement during ground motion can be extracted. Therefore, it is expected that in the near future residual displacement of structures after the earthquake can be simply and effectively estimated.

To achieve this, the IMU, Epson M-V340PD (Seiko Epson Corporation 2017), was used and tested in this study. As the main research object, the three-axis acceleration and three-axis angular velocity in its local coordinates are first received and these six-axis data are processed by a low-pass filter in order to remove noise. The processed data are used to calculate

¹ Master Student, Department of Civil Engineering, National Taiwan University

² Assistant Professor, Department of Civil Engineering, National Chung-Hsing University

³ Associate Professor, Department of Civil Engineering, National Taiwan University

the quaternion and the technique of orientation estimation is utilized to evaluate the attitude of the sensor during the movement. Furthermore, by using a quaternion transformation matrix, the acceleration is transferred from the local coordinates to global (reference) coordinates and, after gravity compensation, the measured acceleration becomes the true acceleration in the global (reference) coordinate system. Finally, the trajectory can be successfully reconstructed by using the double integration of the true acceleration

Trajectory Reconstruction

In this section, we describe how we use the three-axis acceleration and three-axis angular velocity for trajectory reconstruction. These six-axis data are measured by the IMU and are first processed through a low-pass filter to eliminate the effect of noise. Then, the filtered data are used to calculate the Euler angle and quaternion during the movement, and the useful information is multiplied by the quaternion transformation matrix to obtain the acceleration in global (reference) coordinates. Subsequently, gravity is compensated and the true value of acceleration is integrated once to obtain velocity and twice to get displacement, which is the reconstructed trajectory.

Introduction of the IMU

The IMU used in this study is Epson M-V340PD (Seiko Epson Corporation 2017). It is a small-sized IMU implemented with six degrees of freedom. This IMU is also known for its low noise, high stability, and high-precision measurement capabilities. The three-axis acceleration and three-axis angular velocity can be obtained with fair accuracy under movement. The angular velocity is measured by the embedded gyroscope with a dynamic range of ± 450 deg/s, and the acceleration is measured by the embedded accelerometer with a dynamic range of ± 5.8 G. It has been used in the fields of dynamic analysis, dynamic control, unmanned systems, navigation systems, vibration control, and stability analysis.

Preprocessing for the Signals

Because the IMU digitalizes the measurement immediately after data acquisition, the raw data are accordingly scaled up or down to the physical unit first. The measured signals from the IMU are also filtered to remove noise. These processed data are then ready for subsequent data analysis.

The purpose of the filter is to eliminate the effect of noise by passing the data through the specified cutoff frequencies; therefore, the content outside this specified frequency range is regarded as noise and is filtered out. Filters can be roughly divided into four categories according to their frequency response functions: low-pass filters, high-pass filters, band-pass filters, and band-stop filters (Pozar 1998). Low-pass filters allow signals with low-frequency content to pass and prevent signals with higher frequency content from passing. A low-pass filter is used in this study because of the assumption that noise only exists in the high-frequency range.

Orientation Estimation using the Quaternion

To provide accurate orientation estimation, this study evaluates the attitude of the sensor using the quaternion formulation instead of simply using the Euler angle. The quaternion has no singularity problem; on the other hand, the use of the Euler angle may cause the gimbal lock problem during coordinate transformation and, eventually, lose a rotational degree of freedom. Most importantly, the quaternion can be easily obtained from the Euler angle through trigonometric functions (Kim and Golnaraghit 2004). Therefore, although the estimation using the Euler angle is more intuitive, it is only used to calculate the initial attitude.

Coordinate Transformation and Gravity Compensation

Because the IMU simultaneously measures the sensor's acceleration (in the local coordinate) and the gravity during the movement, the measurement in each axis will contain the gravitational acceleration components. Therefore, it is necessary to use the quaternion transformation matrix to transfer the local acceleration to global acceleration for further gravity compensation. In this way, the gravitational acceleration components in each axis all convert to the z-axis in global (reference) coordinates and can be conveniently eliminated by removing the gravity in the z-axis.

Integration using Fourth-order Runge-Kutta Method

The last step in trajectory reconstruction is integration using the fourth-order Runge-Kutta method. It is a numerical method for first-order ordinary differential equations (ODEs) and can generate higher-order solutions compared to conventional integration using Taylor series expansion or Simpson's rule. Most importantly, the method is easy to calculate and can dramatically increase the accuracy of velocity and displacement values while performing integration.

Results and Discussion

In this study, the simulation incorporates the MATLAB toolbox (Sensor Fusion and Tracking Toolbox) and the specifications of Epson M-V340PD, including measurement range, resolution, and noise density of the accelerometer and gyroscope. The simulated responses under different motions are regarded as true values and compared with results obtained through trajectory reconstruction. This section will present the comparison of two examples: backward-forward movement and circular movement with a constant velocity. Observation between true and estimated values is also discussed.

Backward-forward Movement in the Y-axis

The velocity of the backward-forward movement in the y-axis is 10 m/s, the total displacement is 1 m, the total time of motion is around 20 s, and the sampling rate of simulation is set as 1000 Hz. The acceleration and angular velocity simulated

by the toolbox can be effectively converted to global (reference) coordinates via the trajectory reconstruction method proposed in this study.

The velocity and displacement after numerical integration show that, even though the initial conditions of the integration are unknown, the difference between reconstructed and true values is extremely small. The maximum error of the residual displacement is less than 5 cm, as shown in Figure 1, where the ratio of the error to the total displacement is only 5.00%.

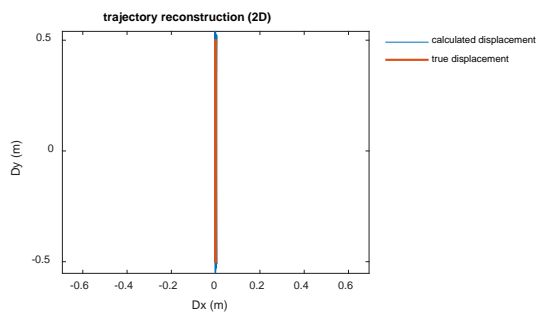


Fig. 1. Result of trajectory reconstruction in the backward–forward movement in the y-axis

Circular Movement with A Constant Velocity

The velocity of the circular movement is again 10 m/s, the radius of the circle is 5 m, the total time of motion is approximately 20 s, and the sampling rate of simulation is set as 500 Hz. Consequently, the acceleration and angular velocity simulated by the toolbox are once again converted to global (reference) coordinates via the trajectory reconstruction method.

The velocity and displacement after numerical integration show that there is still a small difference between the reconstructed and true values. Under the assumption of unknown initial conditions, the maximum error of the residual displacement is approximately 2 m, as shown in Figure 2. The error may arise from the unknown initial conditions for integration and the linear trend produced by the two steps of integration. After removing some points where the true value approaches zero, the overall ratio of the error to the perimeter is approximately 6.37%.

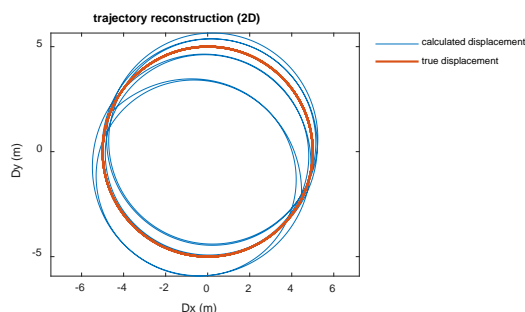


Fig. 2. Result of trajectory reconstruction in the circular movement with a constant velocity

Conclusions

This study utilized sensor fusion technology to estimate the sensor orientation through the quaternion, and then transferred the acceleration from local

coordinates to global (reference) coordinates. After the two-step integration using the Runge–Kutta method, the velocity and displacement of the IMU can be estimated and the trajectory can be reconstructed. Compared to the conventional Euler angle and rotation matrix method, this approach reduces tedious computations of trigonometric functions and avoids the singularity problem of the gimbal lock.

In the simulation study, for both backward–forward movement in the y-axis and circular movement with a constant velocity, the trajectory was effectively reconstructed and successfully verified. The error in these two examples was less than 7%. This shows that the proposed method can successfully carry out trajectory reconstruction under limited conditions and can be applied to three-dimensional structures in the future. It can also be implemented to estimate the residual displacement after an earthquake.

References

- Tiliakos, N. (2013). MEMS for harsh environment sensors in aerospace applications: selected case studies. In *MEMS for Automotive and Aerospace Applications*, 245-282.
- Wang, C. F. (2009). *GPS/INS System Design and Integration*. Master Thesis, Chung Hua University.
- Teng, Y. C. (2018). *Combined-Gesture Recognition using Wearable Devices with Inertial Measurement Units*. Master Thesis, National Tsing Hua University.
- Kim, A. & Golnaraghi, M. F. (2004). A quaternion-based orientation estimation algorithm using an inertial measurement unit. *Position Location and Navigation Symposium*, 268-272.
- Wu, J., Zhou, Z., Chen, J., Fourati, H., & Li, R. (2016). Fast complementary filter for attitude estimation using low-cost MARG sensors. *IEEE Sensors Journal*, 16(18), 6997-7007.
- Großekathöfer, K., & Yoon, Z. (2012). Introduction into quaternions for spacecraft attitude representation. *TU Berlin*, 16.
- Smaiah, S., Sadoun, R., Elouardi, A., Larnaudie, B., Bouaziz, S., Boubezoul, A., Vincke, B., & Espié, S. (2018). A Practical Approach for High Precision Reconstruction of a Motorcycle Trajectory Using a Low-Cost Multi-Sensor System. *Sensors*, 18(7), 2282.
- Renaudin, V., & Combettes, C. (2014). Magnetic, acceleration fields and gyroscope quaternion (MAGYQ)-based attitude estimation with smartphone sensors for indoor pedestrian navigation. *Sensors*, 14(12), 22864-22890.
- Zhang, J., Feng, J., & Zhou, B. (2018). Sensor-fusion-based Trajectory Reconstruction for Mobile Devices. In *VISIGRAPP*, 48-58.
- Seiko Epson Corporation. (2017). “M-V340PD Datasheet”, website: https://global.epson.com/products_and_drivers/sensing_system/download_hidden/pdf/m-v340pd_datasheet_e_rev20170904.pdf
- Pozar, D. M. (2009). *Microwave engineering*. John Wiley & Sons.

Analysis of an Experimental Database of the Deformation Capacity of Reinforced Concrete Rectangular Column Members

Kai-Ning Chi¹ Ker-Chun Lin² Sheng-Jhih, Jhuang³ and Jun-Wei Wu⁴

紀凱甯¹、林克強²、莊勝智³、吳峻維⁴

Abstract

The lateral deformation demand for column members under an axial force can be obtained using inelastic dynamic analysis. The purpose of this research is to establish a relationship between the axial force ratio (P/P_0) and the lateral deformation capacity of reinforced concrete (RC) column members, which can be used to design the confinement of these members. The study provides an empirical formula for the confinement and an effective and economical design for RC column members. This was achieved by collecting domestic and foreign basic design parameters and experimental results under the repeated loading of rectangular RC column members, creating a database of these members, and focusing on the parametric analysis for design conditions and their lateral deformation capacity. The analysis shows that the axial force ratio and the details of the transverse reinforcement are the main parameters that affect the lateral deformation capacity of RC column members. When the axial force ratio increases or the confinement decreases, the lateral deformation capacity of the column member decreases. The empirical formula for describing the confinement of RC column members can be used as a reference for design engineers.

Keywords: ratio of axial force, lateral deformation capacity, confinement, inelastic dynamic analysis.

Introduction

It follows from the concept of strong column-weak beam in seismic design that plastic hinges are generally expected to occur at the end of beam members or at the bottom of first-floor column members in moment-resisting frames. Under the action of earthquakes, plastic hinges not only develop on the first-floor column members, but lower story column members are also subject to nonlinear deformation. Generally, the deformation can be evaluated using Inelastic Dynamic History Analysis (IDHA). For the seismic design of reinforced concrete (RC) column members, the lateral deformation capacity mainly depends on the design details of the transverse reinforcement and the axial force ratio. For RC columns having the same deformation capacity, larger axial forces require greater transverse reinforcement.

For areas with high seismic risk, the lateral deformation demand of column members prescribed in seismic design code is generally based on a total rotation angle of 3% radians. Thus, column members on the lower stories of high-rise buildings must provide a rotation capacity of 3% radians. However, the deformation demands of the column members are smaller for higher stories, and the requirement for a 3% radian rotation should be reduced. Therefore, the IDHA can be used to obtain the deformation demands for the column members on each floor to provide an effective and economical design for transverse reinforcement. Depending on the conditions of the axial loads and the lateral deformation demand of the column member, the confinement details can be designed according to performance design principles. For column members with small deformation demands, it is also not necessary to follow the minimum requirement of a 3% radian rotation angle.

¹ Assistant Researcher, National Center for Research on Earthquake Engineering

² Research Fellow, National Center for Research on Earthquake Engineering

³ Assistant Researcher, National Center for Research on Earthquake Engineering

⁴ Master Student, National Taiwan University of Science and Technology

Experimental Database for RC Column Members

To discuss the relationship between the configuration details of the transverse reinforcement of RC column members and their ductility capacity, the design details and test results related to RC column members in domestic and foreign contexts must be compiled. The data sources include the experimental database of the Pacific Earthquake Engineering Research Center (PEER) in the United States, DEEDS in Japan, and the National Center for Research on Earthquake Engineering (NCREE) in Taiwan. Because of the inconsistency between the research objectives and the test conditions for each experiment, this study screens the experimental data base. We used the following screening principles:

- (1) The ultimate strength of the specimen must be reduced to 80% of the maximum strength
- (2) The hysteresis behavior of the specimen must be reasonable, and the loading displacement must continue to increase
- (3) The lateral force loading must be unidirectional, and the axial force must remain constant.

After applying these screening conditions, 124 sets of data were finally selected for the parameter analysis in this study. The parameters used for the data analysis are listed in Table 1.

Table 1. Parameters for the ER column member analysis data

Parameter	Symbol	Units	Min.	Mean	Max.
Concrete compressive strength	f_c'	MPa	21	51	175
Yield stress of longitudinal reinforcement	f_y	MPa	331	461	869
Yield stress of transverse reinforcement	f_{yt}	MPa	249	465	1424
Axial load ratio 1	P/P_0	-	0	0.27	0.59
Axial load ratio 2	$P/A_g f_c'$	-	0	0.28	0.65
Aspect ratio	a/d	-	2.5	3.5	6.6
Transverse reinforcement ratio	ρ_s	%	0.08	0.98	3.2
Ultimate drift ratio	Δ_{80}	%	0.93	3.81	8.3

According to the analysis data, the axial force in the RC column member is strongly correlated with the lateral deformation capacity. In the past, it was generally related to the axial force ratio $P/A_g f_c'$, which means that the contribution of the longitudinal reinforcement to the axial force (P_0) does not need to be considered. Therefore, this study will compare the axial force ratio $P/A_g f_c'$ with P/P_0 , where P_0 is the axial compressive strength of the section of the RC column member ($P_0=0.85(A_g-A_{st})f_c'+A_{st}f_y$), where A_{st} is the total cross-sectional area of the longitudinal reinforcement, and f_y is the yield strength of the longitudinal reinforcement. The axial force ratio ranged from 0 to a maximum value of $0.52P/P_0$ according to the axial force-flexural moment (P-M)

curve design of the RC column, where the ratio $0.52P/P_0$ is equal to $0.65 P/A_g f_c'$.

For the transverse reinforcement configuration, the longitudinal reinforcement at the corner has a strong confinement effect because it is confined by the outer transverse reinforcement and the seismic hooks; this confinement will increase the ductility of the column members. In accordance with the minimum requirements for confinement defined in Section 18.7.5 of the American Concrete Institute (ACI) 318-19 code (ACI, 2019), we also aimed to investigate the confinement effectiveness factor k_n in this study. Factor k_n is given by a simplified formula ($k_n = n_{ls}/(n_{ls}-2)$) for calculating the effective area of the confined concrete under a uniformly configured longitudinal reinforcement. However, the n_l value specified in the ACI 318-19 code does not include reinforcement in the central area. This study suggests that the steel bars in the central area are also confined by stirrups and concrete. Therefore, n_{ls} is defined as the total number of steel bars confined by the corners of the seismic hooks and stirrups including the central area. The difference between the two parameters and the calculation method are shown in Figure 1. The database established in this study does not yet include the design of longitudinal reinforcement in the center of the member section.

The ACI 318-19 code also specifies that the spacing between the confined longitudinal reinforcement h_x should be less than 350 mm when the axial force ratio $P/A_g f_c'$ is less than 0.3, or h_x should be less than 200 mm when the ratio of axial force $P/A_g f_c'$ is larger than 0.3. This value directly affects the area of effective confined concrete, so its parameters must also be taken into consideration.

This parameter in this study divides into two conditions. One is directly expressed according to the above specifications H_x , and the design configuration h_x . The other is $(H_x)_{limit}$, which is based on the value specified in the provision. When the calculated ratio is less than 1.0, the $(H_x)_{limit}$ is 1.0. Otherwise, the calculated value is used.

Thus, the spacing h_x between the confined longitudinal reinforcement follows the requirements of the specification, and the h_x value is not the main factor affecting the ductility capacity of the column member. The definition of the two parameters is listed in Table 2.

Table 2. Definition of the spacing between the confined longitudinal reinforcements.

H_x	Axial F. Ratio ≤ 0.3	$H_x = h_x / 350$
	Axial F. Ratio > 0.3	$H_x = h_x / 200$
$(H_x)_{limit}$	Axial F. Ratio ≤ 0.3	$(H_x)_{limit} = h_x / 350 \geq 1$
	Axial F. Ratio > 0.3	$(H_x)_{limit} = h_x / 200 \geq 1$

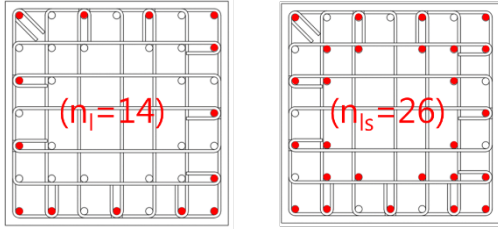


Figure 1. The difference between n_l and n_{ls} .

Regression Analysis of Ductility Index

In the previous section, several analytical parameters were discussed, including n_{ls} /number of total bars, $(n_{ls}-2)/n_{ls}$, H_x , and $(H_x)_{limit}$. These parameters were combined with the product of the yield stress of transverse reinforcement and the transverse reinforcement ratio ($\rho_s \times f_{yt}$) to yield four sets of ductility indices:

- (1) $\rho_s \times f_{yt} \times (n_{ls}/\text{total bars}) / (H_x)_{limit}$ (MPa)
- (2) $\rho_s \times f_{yt} \times (n_{ls}-2) / n_{ls} / (H_x)_{limit}$ (MPa)
- (3) $\rho_s \times f_{yt} \times (n_{ls}/\text{total bars}) / (H_x)$ (MPa)
- (4) $\rho_s \times f_{yt} \times (n_{ls}-2) / n_{ls} / (H_x)$ (MPa)

The four sets of ductility indices were used for regression analysis with two parameters, the axial force ratios $P/A_g f'_c$ and P/P_0 and the ultimate story displacement angle Δ_{80} of column members. Linear, exponential, and natural logarithmic functions were used to evaluate the trends between the parameters. The correlation coefficients (R^2 values) of the regressions are listed in Table 3.

We found that that the correlation coefficient value for the exponential function is the highest in the regression analysis, and that the parameter P/P_0 yields the best analytical result. The ductility index $\rho_s \times f_{yt} \times (n_{ls}-2) / n_{ls} / (H_x)_{limit}$ has the greatest correlation with the deformation capacity of column members. The correlation between the axial force ratio P/P_0 and the ductility index $\rho_s \times f_{yt} \times (n_{ls}-2) / n_{ls} / (H_x)_{limit}$ of the screened data in the database is shown in Figure 2. According to these results, the ultimate story displacement angle Δ_{80} of the column member is lower when the axial strength ratio P/P_0 is higher. Furthermore, higher ductility indices. result in larger lateral deformation capacity.

The results in Table 3 also show that the regression correlation coefficient R^2 is lowest when the axial force ratio ranges from $0.5P/P_0$ to $0.52P/P_0$. This reason for this is related to the four sets of data in this region of the database, shown in Fig. 2. In engineering practice, the column members should not be designed under such axial force ratio conditions. Therefore, this study provisionally excludes data in this region. Figure 3 shows the relationship between

the finally selected axial force ratio P/P_0 , ductility index $\rho_s \times f_{yt} \times (n_{ls}-2) / n_{ls} / (H_x)_{limit}$ and the ultimate story displacement angle Δ_{80} .

Table 3. Correlation coefficient values (R^2) values in the database.

R^2	Index 1			Index 2			Index 3			Index 4		
	Linear	Power	Ln									
0 - 0.1	0.60	0.74	0.85	0.50	0.79	0.87	0.54	0.75	0.87	0.62	0.82	0.91
0.1 - 0.2	0.19	0.56	0.38	0.25	0.64	0.49	0.07	0.48	0.35	0.09	0.51	0.41
0.2 - 0.3	0.44	0.61	0.53	0.58	0.68	0.63	0.53	0.67	0.60	0.63	0.71	0.67
0.3 - 0.4	0.14	0.54	0.36	0.08	0.47	0.28	0.05	0.36	0.24	0.03	0.32	0.20
0.4 - 0.5	0.60	0.67	0.63	0.59	0.62	0.60	0.49	0.66	0.61	0.54	0.66	0.62
0.5 - 0.52	0.00	0.08	0.04	0.01	0.12	0.07	0.00	0.12	0.08	0.01	0.18	0.12
average	0.33	0.53	0.47	0.34	0.55	0.49	0.28	0.51	0.46	0.32	0.53	0.49

R^2	Index 1			Index 2			Index 3			Index 4		
	Linear	Power	Ln									
0 - 0.1	0.76	0.76	0.87	0.58	0.80	0.88	0.65	0.75	0.87	0.69	0.82	0.91
0.1 - 0.2	0.13	0.33	0.25	0.23	0.49	0.41	0.06	0.30	0.23	0.08	0.39	0.33
0.2 - 0.3	0.07	0.38	0.24	0.08	0.42	0.29	0.14	0.46	0.33	0.16	0.51	0.38
0.3 - 0.4	0.07	0.12	0.10	0.07	0.08	0.08	0.04	0.08	0.07	0.06	0.06	0.06
0.4 - 0.5	0.68	0.79	0.67	0.61	0.75	0.63	0.57	0.78	0.67	0.54	0.76	0.65
0.5 - 0.65	0.04	0.30	0.24	0.10	0.31	0.24	0.03	0.36	0.29	0.10	0.38	0.30
average	0.29	0.45	0.39	0.28	0.48	0.42	0.25	0.45	0.41	0.27	0.49	0.44

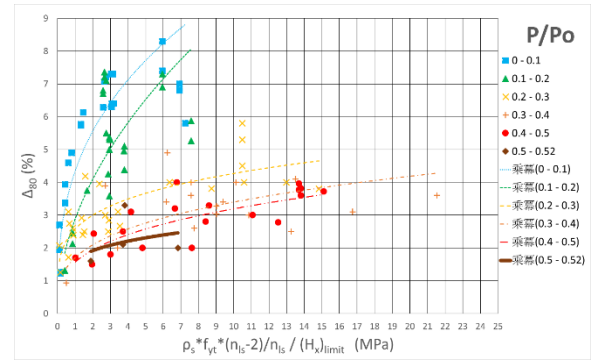


Figure 2. Regression analysis of parameters

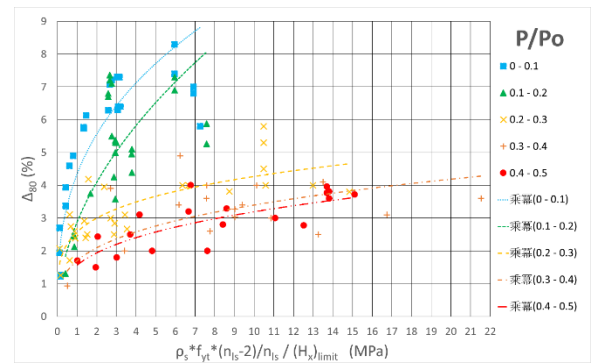


Figure 3. The regression analysis results of selected parameters.

Conclusions and Suggestions

1. This research is based on domestic and foreign experimental data of reinforced concrete (RC) rectangular columns. The analytical results

show that more accurate regression results can be obtained when the axial force ratio includes consideration of the contribution of longitudinal reinforcement.

2. This study derived the following ductility index formula $\rho_s \times f_{yt} \times (n_{ls} - 2) / n_{ls} / (H_x)_{limit}$ through regression analysis, which can be used to predict the relationship between the axial force ratio P/P_0 and the ultimate story displacement angle Δ_{80} of column members.
3. At present, the regression analysis is only valid for predicting the relationship between the ductility index and ultimate story displacement angle under different axial forces. Therefore, seismic performance tests of column members should be carried out in the future to further verify the correlation between the parameters.
4. In the future, the study will continue to examine the relationship between the configuration of longitudinal reinforcement and lateral deformation capacity of column members.

References

- Chai, J.-F., Teng, T.-J. and Liao, W.-I., (2004). "Numerical Simulation of Near-fault Ground Motions and Induced Structural Responses," Proceedings of the 13th WCEE (CD-Rom), Vancouver, Canada, Paper # 3309.
- ACI Committee 318 (2019), Building Code Requirements for Structural Concrete and Commentary., American Concrete Institute (ACI), Farmington Hills.
- Frédéric Légeron and Patrick Paultre, (2000). Behavior of High-Strength Concrete Columns under Cyclic Flexure and Constant Axial Load." ACI Structural Journal, July-August 2000, pp.591-601.
- J. B. Mander, M.J.N. Priestly, and R. Park, (1988), "Theoretical Stress-Strain Model For Confined Concrete," Journal of Structural Engineering, 114(8), pp. 1804-1826.
- Jun-Wei Wu (2020), "Analysis Investigation of Experimental Data Base on Deformation Capacity of Rectangular RC Columns," Master's thesis, University of Science and Technology.
- Kenneth J. Elwood and Marc O. Eberhard (2009), "Effective Stiffness of Reinforced Concrete Columns," ACI Structural Journal, pp.476-484.
- Lehman et al, Jack Moehle, Stephen Mahin, Anthony Calderone, and Lena Henry, (2004), "Experimental Evaluation of the Seismic Performance of Reinforced Concrete Bridge Column," Journal of Structural Engineering, 2004, 130(6): pp.869-879.
- Mizoguchi Mitsuo, Arakawa Takashi, Arai Yasuyuki, Yoshida Minoru (1990), "Shear Resisting Behavior of Short Reinforced Concrete Columns under Biaxial Bending-Shear and Varying Axial Load," Transactions of the Japan Concrete Institute, Vol. 12, pp.347-354.
- Oguzhan Bayrak and Shamim A. Sheikh (1998), "Confinement Reinforcement Design Considerations for Ductile Column," Journal of Structural Engineering, 124(9), pp.999-1010
- Ohno and Nishioka (1984), "An Experimental Study on Energy Absorption Capacity of Columns in Reinforced Concrete Structures," JSCE Structural Eng. Vol 1, No. 2, pp.23-33.
- Paultre, P., and Légeron, F., (2008), "Confining Reinforcement Design for Reinforced Concrete Columns." Journal of Structural Engineering, ASCE, V. 134, No. 5, May., pp.738-749.
- Shamim A. Sheikh and Shafik S. Khoury (1993), "Confined Concrete Columns with Stubs," ACI Structural Journal, pp414-431.
- Shamim A. Sheikh, Dharmendra V. Shah, and Shafik S. Khoury, (1994), Confinement of High-Strength Concrete Columns. ACI Structural Journal, pp414-431, pp100-111.
- Shunsuke Sugano (1996), "Seismic Behavior of Reinforced Concrete Columns Which Used Ultra-high-strength Concrete," Eleventh World Conference on Earthquake Engineering Proceeding, Paper No.1383.
- Tomomi Suzuki, Lucas Laughery, and Santiago Pujol (2018), "Learning from the Japanese Experience with High-Strength Longitudinal Reinforcement," Concrete International, September 2018, pp. 47-58
- Watson and R. Park, Fellow (1994), "Simulated Seismic Load Tests on Reinforced Concrete Columns," Journal of Structural Engineering, 120(6): pp.1825-1849.
- Yan Xiao and Armen Martirosyan, (1998), "Seismic Performance of High-strength Concrete Columns," Journal of Structural Engineering, 124(3): pp.241-251.
- Y. L. Mo and S. J. Wang, (2000), "Seismic Behavior of RC Columns with Various Tie Configurations," Journal of Structural Engineering, Oct. 2000, pp.1122-1130.

Centrifuge Modeling of the Dynamic Behavior of Low-rise Buildings on Sandy Ground with Different Water Table Depths

Lin-Mao Hu¹ Chih-Chieh Lu² Kuan-Yu Chen³

Abstract

In recent decades, Taiwan has experienced serious soil liquefaction disasters that have caused damage to buildings and affected people's safety. This study aims to simulate the behavior of low-rise buildings on liquefiable ground during earthquakes via centrifuge modeling. In addition, different water table depths are used to investigate the effectiveness of the dewatering method for avoiding soil liquefaction disasters. The test results reveal that lowering the water table can effectively limit the excitation of excess pore water pressure and reduce the settlement of structures on liquefiable ground. However, it also reduces the seismic isolation effect of soil liquefaction on a structure. As the water table is lowered, the acceleration amplification in structures built on ground with a higher relative density is greater than that in structures on ground with a lower relative density. This shows that when the water table is lowered, the degree to which specific site conditions may affect acceleration amplification during seismic events must be considered.

Keywords: centrifuge modeling, soil liquefaction, dewatering method.

Introduction

The presence of groundwater in sandy soil is likely to cause soil liquefaction in the event of an earthquake, and this will affect any structures located on the site. In recent decades, Taiwan has experienced severe soil liquefaction disasters, namely the Chi-Chi earthquake in 1999 and the Meinong earthquake in 2016. The latter caused some buildings in Tainan to subside and tilt as a result of soil liquefaction, which drew people's attention to the issue of soil liquefaction disasters. Disaster prevention and the improvement of old buildings on liquefied strata is an essential part of urban renewal. Therefore, in this study, we used centrifuge modeling with a scale model of a low-rise building with a height of approximately 10 m in prototype scale to simulate the behavior of an old building on a liquefied stratum in an earthquake. Different water table depths were specified in each test of the model specimens to investigate the effectiveness of the dewatering method for preventing damage to old buildings in soil liquefaction disasters.

The centrifuge modeling uses a centrifuge to move a scale-model specimen mounted on the end of the rotation arm in a uniform circular motion to provide it with a radial acceleration field. When the

model specimen is subjected to N times the Earth's gravity, Ng , the stress and strain conditions in the model scaled-down by N from the prototype scale can be used to represent the behavior of the target building in prototype. Thus, the scale model can be used to simulate the soil-structure interaction of the building in prototype scale. The advantage of the centrifuge modeling is that a scale model is more economical to use than a full-scale one, and the test conditions are easier to control.

Test Equipment and Materials

In this study, the centrifuge modeling were conducted using the geotechnical centrifuge at the Experimental Center of Civil Engineering (ECCE) at the National Central University (NCU), Taiwan. The other test equipment was a shaking table on the centrifuge, a laminar container, and various measuring sensors and instruments. The NCU centrifuge is shown in Fig. 1. It has a nominal radius of 3 m and a maximum payload of 1000 kg under an acceleration field of 100 g. A 1-Dimension servo-hydraulic shaker was integrated into the swing basket of the centrifuge. The shaker provides a payload mounting area of 1000 mm (length) \times 546 mm (width) \times 500 mm (height). The maximum displacement of the table was ± 6.4 mm,

¹ Assistant Technologist, National Center for Research on Earthquake Engineering

² Research Fellow, National Center for Research on Earthquake Engineering

³ Assistant Researcher, National Center for Research on Earthquake Engineering

and the nominal operating shaking frequency range was 0–250 Hz.

A fine quartz sand was used in all the tests to provide a uniform sand bed. The mean grain size D_{50} was 0.19 mm, which is classified as a poorly graded sand (SP) in the Unified Soil Classification System. The sand had a specific gravity of 2.65, its friction angle with a relative density of 55% was 35.7° , and its maximum and minimum dry unit weights were 16.3 kN/m^3 and 14.1 kN/m^3 , respectively.

Fig. 2 shows the laminar container, which was composed of 38 layers of rectangular aluminum alloy frames. The inner dimensions of the container were 711 mm (length) \times 356 mm (width) \times 353 mm (height). There were roller bearings between each frame, providing a very low friction coefficient of 0.01. The maximum relative displacement between each frame was 2.5 mm, meaning that the volume in the container could provide shear deformation in the long axis.



Fig. 1. The NCU centrifuge.



Fig. 2. The laminar container.

building with a height of 10 m in prototype scale. The length and width of the floors were both 3.95 m, the length and width of the independent footing were both 1.18 m, and the depth of the footing surface was 1.56 m below the surface of the ground. To simulate the cracking of the cement floor on the first floor due to soil liquefaction and subsidence of the building, the central part of the first floor of the model structure was replaced with gypsum flakes.

The accelerometers were installed at floor level on the first, at ceiling height on the second and third floor of the model structure. Two reflection plates for the laser displacement transducer were extended from the ceiling on the first floor to measure the settlement of the structure during the test. The soil stratum in the model was a 15 m thick layer of sand, the scale building was seated at the center of the model ground. There was one accelerometer and pore pressure transducer array in the free field of the model and another underground, at the center of the model. The configuration of the model is shown in Fig. 3.

We conducted ten centrifuge tests in this study. The test conditions are summarized in Table 1. The conditions that were varied were relative density (50% and 65%) and the depth of the water table (0 m, 1 m, 1.56 m, and 3 m). The other two tests were pilot tests in which the first floor was replaced with a solid aluminum alloy plate.

Table 1. Summary of the test conditions.

Test code	Relative density (%)	Ground thickness (m)	Water table depth (m)
Test-65-0-R	65	15	0 (fully saturated)
Test-65-1.56-R	65	15	1.56
Test-65-0	65	15	0 (fully saturated)
Test-65-1	65	15	1
Test-65-1.56	65	15	1.56
Test-65-3	65	15	3
Test-50-0	50	15	0 (fully saturated)
Test-50-1	50	15	1
Test-50-1.56	50	15	1.56
Test-50-3	50	15	3

Model Preparation and Test Procedure

To reduce the complexity of the experiment and analysis, the model structure used a simple rigid frame made by aluminum alloy, and the foundation was four independent footings, in order to simulate old buildings. The model structure was a three-floor

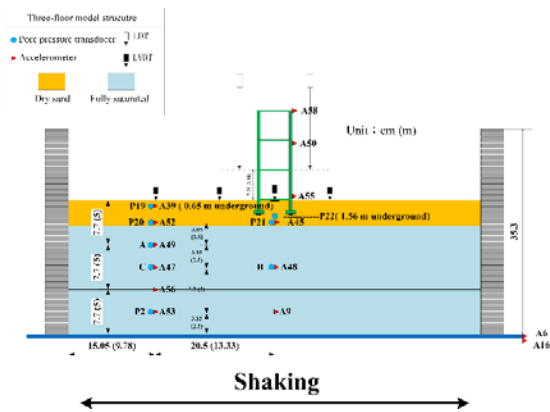


Fig. 3. Configuration of the model.

In this study, the model soil was prepared using the air pluviation method. The drop heights for the sand were 50 cm and 30 cm, respectively, for a relative density of 65% and 50%. Before the model soil was prepared, the laminar container was lined with a waterproof rubber bag to prevent the groundwater from leaking out of the container. Once the pluviation had started, the drop height of the sand had to be adjusted for every additional 1 cm of sand that had accumulated in the container in order to accurately achieve the target relative density. The sensors were installed at specific depths in the model during this stage. When the thickness of the sand layer had reached the predetermined height for the foundation surface, the model structure was installed at the center of the ground surface, and the accelerometer wire were guided to the wall of the container along the ground surface at the foundation ground level to reduce the disturbance to the dynamic behavior of the model structure.

After the model ground had been prepared, the model container was placed in a large chamber for the saturation of the sand. The air in the chamber was pumped out until the inside of the chamber was almost a vacuum. A viscous fluid was then dripped onto the model ground at a rate of less than 0.6 kg per hour. When the saturation was complete, the model was installed on the centrifuge platform and ready for the test. When the test started, the centrifuge accelerated slowly to a predetermined acceleration field of 65 g. The shaking events were controlled using a remote control system, and all sensor data were recorded simultaneously. Five main shaking events were included in every test. The acceleration amplitudes were respectively 0.02 g, 0.2 g, 0.3 g, 0.2 g, and 0.4 g, with a sine wave frequency of 1 Hz and twenty cycles. Before the main shaking events, three smaller events were used to detect the ground's characteristics. They were characterized by an acceleration amplitude of 0.01 g with a sine wave frequency of 2 Hz and one cycle; an acceleration amplitude of 0.01 g with a sine wave frequency of 1 Hz and five cycles; and a white noise signal with an amplitude of 0.01 g and a duration of 40 s.

Test Results

The general definition of soil liquefaction is that when a fully or partially saturated soil stratum is subjected to an external force such as an earthquake, the pore water pressure will be excited, causing the ground to lose its bearing capacity. However, this also means that the shear wave of the earthquake is unable to propagate completely to the surface. Figure 4 shows the acceleration time history for the first main shaking event, with an amplitude of 0.2 g, in Test-65-0. The bottom panel in the figure shows the acceleration of the base, and the top panels show the acceleration at progressively decreasing depths, up to the surface. From this figure, it can be observed that the acceleration attenuated toward the surface. Only a quarter of the waveform was generated near the surface, and the maximum amplitude was only half of that of the base. The lower part of Fig. 5 shows the peak acceleration amplification at 0.65 m underground for the first main shaking event (amplitude of 0.2 g) in each test. It reveals that, although full saturation of the ground may cause severe soil liquefaction, it can also achieve a strong seismic isolation effect. The upper part of Fig. 5 shows the peak acceleration amplification at the top of the structure for the first main shaking event in each test. It shows that the peak acceleration amplification increased as the water table dropped. When the ground was fully saturated, the peak acceleration amplification was little affected by the relative density of the ground. However, when the water table was lower, the higher relative density was associated with a higher peak acceleration amplification in the structure.

Fig. 6 shows the time history of the excess pore water pressure (EPWP) for the first main shaking event in Test-65-1, Test-65-1.56, and Test-65-3 from left to right. The red dashed line indicates the effective overburden stress at each depth. At the bottom of the figure is the EPWP time history at a depth of 12.5 m. At this depth, the EPWP was rapidly excited to the level of the effective overburden stress. However, at depths of less than 7.5 m, the excitation of the EPWP was substantially delayed, and the EPWP ratio was much lower. As the water table dropped, this phenomenon became more pronounced. This shows that when the water table is lowered to below the surface, there is greater void volume over which the excess pore water pressure can dissipate, avoiding the accumulation of EPWP and thus avoiding soil liquefaction.

Figure 7 shows the vertical settlement of the structure. The figure shows that the structure underwent the greatest settlement when the ground was fully saturated, with substantially less settlement as the water table dropped. These results show that the dewatering method may effectively improve the structure's settlement due to soil liquefaction. However, it would also magnify the impact of the

shaking on the structure.

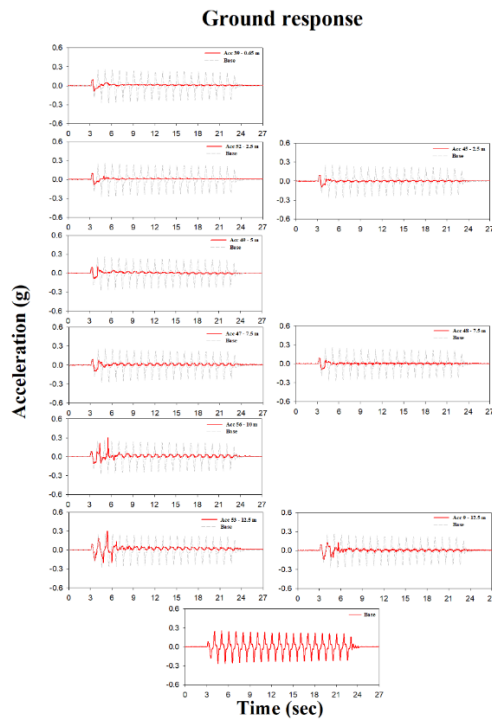


Fig. 4. Acceleration time history for Test-65-0.

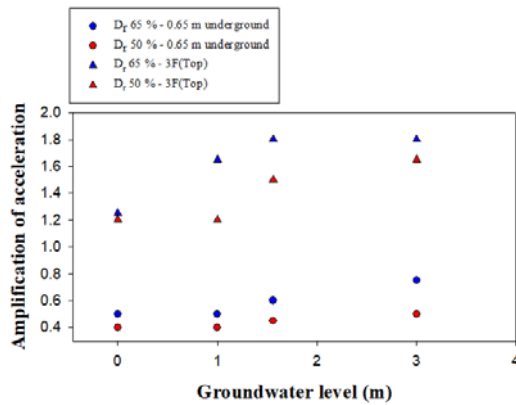


Fig. 5. Peak acceleration amplification at 0.65 m underground and the top of the structure.

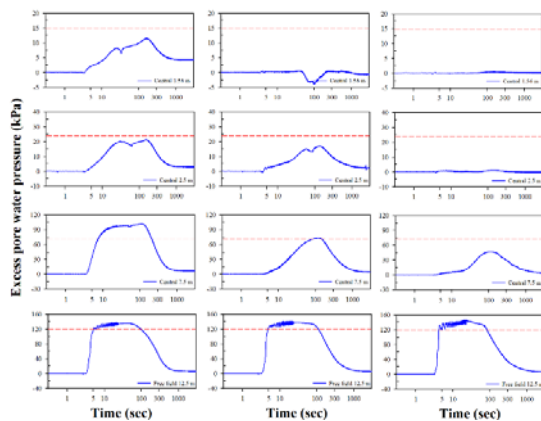


Fig. 6. Time histories of excess pore water pressure for Test-65-1, Test-65-1.56, and Test-65-3.

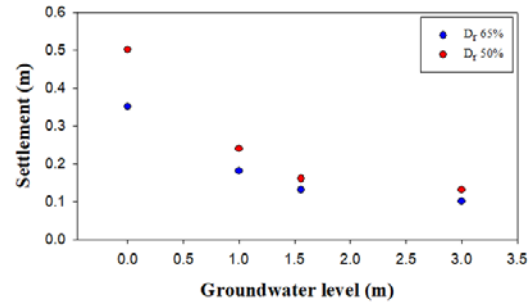


Fig. 7. Vertical settlement of the structure.

Conclusions

In this study, ten centrifuge model tests were conducted to simulate the seismic behavior of low-rise buildings on liquefiable ground and assess the effectiveness of the dewatering method for protecting such buildings against soil liquefaction disasters. The test results showed that as the water table drops, the excitation of EPWP in the soil stratum is effectively reduced. The ground retains most of its bearing capacity, which reduces the settlement of the structure. However, as the water table drops, the structure's peak acceleration amplification increases from 1.2 to approximately 1.7. The tests also show that the peak acceleration amplification in a soil stratum with a relative density of 65% is higher than that in a stratum with a relative density of 50% when the water table is lower. This reveals that when the dewatering method is used, the specific site conditions and their potential effect on acceleration amplification in the structure must be considered. Future research will address the behaviors of the ground and structure under subsequent liquefaction events and fully evaluate the interaction between the dewatering method and structure behavior during seismic events.

References

- Dashti, S., Bray, J.D., Pestana, J.M., Riemer, M., and Wilson, D. (2010), "Mechanisms of seismically induced settlement of buildings with shallow foundation on liquefiable soil." *Geotechnical Engineering*, 136(1), 151-164.
- Qiu, Y.H. (2018), "Study of seismic response of five-floor building with shallow foundation during soil liquefaction by centrifuge model test" Master's thesis, National Central University, Taiwan. [Chinese]

The Soil Liquefaction Potential Map of Taipei Basin Based on a Refined Borehole Database

Chih-Chieh Lu¹ Yuan-Chang Deng² Jin-Hung Hwang³

Abstract

The purpose of this study is to establish a reliable borehole database for the creation of a soil liquefaction potential map of the Taipei Basin. In the example presented here, information from over four thousand boreholes widely distributed across the Taipei Basin is first collected from different databases. For the geological boreholes, the soils are first classified according to the unified soil classification system (USCS), and a brief introduction of the geological characteristics of the area is created according to the analysis of the different soils. Then, external forces are considered to evaluate soil liquefaction, including factors such as the peak ground acceleration of the earthquake and the ground water table. A soil liquefaction evaluation is conducted to determine the factor of safety against soil liquefaction for each soil layer in the boreholes. The concept of a liquefaction potential index (P_L) is adopted to evaluate the soil liquefaction effect in a liquefiable soil column. Finally, the study results are briefly summarized.

Keywords: Soil Liquefaction, Liquefaction Potential Index, Borehole, Database.

Introduction

In 1999, the 921 Chi-Chi earthquake struck central Taiwan and caused extensive soil liquefaction, a problem that drew the attention of researchers and engineers. Since soil liquefaction cases, earthquake records, and geological information are well-documented, many researchers began studying soil liquefaction at that time. Some Taiwanese researchers used the framework proposed by Seed et al. (1985) to develop a local simplified procedure based on SPT-N, namely the hyperbolic function (HBF) procedure (Hwang et al., 2005 and 2012).

In 2016, about seventeen years after the 921 Chi-Chi earthquake, the Meinong earthquake, which had a local magnitude M_L of 6.6, struck southern Taiwan. The earthquake caused serious building damage in the Tainan area due to soil liquefaction. Due to significant public concern over the soil liquefaction risk in urban areas after the earthquake, the Central Geological Survey created the first version of a soil liquefaction potential map. This project, using a limited number of boreholes approximately one month after the Meinong earthquake, ranked the liquefaction risk in terms of the liquefaction potential index P_L . Figure 1 shows the published results for soil liquefaction in the Taipei Basin. In order to provide the public with a better understanding of soil liquefaction risk, the Construction and Planning Agency Ministry of the Interior (CPA/MOI) promoted the “Home Security

Plan” to produce a refined soil liquefaction potential map for local administrative divisions in liquefiable areas. To facilitate the execution of the plan, the National Center for Research on Earthquake Engineering (NCEE) served as advisors to Taipei City and New Taipei City. NCEE set the standard operation procedure and supervised the contractor (CECI Engineering Consultants) to execute the plan according to its requirements. Over approximately two years, the working group has conducted the project and accumulated significant experience.

In this study, factors that may affect the results of the soil liquefaction potential map are addressed including the collection and screening process for the borehole database, the variations resulting from the soil liquefaction evaluations, and the thickness of the un-liquefiable crust on the soil surface. The Taipei Basin will be used as an example to address several factors considered in the generation of a refined soil liquefaction potential map. Additionally, the results generated by different liquefaction evaluation frameworks will be compared.

¹ Research Fellow, National Center for Research on Earthquake Engineering

² Assistant Researcher, National Center for Research on Earthquake Engineering

³ Professor, Department of Civil Engineering, National Central University

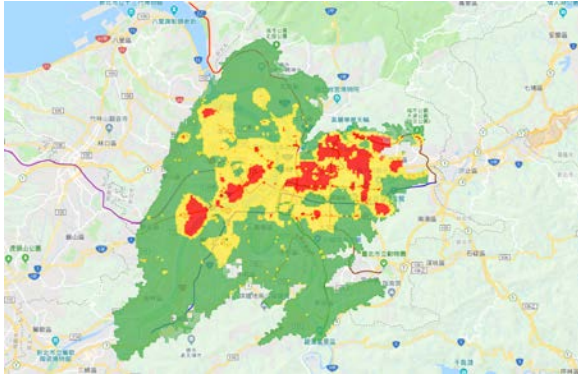


Fig 1. Soil liquefaction potential map of the Taipei Basin from the Central Geological Survey.

The establishment of the borehole database

In addition to seismic data, geological drilling is an essential input parameter for the assessment of soil liquefaction. The Taipei Basin in Taiwan is highly developed. In recent decades, many large projects including large-scale land development projects, public rapid transit systems, freeways, and highways have been completed and in operation for many years. This public infrastructure has provided extensive geological drilling data for sites distributed across the Taipei Basin. Currently, there are as many as 12,962 boreholes in the Taipei Basin. Assuming a uniform spatial distribution of boreholes in this area, this corresponds to approximately 53 boreholes per square kilometer. However, since the quality control system during early geologic drilling was not well established, much of the submitted borehole data is not reliable for use in a liquefaction assessment. Therefore, it is necessary to conduct further inspection and screening before including this data in the liquefaction evaluation. During the screening process, the authors first classified the quality of the drilling data. The classification is based on the completeness of the data, including the USCS information, the SPT-N value, and index properties of the soil. In this classification, drilling data in the first class had almost no need for corrections or supplementary data; the second class required some minor correction or supplementary data; the third class had unreliable data and lacked some essential information; and the data in the fourth class was extremely unreliable and lacked a significant amount of essential information. In this study, boreholes in the third and fourth classes were excluded due to their unreliability, with only the borehole data from the first and second classes used for the following analyses. For soil layers that were missing soil sample information, data from neighboring soil samples was used that had similar USCS classifications. If the soil layers don't have other similar soil layers with similar USGS classifications and sufficient geological information for reference, the missing information was supplemented using the statistical analysis of reliable

soil samples. After this data processing procedure, the remaining number of the boreholes was 4,876. The distribution of all boreholes in the Taipei Basin is shown in Figure 2. In the figure, the solid blue portions represent the drilling from the Home Security Plan, carried out from 2017 to 2018. The purpose of the drilling was mainly to evaluate soil liquefaction in the Taipei Basin. In order to reduce variation in operation, the automatic drop hammer system was adopted, and the drilling quality was improved as a result. Based on the energy measurements from some selected boreholes, the energy ratio of the automatic drop hammer system is approximately 65-70%. According to the statistical results of the boreholes from the Home Security Plan, liquefiable sandy soils, which include SM, ML, CL-ML, and other gravel soils, account for 58.3% of all soils. Among the liquefiable sandy soils, SM soils were most common, accounting for 53.5% of the liquefiable soils. According to the analysis of some typical soils such as SM, CL, and ML, the SM soils have an average N value of approximately 12 and an average fines content of 25%; the CL soils have an average N value of 5 and an average fines content of 94%; and the ML soils have an average N value of 9 and an average fines content of 75%.

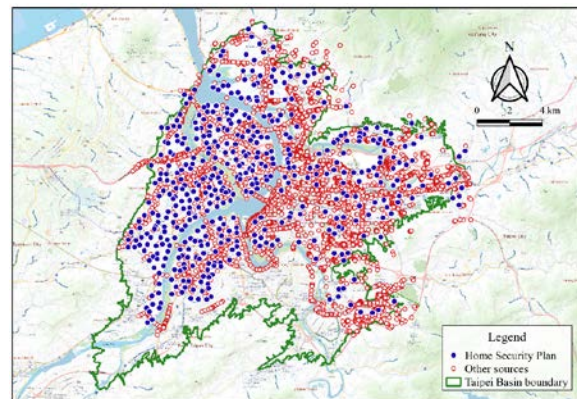


Fig 2. The distribution of boreholes in the Taipei Basin after the screening process.

Soil liquefaction potential evaluation

Design earthquake parameters and ground water table

The moment magnitude M_w scale and the horizontal peak ground acceleration (PGA) are the earthquake parameters used to evaluate soil liquefaction. According to the recommendations from the latest "Seismic design specifications and commentary of buildings" report, soil liquefaction studies must consider a design earthquake with return period of 475 years (10% probability of exceedance in 50 years). In this study, the same concept was used. In the Taipei Basin, the dominant earthquake source is the Sanchiao Fault. The moment magnitude M_w for an earthquake with a return period of 475 years is 7.3, and

its horizontal PGA is 0.24 g. All boreholes in this study are within or near the Taipei Basin, and the M_w and PGA are consistent. In addition to these earthquake parameters, the ground water table (GWT) is also a critical parameter for evaluating soil liquefaction. Since the data on the GWT is insufficient, the ground water tables of the boreholes created by the Home Security Plan were measured during the execution of the plan. Based on the GWT measurements, it is clearly observed that the GWT changes throughout the year. To be conservative, a contour of the average ground water table in the Taipei Basin during the flood season was generated to evaluate the soil liquefaction for the boreholes.

Methods to evaluate soil liquefaction potential

To determine the effect of soil liquefaction in areas experiencing severe liquefaction during the design earthquake, the liquefaction potential index P_L proposed by Iwasaki et al. (1978), which is commonly adopted to evaluate the liquefaction severity, was applied at each site. According to the ranking suggestions determined by Iwasaki et al. (1978), the sites with a $P_L > 15$ can be regarded as having a high liquefaction potential, sites with $5 < P_L \leq 15$ are regarded as having a medium liquefaction potential, and sites with $P_L \leq 5$ have low liquefaction potential. P_L is evaluated using the factors of safety (FS) calculated from the Taiwan local HBF method (Hwang et al., 2012) to predict the likelihood that liquefaction would cause damage at the surface level. It should be noted that the evaluation by different simplified methods would result in a varying FS, even if the borehole data is consistent. To quantify the variation in P_L from different simplified liquefaction analysis procedures, several other common SPT-based simplified procedures in Taiwan, including the NCEER method (Youd et al., 2001), and the JRA method (Japanese Road Association, 1996) were adopted. The results of the analysis can be used to compare the procedures.

Evaluation results

Figure 3 shows the statistics for the evaluated P_L using different simplified liquefaction analysis procedures for all selected boreholes. As shown in the figure, the ratios of the evaluated P_L in each liquefaction potential group are comparable. The ratios of high, middle, and low liquefaction potential are approximately one third for all methods. The variation resulting from the simplified procedures is not evident, which means that the adopted simplified procedures for the liquefaction analysis did not significantly impact the evaluation of the factor of safety against soil liquefaction in the studied cases.

In this study, the liquefaction potential indices calculated using the HBF method and the borehole coordinates were used to evaluate the liquefaction

potential indices of all discretized positions in the analysis domain. To achieve this, the data was interpolated using the Kriging method, and then the refined soil liquefaction potential map was drawn for the Taipei Basin. Figure 4 shows the soil liquefaction potential map using P_L . Table 1 shows the proportion of the liquefaction potentials in the analyzed area. It can be seen that an area of 65.6 km² has a high liquefaction potential, which accounts for 25% of the total area; 95.0 km² has a medium liquefaction potential, which accounts for 36% of the total area; and 101.3 km² has a low liquefaction potential, which accounts for 39% of the total area. The area with high liquefaction potential is widely distributed over the middle- and down- stream regions of the Dansue River and Keelung River. In general, the areas furthest from the rivers have little soil liquefaction potential.

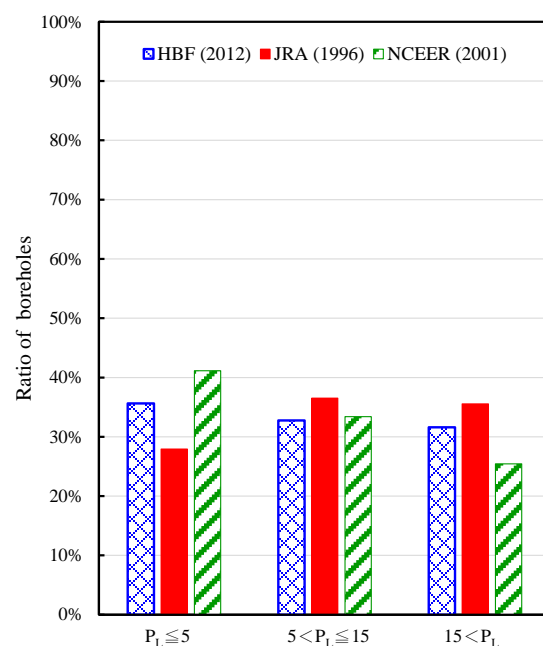


Fig 3. Ratio of the evaluated P_L in each liquefaction risk group.

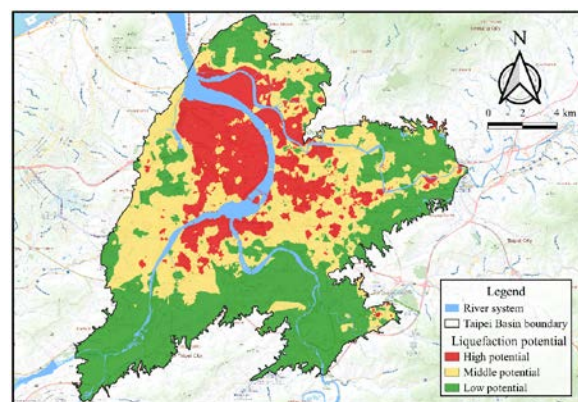


Fig 4. Soil liquefaction potential map of the Taipei Basin.

Table 1. The distribution areas and ratios of the liquefaction potential levels.

Area (km ²)/ proportion (%)		
Low potential	Middle potential	High potential
101.3/39	95.0/36	65.6/25

Conclusions

This study first collected borehole data from different sources and built a reliable borehole database using a data classification and screening process. The database includes 4,876 boreholes for an average of 20 holes per square kilometer throughout the analysis area. In this study, the borehole database was used to produce a refined soil liquefaction potential map, and it is concluded that the results are reliable and can be available for reference.

According to the records from past earthquakes, there were no cases of soil liquefaction in the Taipei Basin. This study collected data from a number of pre-earthquake boreholes. If a strong earthquake in the future induces soil liquefaction, this borehole data in conjunction with the seismic data for the Taipei Basin can be used to verify each simplified procedure for evaluating soil liquefaction and the rationality of the liquefaction potential maps.

The first version of the liquefaction potential map, which had limited reliable data for evaluating soil liquefaction, and the refined soil liquefaction potential map using the HBF method, which had relatively reliable borehole data, are very different. This shows that the accuracy and spatial distribution of boreholes have a significant influence on the results of the analysis. When engineers review the relevant drawings, they should properly understand the accuracy and reliability of the background data.

In the Taipei Basin, most of the surface soil layer belongs to the sixth sublayer of the Sungshan Formation, which is rich in clay and has a thickness of approximately 3-8 m. This implies that the surface of the basin has a layer of non-liquefied materials. According to Ishihara (1985), the non-liquefied surface layer can restrain the manifestation of soil liquefaction at the surface. Considering the surface non-liquefied layer, it is believed that the severe liquefaction area largely decreases, and the area with a low liquefaction potential significantly increases.

Acknowledgements

The authors wish to acknowledge the financial support from the Construction and Planning Agency Ministry of the Interior (CPA/MOI), Taipei City, and New Taipei City. The results and the opinions presented in this study, written or implied, are those of the writers and do not necessarily represent the

opinions and policies of Taipei City.

References

- Hwang, J.H., C.W. Yung, and C.H. Chen (2005). "Simplified methods for assessing liquefaction potential of soil by using hyperbolic cyclic resistance curves," *Sino-geotechnics*, 103, 53-64. (in Chinese)
- Hwang, J.H., C.H. Chen, and C.H. Juang (2012). "Calibrating the model uncertainty of the HBF simplified method for assessing liquefaction potential of soils," *Sino-geotechnics*, 133, 77-86. (in Chinese)
- Ishihara, K. (1985). "Stability of natural deposits during earthquakes," *Proceedings of the 11th International Conference on Soil Mechanics and Foundation Engineering*, 1, A.A. Balkema, Rotterdam, Netherlands, 321-376.
- Iwasaki, T., F. Tatsuoka, K. Tokida, and S. Yasuda (1978). "A practical method for assessing soil liquefaction potential based on case studies at various sites in Japan," *Proceedings of the 2nd international conference on microzonation for safer construction—research and application*, San Francisco, CA, 885-896.
- JRA (Japan Road Association), (1996). *Road bridge specifications: part V Series of earthquake-proof design*. (in Japanese)
- Seed, H.B., K. Tokimatsu, L.F. Harder, and R.M. Chung (1985). "Influence of SPT Procedures in Soil Liquefaction Resistance Evaluation," *J. of Geot. Engr.*, ASCE, 111(12), 1425-1445.
- Youd, T.L., I.M. Idriss, R.D. Andrus, I. Arango, G. Castro, J.T. Christian, R. Dorby, W.D.L. Finn, L.F. Harder Jr, M.E. Hynes, K. Ishihara, J.P. Koester, S.C. Liao, W.F. Marcuson III, G.R. Martin, J.K. Mitchell, Y. Moriwaki, M.S. Power, P.K. Robertson, R.B. Seed, K.H. Stokoe II (2001). "Liquefaction resistance of soils: Summary report from the 1996 NCEER and 1998 NCEER/NSF workshops on evaluation of liquefaction resistance of soils," *Journal of geotechnical and geoenvironmental engineering*, 127(10), 817-833.

Research on Seismogenic and Velocity Structures in the Kaohsiung and Pingtung Areas

Yu-Chih Huang, Yi-Zen Chang², Strong Wen³, Che-Min Lin⁴, Hung-Hao Hsieh², Chih-Wei Chang⁵

黃有志¹、張議仁²、溫士忠³、林哲民⁴、謝宏灝²、張志偉⁵

Abstract

Taiwan is located on a convergent plate boundary in the Circum-Pacific seismic belt and is characterized by intensive seismicity and complex tectonics. In southwest Taiwan, highly active faults and complex seismogenic structures have historically caused serious damage, and this region has always been considered a high seismic hazard zone. The densely populated cities are situated on thick alluvium and are threatened by seismic wave amplification and soil liquefaction. We analyzed the data from broadband seismic networks operated by the National Center for Research on Earthquake Engineering and the National Chung Cheng University in southwest Taiwan and the Hengchun Peninsula. The results show that the seismicity was mainly concentrated at a depth of approximately 20 kilometers in southwest Taiwan. The b values and focal mechanisms were also determined. Since the basic theorem for ambient seismic noise analysis has been verified, we show that the investigations lead to estimates of subsurface velocity structures below the Hengchun Peninsula. The results will be further compared with information for active faults, seismogenic structures, and groundwater distribution. This analysis helps in the understanding of earthquake probabilities and changes in regional stress fields, and permits construction of strong ground motion simulations. The outcomes are particularly important for seismic hazard mitigation, especially in metropolitan areas.

Keywords: southwest Taiwan, Hengchun Peninsula, seismicity, ambient seismic noise, velocity structures

Motivation

Taiwan is located at a complex convergent plate boundary where the Eurasian Plate interacts with the Philippine Sea Plate. This location is characterized by intense seismicity, complex tectonics, and vigorous orogeny (Tsai et al., 1977; Tsai, 1986). According to observations from long-term Global Positioning Systems (GPS), major crustal deformation is concentrated along the suture zones of the Longitudinal Valley and deformation front of the Taiwan orogeny. Active faults and complex seismogenic structures are recognized and have historically caused serious damage in these two areas (Hsu et al., 2009; Ching et al., 2011).

According to the data from historical events, devastating earthquakes occur approximately every 30–40 years in western Taiwan. Therefore, the Taiwan Earthquake Research Center (TEC) and the

Earthquake-Disaster & Risk Evaluation and Management Center (E-DREaM) estimated the probabilistic seismic hazard analysis (PSHA) for active faults and determined possible seismogenic structures (Fig. 1; Wang et al., 2016). This past March, the Central Geological Survey (CGS) also announced the probability of earthquakes with a magnitude greater than 6.5 occurring within a 50-year period for the 33 active faults on land. The results have shown that in addition to the Longitudinal Valley, southwest Taiwan is also a high seismic risk zone.

Additionally, densely populated cities with many unreinforced masonry buildings in the Coastal Plain are situated on thick alluvium and are thus threatened by seismic wave amplification and soil liquefaction (Kuo et al., 2015). Hence, the National Center for Research on Earthquake Engineering (NCREE) has cooperated with the Construction and Planning Agency at the Ministry of the Interior (CPA, MOI) to

¹ Associate Researcher, National Center for Research on Earthquake Engineering

² Assistant Researcher, National Center for Research on Earthquake Engineering

³ Associate Professor, National Chung Cheng University

⁴ Research Fellow, National Center for Research on Earthquake Engineering

⁵ Assistant Technologist, National Center for Research on Earthquake Engineering

promote the reinforcements of public and private buildings in order to prevent extensive disastrous damage from being caused by the next catastrophic earthquake.

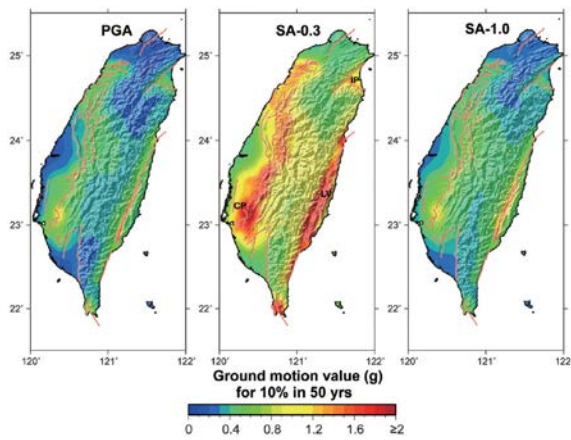


Fig. 1. PHSA maps of the peak ground acceleration (PGA) in Taiwan, pseudo-spectral acceleration (Sa) at 0.3 s (for low-rise buildings), and Sa at 1.0 s (for high-rise buildings) for a 10% probability of exceedance (PoE) over 50 years (Wang et al., 2016).

Seismic Activity in Southwest Taiwan

According to the previous monitoring data from the Southern Taiwan Science Park area by the NCREE, especially intense seismicity was found along the Chukou, Muchilio and Liuchia Faults. Seismic clusters were also located at the north end of the Chishan Fault (Lin et al., 2010). In addition to seismic activity, mud volcano activity has been commonly observed in the Gutingkeng Formation in southwestern Taiwan. The Gutingkeng Formation has a zone of several kilometers thick that is suspected to be a key factor in amplifying ground motion and affecting the distribution of damage (Wen et al., 2020). Mud volcano eruptions may be related to the existence of mud diapirs or may be initiated by nearby seismic activity (Ching et al., 2016).

We analyzed the data from the temporary broadband seismic networks operated by the NCREE and the National Chung Cheng University (CCU), located in southwest Taiwan (Fig. 2). The dataset was routinely collected and processed to monitor seismic activity, determine the focal mechanisms, and determine seismic b values. Figure 3 shows the observed seismicity that was concentrated in the Chishan Transfer Fault Zone (CTFZ) which has a northwest-southeast orientation in the Kaohsiung and Pingtung areas. Relatively few seismic events were detected in the alluvial plains, except for swarms with a magnitude of approximately 3 that occurred offshore near Tainan City. Additionally, Figure 4 shows that large-scale earthquakes were mostly located in areas with low seismic b values.

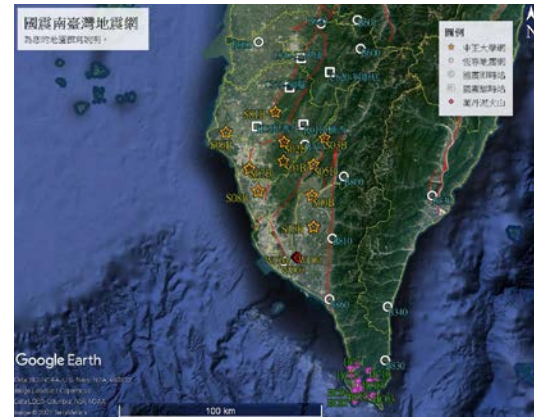


Fig. 2. The broadband seismic networks analyzed in this study, which were operated by the NCREE (white circles, white square, red diamonds, and purple circles) and the CCU (orange stars).

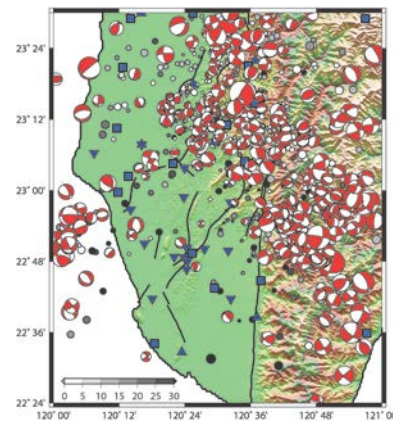


Fig. 3. Observations of seismicity and focal mechanisms in southwest Taiwan.

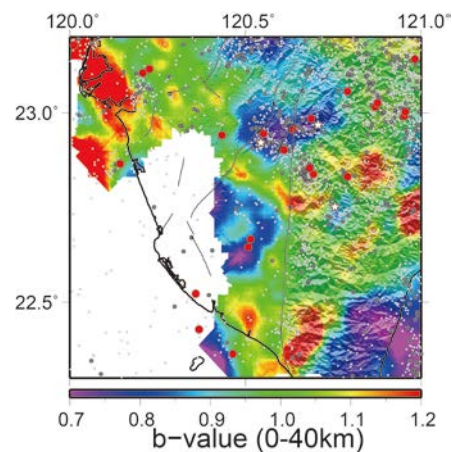


Fig. 4. The seismic b values in the 0-40 km zone of the crust in southwest Taiwan. Large seismic events are marked with red circles ($5 \leq M < 6$) and white stars ($M \geq 6$).

Velocity Structure in Hengchun Peninsula

The Hengchun Peninsula is an accretionary prism formed by plate collision. It is dominated by fold-

thrust belts and is located on the southernmost tip of Taiwan. The Hengchun Fault is an eastward dipping thrust fault, located near the intersection of the foothills and the plains. The fault is generally considered to have a high risk for seismic events. Both ends of the fault are suspected to extend into the sea (Chen et al., 2005).

Since the basic theorem that describes ambient seismic noise analysis has been generally verified, investigations of subsurface velocity structures have provided important insights for various parts of the world. Ambient seismic noise contains diffuse wavefields with passive structural signals, and the signals can be enhanced after long-term stacking. The propagation is similar to that of a surface wave; therefore, it exhibits dispersion properties related to underground velocity structures. Velocity structures can be obtained from the cross-correlation of station pairs with simultaneous and continuous ambient seismic noise signals (Weaver, 2005). The depth range of the velocity structure is positively correlated with the aperture of the seismic network, and its lateral resolution is positively correlated with the density of the path coverage. Figure 5 shows the data analysis procedures of the ambient seismic noise used in this study; it is similar to the procedure reported by Huang et al. (2018).

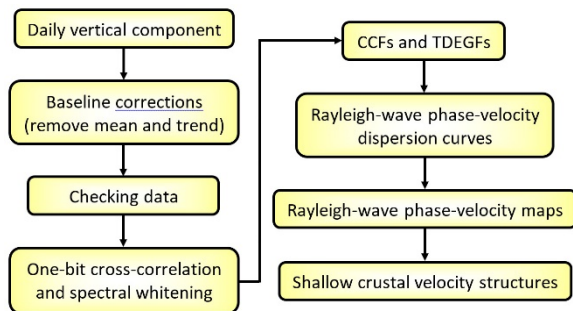


Fig. 5. Data processing of ambient seismic noise analysis in this study.

Recently, a temporary seismic network was operated by the NCREE to monitor the seismic activity in the Hengchun Peninsula. The network used twelve Guralp CMG-6TD broadband seismometers along the Hengchun Fault with an interstation spacing of approximately 5 kilometers. There are eleven more nearby broadband stations, giving a total of twenty-three stations in the network, that could be used to study the velocity structure underneath the peninsula. In 2018, the data qualities of daily vertical components were first assessed and downsampled to 20 Hz. Daily cross-correlation functions (CCFs) were calculated using a 100-s lag time in the 0.5–10-s period band for all station pairs. After the daily CCFs were long-term stacked, relatively stable and representative CCF for each station pair was derived. Figure 6 presents the stacked 0.5–10 s CCFs relative to the interstation distance for all station pairs. The time domain

empirical Green's function (TDEGF) signals propagate with an average apparent velocity of 2.1 km/s. Figure 7 shows the measured 0.5–10 s Rayleigh-wave phase-velocity dispersion curves, including the averages and standard deviations.

Figure 8 displays checkerboard resolution test (CRT) input models for a velocity contrast of 1.5 ± 0.2 km/s at 0.025° and 0.25° anomalies and 0.01° and 0.1° grid spacing, respectively. The recovery results indicate that the regions with high station densities near the Hengchun Fault were recovered with a 0.025° anomaly. In contrast, for other regions with low station densities on the Hengchun Peninsula, CRT could be only recovered with a 0.25° anomaly. Therefore, we applied 0.01° grid spacing for the construction of 1–2 s Rayleigh-wave phase-velocity maps near the Hengchun Fault (Fig. 9). A grid spacing of 0.1° was applied for the construction of 1–10 s Rayleigh-wave phase-velocity maps in other regions of the Hengchun Peninsula (Fig. 10). The predominant lateral velocity variations show dramatic patterns near the Hengchun and Chaochou Faults.

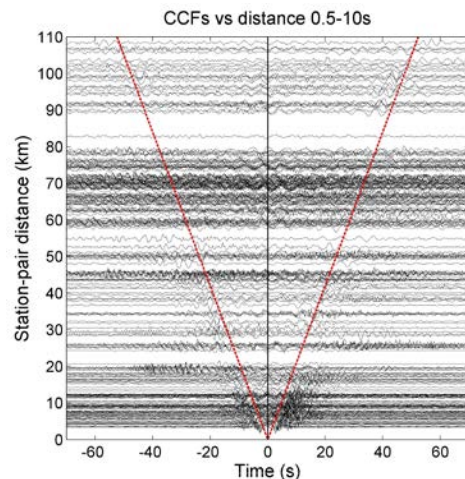


Fig. 6. Stacked 0.5–10 s CCFs versus the interstation distance for all station pairs. Red dashed lines mark the TDEGF signals with an apparent velocity of 2.1 km/s.

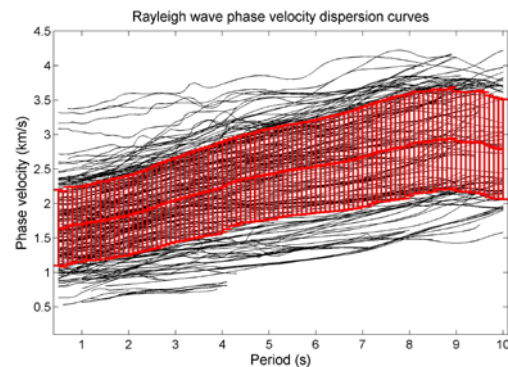


Fig. 7. Measured 0.5–10 s Rayleigh-wave phase-velocity dispersion curves. Black lines indicate individual dispersion curves and the red line represents the average (with standard deviation).

Future Studies

In the near future, we aim to more specifically investigate and integrate the seismic results for southwest Taiwan and the Pingtung Peninsula. We will obtain shallow crustal S-wave velocity structures to provide additional comparisons with the information derived from active faults, seismogenic structures, groundwater distribution, and associated phenomena. Based on the observations of this study, the seismicity of active faults can be evaluated with confidence. The parameters are particularly important for constructing strong ground motion, assessing hazards, and numerically simulating potential seismic risks.

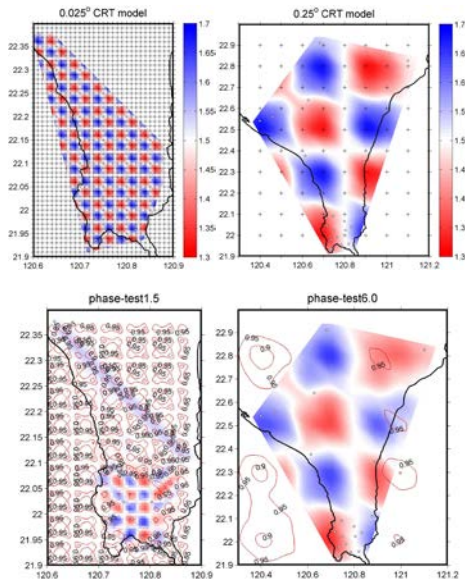


Fig. 8. The 0.025° and 0.25° CRT input models (top) and the recovery results (bottom).

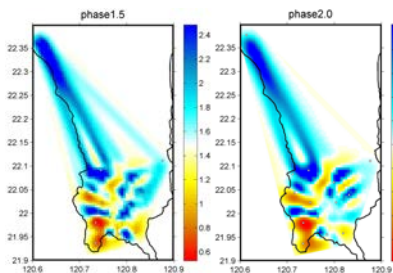


Fig. 9. Rayleigh-wave phase-velocity maps near the Hengchun Fault at periods of 1.5 s and 2.0 s.

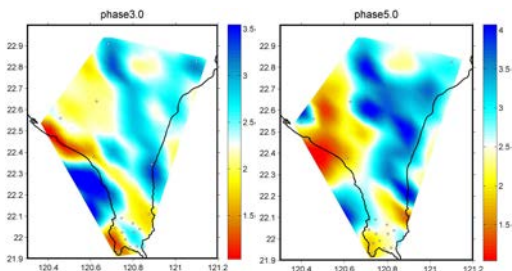


Fig. 10. Rayleigh-wave phase-velocity maps for the Hengchun Peninsula at periods of 3.0 s and 5.0 s.

References

- Chen, W. S., Lee, W. C., Huang, N. W., Yen, I. C., Yang, C. C., Yang, H. C., Chen, Y. C., and Sung, S. H. (2005), "Characteristics of accretionary prism of Hengchun Peninsula, southern Taiwan: Holocene activity of the Hengchun Fault", *Western Pacific Earth. Sci.* 5, 129-154. (in Chinese with English abstract)
- Ching, K. E., Gourley, J. R., Lee, Y. H., Hsu, S. C., Chen, K. H., and Chen, C. L. (2016), "Rapid deformation rates due to development of diapiric anticline in southwestern Taiwan from geodetic observations", *Tectonophysics*. 292, 241-251.
- Ching, K. E., Hsieh, M. L., Johnson, K. M., Chen, K. H., Rau, R. J., and Yang, M. (2011), "Modern vertical deformation rates and mountain building in Taiwan from precise leveling measurements and continuous GPS observations, 2000-2008", *J. Geophys. Res.* 116, B08406.
- Hsu, Y. J., Yu, S. B., Simons, M., Kuo, L. C., and Chen, H. Y. (2009), "Interseismic crustal deformation in the Taiwan plate boundary zone revealed by GPS observations, seismicity, and earthquake focal mechanisms", *Tectonophysics*. 479, 4-18.
- Huang, Y. C., Ohkura, T., Kagiya, T., Yoshikawa, S., and Inoue, H. (2018), "Shallow volcanic reservoirs and pathways beneath the Aso caldera revealed using ambient seismic noise tomography", *Earth Planets Space* 70, 169.
- Kuo, C. H., Chen, C. T., Wen, K. L., Lin, C. M., Hsieh, H. H. (2015), "Investigation of Shallow S-wave Velocity Profile-Western Plain of Taiwan", NCREE-15-005, NCREE, Taipei. (In Chinese)
- Lin, C. M., Chang, T. M., Wen, K. L., Hsieh, H. H., Chen, A. B., Chang, L. C., and Kuo, C. H. (2010), "Micro-Earthquake Monitoring of Science Parks in Taiwan", NCREE-10-020, NCREE, Taipei. (In Chinese)
- Tsai, Y. B. (1986), "Seismotectonics of Taiwan", *Tectonophysics*. 125, 17-37.
- Tsai, Y. B., Teng, T. L., Chiu, J. M., and Liu, H. L. (1977), "Tectonic implications of the seismicity in the Taiwan region", *Mem. Geol. Soc. China* 2, 13-41.
- Wang, Y. J., Chan, C. H., Lee, Y. T., Ma, K. F., Shyu, J. B. H., Rau, R. J., and Cheng, C. T. (2016), "Probabilistic seismic hazard assessment for Taiwan", *Terr. Atmos. Ocean. Sci.* 27, 325-340.
- Weaver, R. L. (2005), "Information from seismic noise", *Science* 307, 1568-1569.
- Wen, Y. Y., Yen, Y. T., Kuo, C. H., and Ching, K. E. (2020), "Source and strong-motion characteristics of two $M > 6$ buried earthquakes in southwest Taiwan", *Earth Planets Space* 72, 188.

Statistical Analysis of Radon Time Series Data from San-Jie Monitoring Station in Northern Taiwan

Vivek Walia¹, Arvind Kumar², Shih-Jung Lin³ and Hsiao-Fen Lee⁴

Abstract

In this study, we statistically examined soil-gas radon time series data from San-Jie monitoring station in northern Taiwan. Pearson correlation method was used to find correlation of radon data with temperature, pressure, humidity, and rainfall. The hourly radon time series data was decomposed into three component series (seasonal, trend, and random) to identify authentic anomalous values. Irregular patterns in hourly and residual radon data could be associated with earthquake events and rainfall. Our preliminary results show that this method is helpful in identifying anomalous radon values, which are suppressed by rainfall or other meteorological parameters.

Keywords: Radon time series, Pearson correlation, Decomposition, Earthquake precursor, northern Taiwan

Introduction

Predicting earthquakes remains a pressing issue in the Earth Sciences. There exists no global model or procedure capable of forecasting the upcoming seismic events. However, possible geochemical precursors have been recorded hours to months before some major earthquakes in different part of the world (Yang et al., 2006; Cicerone et al., 2009; Matsumoto and Koizumi, 2011; Martinelli, 2015; Fu et al., 2017a). Among these precursors, radon (²²²Rn) is recognized as one of the most promising precursor (Walia et al., 2009a, 2009b; Nicoli et al., 2019; Fu et al., 2017b, 2017c). Radon monitoring in both soil and groundwater has shown spatial and temporal variations that can provide clues about geodynamical events.

Soil-gas radon emanation beneath the earth moves towards the surface is also affected by environmental parameters such as rainfall, temperature, relative humidity, and pressure (Kumar et al., 2015; Arora et al., 2017). Radon emanation is thus not only affected by seismic events but also by meteorological parameters, and it is often not possible to distinguish between radon anomalies or irregular patterns caused by seismic events, and those merely caused by climate changes. Some anomalies are hidden, while some are erroneously identified as earthquake precursors. This necessitates the use of statistical and computational tools to minimize the

confounding effects of meteorological parameters on radon emission (Torkar et al., 2010; Kumar et al., 2015; Arora et al., 2017).

We have four radon monitoring stations to study temporal geochemical variations of soil-gas composition. These are located along different faults (Fig.1): in the Hsinchu (HC) (along Hsincheng fault), Tainan (HH) (along Hsinhua Fault), Ilan (at Jaosi (JS)), and Yangmingshan area (SJ) (along Shanchiao fault). In the present study, soil-gas radon time series data from the San-Jie (SJ) monitoring station in northern Taiwan (Fig.1) have been examined statistically. Pearson correlation was employed to find correlations of radon with temperature, pressure, humidity, and rainfall. Radon time series data were decomposed into three component series (seasonal, trend, and random) for analysis.

Methods and Instrumentation

Pearson correlation coefficient:

Pearson's correlation coefficient or Pearson's r is defined in statistics as the measurement of the strength of the relationship between two variables and their association with each other. In simple terms, Pearson's correlation coefficient calculates the effect of change in one variable when the other variable changes.

¹ Research Fellow, National Center for Research on Earthquake Engineering, walia@narlabs.org.tw

² Associate Research Fellow, National Center for Research on Earthquake Engineering, kumar@narlabs.org.tw

³ Assistant Research Fellow, National Center for Research on Earthquake Engineering, sjlin@narlabs.org.tw

⁴ Associate Research Fellow, National Center for Research on Earthquake Engineering, hfllee@narlabs.org.tw

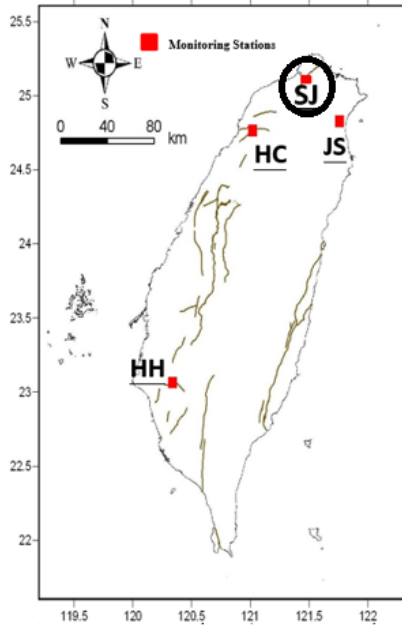


Fig.1. Map showing the location of monitoring stations.

The coefficient takes on values between -1 and 1. It is calculated by the following formula:

$$r = \frac{N\sum xy - \sum x \sum y}{\sqrt{[N\sum x^2 - (\sum x)^2][N\sum y^2 - (\sum y)^2]}} \quad (1)$$

where:

N = number of pairs of scores

$\sum xy$ = sum of the products of paired scores

$\sum x$ = sum of x scores

$\sum y$ = sum of y scores

$\sum x^2$ = sum of squared x scores

$\sum y^2$ = sum of squared y scores

Time Series Decomposition:

Time series data can exhibit a variety of patterns, and it is often helpful to split a time series into several components, each representing an underlying pattern category.

There are three types of time series patterns: trend, seasonality, and cycles. When we decompose a time series into components, we usually combine the trend and cycle into a single trend-cycle component (sometimes called the trend for simplicity). Thus, we think of a time series as comprising three components: a trend-cycle component, a seasonal component, and a remainder component (containing anything else in the time series). If we assume an additive decomposition, then we can write

$$Y_t = S_t + T_t + R_t \quad (2)$$

where Y_t is the data, S_t is the seasonal component, T_t is the trend-cycle component, and R_t is the remainder component, all at period t . Alternatively, a multiplicative decomposition would be written as:

$$Y_t = S_t * T_t * R_t \quad (3)$$

The additive decomposition is the most appropriate if the magnitude of the seasonal fluctuations, or the variation around the trend-cycle, does not vary with the level of the time series. When the variation in the seasonal pattern, or the variation around the trend-cycle, appears to be proportional to the level of the time series, then a multiplicative decomposition is more appropriate. Multiplicative decompositions are common with economic time series. An alternative to using a multiplicative decomposition is to first transform the data until the variation in the series appears to be stable over time, then use an additive decomposition. When a log transformation has been used, this is equivalent to using a multiplicative decomposition because

$$Y_t = S_t * T_t * R_t \text{ is equivalent to:} \\ \text{Log}Y_t = \text{Log}S_t + \text{Log}T_t + \text{Log}R_t.$$

Radon Monitoring:

To carry out the investigation, temporal soil-gas radon composition variations were measured at 15 minute intervals at the above-mentioned continuous earthquake monitoring stations using RAD7 (Durrige, USA). The meteorological and seismic data were procured from the Central Weather Bureau, Taiwan. Rainfall data were only available at hourly resolution, so for the sake of uniformity and compatibility with the hourly rainfall data we reduced 15-minute radon, temperature, humidity, and pressure data to hourly averages.

Results and Discussions

To ensure data continuity and regularity, data intervals with minimal breaks were carefully selected. The selected soil-gas radon concentrations data along with temperature, pressure, humidity, and rainfall from June 01, 2019 to May 31, 2020 are shown in figure 2.

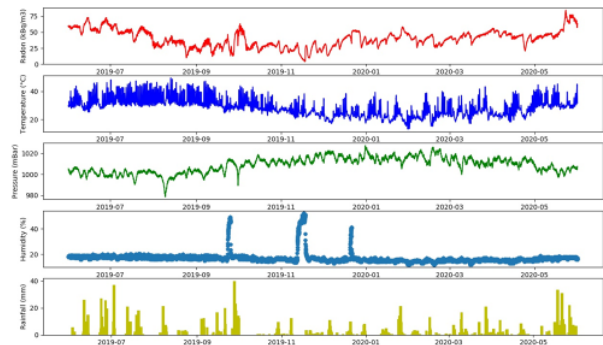


Fig. 2: Recorded soil radon concentrations along with temperature, pressure, humidity, and rainfall at the JS monitoring station from June 01, 2019 to May 31, 2020.

Table 1 and Figure 3 a–d show the calculated Pearson correlation of radon with temperature, pressure, humidity, and rainfall observed in the present study.

The computed overall Pearson's r of radon with temperature, pressure, humidity, and rainfall is 0.11, -0.3, -0.16, and 0.06 respectively.

Table 1: Computed correlation of radon with temperature, pressure, humidity, and rainfall using Pearson's method.

Pearson correlation coefficient			
Radon & Temperature	Radon & Pressure	Radon & Humidity	Radon & Rainfall
0.11	-0.3	-0.16	0.06

The overall Pearson's r is a measure of global synchrony that reduces the relationship between two signals to a single value. However, moment-to-moment local synchrony can also be assessed using Pearson correlation. One approach is to measure the correlation in a small portion of the signal and repeat the process in a rolling window until the entire signal is covered. In our study, we used a rolling window of 30 days. We found that radon was not only controlled by a single but multiple metrological parameters (Fig. 3 a-d). In comparison with the effect of other meteorological parameters, the correlation of exhalation rate with precipitation was found to be significant. We subsequently used Panda's library for the radon time series decomposition, which offers a lot of flexibility when manipulating data and also allows statistical computation using Python. Radon time series decomposition was performed by a polynomial fitting method. We defined a third-order polynomial to fit our data. We first found the overall trend in the radon time series and then subtracted the overall trend component from the original time series. Subsequently, we isolated and subtracted the seasonal component. The remainder is the residual component. Figure 4 shows the decomposition of the radon time series (observed radon, de-trended, de-seasonal, and residual) using the polynomial fitting method. There are irregular patterns in the residual radon data.

To correlate the residual radon data with earthquake recorded in the study area during the observation period, only earthquakes with a local intensity of 1 or greater, depth ≤ 40 km, epicentral distance (R) < 100 km, and D/R ratio ≥ 1 (where $D = 10^{0.43M}$ theoretical strain radii of impending earthquakes; proposed by Dobrovolsky, 1979) were selected. In case a group of earthquakes was close together, we selected the largest earthquake prior to the anomaly (Kumar et al., 2009). The statistical threshold value of gas anomalies or irregular patterns in the radon concentration was fixed at the mean $\pm 2\sigma$. Figure 5 shows hourly radon and residual radon calculated via polynomial fitting, together with seismic events and rainfall that occurred during the study period.

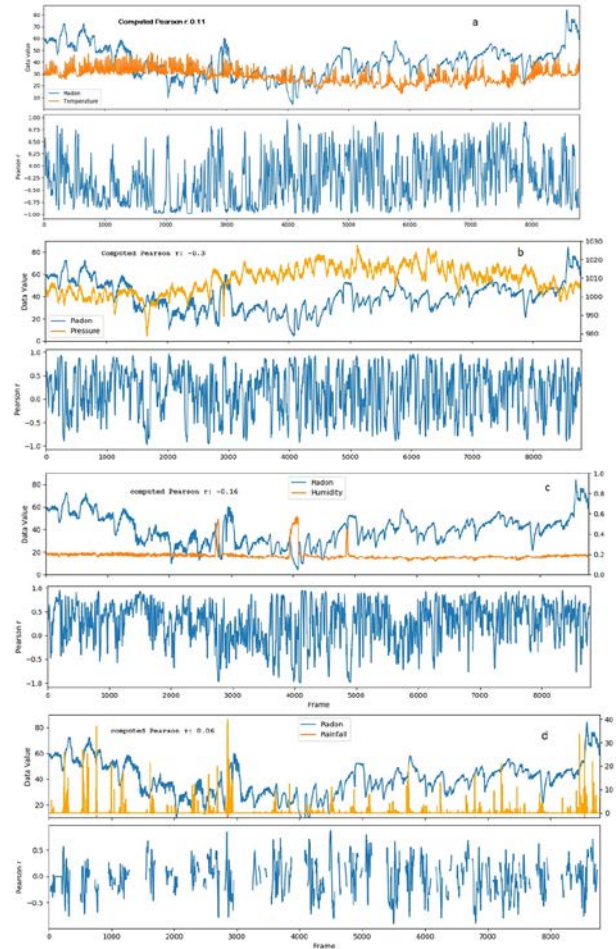


Fig. 3: The computed overall Pearson (r) and moment-to-moment, local synchrony using Pearson correlation, repeated along with a rolling window of 30 days of radon with temperature (a), pressure (b), humidity (c), and rainfall (d).

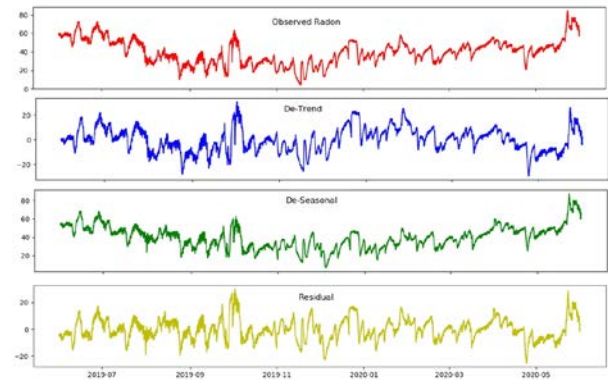


Fig. 4: Decomposition of the radon time series (from top first panel is observed radon, second panel is De-trend, third panel is De-seasonal, and fourth panel is residual) using the polynomial fitting method.

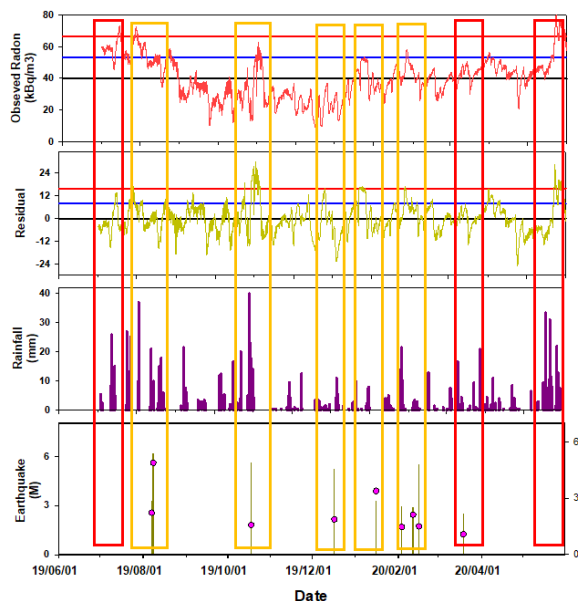


Fig. 5: Correlation of radon anomalies (from top: first panel is hourly radon, second panel is residual from polynomial fitting) with rainfall (third panel) and seismic events (fourth panel) during the study period.

During the study period, eight earthquakes were observed that fit our criteria. Red rectangles indicate that earthquake events which were recorded but no irregular patterns in daily or residual radon data observed and vice versa. Yellow rectangles show earthquake events recorded before and after irregular patterns in hourly or residual radon data. For events 3, 4, and 5, hourly radon data did not show any anomalous values; however residual radon data showed anomalous values before these events. A possible reason for the absence of any anomalous values in hourly radon data is rainfall during this time period, which may have hidden the anomalies.

References

Yang TF, Fu CC, Walia V, Chen CH, Chyi LL, Liu TK, Song SR, Lee M, Lin CW, Lin CC (2006) Seismogeochemical variations in SW Taiwan: multi-parameter automatic gas monitoring results, *Pure Appl Geophys* 163, 693–709.

Cicerone RD, Ebel JE, Britton J (2009). A systematic compilation of earthquake precursors. *Tectonophysics* 476:371–396.

Matsumoto N, Koizumi N (2011) Recent hydrological and geochemical research for earthquake prediction in Japan. *Nat Hazards* 69: 1247-1260.

Martinelli G (2015) Hydrogeological and geochemical precursors of earthquakes: an assessment for possible applications. *Boll di Geofis Teor ed Appl* 56(2): 83-94.

Fu CC, Yang TF, Chen CH, Lee LC, Wu YM, Liu TK, Walia V, Kumar A, Lai TH (2017b) Spatial and

temporal anomalies of soil-gas in northern Taiwan and its tectonic and seismic implications. *J Asian Earth Sci* 149: 64-77.

Walia V, Yang TF, Lin SJ, Hong WL, Fu CC, Wen KL, Chen CH (2009a) Geochemical variation of soil-gas composition for fault and earthquake precursory studies along Hsincheng fault in NW Taiwan. *Appl Radiat Isot* 67:1855-1863.

Walia V, Yang TF, Lin SJ, Hong WL, Fu CC, Wen KL, Chen CH (2009b) Continuous temporal soil-gas composition variations for earthquake precursory studies along Hsincheng and Hsinhua faults in Taiwan. *Radiat Meas* 44:934-939.

Nicoli L, Massimiani G, Segantini S, Zucchetti M (2019) Detection of radon emissions during 2016/2017 earthquakes in abruzzo (Italy). *Fresenius Environ Bull* 28(2): 672-680.

Fu CC, Walia V, Yang TF, Lee LC, Liu TK, Chen CH, Kumar A, Lai TH, Wen KL (2017c). Preseismic anomalies in soil-gas radon associated with 2016 M6.6 Meinong earthquake, Southern Taiwan. *Terr Atmos Ocean Sci* 28(5): 787-798.

Fu CC, Yang TF, Tsai MC, Lee LC, Liu TK, Walia V, Chen CH, Chang WY, Kumar A, Lai TH (2017a) Exploring the relationship between soil degassing and seismic activity by continuous radon monitoring in the Longitudinal Valley of eastern Taiwan. *Chem Geol* 469: 163-175.

Smetanová I, Holý K, Müllerová M, Anna P (2010) The effect of meteorological parameters on radon concentration in borehole air and water. *J Radioanal Nucl Ch* 283: 101-109.

Kumar A, Walia V, Arora BR, Yang TF, Lin SJ, Fu CC, Chen CH, Wen KL (2015) Identifications and removal of diurnal and semi-diurnal variations in radon time-series data of Hsinhua monitoring station in SW Taiwan using singular spectrum analysis. *Nat Hazards* 79(1): 317-330.

Arora BR, Kumar A, Walia V, Yang TF, Fu CC, Liu TK, Wen KL, Chen CH (2017). Cleaning Soil-gas Radon at Hsinchu, Taiwan for Contamination from Meteorological and Hydrological Parameters: A Step Forward to Identify Earthquake Precursors. *J Asian Earth Sci* 149:49-63.

Torkar D, Zmazek B, Vaupotic J, Kobal I (2010) Application of artificial neural networks in simulating radon levels in soil gas. *Chem Geol* 270(1–4), 1–8.

Dobrovolsky IP, Zubkov SI, Miachkin VI (1979). Estimation of the size of earthquake preparation zones. *Pure Appl Geophys* 117:1025–1044.

Kumar A, Singh S, Mahajan S, Bajwa BS, Kalia R, Dhar S (2009) Earthquake precursory studies in Kangra valley of north-west Himalayas, India, with special emphasis on radon emission. *Appl Radiat & Isot* 67:1904–1911.

Draft Revision of Guidelines for Seismic Installation of Suspended Ceiling Systems

Wei-Chung Chen¹, Juin-Fu Chai¹, Fan-Ru Lin¹, George C. Yao²,
Bai-Yi Huang¹, and Wei-Hung Hsu¹

陳威中¹、柴駿甫¹、林凡茹¹、姚昭智²、黃百誼¹、徐瑋鴻¹

Abstract

Many suspended ceilings have been damaged in past earthquakes owing to a lack of proper installation. In 2011, an appendix to the Taiwanese building seismic design code was issued to provide guidance for the seismic installation of suspended ceilings. However, it has been found that ceiling systems implemented according to installation guidelines still collapsed when subjected to near-fault earthquakes with large vertical seismic forces. In addition, practical implementation of the design details has always been a difficult problem, leading to uneven qualities of installed suspended ceilings.

In order to determine the effects and efficiency of the current standard, a series of full-scale shaking table tests of large-area suspended ceilings was conducted in this study. An attempt is made to identify the vertical strength capacity of ceilings and the parameters that influence their capacity based on the test results and the failure mechanisms observed. The experimental results are analyzed and discussed in this paper and a draft revision of the seismic installation guidelines is presented.

Keywords: suspended ceiling systems, seismic installation guideline, shaking table tests, nonstructural components

Introduction

Past earthquakes have conclusively highlighted that losses from damage to nonstructural components can be significant. A suspended ceiling system is among the critical nonstructural components in buildings that can experience major damage during earthquakes and result in endangering the safety of occupants and impeding the continuous operation of buildings and other facilities. In 2011, an appendix referring to ASTM E580-06 and -08 was issued in the Taiwanese building seismic design code. The appendix provides explicit guidance for the seismic installation of suspended ceiling systems. Most construction details are specified for horizontal seismic forces; however, the current standard provides only limited guidance in terms of vertical motions resistance.

In recent years, many studies concerned with suspended ceilings have demonstrated that the

influence of vertical seismic forces should not be underestimated. A ceiling system implemented in accordance with the current standard may not effectively resist vertical motions. This will become more pronounced when subjected to near-fault earthquakes with large vertical seismic forces. The present study examines the seismic performance of suspended ceilings with reference to current construction practice. In order to evaluate and better understand the dynamic response and the vertical strength capacity of the ceiling systems, a series of full-scale shaking table tests of large-area suspended ceilings was conducted to identify the influence of different system conditions and the effects of the protective systems required by the current standard. Based on the test results and the failure mechanisms observed, a draft revision of the seismic installation guidelines is presented in this paper.

¹ National Center for Research on Earthquake Engineering

² Distinguished Professor, National Cheng Kung University

Experimental Setup

Full-scale shaking table tests of suspended ceiling systems were conducted at the National Center for Research on Earthquake Engineering (NCREE) Tainan Laboratory. To effectively simulate the seismic response of a large area ceiling system, an extension steel frame supporting a 10.98 m × 10.98 m ceiling area was mounted on the shaking table (Fig. 1). All test configurations were constructed in compliance with the current standard. Fig. 2 demonstrates the layout of the ceiling system. It is symmetric in layout; red dotted lines show the positions of the lateral bracing assemblies. The plenum height of the ceiling system is 1.58 m.



Fig. 1. The extension steel frame

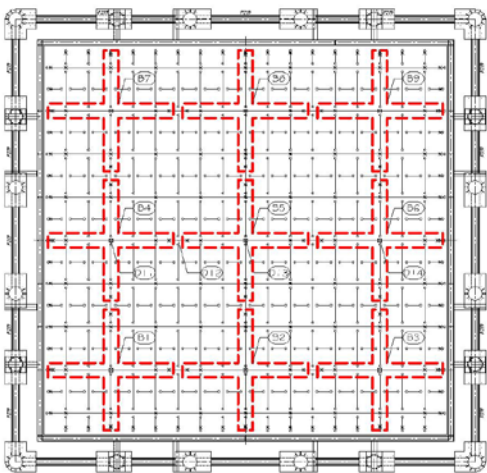


Fig. 2. Typical layout of the ceiling system

To investigate the seismic performance of suspended ceilings subjected to earthquake-induced excitation, the 1999 Chi-Chi Earthquake record (CHY099) and 2018 Hualien Earthquake record (WHABA3) were adopted as the test ground motions. Target motions were generated to match the Required Response Spectrum (RRS) according to ICC-ES-AC156. The RRS was developed based on the Taiwanese design code with a maximum level of $S_{DS} = 1.14g$. The corresponding parameters of $A_{RIG-H} = 1.36g$, $A_{FLX-H} = 1.82g$, $A_{RIG-V} = 0.30g$, and $A_{FLX-V} = 0.76g$ were used as the target spectra for the horizontal

and vertical excitations. To take into account the floor amplification effect of building structures in the vertical direction, an additional vertical excitation three times proportional to the AC156 standard was performed

Experimental Results

Almost no damage to the ceiling specimens was observed in response to horizontal ground excitations, and only a few pop rivets were dislodged at the perimeter-supporting closure. However, several failure patterns occurred once the vertical seismic force was applied, and resulted in consequent global system collapse. The main observations from the tests are as follows:

1. The current standard permits either heavy-duty main runners or intermediate-duty main runners as defined in Specification ASTM C635 to be used in the ceiling systems, with suspension wires spaced at 120 cm or 150 cm. Tests results showed that an intermediate-duty main runner with suspension wires spaced more than 120 cm apart had severely buckled (Fig. 3) once the peak vertical acceleration of the floor motions exceeded 800 gal.
2. Most of the grid splices, latches, and intersection connectors of the main and cross runners could not meet the minimum capacity requirements of 5° offset in the vertical direction. It was observed that the connections of the grid members came apart when suffering large vertical seismic forces. In some cases, cross runner connections even failed prior to the perimeter connections. This might be attributed to the combined axial and shear forces due to multi-directional excitations.
3. Shear failure (Fig. 4) occurred at the connection latches of cross runners when the peak vertical acceleration of the floor motions exceeded 800 gal, and consequently led to ceiling collapse.
4. The load-carrying capacity of cross runners is not specified in the current standard, leading to uneven qualities of suspended ceilings. Test results demonstrated that the capacities of most cross runners on the market were not sufficient and that the grid members deformed when excited by vertical motions
5. Tensile strength between the connection device and the suspension wire was not sufficient for most products prefabricated in factories. The suspension wires were pulled out from the L-shaped connection device when subjected to large vertical excitation (Fig. 5). The failure of a single suspension wire resulted in absence of vertical support and uneven loading distribution of the ceiling grids, which led to a progressive failure of other suspension wires and caused a chaotic global

collapse of the ceiling system.

6. Test results showed that the installation of a lateral bracing assembly may not improve the seismic response of the ceiling system, especially if the system is subjected to vertical excitation. The ineffectiveness of the bracing wire was considered mainly to result from the slack wire effect. Although the bracing wire was installed tightly before each test, it became slacker as experiments progressed. Therefore, the slack wire allowed some lateral movement before it effectively restrained the ceiling. Moreover, the clearance between the end of the ceiling grid to the boundary was only 12 mm, which impeded ideal performance of the wire before the ceiling impacted the boundary.



Fig. 3. Collapse of the ceiling system



Fig. 4. Shear failure of cross runner connection



Fig. 5. Failure of the suspension wire

Draft Revision

This paper aims to determine not only the seismic performance of suspended ceiling systems, but also the efficiency of the current standard. A draft revision of the seismic installation guidelines is presented below.

1. Suspended Ceiling Components

- Only heavy-duty main runners as defined in Specification ASTM C635 and tested per Test Methods ASTM E3090 shall be used.
- The load-carrying capacity of cross runners shall not be less than 18.5 kgf/m when tested per Test Methods ASTM E3090. Cross runners shall be capable of carrying the load specified by the manufacturer without exceeding the maximum allowable deflection equal to 1/360 of their span.
- The main runners and cross runners of the ceiling system and their splices, intersection connectors, and expansion devices shall be designed and constructed to carry a mean ultimate test load of not less than 80 kgf in compression and in tension when tested per Test Methods ASTM E3090. The tensile test shall allow for a 5° offset of the connection in any direction. The connectors at splices and intersections shall be of the mechanical interlocking type.

2. Suspended Ceiling Application

- Main runner or cross runner ends, or both, shall be attached to the perimeter on two adjacent walls (Fig. 6, A-A, B-B). A clearance of 1.2 cm shall be maintained between the main runner and cross runner ends and the perimeter members on the two opposite walls (Fig. 6, C-C, D-D). On the walls where the terminal end runners are not fixed to the perimeter supporting closure, allow for 1.2 cm axial movement.
- Terminal ends of main runners and cross runners not attached to the perimeter closure angle or channel shall be prevented from spreading.
- Suspended ceiling systems shall have positively connected stabilizer bars or mechanically connected cross runners at a maximum spacing of 120 cm perpendicular to the main runners. Stabilization shall occur within 60 cm of each wall.

3. Suspension Wire Application

- Suspension wires of galvanized, soft-annealed, mild steel wire shall not be lighter than No. 12-gauge (2.70 mm) and spaced at 120 cm on center along each main runner.
- The terminal end of each cross runner and main runner shall be supported independently, a

maximum of 20 cm from each wall or ceiling discontinuity with No. 12-gauge (2.70 mm) wire or approved wall support.

- Each vertical wire shall be attached to the ceiling suspension member and to the support above such that the wire loops are tightly wrapped and sharply bent to prevent any vertical movement or rotation of the member within the loops. The wire must be wrapped around itself a minimum of three full turns (360° each) within a 7.5 cm length. Connection devices to the supporting construction shall be tested under tension and demonstrate a mean ultimate load of 90 kgf.
- Suspension wires shall not hang more than one in six out of plumb unless counter-sloping wires are provided.

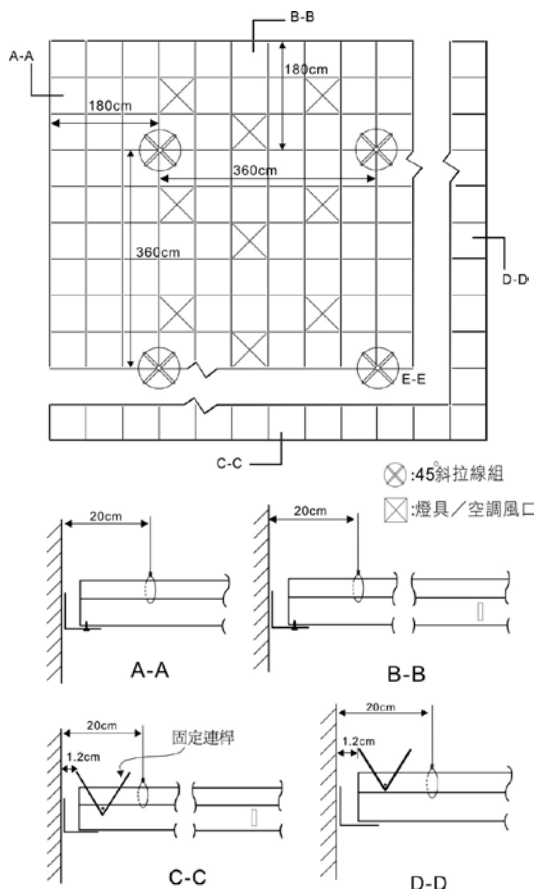


Fig. 6. Perimeter details of ceiling systems

4. Lateral Bracing Assembly Application

- Lateral bracing assembly is required for all ceiling areas greater than 100 m². Horizontal restraints shall be effected by four No. 12-gauge (2.70 mm) wires secured to the main runner within 50 cm of the cross runner intersection and splayed 90° from each other at an angle not exceeding 45° from the plane of the ceiling. These horizontal restraint points shall be placed 360 cm on center in both directions with the first point within 180 cm from

each wall.

- Bracing wires shall be attached to the grid and to the structure in such a manner that they can support a load of not less than 115 kgf when tested per Test Methods ASTM E3090.

Conclusions

Based on the test results, a suspended ceiling system constructed in accordance with the current standard displayed good resistance to horizontal forces but became more vulnerable when subjected to vertical forces. The failure patterns indicated that the vertical motions had substantial influence on the seismic performance of ceiling systems, rendering a revision of the current standard more important.

It was also observed that the lateral bracing assembly may not adequately resist the lateral force due to construction problems. The splayed wire bore only a small portion of the lateral inertial force, and most of the inertial force still acted on the ceiling members. However, it is unclear whether or not a bracing wire is unnecessary. Assuming a large suspended ceiling separates into several floating parts during an earthquake, it is believed that the bracing wire can help restrain the excess movement of the ceiling and reduce the possibility of further damage. The draft revisions in this paper still maintain required lateral bracing assemblies for large area suspended ceilings.

References

- Construction and Planning Agency, MOI, (2011). "Seismic Design Specifications and Commentary of Buildings", Taiwan.
- American Society of Testing and Materials. (2007). "Standard Specification for the Manufacture, Performance, and Testing of Metal Suspension Systems for Acoustical Tile and Lay-in Panel Ceilings" *ASTM C635-07*, ASTM International, PA, USA.
- American Society of Testing and Materials. (2020). "Standard Test Methods for Strength Properties of Metal Ceiling Suspension Systems" *ASTM E3090-20*, ASTM International, PA, USA.
- American Society of Testing and Materials. (2020). "Standard Practice for Installation of Ceiling Suspension Systems for Acoustical Tile and lay-in Panels in Areas Subject to Earthquake Ground Motions" *ASTM E580-20*, ASTM International, PA, USA.

Effects of Near-Fault Ground Motion on Seismic Isolated Buildings and Corresponding Design Strategies

Wang-Chuen Lin¹, Jenn-Shin Hwang², Cho-Yen Yang³, Chung-Han Yu⁴
and Shiang-Jung Wang⁵

林旺春¹、黃震興²、楊卓諺³、游忠翰⁴、汪向榮⁵

Abstract

The concept of seismic isolation design is an accepted and effective method for the seismic mitigation of urban structures. However, in Taiwan, an earthquake prone island, many sites are located in near-fault zones. The recorded seismic waves show near-fault characteristics, such as velocity pulses and displacement pulses. These seismic waves may cause excessive displacement demands on the isolation system and transmit significant acceleration to the superstructure. Consequently, the design of seismically isolated structures located in near-fault areas is challenging.

In this study, the superstructure is modeled as a single degree of freedom system such that the entire structure, including the isolation system, is modeled as a two degree of freedom system. The isolation system is composed of bilinear hysteretic bearings and viscous dampers. The superstructure is assumed to remain elastic during ground shaking. The system is designed using the response spectra of measured near-fault ground motions. Inelastic dynamic analysis is used to investigate the effectiveness of the isolation design. Both the maximum displacement and transmitted force of the isolation system subject to near-fault and far-field ground motions are examined. Further, the responses of the superstructure are discussed. It is concluded that isolation design considering only near-fault ground motions will dramatically reduce isolation effectiveness against far-field earthquakes. Nevertheless, incorporating linear viscous dampers is recommended for future research to meet design goals.

Keywords: Near-fault ground motion; Seismic isolated system; Lead-rubber bearing; Viscous damper.

Introduction

Seismic isolation technology has been regarded as one of the most effective strategies to enhance the safety and functionality of buildings, infrastructure, and equipment. However, seismically isolated structures located on soft ground, such as the Taipei Basin, and in near-fault areas are challenging. Because the recorded seismic waves of soft ground and basin have a long period, they cause a large displacement response of the isolation system. The recorded seismic waves of near-fault ground motions have marked characteristics, such as velocity and displacement pulses. The main

difference between near-fault and far-field ground motions is that the velocity of a near-fault ground motion is accompanied by pulses with long periods (Somerville et al., 1997). These seismic waves for near-fault ground motions may cause excessive displacement demands on the isolation system and transmit significant acceleration to the superstructure (Kasalanati and Constantinou, 1999; Kelly, 1999).

In 2007, Baker (2007) proposed a method based on wavelet analysis to identify quantitatively velocity pulses of near-fault ground motions. In 2014, Shahi and Baker (2014) developed a more reliable method by

¹ Associate Researcher, National Center for Research on Earthquake Engineering, wclin@ncree.narl.org.tw

² Courtesy Researcher, National Center for Research on Earthquake Engineering, jshwang@ncree.narl.org.tw

³ Associate Researcher, National Center for Research on Earthquake Engineering, cyyang@ncree.narl.org.tw

⁴ Assistant Researcher, National Center for Research on Earthquake Engineering, chyu@ncree.narl.org.tw

⁵ Courtesy Researcher, National Center for Research on Earthquake Engineering, sjwang@ncree.narl.org.tw

optimizing criteria to extract the largest velocity pulse from any given near-fault ground motion. The proposed algorithm was then used to classify each record in the NGA-West2 database, with 244 near-fault ground motion records identified. These records have since been used as the foundation for studying the effects of near-fault ground motions on civil infrastructure.

For the purpose of designing an isolation system for near-fault ground motion, isolation buildings developed with a two-degree-of-freedom model were designed using the response spectra of measured near-fault ground motions and an inelastic dynamic analysis was used to investigate isolation design effectiveness. It is concluded that the isolation design adopting linear viscous dampers within the isolation system considering only near-fault ground motion will dramatically reduce isolation effectiveness against far-field and near-fault earthquakes.

Selection of ground motion

To investigate the characteristics of near-fault ground motion, this study used the following two approaches for determining near-fault earthquakes with significant maximum incremental velocity. (1) When two evident velocity values passing through zero do not show any clear peak values, the recorded earthquake histories possess clear maximum incremental velocity. Otherwise, the velocity histories do not pass through zero value between two evident peak values and the peak values show the same direction. (2) When between two evident peak values, velocity histories passing through zero value with clear peak values demonstrate a clear maximum incremental velocity. As stated above, this study also adopted the method from Shahi and Baker (2014) to define near-fault earthquakes for analysis and discussion.

Table 1. Details on the selected near-fault ground motion.

Station	Direction	PGA (g)	PGV (cm/s)	Incremental Velocity (cm/s)	Duration (s)
TCU052	EW	0.36	174.6	260.72	33.705–35.31
HWA014	EW	0.32	146.5	251.83	25–26.145
HWA019	EW	0.41	138.4	220.54	27.29–28.47
MND016	EW	0.31	133.6	212.11	26.52–27.815

Table 2. Details on the selected far-field ground motion.

Station	Direction	PGA (g)	PGV (cm/s)
El Centro	NS	0.28	30.93

Based on the selected approaches, four recorded near-fault earthquake histories were selected, including the TCU052 of strong ground motion station in the E-W direction during the 1999 Taiwan Chi-Chi Earthquake and HWA014, HWA019, and MND016 of strong ground motion stations in the E-W direction during the 2018 Hualien Earthquake (see Table 1). One far-field

1940 El Centro earthquake history was selected, namely the spectrum-compatible earthquake compatible with the seismic zone of Puli District, Taichung City, from the Seismic Design Specifications and Commentary of Buildings (Construction and Planning Agency, MOI, 2011), as shown in Table 2.

Proposed procedure for the isolation system design

A simple linear two-degree-of-freedom model (Kelly, 1990) was used to understand the behavior of isolation buildings with linear springs and linear viscous damping. The parameters of the model are shown in Figure 1. m_b and K_b are the base mass and stiffness of the isolation system, respectively, m_s and K_s are the superstructure mass and stiffness of isolation buildings, respectively, r_m is the mass ratio (m_s/m_b), u_g is the absolute displacement of ground, u_b is the absolute displacement of the base slab of the isolation system, u_s is the absolute displacement of the top of isolation buildings, D_b is the relative displacement of the base slab of the isolation system with respect to the ground ($u_b - u_g$), D_s is the relative displacement of the top of isolation buildings with respect to the base slab of the isolation system ($u_s - u_b$), and α_b and α_s are the absolute acceleration of the base slab of the isolation system and the top of isolation buildings, respectively.

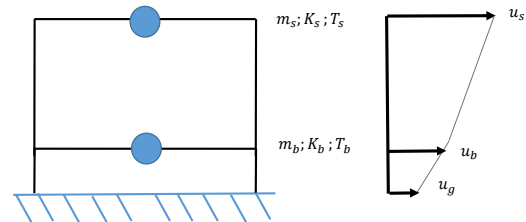


Figure 1. Two-degree-of-freedom model.

As shown in Figure 2, the proposed design procedure provided for the isolation system is composed of lead-rubber bearings and viscous dampers. Based on a structural weight W above the isolation interface of 500 tf and using HWA019 of strong ground motion stations in the E-W direction during the 2018 Hualien Earthquake, a characteristic strength Q_d of the lead-rubber bearings of $0.05W$ and a 40% effective damping ratio ζ_e of the isolation system were used as an example. The calculation formulae and detailed procedure are as follows.

1. Assuming the natural period of the superstructure T_s is 1 s and the strain hardening ratio α_b is 0.05, the isolation system parameters can be calculated as follows:

$$K_u = \frac{4\pi^2 W}{T_s^2 g} = 4.024W \quad (1)$$

$$K_d = \alpha_b \times K_u = 0.2012W \quad (2)$$

$$F_y = \frac{Q_d}{(1-\alpha_b)} = 0.053W \quad (3)$$

$$D_y = \frac{F_y}{K_u} = 0.013 \text{ m} \quad (4)$$

2. The 5% damped acceleration response spectra of the HWA019 of recorded earthquake history was used for design and analysis.
3. An effective damping ratio ξ_e of 40% and a design displacement D_d of 0.3 m were assumed in the first iteration by adopting an iterative method.
4. The maximum force F_d at the corresponding design displacement D_d , the effective stiffness K_{eff} , the effective period T_{eff} , the effective damping ratio ξ_b of lead-rubber bearings, and the design spectral response acceleration S_{ad} can be calculated as follows:

$$F_d = Q_d + K_d \times D_d = 0.11W \quad (5)$$

$$K_{eff} = \frac{F_d^+ + F_d^-}{D_d^+ + D_d^-} = 0.37W \quad (6)$$

$$T_{eff} = 2\pi \sqrt{\frac{W}{K_{eff}g}} = 3.31 \text{ s} \quad (7)$$

$$S_{ad} = 0.61 \quad (8)$$

$$\xi_b = \frac{4Q_d(D_d - D_y)}{2\pi E_s} = 0.276 \quad (9)$$

5. Based on the effective damping ratio ξ_e , the damping factor B_1 can be obtained and the new design displacement D_d can be computed using an iterative method. By repeating Step 4 and 5 as necessary, a more accurate design displacement D_d can be converged upon and obtained.

$$D_d = \frac{g}{4\pi^2 B_1} S_{ad} T_{eff}^2 = 1.08 \text{ m} \quad (10)$$

6. Verifying the design displacement D_d as a practical design value, the updated maximum force F_d at the corresponding design displacement can be calculated. If the design displacement D_d is not reasonable, the design steps should be restarted from Step 3.

7. Assuming that the nonlinear exponent α_d of the nonlinear viscous dampers is 0.3, the damping coefficient C_d can be computed as follows:

$$C_d = \frac{(2\pi)^{3-\alpha_d} T_{eff}^{\alpha_d-2} \xi_d W}{\lambda D_d^{\alpha_d-1} g} \text{ m} = 48.9 \text{ tf} \cdot (\text{s/m})^{0.3} \quad (11)$$

8. The maximum transmitted force of the isolation system can be computed as follows:

$$F_{max} = Q_d + K_d D_d \cos \delta + C_d (2\pi / T_e)^\alpha D_d^\alpha \sin^\alpha \delta \quad (12)$$

$$\frac{\sin^{2-\alpha} \delta}{\cos \delta} = \frac{2\pi \xi_d K_{eff}}{K_d \lambda} \quad (13)$$

The final parameters of the isolation system can be obtained by an iterative method.

Therefore, the characteristic strength Q_d for 0.03W and 0.05W are defined in this study. Moreover, the isolation system is composed of bilinear hysteretic bearings and a viscous damper with a varying damping exponent α , including thenonlinear and linear viscous damper.

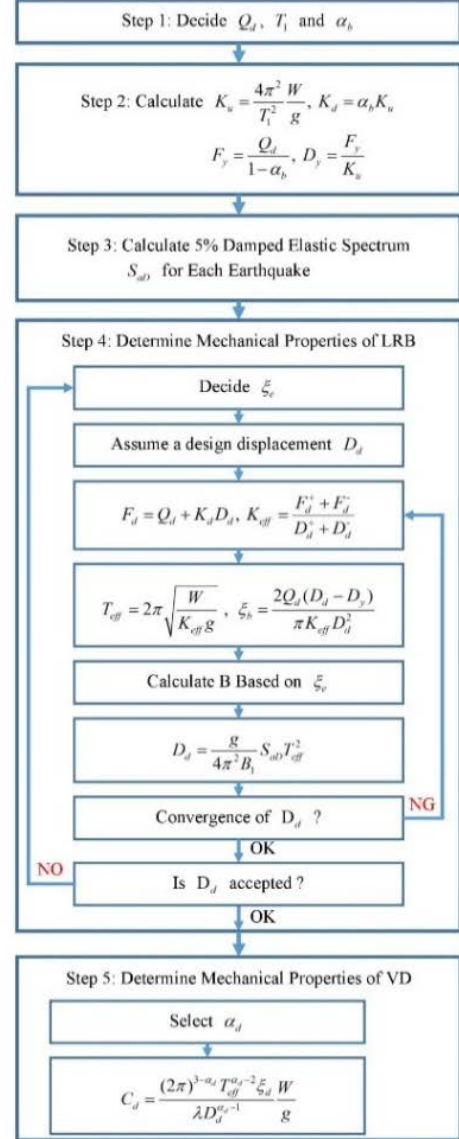


Figure 2. Proposed procedure for the isolation system design composed of lead-rubber bearings and viscous dampers.

Analytical study and discussion

Table 3 and 4 show the parameters and dynamic responses of the isolation system and superstructure assuming a mass ratio r_m of 10 and a superstructure natural period T_s of 0.5 combined with the results of the HWA019 of strong ground motion station and the spectrum-compatible earthquake of El Centro

earthquake history as an example.

Under a total effective damping ratio of 30% and a damping exponent of 0.3, it was revealed that the isolation system could yield sooner and generate larger displacement and less acceleration response when the characteristic strength is reduced from 0.05W to 0.03W. For example, the maximum displacement of the isolation system increased from 83 cm to 87 cm, the acceleration responses of the superstructure reduced from 0.277 g to 0.272 g for near-fault ground motions. However, the results for the near-fault and far-field earthquakes show that the acceleration responses of the superstructure decreased slightly due to the seismic isolation design, with the effectiveness of the design still quite limited.

Under a total effective damping ratio of 30% and characteristic strength of 0.03W, the results for the HWA019 strong ground motion station show that the isolation system with linear viscous dampers can effectively suppress the maximum displacement responses and transmitted force of the isolation system, as well as transmitting an acceptable acceleration to the superstructure. Therefore, an isolation system with linear viscous dampers can enhance isolation design effectiveness better than with nonlinear viscous dampers with a damping exponent less than 1. Although the force of linear dampers is increased, it can be considered a viable design strategy. Moreover, the seismic responses of the isolation system composed of lead-rubber bearings and linear viscous dampers can still provide an effective seismic isolation design for a far-field earthquake.

Table 3. Design results for the recorded earthquake histories of HWA019.

Q_d (W)	ξ_e (%)	α	D_b (m)	D_s (m)	a_b (g)	a_s (g)	F_{VD} (W)	F_{LRB} (W)	F_{max} (W)
0.03W			1.318	0.019	0.489	0.302		0.295	0.300
	30	0.3	0.870	0.016	0.325	0.272	0.088	0.205	0.273
	40	0.3	0.704	0.016	0.311	0.264	0.119	0.172	0.264
	50	0.3	0.562	0.016	0.284	0.261	0.147	0.143	0.261
	30	1.0	0.814	0.014	0.244	0.246	0.122	0.193	0.246
	40	1.0	0.680	0.014	0.253	0.250	0.160	0.166	0.248
0.05W	50	1.0	0.580	0.016	0.265	0.271	0.190	0.146	0.270
			1.250	0.019	0.440	0.310		0.300	0.300
	30	0.3	0.832	0.017	0.330	0.277	0.076	0.220	0.280
	40	0.3	0.650	0.016	0.323	0.267	0.110	0.180	0.270
			0.495	0.016	0.276	0.265	0.139	0.150	0.260

Table 4. Design results for recorded earthquake histories of El Centro.

Q_d (W)	ξ_e (%)	α	D_b (m)	D_s (m)	a_b (g)	a_s (g)	F_{VD} (W)	F_{LRB} (W)	F_{max} (W)
0.03W			0.130	0.004	0.163	0.060		0.056	0.056
	30	0.3	0.060	0.006	0.241	0.096	0.049	0.042	0.091
	40	0.3	0.043	0.007	0.199	0.112	0.068	0.039	0.105
	50	0.3	0.036	0.008	0.227	0.130	0.088	0.036	0.120
	30	1.0	0.109	0.004	0.151	0.069	0.023	0.052	0.065
	40	1.0	0.099	0.005	0.153	0.080	0.032	0.050	0.075
0.05W	50	1.0	0.093	0.005	0.156	0.089	0.039	0.049	0.083
			0.126	0.0048	0.155	0.081		0.075	0.075
	30	0.3	0.055	0.0065	0.225	0.108	0.043	0.061	0.105
	40	0.3	0.039	0.0078	0.222	0.128	0.065	0.058	0.118
			0.032	0.0088	0.226	0.146	0.086	0.056	0.130

Conclusions

The results show that the isolation system composed of lead-rubber bearings and viscous dampers can not only effectively suppress extremely large displacement of the isolation system subjected to near-fault ground motions, but also achieve acceptable maximum displacement responses for practical applications. Further, an isolation design considering only near-fault ground motion will dramatically reduce isolation effectiveness against far-field earthquakes.

Therefore, in order to achieve the expected seismic-resistance performance provided by the isolation design for structures located in near-fault areas, the adoption of linear viscous dampers within the isolation system and the use of a smaller characteristic strength and larger effective damping ratio is suggested to more rapidly reduce earthquake effects and achieve controllable maximum displacement responses and an acceleration responses of the superstructure subject to near-fault and far-field ground motions.

References

- Jack W. Baker, "Quantitative Classification of Near-Fault Ground Motions Using Wavelet Analysis," Bulletin of the Seismological Society of America, Vol. 97, No. 5, pp. 1486–1501, 2007.
- Kasalanati, A. and Constantinou, M. C., Experimental Study of Bridge Elastomeric and Other Isolation and Energy Dissipation Systems with Emphasis on Uplift Prevention and High Velocity Near-Source Seismic Excitation, MCEER Report, MCEER-99-004, SUNY, Buffalo, 1999.
- Kelly, J. M. "The role of damping in seismic isolation," Earthquake Engineering & Structural Dynamics, Vol. 28 Issue 1, pp. 3-20, 1999
- Shahi, S. K., and Baker, J. W. (2014), "An Efficient Algorithm to Identify Strong-Velocity Pulses in Multicomponent Ground Motions." Bulletin of the Seismological Society of America, Vol. 104, No.5, pp. 2456-2466.
- Somerville, P. G., N. F. Smith, R. W. Graves, and N. A. Abrahamson. "Modification of empirical strong ground motion attenuation relations to include the amplitude and duration effects of rupture directivity," Seismological. Research. Letters. 68, no. 1, 199–222. 1997.
- Construction and Planning Agency, Ministry of the Interior, "Seismic Design Specifications and Commentary of Buildings", 2011.
- Kelly, J.M. "Base Isolation: Linear Theory and Design." Earthquake Spectra, Volume 6, No 2, 1990.

Shaking Table Test of a Unidirectional Shear Box

Hsuan-Chih Yang¹, Kuan-Yu Chen², Wei-Kuang Chang³, Shang-Yi Hsu⁴, Che-Yu Chang⁵

楊炫智¹、陳冠羽²、張為光³、許尚逸⁴、張哲瑜⁵

Abstract

Domestic and international earthquake case studies and research have revealed that when an earthquake occurs, fault movement, ground motion, soil liquefaction, and its derivative phenomena can jeopardize life-sustaining pipelines that are either in the ground or on the surface. The domestic practical application of pipeline risk assessments often focus on leakage and deterioration management projects and seldom consider earthquake issues. Furthermore, research on pipelines affected by earthquakes is mostly limited to theoretical analyses and risk assessments. Therefore, considering that an underground pipeline has an exceedingly small diameter-axis ratio, to design for existing facilities, a one-dimensional shear box was modified to explore the effects of soil liquefaction or subsidence on the pipeline. To confirm the effectiveness of the one-dimensional shear box, a frequency characteristic analysis and seismic input analysis were performed on a shaking table, and the ground response analysis was performed using the DEEPSOIL software simultaneously. The one-dimensional shear box test results were confirmed from the ground response. The results of the reaction analysis are consistent, which is sufficient to verify the reliability of the test equipment, and the behavior of the soil interaction with the pipeline structure can be discussed later.

Keywords: unidirectional shear box, DEEPSOIL, site response analysis

1. Introduction

Taiwan is located at the junction of the Eurasian Plate and the Philippine Plate, also known as the Pacific Rim Seismic Belt. According to the active fault data for Taiwan released by the Central Geological Survey in 2012, there are currently 33 type 1 and 2 active faults. Earthquakes, which occur due to fault dislocation, are often accompanied by large social effects and economic losses.

Many important trunk pipelines are buried in the ground due to limitations such as site location or environmental terrain. Although pipelines are designed to avoid passing by geologically fragile areas, pipelines still must pass through certain faults zones, areas with a potential for soil liquefaction, landslide sensitive areas, and other high-risk areas. When an earthquake occurs, fault movement, ground motion, soil liquefaction, and its derivative phenomena will endanger the life-sustaining pipelines set in the ground or on the surface.

In domestic and international earthquake disaster

cases, the damage to underground life-sustaining pipelines caused by earthquakes can be divided into three types: fault dislocation, soil liquefaction, and landslides. When fault dislocation occurs, the underground pipelines passing by the fault will be sheared, pulled, or squeezed, leading to cracks, wrinkles, or joint damage. The pipeline damage will a spill, and if the content is oil, secondary disasters such as fires and serious environmental pollution can occur.

The failure mode of the pipeline caused by the earthquake can be divided into either pipeline fracture (tension, shear, bending), pipeline joint detachment, or pipeline buckling. Pipeline fracture or joint detachment is due to large deformations in the ground surface. The pipeline in the undeformed area is tightly constrained by the soil, and the pipe is pulled, sheared, or loses support where there is excessive soil deformation, which is near violent earthquake zones, faults, and areas with potential landslides or liquefaction.

Pipeline buckling occurs when there is a weak interlayer or liquefied area along the pipeline path. In

¹ Associate Research Fellow, National Center for Research on Earthquake Engineering

² Research Assistant, National Center for Research on Earthquake Engineering

³ Associate Research Fellow, National Center for Research on Earthquake Engineering

⁴ Associate Research Fellow, National Center for Research on Earthquake Engineering

⁵ Assistant Research Fellow, National Center for Research on Earthquake Engineering

this situation, the pipeline can be pushed on both sides in the weak medium area, resulting in buckling. Statistics on pipeline damage after earthquakes in the U.S. show that the extent of pipeline damage is proportional to maximum surface velocity.

The seismic behavior and response of underground pipelines is an important subject. Cornell University in the United States has designed a large laboratory and equipment for researching pipeline crossing faults. However, domestic research on pipelines affected by earthquakes is mostly limited to theoretical analysis and risk assessment. In practical applications, pipeline risk assessments often focus on leakage, ageing, and deterioration management projects. There is minimal research focus on earthquake issues, which is an area for improvement.

In this study, a unidirectional shear box suitable for pipeline testing with length effects was prepared. The unidirectional shear box was used for an in-depth study of the dynamic mechanical behavior of underground pipelines. In order to confirm the characteristic and capacity of the unidirectional shear box, the box was placed on a shaking table for frequency characteristics and seismic input analysis and compared with the results of a ground response analysis.

2. Design of the Unidirectional Shear Box

In the present study, an existing fixed sand box was selected for design modifications. Figure 1 shows the fixed sand box with an internal space of 440 cm x 130 cm x 112 cm (length x width x height), which is used as the unidirectional shear box. The outer box improves the overall rigidity and provides waterproof sealing. The main focus of this design was to effectively use the equipment for pipeline tests, so the design was divided into one main shaft and two target tests.



Figure 1. The shear box with and without sand.

The main purpose of using the unidirectional shear box by applying the sliding layer is to simulate the effect of a semi-infinite domain, which is essential for simulating ground motions and seismic responses. The unidirectional shear box could be used for pipeline

axial and lateral tests. Pipeline axial tests study the impact of soil liquefaction or subsidence on the pipeline. Pipeline lateral tests study the impact of fault displacement on the pipeline.

Considering the internal space of the fixed sand box and the test requirements, in the first stage, ten sliding layers were added to the fixed sand box, each with a height of 8 cm and an interval between layers of 2 cm. The sliding distance was ± 35 cm, so the internal space can reach 360 cm x 100 cm x 110 cm (length x width x height) and can accommodate a 3-m long pipeline. The second stage extended upward based on the same design. The total internal space can reach 360 cm x 100 cm x 260 cm (length x width x height), with a total of twenty-five sliding layers, which can accommodate 3-m (axial) or 2.5-m long pipelines (lateral).

3. Unidirectional Shear Box Testing

In order to verify the integrity of the construction of the unidirectional shear box and its performance in simulating a semi-infinite domain, the box was filled with quartz sand for a shaking table test to compare the sliding layer motion with the performance of the shear box under different conditions.

The test process included installing a rubber mold (within the empty box), loading loose standard quartz sand (without water), adding water to simulate the presence of groundwater, and embedding acceleration gages on the sliding layer frame and the middle and surface of the soil for comparison purposes.

A white noise signal, a sweep signal, and the TCU-084 seismic record were used as input motions for the shaking table test, with the x-direction as the input direction. After each seismic record input, the frequency was swept to confirm the change in soil frequency. The input motions are shown in Table 1.

Table 1. Input motion list.

空箱		乾砂		飽和砂	
運動型態	方向與等級	運動型態	方向與等級	運動型態	方向與等級
White noise	50gal-X 50gal-XYZ	White noise	50gal-X 50gal-XYZ	White noise	50gal-X 50gal-XYZ
Sweep sine 1-50Hz	100gal-X 100gal-XYZ	Sweep sine 1-50Hz	100gal-X 100gal-XYZ	Sweep sine 1-50Hz	100gal-X 100gal-XYZ
TCU084	100gal-X 200gal-X 400gal-X 600gal-X	TCU084	100gal-X 200gal-X 400gal-X 600gal-X	TCU084	100gal-X 200gal-X 400gal-X 600gal-X
				HWA062	100gal-Xtrue 100gal-Xs 600gal-Xs 1000gal-Xs
WN and Sweep after Maximum EQ intensity					

4. Test results

A. Soil liquefaction phenomenon

Since one of the goals of the one-dimensional shear box is to explore the reaction of the pipeline under soil liquefaction, this condition needed to be

meet. The test preparation method involved sprinkling dry sand into the air to a set height, then completing the drying process. After the sand test, water was gradually added until it nearly reached the surface of the sand body, and then the saturated sand test was performed.

Figure 2 shows the state of the sand body surface during the 400 gal and 600 gal shaking table tests for the TCU084 earthquake. It can be observed from the figure that when the maximum acceleration of the earthquake reaches 400 gal, the sand body has already liquefied. After the free water on the surface was absorbed, the 600-gal test was performed. We found that the degree of soil liquefaction was far greater than for 400 gal. This phenomenon is similar to that observed in other studies. When there is a potential for liquefaction, the soil liquefaction may possibly recur. When earthquake intensity increases, soil liquefaction may occur again. From this result, it can be verified that the unidirectional shear box will have soil liquefaction during the earthquake.

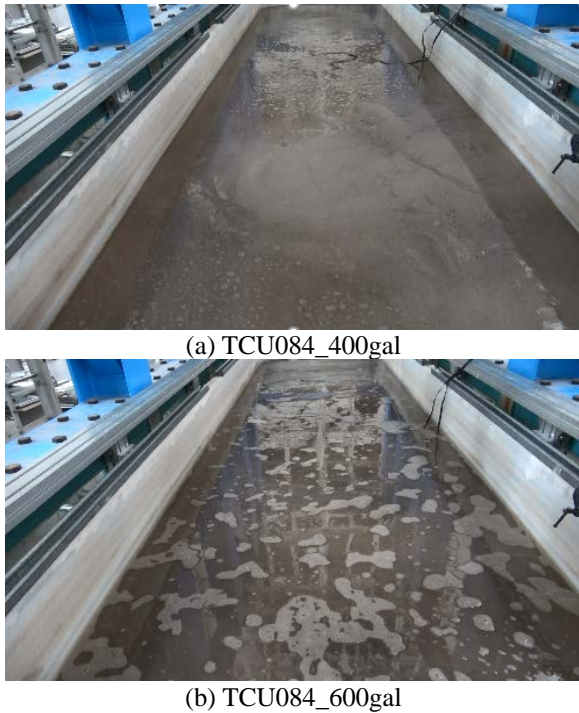


Figure 2. The soil liquefaction phenomenon.

B. Site response analysis result comparison

Considering that the unidirectional shear box models a semi-infinite domain, DEEPSOIL was selected for comparison. The soil wave velocity was obtained by the systematic differentiation of dry and saturated sand, and the same analysis was applied for DEEPSOIL. The model was used for a site response analysis, and the acceleration duration of the frame buried in the sand, the sand surface, and its corresponding sliding layer frame were selected for comparison, as shown in Figure 3 and 4, which

correspond to the dry and saturated sand states, respectively. The dotted line indicates the linear and nonlinear response spectra for DEEPSOIL 40 cm from the soil surface (the middle of the soil), while the solid line represents the sand and frame acceleration response spectra at different depths.

Comparing the solid line on the graph, we found that the acceleration response spectra of the two positions are nearly identical, which means that the sand in the middle moves along with the sliding layer caused by the earthquake input motion, and it reaches the semi-infinite domain. From the trend of the dotted and solid lines, the response in the test under the dry sand state is almost identical to the result from the DEEPSOIL analysis.

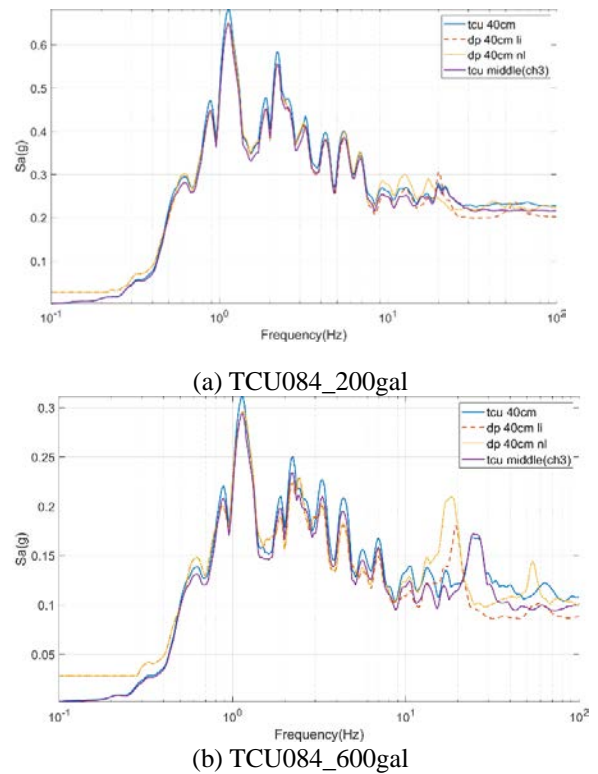
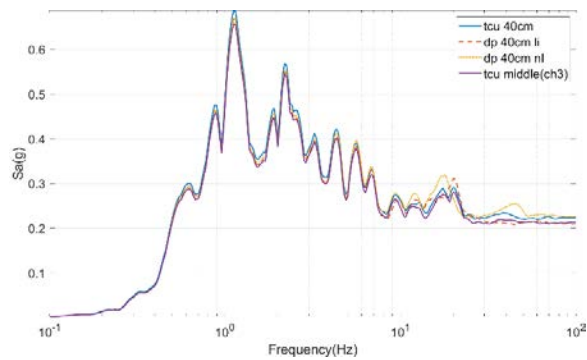
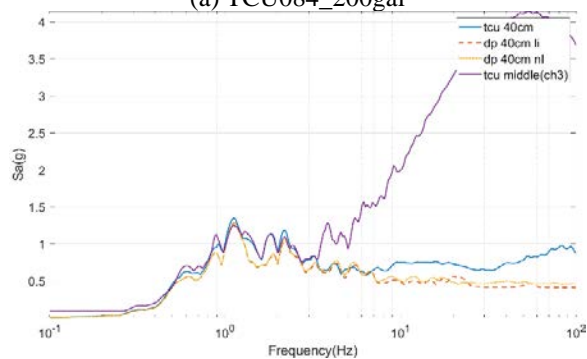


Figure 3. Site response for the dry sand.

In the saturated sand state, when the maximum seismic acceleration is 200 gal, the result is similar to the DEEPSOIL result, indicating that the designed sliding mechanism can achieve isolated layer displacements, and it is not affected by the rubber friction; however, when the seismic acceleration reached 400 gal in the saturated sand state, the earthquake caused soil liquefaction. We found that the response of the measured data and the DEEPSOIL analysis result are apparently inconsistent after 3 Hz. These discrepancies may be attributed to the sensor, which floats during liquefaction.



(a) TCU084_200gal



(b) TCU084_600gal

Figure 4. Site response for the saturated sand.

4. Conclusion

From the analysis and comparison of the test results, we concluded that the design concept and the construction of the one-dimensional shear box from the fixed test sand box can simulate a semi-infinite domain and soil liquefaction. Comparing the theoretical analysis and test results, the unidirectional shear box does meet the expected result. In addition to completing the pipeline dynamic test, the box also is 3 m in the longitudinal direction, so the comparison test body can be arranged inside the box in the same test. Therefore, earth seismic engineering tests such as tank liquefaction, tank pipeline joint, and foundation pile tests can be performed in the future.

Reference

1. Donald Ballantyne(2008). M7.8 Southern San Andreas Fault Earthquake Scenario: Oil and Gas Pipelines. MMI Engineering
2. Chenna Rajaram, Srikanth Terala, Ajay Pratap Singh, Kapil Mohan, Bal Krishna Rastogi, Pradeep Kumar Ramancharla (2014). Vulnerability Assessment of Buried Pipelines: A Case Study. Frontiers in Geotechnical Engineering (FGE) Report No: IIIT/TR/2014/-1,
3. Eren Uckan, Bulent Akbas, Ercan Şerif Kaya, Ferit Çakır, Cengiz Ipek, Murat Makaracı, Şenol Ataoglu, (2016). Design Issues of Buried Pipelines at Permanent Ground Deformation

Zones. DISASTER SCIENCE AND ENGINEERING p. 53-58, 2(2).

4. Durga Prasad, Neelima Satyam(2016). Analysis of continuous and segmented pipeline in liquefiable soil,5th International Conference on Integrity - Reliability - Failure Report No: IIIT/TR/2016/-1.
5. ALA, American Lifelines Alliance, Seismic fragility formulations for water systems, 2001.

Database of Near-Fault Highway Bridge Damage in Recent Taiwan Earthquakes and Preliminary Fragility Investigation

Gee-Yu Liu,¹ Pao-Ching Chou,² and Lee-Hui Huang³

劉季宇¹、周寶卿²、黃李暉³

Abstract

In this investigation, a database of near-fault highway bridges involved in the 1999 Chi-Chi earthquake and 2018 Hualien earthquake is established. Totals of 151 and 24 bridges, respectively, all within the vicinity of the ruptured faults and with or without damage, are included. The structural attributes, strong motion intensity, distance to the fault, and offset experienced (if any) of each bridge are either well calibrated or carefully determined. Furthermore, we classify and record the damage states and modes for the 16 and 5 damaged bridges after the Chi-Chi and Hualien earthquakes, respectively. This database is employed to predict the damage of each bridge using the Thighway software developed by NCREE for the damage and loss estimation of highway bridges. A comparison of the prediction and actual damage is made.

Keywords: Chi-Chi earthquake, 2018 Hualien earthquake, near-fault, highway bridge damage.

Introduction

There are numerous active faults all over Taiwan. Historically, devastating earthquakes occurred very often and were mostly a result of the rupture of these faults. Accordingly, severe casualties and losses were incurred, especially in the near-fault areas. Evidently, it is an important task to develop databases and models for improved seismic loss estimation techniques in near-fault areas. In this investigation, we establish a database of information from highway bridges after recent earthquakes in Taiwan. The structural attributes, strong motion intensity, distance to the fault, and offset experienced (if any) of each near-fault bridge were either well calibrated or carefully determined. Furthermore, the damage state and modes of the damaged bridges were well classified and recorded. These databases were first employed to predict the bridge damage; then, the prediction was compared with the actual record.

Sources of Bridge Damage Information

The database consists of data from the near-fault highway bridges during both the 1999 Chi-Chi earthquake and the 2018 Hualien earthquake, as these two major events were apparently associated with the rupture of active faults and caused the most substantial

highway bridge damage in decades. On the contrary, there was either no damage or no damage related to known active faults in other recent events (for example, the 2016 Meinong earthquake).

According to the reconnaissance report by NCREE, which described highway and roadway bridges after the Chi-Chi earthquake (張國鎮, 1999), there were around 1,000 highway (and roadway) bridges in central Taiwan. About 20% of these bridges in the affected areas sustained damage varying from very minor to collapse. Among these bridges, all those crossed by the Chelungpu fault collapsed as a result of the fault offset. This investigation consulted the documentation and photos from the original paper to decide the inventory, structural attributes, and detailed damage information for the damaged highway bridges, many of which have since been rebuilt and are not the same as before the earthquake.

After the Hualien earthquake, there were five bridges damaged, all by fault offset. One was crossed by the Lingding fault and the rest by the Milun fault. Detailed information about their damage can be found in the paper by Hung *et al.* (洪曉慧等, 2018). The inventory and structural attributes were from the report of post-earthquake examination of bridges by the

¹ Research Fellow, National Center for Research on Earthquake Engineering, karl@narlabs.org.tw

² Assistant Researcher, National Center for Research on Earthquake Engineering, pcchou@narlabs.org.tw

³ Assistant Researcher, National Center for Research on Earthquake Engineering, lhhuang@narlabs.org.tw

Hualien County Government (花蓮縣政府, 2018).

Records of Damage States and Modes

Based on the bridge damage information, we determined a unified classification for damage states and damage modes of the bridges. As summarized in Table 1, there are five different damage states (DS), denoted as (1) N for none, (2) S for slight, (3) M for moderate, (4) E for extensive, and (5) C for complete. The difference between M, E, and C is that any of the major members sustaining damage or displacement will result in no, partial, or major reduction in their bearing capacity.

The damage mode(s) are denoted by the member(s) in which damage occurs followed by the damage state. The member may be non-structural (N), the main structure (S), an expansion joint (EJ), a seismic stopper (SS), a bearing (B), a pier (P), the foundation (F), a girder (G), a deck (D), or an abutment (A). For a bridge with slight damage in the main structure, it is not necessary to note whether it is in the pier, foundation, girder, deck, or abutment. For a bridge beyond extensive damage, it is not necessary to note whether the damage is in a non-structural member, expansion joint or seismic stopper. In addition, the damage mode for a collapse is denoted by [D5+].

Table 1 Classification of damage states and modes for highway bridges of the girder type.

DS	Damage Modes (for girder bridges)
N (1)	• No damage
S (2)	<ul style="list-style-type: none"> • Damage in non-structures [N2] • Slight cracking in structure [S2] • Expansion joints slightly displaced [EJ2] • Bearings slightly displaced [B2] • Seismic stoppers slightly damaged [SS2] • Abutments/ramps slightly cracked [A2]
M (3)	<ul style="list-style-type: none"> • Cracking in structure [S3] • Minor displacement of decks [D3] • Bearings displaced/damaged [B3] • Seismic stoppers failed [SS3] • Abutments/ramps cracked [A3]
E (4)	<ul style="list-style-type: none"> • Piers deformed/damaged [P4] • Foundations deformed/damaged [F4] • Girders deformed/damaged [G4] • Decks cracked/displaced [D4] • Abutments/ramps settled/deformed [A4]
C (5)	<ul style="list-style-type: none"> • Piers severely deformed/damaged [P5] • Foundations severely deformed/damaged [F5] • Girders severely deformed/damaged [G5] • Decks severely cracked/displaced [D5] • Abutments severely damaged/settled [A5] • Collapse [D5+]

Seismic Hazards at Bridge Sites

The strong motions of both earthquakes recorded by the seismic observation network under the Central Weather Bureau, MOTC, were employed to determine the seismic intensities (SI) at the locations of the bridges. The SIs include peak ground acceleration (PGA), peak ground velocity (PGV), and the spectral accelerations at the periods of 0.3 s and 1.0 s (Sa0.3 and Sa1.0). Their values were obtained via interpolation of the measured values at the strong-motion stations. This work was conducted by Dr. Shu-Hsien Chao of NCREE.

The fault traces of both earthquakes employed in this study were from the Central Geological Survey (CGS), MOEA. The fault trace of the Chi-Chi earthquake is according to the field investigation conducted afterward. It includes the entire Chelungpu fault and the northern segment of the Tachienshan fault. The fault trace of the Hualien earthquake is according to the CGS's active fault map of Taiwan, which was issued in 2012. It includes both the Milun and Lingding faults. As the Chi-Chi earthquake has a very high magnitude (M7.3 in the Richter scale) and widespread area of effect, in this study the near-field area is assumed to be the buffer region of the fault tract with a radius of 8 km. While the Hualien earthquake had a much smaller magnitude (M6.4 in the Richter scale) and a narrower affected area, the near-fault area is assumed to have a radius of 2 km.

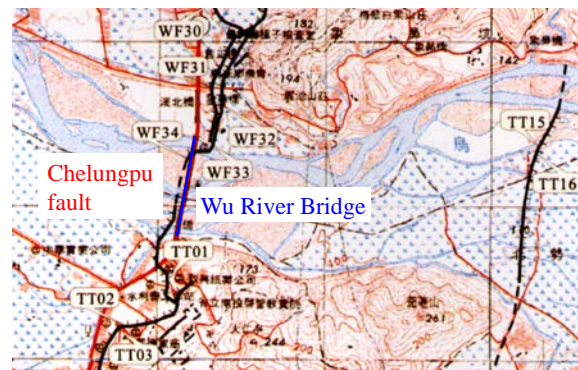


Figure 1 The trace of the Chelungpu fault around the Wu River Bridge (Chi-Chi earthquake).

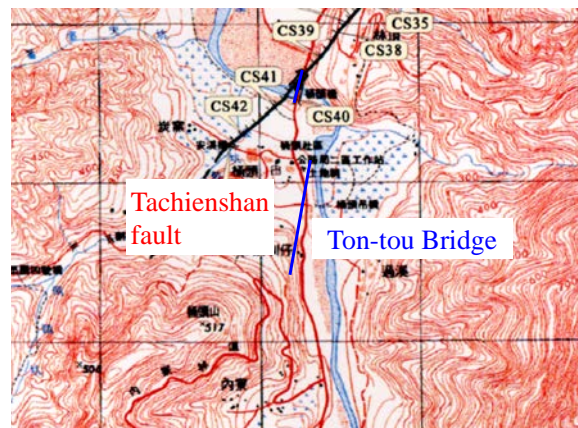


Figure 2 The trace of the Tachienshan fault around the Ton-tou Bridge (Chi-Chi earthquake).

As bridge damage occurred at the fault crossings in both earthquakes, it is very important to quantify the fault offset where these bridges are located. A geological investigation by the CGS following the Chi-Chi earthquake gave detailed observations of the fault rupture from north to south (經濟部中央地質調查所, 1999). Fortunately, all the bridges with a fault crossing were included. For example, an east–west trace of the Chelungpu fault was observed under the Wu River Bridge, as depicted in Figure 1, which has a vertical rise of 1 m. Another trace of the Tachienshan fault was observed crossing the Ton-tou Bridge, as depicted in Figure 2, which orientates 55° north by east and the offset is 30 to 40 cm vertically. The information quantified in the report on the fault offset was all well examined and integrated into the database of this study. Similar work was also conducted for the Hualien earthquake using the CGS report (經濟部中央地質調查所, 2018).

Contents of Database Established

The database established in this investigation consists of an inventory of near-fault highway bridges and their structural attributes. There are 151 and 24 bridges for the Chi-Chi and Hualien earthquakes, of which there are 16 and 5 damaged bridges, respectively. Their damage states and damage modes have been classified and recorded in the database. As arch bridges and cable-stayed bridges usually have a very complicated structural behavior, they are not included in the database for the sake of simplification.

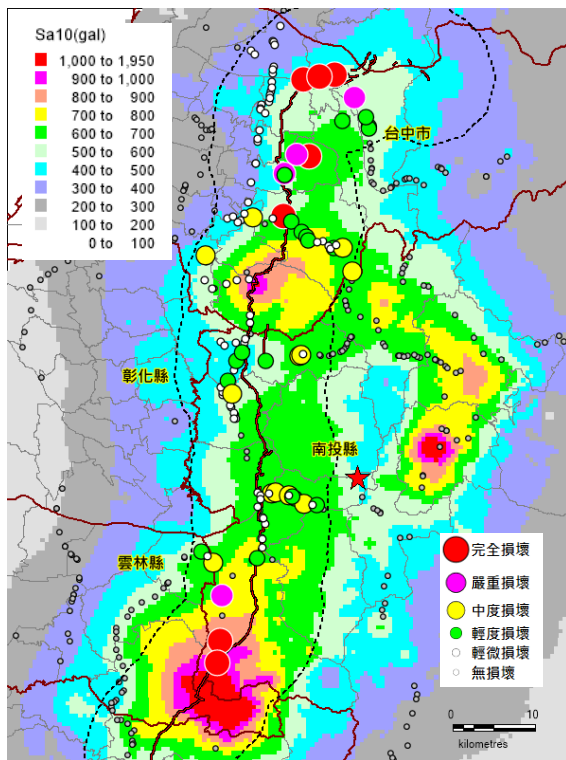


Figure 3 The near-fault area of the 1999 Chi-Chi earthquake and the distribution of highway bridges and their damage states.

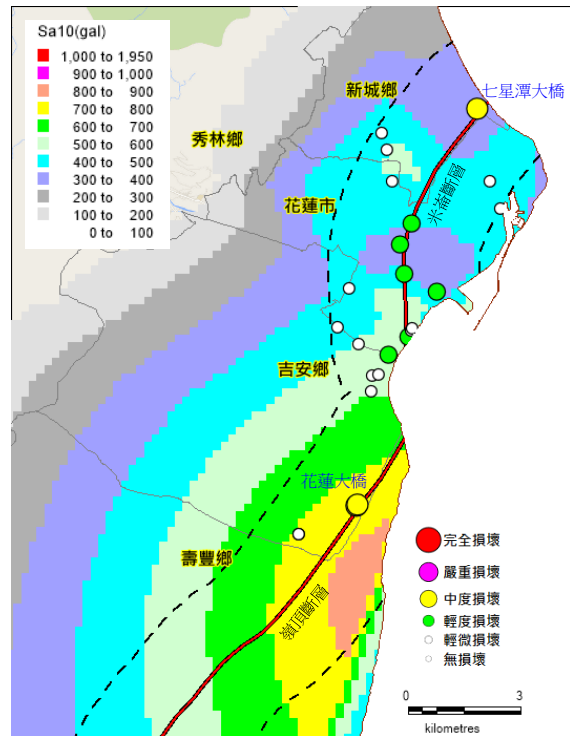


Figure 4 The near-fault area of the 2018 Hualien earthquake and the distribution of highway bridges and their damage states.

In addition, the seismic hazard parameters at the location of each bridge are determined and recorded in the database. They are the values of PGA, PGV, Sa0.3, and Sa1.0, and the fault offset and its components (vertical or horizontal) if there is a fault crossing.

Figures 3 and 4 depict the near-fault areas and the distributions of highway bridges and their damage states for the Chi-Chi and Hualien earthquakes, respectively.

Thighway Model for Bridge Damage Estimation

Thighway is the software developed by NCREC for the damage and loss estimation of highway bridges. In its methodology, bridges are classified into eight categories, which are summarized in Table 2, according to the number of spans, continuity of super-structures, and type of piers. Each category of bridges consists of three sub-categories, *i.e.*, conventional design, seismic design, and conventional design with seismic retrofit. The fragility curves for an evaluation unit of a bridge of any sub-category have been developed based on earlier studies and can be employed to predict the damage state if the seismic hazards to which the bridge is exposed are specified. Since the seismic design force and construction details depend on the design codes and zoning schemes, which have been revised several times in the past, the fragility curves of a specific bridge must be adjusted according to the design year, site condition, seismic zone, and geometry.

Table 2 Classification scheme for highway bridges.

	Girder type	Pier type	Category
Girder bridges: single span	-	-	HWB1
Girder bridges: multiple spans	Simply supported	Single column	HWB2
		Column bent	HWB3
		Pier wall	HWB4
	Continuous	Single column	HWB5
		Column bent	HWB6
Other bridges	-	-	HWB7

Accordingly, damage estimation of highway bridges can be performed following the procedures depicted in Figure 5. Given an earthquake event, the seismic hazards including ground shaking and ground failure where a bridge is located can be determined. The fragility curves (FC) for seismic intensity (SI) and permanent ground displacement (PGD) are then employed, respectively. The joint probabilities for various damage states in each evaluation unit of a prototype bridge can be determined. Finally, the damage state and failure probability of every bridge, single or multiple span, can be decided.

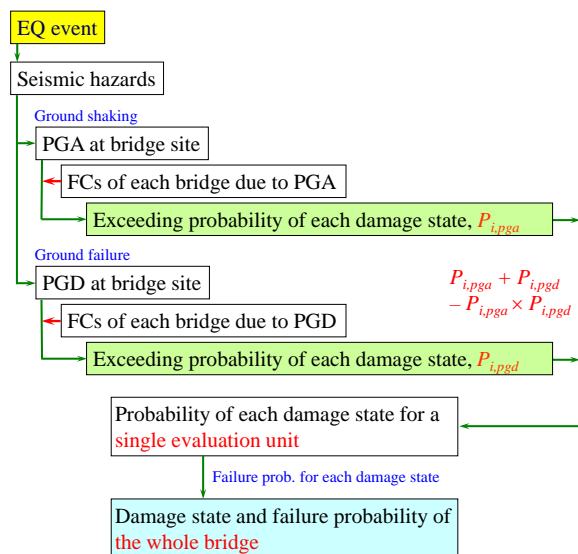


Figure 5 Procedures for damage estimation of highway bridges.

Comparison between Thighway Prediction and Actual Damage

A comparison between the Thighway prediction and observed damage of highway bridges was made using the established database. For the case of the Chi-Chi earthquake, they agree well with each other. However, the observed “moderate” damage states of the Qixingtang Bridge and Hualien Bridge, which both have a fault crossing and experienced a 70 cm horizontal offset in the Hualien earthquake, were less

severe than the predicted “extensive” damage state. Generally speaking, the rupture of a reverse fault (e.g., the Chelungpu and Tachienshan faults in the Chi-Chi earthquake) exerts a compressive and maximum damaging effect to all infrastructures encountering the offset. Meanwhile, the effect from a strike-slip fault (e.g., the Milun and Lingding faults in the Hualien earthquake) varies significantly. It may be tensile, shear, or compressive, depending on the alignment of the infrastructures with respect to the fault trace. Figure 6 depicts the shear effect exerted upon the Hualien Bridge, which was crossed by the Lingding fault at a right angle between piers No. 9 and No. 10, resulting in the shift and rotation of the bridge’s deck between the two piers. The comparison suggests that the current model of bridge damage prediction employed by Thighway should be tuned to minimize the discrepancy between the prediction and observation.



Figure 6 A 70 cm horizontal offset of the Lingding fault beneath the Hualien Bridge results in the shift and rotation of the bridge’s deck between piers No. 9 and No. 10.

References

1. 花蓮縣政府, 2018, 「花蓮地震橋梁特檢表」, 花蓮。
2. 洪曉慧、陳俊仲、蘇進國、李柏翰、江奇融、宋裕祺, 2018, 「0206 花蓮地震橋梁震損調查與分析」, 中華民國第十四屆結構工程研討會暨第四屆地震工程研討會論文集, 論文編號 24014, 台中。
3. 張國鎮等, 1999, 「九二一集集大地震全面勘災報告—橋樑震害調查」, 國家地震工程研究中心研究報告, 編號 NCREE99-055, 台北。
4. 經濟部中央地質調查所, 1999, 「九二一地震地質調查報告」, 台北。
5. 經濟部中央地質調查所, 2018, 「2018 0206 花蓮地震地質調查報告」, 台北。

The Development of the 5D Smart City Platform

Ren-Zuo Wang¹ and Chih-Shian Chen²

王仁佐¹、陳志賢²

Abstract

In response to the future development and application requirements of smart cities and the Internet of Things, the National Center for Research on Earthquake Engineering (NCREE) has researched and developed a 5D smart city platform. The 5D smart city is a combination of a 3D city model, Taiwan satellite imagery, a digital elevation model (DEM), and time data (called a 4D model). The time data is transmitted through sensors to send digital information. Information is sent to the 5D smart digital space via the Internet. Using the 5G network, which can shorten the time required for synchronization between the 5D smart space and real-world data, the 5D digital space becomes a digital twin of the real world. The proposed platform was applied and verified in Zone C of the Shalun Smart Green Energy Science City. By using a 5D visualized platform, many types of information can be integrated for environmental monitoring, energy, images, or other sensing. The platform can be operated interactively in real-time and display characteristics at any viewing angle in the 3D scene. Furthermore, the platform improves the convenience of data access and establishes the relationship between simple data types, the geographical environment, and 3D scenes. This work can expand the value-added application of remote sensing technology in the field of smart cities and disaster prevention.

Keywords: smart city, 3D GIS, IoT, BIM, digital twin

Platform Function Framework

For improved platform operation efficiency, the C++ programming language was used to develop the platform in the Visual Studio integrated development environment (IDE) of the Windows operating system. In addition to strengthening the technical skills of native 3D platform development, self-development platform prevents the high license fees of commercial software and retains flexibility to expand platform functions and different file formats. This prevents a dilemma in platform discontinuation due to interruptions in the technical support of the commercial software. The platform structure is shown in Fig. 1. The base map of the platform is made using satellite imaging merged with the twenty-meter digital elevation model (DEM) in the open data of the Ministry of the Interior. Either the TWD97 or WGS84 coordinate systems can be used. The system can support 3D mesh model types such as *.obj, *.fbx, *.stl, and *.dae. Shapefiles, GeoTiff, GeoJSON, etc., and *.e57 or *.pts are the GIS and point cloud file types supported, respectively.

The monitoring data is received and queried by network protocols such as HTTP, HTTPS, MQTT, SQL database, and Modbus TCP. For images, surveillance images are received by RTSP, RTMP, and MPEG-TS. The weather module can simulate changes in the weather such as clouds, sunshine, rain, snow, lightning, and flooding, as shown in Fig. 2. to Fig. 4.

Platform Features

- (1) The platform can display the city's fine triangular mesh model, which was established from large-scale aerial photography. Base on the stress testing, a fine triangular mesh model of more than twenty square kilometers can be displayed. The total number of triangular meshes is approximately sixty-four million.
- (2) The platform can combine information such as data from the Internet of Things (IoT), images, and 3D spatial information. Monitoring data and surveillance images can be directly displayed next to devices. Users can intuitively observe

¹ Research Fellow, National Center for Research on Earthquake Engineering

² Assistant Researcher, National Center for Research on Earthquake Engineering

relationships between the location of devices, information, and nearby geographical conditions.

- (3) Users can interact with the platform in real-time. Users can use input interfaces such as a keyboard and mouse to interact with the platform, display scenes at any angle in the 3D view and improve the convenience of data access.
- (4) The platform supports multiple projection display methods. In response to requirements for displaying the results of research and development, the platform can support curved projection, virtual reality (VR), and 3D stereo vision projection to provide more diverse visual experiences.

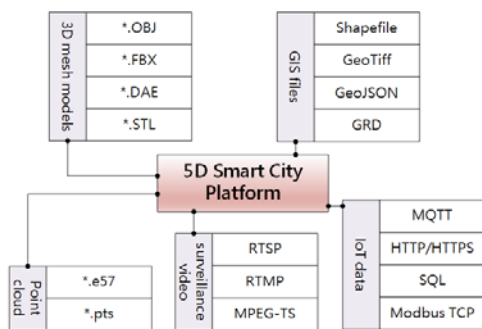


Fig. 1. Functional architecture diagram of the platform's supported file types.

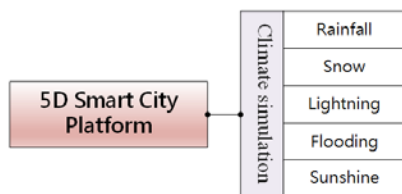


Fig. 2. Functional architecture diagram of the platform's climate simulation.

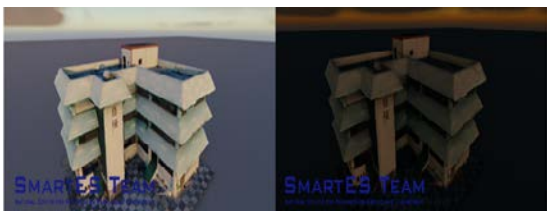


Fig. 3. Climate simulation of changes in sunlight.



Fig. 4. Simulation of rainfall.

Integrated Application in IoT and 3D Urban City Model - Shalun Smart Green Energy Science City - Zone C as an Example

The Tainan Shalun Smart Green Energy Science City (TSSGES-City) includes a core area, business district, industrial research and development, Academia Sinica Southern Campus, and a residential area near the Tainan station on the high-speed rail. Zone C is an application area for smart green energy technology research and development. The goal is to build a smart grid in Zone C, integrating renewable energy and developing intelligent control and energy management technology. In addition, smart streetlights and environmental monitoring facilities have been established to collect surveillance videos and environmental data. 5D display technology has been adopted and integrated with 3D models and IoT data, producing a highly visual display platform.

TSSGES-City was selected to demonstrate the proposed platform. The base map is a digital elevation model (DEM) with a precision of twenty meters (内政部) combined with satellite imagery. Detailed 3D mesh models from aerial modeling are overlain on the Taiwan base map, as shown in Fig 5. The generated models are composed of a 3D model using a massive triangular mesh, copied over the real image texture.

A common method of generating a 3D city is to use an unmanned aerial vehicle (UAV) and oblique photograph technology. After obtaining pictures of many buildings at various angles and using the structure from motion and dense matching techniques, a 3D point cloud or 3D mesh model is produced. The technique improves efficiency and quality, and therefore promotes 3D GIS development (吳錫賢 2017, 林世賢 2018).

Building information models (BIM) with detailed information about the indoor space are also integrated in the platform, as shown in Fig 6.

While there is an extremely high similarity between the model and the real-life scenery, this complexity causes an enormous computational burden as the triangle mesh number is much greater than that of the mockups for the approximated buildings mentioned previously, and the textures are of a high-resolution. Therefore, the program must adjust the fineness of the triangular mesh for different distances. If the distance is increased, the mesh becomes coarser. There is no visual difference for a model with a coarser mesh. However, there is remarkable improvement in computational performance.

The outdoor monitoring equipment of TSSGES-City Zone C consists of (1) two micro weather stations, (2) eighty-six smart streetlights, (3) two scenery

complementary streetlamps, (4) one solar panel, and (5) surveillance videos. The first three items use NB-IoT communication technology to achieve the goal of real-time surveillance (遠傳電信 2019). The fourth item uses the Modbus TCP communications protocol. The surveillance camera adopts the RTSP communications protocol. Besides surveillance videos, the relevant monitoring data is stored long-term in a back-end database for centralized management. The platform captures the corresponding information and displays it in a 3D virtual scene.

The integrated architecture between the BIM model and the monitoring data is shown in Fig. 7. The Revit BIM file is first converted into an FBX file and then imported into the platform. A structured query language (SQL) database is used to search the building model and the databases of the monitoring data. The results are linked through data mapping between the globally unique identifier (GUID) of the virtual object in the BIM model and the actual sensor ID, thus linking the object and its data.

The smart streetlights use wireless controllers, which can control illumination brightness by responding to demand. At the same time, they can integrate the real-time voltage and current of the lamp into the platform. Zone C includes information on eighty-six smart streetlights. The brightness of the virtual lamps in the platform can be used to carry out a light source simulation based on the brightness setting in the actual lamp control system, as shown in Fig. 8.

The traditional surveillance method is to watch many different surveillance images displayed on many small screens. It is not easy to build a connection between the images and the on-site environment. In the 5D platform, images display at the actual location of the surveillance camera. By matching the image with the model, users can observe the site at an arbitrary angle, directly building a relationship between the images and the actual environment to help manage the large number of images from the surveillance cameras. Fig. 9 shows the surveillance videos of an intersection and its corresponding virtual scene.

There is a 33.5 kWp solar energy electricity generation system and a 20 kW/45 kWh lithium battery stored energy system in the parking shed of the Taiwan Car Lab. An energy management system was built by the research team of Professor Hong-Tzer Yang from the National Cheng Kung University (NCKU). This system contains historical data of solar energy generation and weather forecast data (temperature, rainfall, weather description, etc.). Using the fuzzy reasoning method, the system supports the selection of a support vector regression (SVR) model. The system predicts power generation for the next day and performs integrated scheduling of

available power resources by intellectualization prediction, diagnosing, and decision-making. Fig. 10 shows the historical data of the predicted and actual solar energy generation for the platform.

In energy management, the total power consumption of the building (Fig. 11(a)), power consumption of each space, and power consumption of single air-conditioning units can be displayed by collecting the monitoring data of smart meters. The result of the integration is shown in Fig. 11. Using the electric circuit monitored by the smart meters, the power consumption of a single device can be monitored, as shown in Fig. 11(b). The real-time power consumption of the device and the cumulative power consumption for the current month are displayed for an air conditioner. Fig. 11(c)-(d) shows the electricity consumption details for a single space in the room using an information panel. The relevant information can be used to further analyze the proportion of each space's power consumption relative to the total power consumption and evaluate future electricity demand and cost.

The indoor environment monitoring items include temperature, humidity, illuminance, CO, and CO₂. The function setting can be determined; for example, the air conditioning temperature can be automatically adjusted through infrared controllers. Other electrical appliances can be controlled by remote infrared controllers such as fans, lighting, projectors, and electric curtains for energy-saving. The result of the integration is shown in Fig. 12. The monitoring data is displayed next to the sensor installation location, which clearly establishes the correspondence between information and space.

Conclusions

Smart cities embody the integrated value-added applications of big data. Applications of big data, which are widely used in various fields. With the development of the Internet of Things, the importance of integrating various sources of data, such as firefighting, energy management, environmental monitoring, cameras, and smart streetlights, is extended. Presently, commercial software is used at home and abroad for the 3D visualization of smart cities; however, the integration of various IoT monitoring data and techniques for real-time interactive display is still scarce. The results of the 5D smart city platform developed by the NCREC will help develop smart cities in Taiwan and will meet future applications of the Internet of Things and urban disaster prevention.

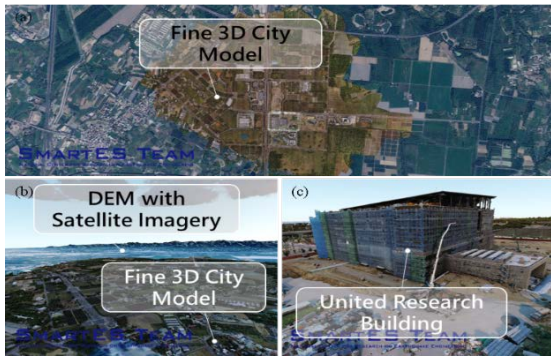


Fig. 5. (a) 3D mesh models of TSSGES-City, (b) model of the entire area, (c) United Research Building.

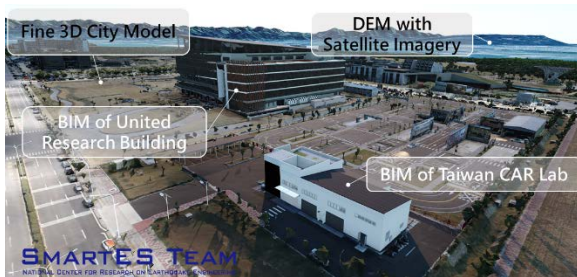


Fig. 6. Integration of the BIM 3D model in the Tainan SSGES-City Zone C.

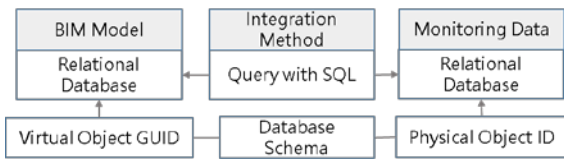


Fig. 7. Integrated architecture of the BIM model and monitoring data.



Fig. 8. Virtual and real integration of the brightness of the smart streetlight and the platform.



Fig. 9. Integrated application of surveillance videos.



Fig. 10. Integrated application of solar power information.



Fig. 11. Indoor power consumption data display.



Fig. 12. Indoor environmental data display.

References

- 吳錫賢, 李明儒, 姜興華, & 鄭宏達 (2017), 三維空間資訊技術之發展與應用. 中華技術 10 週年特刊, 114, 72-89.
- 內政部 20 公尺網格數值地形模型資料, 政府資料開放平台, <https://data.gov.tw/dataset/35430>
- 林世賢, 施錦揮, & 鐘文彥 (2018), 三維實景三角網模型製作規範之研究, 內政部國土測繪中心研究報告(107301000100G003).
- 遠傳電信股份有限公司系統整合分公司(2019), 能源環境智慧管理平台研發與展示案期末報告書, 財團法人國家實驗研究院.

Preliminary Study on Acceleration Control of Seismic Simulator using Deep Learning

Po-Hui Hsieh¹, Pei-Ching Chen² and Chuin-Shan Chen³

謝伯徽¹、陳沛清²、陳俊杉³

Abstract

Seismic shake table testing is one of the most straightforward methods for performance assessment of structural resistance under earthquakes. Since the total weight of shake table and testing specimen is enormous and close to the maximum force capacity of the hydraulic actuator, the control performance of shake table testing is greatly affected by the interaction between the shake table and actuator, leading to difficulties of accurate acceleration control of shake table. Various control strategies such as Proportional-Integral-Derivative, and Three-Variable Control are applied to the seismic shake table testing to overcome the situation. Recently, there were breakthrough in image recognition, audio processing, image generation, and robotic control with deep learning approaches. In this study, deep learning is adopted to improve the control performance of shake tables. The strategy and future work are introduced thoroughly.

Keywords: Control system, Deep Learning, Reinforcement Learning

Introduction

Seismic shake table testing has been recognized as the most straightforward method to investigate seismic performance of structures. In a shake table test, a specimen is mounted on a rigid steel platform, which is driven by servo hydraulic actuators to reproduce desired acceleration time histories. However, during shake table testing, the measured acceleration could be different from the desired acceleration time history due to the control-structure interaction. Therefore, several control strategies such as traditional Proportional-Integral-Derivative (PID) control, and Three-Variable Control (TVC) are adopted in order to overcome the situation. On the other hand, there was an offline tuning approach named transfer function iteration method proposed by Spencer & Yang (1998). In the tuning approach, the shake table test is conducted under small excitation for collecting input and output data. Then, the relationship of input command and measured acceleration is modeled. The command is adjusted by the inverse model offline iteratively. Finally, the command is modified and adopted as the drive profile for shake table testing.

When the specimen collapses during the shake table testing, the system dynamics could be changed, which causes indelible tracking error in acceleration

reproduction. In the past few years, new control methods which could adapt to the time variant system dynamics are proposed such as sliding mode control by Yang (2013) and acceleration trajectory tracking control method by Nakata (2010).

In this study, the non-linear deep learning model is used to fit the system dynamics first to represent the shake table. Then, the parameters of deep learning controller are trained with the shake table model in a reinforcement learning approach.

Shake Table Tests

A deep learning model needs large amount of data to train model parameters such that the predicted results are close to the experimental ones. In this study, a steel structure was designed and fabricated as the specimen for collecting experiment data from shake table testing. Two hundred records of measured data are collected in the small-scale structural laboratory of NCREE. The experimental setup, which is shown in Figure 1, is a one-story steel structure with a length of 50 cm and a width of 45 cm. The total height of the structure is 60 cm. The thickness of each slab is 10 cm. The total weight of specimen is 176 kgf. The natural frequency is 5 Hz and the damping ratio is 0.5%.

¹ Graduate student, National Taiwan University

² Associate Professor, National Taiwan University of Science and Technology

³ Professor, National Taiwan University

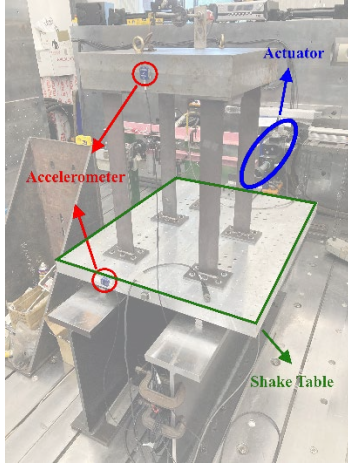


Figure 1. Experiment setup

Deep Learning Modeling

LSTM (long short-term memory) is one of the widely used models in time series prediction. One of the analysis conducted by Zhang (2019) used two kinds of data for the validation of LSTM capacity. One was trained by field measurement data from a 6-story building in San Bernardino, California. The other one was trained by simulation data from a 3-story steel specimen which contained damper at each floor using RTFrame2D. The input ground motions were selected from the PEER strong motion database. The ground motions were the input to the LSTM model and the structural inter-story drifts were the outputs. The LSTM models in both cases could predict the response of the structure accurately.

In this study, acceptable control performance is required in the range of desired frequency bandwidth. The servo-valve commands were selected as the control input and collected measured acceleration data were selected as the output. The dynamics of the system was modeled by one LSTM layer connected with three stacked dense layers. The collected data were preprocessed and split into three subsets, including training dataset, validation dataset, and testing dataset. The LSTM model parameters were updated by Adam optimizer with a learning rate of $1.07e-03$. The modeling error used in this study was a normalized mean squared error in time domain and frequency domain as:

$$RMS_T = \sqrt{\frac{\sum_{k=1}^N (a_r[k] - a_m[k])^2}{\sum_{k=1}^N a_r[k]^2}} \times 100\% \quad (1)$$

$$RMS_F = \sqrt{\frac{\sum_{k=1}^N (s_d[k] - \hat{s}_d[k])^2}{\sum_{k=1}^N s_d[k]^2}} \times 100\% \quad (2)$$

Table 1 shows the simulation result of LSTM modeling. It demonstrates that the shake table acceleration response can be predicted by the deep learning modeling as shown in Figure 2.

Table 1. LSTM model prediction error

	RMS_T	RMS_F
Training	20%	14%
Validation	25%	17%
Testing	27%	19%

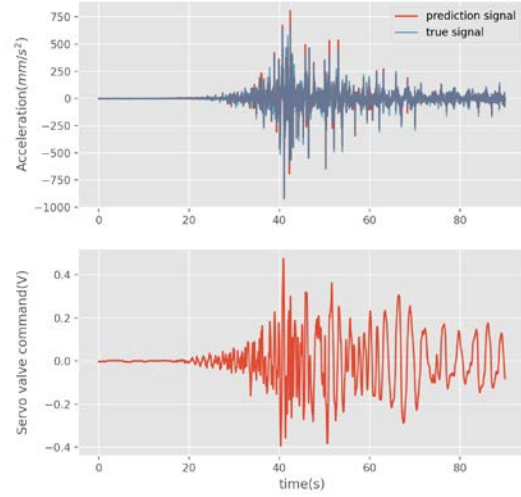


Figure 2. One of the LSTM model prediction results

Reinforcement Learning

The reinforcement learning is formulated by the interaction between the agent and the unknown environment. The action is calculated by the agent (actor) according to the observable states of the system. The environment reacts to the action and switches to the next state. Once an action is taken, the environment delivers a reward as feedback. Figure 3 shows the interaction process in reinforcement learning. The overall interaction procedure can be framed as an Markov Decision Process (MDP). In most cases, the reward function and transition probabilities of the environment is unknown.

In the past decades, most of the researcher use hand-crafted features from raw data as the agent input. The performance of the agent was highly dependent on the feature extraction technique in each domain. Recently, significant progress has been made in solving challenging problems with deep neural networks. Not only higher prediction accuracy but also the end-to-end training provide the opportunity to solve the reinforcement learning with neural network. Agent can directly learn how to extract features from data and produce appropriate action. As a result, the neural network method can be generalized to different reinforcement problems.

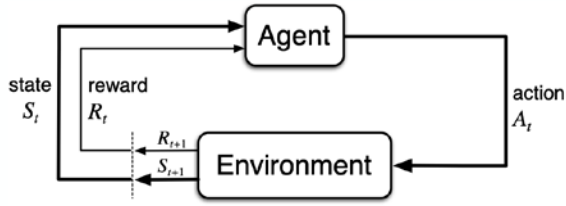


Figure 3. Reinforcement learning architecture

Deep reinforcement learning method can be split into three categories, including value-based method, policy-based method, and actor-critic method. In this study, actor-critic method is implemented in the simulation because of the continuous input command. The actor selects an action a based on the observation s and model parameters θ . The probability of selected action is $\pi(s, a)$. Critic predicts the expected accumulated reward $Q(s, a)$ from current state with observation and action predicted by the actor. The expected accumulated reward in one experiment testing is denoted as ρ . The updating strategy is that the gradient of the actor is proportional to the gradient of the expected accumulated reward in one episode according to the policy gradient theorem

$$\frac{\partial \rho}{\partial \theta} = \sum_s d^\pi(s) \sum_a \frac{\partial \pi(s, a)}{\partial \theta} Q^\pi(s, a) \quad (3)$$

It shows that updating the actor with gradient ascent would also increase the expected accumulated reward in one episode.

Simulation Environment Setup

In theory, the convergence of policy gradient theorem is based on the fully observable MDP. However, there are only part of the system states are measurable, which means a partial observable MDP are available in practice. In order to confirm the required system state for FOMDP, a Simulink shake table simulator model was adopted as the environment in MATLAB for the sake of fully accessing the system states.

The deep learning computation platform and reinforcement learning algorithm codebase is well supported in Python. To incorporate real time communication between the agent in Python and Simulink model in MATLAB. The TCP protocol was adopted as the communication interface. The action was selected by the agent in Python and sent to the environment with TCP connection. Then, the environment received the action, modified the system states and returned feedback at next time step. Figure 4 shows the overall framework stack.

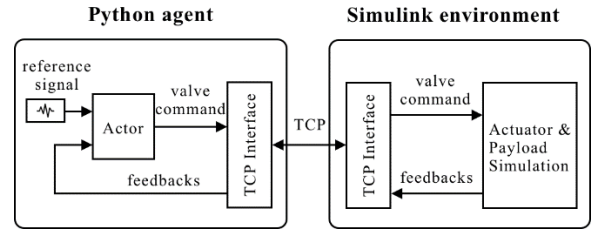


Figure 4. The communication mechanism between agent and environment

Conclusions and Future Work

In this study, deep learning model was used to simulate the dynamics of the shake table system. The modeling of the system was demonstrated to represent the real system fairly well. Due to the partial observable system in the real world, the sufficient condition for agent to work in reinforcement learning settings is still under investigation. Once the fully observable Markov Decision Process is determined, the reinforcement learning algorithm can be applied to obtain the deep learning controller soon.

References

- Degrís, Thomas, Pilarski, Patrick M, and Sutton (2012), Richard S. Model-free reinforcement learning with continuous action in practice. In American Control Conference (ACC), pp. 2177–2182. IEEE, 2012.
- Fujimoto, S., van Hoof, H., and Meger, D. (2018) Addressing function approximation error in actor-critic methods. arXiv preprint arXiv:1802.09477
- Mnih, V., Kavukcuoglu, K., Silver, D., Graves, A., Antonoglou, I., Wierstra, D., and Riedmiller, M. (2013) Playing Atari with deep reinforcement learning. arXiv preprint, arXiv:1312.5602.
- Nakata, N. (2010) “Acceleration Trajectory Tracking Control for Earthquake Simulators” Engineering Structures, 32(8): 2229-2236.
- Sutton, R., McAllester, D., Singh, S. & Mansour, Y. (2000) Policy gradient methods for reinforcement learning with function approximation. In Advances in Neural Information Processing Systems, 1057–1063.
- Spencer Jr., B.F. and Yang, G. (1998), "Earthquake Simulator Control By Transfer Function Iteration," Proceedings of the 12th ASCE Engineering Mechanics Conference, San Diego, California, May 17–20, pp. 776–769.
- Thoen, B., and Laplace, P. (2004). “Offline tuning of shaking tables using dynamic simulation models.” Proc., 13th World Conf. Earthquake Eng, Canadian Association for Earthquake Engineering, Vancouver, British Columbia, Canada, Paper No. 960.
- Yang, T. Y., Li, K., Lin, J. Y., Li, Y., and Zhang, Y. F. (2013) “Implementation of Nonlinear Control Algorithm for Shaking Table Tests”, *Proceedings*, 5th International Conference on Advances in Experimental Structural Engineering, Taipei, Taiwan.
- Zhang, R., Chen, Z., Chen, Su., Zheng, J., Buyukozturk, O., Sun, H. (2019), “Deep long short-term memory networks for nonlinear structural seismic response prediction”, *Computers & Structures*, Vol. 220, pp. 55-68

Benchmark of GPGPU for Artificial Intelligence

Wei-Tze Chang¹

張慰慈¹

Abstract

General-Purpose computing on Graphics Processing Units (GPGPU, GPU cards, or GPUs) plays a key role in Artificial Intelligence (AI) technologies. However, there are an excessive number of GPU cards for different purposes on the market, and there is no clear guide for buyers to help them choose a product for AI applications. This study tested three types of GPU cards to determine their relative increases in acceleration and effectiveness. Their price was also considered, which is useful for users who aim to establish their own AI platform or to rent one.

Keywords: Artificial Intelligence, General-Purpose computing on Graphics Processing Units, speed up

Background

With the advantages of hardware technologies and software algorithms, Artificial Intelligence (AI) is widely applied in various fields. NVIDIA proposed three series of General-Purpose computing on Graphics Processing Units (GPGPU, GPU cards, or GPUs), which include GeForce, Quadro, and Tesla. Ignoring the Quadro series, which focuses on rendering speed, the GeForce and Tesla series can be applied in AI research for designing consumer computers and business servers, respectively. However, the price of a Tesla GPU card can be seven to nine times greater than that of the GeForce series. In this study, two of the top NVIDIA GPU cards of 2020, the RTX 2080 Ti and Tesla V100, were selected to understand their effectiveness in the AI field.

Benchmark Environment and Performance Index

This study chose two types of NVIDIA GPU cards: the GeForce RTX 2080 Ti and the Tesla V100 (16G and 32 GB memory). The Intel Xeon E5 (2.6 GHz) and Xeon Gold (2.1 and 2.6 GHz) CPUs were combined. The CentOS Linux v7.3 Operating System (OS) with kernel v3.10.0-1160.6.1.el7 was chosen to establish the platform. The benchmark program was the “ai-benchmark” (Andrey Ignatov, 2021), which was written in Python using the Tensorflow package v1.12 and v2.1. Six common type of AI problems, classification, image-to-image mapping, image

segmentation, inpainting, sentence sentiment analysis, and text translation, were chosen as the targets for estimating the acceleration and performance score.

Traditional speed-up and efficiency indices were chosen as the performance indices. The speed up s_N is defined as

$$s_N = \frac{T_{ref}}{T_N} < N, \quad (1)$$

in which N is the number of added CPU cores or GPU cards. T_{ref} and T_N are the wall-clock times with and without extra CPU cores or GPU cards, respectively. The ideal value of s_N is N . Furthermore, the efficiency index e_N can be calculated as

$$0 < e_N = \frac{s_N}{N} < 1. \quad (2)$$

The value of e_N should between 0 and 1. A higher e_N indicates improved resource usage with less waste. The efficiency of ideal linear algebra programs can be relatively close to 1. The efficiency for scientific and engineering programs is often between 0.7 and 0.9.

Results and Discussion

Effectiveness of CPU

First, the influence of the number of CPU cores on the performance was tested. Twenty-three extra Intel Xeon E5 (2.6 GHz) CPU cores were added and the speed up was tested as shown in Table 1. It was

¹ Assistant Researcher, National Center for Research on Earthquake Engineering

confirmed that it is helpful to add CPU cores in classification, image-to-image mapping, image segmentation, inpainting, and sentence sentiment analysis. The speed up ranged between 3.6 and 10.2. However, the efficiencies ranged between 0.15 and 0.425, values that are much lower than traditional scientific and engineering programs. This shows that adding CPU cores is not an effective approach for speeding up AI programs.

Table 1 The speed up after adding 23 Intel Xeon E5 CPU cores (2.6 GHz)

Version of Tensorflow		1.12	2.1
Speed up (s_N)	Classification	6.1	7.9
	Image-to-image mapping	3.9	6.0
	Image segmentation	7.0	7.3
	Inpainting	9.2	3.6
	Sentence sentiment analysis	8.6	10.2
	Text translation	1.0	1.0

Program effectiveness with different versions of Tensorflow

Then, the effectiveness of upgrading Tensorflow from v1.12 to v2.1 was tested. 1- and 24-core Intel Xeon E5 CPUs (2.6 GHz) were used as the benchmark environment. The testing results are shown in Table 2. Tensorflow 2.1 showed better speed up in classification, image-to-image mapping, image segmentation, and sentence sentiment analysis, but was worse in inpainting. There was no difference in text translation performance between the different versions of Tensorflow. Considering the continuous development of Tensorflow, which will bring increasing performance and stability, it is suggested that users shift to Tensorflow 2.x as quickly as possible.

Effectiveness of the NVIDIA RTX 2080 Ti GPU Card

The NVIDIA RTX 2080 Ti GPU card is the top GPU card in the GeForce series in 2020. This study tested the influence of combining 1 or 2 RTX 2080 Ti GPU cards with a 1- or 32-core Intel Xeon E5 CPU (2.6 GHz). The testing results are shown in Table 3. There was no obvious difference when adding extra GPU cards to the existing RTX 2080 Ti. This may be because the memory required for testing examples is

smaller than the capacity of a RTX 2080 Ti GPU card, which is 11 GB. One RTX 2080 Ti GPU card can increase the speed by at least 200 times for the classification and image segmentation tasks. The speed up can even reach 460 for image-to-image mapping tasks. For inpainting, sentence sentiment analysis, and text translation tasks, the speed up can reach 14 to 32, which is much improved over the CPU performance shown in Table 1.

When a 32-core CPU was used, there was no obvious difference between the 1 and 2 RTX 2080 Ti GPU card. The speed up of the RTX 2080 Ti GPU card was only 2 to 54 times (Table 3). This increase in speed could only be achieved with a 32-core CPU. Only the text translation task showed an increase of 13 in this case.

Table 2 The speed up when upgrading Tensorflow from v1.12 to v2.1

CPU cores		1	24
Speed up (s_N)	Classification	1.7	2.2
	Image-to-image mapping	1.6	2.4
	Image segmentation	1.5	1.6
	Inpainting	5.5	2.1
	Sentence sentiment analysis	1.1	1.3
	Text translation	1.0	1.0

CPU: Intel Xeon E5 (2.6 GHz)

Effectiveness of the NVIDIA Tesla V100 GPU Card

The NVIDIA Tesla V100 GPU card was the top card in the Tesla series in 2020. Two V100s with different memory sizes, 16 and 32 GB, were tested in this study. The testing results are shown in Table 4.

The difference between the 1 and 2 Tesla V100 GPU cards was not obvious. This may also be because the memory required for the testing examples was smaller than the capacity of the Tesla V100 GPU Card, which is 16 and 32 GB. The speed up performance of the 1-core CPU was also better than the 32-core CPU in this study. However, it should be noted that the speed up for the classification task could reach 186.2 to 197.2 times by adding one Tesla V100 GPU card. The speed up can reach 263.6 to 365.5 for image-to-image mapping tasks. The speed up for the inpainting, sentence sentiment analysis, and text translation tasks ranged between 10.0 and 32.1. Although these values are lower than for other tasks, they are consistent with the RTX 2080 Ti performance.

Benchmark Score

In order to compensate for the difference between the CPUs and GPUs for six testing items, *ai-benchmark* was implemented, which uses a uniform criteria, the “AI score”. A higher score corresponds to a better combination. The testing results are shown in Table 5.

Without GPU cards, the AI scores for the pure, single-core CPU environment were 123, 214, and 170.

Adding 7 to 31 additional cores could increase the score to the 1,000- range.

Extra GPU cards can bring great improvement compared with the pure CPU environment. The score after adding an RTX 2080 Ti GPU card can reach 26,000. The score after adding a Tesla V100 GPU card can reach 30,000 for both 16 and 32 GB memories. Obviously, the acceleration benefits of GPU cards are greater than for multiple-core CPUs.

Table 3 Speed up after adding NVIDIA RTX 2080 Ti GPU cards

CPU cores		1	1	32	32
Extra GPU cards		1	2	1	2
Speed up (s_N)	Classification	271.4	271	21.1	20.4
	Image-to-image mapping	460.7	458.2	54.1	54.1
	Image segmentation	213.7	211.2	17.9	17.3
	Inpainting	14.8	14.6	2.1	2.2
	Sentence sentiment analysis	32.2	31.8	5.9	6.0
	Text translation	14.0	13.8	13.1	13.5

CPU: Intel Xeon E5 (2.6 GHz)

Table 4 Speed up after adding NVIDIA Tesla V100 GPU cards

Environment	CPU	Number of Cores	1	1	28	28	1	1	24	24
		Clock rate (GHz)	2.6	2.6	2.6	2.6	2.1	2.1	2.1	2.1
Speed up (s_N)	GPU	Number	1	2	1	2	1	2	1	2
		Memory	16	16	16	16	32	32	32	32
Speed up (s_N)	Classification		186.2	189.6	19.7	19.6	197.2	187.5	31.1	31.3
	Image-to-image mapping		256.9	263.6	38.0	37.9	365.5	353.9	88.2	86.4
	Image segmentation		129.0	137.2	17.6	17.5	95.7	101.2	19.4	20.3
	Inpainting		10.0	16.5	2.9	2.9	15.2	15.2	3.7	4.3
	Sentence sentiment analysis		29.7	43.7	8.6	8.8	28.7	32.1	9.6	9.8
	Text translation		11.0	16.6	10.3	10.6	16.2	15.7	16.2	16.7

CPU: Intel Xeon Gold

Table 5 AI score using the “ai-benchmark”

Intel CPU			NVIDIA GPU			Benchmark score
Number of cores	Brand	Clock rate (GHz)	Brand	Memory (GB)	Number of cards	
1	Xeon E5	2.6	—	—	—	123
1	Xeon E5	2.6	RTX 2080 Ti	11	1	27,186
1	Xeon E5	2.6	RTX 2080 Ti	11	2	26,934
32	Xeon E5	2.6	—	—	—	1,101
32	Xeon E5	2.6	RTX 2080 Ti	11	1	26,013
32	Xeon E5	2.6	RTX 2080 Ti	11	2	25,732
1	Xeon Gold	2.6	—	—	—	214
1	Xeon Gold	2.6	Tesla V100	16	1	30,141
1	Xeon Gold	2.6	Tesla V100	16	2	32,437
28	Xeon Gold	2.6	—	—	—	1,598
28	Xeon Gold	2.6	Tesla V100	16	1	32,985
28	Xeon Gold	2.6	Tesla V100	16	2	32,797
1	Xeon Gold	2.1	—	—	—	170
1	Xeon Gold	2.1	Tesla V100	32	1	29,258
1	Xeon Gold	2.1	Tesla V100	32	2	28,700
24	Xeon Gold	2.1	—	—	—	829
24	Xeon Gold	2.1	Tesla V100	32	1	30,474
24	Xeon Gold	2.1	Tesla V100	32	2	30,288

Comparing the AI scores of the combinations shown above, it can be observed that the performance of Tesla V100 was obviously higher than RTX 2080 Ti, but only by 12% to 20%. However, the Tesla series can be seven to nine times more expensive than the GeForce series. Thus, for problems requiring less than 11 GB of memory, the RTX 2080 Ti GPU card may be a better choice. The Tesla series only has benefits for problems requiring more memory. It should be noted that the “problem size” is not equivalent to the size of the AI dataset; the dataset will be loaded into the AI program by batch, which controls the real memory requirements for the GPU cards.

Conclusion

This study provides the benchmark for three types of NVIDIA GPU cards when applied to six types of artificial intelligence problems. This study can help those who are aiming to establish their own AI platform or to rent one. It is recommended that planners understand the computing requirements and

the domain problems first. Then, they can avoid spending considerable construction fees on hardware that will not correspondingly improve effectiveness.

References

Andrey Ignatov. (2021) ai-benchmark, <https://ai-benchmark.com/>

Nonlinear Response History Analyses of NCREE Research Building Extension

Ming-Chieh Chuang¹, Keh-Chyuan Tsai², Guan-Hong Lin³, and Jui-Liang Lin⁴

莊明介¹ 蔡克銓² 林冠泓³ 林瑞良⁴

Abstract

This paper presents nonlinear response history analyses (NRHA) of the research building extension of the Taiwan National Center for Research on Earthquake Engineering (NCREE). Through the extension, NCREE's research building becomes a composite structure comprising a strengthened six-story reinforced-concrete (RC) structure and a vertically added seven-story steel structure. A new steel service core was added from the first floor to the roof at the north side of the building. To upgrade the earthquake-resistant performance, novel energy-dissipation devices such as buckling-restrained braces, steel panel dampers, and fluid viscous dampers are utilized. To gain insight into the seismic performance of NCREE's extended building, PISA3D structural analysis software is used for constructing the numerical model to conduct not only modal analysis but also NRHAs. To conduct these NRHAs, a total of twenty-one sets of historic earthquake ground accelerations are chosen and scaled to fit the Taipei Zone II design-basis earthquake (DBE) spectrum. The scale factors of the DBE range from 2.22 to 6.35. The earthquakes corresponding to the hazard levels of a service-level earthquake (SLE) and a maximum-considered earthquake (MCE) are 0.29 and 1.3 times that of the DBE, respectively. Through the NRHAs using the scaled ground accelerations of three different earthquake hazard levels (SLE, DBE, and MCE), it is found that maximum inter-story drifts are distributed evenly in the longitudinal direction but unevenly in the transverse direction. In the DBEs, the means of the maximum inter-story drift ratios are less than 1.5%, and thereby meet the ASCE/SEI 7-10 limitations of the buildings of the risk III category (*e.g.*, lecture halls). In the MCEs, the means of the maximum inter-story drift ratios are less than 2%, and thereby meet the FEMA 356 performance limitation for life safety. Hence, the seismic performance of NCREE's extended building is verified to be satisfactory.

Keywords: buckling-restrained braces, steel panel dampers, fluid viscous dampers, PISA3D, nonlinear response history analysis

Introduction

Preparations began for the National Center for Research on Earthquake Engineering (NCREE) Taipei research building and the large-scale structural laboratory in March 1990. The ground breaking started in August 1993, and the building use permit was obtained in December 1997. The original research building consisted of six levels above ground along

with a basement level (Fig. 1). After the official opening of the NCREE, to meet the needs of earthquake disaster prevention research and applications, business increased dramatically, the number of staff in the NCREE increased from 24 to more than 200 people. Fortunately, the original research building was designed for a foundation and structure based on the standards for 12-story reinforced-concrete (RC) buildings, allowing for the possibility of future

¹ Associate Researcher, National Center for Research on Earthquake Engineering

² Professor, Department of Civil Engineering, National Taiwan University

³ Former Research Assistant, Department of Civil Engineering, National Taiwan University

⁴ Division Head, National Center for Research on Earthquake Engineering

additions to the building.

After understanding the reasons and preliminary ideas for the vertical addition of the research building, the president of Ruentex Group, Dr. Yen-Liang Yin, agreed to donate the vertical addition project. The assessment of the vertical addition suggested that an additional steel structure design could be added up to the thirteenth floor (Figs. 2 and 3). In addition, the vertical addition project adopted the NCREE's patented buckling-restrained braces (BRBs) and steel panel dampers (SPDs). It also received donations of fluid viscous dampers (FVDs) from the US Taylor Devices and Sinodynamics Enterprise, Japan's KYB, and Taiwan's Well Link Industry, allowing the NCREE research building to be a building that integrates various seismic technologies. Construction on the extended research building finally started on October 23, 2019, with the beam-raising on May 27, 2020. On November 9, 2020, it was officially completed and opened.

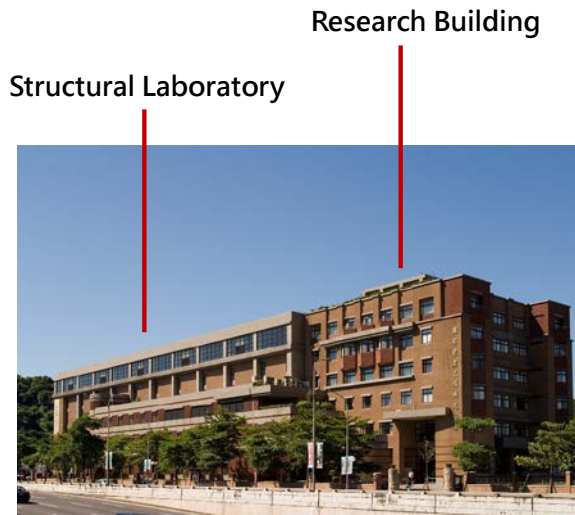


Fig. 1. The six-story RC building.



Fig. 2. The thirteen-story composite building.

Features of the Extended Building

The extended NCREE building (Fig. 3) is a composite structure that includes an existing six-story RC structure and an added seven-story steel structure. In addition, a new service core was added at the north side of the building from the first floor to the roof. Since the 1999 Chi-Chi earthquake, seismic design requirements have increased tremendously. To sustain the added steel structure and meet the latest seismic design requirements, the existing RC structure was strengthened using added RC shear walls and fiber-reinforced polymer (FRP)-strengthened RC beams. Moreover, novel energy dissipation devices (dampers) were adopted for improving the seismic performance of the extended building. Figure 4 shows an elevation view of the dampers installed on-site. To reduce a possible torsional effect and upgrade seismic performance, the BRBs and SPDs, developed by the NCREE, were installed in the new service core. FVDs were installed in the corners of the new building from the seventh to eleventh floors to mitigate the inter-story drift.

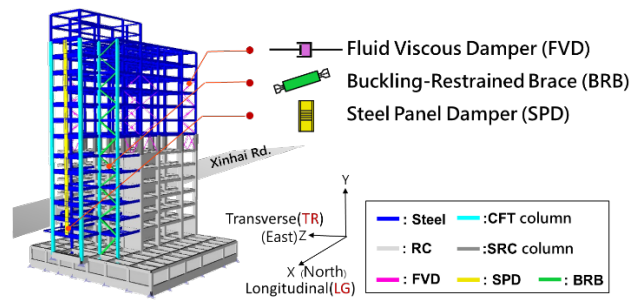


Fig. 3. PISA3D model.

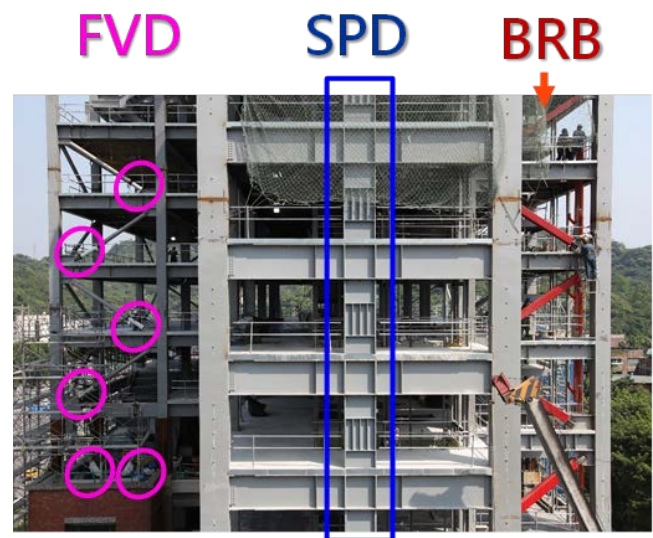


Fig. 4. On-site dampers.

Nonlinear Response History Analyses

To understand the seismic performance of the extended research building, a collaborative research project was conducted by NCREE researchers and Prof. Keh-Chyuan Tsai's research group from the National Taiwan University (NTU). In the research, PISA3D structural analysis software (Lin *et al.*, 2009) was used for constructing the numerical model (Fig. 3) to conduct modal, pushover, and nonlinear response history analyses (NRHA) (Lin *et al.*, 2021). NRHAs for the NCREE's thirteen-story composite building were conducted to gain insight into the effects of possible maximum seismic forces and deformational demands. A total of sixty-three ground accelerations, namely twenty-one at each of three hazard levels—service-level earthquakes (SLE), design-basis earthquakes (DBE), and maximum-considered earthquakes (MCE)—were utilized for the NRHAs. These ground accelerations were scaled separately for the three hazard levels to fit the spectral accelerations in the design response spectra (Chien *et al.*, 2020; Liu *et al.*, 2020). The scale factors for the DBE ranging from 2.22 to 6.35 were used to fit the Taipei Zone II design spectrum (Fig. 5). Subsequently, the ground accelerations corresponding to the hazard levels of the SLE and MCE are 0.29 and 1.3 times that of the DBE, respectively.

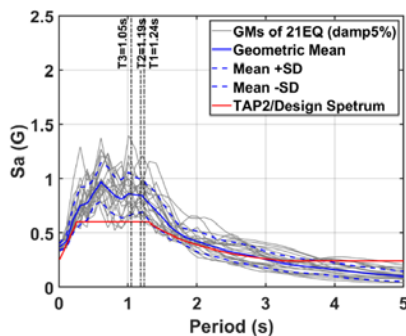


Fig. 5. Twenty-one DBEs and design response spectra.

The twenty-fold amplified deformation shapes and corresponding distributions of the plastic rotations, derived from the NRHA with the ground motions recorded at the TAP042 strong-motion station in the 1999 Chi-Chi earthquake and scaled to the MCE, as the numerical model reached the peak roof displacement (drift ratio: 0.88%) in the transverse (TR) direction are shown in Figs. 6 and 7. As shown in Fig. 6, significant plastic hinges that formed at the RC beam ends indicate flexural failures. Examples of the hysteresis loops for the RC members (*e.g.*, RC beam and RC shear wall) and adopted dampers (*i.e.*, FVD, SPD, and BRB) are indicated in Figs. 6 and 7, respectively.

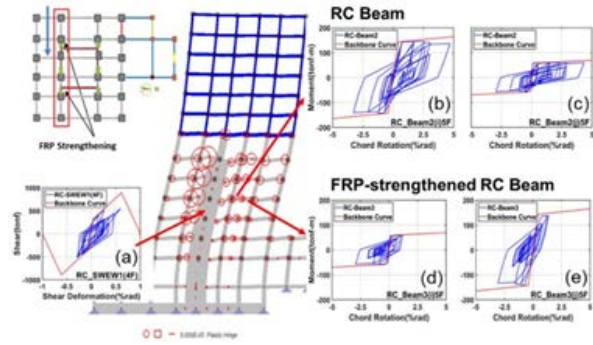


Fig. 6. Side view of the deformation shape (as the numerical model reaches the peak roof displacement) and hysteresis loops for the RC members.

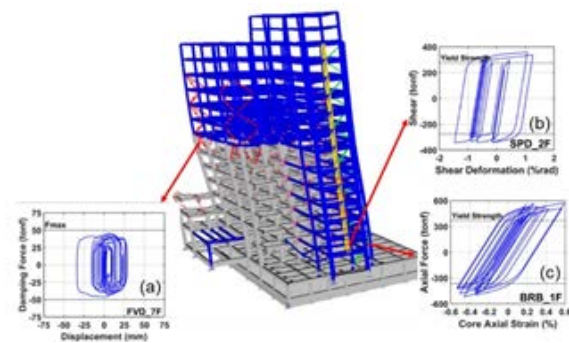


Fig. 7. Perspective view of the deformation shape (as the numerical model reaches the peak roof displacement) and hysteresis loops for the dampers.

From the NRHA results shown in Fig. 8, it can be found that maximum inter-story drifts are distributed evenly in the longitudinal (LG) direction but unevenly in the TR direction. Moreover, the results shown in Fig. 8 indicate that, for the twenty-one MCE ground accelerations, the peak means of the maximum inter-story drift ratios are 1.61% and 1.52% in the LG and TR directions, respectively. In addition, for the twenty-one DBE ground accelerations, the peak means of the maximum inter-story drift ratios are 1.22% and 1.11% in the LG and TR directions, respectively. Obviously, the means of the maximum inter-story drift ratios of DBEs and MCEs can satisfy the requirements of the American Society of Civil Engineers ASCE/SEI 7-10 limitation (1.5%) for buildings of the risk III category (*e.g.*, lecture halls) and the Federal Emergency Management Agency FEMA 356 limitation (2%) for life safety, respectively.

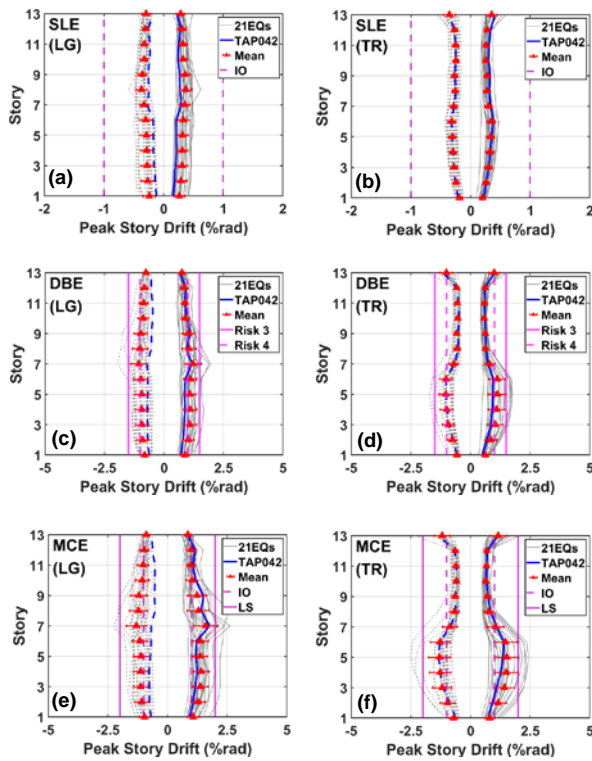


Fig. 8. Means of maximum inter-story drift ratios obtained from NRHAs.

Conclusions

Based on the inter-story drift ratios obtained from the above NRHAs, the seismic performance of the extended NCREE building is satisfactory and meets the requirements of inter-story drift limitations prescribed in the FEMA 356 (life safety) and ASCE/SEI 7-10 (Risk III building) codes.

References

- Lin, B.Z., Chuang, M.C. and Tsai, K.C. (2009), “Object-oriented development and application of a nonlinear structural analysis framework”, *Advances in Engineering Software*, **40**(1): 66-82.
- Chien, W.Y., Liu, H.J., Chang, C.W. and Chang, Y.W. (2020). “A Study on the Design Basis Earthquake for Taipei Basin,” Proceedings of the fifteenth national conference on structural engineering/the fifth national conference on earthquake engineering, Tainan, Taiwan, 2-4 September, 2020. Paper # 104.
- Liu, H.J., Chien, W.Y. and Chang, Y.W. (2020). “A Study on Recorded Ground Motion Selection for Generic Sites in Taiwan,” Proceedings of the fifteenth national conference on structural engineering/the fifth national conference on earthquake engineering, Tainan, Taiwan, 2-4 September, 2020. Paper # 143.
- Lin, G.H., Chuang, M.C., Tsai, K.C. and Lin, J.L. (2021), “Seismic Analysis of NCREE Office

A Case Study of Rescue Route Planning

Cheng-Tao Yang¹ Chi-Hao Lin¹ Zheng-Xuan Li² Ya-Chu Tsao³ I-Tien Lo⁴

楊承道¹、林祺皓¹、李政軒²、曹雅筑³、羅億田⁴

Abstract

In response to major disasters, rescue routes that connect evacuation shelters and rescue spots are the heart of a disaster rescue site. These routes enable delivery of required emergency rescue equipment and supplies. Currently, the Taipei City government has declared “Emergency Rescue Route for Major Disasters” as a tool to address rescue and evacuation. Other cities and counties have performed preliminary studies, but there are still no officially-released procedures for establishing rescue routes. To undertake rescue route planning, multiple factors need attention. These include earthquake risk features in each area, seismic capacity of on-street buildings and critical bridges, regional transportation demands, and the location of emergency medical facilities. Using New Taipei City as an example, our study concentrates on the geographical environment of the region and the principles of rescue route planning to identify rescue routes by applying a developed software, ROSA. Use of such rescue routes promotes precautionary measures in pre-earthquake conditions and aims to help relevant practitioners launch emergency responses during and after earthquakes.

Keywords: Earthquake Disaster, Rescue Route, On-street Buildings, Critical Bridges

Introduction

Taiwan is located in an earthquake-prone zone and has densely populated metropolitan areas. If a large-scale earthquake occurs, avoiding impacts on population, buildings, and road networks would be difficult. Roads are the main connections for daily living and various economic activities and, during major disasters, they connect rescue sites and disaster areas and facilitate delivery of emergency supplies and evacuation. For disaster preparedness, local governments need to consider several regional factors to plan rescue route networks. These include earthquake risk features, seismic resistance of on-street buildings, locations of fire stations and emergency medical services, distribution of evacuation shelters, and mutual rescue between neighboring counties and cities. Old and on-street buildings and critical bridges that are at risk of collapse have priority for repairing or retrofitting. Structural retrofitting aims to reduce the frequency of road network disruption and ensure more fluent and efficient emergency pipelines.

In recent years, our team has constructed a system for simulating the probability of destruction or damage to roads under earthquake events in Taiwan. The following software, called ROSA, was developed to tackle damage events and evaluate rescue efficiency. This software can be applied to emergency rescue and evacuation route planning, making decisions on using alternative roads, and identifying key road components and seismic risks of on-street buildings, especially for

road networks in Taiwan. In this study, we use New Taipei City as a case study and introduce its geographic environment. We then describe our study method, including principles of planning which rescue routes to follow and how ROSA forecasts these potential rescue routes.

The red lines in Figure 1 indicate 27 emergency rescue routes officially declared by the Taipei City government (Taipei City Traffic Engineering Office, 2019). Although the neighboring New Taipei City and Keelung City have related studies and results on this issue (New Taipei City, 2015; Sheu, 2003), the official rescue route has not yet been proclaimed.

A recent study has identified the supplementary transportation pipelines of New Taipei City (New Taipei City, 2015). The transportation principles mainly focus on road widths and intra-regional connections. However, for further application, New Taipei City (2015) still needs to consider other significant factors of the rescue process, such as connections between neighboring districts, rescue in densely populated areas, and mutual rescue between neighboring counties and cities.

As shown in Figure 1, New Taipei City has a vast territory and complex topography with urbanized plains, rivers, and mountains. Taipei City and Keelung City are embedded in this area. Their roads are complex and less organized than grid streets. Further, the population is highly concentrated in some districts

¹ Associate Researcher, National Center for Research on Earthquake Engineering

² Summer Intern, National Center for Research on Earthquake Engineering

³ Research Assistant, National Center for Research on Earthquake Engineering

⁴ Chief of Preparedness and Response Division, Fire Department, New Taipei City

on the left bank of the Tamsui River-Xindian River juncture. Considering these factors, New Taipei City's emergency rescue operations require further consideration.

We recommend the following items to develop a satisfactory rescue route solution.

The first is a consideration of the road networks of neighboring counties and cities, including Taipei City, Keelung City, and Taoyuan City. The most efficient rescue routes in different districts of New Taipei City usually pass through Taipei or Keelung. Therefore, incorporating the total road network around its neighboring cities is recommended.

The second recommendation is to relax road width requirements by setting a wider road width range. The roads in New Taipei City are curved and non-gridded. Roads in the same section may have different widths or contain different lane densities. Therefore, it is difficult to critically follow road width rules under emergency planning principles. We recommend changes to rescue road selection according to individual city conditions, as supported by Sheu (2003).



Figure 1. The distribution of rescue sites and important roads in New Taipei, Taipei, and Keelung

Methodology

The planning principles of rescue routes are primarily based on “Guidelines for Disaster Prevention Roads and Evacuation Sites Planning” (Construction and Planning Agency, Ministry of the Interior, 2011). According to Table 1, the main considerations for disaster rescue route selection are based on road width and whether or not they connect important rescue sites.

Table 1. Guidelines for disaster prevention roads and evacuation sites planning (from the website of Construction and Planning Agency, Ministry of the Interior).

Guidelines for Disaster Prevention Roads Planning
1. Emergency road: main road > 20 meters in width connecting neighboring counties and cities
2. Rescue transportation road: main or secondary roads 15 to 20 meters in width
3. Evacuation service road: roads 8 to 15 meters in width

Guidelines for Evacuation Sites Planning
1. Four types: emergency evacuation, temporary evacuation, temporary shelters, and mid- and long-term shelters.
2. Mid- and long-term shelter priority should be schools and stadiums.
3. These places should be adjacent to roads, hospitals, fire stations, police stations, administrative centers, and supplement distribution centers.

Based on the special geographical environment of New Taipei City and the official rescue route of Taipei City, our study prioritizes the Taipei route and connects subsequent existing rescue routes. We also moderately relax the requirements of road width under topographical restrictions. Overall, the rescue route planning process using ROSA can be divided into the following steps:

Select important rescue sites. Where populations and buildings are densely distributed in each district, we select important rescue sites (e.g., hospitals, fire stations, and evacuation shelters), and major traffic nodes (e.g., river crossing ramps, freeways, and expressways entrance ramps).

Utilize ROSA for solutions. The concepts of ROSA mainly recognize rescue sites as supply nodes, densely populated areas as demand nodes, and others as relay nodes. The estimated cost of node connection is based on travel time by cars driving through certain road sections. The travel cost of each pitch line is multiplied by different weights determined by regional road conditions, preferential path, existing rescue routes of Taipei City, and rescue sites. Individual cases are used to minimize the total travel cost of rescue teams travelling through various paths and determine the most efficient route.

Identify the risks of road blockage. We use an earthquake loss estimation system to obtain simulation results of selected rescue road blockage risks due to broken bridges or collapsed on-street buildings during and after earthquakes. Moreover, we explore alternative roads to cover such blockage cases.

The Planning Case Studies

This section shows the workflow employed by ROSA to determine rescue routes for Yonghe District in New Taipei City as a case study. The locations of emergency medical service, critical bridges, fire stations, and evacuation shelters around Yonghe are shown in Figure 2. The blocks in Figure 3 denote the basic statistical area declared by the Ministry of the Interior. The classification shows the building height ratio using the sum of floor area divided by total land area of each building in every basic statistical area. We highlight four built-up areas around Yonghe District.

ROSA then recognizes densely populated areas as demand nodes and all available rescue sites as supply

The Post-earthquake Crowdedness of a First-aid Hospital by Non-urgent Patients

You-Xuan Lin¹ and Chi-Hao Lin¹

林祐萱¹、林祺皓¹

Abstract

The purpose of this study is to analyze the impact of a group of earthquake-induced non-urgent patients on hospital performance. This paper takes the emergency care system in Taiwan as the research context, where first-aid hospitals are ranked according to three levels, advanced, intermediate, and general, with a current emphasis on a general emergency responsibility hospital. A healthcare performance index, Crowdedness Index (CI), is proposed to measure crowdedness on a daily basis. Results of simulations rendered the establishment of empirical equations, describing the relationship between maximum CIs and patient growth ratios. Findings are provided pertaining to the predication of a recovery curve and the alarming level of patient increase, which are supportive information for preparedness planning as well as response measure formulation to improve resilience.

Keywords: first-aid hospitals, crowdedness, quality, seismic resilience

Introduction

Hospital crowdedness caused by a surge of casualties is one of the major obstacles to healthcare system resilience in the face of seismic disasters. Even if a hospital survives and maintains its full functionality to treat and accommodate patients, long queues may still emerge from rushing patients and overwhelm the emergency department (ED). Thanks to well-developed methodologies for earthquake loss estimation, specialized modules in software tools, like HAZUS [1] and TELES [2], have made casualty estimates of seismic events feasible. Nevertheless, there is a gap between information on estimated medical demand and predictions of likely induced impact on emergency care institutions.

In this paper, we take the emergency healthcare system in Taiwan as the research context and demonstrate the relationship between patient number growth ratios and emergency care performance decline, as well as recovery time (in days after earthquakes) using two performance measures, Crowdedness Index and Quality. In the analysis, patient flow was split into two separate routes, one for urgent patients (AL1 and AL2) and the other for less acute patients (AL3, AL4, and AL5).

Model of patient flow and parameter settings

Discrete event simulation (DES) was conducted with the help of a Python library, SimPy [3], to simulate patient flow within emergency care. Based on Favier et al. [4] and Côté [5], and some modifications made to approximate the emergency care procedure in Taiwan, the patient flow paths throughout first-aid hospitals were modelled, as shown in Fig. 1.

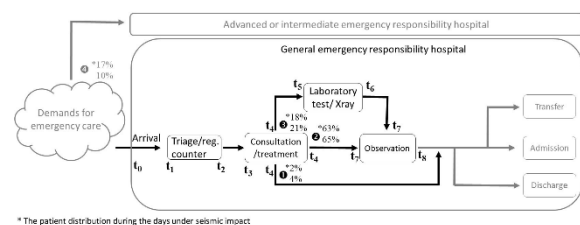


Fig. 1. Patient flow of first-aid hospitals

Based on real data and estimations, Favier et al. [4] proposed the percentage of each triage category and

¹ Assistant Researcher, National Center for Research on Earthquake Engineering

² Associate Researcher, National Center for Research on Earthquake Engineering

the probability of each category being assigned to one of three paths. This study primarily adopted their figures after making the following changes: (1) altering the percentage of AL1 and AL2 patients and (2) altering the path taken by AL5 patients, as shown in Table 1.

Table 1. Distribution of arriving patients to paths

	Path1	Path2	Path3	Path4
Normal	4%	65%	21%	10%
Seismic	2%	63%	18%	17%

This study adapted estimated arrival rates to generate the number of patients over time. As displayed in Fig. 2, instead of being fixed or smoothed, arrival rates fluctuated over time during the busy phase. Arrival rates in five scenarios in Favier et al. [4] were adapted for simulations in this study, with one scenario being applicable during normal conditions and the remaining four after earthquakes (GR1 – GR4).

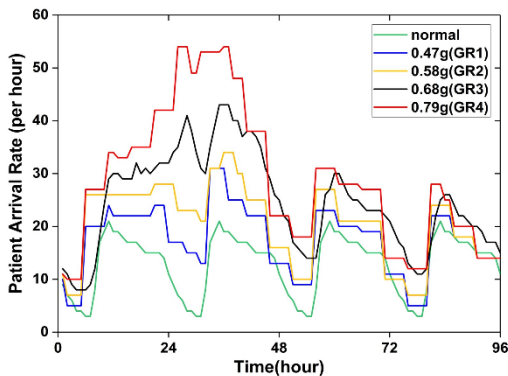


Fig. 2. Patient arrival rates within the 4-day busy phase and on normal days (adapted from Favier et al. [4])

As one patient is generated in the simulation, he/she will be moved forward along the assigned path to receive medical services while simultaneously occupying one resource unit of the assigned service. One resource unit here refers to a combination of all labor and devices needed to serve one patient, instead of referring to specific staff or items. The duration of each medical service and the gross resource number are two set parameters in the program. The time distribution of each service and the resource number are based on previous studies with some adjustments made after initial trials.

The simulation model with a defined set of parameters was tested to ensure that it could by and large represent operations within emergency care institutions. To confirm that the resource number and

service time of each medical service were reasonable, we compared simulation results with real census data. In our model, every patient (AL3–AL5) waits for approximately 9 minutes before receiving treatment on normal days. In real situations, according to a report surveying all EDs in Taiwan [6], the AL3, AL4, and AL5 patient waiting time for treatment is 9–10 minutes on average. These suggest that our model is generally able to, if not accurately, capture normal operations in a general emergency responsibility hospital.

Crowdedness Index (CI) is a measure that evaluates a first-aid hospital by its ability to provide timely treatment for patients of different ALs. The Ministry of Health and Welfare in Taiwan has issued a guide on triage, which prescribes the maximum waiting time for each AL. Using this guide, CI is defined as the quotient of average patient waiting time for treatment over the advised maximum waiting time grouped by ALs. Therefore, each level has its own CI calculated. The calculation to obtain CI is described below in Eq 1, Eq 2, and Eq 3:

$$CI_{AL3,j} = \frac{\sum_{p=1}^{N_{AL3,j}} (t_3^p - t_0^p)}{N_{AL3,j} \cdot T_{AL3}} \quad (1)$$

$$CI_{AL4,j} = \frac{\sum_{q=1}^{N_{AL4,j}} (t_3^q - t_0^q)}{N_{AL4,j} \cdot T_{AL4}} \quad (2)$$

$$CI_{AL5,j} = \frac{\sum_{r=1}^{N_{AL5,j}} (t_3^r - t_0^r)}{N_{AL5,j} \cdot T_{AL5}} \quad (3)$$

where p , q , and r are every single AL3, AL4, and AL5 patient arriving on day j and receiving treatment, $N_{AL3/4/5}$ are the total numbers of p , q , and r , and $T_{AL3/4/5}$ are the advised maximum waiting times. Hospital duration time that CI concerns is from arrival to treatment or the time interval between t_3 and t_0 , as marked in Fig. 1.

Results

In this study, we have highlighted the maximum CI values in different scenarios and provided an overview of changing CIs over time (in days), as shown in Fig 3 and Fig 4. The maximum CI indicates the worst state for different casualty sizes. While CI provides information on emergency care performance on a given day, applying different ways to analyze and interpret these CI data helps to obtain information for practical purposes, as shown in Fig. 3.

Two analyses are provided. First, maximum CI is further analyzed in relation to growth ratios to reach a set of empirical equations (Eq 4–6) that can be adopted to estimate hospital states for different scenarios. Second, CIs are viewed from a different perspective to present both decline and recovery of emergency care quality. In this way, the concept of

resilience can be introduced, as shown in Fig. 5.

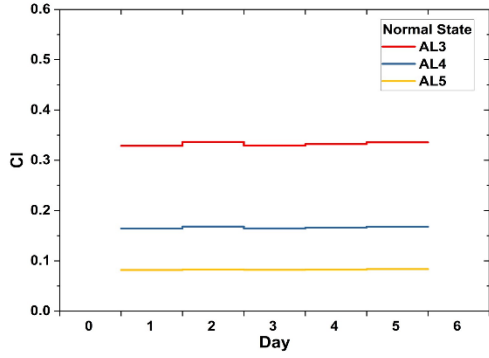


Fig. 3. Crowdedness Index in normal situations

$$MaxCI_{AL3} = \begin{cases} -8.42 + 8.75P & P \leq 1.4 \\ -133.56 + 98.13P & P > 1.4 \end{cases} \quad (4)$$

$$MaxCI_{AL4} = \begin{cases} -4.19 + 4.36P & P \leq 1.4 \\ -66.78 + 49.07P & P > 1.4 \end{cases} \quad (5)$$

$$MaxCI_{AL5} = \begin{cases} -2.08 + 2.16P & P \leq 1.4 \\ -33.4 + 24.53P & P > 1.4 \end{cases} \quad (6)$$

The CI data were analyzed from another perspective to generate a direct representation of emergency care quality. Eq 7 indicates how emergency care quality (Q_i) is achieved using CI_i , where i refers to AL3, AL4, and AL5. In brief, quality (Q) is defined by taking the minimum value between 1 and the reciprocal of CI. A properly functional general emergency responsibility hospital has a Q value of 1, where patients can be treated within an appropriate time. Values lower than 1 signify overloading and a decline in quality. By applying CI in this way, Q also focuses on the ability of a hospital to timely and effectively provide healthcare.

$$Q_i = \min\left(\frac{1}{CI_i}, 1\right) \quad (7)$$

Q is efficient in capturing the reduction and restoration of emergency care quality, as shown in Fig. 5. Fig. 5 illustrates the impact of increased patient volume on emergency care quality for the three patient categories. The results show that Q decreases immediately on the first day of the busy phase, except for AL5 in the GR1 scenario, where Q remains at 1 and the drop is delayed by one day (Fig. 5A).

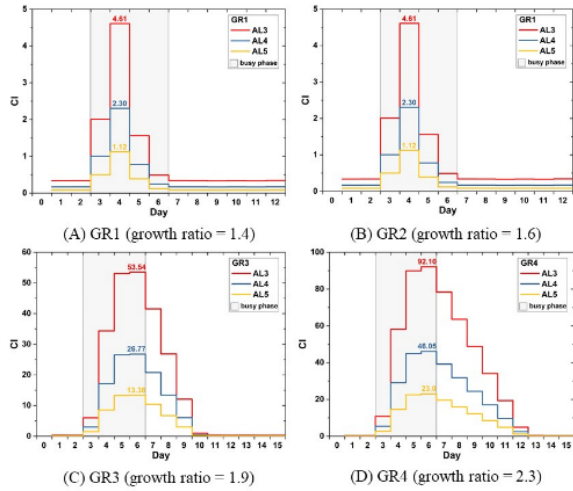
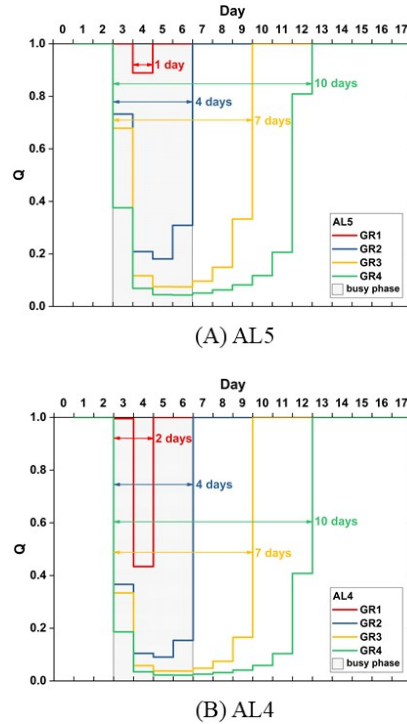


Fig. 4. Crowdedness Index under the influence of earthquakes

We can find that maximum CI has a drastic reaction to the growth of patient numbers especially when the growth ratio is above 1.4. Although the excessively lengthy waiting time may not necessarily be fatal yet for those patients, it cannot be neglected because their suffering, both mental and physical, is prolonged and intensified during the process. Consequently, it would make the already tough recovery period, both personally and for the whole community, even more challenging.



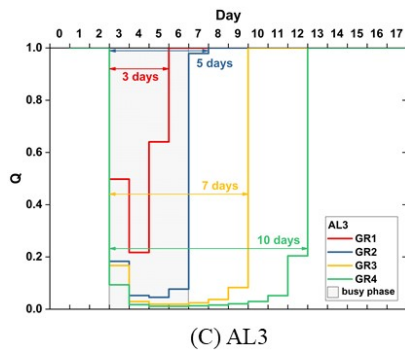


Fig. 5. Emergency care quality decrease and restoration

As to recovery, the process of quality decrease and restoration, the period is prolonged as patient volumes increase. As expected, GR4 results in the longest recovery time and GR1 the shortest. However, when compared across acuity levels, the quality recovery period for more acute injuries is not necessarily prolonged. No difference in the length of recovery period was observed across levels in GR3 and GR4 scenarios. Here, 7 days and 10 days are required respectively for all patient categories. However, it takes additional time in GR1 and GR2 to recover the quality of AL3. In conclusion, this may suggest that when the patient number inflates to a certain extent, the quality loss caused by queuing equally impacts recovery time for patients of all acuity levels.

Conclusions

This study is a preliminary attempt to analyze the post-earthquake congestion of healthcare institutions with its current research target on one single general emergency responsibility hospital. In the current study, we focused exclusively on the impact of a sudden increase in patient visits made up of seismic casualties. By means of discrete event simulation, changes in hospital performance faced with different volumes of patient influx were captured and presented using Crowdedness Index (CI) and Quality (Q) as performance measures. Results of the emergency care quality recovery curve and the level of patient increase as a warning sign forecasting a collapse in medical supply were reported.

References

1. Federal Emergency Management Agency [Internet]. Hazus Earthquake Model Technical Manual. 2020 Oct. Available from: https://www.fema.gov/sites/default/files/2020-10/fema_hazus_earthquake_technical_manual_4-2.pdf [cited 2021 Jan 18].
2. Yeh CH, Loh CH, Tsai KC. Overview of Taiwan earthquake loss estimation system. *Nat Hazards*

(Dordr). 2006;37: 23-37. doi: 10.1007/s11069-005-4654-z.

3. Müller K, Vignaux T. SimPy: Simulating systems in Python. 2003. Available from: <https://simpy.readthedocs.io/en/latest/>
4. Favier P, Poulos A, Vásquez JA, Aguirre P, de la Llera JC. Seismic risk assessment of an emergency department of a Chilean hospital using a patient-oriented performance model. *Earthq Spectra*. 2019;35: 489-512.
5. Côté MJ. Patient flow and resource utilization in an outpatient clinic. *Socioecon Plann Sci*. 1999;33: 231-245.
6. Shiu MN. 2013. Emergency Department Overcrowding Analysis and Countermeasures. Department of Medical Affairs. Ministry of Health and Welfare (Taiwan). Available from: <https://www.mohw.gov.tw/dl-3079-d8ff7291-e302-4a8f-a2a5-8208c4a1ada2.html> [cited 2020 501 Dec 24].

Site-Effect Model for Wide-area Seismic Damage Assessment

Chin-Hsun Yeh¹, Lee-Hui Huang² and Yin-Nan Huang³

葉錦勳¹、黃李暉²、黃尹男³

Abstract

Wide-area earthquake loss assessment has been widely used in disaster prevention planning and emergency response drills to improve various aspects of risk-management feasibility and effectiveness. When evaluating earthquake damage to engineering structures over a wide area, it is necessary to estimate the local seismic hazards for each location. Estimating ground-motion intensity is the basis for evaluating other threats such as soil liquefaction or landslide potential. Because geological data such as V_{s30} (averaged shear-wave velocity to a depth of 30 m) and $Z_{1.0}$ (depth at which shear-wave velocity is 1000 m/s) are not usually available for large areas, the site-effect model used in ground-motion prediction equations is not suitable for seismic hazard analysis or loss assessment for large areas. Based on the Taiwan Earthquake Loss Estimation System (TELES), this study combines new ground-motion prediction equations and ground-motion databases in Taiwan to develop and assess a site-effect model suitable for wide-area seismic damage assessment.

Keywords: wide-area earthquake loss assessment, seismic hazards, ground-motion prediction model, site effect.

Introduction

Based on site-specific seismic source characteristics, rupture fault geometry, and geological data—such as the averaged shear-wave velocity to a depth of 30 m (V_{s30}) and the depth at which shear-wave velocity is 1000 m/s ($Z_{1.0}$)—a ground-motion prediction model can estimate the intensity of motion of the surface of the ground as a result of any earthquake scenario. Using the estimated ground-motion intensity, the extent of other seismic hazards, such as soil liquefaction and landslides, can be assessed. Based on these estimates, it is possible to predict damage to engineering structures, human casualties, social impact, and economic losses caused by earthquakes. The ground-motion prediction model is thus the basis of earthquake loss assessment technology.

The new generation of ground-motion prediction models comprehensively consider source characteristics, path effects, and site effects. For example, they distinguish between crustal earthquakes and subduction earthquakes, and they take into account effects such as magnitude saturation and distance saturation. Based on ground-motion

prediction models developed in other countries but using ground-motion records from Taiwan, Chao (2019) established a ground-motion prediction model suitable for Taiwan, named NCREE 19 GMPE. This model uses V_{s30} and $Z_{1.0}$ as the main factors reflecting site effects.

The Taiwan Earthquake Loss Estimation System (TELES) (Yeh, 2003), developed by the National Center for Research on Earthquake Engineering (NCREE) in Taiwan, has been widely used in earthquake disaster prevention planning, risk assessment, and management. Comparing the early loss estimates following earthquakes with the actual disaster survey data over many years improves the reference value of the TELES assessment results and indirectly demonstrates the validity of the ground-motion prediction model.

When assessing earthquake losses across large areas, most places lack measured V_{s30} and $Z_{1.0}$ values. As a result of complex topography, landforms, and underground soil structures, measured ground-motion intensity varies substantially. It is not possible to fully reflect site effects using V_{s30} and $Z_{1.0}$ alone. This study aims to integrate aspects of the TELES model and the NCREE 19 GMPE model without site effects. It uses the ground-motion records

¹ Research Fellow and Division Head, Seismic Disaster Simulation Division, NCREE, NARL

² Assistant Researcher, Seismic Disaster Simulation Division, NCREE, NARL

³ Associate Professor, Department of Civil Engineering, National Taiwan University

from the Taiwan Central Weather Bureau for recent decades, including the magnitude and location of earthquakes, fault-plane solutions, and geological drilling data for each station, to investigate site-effect models suitable for wide-area seismic damage assessment in Taiwan.

Existing Site-Effect Model for TELES

For seismic damage assessment of various types of structures and buried pipelines, the ground-motion parameters should include the peak ground acceleration (PGA), the short-period structural-response spectral acceleration (S_{a03}), and the one-second-period structural-response spectral acceleration (S_{a10}). Due to the different patterns of attenuation of seismic waves of different periods with distance, the site-effect coefficients of the three ground-motion parameters are different, but the estimation models are roughly similar.

As an example, Fig. 1 uses PGA to illustrate the site-effect model used in the TELES. Based on experience, the seismic intensity at bed-rock can be divided into several intervals. When it is small, the magnification of the ground-motion intensity is greater. This magnification decreases when the seismic intensity at bed-rock increases, owing to the nonlinear response of the soil. It is assumed in Fig. 1 that regression analysis can be used to obtain the median ground-motion intensity (PGA_s) at each site under different seismic intensities at bed-rock (PGA_a). The solid lines of various colors represent site-response characteristics at various locations. The green line represents soft-soil sites, the blue line medium sites, and the red line hard-rock sites.

Under any earthquake scenario, the ground-motion intensity at each site can be assessed initially using the traditional ground-motion attenuation law to obtain the seismic intensity at bed-rock. Depending on the site characteristics, one of the curves in Fig. 1 is chosen to assess the ground-motion intensity.

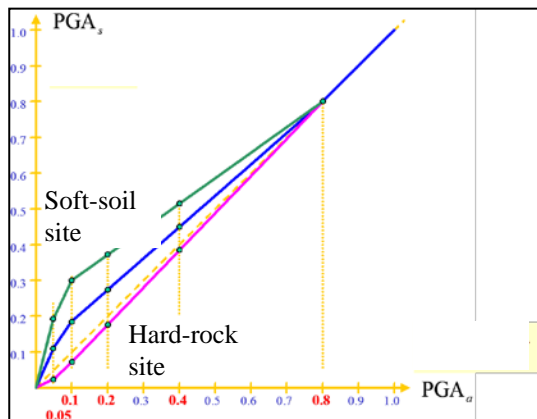


Fig. 1 Schematic diagram of the TELES site-effect model.

Methods and Procedures

This study collected earthquake records from 1981 to 2016, comprising records from 843 seismic stations of the Central Weather Bureau covering 365 seismic events and 44,600 individual earthquake records. Only records with a high resolution that were suitable for site-effect analysis were included, to maximize the accuracy of the analysis results. For example, to meet the seismic damage assessment requirements for structures and buried pipelines, the seismic intensity at bed-rock had to be higher than a specific threshold. For historical earthquakes, the seismic intensity at each station (without considering site effects) was estimated using NCEE 19 GMPE. The shear-wave velocity of the reference site was assumed to be 760 m/s. The comparison of the measured ground-motion intensity for individual stations with the predicted seismic intensity was used as the basis for studying the site-effect model.

Since there were usually not enough earthquake records that met the requirements above (for example, $PGA_a \geq 0.02$ g) for a single station, it was impossible to perform a credible regression analysis using these records alone. To solve the dilemma of poor earthquake records for individual stations, this study classifies the sites based on the V_{s30} values for individual stations. In this way, more stations and earthquake records belonged to a single site classification. Thus, the site-effect curves for the various site classifications under different seismic intensities can be reasonably estimated. Thus when there are not enough data-points for individual stations, one can refer to the site-effect curve for the same site classification.

Site-Effect Model for Site Classifications

The parameter V_{s30} is often used for site classification, and this value has been recorded at each of the Central Weather Bureau's stations. Therefore, this study used V_{s30} values of 760, 630, 540, 450, 360, 270, and 180 m/s as the boundaries to divide the stations into eight classes of site-condition. The seismic intensity at bed-rock was also divided into several intervals to explore the relationship between site magnification and seismic intensity at bed-rock. Considering S_{a03} , the first three intervals of seismic intensity at bed-rock were 0–0.1 g, 0.1–0.2 g, and 0.2–0.4 g. Table 1 shows the number of records for each seismic intensity interval and site classification. It can be seen from the table that, in general, the number of records was much larger for the first seismic intensity interval than for the others.

Figure 2 shows the distribution of data points for the site class with V_{s30} values of 270–360 m/s, as an example. Note that both the horizontal and vertical

axes are logarithmic. The 45° dashed line in the figure indicates the points at which seismic intensity at bed-rock is equal to the seismic intensity at surface, with no amplification due to site effects. The data points in each interval were used to derive regression equations, where the slope of the line is constant, and the best intercept is calculated:

$$\log_{10}(y_s) = \log_{10}(y_a) + c, \quad (1)$$

where y_a is the estimated seismic intensity at bed-rock, y_s is the measured ground-motion intensity at surface, and c is the regression parameter. The larger the intercept c , the greater the site effect. Magnification due to the site effect was 10^c . For the sake of conservatism, the site effect was assumed to be the value at the right-hand end of the intensity interval. The three thick line segments in Fig. 2 represent the regression lines for the three seismic intensity intervals and the magnifications due to site effect were 1.7, 1.2, and 1, respectively.

Table 1 Number of records for each seismic intensity interval and site classification.

V_{s30} (m/s)	Seismic intensity S_{a03}		
	0–0.1 g	0.1–0.2 g	0.2–0.4 g
> 760	423	56	43
760–630	415	64	31
630–540	795	155	60
540–450	1,099	178	78
450–360	702	101	34
360–270	572	95	62
270–180	1,533	179	95
< 180	123	10	8

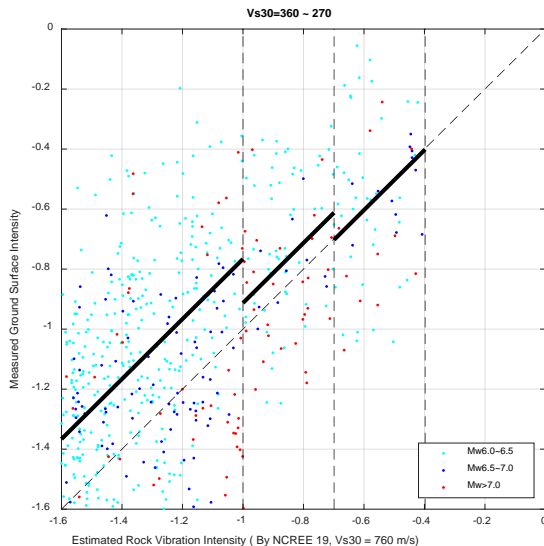


Fig. 2 Spread of S_{a03} values according to seismic intensities at bed-rock and at surface for sites with $V_{s30} = 270\text{--}360$ m/s.

Generally speaking, when the seismic intensity at bed-rock is high, the magnification of the ground-

motion intensity is slight. There were few data points in the third seismic intensity interval, so the regression analysis results for this class are of lower reference value. Therefore, this study only used the regression results for the first and second seismic intensity intervals. Table 2 shows the regression results for the S_{a03} site effects for the eight site classifications.

Table 2 Regression results for the S_{a03} site effects for the eight site classifications

V_{s30} (m/s)	First Interval	Second Interval
> 760	0.0833	0.0000
760–630	0.0850	0.0000
630–540	0.1214	0.0418
540–450	0.1756	0.0662
450–360	0.2790	0.1628
360–270	0.2336	0.0870
270–180	0.3328	0.1344
< 180	0.3478	0.2355

The regression results c in the first seismic intensity interval for the eight site classifications are plotted in Fig. 3. A linear regression analysis was performed for PGA, S_{a03} , and S_{a10} , respectively, according to:

$$c = a \times V_{s30} + b \geq 0, \quad (2)$$

where a and b are the regression coefficients. The results are shown in Table 3 and in Fig. 3 as thick lines. From Fig. 3 or Table 3, if one has the V_{s30} value for a specific location, one can obtain the site-effect magnification for the first seismic intensity interval, as shown in Fig. 4.

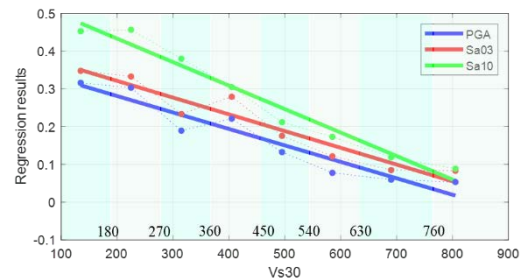


Fig. 3 Regression results for the first seismic intensity interval for the eight site classifications.

Table 3 Coefficients in Eq. (2) for each of the three site-effect variables.

Coeff.	PGA	S_{a03}	S_{a10}
a	–0.000436	–0.000443	–0.000622
b	0.368253	0.409887	0.557492

Site-Effect Model for Individual Stations

It should be noted that there are actual measured ground-motion records for many sites, so the site-effect curve for individual stations should be

somewhat different from the curve obtained entirely based on Eq. (2). The site-effect curve for each station should thus be a weighted average of two analysis results: the regression analysis of seismic records from the station itself, and the site-effect curve for all sites in the same V_{s30} classification. The weights of the two analysis results should be determined using the number of data points in each seismic intensity interval for that station. If the station has more data points (e.g., ≥ 10), then the more reliable regression results can be used, and the site characteristics will be more accurately reflected. Otherwise, it is necessary to refer to the V_{s30} value for the station to obtain the approximate site-effect curve.

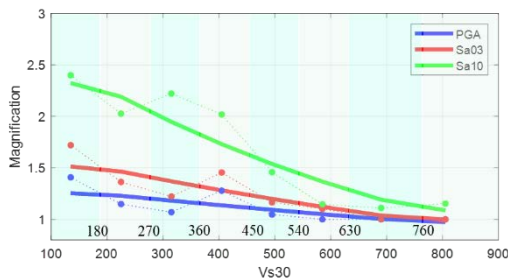


Fig. 4 Site-effect magnification in the first seismic intensity interval for the eight site classifications.

Figure 5 shows the S_{a03} site-effect magnification for all individual stations in the first seismic intensity interval. The thick black line represents the predicted site-effect magnification for the classified sites. It can be seen that the actual site-effect magnification values for individual stations are distributed on either side of that line. The V_{s30} value for individual stations may thus broadly reflect the site effect, but these effects do exhibit considerable variability. If the site-effect magnification for a site classification is used to estimate the ground-motion intensity at a station under any earthquake scenario, the probability of over- or underestimation is approximately 50%.

Based on the coordinates and the site-effect magnification for individual stations, spatial interpolation can be used to calculate the distribution of site-effect magnification, for a specific seismic intensity interval, of PGA, S_{a03} , and S_{a10} , as shown in Fig. 6.

Concluding Remarks

This study combined the site-effect model of the TELES and the ground-motion prediction model NCREE 19 GMPE without site-effect. The proposed site-effect model considers seismic records from recent years and the geological variable V_{s30} for individual stations. Under any earthquake scenario, the new model may predict the ground-motion intensity more accurately for each location. These

results will be integrated into the TELES for wide-area seismic damage assessment in Taiwan.

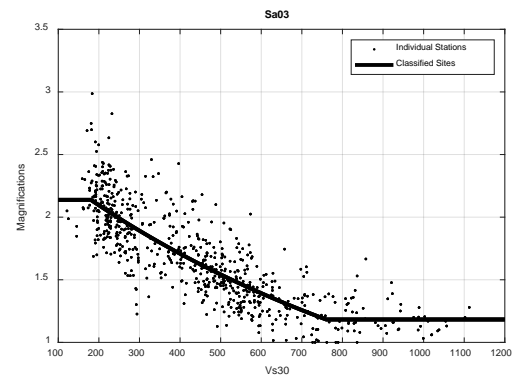


Fig. 5 S_{a03} site-effect magnification for individual stations in the first seismic intensity interval.

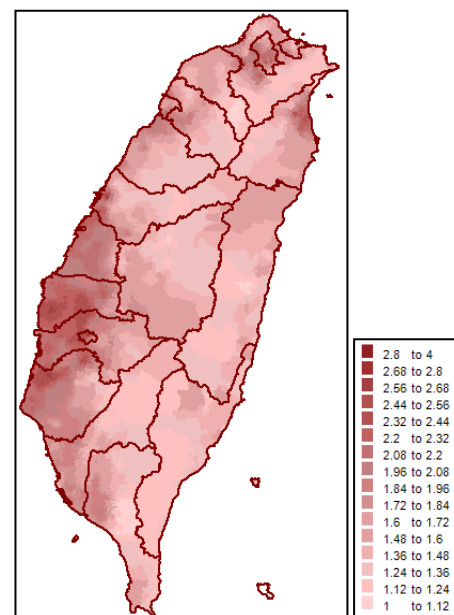


Fig. 6 Distribution of S_{a03} site-effect magnification in the first seismic intensity interval.

References

1. Shu-Hsien Chao, Brian Chiou, Chiao-Chu Hsu, Po-Shen Lin, 2019, "Development of Horizontal and Vertical Ground Motion Models for Crustal Earthquakes and Subduction Earthquakes in Taiwan," NCREE-19-003.
2. Chin-Hsun Yeh, 2003, "Taiwan Earthquake Loss Estimation System (TELES)," NCREE-03-002 (in Chinese).

Assessment of Redundancy Factors for the Seismic Design of Building Structures

Yuan-Tao Weng¹ Lap-Loi Chung² Eliot Chen³ Li-Tzung Huang⁴
Xi-Qing Guo⁵ Tsung-Jen Teng⁶

翁元滔 鍾立來 陳暉欽 黃立宗 郭錫卿 鄧崇任

Abstract

In recent years, the investigation results of the earthquake damage that occurred due to the 2016 Meinong and 2018 Hualien earthquakes has shown that mid-to-high-rise buildings with only one-to-two spans in the direction of the earthquake are prone to significant earthquake damage. However, in the current Taiwanese building seismic code, the impact of structural redundancy on the seismic performance of a building is not considered. This study reports the design requirements of American and Mexican building codes for redundancy and proposes a design plan for structural redundancy that is suitable for the characteristics of buildings in Taiwan for the purpose of safely engineering such buildings.

Keywords: structural redundancy, redundancy factor, seismic codes, ductility, overstrength

Introduction

Nowadays, building construction in large cities worldwide is dominated by the architectural needs of providing large spaces within a relatively reduced land space because of the high cost of land in business and residential districts. Big cities in very active seismic regions are not exempt from this scenario. Building developers often want to implement similar solutions to those used in non-seismic regions for constructing architectural and structural projects given such constraints. Therefore, it is now common in big cities in active seismic regions to construct new building projects based upon moment frames. These buildings possess fewer frames with fewer bays, and therefore exhibit weakly-redundant structural systems under lateral loading.

For example, consider the Weiguan Jinlong Building that collapsed during the Meinong Earthquake on February 6, 2016 [3]. This building was constructed of 16-story reinforced concrete. The height of the 1FL building was about 6 m, and the height of the building from 2FL to 16FL was 2.9 m. The total height of the building was approximately 50 m. It was completed in January 1995. The lower floors were for commercial use while the higher floors were

for residential use. The floor plan of the first floor, shown in Figure 1, is U-shaped, with 9 units in total. In this plan, 7 units are located on the front side (Buildings A to G) and 2 units (H and I) are located on the back side (west side). The vertical movement lines (stairs and elevators) are concentrated on the rear of the building (west side), and they are located at the short-directional single-span extension. Among the 7 units in Buildings A to G on the front side, there are 7 spans in the long direction (north-south direction) with a span of 8 m; there is only 1 span in the short direction with a span of about 10 m, and therefore this direction is comprised of a single-span flexural frame with an overall aspect ratio of approximately 5. The redundancy of this building aspect may thereby have been insufficient.

The practice of using weakly redundant structures in seismic regions is not entirely new. It has been used for decades as a solution for architectural needs related to land space constraints. It is worth noting that the seismic performance of such buildings during past earthquakes has been poor. In particular, buildings in which one-bay frames are used in the slender direction have exhibited poor performances during past earthquakes. Besides being weakly redundant, this type of structure also favors amplified

¹ Associate Researcher, National Center for Research on Earthquake Engineering

² Consultant, National Center for Research on Earthquake Engineering

³ Senior STR Engineer, ARUP Consulting Engineering, Inc.

⁴ Deputy General Manager, Federal Consulting Engineering, Inc.

⁵ Vice Chairman, Evergreen Consulting Engineering, Inc.

⁶ Researcher, National Center for Research on Earthquake Engineering

earthquake responses because of the global slenderness of both the building and plan. For example, the Weiguan Jinlong Building Building in Tainan City (Figure 2), which collapsed during the February 6,, 2016 Meinong Earthquake. This buildings were slender in terms of plan and elevation (Figure 1), and they were weakly redundant in the transverse direction (almost one-bay frames were used). These buildings eventually collapsed in the transverse direction (Figure 2).

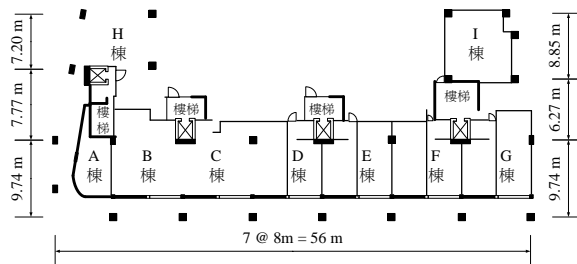


Fig. 1. Schematic of the 1st floor of the Tainan Weiguan Jinlong Building



Fig. 2. Collapse of the Tainan Weiguan Jinlong Building [3]

BUILDING CODES

ASCE 7

In ASCE-7 (2013), the redundancy factor (ρ) is taken into consideration when assessing the horizontal seismic load effect, E:

$$E = \rho Q_E \pm 0.2 S_{DS} D \quad (1)$$

where Q_E is defined as the effects of the horizontal seismic forces resulting from V (i.e., the total design lateral force or shear at the base). The corresponding basic load combinations used for strength design and allowable stress design are established in section 12.4.2.3 of ASCE-7 (2010).

According to ASCE-7, the redundancy factor is taken into consideration to amplify or diminish seismic lateral forces based upon the seismic design category, which is a classification assigned to a structure based on its occupancy and the severity of the design earthquake ground motion at the site, as described in detail in sections 11.6, 11.7, and 11.8 of ASCE-7 (2010). In general, seismic design categories A to C are given to common structures for which the risk of earthquake hazards is not high and soil site effects are not very important. Conversely, seismic

design categories D to F are used for structures for which the earthquake hazard is higher and soil site effects are important.

Two values are proposed for the redundancy factor in ASCE-7 (2010): $\rho=1$ for all cases identified in section 12.3.4.1 (among them, structures assigned to seismic design categories B and C), as well as the exemptions described in section 12.3.4.2 for structures assigned to seismic design categories D to F; and $\rho=1.3$ for structures assigned in seismic design categories D to F according to section 12.3.4.2. Therefore, the redundancy factor ρ in ASCE-7 is used to magnify horizontal seismic forces in structures found to belong to seismic design categories of greater risk, unless one of the two following conditions are met (for exemptions, $\rho=1$ is used for the seismic design categories D to F):

- I. Each story must resist more than 35% of the base shear in the direction of interest while complying with the requirements provided in ASCE-7 Table 12.3-3 for the identified lateral-force-resisting elements.
- II. Structures must be regular in plan at all levels provided that the seismic force-resisting systems consist of at least two bays of seismic-force-resisting perimeter framing on each side of the structure in the orthogonal direction at each story to resist more than 35% of the base shear. The number of bays for a shear wall shall be calculated as the length of the shear wall divided by the story height or as twice the length of the shear wall divided by the story height for light-frame constructions.

From these definitions, we could make the following general observation about the ASCE-7 recommendations for the redundancy factor ρ . The lack of redundancy is only penalized in the design of structures for which the earthquake hazard is high according to its seismic design category (D to F). However, the lack of redundancy is not taken into account in the design of structures with one-bay frames in other seismic design categories (A to C). It would be very valuable to know why the ASCE-7 committee made this decision, but to our knowledge, no documents are available that provide specific comments regarding this topic.

MOC-2008

In MOC-2008 (MOC-2008 2009, Tena-Colunga et al., 2009), the redundancy factor ρ is taken into consideration when defining the spectral design forces (Figure 4a). Moreover, ρ is a factor that basically corrects the previous assessment of the overstrength factor (denoted as R in Mexican codes) and the ductility factor (denoted as Q in Mexican codes), as depicted in Figure 4b. Most of the studies consulted in

MOC-2008 for defining R values were performed using 2-D models with different degrees of redundancy (MOC-2008 2009, Tena-Colunga et al., 2009). In addition, this factor considers the unfavorable performances of weakly redundant structures in strong earthquakes that have occurred worldwide over the last 30 years (for example, see Figures 1 to 3).

The proposed values for ρ in the MOC-2008 code are the following:

- I. $\rho=0.8$ for structures with at least two earthquake-resistant parallel frames or lines of defense in the direction of analysis if such frames are one-bay frames (or equivalent structural systems).
- II. $\rho=1.0$ for structures with at least two earthquake-resistant parallel frames or lines of defense in the direction of analysis if such frames have at least two bays (or equivalent structural systems).
- III. $\rho=1.25$ for structures with at least three earthquake-resistant parallel frames or lines of defense in the direction of analysis if such frames have at least three bays (or equivalent structural systems).

The above regulations show that in terms of their seismic design, single-span structured buildings often have poor seismic performances in strong earthquakes due to their lack of redundancy. In an earthquake damage investigation report conducted for several buildings, the collapse or partial collapse of such buildings was recorded (as shown in Figure 2), and the degree of structural super strength was also observed to be relatively small [6].

According to the research of Arturo and Antonio [7], ρ_{Ω} is the ratio of the structural super-strength factor for the same number of floors and different beam spans to the double-span frame. The ratio of the structural toughness capacity is shown in Figure 3(a). When the number of spans of the seismic frame of the structure is small, the structural super-strength factor is reduced and the demand of the design seismic force is large. When the number of spans is the same, a higher value corresponds to a reduced structural super-strength factor. Figure 3(b) shows that when the structural seismic frame span is small, the structural toughness capacity is low and the design seismic force demand is large. When the number is the same, a high number of floors will result in a decreased structural toughness capacity. Therefore, when the degree of structural redundancy is low, decreases in the structural super strength and toughness capacity will occur; when the number of floors of a building is high, the structural super strength and toughness capacity will be reduced.

Revision Methods and Principles

Considering that the degree of redundancy of building structures in engineering practice mainly depends on the stiffness, strength, and degree of non-linear behavior, as well as the location of the middle and lower floors, only the lower floors (considered to be 1/3 of the total number of floors above the base of the building) are considered. Based on the implications of the relevant provisions of MOC-2008 [5] and ASCE 7-16 [4] regarding redundancy factors and considering the current Taiwanese building seismic codes, the structural super-strength factor of general building structures is 1.4. As a comparison, the US ASCE 7-16 [4] structural super-strength factor is typically 2.5 or 3.0. The structural super-strength factor specified in the Taiwan seismic code [8] is quite conservative; therefore, the degree of structural redundancy should be considered. Considering the impact of this factor on the structural toughness capacity, Figures 4 and 5 show the ratio of the design base shear force before and after undergoing ductility reduction when the ductility capacity R is 4.8 and 3.2, respectively. It can be seen that when the structural toughness capacity R is 4.8, the toughness capacity is reduced to the original value of 0.95. The design seismic force is maximized when the design seismic force is increased by approximately 5% and 10% and the structural toughness capacity R is 3.2, if the toughness capacity is reduced by 0.95 and 0.9 times, respectively. These reductions correspond to approximate increase of the design seismic force of 4.8% and 9.5%, respectively.

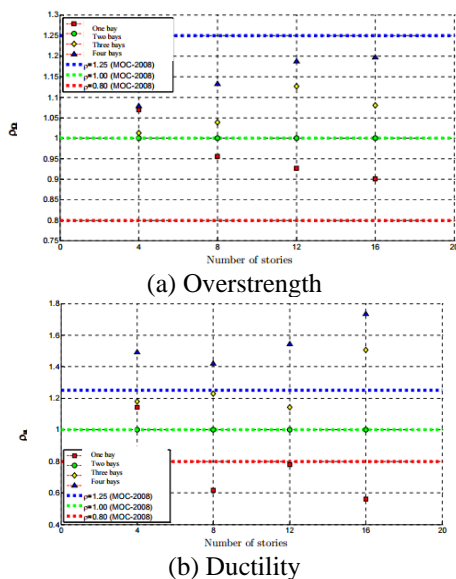


Fig. 3 Effects of the redundancy factor on the (a) structural overstrength factor and (b) ductility capacity

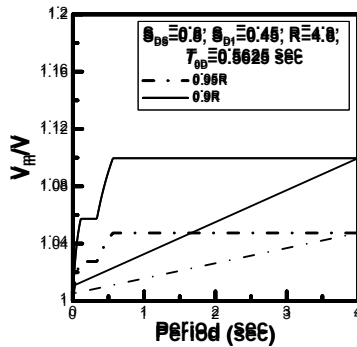


Fig.4 the design base shear force ratio before and after ductility reduction (R is 4.8)

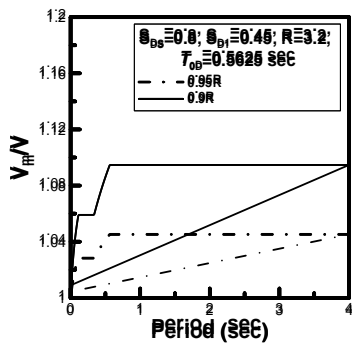


Fig.5 the design base shear force ratio before and after ductility reduction (R is 3.2)

In this study, we considered ASCE 7-16 [4], MOC-2008 [5], and the aforementioned two plans (A and B), which were used to simplify the concept. A plan C may be defined as follows:

If the single-span flexural frame (excluding shear walls or diagonal braces) of any low floor in a building (defined as being within 1/3 of the total number of floors above the base of the building) bears 33-67% of the floor shear force (inclusive), then the design seismic force of the floor must be amplified by 5%. If the single-span bending frame of any floor bears more than 67% of the floor shear force, the design seismic force of the floor must be amplified by 10%, and the adjacent floor must be considered. The continuity of stiffness and strength should be assumed.

Conclusions

According to the aforementioned results, when the number of floors in a building is constant, a lower span (redundancy) of the seismic frame of the structure will result in reductions in the structural super-strength factor and toughness capacity, and therefore the design seismic force demand will be large. When the number of spans is constant, a larger number of floors, which corresponds to the first vibration modal period of the structure, will result in a greater structural super-strength factor, and resilience capacity will be reduced. Therefore, the design seismic force demand will be greater.

This study provides a method that does not require the calculation of resilience capacity

correction values for the design of buildings. The proportion of the shear force of a floor that is borne by a single-span bending frame is instead used to appropriately amplify the design seismic force of the floor.

References

1. National Center for Research on Earthquake Engineering (2018), "2016 Meinong Earthquake Tainan City Building Seismic Damage Database", NCREE-18-004.
2. National Center for Research on Earthquake Engineering, "Hualien Earthquake Investigation Report on February 6, 2018", NCREE-18-005, March 107, Republic of China.
3. ABRI (2017), "Evaluation of Weak Floors and Reversing Irregularities in Mid-to-High-Rise Buildings", Project Results Report of the Institute of Architecture, Ministry of the Interior.American Society of Civil Engineers (ASCE). 2016. "Minimum Design Loads for Buildings and Other Structures," ASCE 7, ASCE Standard, ASCE / SEI 7-16, Reston, VA.
4. MOC-2008 (2009), Manual de diseño de obras civiles, diseño por sismo. Comisión Federal de Electricidad, México, November (in Spanish).
5. Tena-Colunga, A. (2004). Evaluation of the seismic response of slender, setback RC moment-resisting frame buildings designed according to the seismic guidelines of a modern building code. Proceedings, 13th World Conference on Earthquake Engineering, Vancouver, Canada, Paper No. 2027, CD-ROM, August.
6. Arturo Tena-Colunga and José Antonio Cortés-Benítez, (2015), "Assessment of Redundancy Factors for the Seismic Design of Special Moment Resisting Reinforced Concrete Frames", Latin American Journal of Solids and Structures, No.12, pp.2330-2350.
7. The Ministry of the Interior Construction Department (2011), "Specifications and Explanations for Seismic Design of Buildings", 100.01.19 Taineiyingzi No. 0990810250 Amendment Part Provisions, effective from July 1, 100th of the Republic of China.
8. Ministry of Communications (2019), "Code for Seismic Design of Highway Bridges", Jiaoji (108) No. 1085000530.
9. International Code Council (ICC), 2012. *International Building Code*, Falls Church, VA.
10. Tena-Colunga, A., Mena-Hernández, U., Pérez-Rocha, L. E., Avilés, J., Ordaz, M. and Vilar, J. I. (2009). Updated seismic design guidelines for buildings of a model code of Mexico. *Earthquake Spectra*, 25 (4): 869-898, November, doi: 10.1193/1.3240413.

Influence of Prestressing on the Fundamental Frequency of Uncracked Concrete Beams

Marco Bonopera¹

馬爾科¹

Abstract

In this study, a series of laboratory experiments were conducted on a large-scale Prestressed Concrete I (PCI) beam with a straight unbonded tendon. Specifically, the simply supported PCI beam was subjected to free bending vibrations under varying prestress forces. Numerical modeling results, based on the Euler-Bernoulli beam theory, were then compared with experimental data. It was shown that the fundamental frequency of uncracked PC beams is unaffected by increasing applied prestress force when these members are subjected to small second-order effects. Moreover, the compression-softening effect is prominent even if its classical decreasing trend is modified by variations in the concrete elastic modulus over time. The experimental results also confirmed that the fundamental frequency is not a reliable indicator of prestress losses in PC beams.

Keywords: concrete beam, elastic modulus, frequency, prestress force

Introduction

The fundamental frequency of prestressed concrete beams is an important parameter defining bridge load-carrying capacity. Therefore, questions arise on how the dynamic response of prestressed beams is affected by the applied prestress force. In this study, a large-scale Prestressed Concrete I (PCI) beam with a straight unbonded tendon was adopted for simulating a typical prestressed member. Free bending vibrations with different prestress forces were performed. A set of accelerometers were installed along the PCI beam to measure variations in fundamental frequency. The results of numerical modeling based on conventional beam theory, in which the cross-sectional second moment of area corresponds to the composite section formed by the concrete and tendon, were then compared with experimental data. Specifically, the reference solution was a simply supported Euler-Bernoulli beam, where the prestress force was modeled as an external compressive axial force. Results indicated that experimental data can be simulated, thus demonstrating the correctness of the model as predicted by compression-softening according to the dynamic theory. The fundamental frequencies were well approximated by the first-order dynamic formula for the Euler-Bernoulli beam (Young & Budynas

2002). Generally, the fundamental frequency of uncracked PC beams is unaffected by prestress force under small second-order effects. The compression-softening effect is prominent even if its classical decreasing trend is modified by variations in the concrete elastic modulus over time. The results confirmed that fundamental frequency is an unreliable parameter for prestress losses in PC beams.

Large-Scale Laboratory Testing

A PCI beam with a width b and height h of 450 and 900 mm was adopted, respectively (Fig. 1). The straight unbonded tendon had an eccentricity of 220 mm from the cross-section centroid and was composed of 15 cables with a “seven wire strand” 15.2 mm in diameter and inserted in a metallic duct (Fig. 1). Two pinned-end supports were placed at the beam ends, resulting in a span L of 14.5 m (Fig. 1). The cross-sectional second moment of area of the PCI beam’s composite section was $I_{\text{exact}} = 2.696479 \times 10^{10} \text{ mm}^4$, whereas the cross-sectional area was $A_{\text{exact}} = 2.98146 \times 10^5 \text{ mm}^2$. Finally, the slenderness ratio was 49. The concrete elastic modulus was evaluated

¹ Postdoctoral Researcher, National Center for Research on Earthquake Engineering

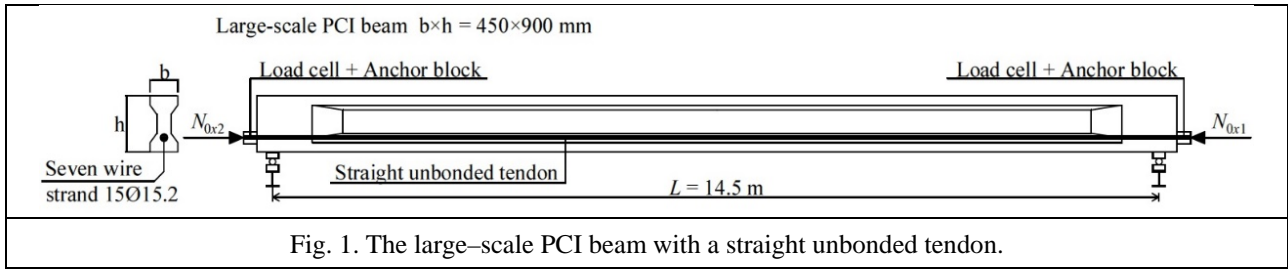


Fig. 1. The large-scale PCI beam with a straight unbonded tendon.

by compression tests at 28 days of curing and during the experimental period. The PCI beam was then inserted in a test frame using a test rig. At one beam end, a hydraulic oil jack with a force capacity of 4,000 kN was used to apply different prestress forces by pulling the tendon outwards. At both ends, respectively, a 4,000 kN load cell with an accuracy of 2 mV/V measured the applied prestress forces N_{0x1} and N_{0x2} . Four distinct prestress forces $N_{0x,aver}$ were applied with average values of approximately 1,563, 1,722, 1,819, and 1,921 kN. Differences in prestress forces N_{0x1} and N_{0x2} , measured at the beam ends, were due to friction losses along the tendon (Fig. 1). The measurement system included four VSE-15D accelerometers, manufactured by Tokyo Sokushin Co., with a sensitivity of 5 mV/gal. One, marked A4, was placed on the top of the PCI beam to correspond with the midspan cross-section at $i = 4$ and collect acceleration for the strong axis (Fig. 3). Two accelerometers, A0 and A8, were instead fixed at the beam ends at $i = 0$ and 8, respectively. One reference accelerometer, marked Af, was fixed to the floor, close to the beam end at $i = 0$. The test layout in Fig. 3 shows the corresponding positions in red.



Fig. 2. (a) Arrangement of the hydraulic oil jack on a steel rebar. (b) Arrangement of the hydraulic pump before activation.

Free Bending Vibrations

Free bending vibrations were performed at each applied prestress force $N_{0x,aver}$ to obtain accelerations at the sensing point $i = 4$ (Fig. 3). Four test cases were considered: $N_{0x,aver} = 1,563, 1,722, 1,819,$ and $1,921$ kN (Fig. 1). All accelerometers acquired accelerations at a sampling rate of 200 Hz and with a block size of 2,048 samples. For each applied prestress force $N_{0x,aver}$, vibrations were performed thrice for a total of twelve experiments. Specifically, free vibrations were imposed by rupturing a 10-mm diameter steel rebar anchored close to the midspan of the PCI beam (Fig. 2(a)). The ultimate strength of the steel rebar ($f_{sk} = 540$

MPa) was reached using a hydraulic oil jack with a force capacity of 100 kN and pulling up each rebar until rupture (Fig. 2(a)). The hydraulic oil jack was actuated by a hydraulic pump positioned on the floor (Fig. 2(b)). Therefore, the PCI beam was vertically excited by a release force F_d of approximately 42.4 kN and its dynamic response was measured along the strong axis (Fig. 3). The prestress forces N_{0x1} and N_{0x2} were recorded every second over two-hundred seconds by a data acquisition unit using a unique data logger (Fig. 1).

Evaluation of the Time-Dependent Elastic Modulus of Concrete

Together with the PCI beam, a set of 100×200 mm² cylinders were cast to measure the time-dependent elastic modulus of the concrete via compression tests. The elastic modulus E of each cylinder was estimated according to ASTM C 469/C 469M-14 (Annual Book of ASTM Standards 2016) as

$$E = \frac{\sigma_2 - \sigma_1}{\varepsilon_2 - 0.00005}. \quad (1)$$

The elastic moduli E of the concrete at 28 days and during the experimental period are listed in Table 1. The average elastic modulus E_{aver} experienced a progressive increment of 1.8%, 1.5%, and 2.6% above the day 28 baseline. Therefore, the average reference elastic modulus E_{ref} was 37,205 MPa. The average value of the concrete characteristic strength f_{ck} was 102.67 MPa for all compression tests reported in Table 1. The experimental unit weight of concrete, $\rho_c = 24.26$ kN/m³, was obtained from the average value of each cylinder (Table 1).

Influence of Prestressing on the Fundamental Frequency

A simply supported Euler-Bernoulli beam of $L = 14.5$ m was used as an exact reference solution (Fig. 4). The end constraints of a PC bridge-girder can mostly be assumed as pinned-end supports. The cross-sectional area A_{exact} and the second moment of area I_{exact} were likewise established according to the design. The elastic modulus of concrete E_{aver} was also assumed to be a known parameter. Under the second-order theory, the PCI beam was subjected

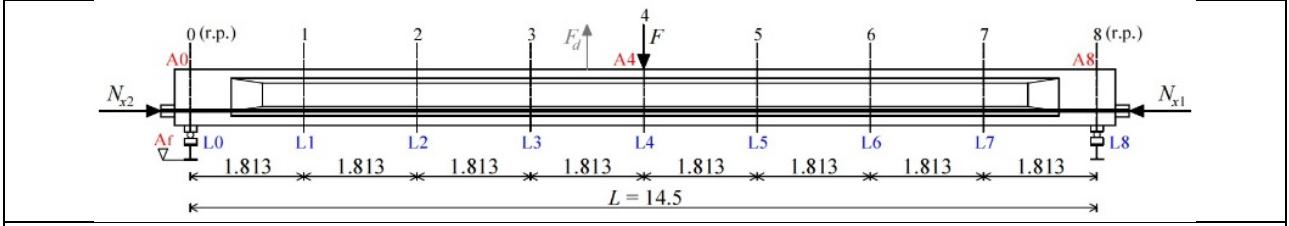


Fig. 3. Test layout showing the location of the instrumented sections with accelerometers. Units in m.

to an eccentric prestress force N from the centroid of the cross-section (Fig. 4), with the prestress force N applied externally (Fig. 4). The deflected shape at the PCI beam's fundamental frequency f_1 for the first- and second-order theory is marked as $v^{(0)}$ in Fig. 4. By assuming a concrete characteristic strength of $f_{ck} = 102.67$ MPa, the decompression serviceability limit state in the PCI beam was satisfied until a prestress force N_x of 4,300 kN, corresponding to 9.1% of its Euler buckling load where $N_{crE} = \pi^2 E_{ref} I_{exact} / L^2 = 47,094$ kN.

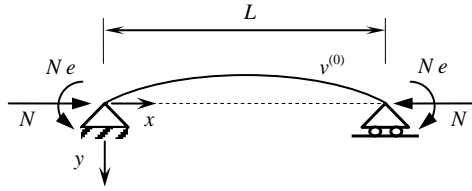


Fig. 4. Reference solution of the PCI beam. Deflected shape $v^{(0)}$ at the fundamental frequency f_1 under the first- and second-order theories.

Integration of Free Bending Vibrations and the Analytical Solution

A Fast Fourier Transform (FFT) was used to transform the acceleration time domain of the vibration experiments (Fig. 5(a)) to the frequency domain of the midspan cross-section at $i = 4$ (Fig. 3). Here, the peak-picking method was adopted. In total, twelve FFT functions were constructed where each experiment was repeated thrice for each prestress force $N_{0x,aver}$. The maximum applied prestress force, $N_{0x,aver,max} = 1,921$ kN, was 44.7% of $N_x = 4,300$ kN. The average fundamental frequencies f_1 from the three repetitions are shown in Fig. 6. The fundamental frequency of an axially-loaded simply supported beam (Fig. 4) was calculated using Eq. (2) according to the compression-softening theory, which does not consider the effect of the distributed load due to the straight tendon under tensile force (Young & Budynas 2002):

$$f_1 = \frac{\pi}{2} \sqrt{\frac{E_{aver} I_{exact} g}{m L^4}} \sqrt{1 - \frac{N_{0x,aver}}{N_{crE}}} \quad (2)$$

The concrete mass per unit length was $m = \rho_c \times A_{exact} = 7.233$ kN/m. Table 1 shows the elastic modulus E_{aver}

on each test day according to concrete curing levels. The cross-sectional second moment of area was considered for the composite section area formed from the concrete and tendon, I_{exact} , according to this design. Moreover, the Euler buckling load of the PCI beam was obtained by $N_{crE} = \pi^2 E_{aver} I_{exact} / L^2$, in which variations in elastic modulus E_{aver} were respectively imposed on each test day (Table 1). The gravitational acceleration g was 9.81 m/s². Despite some errors, as illustrated in Fig. 6, the fundamental frequencies f_1 can be simplified by neglecting the term containing the compressive axial force, $N_{0x,aver}$, as

$$f_1 = \frac{\pi}{2} \left(\frac{E_{aver} I_{exact} g}{m L^4} \right)^{1/2} \quad (3)$$

Fig. 6 compares the experimental beam frequencies with the corresponding analytical values f_1 from Eq. (3). An average error of 1.3% was obtained among the test combinations. When using the reference elastic modulus $E_{ref} = 37205$ MPa from Eq. (3), an average error of 1.2% was instead gained. Specifically, variations in the analytical frequency f_1 (solid green line), i.e., by using Eq. (3), increased by 0.3%, whereas the experimental frequency (solid red line) increased by 1.1%. The prestress force range was $\Delta N_{0x,aver} = (1,921 \text{ kN} - 1,563 \text{ kN}) / 1,563 \text{ kN} = 22.9\%$. The fundamental frequency of the PCI beam was sensitive to variations in concrete elastic modulus E_{aver} over time. This trend confirmed the results by Jaiswal (2008) and Wang et al. (2013) in which the natural frequencies of PC beams was unaffected by prestress force.

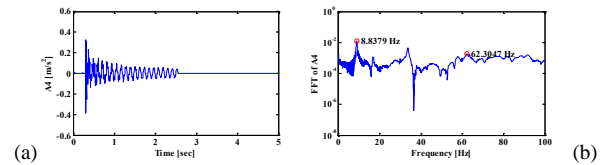


Fig. 5. (a) Acceleration time history. (b) Identified peaks in the FFT function for the A4 section when $N_{0x,aver} = 1,563$ kN was applied.

The Euler-Bernoulli beam model based on the first-order theory (Eq. (3)) can describe PC beam dynamics (Young & Budynas 2002) since the second-order effects in these members are usually less than 10%. Specifically, the maximum applied prestress force, $N_{0x,aver,max} = 1,921$ kN, was 4.1% of

Table 1. Measured unit weight ρ_c , characteristic strength f_{ck} , and elastic modulus E of the concrete.

Days of concrete curing	Cylinder	ρ_c (kN/m ³)	f_{ck} (MPa)	E (MPa)	E_{aver} (MPa)	E_{ref} (MPa)	Variation (%)
28	A	–	–	37,458	36,490	–	–
28	B	–	–	34,752			
28	C	–	–	37,365			
28	D	–	–	36,384			
87	1	24.17	98.25	36,061	37,139		1.8
87	2	24.39	113.82	37,712			
87	3	24.89	98.3	38,669			
87	4	24.07	98.2	36,112			
88	1	24.14	100.59	36,627	37,050	37,205	1.5
88	2	24.11	86.52	35,253			
88	3	24.39	104.34	38,108			
88	4	23.68	107.28	38,211			
90	1	24.35	114.78	38,080	37,425		2.6
90	2	24.38	104.62	36,769			

$N_{crE} = 47,094$ kN, corresponding to 4.1% of the second-order effects induced in the experiments. Within this range, the compression-softening effect was prominent in the PCI beam preserved against crack and micro-crack formation, even if its classical decreasing trend was modified by variations in concrete elastic modulus over time, with $\Delta E_{aver} = (37,425 \text{ MPa} - 37,139 \text{ MPa}) / 37,139 \text{ MPa} = 0.8\%$ (Fig. 6). In previous studies, natural frequencies were proposed as indicators of prestress losses (Bu & Wang 2011, Li et al. 2013). The present study shows that the fundamental frequency is an unreliable indicator for prestress losses in PC members.

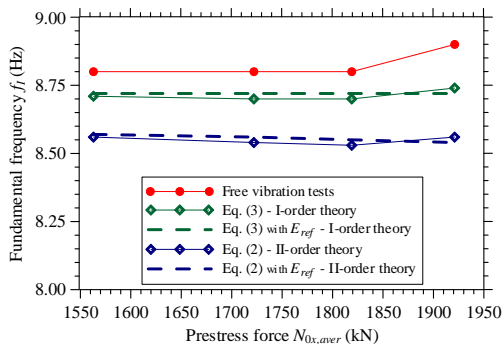


Fig. 6. Observed changes in fundamental frequency from free bending vibrations and analytical tests using Eq. (2) and (3).

Conclusions

The fundamental frequency of uncracked PC beams is sensitive to variations in the concrete elastic modulus over time during its early curing process. Moreover, the fundamental frequency is unaffected by prestress force. A variation of 1.1% was obtained for

variations in prestress force of 22.9%. Therefore, frequency is not a reliable parameter for estimating prestress losses. This finding, analytically suggested by Jaiswal (2008), was experimentally verified in this study. In conclusion, the relationship between prestress force and fundamental frequency is well approximated by the Euler-Bernoulli beam model based on a first-order theory, even when considering variations in concrete elastic modulus over time. Specifically, an average error of 1.3% was obtained when comparing experimental and analytical functions of the prestress force effect on the fundamental frequency.

References

- Bu, J.-Q. and Wang, H.-Y. (2011), "Effective pre-stress identification for a simply supported PRC beam bridge by BP neural network method", *J. Vib. Shock* 30, 155-159.
- Jaiswal, O.R. (2008), "Effect of prestressing on the first flexural natural frequency of beams", *Struct. Eng. Mech.* 28, 515-524.
- Li, H., Lv, Z. and Liu, J. (2013), "Assessment of pre-stress force in bridges using structural dynamic responses under moving vehicles", *Math. Probl. Eng.*, 435939.
- Wang, T.-H., Huang, R. and Wang, T.-W. (2013), "The variation of flexural rigidity for post-tensioned prestressed concrete beams", *J. Mar. Sci. Technol.* 21, 300-308.
- Young, W.-C. and Budynas, R.-G. (2002). *Roark's Formulas for Stress and Strain*; McGraw-Hill: New York, NY, USA; pp. 767-768.

Bridge Displacement Monitoring using a Fiber Bragg Grating–Differential Settlement Measurement Sensor System

Marco Bonopera¹ and Zheng-Kuan Lee²

馬爾科¹、李政寬²

Abstract

Bridge managers are always looking for an easy method to measure vertical displacements of bridges. With the advancement of fiber-optic technologies, fiber Bragg grating (FBG) sensors are nowadays commonly used in structural health monitoring due to their outstanding advantages, including multiplexing capability as well as high resolution and accuracy. In this study, FBG–differential settlement measurement (DSM) sensors, connected by a hydrostatic leveling system of communicating vessels, were used for displacement measurements along a large-scale Prestressed Concrete I (PCI) beam in the laboratory. The measured displacements matched well with the corresponding experimental values from linear variable differential transformers.

Keywords: FBG–DSM sensor, optical fiber, PCI beam, vertical displacement

FBG–DSM Sensors

The principal method for monitoring bridge displacement proposed by the National Center for Research on Earthquake Engineering of Taiwan is to clamp the optical fiber with heat-shrinkable sleeves for a total length of 100 mm (Fig. 1; expressed as S1 + FBG + S2). The sleeves are used as connectors between the bare fiber and additional elements are used to introduce external forces into the fiber Bragg grating (FBG). In this way, instrument components can exert prestress, which serves as the sensing origin. The FBG–differential settlement measurement (FBG–DSM) sensor comprises a suspended mass, FBG unit and two sleeves. One sleeve is directly connected to the suspended float mass, whereas the other is connected to the upper fixed end of the customized container (Fig. 1). The communicating vessels contain a homogeneous fluid, and the elastic range of the FBG is governed by floatation mechanics and Hooke's law. According to the buoyancy principle, the magnitude of the buoyancy force is equal to the weight of an equal volume of fluid. Therefore, the force detected by the FBG from pulling the suspended object increases with the immersed volume of the suspended object. Specifically, the maximum prestress force of the fiber is equal to the weight of the suspended float mass less half of the volume of the floating body multiplied by the fluid density. Several FBG–DSM sensors can be

linked using a connecting pipe. When an FBG–DSM sensor displaces downward with the beam span under monitoring, the suspended internal cylindrical object also moves downward. At the same time, the associated liquid level moves relatively upward inside the sensor until the same level has been obtained within the connected FBG–DSM sensors. Variations in the buoyancy of the floats thus modify the force exerted on the FBG and thereby change the reflective light wavelength. With respect to the linear behavior of the material of FBG, the function of the FBG–DSM sensor can be expressed as $\Delta \text{liquid surface height} \propto \Delta \text{buoyancy} \propto \Delta \text{fiber stress} \propto \Delta \text{fiber strain} \propto \Delta \text{wavelength of the reflective light}$.

The data logger can be located on the ground, whereas the optical wires run externally and internally through the FBG–DSM sensors. Once the logger instrument has measured the $\Delta \text{central wavelength of the reflective light}$, the $\Delta \text{liquid surface height}$ can be obtained, which in turn yields the corresponding displacement. In short, the FBG–DSM sensor can furnish settlement measurements derived from the change in wavelength transmitted by the fiber within the container. The liquid height variation of the fluid in the vessel produces a difference in the wavelength of the installed fiber. In our tests, the maximum stroke of the employed FBG–DSM sensor was 180 mm. We found a linear variation in the wavelength, caused by

¹ Postdoctoral Researcher, National Center for Research on Earthquake Engineering

² Associate Researcher, National Center for Research on Earthquake Engineering

the internal dimensions of the suspended cylindrical object (38.5 mm in diameter) and customized volume of the packaging case of the FBG–DSM sensor. When the maximum stroke of 180 mm is reached, the elongation of the acrylic fiber is ≈ 0.103 mm with a wavelength shift of 3.04 nm. The ultimate elongation of the used fiber, corresponding to its ultimate tensile strength of ≈ 0.20 mm, corresponded to a wavelength shift of ≈ 6 nm (value obtained from tensile test on the fiber). More details are furnished in the patents proposed by Lee 2014, 2015 and 2020.

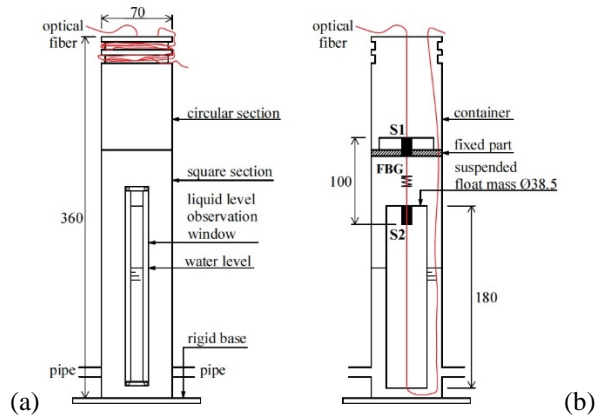


Fig. 1. (a) External view and (b) internal system layout of the employed FBG–DSM sensor (dimensions: mm)

Calibration Tests of the Measured Displacements

The FBG–DSM sensor used in this study can measure vertical displacements with an accuracy of 0.1 mm. Thirty-six three-point bending tests were performed on a large-scale prestressed concrete I (PCI) beam to verify the accuracy of numerous measured displacements obtained by the FBG–DSM sensors. Calibration was carried out using linear variable differential transformers (LVDTs) of 0.01 mm accuracy, positioned at the same cross sections of the FBG–DSM sensors. The tensile elongation of the fiber corresponding to the maximum measured displacement of $v_3 = 14.0$ mm (Table 1) was ≈ 0.008 mm, which was considerably lower than its maximum tensile elongation of ≈ 0.20 mm.

Prestressed Concrete I (PCI) Beam

A large-scale PCI beam of $b = 450$ mm in width and $h = 900$ mm in height was employed in testing (Fig. 2). The straight unbonded tendon had an eccentricity of 220 mm with respect to the centroid of the cross section. The tendon was formed by 15 seven-strand steel cables of 15.2 mm diameter (Fig. 2). Two pinned-end supports were arranged at the beam ends to reproduce the most common boundary conditions of bridge girders, resulting in a clear span of $L = 14.5$ m

(Fig. 2). The PCI beam was inserted in a test rig (Fig. 3). At one beam end, a hydraulic oil jack of 4,000 kN force capacity was used to apply a prestress force by pulling the tendon outward. At both ends, a 4,000 kN load cell with 2 mV/V accuracy was placed to measure the assigned prestress forces N_{0x1} and N_{0x2} (Table 1). In total, four prestress forces $N_{0x,aver} \approx 1,565, 1,722, 1,819,$ and $1,920$ kN were applied. The different prestress forces N_{0x1} and N_{0x2} were caused by the friction losses along the tendon (Fig. 2). For every prestress force $N_{0x,aver}$, a vertical load F was applied by a transverse steel beam at the PCI beam's midspan (Fig. 3). The load F was increased from its initial magnitude, then gradually to two different values, depending on the magnitude of $N_{0x,aver}$ (Table 1). F was always pulled both up and down using two hydraulic oil jacks, of 1,000 kN force capacity, fixed to the floor, and two other jacks of the same strength fastened at the top of the transverse beam (Fig. 3). All values of F were obtained from the sum of the measurements of two load cells of 1,000 kN force capacity and 2 mV/V accuracy, located between the upper oil jacks and two steel plates (Fig. 3 and Table 1). This test condition was repeated thrice for every vertical load F , resulting in a total of thirty-six tests. Seven FBG–DSM sensors and seven LVDTs (labeled L0, ..., L6) were located along the PCI beam's length at the cross sections $i = 0, \dots, 6$, based on the test layout shown in Fig. 2. Specifically, the reference FBG–DSM sensors and LVDTs (marked r.p. and L0, L6 in Fig. 2) were located at the beam ends $i = 0$ and 6 to form a reference line for the measurement system between the boundary conditions. The FBG–DSM sensors were connected by optical wires along the PCI beam and linked by a connecting pipe. A static full-spectrum optical interrogator fixed to the floor was used as the data logger to acquire the FBG–DSM signals.

Comparison between the Measured Displacements

The vertical displacements v_i for $i = 0, \dots, 6$ (Fig. 2) were measured by the FBG–DSM sensors and LVDTs after applying each vertical load F . The initial reference deflection shape corresponds to that after the assignment of prestress forces N_{0x1} and N_{0x2} (Table 1). All test measurements were recorded every second for nearly 200 seconds by a data acquisition unit. The average measurements of the initial prestress forces ($N_{0x2}, N_{0x1}, N_{0x,aver}$), prestress forces with loads F applied ($N_{x2}, N_{x1}, N_{x,aver}$), loads F and deflections v_i for one repetition of the test combinations are listed in Table 1. Twelve test cases were defined, yielding a total of thirty-six tests via three replicates. Replicability was high, with reciprocal errors lower than 2%. No mean error was obtained across the measured displacements $v_1, v_3,$ and v_4 .

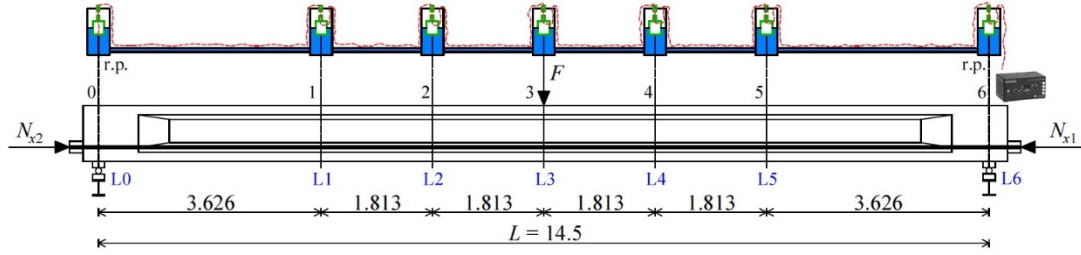


Fig. 2. Test layout with locations of the instrumented sections of the FBG–DSM system (dimensions: m)

Table 1. Comparison between the measured displacements v_i corresponding to the test layout depicted in Fig. 2

Days of concrete curing	N_{0x2} [kN]	N_{0x1} [kN]	$N_{0x,aver}$ [kN]	N_{x2} [kN]	N_{x1} [kN]	$N_{x,aver}$ [kN]	F [kN]		v_1 [mm]	v_2 [mm]	v_3 [mm]	v_4 [mm]	v_5 [mm]
87	1514	1614	1564	1524	1620	1572	80.5	LVDT	3.68	4.85	5.29	4.80	3.59
								FBG–DSM	3.8	5.0	5.5	5.0	3.7
87	1514	1614	1564	1526	1622	1574	100.9	LVDT	4.58	6.08	6.67	6.03	4.47
								FBG–DSM	4.6	6.2	6.8	6.0	4.6
87	1520	1613	1567	1529	1624	1577	139.7	LVDT	6.26	8.35	9.21	8.34	6.25
								FBG–DSM	6.3	8.5	9.3	8.3	6.4
88	1668	1775	1722	1678	1789	1733	160.3	LVDT	7.29	9.64	10.56	9.60	7.37
								FBG–DSM	7.3	9.7	10.5	9.6	7.4
88	1668	1775	1722	1679	1790	1735	171.4	LVDT	7.85	10.40	11.42	10.36	7.93
								FBG–DSM	8.0	10.6	11.4	10.5	8.1
88	1668	1775	1722	1681	1792	1737	182.4	LVDT	8.43	11.20	12.31	11.14	8.51
								FBG–DSM	8.4	11.3	12.2	11.1	8.5
88	1754	1882	1818	1776	1896	1836	179.8	LVDT	8.13	10.77	11.84	10.73	8.18
								FBG–DSM	8.2	11.0	11.8	10.7	8.3
88	1764	1880	1822	1775	1895	1835	180.7	LVDT	8.16	10.81	11.86	10.79	8.24
								FBG–DSM	8.2	11.0	11.8	10.8	8.3
88	1754	1882	1818	1779	1898	1838	196.8	LVDT	9.06	12.05	13.30	12.00	9.10
								FBG–DSM	9.1	12.3	13.2	11.9	9.2
90	1848	1989	1918	1872	2002	1937	190.2	LVDT	8.52	11.26	12.37	11.18	8.51
								FBG–DSM	8.5	11.4	12.4	11.2	8.6
90	1859	1987	1923	1871	2002	1937	191.8	LVDT	8.68	11.48	12.55	11.44	8.77
								FBG–DSM	8.7	11.5	12.5	11.4	8.7
90	1848	1989	1918	1876	2006	1941	210.6	LVDT	9.64	12.80	14.10	12.71	9.61
								FBG–DSM	9.6	12.9	14.0	12.7	9.7
Mean relative error [%]									0.6	1.5	0.2	0.2	1.3
Mean absolute error [mm]									0.0	0.1	0.0	0.0	0.1

The displacement v_2 was characterized by a mean error of 0.1 mm, corresponding to a relative error of 1.5%. The displacement v_5 close to the end constraint was characterized by a mean error of 0.1 mm (1.3%). The mean relative and absolute errors of each measure v_i , for $i = 1, \dots, 5$, are reported at the bottom of Table 1.

Conclusions

Our results suggest the following conclusions:

1. Bridge beams are characterized by second-

order effects lower than 10% of their Euler buckling load. These small second-order effects require highly accurate vertical displacement measurements. The displacements obtained using the FBG–DSM sensors well matched the corresponding experimental displacements obtained by LVDT, resulting in a mean error of -0.3% .

2. The FBG–DSM sensing system has high potential for short-term displacement measurements against an absolute reference and without any external physical reference to the ground.

3. The FBG–DSM sensing system can be substituted for the manual geodetic technique required to survey the level of bridge decks for routine management.

4. Dial indicators and LVDTs require fixed references below the measurement points. By contrast, FBG–DSM sensors can be located inside the girders of slab-on-girder and box-girder bridges without requiring any fixed ground reference points.



Fig. 3. FBG–DSM sensors and LVDTs along the PCI beam

References

- Lee, Z.-K., (2014). “Bridge safety monitoring integrated system with full optical fiber and the method for sensing thereof”. J.P. Patent No. 5,542,980.
- Lee, Z.-K., (2015). “Bridge safety monitoring integrated system with full optical fiber and the method for sensing thereof”. U.S. Patent No. 9,183,739.
- Lee, Z.-K., (2020). “Optical fiber sensing method”. Unitary Patent No. EP3457105.

Mapping a 3D Geometric Model of the Décollement in the Western Foothills of Central Taiwan

Chiu-Ping Fan¹, Kuan-Yu Chen², Yu-Wen Chang³, Chih-Wei Chang⁴, and Hsun-Jen Liu⁵

范秋屏¹、陳冠宇²、張毓文³、張志偉⁴、劉勛仁⁵

Abstract

The underground geometries the active faults are very complex in the western foothills (WF) of central Taiwan. In previous studies, it has been difficult to identify the correlations between the seismogenic structures and active faults in the area using geophysical explorations or theoretical seismological modes. Therefore, if a three-dimensional geometric model of the décollement in the WF could be constructed, it would benefit morphological studies of this region.

Keywords: décollement、detachment、seismicity、western foothills、GIS、Geographic Information System

Introduction

Geologists use geological cross sections to represent the underground morphology and compression of the fault-fold belts, as well as to investigate the evolution of shallow crustal deformations (Suppe 1980a). The fold-thrust belts and thrust-fault systems in central Taiwan are affected by the compressive plate boundaries and are tiled from east to west (Suppe, 1980b). In the thin-skinned tectonic models, formations majorly deform in the shallow zone in which the depth is approximately 10 km. The geological cross section shows the detachment as an east-inclined and low-dip angle interface (Suppe, 1980a, Davies et al., 1983, 黃旭燦等, 2004). This interface represents a weak component between blocks. When the compression progresses, small earthquakes frequently occur to release the accumulated energy. Carena et al (2002) considered approximately 110,000 small earthquakes ($M_L \leq 4$, from 1991 to 2000) from a seismic database. These earthquakes could visually generate the three-dimensional geometry of a detachment underneath the island of Taiwan, which is perpendicular to the Chelongpu fault but is relatively rough because it does not extend to form a continuous detachment in central Taiwan. As seismic technology improves, a more

accurate seismic catalog will assist in investigating this detachment.

The thin-skinned tectonic model had been well verified through the sandbox experiments. Dahlen et al (1984) reconstructed the mechanics above the basal detachment and found that there are similar to those of the western foothills (WF) of Taiwan. Their results showed that the slope of the terrain (α) and predicted inclination (β) could be related as:

$$\alpha = (5.7^\circ \pm 0.2^\circ) - (0.66 \pm 0.14)\beta$$

Statistically the topographic gradient of western Taiwan is $\alpha = 2.9^\circ \pm 0.3^\circ$, and therefore the inclination β of the detachment should be $6^\circ \pm 1^\circ$.

A series of geological cross sections of the western foothills and plains in Taiwan were constructed by the Chinese Petroleum Corporation in 2004, which was entrusted by Central Geological Survey (CGS) (黃旭燦等, 2004). These findings were integrated with downhole geological data, field investigations, and seismic explorations to comprehensively represent the terrestrial compositions of the western foothills and plains in Taiwan. The basal detachment was shown to appear at depths ranging from around 5 to 10 km, and the

¹ Project Assistant Researcher, National Center for Research on Earthquake Engineering

² Assistant Researcher, National Center for Research on Earthquake Engineering

³ Associate Researcher, National Center for Research on Earthquake Engineering

⁴ Assistant Technologist, National Center for Research on Earthquake Engineering

⁵ Assistant Researcher, National Center for Research on Earthquake Engineering

statistical mode of inclination was 7°.

To summarize these research results, this study uses well-arranged dense seismicity values to map the three-dimensional geometry of the detachment using grids. The study area was designed to be 90 km in the east-west direction and 150 km in the north-south direction, an area which has a distribution of active faults and is located in the central parts of the coastal plains and foothills in Taiwan

Earthquake Catalog

This study uses the earthquake catalog (Wu et al., 2017) which is a database from the "Reevaluation of Probabilistic Seismic Hazard of Nuclear Facilities in Taiwan Using SSHAC Level 3 Methodology" project conducted by NCREE. Seismic events are not only collected from the Central Weather Bureau Seismographic Network (CWBSN), but also from the seismic records of the International Seismological Centre and China Earthquake Network. This data utilizes a 3D velocity model, which greatly improves the accuracy of the epicenters.

The Central Weather Bureau has been actively promoting the Taiwan Strong-Motion Instrument Program (TSMIP) since 1991. This entire system was upgraded comprehensively as a continuous earthquake real-time monitoring system in the same year (交通部中央氣象局, 2019) which hugely improved the quality of the recordings from this system. As errors should be eliminated from this data, the database was filtered using 1991 as the year in the time domain. The total number of events is 553,363, and 233,608 earthquakes occurred within the study area during the study timeframe.

Seismogenic Structures in the WF

In the thin-skin tectonic model, the blocks are thrust toward the west along the detachment interface and the folds and thrust fault zones are developed because of the compressive forces. To investigate the patterns of underground seismic activities and clarify the correlations between the earthquake-enriched areas and active faults, the rotated seismic profiles are drawn at specific locations (see Fig. 1). Therefore, four chosen rotating centers were chosen, which are referred to by the fault traces on the surface. The northern portion of the Chelungpu fault, southern portion of the Chelungpu fault, southern portion of the Tachien-shan Fault, and the Luhou fault are used. It is shown that earthquakes frequently occurred in the hanging wall of the Chelongpu fault, while they rarely occurred in the foot wall. The seismic events are enriched within a 20-km depth, but no further analytical details concerning the seismic structures within the same area are provided, and these events could possibly have resulted due to the 921 earthquake. The patterns in the southern portion of Tachien-shan

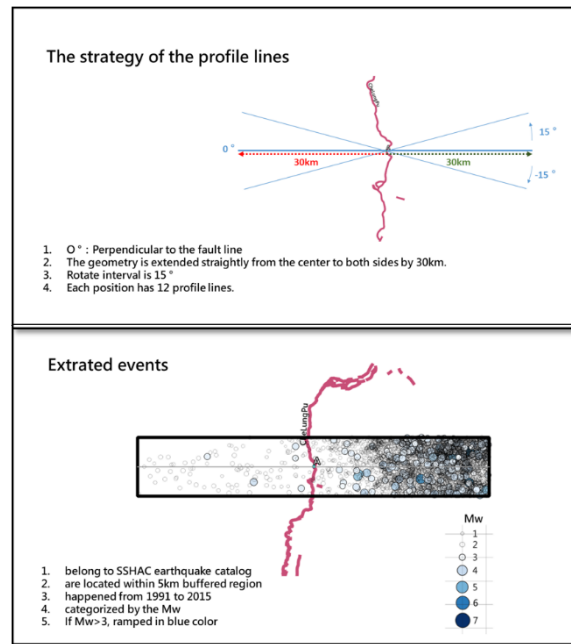


Fig. 1. Methodology of rotating profiles

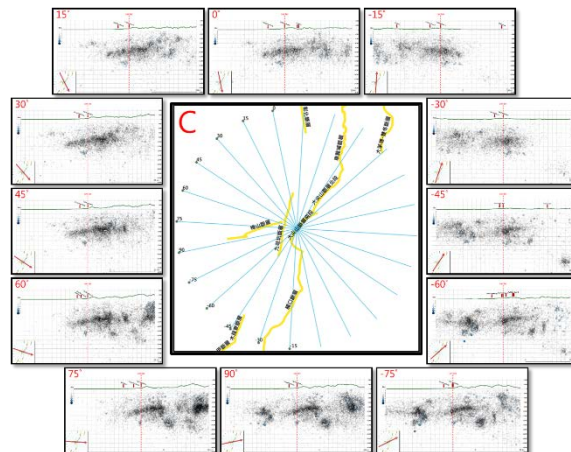


Fig. 2. Rotating profiles of the southern portion of the Tachien-shan Fault

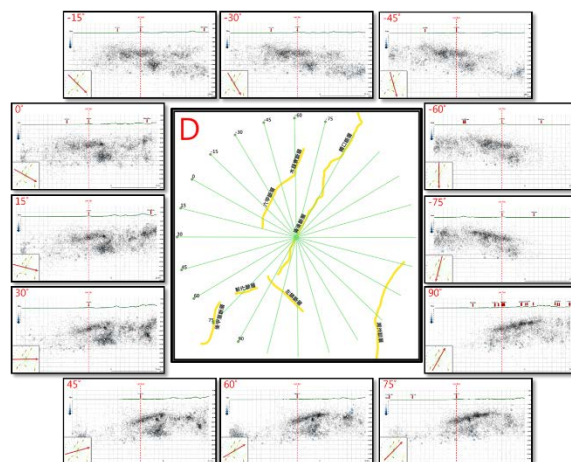


Fig. 3. Rotating profiles of the Luhou fault

Fault and the Lunhou fault clearly demonstrate that events are clustered into multiple and distinguishable structures in each profiles (Fig. 2 and Fig. 3).

According to the correlations shown above, the grid seismic profiles are constructed to identify the locations of the earthquake-enriched structures. Two sets of grid profiles, which are generated parallel and perpendicular to the fault traces of the Luhou and Chukou faults, are provided using 5km intervals (see Fig. 4). Each point in this grid has 2 profiles that are perpendicular to one another.

Using this strategy, the structure may be identified clearly in the parallel profiles. Under the Lunhou fault, there is a structure that extends for 20 km to the south at a depth of around 5-10 km (Fig. 5), and a structure also inclines to the east in

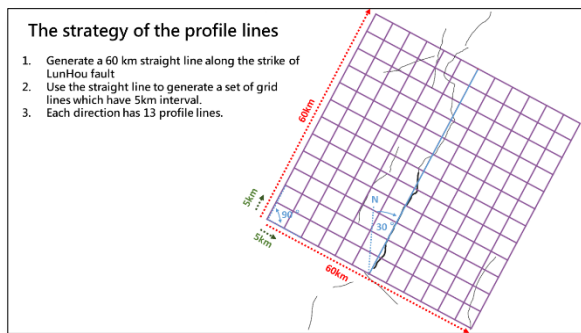


Fig. 4. Grid profile methodology

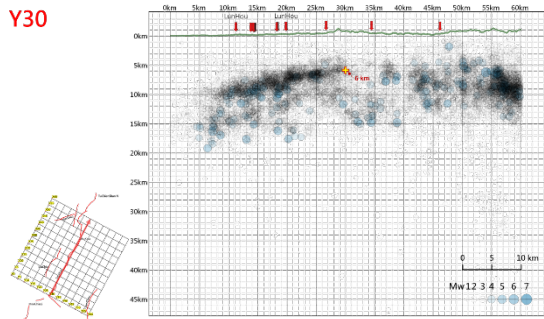


Fig. 5. Seismicity along the Luhou and Chukou faults

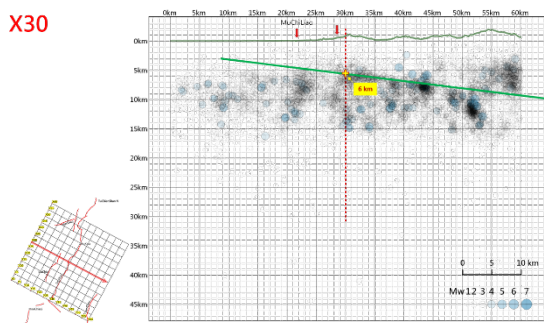


Fig. 6. Seismicity perpendicular to the Chukou faults

perpendicular profiles (Fig. 6). The trends demonstrated by these profiles are consistent with an inclining line of 7°. From our perspective, these two profiles may be regarded as references for the décollement.

Just under the fault trace of the Luhou fault, the décollement could be observed at a 6-km depth (see the yellow cross mark in Fig. 5). We used this depth as the reference depth. On the other side, this reference depth is used to determine the décollement interface that inclines 7° eastward (indicated by the green line in Fig. 6).

Modeling Method and Results

This study uses the methodology of well-arranged, dense seismicity values to map the three-dimensional geometry of the décollement using grids. The entire study area is arranged into 2 sets of seismic profiles that are perpendicular to each other (see Fig. 7). The interval is 5 km and earthquakes are extracted using a 5 km buffer. The characteristics of the décollement from the reference are pre-drawn in the same location within each the perpendicular profile of each fault-trace. We adjusted the possible depth of the décollement according to the seismic distributions and obtained the perspective results of each profile (Fig. 8).

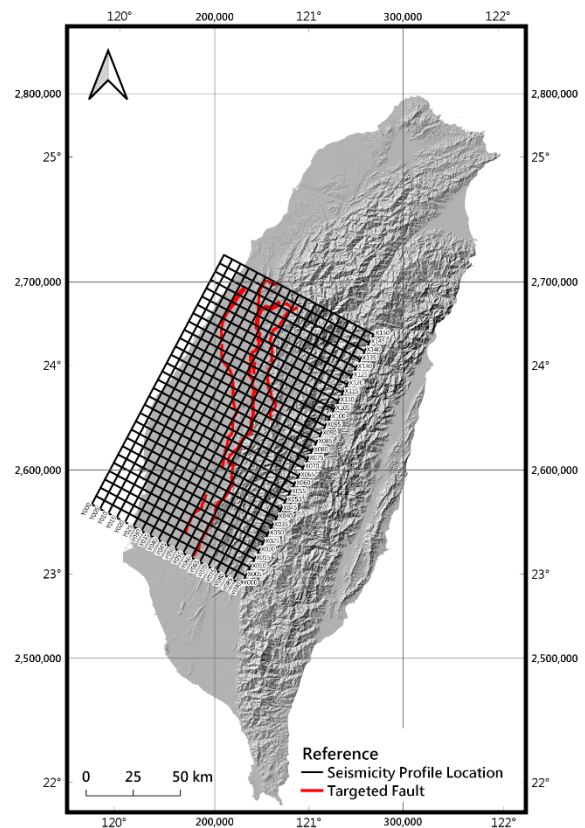


Fig. 7. Methodology of the grid profiles in the study area

Although the décollement cannot be well explained by the seismic distributions due to the limitations of the seismic records, the depth of the décollement may be determined using subjective judgements.

Finally, GIS software is used to map our first 3D geometric model of the décollement in the western foothills of central Taiwan (Fig. 9).

Conclusions

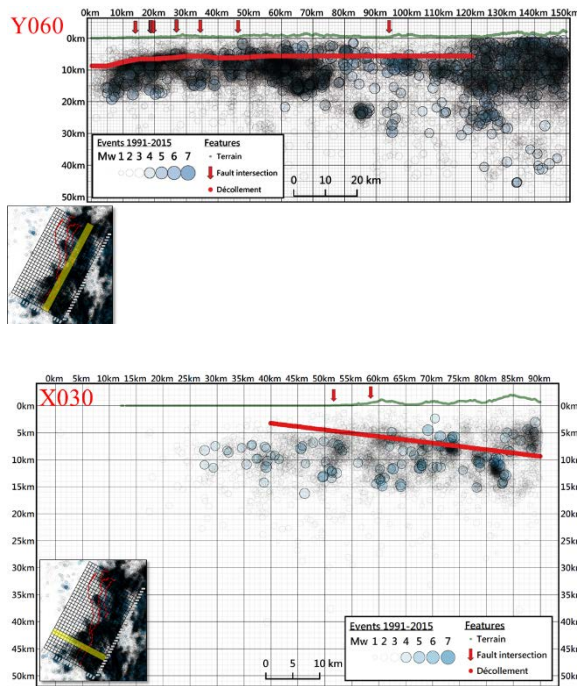


Fig. 8. Décollements drawn using the methodology provided in this study. The upper region shows the direction along the fault trace while the bottom region shows the direction perpendicular to the fault trace.

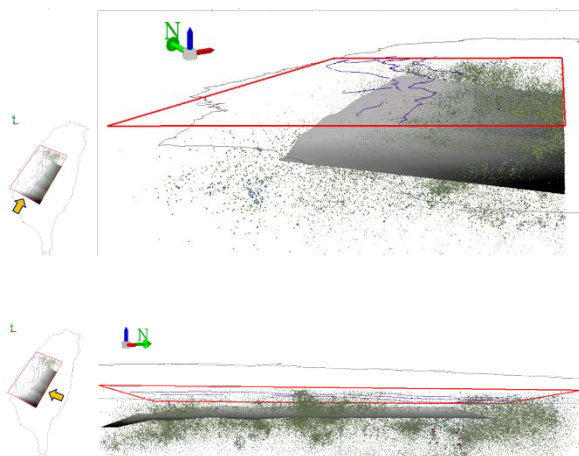


Fig. 9. Visualized 3D geometry of the décollement

In this study, we use GIS to obtain a three-dimensional geometric model of a décollement. The main tools used to achieve this are the built-in functions of QGIS (version 3.10) and ArcGIS (version 10.5.1). The coordinate reference system is the two-degree zoning projection of the Taiwan Transverse Mercator (EPSG: 3826). This is helpful because the coordinate values represent the distance from the origin of the coordinate system. If the values are all provided in meters, an accurate three-dimensional model may be obtained.

The construction of the 3D geometry of the fault system encounters many challenges. We believe that determining the occupied area of the décollement initially would be beneficial for obtaining a geometric model of the faults. This area may be used to represent the boundary conditions of the fault geometry; additionally, overlaps between adjacent faults may be effectively eliminated. The active faults issued by the CGS may be also be considered to better understand the three-dimensional geometric model of active faults in the western foothills of Taiwan in a future study.

References

- 交通部中央氣象局 (2019) 中央氣象局地震測報中心成立三十週年紀念專刊, 共 170 頁。
- 黃旭燦、楊耿明、吳榮章、丁信修、李長之、梅文威、徐祥宏(2004)斷層活動性觀測與地震潛勢評估調查研究, 台灣陸上斷層帶地構造與地殼變形調查研究(V), 經濟部中央地質調查所報告 93-13 號。
- Carena, S., Suppe, J. and Kao, H. (2002). Active detachment of Taiwan illuminated by small earthquakes and its control of first-order topography. *Geology*. 30. 935-938.
- Dahlen, F. A., Suppe, J. and Davis, D. (1984). Mechanics of fold-and-thrust belts and accretionary wedges: Cohesive Coulomb Theory. *Journal of Geophysical Research*. 89. 10087-10101.
- Davis, D., Suppe, J. and Dahlen, F. A. (1983) Mechanics of fold-and-thrust belts and accretionary wedges. *J. Geoph. Res.*, 88, 1153-1172
- Suppe, J. (1980a) A retrodeformable cross section of northern Taiwan, *Geol. Soc. China Proc.*, 23, 46-55.
- Suppe, J. (1980b) Imbricated structure of western Foothills belt, southcentral Taiwan. *Petrol. Geol. Taiwan*, 17, 1-16.
- Wu, Y. M., Cheng, S. N. and Liu, T. Y. (2017). A foundation and Basic Analysis of Earthquake Catalog and Historical Earthquakes Database, NCREC Commissioned project report.

Taiwan Seismic Microzonation Map of the Design Basis Earthquake: Construction of A Geometric Model of the Chukou and Lunghou Faults

Kuanyu Chen¹, Chiuping Fan¹, Yuwen Chang², Chihwei Chang², Hsunjen Liu²

陳冠宇¹、范秋屏²、張毓文³、張志偉⁴、劉勛仁⁵

Abstract

The National Center for Research on Earthquake Engineering (NCREE) constructed a comprehensive model of active faults for nuclear sites when executing the project “Reevaluation of Probabilistic Seismic Hazard of Nuclear Facilities in Taiwan Using SSHAC Level 3 Methodology.” However, the models for other faults are not detailed enough for application in PSHA hazard maps and require continued research.

The scope of this project is the construction of an applicable fault geometric model for PSHA hazard map. At the current stage, we have constructed a geometric model of active faults of central Taiwan. We here briefly describe how the fault geometric model was created, and we evaluate its uncertainty based on integrated data, including surface geological surveys, boreholes, balanced cross-sections, and seismic reflection data.

The lengths of the Chukou and Lunghou fault are 25 km and 50 km, respectively. The dipping angles of both faults are 25/40/50 degrees, and their down-dip depth contacts the 7 degrees décollement. We propose a rupture model of three scenarios: (1) individual rupture of the Chukou or Lunghou fault; (2) linked rupture, and (3) Entire rupture with the southern segment of the Tachienshan fault.

Keywords: PSHA, Chukou fault, Lunghou fault, décollement, rupture model

1. Introduction

The National Center for Research on Earthquake Engineering (NCREE) constructed a comprehensive model of active faults in relation to nuclear sites when executing the project “Reevaluation of Probabilistic Seismic Hazard of Nuclear Facilities in Taiwan Using SSHAC Level 3 Methodology”. Primary faults are defined as seismic sources with high contribution to seismic hazards within 20 km radius of target sites. Following the SSHAC (Senior Seismic Hazard Analysis Committee) level 3 guideline, such sources require increased attention when discussing and constructing fault models. Seismic sources beyond the 20 km radius are defined as “other” faults and will have less or negligible contributions to the hazard of target sites. These significant sources must be considered in technically defensible models, whose construction is highly work intensive. At present,

NCREE plans to provide a hazard map of Taiwan, offering a useful opportunity to develop more refined fault models for Probabilistic Seismic Hazard Analysis (PSHA) hazard map and other expected applications in the future.

The scope of this project is the construction of an applicable fault geometric model for PSHA hazard map. At the current stage, we have constructed the geometric model of active faults of central Taiwan. This short report describes the construction of the model and evaluates its uncertainty using integrated data, including surface geological surveys, boreholes, balanced cross-sections, and seismic reflection data.

2. Modeled faults

The structural lineament of the Chukou-Lunghou fault is a significant boundary in southwest Taiwan. It

¹Assistant Research Fellow, National Center for Research on Earthquake Engineering

²Project Associate Research Fellow, National Center for Research on Earthquake Engineering

³Associate Research Fellow, National Center for Research on Earthquake Engineering

⁴Assistant Technologist, National Center for Research on Earthquake Engineering

⁵Assistant Research Fellow, National Center for Research on Earthquake Engineering

divides the western foothills into the inner foothills with intensive folds and imbricated thrusts on the east, and the outer foothill with scattered folds and thrusts on the west (Ho, 1982).

The Chukou fault, which is characterized as a thrust fault, extends for 28 km from the Shuisheliao fault at its northern end to the Guanziling area at its southern end (Lin et al., 2007). It gradually turns into an antiform and merges with the Lunghou fault at depth as it extends southward toward the Guanziling area (Hung et al., 1999).

The Lunghou fault, a thrust with a length of 48 km, is generally considered a southward extension of the Chukou fault (CPC, 1986; Chang et al., 1998; Lin et al., 2000). In the north of the Guanziling area, it parallels the east side of the Chukou fault and is bounded by the Laitou fault at its northern tip, then merges with the Chukou fault in the Guanziling area and substitutes for it as it extends southward until it was bounded by the Tsochen fault (Hung et al., 1999).

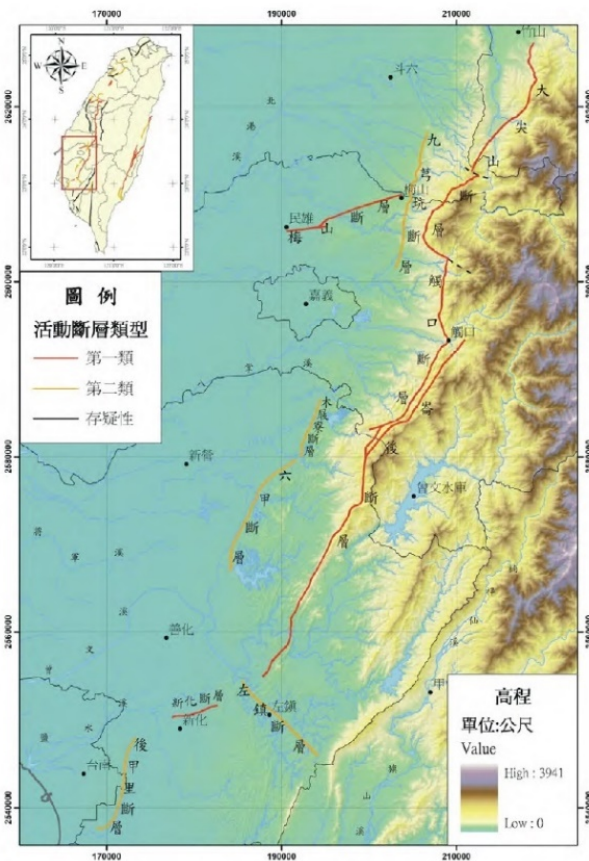


Figure 1. Distribution of active faults in southwest Taiwan. We here focus on the Chukou fault and Lunghou fault (from Lin et al., 2007).

3. Data

In the Chukou fault, the Liuchungchi formation, on foot wall, underlain Nanchuang formation on

hanging wall; the offset across the fault decreases southward starting from over 2000 m (Huang et al., 1994). The balanced cross-sections, constructed from seismic reflection data and boreholes, show a dipping angle of Chukou fault of 30° in Line2', 40° in Line4, and 50° in Line2 (Yang et al., 2001). Relocated seismicity, focal mechanism, and stress inversion analysis indicate a fault plane angle would be 40°. The Chukou fault plane initiates with a high angle (60°) in the shallow part (30 m) then turns into 30°–40° along a down-dip that is suggested by the electrical resistivity imaging profile (Shih et al., 2003). Shallow seismic reflection data show a dipping angle of 35° in profile C, 40° in profile DP, and 42° in profile E from north to south (Chen, 2006). A balanced cross-section (BB') indicated a 65°–55° dipping angle in the shallow part then turns into 30° at depth (Hung et al., 1999). An obvious shear zone is observed at 147 m in Chukou 1st borehole. An angle of 51° was inferred from geometric calculations based on the location of surface topographical features to the shear zone in the borehole (Lin et al., 2007). The 1988 ML6.2 event, RueyLi earthquake sequence, seemed to trigger the Chukou fault with a few events placed in a 60° east-dipping plane beneath the fault (Chen and Wang, 1999). The locations of these features and profiles are mark in Figure 2.

In the Lunghou fault, the Nankang formation as a hanging wall overrides the footwall of the Kueichulin formation, the offset between both sides gradually increasing toward the South (CPC, 1986; Lin et al., 2007). The surface topography, exposed strata on the hanging wall and foot wall, variation in GPS cross-fault velocity traces and balanced cross-sections all reveal that the offset of the Chukou fault is southwardly decreasing from Chukou to Guanziling area (Yu and Chen, 1998; Hung et al., 1999; Yang et al., 2003; Huang et al., 2004). The parallel Lunghou fault concurrently develops from it and gradually increases toward the South. The balanced cross-sections provide a branch fault system to interpret how these two faults merge with each other in the Chukou and Guanziling areas. Therefore, the Chukou and Lunghou faults are generally considered as an identical linked fault (CPC, 1986; Chang et al., 1998; Lin et al., 2000).



Figure 2. Location of geological and geophysical investigation sources along the Chukou fault.

4. Fault Geometric Model

The above data show that the dipping angle of the Chukou fault ranges from 30° to 65° . High dipping angles are all located in the shallow part near the surface (Hung et al., 1999). An electrical resistivity imaging profile also indicated a high angle (60°) located at only 30 m depth (Shih et al., 2003).

The Chukou fault may have been triggered by the Ruyeli earthquake sequence, with few instances of seismicity distributed in a 60° east-dipping plane beneath it (Chen and Wang, 1999). However, as only two seismic sources could be used for mapping the fault plane, this evaluation with highly uncertainty. Moreover, the Chukou 1st borehole indicated a clear 51° shear zone at 147 m depth (Lin et al., 2007). A series of seismic reflection investigations, focal mechanisms, and stress inversion analyses shows that the angle of Chukou fault would range from 30° to 50° .

Although the geological map shows that the Chukou fault and the southern segment of the

Tachianshan fault may be divided by the Shuisheliao fault (CPC, 1986), the features of the Shuisheliao fault have not been observed and identified on outcrops (Hung et al., 1994). Therefore, we do not exclude the possibility of a linkage of the Chukou fault and the southern segment of the Tachianshan fault. The boreholes along the southern segment of the Tachianshan fault (3B, 4B, and 6B) show low dipping angles of, respectively, 25° , 25° , and 20° – 40° (Liu et al., 2014). This indicates that the segment of the Tachianshan fault could have a low angle dipping plane of 25° .

In Figure 3, we contrast angles of 25° , 30° , 40° , and 50° (blue, orange, red, and dark yellow lines) with projected seismicity. The orange line (30°) appears to be a mismatch with the surrounding seismicity. We therefore consider the dipping angles of the Chukou and Lunghou faults should as $25^{\circ}/40^{\circ}/50^{\circ}$.

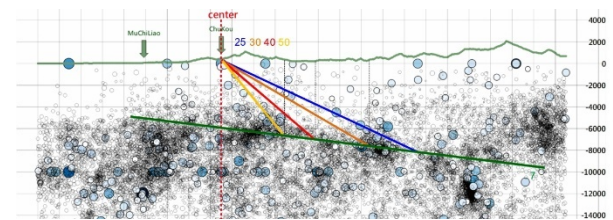


Figure 3. Correlation of dipping angle and projected seismicity. Blue, orange, red, and dark yellow lines indicate angles of 25° , 30° , 40° , and 50° , respectively. The green line represents the location of décollement.

5. Rupture Model

Although we did not have enough rupture history data to determine the rupture sequence of the two faults, the results of previous studies suggest that the Chukou and Lunghou faults could be considered as a single fault system based on geological observations. We therefore consider the possibility of linked rupture of these faults. In the area from Chukou to Guanziling, the two faults are in contact as a branch fault system with a balanced cross-section interpretation. The branch shape of these two faults may indicate that ruptures may not propagate through it easily during small-magnitude earthquakes connected with individual ruptures of the faults. As the stress accumulates due to the irregularity along the strike between the Chukou fault and the southern segment of the Dachianshan fault, a combined rupture may occur leading to a large-magnitude earthquake. Overall, we suggest a rupture model consisting of three scenarios: (1) individual rupture of the Chukou fault and Lunghou fault; (2) linked rupture of both faults, and (3) Entire rupture with the southern segment of the Tachianshan fault.

6. 3D Model

A 3D model was created by our colleague Chiu-Ping Fan. We used the strike of the longitudinal valley and the active faults to arrange intensity profiles at 5 km intervals (Fig. 4). These profiles enabled us to correlate the dipping angle and the projected seismicity for determining fault plane locations (Fig. 3). The 5×5 grid is also useful for verifying the down dip fault plane by depth in each profile, providing 3D grid images of faults for use in GIS representation (Fig. 5).

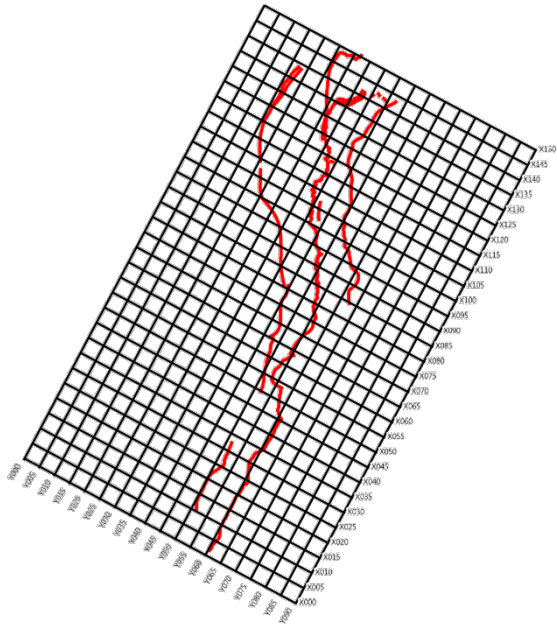


Figure 4. We arranged intensive profiles at 5 km intervals to compare the fault geometry with seismicity and construct the 3D geometric model.

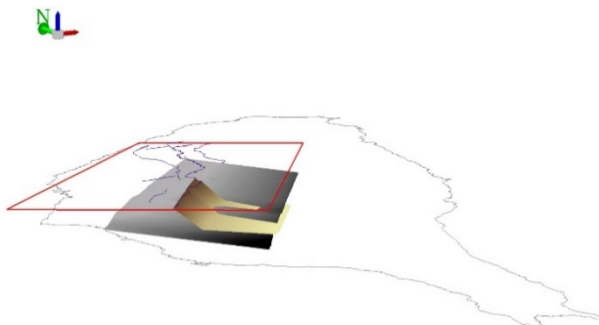


Figure 5. Constructed 3D geometric model of Chukou and Lunghou faults. The gray plane shows the location of décollement. The brown polygon indicates the faults' dipping angle of 40°.

References

1. Hung, J. H., D. V. Wiltschko, H. C. Lin, J. B. Hickman, P. Fang, and Y. Bock (1999), Structure and motion of the southwestern Taiwan fold and thrust belt, TAO, 10(3), p.543–568.
2. Yu, S.B. and Chen, H.Y. (1998) Strain

accumulation in southwestern Taiwan: TAO, Vol.9, no.1,31-50.

3. 中國石油公司(1986)十萬分之一地質圖—嘉義幅。中國石油公司臺探總處出版。
4. 石瑞銓、陳平護、呂明達、陳文山 (2003) 地震地質調查及活動斷層資料庫建置計畫-地球物理探勘計畫(2/5)，經濟部中央地質調查所九十二年度委辦計畫期末報告，共 218 頁。
5. 林啟文、張徽正、盧詩丁、石同生、黃文正(2000)台灣活動斷層概論—五十萬分之一臺灣活動斷層分布圖說明書，第二版。經濟部中央地質調查所特刊，第 13 號，共 122 頁。
6. 林啟文、盧詩丁、石同生、劉彥求、林偉雄、林燕慧 (2007)臺灣西南部的活動斷層。經濟部中央地質調查所特刊，第 17 號，共 132 頁。
7. 張徽正、林啟文、陳勉銘、盧詩丁(1998)台灣活動斷層概論，五十萬分之一臺灣活動斷層分布圖說明書，經濟部中央地質調查所特刊，第 10 號，共 103 頁。
8. 陳郁文(2006)以反射震測法研究觸口斷層及其附近構造。國立中央大學地球物理研究所碩士論文，共 109 頁。
9. 陳朝輝與王維豪 (1999)瑞里地震系列和構造活動之初步研究。地質，19(1)，34–41 頁。
10. 黃旭燦、楊耿名、吳榮章、丁信修、李長之、梅文威、徐祥宏 (2004) 台灣陸上斷層帶地質構造與地殼變形調查研究(5/5)-台灣西部麓山帶地區地下構造綜合分析。斷層活動性觀測與地震潛勢評估調查研究，經濟部中央地質調查所報告 93-13 號。
11. 黃鑑水、張憲卿、劉桓吉 (1994) 台灣南部觸口斷層地質調查與探勘。經濟部中央地質調查所彙刊，第九號，51-76 頁。
12. 楊耿明、洪日豪、吳榮章、黃旭燦 (2001) 斷層活動性觀測與地震潛勢評估調查研究_台灣陸上斷層帶地質構造與地殼變形調查研究(1/5)-西南地區(觸口斷層)，經濟部中央地質調查所報告第 89-4 號，共 93 頁。
13. 饒瑞鈞 (2003) 台灣南部地震活動性研究及潛能分析，行政院國家科學委員會專題研究計畫精簡版成果報告(p. 5)

Discussion on seismic and geochemical monitoring of the Tatun Volcano Group in 2020

Ya-Chuan Lai¹, Hsiao-Fen Lee¹, Min-Hung Shih¹, Li-Chin Chang¹, Chin-hsing Liu¹

and Chia-Jui Teng¹, Teng-Yang Shao¹

Abstract

Northern Taiwan has considerable volcanic activity, and the Tatun Volcano Group (TVG) is a noteworthy area. Surveying and monitoring data taken over two decades indicate that the TVG is an active volcanic group. A volcano observatory was established in 2011 to monitor the volcanic activity using various methods, including seismic activity, fluid geochemistry, and ground deformation. The mission of the volcano observatory is to understand the characteristics of the TVG, monitor possible activity of the magma reservoir, and forecast its future activity.

The number of seismic events in the TVG increased in 2019 by approximately 1.5 times the background value. In 2020, the number increased by as much as twice the background value. In addition to the significant increase in the number of microseisms, earthquakes with magnitudes greater than 3.0 have also increased. Over the same period, the geochemical results were also abnormal, and specifically include a significant increase in the emission of helium and hydrogen chloride. Combining the geochemical and seismic results, it is evident that the TVG has become more active in 2019 and 2020, and that the activity is dominated by hydrothermal activity. At present, no obvious magmatic activity is suggested from observations of the TVG; however, monitoring must continue to forecast possible disasters caused by hydrothermal activity, such as phreatic eruptions.

Keywords: Tatun Volcano Group (TVG), volcano monitoring, micro-earthquake, geochemistry

Introduction

Hot springs and other manifestations of geothermal activity of the Tatun Volcano Group (TVG) are still quite evident. The results of investigations over past decades, including active seismicity, high helium isotope ratios ($\sim 5-7 R_A$), emission of volcanic gases, as well as the geothermal activity, indicate that volcanic activity may not have ceased. Such observations imply that a magma reservoir exists beneath the TVG (Song et al., 2000; Yang et al., 1999). The last eruption in the TVG was five to six thousand years ago as determined from ash dating (Belousov et al., 2010). Furthermore, a magma reservoir at a depth of 20 km has been identified from S wave shadows and P wave delays in seismic travel times (Lin, 2016). It has been concluded that the TVG is still an active volcano.

A conduit-like clustering of seismicity was found beneath Dayoukeng, which is one of the strongest fumaroles in the TVG and is connected to a fracture zone. Such clustered seismicity may be triggered by volcanic gases and fluids ascending from the deep

magma reservoir and would likely be a pathway for ascending magma in a future TVG eruption (Pu et al., 2020).

The results from the monitoring of the TVG over the past few years suggest that the magmatic system is stable overall, and as such, no immediate eruption may be expected. However, the possibility of future re-eruption must be considered, especially as phreatic eruption may occur given the substantial hydrothermal activity of the TVG. Hence the continuous detailed monitoring of volcanic indicators is necessary. Recently, observations from geochemical and seismic monitoring have shown varying results, with a key observation being numerous earthquakes with a magnitude greater than M3.0 occurring in the TVG, especially in 2019 and 2020. Meanwhile, several important indicators from geochemical observations have also changed, suggesting a change in activity in the Tatun volcanic area. This study focuses on the unusual phenomena of the TVG, as part of ongoing efforts to investigate and monitor possible hazards caused by hydrothermal activities.

Seismic observations

When magma or hydrothermal system migrates upwards, many micro-earthquakes would be triggered along their travel paths. Such micro-earthquakes typically accompany other microseisms caused by stress change in the rocks. This means that seismic observations can be used to evaluate the eruption time, location, and scale of volcanic events.

Since 2003, a dense seismic network has been established to monitor and investigate the seismicity of the TVG. Forty broadband seismic stations have been installed thus far in the TVG (Figure 1), with the majority distributed southeast of the Shanjiao Fault. With the network coverage of the Mt. Cising, Dayoukeng, and Bayan areas, the microseisms can be substantially detected. To understand the seismic characteristics of the TVG, continuous waveform data were processed to provide details such as micro-earthquake characteristics and spectrum analyses. Events were selected based on experience, and the P and S wave arrivals were carefully picked for further locating of the events.

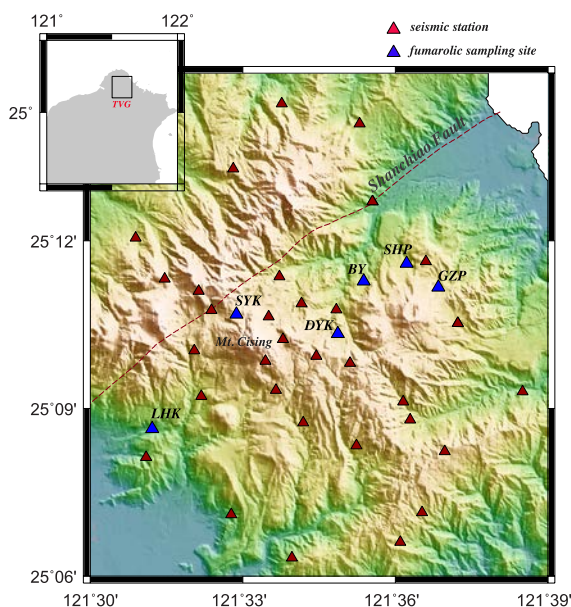


Fig. 1. Distribution of seismic stations and fumarole sampling sites

In the Tatun Volcano area, a total of 4550 micro-earthquakes was detected in 2020, which is double that of the average number (2000-2500) over the past decade. The seismicity first increased significantly in 2019, with approximately 3500 earthquakes occurring in total, before the rapid rise in 2020.

In addition to the significant increase in the number of micro-earthquakes, the number of large events has also increased. The active seismicity in 2020 was mainly observed in the period January to June, when approximately 75% of the events occurred.

Of these, nine earthquakes had a magnitude greater than 3.0. These results demonstrate a significant variation in the temporal distribution of seismicity in 2020.

The number of micro-earthquakes varies greatly each month, mainly because larger earthquakes are usually accompanied by a large number of aftershock sequences. The Bayan earthquake sequence that occurred in January 2020 involved 658 micro-earthquakes. In a subsequent Bayan earthquake sequence in May, the number of micro-earthquakes increased to 825, the highest monthly occurrence detected in 2020. From July to December, the seismicity decreased gradually. By December, the number of micro-earthquakes was lower than the monthly average of 150, indicating that the activity of the TVG had stabilized. Similar temporal variations in seismicity over a period of several months were also observed in 2018 and 2019.

The seismic activity of the Tatun volcanos in 2020 was mainly clustered in the Mt. Cising, Dayoukeng, and Bayan areas (Figure 2), which is consistent with the background seismicity. However, the distribution of seismic activity shows clear spatial and temporal variations. In January, micro-earthquakes mainly occurred in the eastern part of the TVG, from Mt. Huangzui to the Bayan area. By contrast, from February to March, the micro-earthquake distribution moved westward, clustering at the Mt. Cising and Dayoukeng area. Subsequently, the seismic activity in the eastern part of the TVG gradually increased again, with more events occurring near Bayan. A critical increase in seismicity occurred in eastern TVG in May and June and expanded eastward to the Mt. Huangzui. Meanwhile, the seismicity south of Mt. Cising increased in July and even more significantly in August. From September until the end of year, the seismic activity in the TVG decreased overall to the background level, with events mainly occurring in the Mt. Cising and Dayoukeng area. In this period, few events occurred in the Mt. Huangzui and Bayan area where seismic activity had been significantly higher in the first half of the year.

In 2020, many earthquake sequences comprising earthquakes with magnitudes larger than magnitude 3.0 occurred in the TVG. These include: (1) the ML 3.8 earthquake sequence in the Mt. Huangzui area on January 15; (2) the ML 3.8 earthquake sequence on the south part of Mt. Cising on February 3 (which occurred in an area with low background seismicity and a relatively scattered epicenter distribution); (3) the ML 3.8 earthquake sequence in Dayoukeng on February 10; (4) the ML 3.1 earthquake sequence at Mt. Cising on March 18; (5) the ML 3.1 earthquake sequence that occurred north of Bayan on April 21 (where the distribution of epicenters is quite concentrated although they are in an area with low background seismic activity); and (6) the Mt.

Huangzui earthquake sequence that occurred between May 19 to 21 with a ML 3.2 main shock, accompanied by hundreds of aftershocks. The hypocenters of events in the sixth sequence were clustered in the area from Mt. Huangzui to the west and had focal depths concentrated at 3-4 km. This sequence includes another ML 3.0 earthquake and many earthquakes with magnitudes larger than 2.0, indicating that a large amount of energy was released. Finally, on June 27, an earthquake sequence at Mt. Huangzui included two earthquakes with magnitudes of 3.0, which occurred within 74 seconds and were closely located.

gradual shallowing of the focal depth from Mt. Huangzui to Bayan.

In addition to the high level of seismicity in the eastern area of the TVG, an increase in seismic activity was observed over short time periods, especially in August, south of Mt. Cising. This is a region where the most recent large event occurred (the 2014 Shilin earthquake), yet where there is a low TVG background seismicity level.

Geochemical observations

Geochemical monitoring methods, such as direct sampling, soil gas monitoring, and remote sensing are commonly used by volcanologists. Each method has its advantages and disadvantages. The methods used by the Tatun Volcano Observatory include direct sampling and continuous soil gas monitoring. The method discussed in the present study is direct sampling. Currently, more than ten fumaroles are active in the TVG. Six primary fumaroles were selected as regular sampling sites. The sampling frequency was once per month, and the gas compositions and helium isotopes were analyzed to monitor volcanic activity. The sampling locations are shown in Figure 1. Fumarolic gas was sampled using a Giggenbach bottle, which is commonly used by volcanologists. The volume of the Giggenbach bottle was approximately 170 mL, with 50 mL of alkali hydroxide solution in the bottle. The analysis covered H₂O, CO₂, H₂S, SO₂, HCl, CH₄, N₂, H₂, He, Ar, and CO. Iodine was used to obtain SO₂/H₂S ratios. Helium was collected and stored in vacuum glass bottles equipped with stopcocks at both ends. Helium isotopes were analyzed using a rare gas mass spectrometer (VG 5400) at the Department of Geosciences, National Taiwan University.

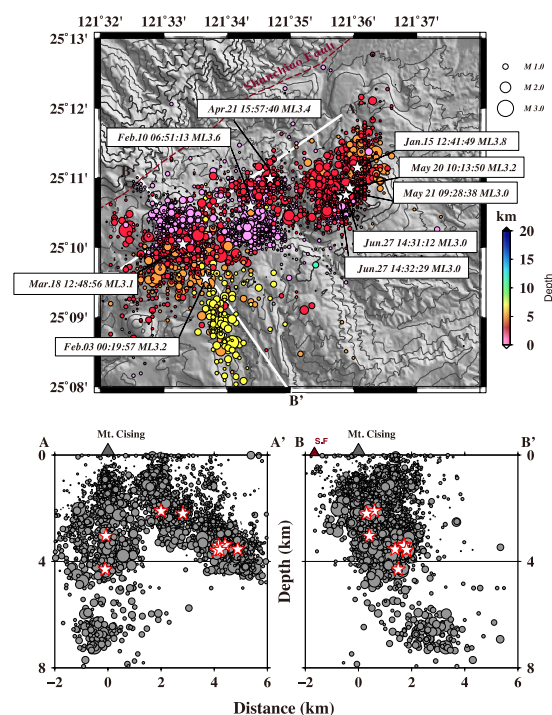


Fig. 2. Seismicity in 2020

The most active seismicity in 2020 was observed in the area between Bayan and Mt. Huangzui. This area is located in the eastern part of the TVG, where the background seismicity is the lowest among the three areas of concentrated seismicity. However, the Bayan earthquake sequence that occurred on 28 January 2019 included many earthquakes with magnitudes larger than 3.0, and was accompanied by a large number of aftershocks. The sequence consists of more than 1000 earthquake, which it is the most active one of the TVG. This high level of activity did not continue in the area until three large earthquakes occurred sequentially in January, May, and June of 2020. It is worth noting that the distribution of these three sequences trends towards the southwest with time; the first event occurred on the northeast side of Mt. Huangzui, seismic activity then increased between Mt. Huangzui and Bayan in May, and finally the distribution of seismicity moved westward toward the Bayan area in June. The northeast-southwest trend of the hypocenters was accompanied by a corresponding

The following discussion focuses on long-term variations in recent years since the sampling interval is relatively long and the record length is limited. The amount of hydrogen chloride and helium from most fumaroles increased towards the end of 2018 and remained high during 2019, especially in the Bayan and Dayoukeng geothermal areas. The levels in these two regions remained high in 2020 while the changes in other areas slowed, as shown in Figures 3 and 4. The ternary diagrams of N₂-He-Ar clearly show that the amount of helium from most fumaroles increased in 2019, and then decreased slightly towards the background value in 2020. In addition, the CO₂-HCl-S_{total} ternary diagrams indicate an increase in HCl at all sampling sites, as well as an increase in hydrothermal activity. The changes in Dayoukeng and Bayan are particularly evident in 2020.

Although the geochemical monitoring results showed a significantly increased amount of helium in 2019 and 2020, the helium isotopic ratio (³He/⁴He ratio) did not change significantly during this period.

The S_T/CO_2 ratio, another important parameter that indicates a magmatic source, also did not increase. In fact, the S_T/CO_2 ratio decreased slightly in recent years. These parameters all indicate that the volcanic system is dominated by hydrothermal activity. Integration of the geophysical and geochemical data suggests that seismic events may open the pathways through which helium is emitted so that more helium gas can escape. However, the helium isotopic ratio does not change because the source is the same. These seismic events would also disturb the volcanic-hydrothermal system. The migration of a deeper fluid or other volcanic brine into the original hydrothermal reservoir might be responsible for the variation in the concentration of hydrogen chloride. Because there are several indicators of magmatic activity in the Dayoukeng area during this period, careful follow-up monitoring is warranted.

second half of 2019. In the second half of 2020, this activity seemed to gradually wane. However, in November and December, strong groundwater signals were observed in the Bayan and Dayoukeng areas. Close attention should be paid to the variation of these parameters in the future.

Conclusions

A large number of seismic events were observed in 2019, and this increased significantly in 2020, especially in the area from Bayan to Mt. Huangzui. The geochemical monitoring results also demonstrate clear anomalies in 2019. In 2020, although the frequency of abnormal changes in the volcanic gas was reduced, there remained significant changes in the Bayan area. The seismic and geochemical results do not reveal details due to the long sampling interval of the volcanic gases. It is evident that both the seismic and geochemical monitoring results from 2019 to 2020 demonstrate that volcanic activity in the TVG area has increased relative to previous years and is dominated by hydrothermal activity. While there are a few signals of suspected magmatic events during this period, no substantial eruption is likely to occur in the near future. At present, the volcano monitoring focuses on possible disasters caused by hydrothermal processes such as phreatic eruptions.

Reference

1. Belousov, A., Belousova, M., Chen, C. H., Zellmer, G. F., 2010. Deposits, character and timing of recent eruptions and gravitational collapses in Tatun Volcanic Group, Northern Taiwan: Hazard-related issues. *J. Volcanol. Geotherm. Res.*, 191, 205-221.
2. Lin, C.H., 2016. Evidence for a magma reservoir beneath the Taipei metropolis of Taiwan from both S-wave shadows and P-wave delay, *Scientific Reports*, Vol. 6, 39500.
3. Pu, H. C., Lin, C. H., Lai, Y. C., Shih, M. H., Chang, L. C., Lee, H. F., Lee, P.T., Hong, G.T., Li, Y.H., Chang, W.Y., Lo, C. H., 2020. Active Volcanism Revealed from a Seismicity Conduit in the Longresting Tatun Volcano Group of Northern Taiwan, *Scientific Reports*, 10.
4. Song, S.R., Yang, T.F., Yeh, Y.H., Tsao, S.J., Lo, H.J., 2000b. The Tatun volcano group is active or extinct? *J. Geol. Soc. China*, 43, 521-534.
5. Yang, T. F., Sano, Y., Song, S. R., 1999. $3He/4He$ ratios of fumaroles and bubbling gases of hot springs in Tatun Volcano Group, North Taiwan. II *Nuovo Cimento Soc. Ital. Fisica C*, 22, 281-286.

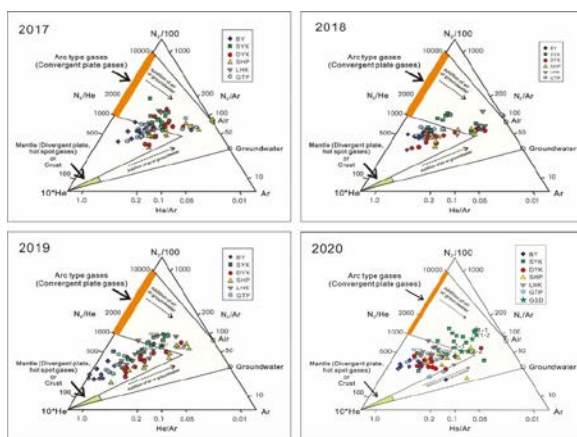


Fig. 3. Ternary diagrams of N_2 -He-Ar

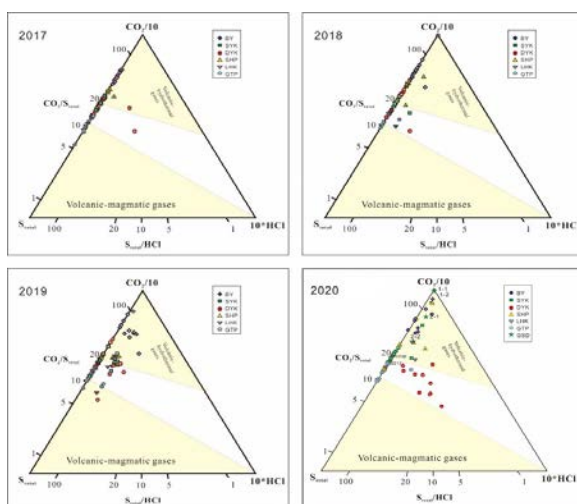


Fig. 4. Ternary diagrams of CO_2 -HCl- S_{total}

On the whole, while hydrothermal activity was dominant in 2017 and 2018, these years were quieter than previous years. From the end of 2018 until present, the TVG area has become more active. Although this activity is still dominated by hydrothermal processes, some magmatic related events were observed in the

Taiwan Recorded Ground Motion Database for Structural Response History Analysis

Hsun-Jen Liu¹, Wen-Yu Jean², and Yu-Wen Chang³

劉勛仁¹、簡文郁²、張毓文³

Abstract

Nonlinear response-history analysis is beneficial for obtaining inelastic structural responses that resemble reality, especially for high-rise, long-span, damping, or base-isolated structures. However, to obtain reliable responses, one of the key issues is proper input excitation selection. In this study, we develop the Taiwan recorded ground motion database for structural response history analysis, which is based on ten target response spectra, local recorded ground motions, and the mean-squared error (MSE) of the major selection index. Target spectra for seven general sites, with corner periods ranging from 0.4 s to 1.0 s, and three Taipei Basin seismic microzonation sites were chosen, all of which have a return period of 475 years. A total of 30 records were selected for each target spectrum to provide an initial reference for choosing input excitations before executing time-history analysis. The ground motion selection fitness index was based on the MSE. This study concludes by providing suggestions for addressing practical issues in database applications, such as methods for selecting reference scale factors (SFs) for bidirectional ground motions, SF and MSE thresholds, and principles for selecting multiple records.

Keywords: recorded ground motion database, response history analysis, Taiwan Building Code, Taiwan general sites, Taipei Basin sites

Introduction

Time-history analysis studies the behavior of a structure to obtain detailed displacement and internal force information at specific time steps and thus gain a better understanding of structural nonlinearity. This approach is widely used for dynamic structural analysis. Input excitations are extremely important elements impacting the reliability of structural responses, and this stability of solutions of structural analysis is mainly influenced by two requirements: the number of recorded time-histories and the characteristics of recorded response spectra. The first requirement, for design purposes, is that a sufficient number of records with sufficient variability is selected in order to achieve unbiased structural response results. For the second requirement, recorded spectral shapes should reflect the site-specific characteristics generated by seismic hazards and site effects.

The motivation for this study was to provide an initial reference and proper data source for dynamic time-history analysis in engineering practices. Using

basic principles for generic applications and the Taiwan Building Code (TBC) regulations, we developed the Taiwan recorded ground motion database for structural response history analysis. A total of ten datasets are grouped in this database. Seven datasets are for general sites, which do not incorporate consideration of near-fault effects (Liu et al., 2020), and three datasets are for Taipei Basin sites. Each dataset includes 30 selected ground-motion records based on a target design spectrum that reflects one of the representative site characterizations in Taiwan.

For generic applications and to ensure equivalence to shape characteristics of recorded response spectra, the observed range of target spectral periods and modified decay of spectral acceleration (S_a) after certain corner periods (T_0) were applied. For general sites, the period ranges from 0.03 s to 3 s and S_a is proportional to T^{-1} after T_0 . For Taipei Basin sites, the period range is 0.01-8.0 s, and S_a is proportional to T^{-1} and T^{-2} , respectively, after T_0 and a period of 4.0 s. The corner period T_0 is defined as the intersection of regions

¹ Assistant Research Fellow, National Center for Research on Earthquake Engineering

² Research Fellow, National Center for Research on Earthquake Engineering

³ Associate Research Fellow, National Center for Research on Earthquake Engineering

of the spectrum where spectral acceleration is constant and where spectral velocity is constant, which is highly dependent on site condition.

Target Design Spectra

Under the current seismic design code regulations in Taiwan, a site can be classified into one of three categories according to regional characteristics: general sites, near-fault sites, and Taipei Basin sites. In this study, which does not consider near-fault effects, the target design spectra for developing the Taiwan recorded ground motion database include seven sets for general sites (Figure 1) and three sets for Taipei Basin sites (Figure 2).

General Sites

If all combinations of S_s^D and S_1^D for general sites with a return period of 475 years are considered, a first class site (a hard site) without near-fault effects, can be categorized into three groups depending on the distribution of T_0 for code-based normalized design spectra (with an effective peak acceleration (EPA) of 0.4 g): T_0 equal to 0.5, 0.6, and 0.7 s. The T_0 range can be extend to 0.4-1.0 s if the site amplification factors (F_a and F_v) follow a semi-logarithmic empirical model (Jean, 2020), which is formulated in terms of V_{s30} and designed ground motion intensities (S_s and S_1). Rather than setting a constant S_a (e.g., $0.4S_{DS}$ or $0.4S_{MS}$) after a spectral period larger than $2.5T_0$, as is done for a conservative consideration of seismic design force in the current TBC, in this study, the S_a after T_0 is assumed to continue to be proportional to T^{-1} for general sites so that real ground motion characteristics are reasonably approximated.

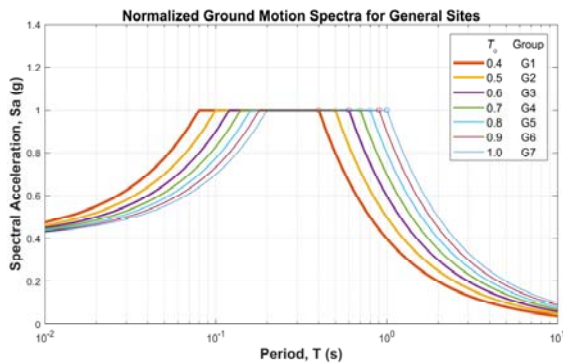


Fig. 1 Seven normalized target design spectra for general sites (EPA of 0.4 g).

Taipei Basin Sites

For Taipei Basin seismic microzonation sites 1, 2, and 3 (TAP1, TAP2, and TAP3) with a return period of 475 years from the current TBC, all S_{DS} values are 0.6 and the T_0 values are 1.6, 1.3, and 1.05 s, respectively. In addition, with reference to past earthquake data, in this study the corner period defined by the intersection of regions of constant spectral velocity and spectral displacement is designated as T_L , which is the cut-off

point for S_a being proportional to T^{-1} and T^{-2} . T_L is chosen to be 4.0 s in accordance with seismic hazard analysis results (Jean et al., 2020).

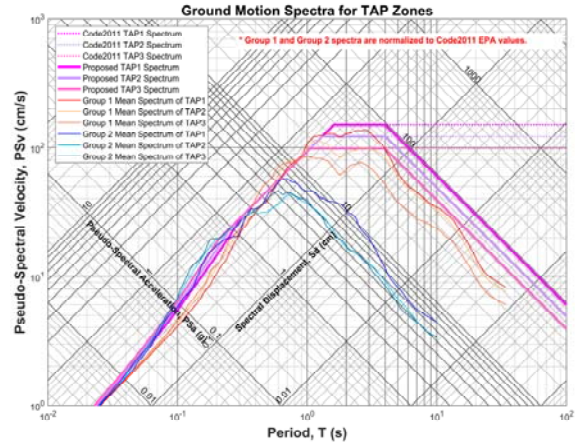


Fig. 2 Three target design spectra for Taipei Basin sites (thick solid lines).

Ground Motion Selection Approach

In accordance with the above-mentioned ten target design spectra, TBC regulations, and application limits of target design spectra at long period ranges, we propose the following methodology for recorded ground motion selection (after Liu et al., 2020):

1. The recorded response spectrum is presented as the geometric mean of both horizontal spectra, which is the basis for spectral amplitude scaling and spectral shape goodness-of-fit testing of horizontal components. S_a is computed at 50 points, which are uniformly spaced over the log period scale from 0.01 s to 10 s.
2. The period range for the spectral shape goodness-of-fit estimation is 0.03 s to 3 s for general sites; this range avoids celebrated earthquake events (e.g., 921 and 331 severe earthquakes) that dominate selection results and have unrealistic target spectral shapes at long periods. The period range for spectral shape goodness-of-fit estimation is 0.01 s to 8.0 s for Taipei Basin sites; this reflects the actual spectral trends after T_L , including those at long period ranges.
3. The ranking method for recorded response spectra uses a scale factor (SF) and mean-squared error (MSE). The calculation process for the rank index is as follows:

(a) Calculate SF_0 from:

$$SF_0 = \exp\left(\frac{\sum_i^N [\ln(Sa_{target}(T_i)) - \ln(Sa_{record}(T_i))]}{N}\right) \quad (1)$$

where T_i is the i^{th} spectral period in a specified range, N is the total number of points of the specified periods, Sa_{target} is the target S_a , and Sa_{record} is the recorded S_a , which is defined as the geometric mean spectrum of both horizontal components.

(b) Calculate MSE_0 from:

$$MSE_0 = \frac{\sum_{i=1}^N \left[\ln(Sa_{target}(T_i)) - \ln(Sa_{record}(T_i) \times SF_0) \right]^2}{N} \quad (2)$$

(c) Calculate SF_m for reference scaling from:

$$SF_m = \begin{cases} SF_0 \times (0.9/RTR_{min}), & RTR_{min} < 0.9 \\ SF_0, & RTR_{min} \geq 0.9 \end{cases} \quad (3)$$

where $RTR_{min} = \min(Sa_{record}(T_i) \times SF_0 / Sa_{target}(T_i))$

is the minimum record-to-target ratio in a specified spectral period range.

(d) Calculate MSE_m for rank index from:

$$MSE_m = \frac{\sum_{i=1}^N \left[\ln(Sa_{target}(T_i)) - \ln(Sa_{record}(T_i) \times SF_m) \right]^2}{N} \quad (4)$$

MSE_0 or MSE_m denote fitness index. The lower the MSE, the more similar the shapes between target and scaled recorded spectra. MSE_m is larger than MSE_0 because of the criteria restricting recorded spectra from falling more than 10 percent below the target spectrum at any one period. In addition, SF_0 or SF_m denote scaling index, which can be applied to scale the amplitude for both horizontal components of the accelerograms. The scaled recorded spectrum may present a certain design level and conforms to the TBC requirements. In general, lower MSE and SF values are preferable in practice.

Taiwan Recorded Ground Motion Database

The earthquake data used in this study are from the Taiwan Strong Motion Instrumentation Program (TSMIP) operated by the Central Weather Bureau (CWB) from January 1991 to June 2018. In accordance with the above ten target design spectra, ground motion selection approach, and data sources, Figure 3 shows the complete procedure and statistics for the construction of the Taiwan recorded ground motion database for structural response history analysis.

The purpose for recorded ground motion candidate selection is to set adequately relaxed restrictions and then collect as many records as possible. Regarding the strong-motion station criteria, for general sites, the V_{s30} level decreases while T_0 rises and the division points of the V_{s30} range are 270, 360, and 520 m/s. For Taipei Basin sites, the range of selected stations is extended to the group with next lowest T_0 .

Each dataset corresponding to each group of target spectra contains the first 30 recorded ground motions with the smallest MSE_0 . The number of earthquake events decreases with increasing T_0 , which means that in Taiwan, few earthquake events with large magnitudes inducing long energy periods occurred. The number of stations in each group is greater than 24, which is sufficiently large to cover the range for strong-motion station distributions. In addition, the statistics for the MSE_0 range are within 0.038 for general sites and 0.079 for Taipei Basin sites, which are less than the

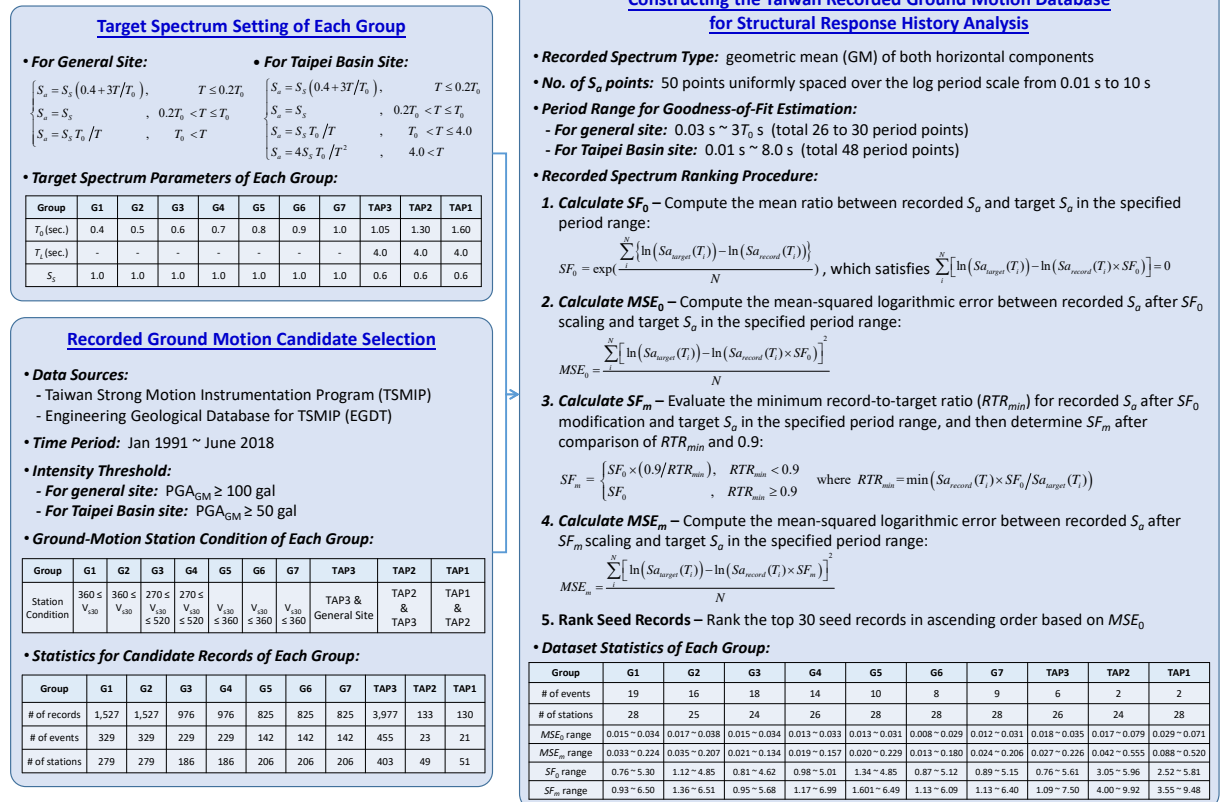


Fig. 3 Procedure and statistics for construction of the Taiwan recorded ground motion database for structural response history analysis.

0.164 required in the New Zealand structural design standard (NZS 1170.5:2004-A1, 2016). This comparison shows that the database developed in this study is appropriate for practical applications. Figure 4 presents scaled recorded spectra for the smallest MSE_0 compared with corresponding target spectra for group G4 (general site; $T_0 = 0.7$ s) and group TAP2 (Taipei Basin site; $T_0 = 1.05$ s).

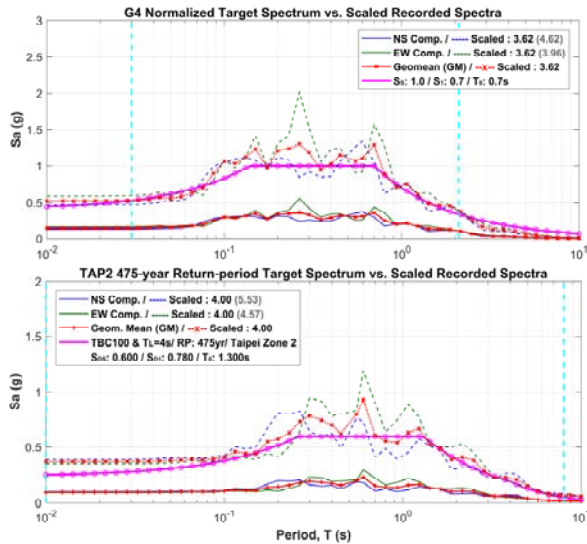


Fig. 4 Scaled and non-scaled recorded spectra of the smallest MSE_0 for group G4 (top plot) and group TAP2 (bottom plot).

Key parameters are classified into four categories listed in the metafile of each dataset in the Taiwan recorded ground motion database:

1. *Seismic Source*: earthquake time (UTC), epicentral coordinates (WGS-84), moment magnitude, focal depth, epicentral distance, and hypocentral distance.
2. *Strong-Motion Station*: station code, station coordinates (WGS-84), V_{330} value, located seismic zone, component, and CWB record filename.
3. *Rank Parameter*: SF_0 , MSE_0 , SF_m , and MSE_m .
4. *Ground Motion* (after baseline correction): PGA (A), PGV (V), PGD (D), V/A , AD/V^2 , cumulative absolute velocity (CAV), strong-motion durations (5%–75% and 95% Arias intensity), record length, and S_a at 50 specified periods.

Conclusions and Suggestions

This study describes the construction of the Taiwan recorded ground motion database, which contains seven datasets for general sites and three datasets for Taipei Basin sites. Each dataset includes 30 recorded time histories and information related to spectral fitness and scale factors (SFs), seismic source, strong-motion stations, and ground motion intensity. This database provides a useful reference for selecting input motions during practical response history analysis. We suggest the following for bidirectional dynamic analysis when utilizing this database:

1. Each record listed in the metafile contains both horizontal components, and its geometric mean has its own rank parameter. The SF in these parameters offers a reference for generating uni- or bi-directional input excitations. It is appropriate to use one SF from the geometric mean for bidirectional input excitations.
2. The criterion for better spectral fitness is an MSE less than 0.045 estimated from empirical observations. In practice, however, this could be relaxed to be less than 0.164, in accordance with the New Zealand standards. An SF less than 5.0, is recommended and an SF larger than 7.0 is regarded as inadequate.
3. When selecting multiple ground motions, all earthquake events should be unique and should consider a minimum of three ground motions. In addition, each earthquake event should not exceed two records when considering a minimum of seven or eleven ground motions. The SF determination for multiple ground motions can be compared with the k_1 – k_2 approach outlined in New Zealand standards.
4. Structures with a longer predominant period (T_p) should be examined more carefully. If 1.5 times T_p exceeds the applicable limits ($3T_0$ or 8.0 s), the suitability of the specific spectral shape should be specially confirmed. It is worth noting that the SFs listed in the database for general sites are calculated via normalized target spectra with generic application purposes; these SFs should therefore be corrected depending on the actual demands.

References

- CPAMI, (2011). “Seismic Design Code for Buildings in Taiwan”, Construction and Planning Agency, Ministry of the Interior, Taiwan. (In Chinese)
- Hsun-Jen Liu, Wen-Yu Jean, and Yu-Wen Chang, (2020). “A Study on Recorded Ground Motion Selection for Generic Sites in Taiwan”, *15NCSE*, paper no. 143, Tainan, Taiwan. (In Chinese)
- NCREE, (2019). “Recommended Provisions for Seismic Design Code for Buildings in Taiwan”, <https://www.ncree.narl.org.tw/service/codeworking>, prepared for CPAMI. (In Chinese)
- NZS 1170.5:2004-A1, (2016). “Structural Design Actions - Part 5: Earthquake Actions - New Zealand”, *Standards New Zealand*, Wellington, New Zealand.
- Wen-Yu Jean, (2020). “Proceedings of Seismic Design Specifications and Commentary of Building, 2020 - Recommended Provisions for Site Amplification Coefficients”, 2020 NCREE Technical Report, NCREE-20-015. (In Chinese)
- Wen-Yu Jean, Hsun-Jen Liu, Chih-Wei Chang, and Yu-Wen Chang, (2020). “A Study on the Design Basis Earthquake for Taipei Basin”, *15NCSE*, paper no. 104, Tainan, Taiwan. (In Chinese)

Evaluation of DIP with CLSM Backfill under Truck Loading for the Water Pipeline System

Hsuan-Chih Yang¹, Che-Yu Chang², Gee-Yu Liu³, Pao-Ching Chou⁴

楊炫智¹、張哲瑜²、劉季宇³、周寶卿⁴

Abstract

In the design of buried water pipelines, most of the pipes are buried more than one meter deep due to roadway usage. However, besides water pipelines, telecommunication cable systems and other utility systems are also located underground, especially in densely populated urban areas. Such occupation leads to burying newly constructed water pipelines in deeper or shallower locations. Nowadays, controlled low-strength material (CLSM) is used as backfill to enhance the capacity of shallow buried water pipelines. The performance of CLSM as a backfill material cannot be easily assessed empirically. Therefore, this study analyzed ductile iron pipe (DIP), which is commonly used in water pipeline systems, with CLSM backfill under the impact of truck loading. Five different sizes of DIP were evaluated at four different buried depths. The effect of CLSM strength was also discussed. Analyses were conducted with the finite element software LS-DYNA. The results of this study could provide a reference for designing shallow buried DIP systems for future engineering projects.

Keyword: Ductile iron pipe (DIP), controlled low-strength materials (CLSM), numerical simulation, truck loading analysis

1. Introduction

There has been a long history of using cast iron pipe for water pipeline systems. Through the development of technology and industry, other materials have become available, such as steel pipe (SP), stainless steel pipe (SSP), polyvinyl chloride (PVC) pipe, polyethylene (PE) pipe, and high-density polyethylene (HDPE) pipe. However, the strength, toughness, and ductility of cast iron pipe have also improved over time. In addition, the connections of cast iron piping have been designed to be earthquake resistant. Therefore, ductile iron pipe (DIP) is still the primary choice of material for water pipeline systems worldwide, especially in Taiwan.

Due to the dense population in Taiwan, utilities, including telecommunications, gas, and water, have become underground systems. Newly constructed systems therefore need to be placed either at deeper or shallower levels. Considering the higher cost of burying pipelines deeper, a shallower placement might be preferable. To overcome the safety concerns of shallowly buried pipelines, controlled low-strength material (CLSM) has been used as backfill material in

Japan and Taiwan. Besides its higher strength compared to soil, its ease of removal also makes it a desirable backfill material. However, the impact of using CLSM on DIP performance still requires further study.

We conducted numerical simulations with finite element models to analyze five different sizes of DIP with two kinds of CLSM with different strengths as backfill. The five different DIP sizes include those with the nominal diameters of 100 mm, 300 mm, 500 mm, 1000 mm, and 2600 mm. The analyses summarize and discuss the performance of DIP under truck loading with a 20 cm, 50 cm, 80 cm, and 110 cm depth of cover.

2. Parameters of the Numerical Model

The numerical modeling in this study was conducted using the finite element program called LS-DYNA. The model is based on current designs from the Taiwan water power company with a DIP length of 6 m. The DIP and model dimensions are shown in Table 1 and the layout is illustrated in Figure 1.

The interaction and behavior of the DIP, CLSM, and soil were evaluated. DIP was modeled using shell

¹ Associate Research Fellow, National Center for Research on Earthquake Engineering

² Assistant Research Fellow, National Center for Research on Earthquake Engineering

³ Research Fellow, National Center for Research on Earthquake Engineering

⁴ Assistant Research Fellow, National Center for Research on Earthquake Engineering

elements, while the backfill CLSM and the surrounding soil were modeled with solid elements.

The DIP performance under truck loading was analyzed with elastic linear material properties, shown in Table 2. The ultimate DIP strength in this study was 420 MPa.

Considering the connectivity of the DIP in the longitudinal direction (Z-direction), a longitudinal translation constraint was applied on the Z-plane of the model, which leads to a symmetric layout. On the transverse direction, only vertical (Y-direction) movement was allowed. The bottom of the model had constraints in all directions.

Table 1. Dimensions of the numerical model

Nominal diameter	Thickness	Backfill width	Model width	Depth below DIP	Depth of cover
2600	26.55	3600	25200	10800	
1000	11.7	1700	11900	5100	200
500	7	1000	7000	3000	500
300	5.5	700	4900	2100	800
100	5	500	3500	1500	1100

Units: mm

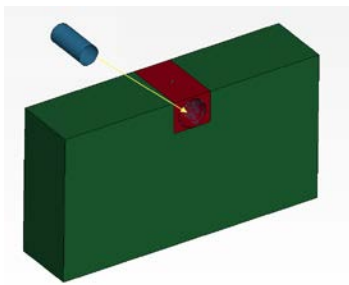


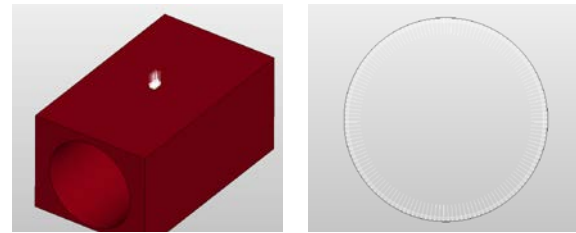
Figure 1. Illustrative scheme of the numerical model with 2600 mm diameter DIP

Table 2. Material properties of the numerical model

Material	Density (ton/mm ³)	Young's modulus (N/mm ²)	Poisson's ratio
DIP	7.15e-9	1.6e5	0.28
CLSM	1.8e-9	8.7e2	0.25
	1.8e-9	2.0e2	0.25
Soil	1.8e-9	20	0.3

Truck loading was modeled by a uniform load of 10 tons applied over an area of 30 cm by 20 cm, which represents the area of contact between the tire and the ground. The DIP centerline was located right underneath the loading area. In addition, a hydrostatic pressure of 0.75 MPa and a hydrodynamic pressure of 0.5 MPa with a total of about 1.3 MPa are also considered in this study. The water pressure was applied on the inner surface of the DIP. Figure 2 shows the loading scheme.

Based on the DIP design guidelines from DIPRA (Ductile Iron Pipe Research Association), a strength safety factor of at least 2 is required. Therefore, in this study, a DIP stress less than 210 MPa was allowed.



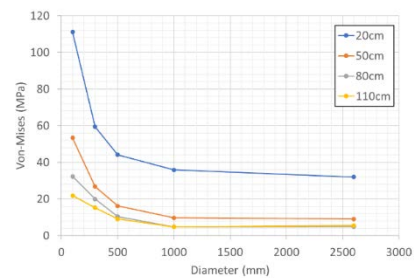
(a) 10 ton truck load (b) Water pressure on the inner surface of DIP

Figure 2. Illustrated loading scheme

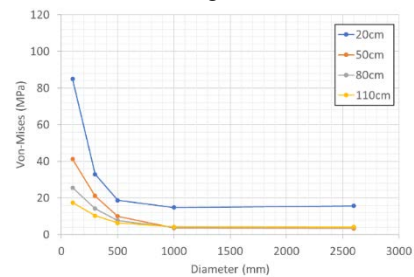
3. Analysis and Results

i. Without water pressure

Figure 3 shows the von Mises stress for various diameters of DIP with varying depths of cover under truck loading without water pressure. When the Young's modulus of CLSM is lower, the DIP stress is higher. Additional attention is thus required when using CLSM with a lower Young's modulus. In terms of the sensitivity to diameter, the DIP von Mises stress decreases while the diameter increases from 100 mm to 1000 mm. For diameters larger than 1000 mm, the DIP von Mises stress is not sensitive to diameter and performance is similar with the same depth of cover.



(a) CLSM with a Young's modulus of 200 MPa

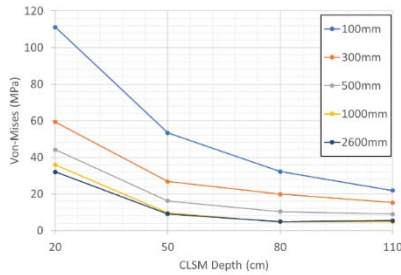


(b) CLSM with a Young's modulus of 870 MPa

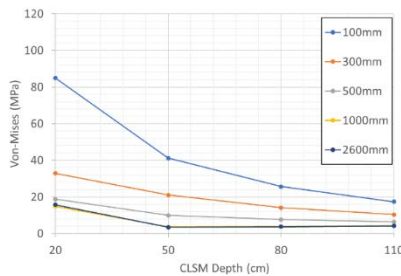
Figure 3. The von Mises stress for various diameters of DIP without water pressure

Figure 4 shows the effect of the depth of cover on the DIP von Mises stress. When the depth of cover is over 50 cm, DIP with diameters of 1000 mm and 2600 mm perform similarly. The difference between these two sizes with a depth of cover of 20 cm is also minor. This phenomenon echoes the one presented in Figure 3. In summary, DIP performance is similar under truck loading without water pressure when the depth of cover is deeper than 80 cm and the DIP diameter is larger than 500 mm. Comparing Figure 4(a) and 4(b), CLSM with a lower Young's modulus results in a larger difference in DIP von Mises stress between different depths of

cover. The CLSM strength affects the sensitivity of DIP performance to the depth of cover.



(a) CLSM with a Young's modulus of 200 MPa



(b) CLSM with a Young's modulus of 870 MPa

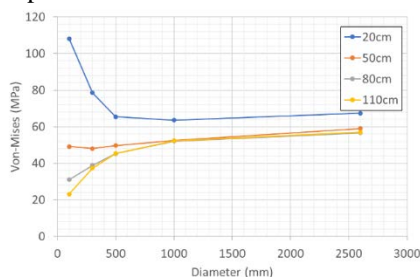
Figure 4. The DIP von Mises stress with varying depths of cover without water pressure.

ii. With water pressure

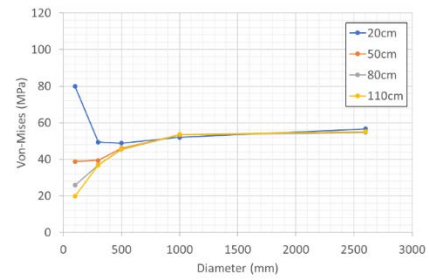
Figures 5 and 6 show the von Mises stress for DIP of various diameters and varying depths of cover under truck loading with the effect of water pressure. When the CLSM Young's modulus is lower, the DIP stress is higher, which is similar to what was observed without water pressure.

With the effect of water pressure, the DIP von Mises stress increases when its diameter increases and the depth of cover is 50 cm. When the depth of cover is deeper than 50 cm, the DIP stress trend goes in the opposite direction compared to the trend without water pressure. With a depth of cover of 20 cm, the DIP stress is similar with and without the effect of water pressure. Water pressure thus controls DIP with diameters larger than 300 mm, especially for those larger than 1000 mm, while truck loading controls DIP with a diameter of 100 mm.

Figure 6 shows that when the CLSM Young's modulus is 200 MPa, the DIP von Mises stress is not sensitive to the depth of cover when the DIP diameter is larger than 800 mm and the depth of cover is over 80 cm. In the case of a CLSM Young's modulus of 870 MPa, the DIP von Mises stress is not sensitive to depth of cover when the DIP diameter is larger than 300 mm and the depth of cover is over 50 cm.

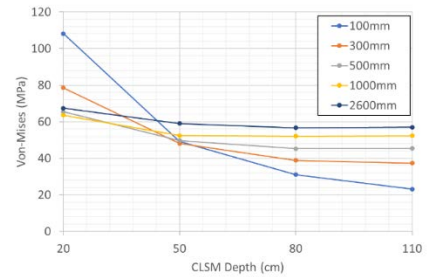


(a) CLSM with a Young's modulus of 200 MPa

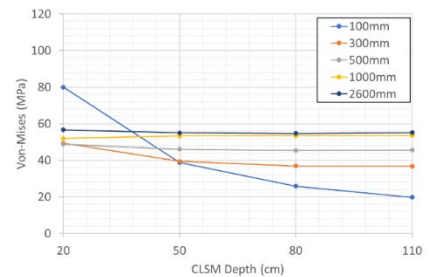


CLSM with a Young's modulus of 870 MPa

Figure 5. The von Mises stress for various diameters of DIP with water pressure



(a) CLSM with a Young's modulus of 200 MPa



(b) CLSM with a Young's modulus of 870 MPa

Figure 6. The DIP von Mises stress with varying depths of cover with water pressure

4. Conclusions and Future Directions

This study analyzed DIP with CLSM backfill of different Young's moduli under truck loading. Our findings are as follows:

Although using CLSM as backfill provides a higher strength compared with soil, attention is still necessary when lower strength CLSM is used, which causes an increase in DIP stress.

When using DIP with small diameters, the stress from truck loading is sensitive to the depth of cover. The water pressure effect shows its significance in this study and requires further observation and analysis in future research.

References

1. 中國國家標準規範·CNS10808 G3219 延性鑄鐵管·2019。
2. 台灣自來水股份有限公司，自來水管埋設工程施工說明書，2020。
3. Duc-Hien Le, "Engineering properties and strength prediction of soil-based controlled low-strength materials", National Kaohsiung university of applied sciences, doctoral dissertation, 2014.
4. DIRPA (Ductile Iron Pipe Research Association), 2016. Design of Ductile Iron Pipe.



NAR Labs

National Center for Research on Earthquake Engineering

No. 200, Sec. 3, Xinhai Rd., Taipei 106219, Taiwan(R.O.C.)

Tel: +886-2-6630-0888 Fax: +886-2-6630-0858

<http://www.ncree.org.tw>

